E85-10069 STAR (H22)

NASA Conference Publication 2355

Landsat-4 Science Characterization Early Results

Volume III—Thematic Mapper (TM), Part 2

(E85-10069 NASA-CP-2355-Vol-3-Pt-2)
LANDSAT-4 SCIENCE CHARACTERIZATION EARLY
RESULTS. VOLUME 3, PART 2: THEMATIC MAPPER
(TM) (NASA) 591 p HC A25/MF A01 CSCL 08B
N85-21724
THRU
N85-21746
Unclas
G3/43 00069

*Proceedings of the Landsat-4 Science Characterization
Early Results Symposium, February 22-24, 1983
held at NASA Goddard Space Flight Center
Greenbelt, Maryland*

NASA

NASA Conference Publication 2355

Landsat-4 Science Characterization Early Results

Volume III—Thematic Mapper (TM), Part 2

John L. Barker, *Editor*
NASA Goddard Space Flight Center
Greenbelt, Maryland

Proceedings of the Landsat-4 Science Characterization
Early Results Symposium, February 22–24, 1983
held at NASA Goddard Space Flight Center
Greenbelt, Maryland

Original photography may be purchased
from EROS Data Center
Sioux Falls, SD 57198

NASA
National Aeronautics
and Space Administration

Scientific and Technical
Information Branch

1985

LANDSAT-4 SCIENCE CHARACTERIZATION EARLY RESULTS

CONTENTS

Volume I: MULTISPECTRAL SCANNER

Page

FOREWORD iii

SUMMARY OF MSS CHARACTERIZATION INVESTIGATIONS
William L. Alford and Marc L. Imhoff
NASA/Goddard Space Flight Center I-1

RADIOMETRIC ACCURACY ASSESSMENT OF LANDSAT-4 MULTISPECTRAL SCANNER DATA
William L. Alford and Marc L. Imhoff
NASA/Goddard Space Flight Center I-9

SPECTRAL CHARACTERIZATION OF THE LANDSAT-4 MSS SENSORS
Brian L. Markham and John L. Barker
NASA/Goddard Space Flight Center I-23

INVESTIGATION OF RADIOMETRIC PROPERTIES OF LANDSAT-4 MSS
Daniel P. Rice and William A. Malila
Environmental Research Institute of Michigan I-57

RADIOMETRIC CALIBRATION AND GEOCODED PRECISION PROCESSING OF LANDSAT-4 MULTISPECTRAL SCANNER PRODUCTS BY THE CANADA CENTRE FOR REMOTE SENSING
J. Murphy, D. Bennett and F. Guertin
Canada Centre for Remote Sensing I-77

LANDSAT SCENE-TO-SCENE REGISTRATION ACCURACY ASSESSMENT
James E. Anderson
NASA/National Space Technology Laboratories I-119

GEOMETRIC ACCURACY OF LANDSAT-4 MSS IMAGE DATA
R. Welch and E. Lynn Usery
University of Georgia I-123

GEODETIC ACCURACY OF LANDSAT-4 MULTISPECTRAL SCANNER AND THEMATIC MAPPER DATA
J. M. Thormodsgard and D. J. DeVries
U.S. Geological Survey, EROS Data Center I-133

GEOMETRIC ACCURACY ASSESSMENT OF LANDSAT-4 MULTISPECTRAL SCANNER (MSS) DATA
Marc L. Imhoff and William L. Alford
NASA/Goddard Space Flight Center I-143

IMPACT OF LANDSAT MSS SENSOR DIFFERENCES ON CHANGE DETECTION ANALYSIS
William C. Likens and Robert C. Wrigley
NASA/Ames Research Center I-159

PRECEDING PAGE BLANK NOT FILMED

CONTENTS (Continued)

Page

LANDSAT-4 MSS GEOMETRIC CORRECTION: METHODS AND RESULTS
J. Brooks, E. Kimmer and J. Su
General Electric Company I-177

INDEX OF AUTHORS I-201

Volume II: THEMATIC MAPPER

INTRODUCTION TO THEMATIC MAPPER INVESTIGATIONS
John L. Barker and Brian L. Markham
NASA/Goddard Space Flight Center II-1

AN OVERVIEW OF LANDSAT-4 AND THE THEMATIC MAPPER
James R. Irons
NASA/Goddard Space Flight Center II-15

RADIOMETRIC CALIBRATION AND PROCESSING PROCEDURE FOR REFLECTIVE BANDS ON LANDSAT-4 PROTOFLIGHT THEMATIC MAPPER
John L. Barker
NASA/Goddard Space Flight Center

R. B. Abrams, D. L. Ball and K. C. Leung
Computer Sciences Corporation II-47

AN OVERVIEW OF THE THEMATIC MAPPER GEOMETRIC CORRECTION SYSTEM
Eric P. Beyer
General Electric Company II-87

TM DIGITAL IMAGE PRODUCTS FOR APPLICATIONS
John L. Barker
NASA/Goddard Space Flight Center

Fred J. Gunther, Rochelle B. Abrams and Dave Ball
Computer Sciences Corporation II-147

CANADIAN PLANS FOR THEMATIC MAPPER DATA
W. M. Strome, F. E. Guertin, A. B. Collins and D. G. Goodenough
Canada Centre for Remote Sensing II-221

SPECTRAL CHARACTERIZATION OF THE LANDSAT THEMATIC MAPPER SENSORS
Brian L. Markham and John L. Barker
NASA/Goddard Space Flight Center II-235

PRELAUNCH ABSOLUTE RADIOMETRIC CALIBRATION OF THE REFLECTIVE BANDS ON THE LANDSAT-4 PROTOFLIGHT THEMATIC MAPPER
John L. Barker
NASA/Goddard Space Flight Center

D. L. Ball and K. C. Leung
Computer Sciences Corporation

J. A. Walker
Santa Barbara Research Center II-277

CONTENTS (Continued)

Page

CHARACTERIZATION OF RADIOMETRIC CALIBRATION OF LANDSAT-4 THEMATIC MAPPER REFLECTIVE BANDS
John L. Barker
NASA/Goddard Space Flight Center

R. B. Abrams, D. L. Ball and K. C. Leung
Computer Sciences Corporation II-373

INDEX OF AUTHORS II-475

VOLUME III: THEMATIC MAPPER (Continued)

RELATIVE RADIOMETRIC CALIBRATION OF LANDSAT TM REFLECTIVE BANDS
John L. Barker
NASA/Goddard Space Flight Center . . . . III-1 ✓

EVALUATION OF THE RADIOMETRIC INTEGRITY OF LANDSAT-4 THEMATIC MAPPER BAND 6 DATA
John R. Schott
Rochester Institute of Technology . . . . III-221 ✓

THERMAL BAND CHARACTERIZATION OF THE LANDSAT-4 THEMATIC MAPPER
Jack C. Lansing
Santa Barbara Research Center

John L. Barker
NASA/Goddard Space Flight Center . . . . III-233 ✓

A PRELIMINARY ASSESSMENT OF LANDSAT-4 THEMATIC MAPPER DATA
D. G. Goodenough, E. A. Fleming and K. Dickinson
Department of Energy, Mines and Resources, Canada . . . . III-257 ✓

PRELIMINARY EVALUATION OF THE RADIOMETRIC CALIBRATION OF LANDSAT-4 THEMATIC MAPPER DATA BY THE CANADA CENTRE FOR REMOTE SENSING
J. Murphy, W. Park and A. Fitzgerald
Canada Centre for Remote Sensing . . . . III-275 ✓

A PRELIMINARY ANALYSIS OF LANDSAT-4 THEMATIC MAPPER RADIOMETRIC PERFORMANCE
C. Justice and L. Fusco
European Space Agency/EPO, Frascati, Italy

W. Mehl
Commission of the European Communities/JRC, Ispra, Italy . . . . III-309 ✓

EVALUATION OF THE RADIOMETRIC QUALITY OF THE TM DATA USING CLUSTERING, LINEAR TRANSFORMATIONS AND MULTISPECTRAL DISTANCE MEASURES
L. A. Bartolucci, M. E. Dean and P. E. Anuta
Purdue University . . . . III-321 ✓

CONTENTS (Continued)

Page

TM GEOMETRIC PERFORMANCE: LINE-TO-LINE DISPLACEMENT ANALYSIS (LLDA)
L. Fusco
European Space Agency/EPO, Frascati, Italy

W. Mehl
Commission of the European Communities/JRC, Ispra, Italy . . . . III-359 ✓

IN-PROGRESS ABSOLUTE RADIOMETRIC INFLIGHT CALIBRATION OF THE LANDSAT-4 SENSORS
R. G. Holm, K. R. Castle, C. J. Kastner, J. M. Palmer and P. N. Slater
University of Arizona

M. Dinguirard
Centre d'Etudes et de Recherches de Toulouse

C. E. Ezra and R. D. Jackson
USDA/Agricultural Research Service

R. Savage
Atmospheric Sciences Laboratory, White Sands Missile Range . . . . III-389 ✓

LANDSAT-4 THEMATIC MAPPER CALIBRATION AND ATMOSPHERIC CORRECTION
Warren A. Hovis
NOAA/National Environmental Satellite, Data, and Information Service . . . . III-411 ✓

SCAN ANGLE AND DETECTOR EFFECTS IN THEMATIC MAPPER RADIOMETRY
Michael D. Metzler and William A. Malila
Environmental Research Institute of Michigan . . . . III-421 ✓

THEMATIC MAPPER SPECTRAL DIMENSIONALITY AND DATA STRUCTURE
E. P. Crist and R. C. Cicone
Environmental Research Institute of Michigan . . . . III-443 ✓

MTF ANALYSIS OF LANDSAT-4 THEMATIC MAPPER
Robert Schowengerdt
University of Arizona . . . . III-467 ✓

INTRABAND RADIOMETRIC PERFORMANCE OF THE LANDSAT-4 THEMATIC MAPPER
Hugh H. Kieffer, Eric M. Eliason and Pat S. Chavez, Jr.
U.S. Geological Survey . . . . III-471 ✓

A PRELIMINARY EVALUATION OF LANDSAT-4 THEMATIC MAPPER DATA FOR THEIR GEOMETRIC AND RADIOMETRIC ACCURACIES
M. H. Podwysocki, N. Falcone, L. U. Bender and O. D. Jones
U.S. Geological Survey . . . . III-497 ✓

THE USE OF LINEAR FEATURE DETECTION TO INVESTIGATE THEMATIC MAPPER DATA PERFORMANCE AND PROCESSING
Charlotte M. Gurney
Systems and Applied Sciences Corporation . . . . III-513 ✓

CONTENTS (Continued)

Page

SPATIAL RESOLUTION ESTIMATION OF LANDSAT-4 THEMATIC MAPPER DATA
Clare D. McGillem, Paul E. Anuta and Erick Malaret
Purdue University . . . . III-527 ✓

AN ANALYSIS OF THE HIGH FREQUENCY VIBRATIONS IN EARLY THEMATIC MAPPER SCENES
John Kogut and Eliane Larduinat
Research and Data Systems, Inc. . . . . III-537 ✓

ASSESSMENT OF THEMATIC MAPPER BAND-TO-BAND REGISTRATION BY THE BLOCK CORRELATION METHOD
Don H. Card and Robert C. Wrigley
NASA/Ames Research Center

Frederick C. Mertz and Jeff R. Hall
Technicolor Government Services, Inc. . . . . III-553 ✓

TESTS OF LOW-FREQUENCY GEOMETRIC DISTORTIONS IN LANDSAT-4 IMAGES
R. M. Batson and W. T. Borgeson
U.S. Geological Survey . . . . III-565 ✓

INVESTIGATION OF TM BAND-TO-BAND REGISTRATION USING THE JSC REGISTRATION PROCESSOR
S. S. Yao and M. L. Amis
Lockheed Engineering and Management Service Company, Inc. . . . . III-571 ✓

GEODETIC ACCURACY OF LANDSAT-4 MULTISPECTRAL SCANNER AND THEMATIC MAPPER DATA
J. M. Thormodsgard and D. J. DeVries
U.S. Geological Survey, EROS Data Center III-581

INDEX OF AUTHORS III-591

Volume IV: APPLICATIONS

OVERVIEW OF TM "APPLICATIONS" RESEARCH REPORTS
Darrel L. Williams
NASA/Goddard Space Flight Center IV-1

IMPACT OF THEMATIC MAPPER SENSOR CHARACTERISTICS ON CLASSIFICATION ACCURACY
Darrel L. Williams, James R. Irons, Brian L. Markham, Ross F. Nelson and David L. Toll
NASA/Goddard Space Flight Center

Richard S. Latty
University of Maryland

Mark L. Stauffer
Computer Sciences Corporation IV-7

CONTENTS (Continued)

Page

ANALYSIS AND EVALUATION OF THE LANDSAT-4 MSS AND TM SENSORS AND GROUND DATA PROCESSING SYSTEMS -- EARLY RESULTS
Ralph Bernstein and Jeffrey B. Lotspiech
IBM Palo Alto Scientific Center IV-25

CHARACTERIZATION OF LANDSAT-4 TM AND MSS IMAGE QUALITY FOR THE INTERPRETATION OF CALIFORNIA'S AGRICULTURAL RESOURCES
Stephen D. DeGloria and Robert N. Colwell
University of California, Berkeley IV-91

EVALUATION OF THEMATIC MAPPER PERFORMANCE AS APPLIED TO HYDROCARBON EXPLORATION
John R. Everett, Charles Sheffield and Jon Dykstra
Earth Satellite Corporation IV-119

GEOLOGIC UTILITY OF LANDSAT-4 TM DATA
Michael Abrams, Anne Kahle, Alan Gillespie, James Conel and Harold Lang
Jet Propulsion Laboratory IV-127

AN INITIAL ANALYSIS OF LANDSAT-4 THEMATIC MAPPER DATA FOR THE DISCRIMINATION OF AGRICULTURAL, FORESTED WETLANDS, AND URBAN LAND COVERS
Dale A. Quattrochi
NASA/National Space Technology Laboratories IV-131

PRELIMINARY EVALUATION OF THEMATIC MAPPER IMAGE DATA QUALITY
R. B. MacDonald, F. G. Hall, D. E. Pitts and R. M. Bizzell
NASA/Johnson Space Center

S. Yao, C. Sorensen, E. Reyna and J. Carnes
Lockheed Engineering and Management Services Company, Inc. IV-153

ASSESSMENT OF COMPUTER-BASED GEOLOGIC MAPPING OF ROCK UNITS IN THE LANDSAT-4 SCENE OF NORTHERN DEATH VALLEY, CALIFORNIA
Nicholas M. Short
NASA/Goddard Space Flight Center IV-163

A CONCEPT FOR THE PROCESSING AND DISPLAY OF THEMATIC MAPPER DATA
Rupert Haydn
University of Munich IV-217

QUICK LOOK ANALYSIS OF TM DATA OF THE WASHINGTON, D.C. AREA
Darrel L. Williams, James R. Irons, Brian L. Markham, Ross F. Nelson and David L. Toll
NASA/Goddard Space Flight Center

Richard S. Latty
University of Maryland

Mark L. Stauffer
Computer Sciences Corporation IV-237

CONTENTS (Continued)

Page

REMOTE SENSING OF COASTAL WETLANDS BIOMASS USING THEMATIC MAPPER WAVEBANDS
Michael A. Hardisky and Vytautas Klemas
University of Delaware IV-251

A PRELIMINARY COMPARISON OF THE INFORMATION CONTENT OF DATA FROM THE LANDSAT-4 THEMATIC MAPPER AND MULTISPECTRAL SCANNER
John C. Price
USDA/Agricultural Research Service Hydrology Laboratory IV-271

EARLY RESULTS OF INVESTIGATIONS OF LANDSAT-4 THEMATIC MAPPER AND MULTISPECTRAL SCANNER APPLICATIONS
F. G. Sadowski, J. A. Sturdevant, W. H. Anderson, P. M. Seevers, J. W. Feuquay, L. K. Balick and F. A. Waltz
Technicolor Government Services, Inc.

D. T. Lauer
U.S. Geological Survey, EROS Data Center IV-281

THEMATIC MAPPER DATA QUALITY AND PERFORMANCE ASSESSMENT IN RENEWABLE RESOURCES/AGRICULTURE/REMOTE SENSING
R. M. Bizzell and H. L. Prior
NASA/Johnson Space Center IV-299

PRELIMINARY COMPARISONS OF THE INFORMATION CONTENT AND UTILITY OF TM VERSUS MSS DATA
Brian L. Markham
NASA/Goddard Space Flight Center IV-313

ASSESSING LANDSAT TM AND MSS DATA FOR DETECTING SUBMERGED PLANT COMMUNITIES
Steven G. Ackleson and Vytautas Klemas
University of Delaware IV-325

A FIRST EVALUATION OF LANDSAT TM DATA TO MONITOR SUSPENDED SEDIMENTS IN LAKES
F. R. Schiebe, J. C. Ritchie and G. O. Boatwright
USDA/Agricultural Research Service IV-337

SNOW REFLECTANCE FROM THEMATIC MAPPER
Jeff Dozier
University of California, Santa Barbara IV-349

PRELIMINARY EVALUATION OF TM FOR SOILS INFORMATION
David R. Thompson, Keith E. Henderson, A. Glen Houston and David E. Pitts
NASA/Johnson Space Center IV-359

CONTENTS (Continued)

Page

THE USE OF THEMATIC MAPPER DATA FOR LAND COVER DISCRIMINATION - PRELIMINARY RESULTS FROM THE UK SATMAP PROGRAMME
M. J. Jackson and J. R. Baker
Natural Environment Research Council, UK

J. R. G. Townshend, J. E. Gayler and J. R. Hardy
Reading University, UK IV-369

PRELIMINARY STUDY OF INFORMATION EXTRACTION OF LANDSAT TM DATA FOR A SUBURBAN/REGIONAL TEST SITE
David L. Toll
NASA/Goddard Space Flight Center IV-387

COMPARATIVE TECHNIQUES USED TO EVALUATE THEMATIC MAPPER DATA FOR LAND COVER CLASSIFICATION IN LOGAN COUNTY, WEST VIRGINIA
J. O. Brumfield
Marshall University

R. G. Witt and H. W. Blodget
NASA/Goddard Space Flight Center

R. F. Marcell
Computer Sciences Corporation IV-403

COMPARISON OF MSS AND TM DATA FOR LANDCOVER CLASSIFICATION IN THE CHESAPEAKE BAY AREA - A PRELIMINARY REPORT
P. J. Mulligan and J. C. Gervin
NASA/Goddard Space Flight Center

Y. C. Lu
Computer Sciences Corporation IV-415

COMPARISON OF LAND COVER INFORMATION FROM LANDSAT MULTISPECTRAL SCANNER (MSS) AND AIRBORNE THEMATIC MAPPER SIMULATOR (TMS) DATA FOR HYDROLOGIC APPLICATIONS
J. C. Gervin
NASA/Goddard Space Flight Center

Y. C. Lu and R. F. Marcell
Computer Sciences Corporation IV-421

RELATIVE ACCURACY ASSESSMENT OF LANDSAT-4 MSS AND TM DATA FOR LEVEL I LAND COVER INVENTORY
E. M. Middleton and R. G. Witt
NASA/Goddard Space Flight Center

Y. C. Lu and R. S. Sekhon
Computer Sciences Corporation IV-431

INDEX OF AUTHORS IV-447

N85-21725

RELATIVE RADIOMETRIC CALIBRATION OF LANDSAT TM REFLECTIVE BANDS

John L. Barker

LANDSAT ASSOCIATE PROJECT SCIENTIST

EARTH RESOURCES BRANCH, CODE 923

NATIONAL AERONAUTICS AND SPACE ADMINISTRATION

GODDARD SPACE FLIGHT CENTER

GREENBELT, MARYLAND 20771

(301) 344-8978

(Revised 26 April 1984)

FOREWORD

This paper presents results and recommendations pertaining to the characterization of the relative radiometric calibration of the protoflight Thematic Mapper (TM/PF) sensor. TM/PF is the primary experiment on the Landsat-4 satellite, launched on July 16, 1982. Some preliminary pre-launch and in-orbit results are also included from the flight model (TM/F) on Landsat-5, which was launched on March 1, 1984. The goals of this paper are:

- Outline a common scientific methodology and terminology for characterizing the radiometry of both TM sensors
- Report on the magnitude of the most significant sources of radiometric variability
- Recommend methods for achieving the exceptional potential inherent in the radiometric precision and accuracy of the TM sensors.

The radiometric characteristics of TM digital imagery that are important for scientific interpretation include mean values of absolute and relative calibration constants, and estimates of the uncertainty in the relative and absolute post-calibration radiances. Mean values and uncertainties in the pre-launch absolute radiometric calibration are discussed elsewhere (Barker, Ball, et al., 1984). This paper focuses on characterizing variability and uncertainty of TM relative radiometry, including total variability as well as its systematic and random components. Emphasis is placed on identifying the magnitude and types of systematic error, since these have the potential for being reduced during ground processing. Estimates of innate random variability, such as the standard deviation or a signal of its signal-to-noise ratio, are also important since they place limits on the inferences that can be drawn from single and multiple pixel radiances. However, accurate estimates of random error require the prior removal of all types of systematic variability.

While the recommendations contain ideas from many people, including scientific investigators on NASA's team for characterizing the quality of the imagery from the sensors on Landsat-4 and Landsat-5, they are the creation and sole responsibility of the author. These recommendations have not been approved by either the Landsat Science Office or the Landsat Project. Evaluation, and possible implementation, of the recommendations will pose significant difficulties both during the research period before the transition of the TM Image Processing System (TIPS) from NASA to NOAA near the end of 1984, and afterwards, during the operational period.

TABLE OF CONTENTS

Section 1 - Introduction. III-9

1.1 Radiometric Characterization III-10
1.2 Post-Calibration Dynamic Range III-11
1.3 Sources of Radiometric Variability III-11
1.4 Research Objectives III-13
1.5 TM Radiometric Calibration III-14
1.6 Approach to Radiometric Characterization III-16

Section 2 - Between-Scene Changes in TM/PF Gain . . . III-19

Section 3 - Between-Band Changes in TM/PF Gain. . . . III-26

Section 4 - Within-Scene Variability in TM Radiometry. III-31

4.1 Bin-Radiance Dependence. III-32
4.2 Within-Line Droop. III-35
4.3 Bright-Target Saturation III-37
4.4 Coherent Noise III-43
4.5 Scan-Correlated Shifts III-48
4.6 Forward/Reverse-Scan Differences III-55
4.7 Total Noise. III-57
4.8 Within-Scene Error Models. III-57
4.9 Summary of Within-Scene Variability III-65

Section 5 - Processing Effects on Radiometry. III-76

5.1 Calibration with Internal Calibrator III-76

5.1.1 Background Calculation. III-77
5.1.2 Pulse Window Locations. III-79
5.1.3 Pulse Integration Parameters. III-80
5.1.4 Pulse Averaging Parameters. III-83
5.1.5 Regression Strategy III-86
5.1.6 Within-Scene Smoothing. III-87
5.1.7 Within-Path Smoothing III-88
5.1.8 Between-Date Smoothing. III-89

5.2 Image Calibration. III-89

5.2.1 Histogram Equalization. III-89
5.2.2 Replacement of Channels III-92
5.2.3 Post-Calibration Dynamic Range. III-94
5.2.4 Unbiased Pixel Calibration. III-95
5.2.5 Geometric Resampling. III-96

TABLE OF CONTENTS (Cont'd)

Section 5 (Cont'd)

5.3 Radiance-To-Reflectance Conversion III-98

- 5.3.1 Irradiance Normalization. III-98
- 5.3.2 Atmospheric Peeling III-99

5.4 Information Extraction III-103

- 5.4.1 Spectrometry. III-105
- 5.4.2 Radiometry. III-108
- 5.4.3 Geometry. III-109

Section 6 - Recommendations III-111

6.1 Engineering Characterization III-111

- 6.1.1 Absolute Radiometric Calibration. . . . III-111
- 6.1.2 Relative Radiometric Calibration. . . . III-112
- 6.1.3 Modeling of Systematic Variabilities. . III-113
- 6.1.4 TM Sensor Report. III-114

6.2 Flight Segment Operations. III-115

- 6.2.1 Changes in Operational Procedures . . . III-115
- 6.2.2 In-Orbit Calibration Tests. III-117
- 6.2.3 In-Orbit Characterization Tests III-117
- 6.2.4 In-Orbit Scientific Mission Tests . . . III-118

6.3 TIPS Ground Processing III-120

- 6.3.1 Radiometric Calibration Parameters. . . III-121
- 6.3.2 IC Systematic Radiometric Corrections . III-122
- 6.3.3 Histograms Equalization III-125
- 6.3.4 Geometric Processing. III-128
- 6.3.5 Three-Sectioned Post-Calibration Dynamic Range III-129
- 6.3.6 Image Calibration III-130
- 6.3.7 Products. III-130
- 6.3.8 Research and Development. III-134

6.4 Contingency Experiments. III-135

- 6.4.1 Scientific Experiments. III-135
- 6.4.2 Engineering Experiments III-135

Section 7 - Acknowledgments III-137

TABLE OF CONTENTS (Cont'd)

Section 8 - Selected Bibliography III-139

Section 9 - Appendices. III-144

9.1 TIPS Post-Calibration Dynamic Range. III-144
9.2 Integrating Sphere Spectral Radiances. III-147
9.3 TM/F Gains III-148
9.4 TM/F Offsets III-149
9.5 TM/PF Apparant Gain Change With Time III-150
9.6 Landsat-4 Images Processed by TRAPP. III-157
9.7 TM/PF Plots of "Shifted" Background Versus Scan III-159
9.8 TM/PF Tables of Scan-Correlated Shifts III-167
9.9 TM/PF Plots of Shutter background Versus Scan III-174
9.10 TM/F Plots of "Shifted" Background Versus Scan. III-187
9.11 TM/F Tables of Scan-Correlated Shifts. III-196
9.12 Shutter Backgrounds. III-203
9.13 Recommendations. III-209
9.14 Key Words. III-215

LIST OF ILLUSTRATIONS

Figure

2-1 Apparent Change in IC-Determined PFP Gain (Gain with time for Band 4 on Landsat-4 TM/PF, as an example of monotonic decrease for the four bands on the Primary Focal Plane (PFP)) III-20
2-2 Apparent Change in IC-Determined SWIR Gain (Gain with time for Band 5 on Landsat-4 TM/PF, as an example of cyclic pattern of two SWIR bands on the Cold Focal Plane (CFP)). III-21
4-1 In-Orbit Landsat-4 TM/PF Frequency Histogram (Number of pixels as a function of DN value, before and after normalization for bin-radiance dependence based on pre-launch measurements of bin size). III-34
4-2 Bright-Target Saturation Effects on Background III-42
5-1 Landsat-4 and -5 Calibration-Pulse and Light Leak III-81
5-2 Parametric Study on Landsat-4 TM/PF Calibration-Pulse Integration Width. . . . III-84
5-3 Parametric Study of Landsat-5 TM/F Calibration-Pulse Integration Width. . . . III-85

LIST OF TABLES

Table

1-1 Post Calibration Dynamic Range (TIPS processings after 15 January 1984) III-12
1-2 Illustration of an 8-Window General Purpose Collect (GPC) on a BRU Tape used during ambient atmospheric prelaunch tests on Landsat-5 TM/F) These particular minor frame (mf) locations were taken for "droop" tests with the scanning mechanism locked III-18

LIST OF TABLES (Cont'd)

Table

3-1 Apparent Percentage Changes in Band-Averaged Gain (for four times relative to time of absolute radiometric calibration for six reflective bands on Landsat-4 TM/PF). The four times are the expected postlaunch value from a pre-launch test in thermal vacuum (TV), the actual first calibration after launch (INIT), and highest (MAX) and lowest (MIN) values observed in space, i.e., the range of change (MAX-MIN). This range is an indication of a possible uncertainty of 3 to 9% in the absolute radionetric calibration of TM/PF reflective bands. III-27

4-1 32 KHz Coherent Noise (every 3.2 pixels), measured by peak-to-peak amplitude in DN from midscan digital data for 96 reflective channels on Landsat-4 TM/PF (ID 40037-16033, 22 AUG 82, Memphis, TN) III-44

4-2 In-Orbit Coherent Noise at Frequency 3.17 Pixels White Sands (3 January 83) . . III-46

4-3 In-Orbit Coherent Noise at Frequency 17.6 pixels White Sands (3 January 83) . . III-47

4-4 Between-Channel Linear Correlation Coefficients, before and after making corrections for scan-correlated shifts in Landsat TM sensor, illustrating with two channels the fact that "if a shift is present in one channel, it is present in all channels of that band." III-53

4-5 TM Radiometric Reference Channels. III-54

4-6 Apparent rms Noise in Background Data for Landsat-4 TM/PF III-58

4-7 Apparent rms Noise in Image Data for Landsat-4 TM/PF III-58

4-8 Definition of Size of Uncertainty in TM Radiometry III-64

LIST OF TABLES (Cont'd)

Table

4-9 Within-Scene Variability TM Shutter Background in "Quiet" Scenes III-66
4-10 Within-Scene Variability TM Shutter Background in Cloudy Scene III-67
4-11 Band 1 on Landsat-4 TM/PF, Within-Scene Variability (IN DN). III-68
4-12 Band 2 on Landsat-4 TM/PF, Within-Scene Variability (IN DN). III-69
4-13 Band 3 on Landsat-4 TM/PF, Within-Scene Variability (IN DN). III-70
4-14 Band 4 on Landsat-4 TM/PF, Within-Scene Variability (IN DN). III-71
4-15 Band 5 on Landsat-4 TM/PF, Within-Scene Variability (IN DN). III-72
4-16 Band 7 on Landsat-4 TM/PF, Within-Scene Variability (IN DN). III-73
4-17 Landsat-5 TM/F Within-Scene Variability (IN DN). III-74
4-18 TM Radiometric Variability (IN DN) III-75
5-1 Thematic Mapper Tasseled Cap Transformation Coefficients from In-Orbit Data (Crist and Cicone, 1984) III-107

SECTION 1 - INTRODUCTION

The Landsat system for observing the land areas of the surface of the Earth is composed of three elements: 1) the spacecraft with the sensors; 2) the ground-processing facilities and the image-processing software of that facility; and 3) the image distribution facility in Sioux Falls, South Dakota. This paper characterizes some of the radiometric aspects of the first two.

The first three Landsat spacecraft were modified meteorological satellites, carrying "old-reliable" return-beam vidicon television sensors and "experimental" multispectral scanner (MSS) imaging radiometers. In this configuration, they provided images of the surface of the Earth that have received wide use in atlases (Short, et al., 1976; Sheffield, 1981) and research (Colwell, 1983; Williams and Carter, 1976).

The last two Landsat spacecraft contain instrument packages mounted on the Multimission Modular Spacecraft (MMS), which can be retrieved using the shuttle transportation system (STS) (Salomonson and Park, 1979). The Multispectral Scanner (MSS) provides data continuity with previous Landsat satellites (Engel et al., 1983). Thematic Mapper (TM) is a new experimental system which is being evaluated as a possible replacement for MSS-type systems (Engel, 1980).

The TM, which was the principal experiment on Landsat-4, was intended to be a second-generation land-scanning radiometer. Since launch on July 16, 1982, the protoflight (PF) instrument on Landsat-4 has provided about 6000 scenes of northern North America through X-band direct-readout ground facilities located at Goddard Space Flight Center, Greenbelt, MD, and at Prince Albert, Canada. Additional images have been acquired through indirect satellite communication networks and by other X-band ground stations.

Images from the TM/PF sensor have met or exceeded expectations, and are "... of excellent quality as examined in image or CCT /computer readable/ form. Besides the excellent geometric qualities of the data, the spatial, spectral, and radiometric qualities of the TM data represent a capability substantially advanced over that provided by the MSS" (Salomonson and Mannheimer, 1983).

The TM sensor is designed to provide increased spectral, radiometric, and geometric performance (Engel et al., 1983). The primary improvement of the TM over MSS is in spatial resolution (Salomonson and Park, 1979). Each TM pixel represents a 30m by 30m area on the ground, instead of the 80m by 80m instanteous field-of-view for MSS. A second major improvement is in new and more precisely located spectral bands. Finally, TM has higher radiometric resolution, namely 8-bit precision as compared to 6-bit for MSS. These improvements are expected to provide many new and improved capabilities (Salomonson and Park, 1979), including:

- Mapping of coastal water areas to water depths of 20-40 meters
- Differentiation between soil and vegetation
- Biomass surveys
- Differentiation between coniferous and deciduous vegetation
- Differentiation between plant species
- Differentiation between clouds and snow cover
- Discrimination of hydrothermal alteration zones in rock units
- Studies of plant heat stress and rock-unit thermal characteristics.

Preliminary evaluation indicate that TM image products have "... spectral and spatial detail clearly surpassing that provided by ... MSS" (Salomonson and Koffler, 1983).

1.1 RADIOMETRIC CHARACTERIZATION

The radiometric characteristics of TM digital imagery that are important for scientific interpretation include mean values of absolute and relative calibration constants, and estimates of the uncertainty in the relative and absolute post-calibration radiances. Mean values and uncertainities in the pre-launch absolute radiometric calibration are discussed elsewhere (Barker, Ball et al., 1984). This paper focuses on characterizing variability and uncertainty of TM relative radiometry, including total variability, as well as both the systematic and random components. Emphasis is placed on identifying the magnitude and types of systematic error, since these have the potential for being reduced during ground processing. Estimates of innate random variability, such as the standard deviation of a signal or its signal-to-noise ratio, are also important since they place limits on the inferences that can be drawn from single and multiple pixel radiances. However, accurate estimates of random error require the prior removal of all types of systematic variability.

1.2 POST-CALIBRATION DYNAMIC RANGE

Pre-launch absolute radiometric calibration of the reflective bands on TM-Flight instrument (TM/F) were used to identify the pre-calibration range of sensitivity for each of these channels (Appendixes 9.3 and 9.4). These results were combined with similar pre-launch calibration ranges of sensitivity for TM/PF (Barker, Ball, et al., 1984), to provide a common post-calibration dynamic range for any TM imagery processed after 15 January 1984 on the TM Image Processing System (TIPS) (Appendix 9.1). This post-calibration dynamic range is defined by the minimum spectral radiance, RMIN, and the maximum, RMAX, given in Table 1-1. Equations are also given in Table 1-1 for relating RMIN and RMAX to the post-calibration offset, $O^o(B)$, and gain $G^o(B)$, for all channels in the band, as well as an equation for calculating the absolute spectral radiance, L_λ, from calibrated radiance on a digital image in units of DN (digital number), L_{cal}. RMIN and RMAX values, for the dynamic range after radiometric calibration on TIPS, are expected to be up-dated based on recalibration of the integrating sphere used for absolute calibration and on reduction of certain systematic errors in the raw digital data.

1.3 SOURCES OF RADIOMETRIC VARIABILITY

Radiometric variability in the final TM image can be divided into three components, based on origin:

- Scene variability (the source of potential information)
    - Solar irradiance
    - Atmospheric transmission, absorption and scattering (reflection)
    - Transmission, absorption and reflection (scattering) of the target, including shadows

Table 1-1. Post-Calibration Dynamic Range (TIPS processings after 15 January 1984)

	BAND 1	BAND 2	BAND 3	BAND 4	BAND 5	BAND 7
RMIN[a] AT $L_{cal} = 0$ DN	−0.15	−0.28	−0.12	−0.15	−0.037	−0.015
RMAX[b] AT $L_{cal} = 255$ DN	15.21	29.68	20.43	20.62	2.719	1.438

[a] $RMIN = \dfrac{-0^{\circ}(B)}{G^{\circ}(B)}$ [b] $RMAX = \dfrac{RANGE - 0^{\circ}(B)}{G^{\circ}(B)}$

$$L_{\lambda} = \frac{L_{cal} - 0^{\circ}(B)}{G^{\circ}(B)} = RMIN + \left[\frac{RMAX - RMIN}{RANGE}\right] L_{cal}$$

- Optical and electrical variability of the sensor
  - Reflected radiance from the TM scanning mirror
  - Radiance from the TM internal calibrator (IC)
- Variability introduced during processing
  - "Active-scan" imagery
  - "End-of-scan" shutter calibration data
  - Housekeeping telemetry

Once the total variability from all non-information sources is characterized, then an evaluation can be made as to the adequacy of the precision for specific requirements. If the sensor has already been placed in orbit, as with TM/PF and TM/F, then only the systematic errors from the sensor and any possible additional errors introduced by data processing can be reduced.

1.4 RESEARCH OBJECTIVES

This paper reports on the results of and recommendations from the scientific characterization of the relative radiometric performance for the "protoflight" Thematic Mapper sensor (TM/PF) carried on the Landsat-4 satellite. Emphasis is placed on the analysis of raw background and calibration data for the six reflective bands. These data consist of the detector responses to the internal calibrator (IC) system and to the surface of a shutter which passes in front of the detectors after each scan. The shutter surface is not illuminated, therefore responses to it are considered "background" data. These unprocessed data are not in products available to users. Specific objectives of this research effort to characterize TM radiometric performance included:

- Monitoring radiometric performance of TM sensor with time (Sections 2 and 3)
- Characterizing sources of within-scene variability and uncertainty in measuring radiance with the TM sensor (Section 4)
- Outlining possible pre-distribution methodologies for optimizing TM radiometric calibration parameters based on required scientific information extraction and on radiometric characteristics of the TM sensor (Section 5)

- Recommending changes in operational or processing procedures as well as areas for further calibration, experimentation, and research (Section 6)

Some results are also reported for the flight model of TM (TM/F) on Landsat-5, which was launched on March 1, 1984.

1.5 TM RADIOMETRIC CALIBRATION

Radiometric pre-processing for de-striping and calibration of TM digital images during both the Scrounge-era (prior to July 1983) and subsequently in the TIPS-era has been based on individually correcting each of the 100 channels by calculating a scene-specific radiometric look-up table (RLUT). This RLUT converts the potential range, L_R, of 256 raw digital numbers (DN) into a new set of 256 calibrated DN values, L_{cal}. Thus,

$$L_{cal} = \frac{L_R - NB_A}{NG_A} \qquad (1\text{-}1)$$

where L_R = raw radiance in DN

NB_A = applied normalized bias in DN; it is usually near zero (Barker, Abrams, et al., 1984b)

NG_A = dimensionless applied normalized gain; it is usually near unity

L_{cal} = radiometrically corrected radiance in DN.

Users of standard TM digital tapes, namely radiometrically corrected and geometrically resampled TM digital imagery from "CCT-PT" tapes, receive values of L_{cal} that can be converted from DN units to units of spectral radiance or in-band radiance using equations given in Table 1-1 (Barker, Ball, et al., 1984). Users of calibrated but unresampled TM digital imagery from "CCT-AT" tapes receive L_{cal} values and also have calibration constants from Equation 1-1, NB_A and NG_A, at the end of each line (Barker, Gunther, et al., 1984).

Procedures for creating these RLUTs are discussed elsewhere (Barker, Abrams, et al., 1984b, p. 27). In brief, the radiometric correction applied to almost all scenes has consisted of two steps:

- Calculation of the change in digital number based upon the on-board IC pulse for each channel

- Histogram equalization of the channels within a band to the mean and standard deviation of a subsampled set of the scene data in the band.

Normalized change for each channel has been determined from the regression of the measured and averaged IC pulse, $P(\ell,C)$ for each of eight lamp configurations (ℓ), for the reflective channels (C), on "nominal" reference values, $P_n(\ell,C)$, calculated to bring all channels in a single band, B, into a common dynamic radiance range from RMIN(B) to RMAX(B) (Barker, Abrams, et al., 1984b, p. 24):

$$\bar{P}(\ell,C) = NB_{IC}(C) + NG_{IC}(C) * P_n(\ell,C) \qquad (1\text{-}2)$$

where $NB_{IC}(C)$ = IC-measured normalized bias for channel C in DN

$NG_{IC}(C)$ = IC-measured normalized gain for channel C (dimensionless)

The absolute radiometric sensitivity of the sensor can be given by a least square fitting:

$$\bar{P}(\ell,C) = O(C) + G(C) * L^{o}_{\lambda,s,t,f}(\ell,C) \qquad (1\text{-}3)$$

where $O(C)$ = apparent offset in DN

$G(C)$ = apparent gain in DN per $mWcm^{-2}ster^{-1}\mu m^{-1}$

$L^{o}_{\lambda,s,t,f}(\ell, C)$ = reference spectral radiance of channel C in units of $mWcm^{-2}ster^{-1}\mu m^{-1}$ for lamp state ℓ based on three calibrations:

test s: sphere calibration
test t: channel calibration of TM
test f: IC calibration

$\bar{P}(\ell,C)$ = observed average IC pulse in DN of channel C for lamp state ℓ.

The above assumes constant "effective" spectral radiance, $L^{o}_{\lambda}(\ell,C)$, from the three IC lamps. The absolute radiometric accuracy of the $L^{o}_{\lambda}(\ell,C)$ values which determine the TM dynamic range is specified to be within 10 percent of the full scale value of DN = 255 (Engel, 1980). Sections 2 and 3 of this paper summarize the average change in gain, for each band, $\overline{G}(B)$, with time since launch. This paper identifies sources and estimates the variability or uncertainty associated with measuring this radiance; i.e., the precision of the measurements. Assuming that the calibration measured in Equation 1-2, and applied in Equation 1-1, is correct, then the radiometrically calibrated digital data for every pixel in Band B, L_{cal}, can be converted to absolute spectral radiance, L_λ, by:

$$L_\lambda = \frac{L_{cal} - O^o(B)}{G^o(B)} \qquad (1\text{-}4)$$

where L_{cal} = calibrated radiance in DN
$O^o(B)$ = common offset for all channels in band B in DN
$G^o(B)$ = common gain for all channels in band B in DN per $mWcm^{-2}ster^{-1}\mu m^{-1}$
L_λ = spectral radiance in $mWcm^{-2}ster^{-1}\mu m^{-1}$

and values for $O^o(B)$ and $G^o(B)$ are determined in the absolute calibration experiments for TM/PF on Landsat-4 (Barker, Ball, et al., 1984).

A few of the absolute radiometric calibration numbers for TM/F on Landsat-5 are given in the appendices. The data in the appendices include: TIPS post-calibration dynamic range (Appendix 9.1), spectral radiances of twenty-one levels of 48" integrating sphere (Appendix 9.2), pre-launch radiometric gains of reflective channels of TM/F sensor on Landsat-5 (Appendix 9.3), and pre-launch offsets of TM/F for fit of raw midscan radiance versus IS spectral radiance (Appendix 9.4).

1.6 APPROACH TO RADIOMETRIC CHARACTERIZATION

In order to characterize and monitor TM radiometric performance, and to provide for possible changes in ground processing procedures, hundreds of tapes of raw video and calibration data have been and are being collected. These pre-launch and in-orbit tapes for Landsat-4 and -5 form the data base for these studies. Data on these tapes consist of 7400 minor frames (mf) for each scan; a minor frame is one sample of all 100 channels. General purpose collects

(GPC) of approximately 30 seconds each sampled 5 to 8 pre-launch collection windows (Table 1-2). Pre-launch data were stored on computer compatible tapes (CCTs) generated by the "BRU," back-up restore utility, program on the bench test equipment. In addition to the 30-second GPC, a few collects, called "BURST" collects, were also made of all data for the 100 channels from a single forward or reverse scan, consisting of about 7400 mf. During the Scrounge-era, 200 mf of in-orbit calibration data were archived a couple of times a week on "CCT-ADDS" tapes (Anon., 1982). A similar type of raw data, called a "CALDUMP" tape, is being planned for internal engineering evaluation during the TIPS-era.

This paper concentrates on an analysis of raw TM calibration data from prelaunch tests and from in-orbit acquisitions. A library of approximately one thousand pre-launch test tapes, each of which samples the equivalent of a scene, is currently maintained for characterization. About 25-50 percent have been examined. Most of the analyses on these tapes used a software program called TRAPP, TM Radiometric and Algorithmic Performance Program, which requires as input both the raw IC calibration data from the shutter region and the raw uncalibrated TM digital imagery. These raw data are not available to the general public. They are used primarily to characterize the sensor, rather than the performance of the ground processing system, for either the initial "Scrounge-era" prior to July, 1983, or for the current "TIPS-era".

Table 1-2. Illustration of an 8-Window General Purpose Collect (GPC) on a BRU Tape (used during ambient atmospheric prelaunch tests on Landsat-5 TM/F) These particular minor frame (mf) locations were taken for "droop" tests with the scanning mechanism locked

	FORWARD SCAN		REVERSE SCAN	
	START	STOP	START	STOP
TIME	1	5	1	5
VIDEO	3148	3172	3148	3172
LINE END	6315	6330	6315	6330
CAL LAMP	7060	7224	6496	6660
SHUTTER	6468	6492	6748	6776
SHUTTER	6924	6952	7204	7228
VIDEO	8	20	8	20
VIDEO	6200	6212	6200	6212

SECTION 2 - BETWEEN-SCENE CHANGES IN TM/PF GAIN

This section summarizes results on the radiometric stability of TM/PF with time. Multi-date, multi-sensor, and/or multi-band comparisons of digital images require known or constant radiometric characteristics for each image in order to allow conversion from digital brightness counts to relative radiance values measured in energy units. Therefore, intercomparable radiometric performance of a sensor requires that its sensitivity is either constant with time or that the raw radiance range in each channel can be corrected to a constant range of sensitivity within each band, namely its post-calibration dynamic range.

The use of Equation 1-2 to de-stripe individual images assumes that the TM sensor can be radiometrically corrected. One method of testing that assumption is to follow apparent changes with time. This has been done on TM/PF on approximately fifty sets of in-orbit calibration data. In particular, the apparent gain of each channel, G(C), from Equation 1-3, was calculated from the IC pulses for each image. An examination of the gains revealed systematic differences between the eight odd and eight even channels, but no single channel appeared to behave in a unique manner (Barker, Abrams, et al., 1984b, Appendix). Therefore, for convenience in summarizing all the data in a band, the odd and even average values have been averaged to give G(B) for Band B:

$$\overline{G}(B) = \frac{\overline{G}\ (\text{odd channels}) + \overline{G}\ (\text{even channels})}{2} \cdot \qquad (2\text{-}1)$$

Within-band TM radiometric trends can be characterized by plotting $\overline{G}(B)$ as a function of time. Points plotted in Figures 2-1 and 2-2 are representative of the available in-orbit data from Landsat-4. Figures of gain versus time for all six reflective bands on TM/PF are given in Appendix 9.5. Raw digital images, from which TRAPP runs for these plots of gain versus time were made, are listed in Appendix 9.6.

The nearly monotonically decreasing pattern shown in Figure 2-1, from the time of launch through the end of regular data acquisition by direct X-band link in February 1983, is the least noisy of what appear to be similar patterns for all four bands on the primary focal plane (PFP), namely Bands 1-4 (Appendix 9.5). One hypothesis is that this asymptotic drop of 3 to 6 percent in 300 days in

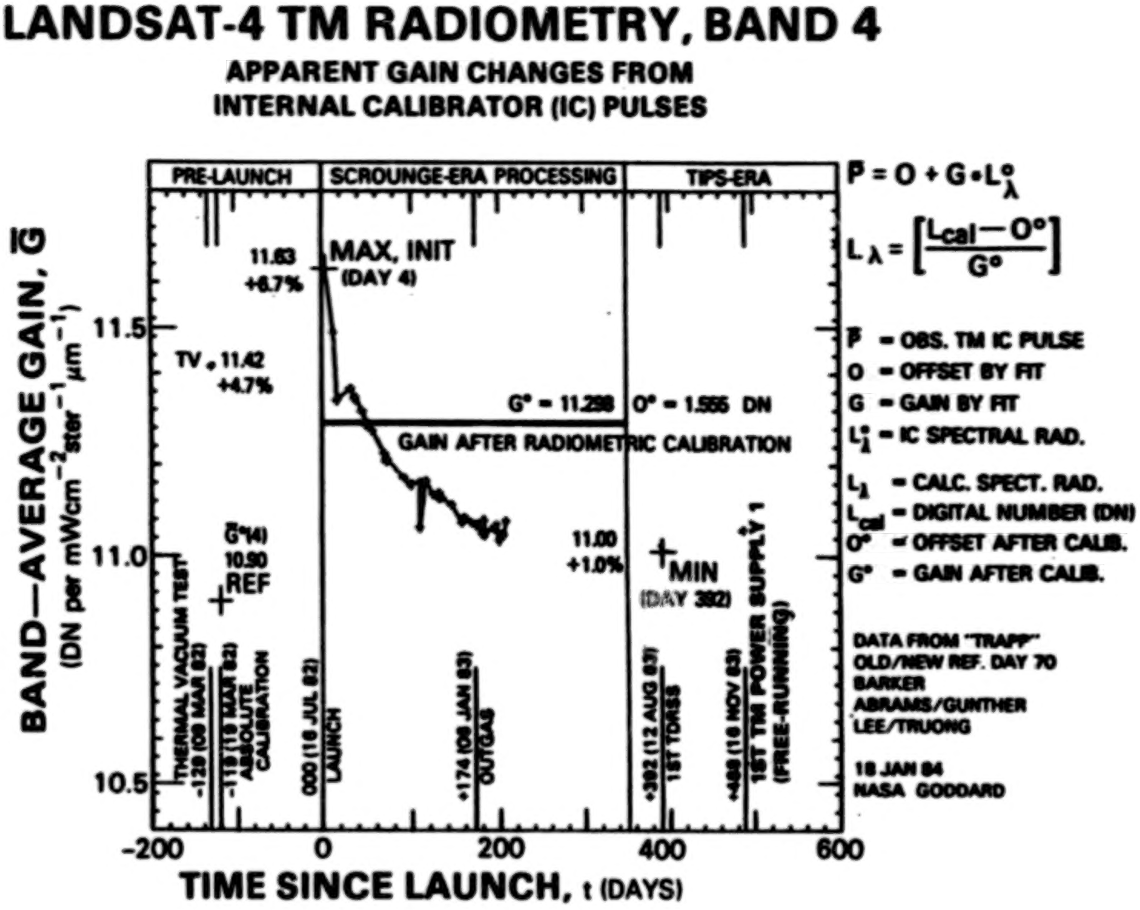

Figure 2-1. Apparent Change in IC-Determined PFP Gain (Gain with time for Band 4 on Landsat-4 TM/PF, as an example of monotonic decrease for the four bands on the Primary Focal Plane (PFP))

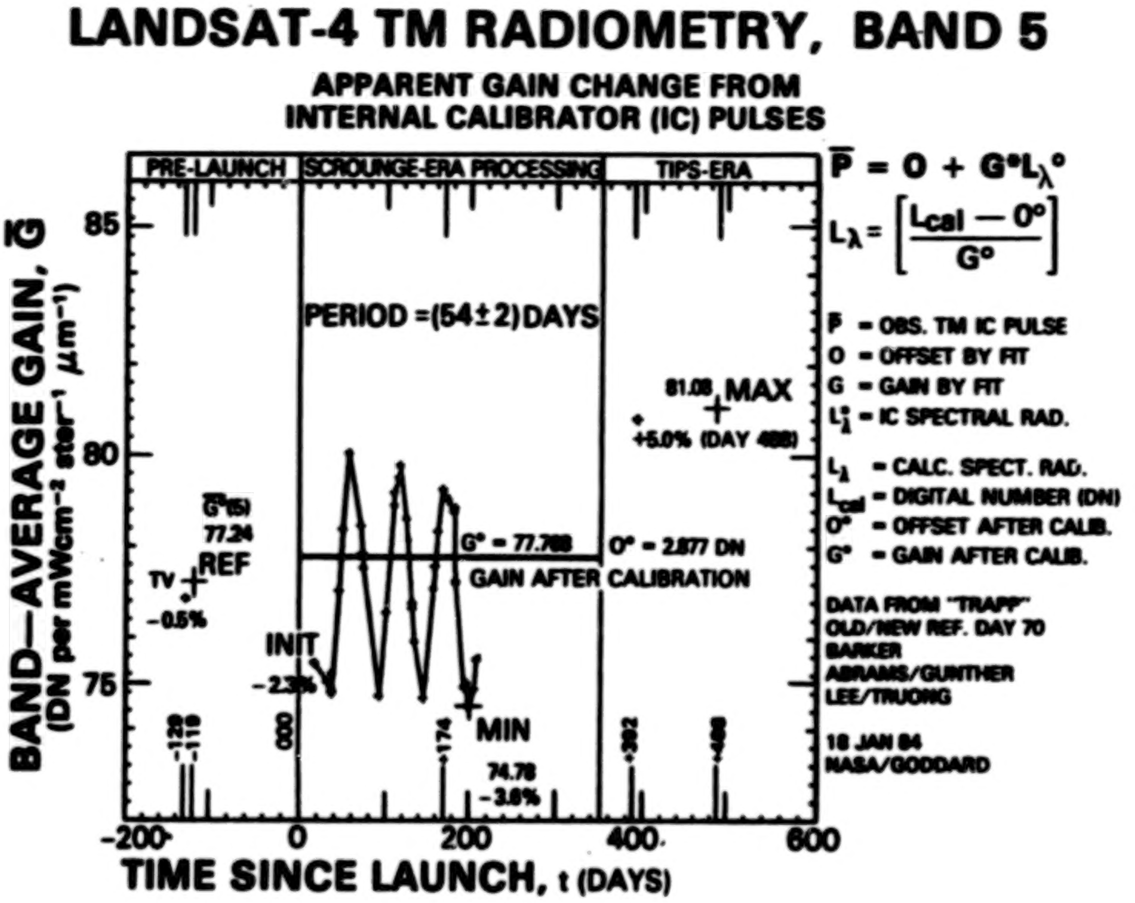

Figure 2-2. Apparent Change in IC-Determined SWIR Gain (Gain With Time for Band 5 on Landsat-4 TM/PF as an Example of Cyclic Pattern of Two SWIR Bands on the Cold Focal Plane (CFP))

orbit is the long-term curve of the "vacuum shift" between IC pulses measured during pre-launch absolute calibration under ambient atmspheric conditions and the IC pulse values observed during pre-launch thermal vacuum testing. This justifies the use of the IC pulses for radiometric calibration of the PFP under the assumption that the "vacuum shift" is due to an optical, physical, or electrical property of the detector and channel itself, rather than to some characteristic of the IC system.

The cyclic pattern in Figure 2-2 is the clearer of the two cyclic patterns for the short-wave infrared (SWIR) bands on the cold focal plane (CFP). Periods for the Band 5 and 7 cycles were estimated at (54 ± 2) and (75 ± 6) days, respectively. These periods are different at the 99 percent level of confidence. Prior to outgassing of the CFP on day 174, the peak-to-peak amplitudes of these cycles were approximately (6.5 ± .5) and (4.0 ± .5) percent for Bands 5 and 7, respectively. For all in-orbit observations, the range of gain changes was about 9 percent for Band 5 and 6 percent for Band 7.

The origin of these cyclic patterns on the CFP is not known. If the cyclic SWIR pattern is due to something independent of the detectors and their electronics, and external to the IC system, there are several possibilities:

- The composite filters over the detectors could be changing; thin film scattering can be both wavelength and thickness dependent

- The CFP itself is moving cyclically relative to the IC beams of light. One problem with this hypothesis is that it would seemingly produce identical periods for the two SWIR bands

- A monotonic, rather than cyclic, change in the opitcal path length inside the "relay optics," i.e., between the PFP and the CFP, might be consistent with the apparent direct relationship of the periods and the wavelengths of the SWIR bands. since the velocity of a wave is equal to its wavelength divided by its period, the observed periods for Bands 5 and 7 both imply a velocity of 11 nm/yr.

- The whole relay optics itself, CFP and all, could be moving at a fixed rate of 11 nm/yr relative to the lens on the shutter and the PFP. This alternative hypothesis is at least possible since the relay optics containing the CFP was designed to be moved in order to bring it into focus with the PFP.

An additional hypothesis is that the amplitude of the cyclic patterns is a function of how close the optics are to the difraction limit, where the amplitude will vary with phase. One test of these hypotheses would be to look for a cyclic pattern in the third band on the CFP, nameliy the Band 6 thermal band, and relate its period to its wavelength and its amplitude to the relative sizes and areas of the detectors on the CFP. Proof of this model for the cyclic pattern of the SWIR band would justify the continued use of the IC to calibrate these bands.

Conversely, the cyclic pattern may arise from a characteristic of the IC system that is unique to Bands 5 and 7. One such possibility is that the silicon photodiodes used to monitor the output of the three IC lamps may not be sensitive to some type of cyclic wavelength-dependence of the output of the three 1900°K lamps or to the energy balance filters used to bring IC radiance into a range commensurate with the sensitivities of each of the six reflective bands. However, it is hard to imagine that these mechanisms for the IC system would produce such pronounced cycles on the SWIR bands and no observable effects on the PFP bands, except, perhaps, in the SWIR filters for the IC.

By process of elimination, the current assumption is that the cyclic patterns are unique characteristics of the detector systems for Bands 5 and 7. This justifies using the IC, as it was designed, to radiometrically correct them. In-orbit intercomparison of sensors and accurate simultaneous measurements of absolute radiance on the ground at White Sands and from TM at minimum and maximum times of these two cycles may provide enough sensitivity to resolve this question of absolute calibration. However, at this time, definitive origins of the monotonically decreasing or cyclic patterns are unknown.

Assuming perfect operation of the IC, all of these slowly varying trends in gain have been corrected out during the calibration of the TM imagery.

On August 22, 1983, the first TM digital imagery was received via the indirect transmission to the Tracking and Data Relay Satellite System (TDRSS) followed by relay to the receiving station at White Sands, New Mexico. All subsequent Landsat-4 TM acquisitions have been, and will be, via the TDRSS. On November 16, 1983, TM power supply 1 was turned on for the first time. Power supply 1 is "free-running," whereas power supply 2 is synchronized with the start of scan. Unlike Landsat-4, both power supplies on Landsat-5 are free-running.

The results of two Landsat-4 "pre-launch" tests for the absolute radiometric calibration are recorded on Figures 2-1, and 2-2, namely an average gain for a test in thermal vacuum (TV) on March 9, 1982 (test f = 9) and for a subsequent test (t = C) under ambient conditions on March 19, 1982 (Barker, Ball, et al., 1984). All data except the absolute reference (REF; $G^o(B)$) gain values of March 19 are referred to an IC reference test on March 20, 1982, called test f = 7, and to a recalibration of the sphere, namely test s = 2, in May 1982. TRAPP analyses that were run using the March 9 IC reference were normalized by band specific factors to the March 20 IC reference.

With the exception of some apparent outliers, the root-mean-square (rms) coefficient of variation for the gain measurements of the band averages, $CV_{\overline{G}(B)}$, as estimated from the range of variability around a smoothly varying curve, is approximately ±.05 percent, for Bands 4 and 5:

$$CV_{\overline{G}(B)} \equiv \frac{\sigma_{\overline{G}(B)}}{\overline{G}(B)} 100 \approx \pm 0.05\% \qquad (2\text{-}2)$$

where $\sigma_{\overline{G}(B)}$ = standard deviation of average gain for band B, namely $\overline{G}(B)$, in units of DN per $mWcm^{-2}ster^{-1}\mu m^{-1}$

$CV_{\overline{G}(B)}$ = coefficient of variation of $\overline{G}(B)$ in %

While the curves of IC-determined gain versus time for each individual channel appear to be even more well defined, the statistical square root of 16 channels indicates that the radiometric predictability of individual channels is at least better than an rms error of 0.2 percent. Therefore, the coefficient of variation is defined as:

$$CV_{G(C)} \equiv \frac{\sigma_{G(C)}}{G(C)} 100 \approx \pm 0.2\% \qquad (2\text{-}3)$$

where $\sigma_{G(C)}$ = standard deviation of G(C)
$CV_{G(C)}$ = coefficient of variation of G(C) in percent.

There were changes in the TRAPP procedures used to calculate the gains and offsets. The smoothly varying patterns in Bands 4 and 5 validate the normalization scheme used in about half of the TRAPP outputs to the level of uncertainty in the curves, namely ±0.05 percent. There is more variation in the other bands (Appendix 9.5). The total noise being lowest in Band 4 on Landsat-4, the other bands would be expected to show greater variability in gain versus time due to the lower precision of the estimation of gain. Alternatively, this greater variability in the gain with time in other bands may indicate that this normalization procedure is not as effective for them. Raw calibration data for these bands could be reprocessed to eliminate the need for this normalization.

The uncertainty in the least-squares calculation of the gain from individual IC pulse averages is greater than the uncertainty observed around the slowly varying patterns. This suggests that future analyses might provide a more quantitative systematic correction for gains and offsets by including trend analysis, or provide alternative radiometric correction procedures that do not show these systematic trends.

Regardless of the origin of this uncertainty, it means that there is the potential for estimating mean values of in-orbit TM radiometry to a precision of ±0.2 percent, at least for channels within Bands 4 and 5.

SECTION 3 - BETWEEN-BAND CHANGES IN TM/PF GAIN

In addition to maintaining scene-to-scene calibration of each band, it is also necessary to maintain band-to-band calibration. Current TIPS procedures do not provide for any between-band correlation of channels. If the IC system has been working as designed, then the radiometric calibration of TM imagery with the IC data will maintain the relative calibration of the channels in each band to ± 0.2 percent (Equation 2-3), and therefore will also maintain the samme precision for band-to-band calibration. If, on the other band, patterns of gain versus time reflect changes in the IC system, then they can be used to estimate the possible absolute error in the radiometrically calibrated TM imagery. Use of IC calibration implies faith in the IC system.

Between-band TM/PF radiometric trends can be characterized from apparent gain changes with time in all six reflective bands (Appendix 9.5). Gains for four specific times are tabulated in Table 3-1 for each band relative to the band-average absolute calibration reference gain, $\overline{G^o}$: (1) TV is the March 9 pre-launch thermal vacuum test; (2) INIT is the initial in-orbit data which occurred on day 4 for PFP bands and day 17 for the CFP bands; (3) MAX is the maximum observed in-orbit gain, which coincides with day 4 initial turn-on for Bands 1-4 and was day 488 for Band 5 and day 392 for Band 7; and (4) MIN is the minimum observed in-orbit gain which occurred on days 392, 200, 200, 392, 200, and 56 for Bands 1-5 and 7, respectively.

Several observations and inferences apply to more than one band and to the radiometric relations between bands:

- IC Temperature-Dependence. The difference between pre-launch gains measured under ambient REF and TV conditions ranged from -1 to +5 percent. While the 6 percent range of differences in gain may be related to the "vacuum shift" of the individual channel responsivity, it is also consistent with a recently-observed temperature-dependence of the IC pulse. Both need to be quantitatively understood to reduce this uncertainty in absolute radiometric calibration of TM digital imagery.

The "IC temperature-dependence" was observed on the PFP bands on Landsat-5 during thermal cycling and is unique for each channel in a band. The dependence can increase or decrease pulse values and appears to be linear with a slope of up to 1 percent per ^{o}C. REF and TV IC shutter

Table 3-1. Apparent Percentage Changes in Band-Averaged Gain (for four times relative to time of absolute radiometric calibration for six reflective bands on Landsat-4 TM/PF). The four times are the expected post-launch value from a pre-launch test in thermal vacuum (TV), the actual first calibration after launch (INIT), and highest (MAX) and lowest (MIN) values observed in-orbit, i.e., the range of change (MAX-MIN). This range is an indication of a possible uncertainty of 3 to 9 percent in the absolute radiometric calibration of the TM/PF reflective bands.

APPARENT CHANGES IN TM/PF GAIN

	RELATIVE CHANGE IN %, $100\left[\frac{\overline{G}-\overline{G^o}}{\overline{G^o}}\right]^*$					
BAND	**1**	**2**	**3**	**4**	**5**	**7**
REF, $\overline{G^o}$	15.78	8.10	10.62	10.90	77.24	147.12
TV (PRE-LAUNCH)	−1.2	−1.0	3.2	4.7	−0.5	−0.5
INIT (IN-ORBIT)	−1.1	−1.0	3.6	6.7	−2.3	−0.8
(INIT-TV)	0.1	0.0	0.5	2.0	−1.8	−0.3
MAX (IN-ORBIT)	−1.1	−1.0	3.6	6.7	5.0	3.3
MIN (IN-ORBIT)	−8.2	−4.5	−2.8	1.0	−3.6	−2.5
MAX-MIN	7.1	3.4	6.5	5.7	8.5	5.8

*GAINS CALCULATED FROM LANDSAT-4 TM/PF INTERNAL CALIBRATION (IC) PULSES, $\overline{P}$, REGRESSED AGAINST IC EFFECTIVE SPECTRAL RADIANCE, L_λ^*:

$$\overline{P} = O + G \cdot L_\lambda^*$$

WHERE O IS FITTED OFFSET AND G IS FITTED GAIN FOR A CHANNEL.

BAND-AVERAGE GAINS, $\overline{G}$, ARE COMPARED TO AN AMBIENT ABSOLUTE CALIBRATION REFERENCE $\overline{G^o}$ OF 19 MARCH 1982, WHERE GAINS ARE IN DN per $mWcm^{-2}\,ster^{-1}\mu m^{-1}$.

BARKER
FEB 84

temperatures were approximately 25°C and 8°C, respectively.

One hypothesis for the origin of the IC temperature-dependence is a thermally induced physical movement of the IC shutter and its seven pencils of light. Higher pulse values for either odd or even channels would be observed if the pencil of light was not completely uniform across the two rows of detectors. This would be especially true if the optimized initial location of the peak radiant intensity was between the odd and even channels. If this hypothesis is true, then regular midscan image data would not be expected to show any temperature-dependence.

The TM/F midscan pulse on Landsat-5 has been observed to be nearly independent of temperature as measured under ambient conditions from the initial turn-on near 20°C to the automatic shutdown at the peak thermal threshold near 30°C. Data are needed under vacuum conditions to characterize possible in-orbit temperature-dependence, especially for the CFP bands for which no pre-launch data were collected. Therefore, it is recommended that TDRSS be used to take in-orbit data over a long duty cycle of Landsat-4 and -5 in order to calibrate the magnitude of the effect and to provide for possible normalization.

- Expected Gains. The difference between pre-launch TV and initial in-orbit (INIT) gains in Table 3-1 ranges from -2 to +2 percent. This is less than half of the -2 to +7 percent range between INIT and the pre-launch ambient REF. In-orbit Landsat-4 digital data have been acquired on a low duty cycle with an IC shutter temperature of 8 to 9°C. Therefore, one hypothesis is that the closer agreement of in-orbit INIT and TV, as compared to INIT and REF gains, is a reflection of at least partial normalization of the "IC temperature-dependence." The residual difference between INIT and TV gains may reflect a combination of measurement error and dependence of "vacuum shift" on length of time in vacuum.

- Vacuum Shift. The first INIT and highest MAX observed in-orbit gains are the same for the four PFP bands (Table 3-1). This would be consistent with an hypothesis of monotonic change in "vacuum shift" with time in vacuum since the maxima are near day 4 and the minima are near day 200 for all four of the PFP bands.

- Thermal Expansion or Contraction. The relative change in gain monotonically increases from band 1 to band 4 for both the MAX and MIN in-orbit observations. This suggests an hypothesis associated with differential thermal expansion of the PFP from its one-sided place of attachment to the bulkhead. The place of attachment is located such that physical expansion of the PFP would move detectors for band 1 the most, and those for band 4 the least. Such a physical expansion would justify the current use of IC data for making radiometric correction, and might suggest a need for using the IC peak location to measure fractional mf movements with time, within the PFP, and between the PFP and CFP. If this expansion exists, it probably does not exceed 0.2 pixels.

Alternative hypotheses implicating the IC system are also possible, such as a different physical expansion or contraction out along the radial arm of the IC shutter. This latter hypothesis seems less likely since an assumption of similar patterns of light for each array suggests that radial movements would produce a related change across all six reflective band optics on the IC shutter; this change is not observed.

- Gain Increase After Outgassing. Band 7, and perhaps Band 5, showed an apparent increase in gain following the turning on of the heaters for about 12 house on the CFP to outgas the thermal band. Measurements of gain were resumed on January 13, 1983, after a period of approximately 26 hours to recool the CFP. An apparent 2 percent increase in gain at 2.2 μm (band 7) would be consistent with the hypothesis that ice on the dewar window for the CFP caused a 30 percent loss in gain for Band 6 at 10 μm after approximately 160 days of operation. Band 7 has the most difficult to interpret patterns and may have band specific dependencies that are as yet unrecognized. Observed maximum values of Band 5 gain at day 392 and 488 are consistent with projected maxima at day 384 and day 492. A possible 2 percent increase in gain in band 5 (1.6 μm) has been estimated.

- Power Supplies. There is no obvious change in any patterns with the first use of the free-running TM power supply on day 488. None were expected, since there is a high degree of regulation on the power supplies.

- Absolute Radiometric Uncertainty. The MAX-MIN range of observed relative in-orbit gain changes for the six reflective bands on Landsat-4 is from 3 to 9 percent. Part of that range is associated with extreme values in Band 1, which are probably not real differences in gain but uncertainties in the measurement. Nevertheless, these extreme limits imply that the uncertainty in the absolute calibration associated with using the IC for radiometric correction is no worse than the range in relative in-orbit gain observed in that particular band. The apparent asymptotic decay of gain with time over the first year inorbit to a nearly constant value for the PFP bands is consistent with the proposed monotonic "vacuum shift" with time. The uncertainty associated with an understanding of these patterns of band-average gain change with time is a measure of the uncertainty in between-band absolute radiometry.

SECTION 4 - WITHIN-SCENE VARIABILITY IN TM RADIOMETRY

If radiometric calibration is done on one scene at a time, as in the case of Scrounge-era and TIPS-era processing, then any sources of systematic variation that occur during the 23 seconds it takes to acquire a scene will remain uncorrected. This section provides an overview of residual uncertainties after radiometrically correcting TM digital imagery. Emphasis is placed on relative errors within a band and within a scene, since between-band and between-scene variability were discussed in the previous sections and current procedures are scene- and band-specific. Even if it were possible to apply radiometric corrections perfectly for mean differences in relative bias and gain for each channel in a band, residual uncertainties, which are associated with the sensor itself, would still produce channel related striping or other patterns of noise in the corrected TM image.

In addition to the uncertainties in radiometric calibration associated with using the sensor's IC over time and with looking at a point source of constant radiance, rather than a full aperture source external to the entire optical path (Section 3), the TM scanning radiometer has the following six types of variability:

- bin-radiance dependence
- Within-line droop
- Bright-target saturation
- coherent noise
- scan-correlated shifts
- forward/reverse-scan differences.

These sources of "noise" range up to 2 DN in value and are channel-dependent. All six of these types of variability are presumably systematic, or slowly varying in nature. They are potential candidates for at least partial, or statistical, removal during ground processing to leave only inherent random noise.

During the process of building the TM sensor, sources of systematic variation or high random noise were removed or brought within specifications by improving the hardware at Santa Barbara Research Center (SBRC) in California. During pre-launch testing and calibration phases, some data were collected for potential future processing, but were not completely analyzed. Subsequent and still partial analyses have revealed several instrumental sources of discontinuous or slowly varying signal changes. Since launch, it has been possible, because of availability of more data under the nearly constant environmental conditions in space, to identify additional types of signal modulation. It is important to characterize the signal modulation because the stability of the TM radiometer and sensitivity of image processing techniques mean that even when scene-specific radiometric correction procedures remove striping between channels down to a few DN, users can display the systematic residual striping by stretching or classifying images.

This section reports on the identification and relative significance of some of these sources of noise. Exact modeling of possible ground processing corrections are in progress. The modeling must precede questions as to whether or not it is feasible to recalibrate the absolute radiometry and incorporate such procedures into the TIPS system, and if so, whether the corrections significantly reduce the errors in value-added products derived from digital imagery. A discussion of the six types of variable noise in TM imagery that are sensor specific and independent of processing procedures is given below.

4.1 BIN-RADIANCE DEPENDENCE

Bin-radiance dependence is a TM noise type associated with error in the analog-to-digital (A/D) converter's bin size and location. This noise can result in any specific DN value being mislocated by up to two levels and varying in size from nearly zero to 2 DN values. The 8-bit A/D converters in both TM/PF and TM/F exhibit this error. While as yet unmodeled for dependence on time and temperature, it has been quantitatively characterized in pre-launch unit-level testing of the multiplexer and A/D converters. Sizes of the unequal bins and sizes of displaced locations are of the same magnitude in all bands since a common design was used for the six A/D converters in a TM sensor. There is an even higher degree of correspondence between the threshold bin voltages of channels within a band because the parallel signals are fed into a track-and-hold storage buffer and serially switched by the multiplexer into the A/D converter for that band. The unequal bin errors, as well as quantization errors, are probably significant sources of variability in the signal-to-noise and absolute radiometric calibration tests. While local variability can be up to two DN values, the full 255 level range of the A/D system is linear to an rms error of ±.4 percent in the slope of raw radiance, L_R, versus known spectral radiance from the integrating sphere, L_{IS}. However, this bin-radiance dependence does result in saw-toothed histograms of raw digital-image data. It has been demonstrated for one channel (Band 1 channel 1 for a Landsat-4 January 3, 1983, scene over White Sands, New Mexico) that normalization for bin size based on pre-launch A/D thresholds can produce a smoother histogram of frequency versus L_R (Figure 4-1). Saw-toothed histograms illustrating bin-radiance dependence have also been noticed on preliminary in-orbit data from Landsat-5 (a 4-band scene over the Atlantic Ocean taken on March 4, 1984) in which local minima corresponded to the narrow size of bins observed in unit-level tests of the A/D converter.

An approximate rms "noise" associated with this systematic A/D bin-radiance dependence is about $\underline{+}0.3$ DN, and is therefore of the same order as the $\underline{+}0.3$ DN noise from digital quantization. It remains to be demonstrated that a time-independent bin-radiance model can be developed that would take raw radiance values, L_R, and replace them with A/D corrected values, $L'_{RA}(C, L_R, t, T)$, which would depend on the channel (C), on time (t) and perhaps on the temperature (T) of the A/D converter for long-duty cycles of TM acquisitions. Such a mean-value correction model for bin-radiance dependence would be most valuable if applied before other types of corrections, or calibrations, and retained in more than 8-bit precision. One form for this correction for each channel would be:

$$L'_{RA} = L_R + CA(L_R) \qquad (4\text{-}1)$$

where $CA(L_R)$ = a function in DN units for making an arithmetic correction for the A/D bin-radiance dependence which is dependent on L_R but independent of t and T, i.e. identical for all occurrences at a given bin number.

L'_{RA} = raw radiance, in DN, which has been corrected for A/D bin-radiance dependence

The apparent correspondence between both pre-launch system-level tests and in-orbit Landsat-5 bin-radiance dependence from histograms, and the pre-launch unit level electronic measurements of the threshold voltage of each bin, suggests that the A/D voltage measurements taken on different dates and at different temperatures will be usable for making corrections for bin-radiance dependence.

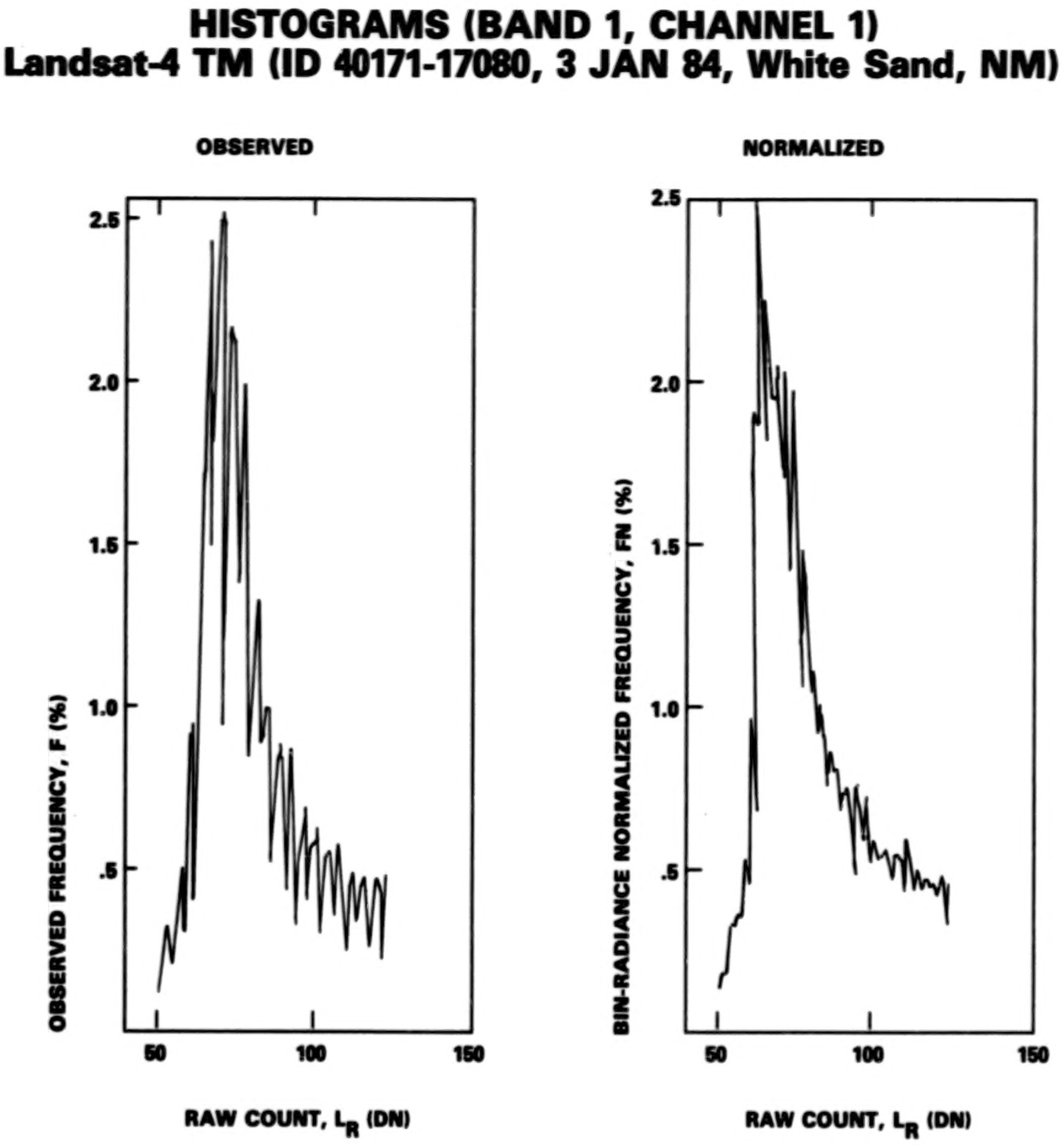

Figure 4-1. In-Orbit Landsat-4 TM/PF Frequency Histogram (Number of Pixels as a function of DN value, before and after normalization for bin-radiance dependence based on pre-launch measurements of bin size)

There are alternative ways to implement this correction, such as:

- Mean value of bin center
- Randomized distribution into bins based on proportion of overlap; this is preferred over the mean value method.

4.2 WITHIN-LINE DROOP

"Droop" is one of three types of "within-line, sample-location dependent noise." Malila et al. (1984) have characterized this noise as a sensor-related scan-angle artifact, partially because of the necessity to remove systematic atmospheric variations from the scene that are scan-angle dependent before observing this residual within-line droop. By comparing forward west-to-east scans to reverse east-to-west scans, a systematic droop of the signal was observed to be about 2 percent, or 1 DN, for Band 1 between the maximum value and the end of active scanning. This was the largest droop for the reflective bands.

The correction model (Malila et al., 1984) for the exponential decay constant required for a 1/e (63 percent decay) was approximately 10 msec, or 1000 samples, based on one Landsat-4 scene. Their model assumed a uniform scan-direction independent exponential decay of the difference, D^{∞}, between the true radiance before droop, L'_{RD} and the apparent radiance after drooping to infinity, L^{∞}_{RD}:

$$D^{\infty} \equiv L'_{RD} - L^{\infty}_{RD} \qquad (4\text{-}2)$$

Within-line "droop" can be positive or negative and is probably dependent on the time, t, or samples after the end of direct current (DC) restoration rather than on the pixels from the west edge of the scan, which was assumed in their model (Malila et al., 1984), and therefore:

$$CD(ADC, S) = D^{\infty} \exp [-KD*ADC] \qquad (4\text{-}3)$$

where ADC = # samples, at sample location S, after end of DC restoration

KD = within-line droop time constant for 1/e (63 percent) decay, in units of reciprocal samples or reciprocal msec. The half-time, $t_{1/2}$, for a drop, or increase, of 50 percent of D^{∞} is:

$$t_{1/2,D} = \frac{\ell n\ 2}{KD}$$

CD (ADC, S) = correction for within-line droop at sample S in DN.

Using nomenclature that is more consistent with this paper, their modified model is:

$$L'_{RD}(S) = \frac{L_R\ (S)}{1 - f_D^{\infty}\ [1 - \exp(-KD*ADC)]} \qquad (4\text{-}4)$$

where f_D^{∞} = fractional decay, or increase, at infinity of an undecayed radiance, L'_{RD}

$L_R(S)$ = observed raw radiance at S in DN

$L'_{RD}(S)$ = raw radiance at S in DN after correction for droop.

The additive correction term for within-line droop, CD (ADC), for each channel in a scan, is computed as follows:

$$L'_{RD}(S) = L_R(S) + CD(ADC,\ S) \qquad (4\text{-}5)$$

where CD(ADC, S) = correction for within-line droop at sample location S, which is ADC samples after DC restoration, in units of DN

$L'_{RD}(S)$ = raw radiance at S, in DN, corrected for within-line droop.

Equation 4-5 is the within-line droop equivalent of the linear correction applied for A/D bin-radiance dependence in Equation 4-1. One of the reasons for expressing corrections in this form is that the combined correction for both of these effects can then be viewed, under an assumption of separability, as the sum of two corrections, $CA(L_R)$ and $CD(ADC,S)$. This linear formulation is also useful in the implementation of corrections to the image.

- Overshoot and Undershoot. Another type of within-line electronic "droop" is called overshoot or undershoot. It is most significant at boundaries between highly contrasted regions and can be as high as tens of DN values if the contrast is high enough. However, this is not expected to pose a problem since the multi-pole electronic filter on each channel is designed to damp the first most excessive swing of this recovery in a fraction of a sample, i.e. in less than 9.6 µsec (microseconds). Overshoot and undershoot were electronically characterized in analog unit-level tests prior to launch and would be hard to locate in digital imagery. There have been no reports of suspected overshoot or undershoot in any TM imagery. The less well characterized within-line droop referred to in Equation 4-3 appears to have a maximum amplitude of a couple of DN, and a time constant KD of the order of hundreds to thousands of samples, i.e. tens of milliseconds.

- Within-Line Droop in TM/F. Preliminary examinations of special pre-launch droop tests on Landsat-5 indicate up to 1.5 DN droop in the PFP bands, with a systematic decrease from the largest effect in Band 4 to the lowest in Band 1. Bands 5, 6 and 7 on TM/F do not seem to show significant within-line droop.

There is a possibility that droop is some form of bright-target saturation or vice versa. An alternative hypothesis is that these effects arise from independent electronic causes, such as droop being associated with the circuity trying to maintain a constant reference voltage and bright-target saturation being a characteristic of detector-type and pre-amplifier electronics.

4.3 BRIGHT-TARGET SATURATION

Bright-target saturation is a second type of "within-line sample-location dependent noise." It is characterized by a memory effect after exposure to a bright target, such as a cloud. The time constant of the hysteresis is such that the effect may last for thousands of samples. There may be two separate physical effects on the detectors, one which has a shorter time constant and decreases the detector sensitivity, and the other, which has a longer time constant and increases the sensitivity.

- Broken-Cloud Saturation Effects. A qualitative observation of the effects of bright-target saturation was first seen by Fischel (1984) on a cloudy TM scene of Terrebonne Bay, LA (ID 40174-16011, 6 JAN 83). Clouds were scattered throughout, but were most prominent in the east and bottom of the scene. The effect was most noticeable as a change in the background observed on the shutter before and after DC restoration, with recovery made more observable by applying a radiometric correction for bias on a line-by-line basis. DN values in alternating sweeps of 16 lines were observed to be lower to the east of bright clouds on forward scans and to the west of bright clouds on reverse scans. After apparent saturation from several kilometers of clouds, there were depressed DN values for about a thousand samples (pixels). At the end of each active scan, the observed differences in averaged background before and after DC restoration were as high as 1 DN in Channel 4 of Band 1.

- Arithmetic Application of Correction. A correction for bright-target saturation can be expressed additively. For each channel in a scan:

$$L'_{RB}(S) = L_R(S) + CB(SB, S) \qquad (4-6)$$

where CB(SB, S) = correction for bright-target saturation in DN at sample S after coming out of saturation SB samples earlier

$L_R(S)$ = observed raw radiance at S in DN

$L'_{RB}(S)$ = raw radiance at S in DN, which has been corrected for bright-target saturation.

- Exponential Form of Cloud Correction. One possibility is that the bright-target saturation effect has a recovery of the same analytical form as droop. By analogy to Equation 4-3, an equation for the expected additive correction term for bright-target saturation in Equation 4-6 would be:

$$CB(SB, S) = BD \exp [-KS*SB] \qquad (4-7)$$

where SB = samples since bright-target saturation at sample S

KS = time constant for bright-target saturation

BD = maximum initial drop in DN

CB(SB, S) = correction in DN at S for bright-target saturation

The exact form of the correction for bright-target saturation remains to be determined. Preliminary analyses of the "solid-cloud" example below indicate two independent physical phenonema may be occuring in the detectors. One causes a decreased sensitivity in the detectors and the correction for this depletion effect can be modeled by Equation 4-7. The other phenomenon gives the appearance of an increased sensitivity in the detectors after exposure to bright targets. This second phenomenon may have a similar correction, except that there would be a new amplitude constant with a changed sign to replace BD, perhaps BI for increased background. There would also be a new time constant to replace KS, perhaps KSI, and it is possible that this second term might require a displaced start from the end of saturation. The correction for bright-target saturation would then be the sum of these two opposing effects. An alternative interpretation of the deeper shorter undershoot and longer lower amplitude overshoot observed in the solid-cloud example below is an underdamped alternating oscillation of decreasing amplitude. This underdamped alternative was tentatively rejected because there was no evidence for a second undershoot and the period of overshoot and undershoot were not the same.

- "Solid-Cloud" Examples. In order to facilitate the interpretation of the data in terms of bright-target saturation, a TM scene was chosen which had one solid formation of clouds. The initial "solid-cloud" scene was of San Francisco, CA (ID 40392-18152, 12 AUG 83). A solid formation of clouds along the coast of the Pacific Ocean on the western edge of this scene starts at about scan 80 and reaches eastward until there is nearly 75% cloud-cover in the lower quarter of the scene. Backgrounds were taken from two shutter regions, "background 1" and "background 2", before and after DC restoration, respectively, namely B-BDC and B-ADC. Uncorrected raw scene-average backgrounds are given in Appendix 9.12. These averaged backgrounds were corrected on a line-by-line basis for scan-correlated shifts (Section 4.5). The corrected backgrounds were plotted separately versus scan number for forward and reverse scans in both regions for all reflective channels (Appendix 9.9), giving four plots for each band, namely, BF-BDC, BR-BDC, BF-ADC and BR-ADC.

If there were no bright-target saturation effects, then four identically flat plots of the same constant background, independent of scan number would be expected. This is not the case. Slowly varying trends are visible in the PFP bands. These trends of the background as a function of scan number are most visible in Band 2 (Appendices 9.9.3 and 9.9.4), especially when related to the known patterns of cloud cover, and can be summarized as follows:

- A "1st transition" occurs between scans 80 and 120.
- All four PFP bands show a 1st transition.
- The 1st transition is correlated to cloud cover.

  Cloud cover is zero down to scan 80.

  About 30% of the western edge of the image is cloud covered by scan 120
- A "2nd transition" occurs between scans 290 and 320.
- The 2nd transition is correlated to cloud cover.

  Cloud cover increases toward the east from 30% to 75% between scans 120 and 290.

  Cloud cover is nearly constant at 75% of western side of image for last 80 scans.
- All channels change at approximately the same time.
- All channels have approximately the same change in DN.
- Band 2 backgrounds depend on region and scan direction.

Estimated changes in Band 2 at 1st transition:

Δ BR-ADC = -2.0 DN, From 2.0 to 0.0 DN
Δ BF-BDC = +1.4 DN, From 2.2 to 3.4 DN
Δ BF-ADC = +1.0 DN, From 2.2 to 3.2 DN
Δ BR-BDC = 0.2 DN, From 2.0 to 1.8 DN

Estimated changes in Band 2 at 2nd transition:

Δ BF-BDC = -0.7 DN, From 4.0 to 3.3 DN
Δ BR-ADC = +0.4 DN, From 0.0 to 0.4 DN
Δ BF-ADC = -0.2 DN, From 3.8 to 3.6 DN
Δ BR-BDC = +0.1 DN, From 1.8 to 1.9 DN

A specific channel was chosen from each band to test the background dependence on distance from the end of the exposure to the bright clouds, SB. For Channel 7 in Band 2, data from both regions can be combined to give a nearly self-consistent curve of B versus SB, starting at about 2.1 DN at the edge of the cloud, to a minimum of about 0.0 DN near pixel 800, and then to a maximum of about +3.8 DN near pixel 4000, followed by a decline to within 0.3 DN of the original background of 2.1 DN near SB = 7000 pixels. This slowly and smoothly varying curve of B versus SB is the justification for the two component bright-target correction model given above. There is a difference of about 0.3 DN between the maxima in forward scan backgrounds before and after DC restoration.

The estimates of actual backgrounds in the San Francisco example were uncertain to varying degrees because of an incomplete printing of the line-by-line backgrounds for any channel in Band 2. Furthermore, there were no normalizations for bin-radiance dependence, and the lower backgrounds are probably biased to the high side because values of L_R = 0 DN undoubtedly include real values that were below zero.

The model for bright-target saturation effects is that they are related to the distance from the end of bright target, or cloud. This hypothesis was tested in this study and the results are shown in Figure 4-2, where the backgrounds from all four regions on the shutter are plotted against the distance from the cloud edge. The initial 1000 mf undershoot and a 6000 mf overshoot suggests that all of the background data can be fit on a single slowly varying curve, thereby justifying the two component model mentioned above.

Some additional verification for this correction model is evident from an examination of the change in the shutter backgrounds in the bottom 100 scans of a Washington, DC scene (ID 40109-15140, 2 NOV 82), in which the eastern 10% is cloud covered at the bottom of the scene. Changes in the background of this eastern solid cloud example are in the opposite direction from the western case, as expected.

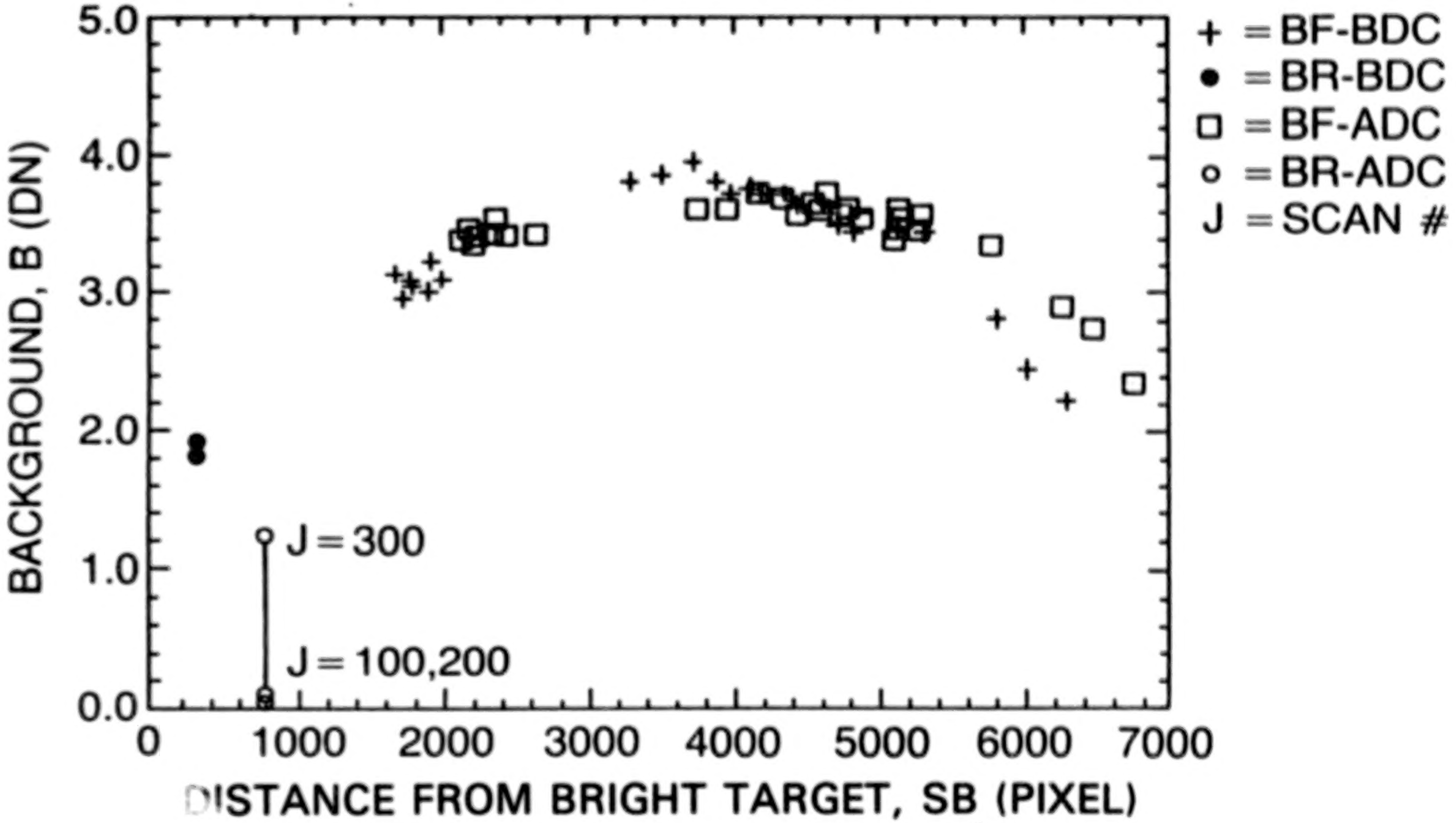

Figure 4-2. Bright-Target Saturation Effects on Background

- Cloud Mask. For real scenes, with single or multiple clouds, implementation of a bright-target correction will probably require initial creation of cloud mask. Corrections may need to be aggregated when there is more than one bright target either within a scan or within a couple of scans, unless it can be shown that the "clock" is reset each time the detector is exposed to a bright target.

- Between-Scan Correction. Because the DC restoration circuit, which is activated by switches on the shutter for about 3.1 milliseconds at the end of each scan, has a 1/e time constant of about 6.2 milliseconds, it is possible that there may be a "between-scan trend-dependent noise" from bright-target saturation effects. The nearly overlapping and smoothly varying curves of B versus SB for both regions suggest that changes which are independent of SB and due to changes during DC restoration are small, less than 0.3 DN.

- Bright-Target Drop-Out during Saturation. During pre-launch testing of Landsat-5 TM/F, occassional major drops in signal were observed in Band-4 during exposure to sources whose radiance was more than about 30% above the nominal limit at a DN value of 255. If such bright targets are observed over land, perhaps in a summer scene of a bright desert, then apparent holes may appear in the saturated imagery.

- Absolute Radiometric Recalibration. If the bright-target saturation effect is radiance-level dependent, then a re-examination of the absolute calibration methodology may be necessary. The re-examination would include the potential impact of the brightest 111 all-lamps-on IC state on video data for 40 scans out of every 360 scans, when the normal IC automatic sequencer mode is used. If the scan mirror is locked, the re-examination needs to include the effect of bright-target saturation in the video on background and calibration data.

4.4 COHERENT NOISE

Coherent noise is a "within-scan, sample-location dependent noise" which has been observed by Fourier analysis in TM scenes (Anuta et al., 1984). Peak-to-peak amplitudes at the 32 KHz peak are given in Table 4-1 for a similar analysis using a Fast Fourier Transform (FFT) on an in-orbit scene (ID 40037-16033, August 22, 1982, Memphis, TN). A scene-independent analysis was performed on 512 mf of in-orbit calibration data from the shutter region (ID 40171-17080, January 3, 1982, White Sands, NM). The

Table 4-1. 32 KHz Coherent Noise (every 3.2 pixels), measured by peak-to-peak amplitude in DN from midscan digital data for 96 reflective channels on Landsat-4 TM/PF (ID 40037-16033, 22 AUG 82, Memphis, TN)

IN-ORBIT LANDSAT-4 TM RADIOMETRIC COHERENT NOISE (DIGITAL COUNTS)

	Peak-to-Peak Coherent Noise at 32 KHz (DN)					
Channel No.	Band 1	Band 2	Band 3	Band 4	Band 5	Band 7
1	.54	.08	.09	.28	.25	.16
2	.98	.13	.13	.39	.50	.28
3	.74	.07	.07	.42	—	.20
4	.03	.15	.86	.77	.19	.37
5	.83	.15	.20	.76	.33	.35
6	1.02	.16	.19	.49	.25	.21
7	.39	.10	.15	.58	.59	.46
8	.93	.00	.80	.70	.34	.29
9	.44	.08	.16	.43	.38	.25
10	.33	.14	.08	.35	.19	.28
11	.54	.13	.17	.37	.29	.18
12	.47	.13	.10	.35	.41	.31
13	.52	.05	.21	.43	.20	.26
14	.76	.00	.12	.28	.25	.34
15	.57	.06	.09	.34	.32	.18
16	1.43	.06	.35	.37	.49	.20

Data Measured Peak-to-Peak, With Background Subtracted in Digital Counts
Data from Scene W023036 ID = 40037-16033 (22 Aug 82) Memphis, TN

TM/PF exhibits coherent noise in the PFP bands at two frequencies, f_2 = 32.8 KHz (a period of every 3.2 pixels) and at f_1 = 5.9 KHz (a period of 17.6 pixels). Results are tabulated in Tables 4-2 and 4-3 for the integrated area under the peaks in the Fourier domain, instead of peak-to-peak amplitudes. A standard method for reducing this noise would be to perform a FFT on each line, apply a notch filter at the two spikes, and apply an inverse Fourier Transform. Given the reproducibility of the frequencies, it might be possible to avoid the need for FFTs by applying a filter in the spatial domain. This could be done by using one channel with a high amplitude to calculate the phase location for all channels, SP, from the start of a period in the shutter region. For each channel in a scan:

$$L'_{RC}(S) = L_R(S) + CC(f, S, SP) \tag{4-8}$$

where CC(f, S, SP) = correction in DN for coherent noise of frequency f, at sample S, and where the start of a cycle is at SP

$L'_{RC}(S)$ = raw radiance at S in DN after correction for coherent noise.

There are no observable coherent noise peaks for the SWIR bands, only a steadily rising amplitude with frequency.

Landsat-5 TM/F has a different coherent noise pattern. It does not have as significant a peak at 32 KHz. Most channels on the primary focal plane in TM/F have only one peak, or multiples of it, near 8.5 n KHz, where n is an integer, and the periods are about (12.5/n) pixels. Two tests on pre-launch data differed in apparent frequency of the coherent noise by about 10 percent. If this magnitude of variability is real, its origin might be traceable and modelable from engineering telemetry. Channel 1 in Band 3 appears to have the largest 8.5 KHz noise on Landsat-5 TM/F.

Systematic corrections for coherent noise are possible. If bin-radiance dependencies are removed first, then the characterization of the coherent noise will be more precise. Coherent noise corrections need to be made before characterizing the between-scan shifts and other types of systematic noise with periods longer than that for coherent noise. When fractional DN corrections are applied to

Table 4-2. In-Orbit Coherent Noise at Frequency 3.17 Pixels
White Sands (3 January 83)

CHANNEL	BAND 1	BAND 2	BAND 3	BAND 4	BAND 5	BAND 7
1	0.976 ± 0.258	0.230 ± 0.052	0.282 ± 0.056	0.556 ± 0.091	0.165 ± 0.333	0.080 ± 0.024
2	1.642 ± 0.346	0.345 ± 0.051	0.233 ± 0.037	0.288 ± 0.057	0.102 ± 0.010	0.233 ± 0.076
3	1.194 ± 0.243	0.166 ± 0.025	0.069 ± 0.013	0.401 ± 0.080	±	0.083 ± 0.017
4	0.253 ± 0.029	0.106 ± 0.037	1.193 ± 0.212	0.453 ± 0.065	0.043 ± 0.012	0.201 ± 0.024
5	1.116 ± 0.201	0.227 ± 0.033	0.057 ± 0.027	0.259 ± 0.029	0.127 ± 0.026	0.037 ± 0.003
6	1.908 ± 0.380	0.349 ± 0.074	0.338 ± 0.074	0.345 ± 0.074	0.187 ± 0.044	0.129 ± 0.042
7	0.569 ± 0.171	0.086 ± 0.008	0.077 ± 0.013	0.191 ± 0.025	0.176 ± 0.044	0.103 ± 0.018
8	1.787 ± 0.343	0.203 ± 0.026	1.609 ± 0.282	0.766 ± 0.132	0.247 ± 0.040	0.075 ± 0.008
9	0.722 ± 0.192	0.046 ± 0.003	0.136 ± 0.029	0.224 ± 0.017	0.035 ± 0.000	0.081 ± 0.022
10	0.601 ± 0.169	0.127 ± 0.018	0.275 ± 0.056	0.305 ± 0.038	0.157 ± 0.019	0.283 ± 0.041
11	1.054 ± 0.200	0.083 ± 0.017	0.049 ± 0.012	0.312 ± 0.023	0.084 ± 0.039	0.122 ± 0.041
12	0.861 ± 0.179	0.192 ± 0.027	0.078 ± 0.022	0.063 ± 0.015	0.039 ± 0.002	0.204 ± 0.030
13	0.787 ± 0.248	0.116 ± 0.024	0.155 ± 0.038	0.221 ± 0.024	0.052 ± 0.021	0.059 ± 0.025
14	1.683 ± 0.313	0.106 ± 0.027	0.416 ± 0.084	0.150 ± 0.010	0.096 ± 0.008	0.048 ± 0.000
15	0.995 ± 0.224	0.098 ± 0.010	0.151 ± 0.031	0.235 ± 0.034	0.259 ± 0.063	0.100 ± 0.016
16	2.626 ± 0.447	0.180 ± 0.039	0.918 ± 0.145	0.218 ± 0.017	0.168 ± 0.026	0.171 ± 0.041

Table 4-3. In-Orbit Coherent Noise at Frequency 17.6 Pixels
White Sands (3 January 83)

CHANNEL	BAND 1	BAND 2	BAND 3	BAND 4	BAND 5	BAND 7
1	0.352 ± 0.118	0.161 ± 0.050	0.469 ± 0.078	0.186 ± 0.078	0.012 ± 0.006	0.066 ± 0.015
2	0.103 ± 0.028	0.062 ± 0.000	0.256 ± 0.058	0.091 ± 0.012	0.114 ± 0.009	0.141 ± 0.018
3	0.374 ± 0.087	0.076 ± 0.014	0.213 ± 0.087	0.185 ± 0.024	±	0.022 ± 0.005
4	0.417 ± 0.237	0.082 ± 0.020	0.198 ± 0.051	0.045 ± 0.007	0.057 ± 0.011	0.119 ± 0.030
5	0.270 ± 0.108	0.111 ± 0.028	0.113 ± 0.038	0.059 ± 0.010	0.033 ± 0.008	0.134 ± 0.017
6	0.158 ± 0.028	0.061 ± 0.010	0.167 ± 0.070	0.115 ± 0.024	0.094 ± 0.029	0.045 ± 0.014
7	0.357 ± 0.081	0.082 ± 0.006	0.157 ± 0.023	0.101 ± 0.009	0.159 ± 0.018	0.223 ± 0.092
8	0.092 ± 0.031	0.017 ± 0.006	0.082 ± 0.031	0.146 ± 0.009	0.009 ± 0.000	0.114 ± 0.022
9	0.184 ± 0.063	0.049 ± 0.008	0.221 ± 0.053	0.126 ± 0.053	0.023 ± 0.000	0.012 ± 0.000
10	0.307 ± 0.060	0.043 ± 0.004	0.088 ± 0.050	0.044 ± 0.009	0.031 ± 0.000	0.003 ± 0.000
11	0.206 ± 0.094	0.049 ± 0.004	0.167 ± 0.023	0.085 ± 0.010	0.128 ± 0.022	0.046 ± 0.000
12	0.366 ± 0.138	0.047 ± 0.004	0.102 ± 0.030	0.092 ± 0.019	0.146 ± 0.016	0.067 ± 0.027
13	0.348 ± 0.143	0.110 ± 0.025	0.142 ± 0.069	0.052 ± 0.009	0.052 ± 0.012	0.138 ± 0.016
14	0.195 ± 0.044	0.032 ± 0.009	0.138 ± 0.047	0.015 ± 0.002	0.067 ± 0.032	0.141 ± 0.032
15	0.308 ± 0.090	0.122 ± 0.012	0.273 ± 0.069	0.060 ± 0.010	0.142 ± 0.016	0.212 ± 0.010
16	0.209 ± 0.106	0.074 ± 0.028	0.338 ± 0.109	0.267 ± 0.032	0.051 ± 0.014	0.116 ± 0.009

digital imagery to partially reduce coherent noise, a statistical randomization can be used to assure a zero mean quantization error (Section 5.2.4).

4.5 SCAN-CORRELATED SHIFTS

Scan-correlated shifts are one of two types of "between-scan, line-dependent noise." Malila et al., (1984) referred to them, on Landsat-4 TM/PF, as level-shift artifacts of Form 1 (exemplified by Channel 4 of Band 1) and Form 2 (exemplified by Channel 7 of Band 7). In this paper, these shifts will be called scan-correlated shifts of Type 4-1 and 4-7, respectively. Malila et al., (1984) observed these shifts most clearly in scenes of raw or geometrically unresampled data taken at night (ID 40037-02243 and ID 40161-02481) and over the clear waters of the Bahamas. Type 4-1 shifts were absent in many scenes but, when present, were largest for Channels 4, 12, 10 and 8 in Band 1, with respective amplitudes of approximately 2.2, 1.8, 1.0 and 0.75 DN. Type 4-7 shifts were present in all examined scenes and occurred with a higher within-scene frequency approaching every 2 sweeps. The largest amplitudes for Type 4-7 shifts were 1.0, 0.5 and 0.4 DN for Channels 7, 10 and 8, respectively, in Band 7. Murphy et al. (1984) have observed that these Type 4-1 shifts start and end at the beginning of a scan line. Their magnitude and consistency suggest a line-by-line radiometric correction procedure for each channel:

$$L'_{RS} = L_R + CS(T,J) \tag{4-9}$$

where $CS(T,J)$ = correction in DN for scan-correlated shift of Type T in scan number J

L'_{RS} = raw radiance in DN corrected for scan-correlated shift

A procedure for correcting for scan-correlated shifts has been developed and tested as part of this study. Assumptions that were made include:

- Shifts are constant within a line; they are either present or absent
- If a shift is present in one channel, it is present in all channels

- The direction and magnitude of the shifts are constant within a scene for each channel (Appendices 9.8 and 9.11)

- There can be as many different types of shifts as there are bands. Two types are tested for Landsat-4 TM/PF (Type 4-1 and 4-7). Two types were also tested for Landsat-5 TM/F (Type 5-3 and 5-7), but only Type 5-3 was significant

- Backgrounds are not constant within a line or between lines because of effects such as bright-target saturation. In this study, the average of 24 or 28 mf on the shutter, before and after DC restoration, were used as background, B, for testing the procedures for correcting for shifts. Forward and reverse scans were calculated separately. Therefore, there were four distinct sets of backgrounds:

  BF-BDC = Background from a forward scan before DC restoration, i.e. from shutter region 1

  BF-ADC = Background from a forward scan after DC restoration, i.e. from shutter region 2

  BR-BDC = Background from a reverse scan before DC restoration, i.e. from shutter region 1

  BR-ADC = Background from a reverse scan after DC restoration, i.e. from shutter region 2.

The steps in the correction procedure were:

- Separately process forward and reverse scans

- Use a reference channel for each type of shift:

  Type 4-1 = Channel 4 in Band 1 on Landsat-4
  Type 4-7 = Channel 7 in Band 7 on Landsat-4
  Type 5-3 = Channel 1 in Band 3 on Landsat-5

- Use the line-averaged background to monitor for shifts

- Separate the backgrounds of the references into two states, thereby creating a binary mask for each type, indicating its presence or absence in each scan of the scene. In future tests, this step could be done for the most significant shift first, and a correction applied for this shift before searching for a second type of shift

- For each channel, calculate the average size of the correction for scan-correlated shift, CS(T), of each type, by averaging the difference between the high and low states at each transition, i:

$$CS(T) = \frac{1}{t} \sum_{i=1}^{t} \left(B_H - B_L \right)_i \qquad (4\text{-}10)$$

- Apply corrections, CS(T), on a line-by-line basis. Illustrative results for all channels are given in Appendices 9.7 through 9.11, before and after backgrounds were corrected for both TM/PF and TM/F.

An initial test of this correction procedure was made for type 4-1 noise on a pre-launch single background collect of ambient data from March 22, 1982. A simultaneous test for Type 4-7 correction, CS, could not be made because the CFP was not cooled. Linear within-band correlations were run for all channels in forward and reverse scans, both with and without corrections from Equation 4-10. For uncorrected data, the apparent linear correlations from this binary level phenomenon were highest for pairs of channels which both had large Type 4-1 shifts. Correlation coefficients, R, were highest between forward and forward scans and lowest between adjacent forward and reverse scans, i.e.:

$$R^2_{FF}(B_i, B_j) \approx R^2_{RR}(B_i, B_j) >> R^2_{RF}(B_{i,F}, B_{i,F+1})$$

where

B_i = average background in DN on shutter for channel i for a single line

B_j = average background in DN on shutter for channel j where j and i are in the same band

$R_{FF}(B_i, B_j)$ = linear correlation coefficient for pairs (B_i, B_j) versus scan number, 2J, for 200 forward scans

$R_{RR}(B_i, B_j)$ = correlation of (B_i, B_j) versus $(2J + 1)$, for 200 reverse scans

$R_{RF}(B_{i,F}, B_{i,F+1})$ = correlation of 200 adjacent forward and reverse scan pairs for channel i.

All channels in all four bands appear to shift at the same time. This led to the original name of channel-correlated shifts, which was later broadened to scan-correlated shifts since all channels within a scan are affected. The low correlation of pairs of adjacent forward and reverse scans versus scan number is due to shifts occurring randomly at the start of any scan, forward or reverse. When comparing pairs within, rather than between, a scan, the pairs of channels always change states at the same time. Illustrative correlation coefficients for the backgrounds in two specified channels for these initial tests are summarized in Table 4-4, both before and after applying corrections for scan-correlated shifts, and for both TM/PF and TM/F. These results, especially the near-unity correlations of forward-to-forward backgrounds, justify the assumption that "if a shift is present in one channel, it is present in all channels in that band."

For Landsat-5 TM/F, the reference channel is Band 3 Channel 1 for Type 5-3, with the largest prelaunch shifts being 0.5, 0.5, 0.4 and 0.3 DN in Band 2 Channel 1, Band 3 Channel 1, Band 3 Channel 3 and Band 4 Channel 1, respectively, for the "Golden Tape," which was an ambient 7-band integrating sphere GPC collect on August 30, 1983 at 16:14:15, labeled as Goddard BRU tape #517 (GE/VF # CIS1B, Scene ID 5-198-10563). This scan-correlated shift is lower in magnitude in Landsat-5 (Appendix 9.11), however, it is more uniformly present in Band 3 than in any bands on Landsat-4 (Appendix 9.8).

For the Landsat-4 San Francisco scene on day 392 after launch, there were approximately 70 changes of state in 380 scans for Type 4-1 noise, and many more for Type 4-7. Type 4-1 shifts were present before and after DC restorations, which is consistent with the assumption that "shifts are constant within a line." This scene was acquired using the synchronized second or redundant TM/PF power supply, The presence of scan-correlated shifts of Landsat-5 TM/F, where both primary and redundant power supplies are free-running, exonerates the synchronization as the sole source of the shift.

The A/D converter is a possible source of this scan-correlated noise. Corrections were possible on Bands 5 and 7 for pre-launch Landsat-4 data even though these detectors were turned off (Table 4-4, and Appendices 9.10 and 9.11). When the bands are off, a constant reference voltage is expected from the A/D converter. In fact, the reference voltage must have a small but finite variability relative to the size of the bin. Therefore, if such a reference signal happens to fall near the upper threshold of bin 2, then a mix of counts 2 and 3 would be expected from quantization error. Values other than 2 are indeed observed when the CFP bands are off. The observed correlation and correctability of these noise counts in Table 4-4, and in Appendix 9.10 and 9.11, suggests that a variable reference voltage in the A/D converter may be a source of scan-correlated shifts.

Observations of the shutter backgrounds lead to suggestions for least-noisy and most-noisy references. Results are given in Table 4-5. The largest shift was used to define the noisiest. Small shift, low random variability, and minimum differences between forward and reverse scans were used as criteria to identify the quiet references. These reference channels are used in preference to earlier ones, such as Channels 1 and 9. Channel 1 was the first reference but it also has the largest offset. Channel 9 was chosen because it was the middle of the focal plane. Criteria cited here provide a basis for choosing a reference channel, based on the stability of its signal.

Since the magnitude of the scan-correlated shifts range from zero to two DNs, uncorrected attempts to normalize gains and offsets will be uncertain by this amount when full-scene histogram-equalization procedures are used. This is also the reason that there are some values of relative biases in Equation 1-1 that are nearly a DN different from zero. Scan-correlated shifts are a large source of noise and are at least partially correctable.

Application of corrections for scan-correlated shifts needs to be scan-specific. It appears that this may have contributed to some residual errors in bias by Fischel (1984, Equation 4-12) and Kogut (1984, Equation 4-5). Estimating background by averaging between scans is not desirable, unless these corrections have been made.

A single unconfirmed case has been reported of a discontinuous change in sensitivity part way through the image. If such a discontinuous bias or gain change does occur, it has not been fully characterized. Such "multi-scan bands" are potentially subject to line-by-line application of the normal IC system radiometric calibration, except that the IC data has to be separated into as many separate calibration sets as there are multi-scan bands.

Table 4-4. Between-Channel Linear Correlation Coefficients, before and after making corrections for scan-correlated shifts in Landsat TM sensor, illustrating with two channels the fact that "if a shift is present in one channel, it is present in all channels of that band."

(TM/PF REF: BAND 1 CHANNEL 4 NOISE TYPE 4-1) (TM/F REF: BAND 3 CHANNEL 1, NOISE TYPE 5-3)

CHANNEL-TO-CHANNEL WITHIN-BAND FORWARD-FORWARD CORRELATIONS (R) BEFORE AND AFTER CORRECTIONS FOR SCAN-CORRELATED SHIFTS IN AVERAGE SHUTTER BACKGROUND

	BAND 1	BAND 2	BAND 3	BAND 4	BAND 5	BAND 7	BAND 6
LANDSAT-4 (TM/PF)					OFF	OFF	OFF
CHANNEL PAIR	4/12	1/14	1/15	6/16	2/4/12 13/14/15	14/16	1/3
100R^2, BEFORE	98	75	92	92	99	91	97 REV
100R^2, AFTER	10	5	15	18	15	2	98 REV
LANDSAT-5 (TM/F)					ON	ON	ON
CHANNEL PAIR	10/12	1/3	1/3	1/4	1/3	7/9	1/2
100R^2, BEFORE	60	84	90	72	47	56	78
100R^2, AFTER	5	3	4	0	0	0	78

Table 4-5. TM Radiometric Reference Channels

	BAND 1	BAND 2	BAND 3	BAND 4	BAND 5	BAND 7	BAND 6
LANDSAT-4 TM/PF							
LOWEST NOISE							
SHUTTER rms	**9**	**14**	**12**	**7**	**2**	**15**	**4F**
HIGHEST NOISE							
SHUTTER rms	16	2	1	8	7	7	1
SHIFT TYPE 4-1	4	–	1	16	15	–	–
SHIFT TYPE 4-7	–	1	16	–	10	7	–
32 KHz (3.2 mf)	16	6	8	8	[8]	[10]	–
6 KHz (18 mf)	4	1	1	16	[7]	[7]	–
LANDSAT-5 TM/F							
LOWEST NOISE							
SHUTTER rms	**15**	**10**	**2**	**1**	**2**	**15**	**4**
HIGHEST NOISE							
SHUTTER rms	4	1	12	3	10	9	1
SHIFT TYPE 5-3	10	1	1	1	3	–	–

This type of between-scan change is not called noise because its apparent correction involves processing of IC data. Multi-scan banding may also prove to be a gain-free offset shift, such as those associated with bright-target saturation or with the scan-correlated shifts discussed in this section.

4.6 FORWARD/REVERSE-SCAN DIFFERENCES

Forward/reverse-scan differences are the second type of "between-scan, line-dependent noise." If a forward/reverse-scan difference actually exists, it has not been definitively demonstrated to be independent of expected forward/reverse manifestations from one or more of the types of noise referred to above (Sections 4.2, 4.3, and 4.5). For background in the shutter region, the apparent magnitude of the average value of (BFWD-BREV) in Landsat-4 is 0.1 DN in the PFP bands, except for scenes with clouds (Appendix 9.12).

In most of the pre-launch tests, calculated values of forward/reverse-scan differences are nearly zero in all bands of Landsat-5, with the exception of a value for Band 4 Channel 16 of -0.1 DN (Appendix 9.12). In the worst cases with calculated DN values as large as 2, the test procedure called for a light source in front of the TM/F. This indicates that the forward/reverse difference is scene dependent. Indeed, initial in-orbit data indicate a background difference as high as 3 DN for band 1 on Landsat-5 TM/F.

It is necessary to process calibration pulses, P, separately in order to avoid scan-correlated shifts. For forward scans, each line has a corrected pulse value of:

$$P' = P - \text{BF-ADC}' \qquad (4\text{-}11)$$

and

$$\text{BF-ADC}' = \text{BF-ADC} + \text{CS} \qquad (4\text{-}12)$$

where BF-ADC = background on shutter after DC restoration, in DN

CS = correction for scan-correlated shift (see Equation 4-10).

For reverse scans:

$$P' = P - BR\text{-}BDC' \qquad (4\text{-}13)$$

and

$$BR\text{-}BDC' = BR\text{-}BDC + CS \qquad (4\text{-}14)$$

where BR-BDC = background of shutter before DC restoration, in DN.

These are net pulses rather than gross pulses. Useful net pulses cannot be created from the 000 all-lamps-off configuration of the IC unless corrected for between-scan shifts. In general, uncorrected or gross pulse values cannot be used. The same procedure applies to conversion of digital imagery values to net counts. For forward and reverse scans:

$$L_R' = L_R - BDC' \qquad (4\text{-}15)$$

When using shutter background, threshold checks are feasible for removing noise from sources such as resetting the scan-line corrector (SLC) and incomplete obscuration. This removal requires an outlier rejection strategy. All such possible forward/reverse-scan differences can be avoided if one chooses to calibrate forward and reverse scans separately. However, if a need to make this correction exists, it can take the form:

$$L_{RF}' = L_R + CF(J) \qquad (4\text{-}16)$$

where CF(J) = correction in DN for normalization to forward scans as a function of scan number, J.

Some authors (Engel et al., 1983) have chosen to use the term "banding" to distinguish this forward/reverse difference between adjacent sweeps of 16 channels and the repeated radiometric striping which is associated with a specific channel.

4.7 TOTAL NOISE

In earlier descriptions of absolute calibration, signal-to-noise values were calculated at two specific radiances (Barker, Ball et al., 1984). The rms noise of that signal can now be seen to be the upper limit on the rms random noise, since it contains a finite number of systematic noise components. For later use in error models, the random noise of each channel is defined as the standard deviation, σ_r.

An rms estimate of the apparent total background noise in the TM/PF sensor ranges from ±0.4 to ±1.3 DN, depending on the band (Table 4-6). If one assumes a range of plus or minus three standard deviations, then this implies that the range of uncertainty in DN values, prior to any systematic corrections outlined in this section, is from 2 to 8 DN. As expected from real sources, estimates of rms noise, for either a pre-launch flooding lamp or for an apparently homogeneous part of an ocean scene, have a slightly higher range from ±0.5 to ±1.7 DN, depending on the band (Table 4-7). This implies that the range of uncertainty in DN, prior to any systematic corrections outlined earlier in this section, is from 3 to 9 DN values.

One measure of the total noise is the standard deviation on shutter backgrounds (Appendix 9.12). The true random error can be estimated from shutter counts after correction for systematic errors.

4.8 WITHIN-SCENE ERROR MODELS

In order to incorporate the within-scene corrections mentioned above, the basic radiometric calibration equations have to be restructured for each channel. Equation 1-2, for regressing observed pulses against nominal pulses, becomes:

$$\overline{P'}(\ell) = NB'_{IC} + NG'_{IC}P'_n(\ell) \qquad (4\text{-}17)$$

Equation 1-1, for applying the normalized gain and bias to the raw image data, becomes:

$$L'_{cal} = \frac{L'_R - NB'_A}{NG'_A} \qquad (4\text{-}18)$$

Table 4-6. Apparent rms Noise in Background Data for Landsat-4 TM/PF

		BAND 1	BAND 2	BAND 3	BAND 4	BAND 5	BAND 7
ODD CHANNEL	FLOODING LAMP[1]	1.24	0.450	0.539	0.333	0.948	1.25
EVEN CHANNEL	FLOODING LAMP[1]	1.27	0.567	0.669	0.406	0.939	1.13
ODD CHANNEL	WATER[2]	1.12	0.393	0.518	0.496	0.872	1.03
EVEN CHANNEL	WATER[2]	1.33	0.523	0.657	0.575	0.818	1.01

Table 4-7. Apparent rms Noise in Image Data for Landsat-4 TM/PF

		BAND 1	BAND 2	BAND 3	BAND 4	BAND 5	BAND 7
ODD CHANNEL	FLOODING LAMP[1]	1.45	0.606	0.859	0.483	1.19	1.67
EVEN CHANNEL	FLOODING LAMP[1]	1.50	0.684	0.952	0.532	1.19	1.40
ODD CHANNEL	WATER[2]	1.51	0.589	0.842	0.462	0.921	1.13
EVEN CHANNEL	WATER[2]	1.71	0.655	0.942	0.461	0.840	1.06

---

[1] Flooding Lamp, March 1982.

[2] Boston Water Scene, September 10, 1982 (ID 40056-14541).

and Equation 1-4, for converting calibrated counts into spectral radiance, becomes:

$$L_\lambda = \frac{L'_{cal} - O^{o}(B)}{G^{o}(B)} \; . \qquad (4\text{-}19)$$

The construction of this correction model has proceeded from the fact that, in general, if the raw radiance, L_R, is corrected for v correction variables, C_i, then the corrected radiance, L'_R, is a function of all these variables:

$$L'_R = L'_R \left(L_R, C_1, C_2, \ldots C_i \ldots C_v\right) \qquad (4\text{-}20)$$

and the standard deviation of this corrected radiance, $\sigma_{L'}$, is the square root of the variance:

$$\sigma^2_{L'} = {\frac{\partial L'_R}{\partial L_R}}^2 \sigma^2_{L_R} + \sum_{i=1}^{v} {\frac{\partial L'_R}{\partial C_i}}^2 \sigma^2_{C_i} \qquad (4\text{-}21)$$

Assuming that the variables are separable, a formulation of the corrections in additive terms is:

$$L'_R = L_R + \sum_{i=1}^{v} C_i \qquad (4\text{-}22)$$

which for the six currently identified sources of within-scene systematic variation could be written as:

$$L'_R = L_R + CA + CD + CB + CC + CS + CF \qquad (4\text{-}23)$$

which are defined by Equations 4-1, 4-3, 4-7, 4-8, 4-10 and 4-16.

The variance in the corrected signal can be derived from Equations 4-21 and 4-22, and the assumption that the only variance in L_R is from the random noise, σ_r:

$$\sigma_{L'}^2 = \sigma_r^2 + \sum_{i=1}^{v} \sigma_{C_i}^2 \qquad (4\text{-}24)$$

or more explicitly from Equation 4-23:

$$\sigma_{L'}^2 = \sigma_r^2 + \sigma_{CA}^2 + \sigma_{CD}^2 + \sigma_{CB}^2 + \sigma_{CC}^2 + \sigma_{CS}^2 + \sigma_{CF}^2 \qquad (4\text{-}25)$$

One of the advantages of formulating the corrections linearly is that optimization of the fitting parameters can now be done in each correction term separately. Minimizing individual correction errors produces the minimum error for the fully corrected raw radiance. For the magnitude of systematic corrections for TM of less than 2 DN, the assumption of separability of primary causes implied by additive corrections in Equation 4-23 is a useful approximation if the coupling between these sources of radiometric variability is small relative to the uncertainties in making the corrections. Use of additive corrections also implies that the multiplicative corrections, such as droop, have an overall correction that is small relative to the size of the raw signal.

Time is one physical variable which can be used to quantify the degree of separability of individual types of systematic variations in the TM sensor's response to radiance. The period of a phenomenon, in pixels or seconds, or the frequency, in cycles per second (Hz), can be used as surrogates for time. For the currently-identified systematic corrections to TM data, an approximate order by frequency is:

$$f_A >> f_C >> f_D \sim f_B > f_{FR} > f_S >> f_P >> f_{BD} \qquad (4\text{-}26)$$

where the symbols are:

$>$ = greater than
$>>$ = factor of more than ten greater than
$\sim$ = approximately equal

and the frequency, f, subscripts are:

A = A/D Bin-Radiance Dependence (Section 4.1)
C = Coherent Noise (Section 4.4)
D = Within-Line Droop (Section 4.2)
B = Bright-Target Saturation (Section 4.3)
FR = Forward/Reverse-Scan Differences (Section 4.6)
S = Scan-Correlated Shifts (Section 4.5)
P = Within-Path Smoothing (Section 5.1.7)
BD = Between-Date Smoothing (Section 5.1.8).

If a sufficient criterion for separability is a difference in period or frequency of more than a factor of ten, then Equation 4-26 is a guide to which corrections might not be separable.

Errors associated with applying systematic corrections will be reduced if the corrections are calculated in the order of their occurrence, as well as in the order of their absolute magnitude. Order of occurrence is given by Equation 4-26. If the phenomena cannot be uncoupled sufficiently by serial linear corrections, then iterative procedures can be used to reduce the random errors in applying these systematic corrections.

An additional use of error models is to decide whether or not to make a correction. Using the correction for scan-correlated shifts, calculated for t transitions, as an example, the variance of Equation 4-10 is:

$$\sigma_{CS}^2 = \frac{1}{t}\sum\left(\sigma_{B_H}^2 + \sigma_{B_L}^2\right) \approx \frac{2}{t}\,\sigma_B^2 \qquad (4\text{-}27)$$

Since the corrected shutter background for a line is:

$$B' = B + CS \qquad (4\text{-}28)$$

then its variance is:

$$\sigma_{B'}^2 = \sigma_B^2 + \sigma_{CS}^2 \qquad (4\text{-}29)$$

which by substitution becomes:

$$\sigma^2_{B'} = \left\{1 + \frac{2}{t}\right\} \sigma^2_B \qquad (4\text{-}30)$$

Equation 4-30 illustrates the generically true statement that the random error in an arithmetically corrected raw radiance value will always be larger than the random error in the uncorrected value. However, Equation 4-30 also illustrates the fact that a correction for scan-correlated shifts can be made to as high a precision as desired by using a sufficient number of transitions, t, between high and low states. For certain channels, this assumption is adequately valid, while for others, there is a possibility that each of these states might themselves be split into two states. One empirical method to use in deciding the validity of the assumption is to use Equation 4-27 in a linear plot of observed variance in CS, σ^2_{CS}, versus the number of transitions within a pass and then between passes to check for systematic displacement of the lines.

At some value of t, the value of σ^2_{CS} will stop decreasing linearly due to the start of some as yet unaccounted for variability, such as a further two-state splitting. The utility of deriving equations such as 4-27 and 4-30 is that they lead to methods for testing the validity of the assumptions in the model. Furthermore, they also provide a method for testing the statistical significance, at a given level α, of any correction C with a standard deviation σ_C. The correction is statistically significant if:

$$\frac{|C|}{\sigma_C} > t_\alpha \qquad (4\text{-}31)$$

where t_α = the student t distribution number for an α level of significance.

This has the implication for TM, that if the correction is constant with time, then a single experimental collection of data can be used to derive an average value for the correction to a specific level of precision for use on any scene.

This empirical formulation of a correction model might be usefully augmented by using the engineering model of TM that is still available to identify the causes of these radiometric variations.

A causitive engineering model of these systematic variations could produce a more stable set of correction procedures for radiometric ground processing, whether the corrections are done line-by-line between scans or sample-by-sample within scans.

Without within-scene corrections, the TM/PF sensor has a range of radiometric uncertainty of 3 to 8 DN, depending on the band (Table 4-6). This is a second order effect, as defined in Table 4-8. It is of the same order as the current uncertainty, or accuracy, of the absolute radiometry. Relative precision might be improved by an order of magnitude, and thereby reduced to a third order effect, by applying the systematic corrections suggested in this section.

Historically, scientists have wanted to start with raw data rather than processed or "corrected" digital imagery. This has led to a generation of discipline scientists in remote sensing being converted into self-made image processing scientists. The amount of computer capacity and time required to develop calibration procedures and analyze TM imagery no longer affords more than a small number of such scientists that luxury. For multidisciplinary general use of TM digital imagery, the preprocessing steps associated with radiometric and geometric resampling must be an accepted starting place. Ideally, the final corrected product needs to be ready for immediate use in scientific studies, i.e., the final systematically corrected product needs to have minimal errors in absolute and relative radiometry.

Table 4-8. Definition of Size of Uncertainty in TM Radiometry

SIZE OF EFFECT	RELATIVE UNCERTAINTY (%)	ABSOLUTE UNCERTAINTY (DN)
ZERO ORDER	∞	∞
1ST ORDER	10 TO 100	26 TO 255
2ND ORDER	1 TO 10	3 TO 26
3RD ORDER	0.1 TO 1	0.3 TO 3
4TH ORDER	0.01 TO 0.1	0.03 TO 0.3

5822 (50)-84

4.9 SUMMARY OF WITHIN-SCENE VARIABILITY

The effect of bright-target saturation was shown as a function of the distance from the end of exposure to the bright target (see Figure 4-2). This means that the variability introduced into the background will be a function of the scene content and is not a fundamental characteristic of the sensor system. Tables 4-9 and 4-10 illustrate this point. In Table 4-9, per-band average forward-reverse differences are presented for "quiet" scenes (nighttime data for Landsat-4, integrating sphere data for Landsat-5). These measured differences are insignificant (near zero) especially when compared to the same per-band averages taken from Landsat-4 data of a cloudy scene, given in Table 4-10.

Total within-scene variability for individual detectors of Landsat-4 reflective bands is given in Tables 4-11 through 4-16, along with data on forward-reverse differences, scan-correlated shifts and coherent noise. Early data taken on within-scene variability for Landsat-5 (total shutter noise and scan-correlated shifts) is given in Table 4-17. Finally, in Table 4-18, lowest and highest noise measures are given for reference channels of Landsats-4 and 5 reflective bands. (Note, reference channels are identified in Table 4-5.)

Table 4-9

WITHIN-SCENE VARIABILITY
TM SHUTTER BACKGROUND IN "QUIET" SCENES TM/PF ON LANDSAT-4 AND TM/F ON LANDSAT-5
(AVERAGE OF ALL CHANNELS IN A BAND)

BAND	TOTAL VARIABILITY (SD) TM/PF[a] (DN)	TOTAL VARIABILITY (SD) TM/F[b] (DN)	(FWD-REV) DIFFERENCE TM/PF[a] (DN)	(FWD-REV) DIFFERENCE TM/F[b] (DN)
1	±1.24	±0.89	0.20	0.04
2	±0.56	±0.29	0.12	0.06
3	±0.73	±0.51	0.13	0.03
4	±0.41	±0.37	0.09	0.01
5	±0.89	±0.93	0.01	0.08
7	±1.03	±0.93	0.03	0.10

[a] LANDSAT-4 IN-ORBIT NIGHT SCENE OF BUFFALO, NY (40037-02243, 22 AUG 82)

[b] LANDSAT-5 PRE-LAUNCH AMBIENT INTEGRATING SPHERE (5-198-10563, 30 AUG 83)

Table 4-10

WITHIN-SCENE VARIABILITY

TM SHUTTER BACKGROUND IN CLOUDY SCENE
CLOUDS ON WESTERN EDGE OF SCENE
SAN FRANCISCO, CA (40392-18152, 12 AUG 83)
(AVERAGE OF ALL CHANNELS IN A BAND)

	TOTAL VARIABILITY (SD) BEFORE AND AFTER DC RESTORE		(FWD-REV) DIFFERENCE BEFORE AND AFTER DC RESTORE	
BAND	B-BDC (DN)	B-ADC (DN)	B-BDC (DN)	B-ADC (DN)
1	±1.45	±1.42	−0.54	1.53
2	±1.11	±1.51	1.29	2.56
3	±1.24	±1.46	1.31	2.44
4	±0.71	±1.02	0.39	1.62
5	±0.93	±0.89	−0.21	0.02
7	±1.05	±1.01	−0.15	0.05

Table 4-11

BAND 1 ON LANDSAT-4 TM/PF, WITHIN-SCENE VARIABILITY (IN DN)

	TOTAL VARIABILITY STANDARD DEVIATION OF SHUTTER IN AND AROUND DC RESTORATION			(FWD-REV) DIFFERENCE BACKGROUND ON SHUTTER IN AND AROUND DC RESTORATION			SCAN-CORRELATED SHIFTS		COHERENT NOISE	
	PM SCENE[a]	CLOUDY SCENE[b]		PM SCENE[a]	CLOUDY SCENE[b]		TYPE 4-1.4 AVERAGE[b]	TYPE 4-7.7 AVG[a,b]	32 KHz (3.2 mf) (area ± 2 mf of peak)	6 KHz (18 mf)
CHANNEL	SD(B)	SD(B-BDC)	SD(B-ADC)	ΔBFR	ΔBFR (BDC)	ΔBFR (ADC)	CS(4-1)	CS (4-7)	CC (32)	CC(6)
16	±1.5	±1.7	±1.7	0.1	-0.6	1.2	0.1	0.0	2.6	0.2
15	±1.4	±1.5	±1.6	0.3	-0.1	2.5	0.0	-0.1	1.0	0.3
14	±1.3	±1.5	±1.4	0.1	-0.6	1.6	0.2	0.0	1.7	0.2
13	±1.3	±1.4	±1.4	0.3	-0.2	2.0	0.1	-0.1	0.8	0.3
12	±1.1	±1.6	±1.4	0.2	-0.4	1.3	1.7	0.0	0.9	0.4
11	±1.3	±1.4	±1.4	0.3	-0.4	2.0	0.0	-0.1	1.0	0.2
10	±1.0	±1.4	±1.4	0.1	-0.6	1.8	1.0	0.0	0.6	0.3
9	±1.1	±1.2	±1.2	0.2	-0.5	1.4	0.0	0.0	0.7	0.2
8	±1.2	±1.5	±1.5	0.1	-1.1	1.3	0.8	-0.1	1.8	0.1
7	±1.3	±1.4	±1.3	0.2	-0.5	1.4	0.0	-0.1	0.6	0.4
6	±1.3	±1.6	±1.5	0.1	-1.3	1.2	0.2	0.0	1.1	0.2
5	±1.1	±1.2	±1.0	0.2	-0.4	1.0	0.0	-0.1	1.1	0.3
4	±1.2	±1.8	±1.6	0.2	-0.5	1.6	2.0	0.0	0.3	0.4
3	±1.1	±1.2	±1.2	0.2	-0.6	1.4	0.0	-0.1	1.2	0.4
2	±1.3	±1.6	±1.6	0.2	-0.7	1.7	0.1	-0.1	1.6	0.1
1	±1.3	±1.4	±1.3	0.2	-0.4	1.3	0.3	-0.1	1.0	0.4

[a] PM BUFFALO, NY (40037-02243), [b] SAN FRANCISCO, CA (40392-18152), [c] WHITE SANDS, NM (40171-17080)

Table 4-12

BAND 2 ON LANDSAT-4 TM/PF, WITHIN-SCENE VARIABILITY (IN DN)

	TOTAL VARIABILITY STANDARD DEVIATION OF SHUTTER IN AND AROUND DC RESTORATION			(FWD-REV) DIFFERENCE BACKGROUND ON SHUTTER IN AND AROUND DC RESTORATION			SCAN-CORRELATED SHIFTS		COHERENT NOISE	
	PM SCENE[a]	CLOUDY SCENE[b]		PM SCENE[a]	CLOUDY SCENE[b]		TYPE 4-1.4 AVERAGE[b]	TYPE 4-7.7 AVG[a,b]	32 KHz (3.2 mf) (area ± 2 mf of peak)	6 KHz (18 mf)
CHANNEL	SD(B)	SD(B-BDC)	SD(B-ADC)	ΔBFR	ΔBFR (BDC)	ΔBFR (ADC)	CS(4-1)	CS (4-7)	CC (32)	CC(6)
16	±0.5	±1.7	±1.6	0.1	1.5	2.9	0.0	0.0	0.2	0.1
15	±0.6	±1.5	±1.5	0.3	1.3	2.6	0.0	0.0	0.1	0.1
14	±0.4	±1.5	±1.5	0.1	1.2	2.5	0.0	0.0	0.1	0.0
13	±0.6	±1.4	±1.6	0.3	1.5	2.8	0.0	0.0	0.1	0.1
12	±0.5	±1.6	±1.5	0.2	1.3	2.7	0.0	0.0	0.2	0.0
11	±0.5	±1.4	±1.4	0.3	1.3	2.4	0.0	0.0	0.1	0.0
10	±0.4	±1.4	±1.4	0.1	1.2	2.5	0.0	0.0	0.1	0.0
9	±0.5	±1.2	±1.5	0.2	1.3	2.6	0.0	0.0	0.0	0.0
8	±0.5	±1.5	±1.5	0.1	1.3	2.7	0.0	0.0	0.2	0.0
7	±0.5	±1.4	±1.4	0.2	1.2	2.3	0.0	0.0	0.1	0.1
6	±0.5	±1.6	±1.5	0.1	1.3	2.7	0.0	0.0	0.3	0.1
5	±0.5	±1.2	±1.4	0.2	1.3	2.4	0.0	−0.1	0.2	0.1
4	±0.7	±1.8	±1.4	0.2	1.1	2.2	0.1	0.0	0.1	0.1
3	±0.6	±1.2	±1.5	0.2	1.3	2.6	0.0	−0.1	0.2	0.1
2	±1.0	±1.6	±1.7	0.2	1.1	2.6	0.0	0.0	0.3	0.1
1	±0.7	±1.4	±1.5	0.2	1.3	2.6	0.1	−0.2	0.2	0.2

[a]PM BUFFALO, NY (40037-02243), [b]SAN FRANCISCO, CA (40392-18152), [c]WHITE SANDS, NM (40171-17080)

Table 4-13

BAND 3 ON LANDSAT-4 TM/PF, WITHIN-SCENE VARIABILITY (IN DN)

	TOTAL VARIABILITY STANDARD DEVIATION OF SHUTTER IN AND AROUND DC RESTORATION			(FWD-REV) DIFFERENCE BACKGROUND ON SHUTTER IN AND AROUND DC RESTORATION			SCAN-CORRELATED SHIFTS		COHERENT NOISE (area ± 2 mf of peak)	
	PM SCENE[a]	CLOUDY SCENE[b]		PM SCENE[a]	CLOUDY SCENE[b]		TYPE 4-1.4 AVERAGE[b]	TYPE 4-7.7 AVG[a,b]	32 KHz (3.2 mf)	6 KHz (18 mf)
CHANNEL	SD(B)	SD(B-BDC)	SD(B-ADC)	ΔBFR	ΔBFR (BDC)	ΔBFR (ADC)	CS(4-1)	CS (4-7)	CC (32)	CC(6)
16	±1.0	±1.5	±1.6	0.1	1.3	2.7	0.1	0.6	0.9	0.3
15	±0.9	±1.4	±1.4	0.2	1.4	2.3	0.2	-0.3	0.2	0.3
14	±0.5	±1.2	±1.6	0.0	1.6	2.7	0.0	0.0	0.4	0.1
13	±0.8	±1.3	±1.4	0.2	1.4	2.3	0.1	-0.1	0.2	0.1
12	±0.4	±1.1	±1.6	0.1	1.4	2.8	0.0	0.0	0.1	0.1
11	±0.7	±1.2	±1.4	0.1	1.3	2.3	0.0	-0.1	0.0	0.2
10	±0.5	±1.1	±1.7	0.1	1.4	3.0	0.0	0.0	0.3	0.1
9	±0.8	±1.3	±1.6	0.2	1.5	2.8	0.0	0.0	0.1	0.2
8	±0.9	±1.2	±1.6	0.1	1.2	2.6	0.0	0.0	1.6	0.1
7	±0.7	±1.2	±1.4	0.1	1.2	2.3	0.0	-0.1	0.1	0.2
6	±0.5	±1.0	±1.5	0.1	1.4	2.6	0.0	0.0	0.3	0.2
5	±0.8	±1.2	±1.4	0.2	1.2	2.4	0.1	-0.2	0.1	0.1
4	±0.7	±1.1	±1.4	0.1	1.0	2.2	0.0	0.0	1.2	0.2
3	±0.8	±1.2	±1.2	0.2	1.1	2.0	0.1	-0.2	0.1	0.2
2	±0.6	±1.0	±1.3	0.1	0.9	2.1	0.0	0.1	0.2	0.3
1	±1.3	±1.7	±1.3	0.3	1.4	2.0	0.3	0.5	0.3	0.5

[a] PM BUFFALO, NY (40037-02243), [b] SAN FRANCISCO, CA (40392-18152), [c] WHITE SANDS, NM (40171-17080)

Table 4-14

BAND 4 ON LANDSAT-4 TM/PF, WITHIN-SCENE VARIABILITY (IN DN)

	TOTAL VARIABILITY STANDARD DEVIATION OF SHUTTER IN AND AROUND DC RESTORATION			(FWD-REV) DIFFERENCE BACKGROUND ON SHUTTER IN AND AROUND DC RESTORATION			SCAN-CORRELATED SHIFTS		COHERENT NOISE	
		CLOUDY SCENE[b]			CLOUDY SCENE[b]				32 KHz (3.2 mf)	6 KHz (18 mf)
									(area ± 2 mf of peak)	
CHANNEL	PM SCENE[a] SD(B)	SD(B-BDC)	SD(B-ADC)	PM SCENE[a] ΔBFR	ΔBFR (BDC)	ΔBFR (ADC)	TYPE 4-1.4 AVERAGE[b] CS(4-1)	TYPE 4-7.7 AVG[a,b] CS (4-7)	CC (32)	CC(6)
16	±0.3	±0.7	±0.9	0.0	0.5	1.4	0.2	0.0	0.2	0.3
15	±0.4	±0.6	±1.1	0.1	0.4	1.7	0.1	0.0	0.2	0.1
14	±0.3	±0.8	±1.2	0.1	0.6	1.9	0.0	0.0	0.2	0.0
13	±0.4	±0.6	±0.8	0.1	0.4	1.3	0.0	0.0	0.2	0.1
12	±0.3	±0.7	±1.1	0.1	0.4	1.8	0.1	0.0	0.1	0.1
11	±0.3	±0.6	±0.9	0.1	0.3	1.4	0.1	0.0	0.3	0.1
10	±0.3	±0.7	±1.0	0.1	0.4	1.6	0.0	0.0	0.3	0.0
9	±0.3	±0.6	±1.1	0.1	0.3	1.8	0.0	0.0	0.2	0.1
8	±0.6	±0.9	±1.1	0.1	0.3	1.6	0.0	−0.1	0.8	0.1
7	±0.3	±0.6	±0.9	0.1	0.4	1.5	0.0	0.0	0.2	0.1
6	±0.5	±0.7	±1.1	0.1	0.4	1.8	0.0	0.0	0.3	0.1
5	±0.4	±0.7	±1.0	0.1	0.5	1.7	0.0	0.0	0.3	0.1
4	±0.5	±0.8	±1.0	0.1	0.2	1.6	0.0	−0.1	0.5	0.0
3	±0.6	±0.7	±1.1	0.2	0.4	1.9	0.0	0.0	0.4	0.2
2	±0.4	±0.8	±1.1	0.1	0.3	1.7	0.0	−0.1	0.3	0.1
1	±0.6	±0.7	±0.8	0.1	0.5	1.3	0.2	−0.1	0.6	0.2

[a] PM BUFFALO, NY (40037-02243), [b] SAN FRANCISCO, CA (40392-18152), [c] WHITE SANDS, NM (40171-17080)

Table 4-15

BAND 5 ON LANDSAT-4 TM/PF, WITHIN-SCENE VARIABILITY (IN DN)

	TOTAL VARIABILITY STANDARD DEVIATION OF SHUTTER IN AND AROUND DC RESTORATION			(FWD-REV) DIFFERENCE BACKGROUND ON SHUTTER IN AND AROUND DC RESTORATION			SCAN-CORRELATED SHIFTS		COHERENT NOISE	
	PM SCENE[a]	CLOUDY SCENE[b]		PM SCENE[a]	CLOUDY SCENE[b]				32 KHz (3.2 mf)	6 KHz (18 mf)
CHANNEL	SD(B)	SD(B-BDC)	SD(B-ADC)	ΔBFR	ΔBFR (BDC)	ΔBFR (ADC)	TYPE 4-1.4 AVERAGE[b] CS(4-1)	TYPE 4-7.7 AVG[a,b] CS (4-7)	(area ± 2 mf of peak) CC (32)	CC(6)
16	±0.8	±0.9	±0.8	0.1	-0.3	0.2	0.0	-0.1	[0.2]	[0.1]
15	±0.9	±0.9	±0.9	0.1	-0.3	0.1	-0.1	-0.1	[0.3]	[0.1]
14	±0.9	±0.9	±0.9	0.0	-0.1	0.0	0.0	-0.1	[0.1]	[0.1]
13	±0.9	±0.9	±0.9	0.0	-0.1	0.0	0.0	0.0	[0.1]	[0.1]
12	±0.9	±0.9	±0.9	0.0	-0.1	0.0	0.0	0.0	[0.0]	[0.1]
11	±0.9	±1.0	±0.9	0.0	-0.1	0.0	0.0	0.0	[0.1]	[0.1]
10	±0.9	±1.0	±0.9	0.0	-0.1	0.0	0.0	0.6	[0.1]	[0.0]
9	±0.9	±0.9	±0.9	0.0	-0.1	-0.1	0.0	0.0	[0.0]	[0.0]
8	±0.9	±0.9	±0.8	0.0	-0.1	0.0	0.0	-0.2	[0.2]	[0.0]
7	±1.1	±1.1	±1.1	0.0	-0.1	0.0	0.0	0.1	[0.2]	[0.2]
6	±0.9	±0.9	±0.9	0.0	-0.1	0.0	0.0	-0.1	[0.2]	[0.0]
5	±0.9	±0.9	±0.9	0.0	-0.1	-0.1	-0.1	0.0	[0.1]	[0.0]
4	±0.8	±0.9	±0.9	0.0	-0.1	0.0	0.1	-0.1	[0.0]	[0.1]
3	—	—	—	—	—	—	0.0	0.0	—	—
2	±0.8	±0.9	±0.8	0.1	-0.7	-0.1	0.1	-0.1	[0.1]	[0.1]
1	±0.8	±0.9	±0.9	0.0	-0.7	-0.1	0.0	0.1	[0.2]	[0.0]

[a]PM BUFFALO, NY (40037-02243), [b]SAN FRANCISCO, CA (40392-18152), [c]WHITE SANDS, NM (40171-17080)

Table 4-16

BAND 7 ON LANDSAT-4 TM/PF, WITHIN-SCENE VARIABILITY (IN DN)

CHANNEL	TOTAL VARIABILITY STANDARD DEVIATION OF SHUTTER IN AND AROUND DC RESTORATION			(FWD-REV) DIFFERENCE BACKGROUND ON SHUTTER IN AND AROUND DC RESTORATION			SCAN-CORRELATED SHIFTS		COHERENT NOISE	
	PM SCENE^a SD(B)	CLOUDY SCENE^b		PM SCENE^a ΔBFR	CLOUDY SCENE^b		TYPE 4-1.4 AVERAGE^b CS(4-1)	TYPE 4-7.7 AVG^{a,b} CS (4-7)	32 KHz (3.2 mf) (area ±2 mf of peak) CC (32)	6 KHz (18 mf) CC(6)
		SD(B-BDC)	SD(B-ADC)		ΔBFR (BDC)	ΔBFR (ADC)				
16	±1.0	±1.0	±1.0	0.1	−0.2	0.2	0.1	−0.2	[0.2]	[0.1]
15	±0.8	±0.8	±0.8	0.1	−0.2	0.1	0.0	0.2	[0.1]	[0.2]
14	±1.1	±1.1	±1.1	0.0	−0.1	0.0	0.1	−0.1	[0.0]	[0.1]
13	±0.8	±0.9	±0.8	0.0	−0.1	0.0	0.0	0.2	[0.1]	[0.1]
12	±1.0	±1.0	±1.0	0.0	0.0	0.0	0.1	−0.2	[0.2]	[0.1]
11	±1.0	±1.0	±0.9	0.0	0.0	0.0	0.0	−0.2	[0.1]	[0.0]
10	±1.1	±1.1	±1.1	0.0	0.0	0.0	0.1	−0.4	[0.3]	[0.0]
9	±1.0	±1.0	±1.0	0.0	−0.1	0.0	−0.1	0.2	[0.1]	[0.0]
8	±1.0	±1.0	±0.9	0.0	−0.1	0.0	0.0	−0.3	[0.1]	[0.1]
7	±2.0	±1.8	±1.8	0.0	−0.2	0.2	−0.1	0.9	[0.1]	[0.2]
6	±1.0	±1.0	±1.0	0.0	0.0	0.0	0.1	−0.3	[0.1]	[0.1]
5	±0.9	±1.0	±0.9	0.0	0.0	0.0	0.0	0.2	[0.0]	[0.1]
4	±1.0	±1.0	±1.0	0.0	−0.1	0.0	0.1	−0.2	[0.2]	[0.1]
3	±0.9	±0.9	±0.9	0.0	−0.1	0.0	−0.1	0.3	[0.1]	[0.0]
2	±1.0	±1.0	±1.0	0.1	−0.6	0.1	0.0	−0.3	[0.2]	[0.1]
1	±1.0	±1.0	±1.0	0.0	−0.6	0.1	0.0	0.3	[0.1]	[0.1]

^{a}PM BUFFALO, NY (40037-02243), ^{b}SAN FRANCISCO, CA (40392-18152), ^{c}WHITE SANDS, NM (40171-17080)

Table 4-17

LANDSAT-5 TM/F WITHIN-SCENE VARIABILITY (IN DN)

	BAND 1		BAND 2		BAND 3		BAND 4		BAND 5	BAND 7
CHANNEL	TOTAL SHUTTER NOISE[a] SD(B)	SHIFT TYPE 5-3.1 AVERAGE[b] CS (5-3)	TOTAL SHUTTER NOISE[a] SD(B)	SHIFT TYPE 5-3.1 AVERAGE[b] CS (5-3)	TOTAL SHUTTER NOISE[a] SD(B)	SHIFT TYPE 5-3.1 AVERAGE[b] CS (5-3)	TOTAL SHUTTER NOISE[a] SD(B)	SHIFT TYPE 5-3.1 AVERAGE[b] CS (5-3)	TOTAL SHUTTER NOISE[a] SD(B)	TOTAL SHUTTER NOISE[a] SD(B)
16	±0.9	−0.2	±0.3	0.7	±0.5	0.3	±0.5	0.0	±0.8	±0.9
15	±0.8	0.0	±0.3	0.3	±0.4	0.3	±0.3	0.1	±0.8	±0.8
14	±1.0	−0.3	±0.2	0.2	±0.4	0.3	±0.4	0.0	±0.8	±0.9
13	±0.8	0.0	±0.3	0.4	±0.5	0.3	±0.3	0.2	±0.9	±0.8
12	±0.9	−0.2	±0.2	0.1	±0.7	0.3	±0.3	0.0	±1.0	±1.0
11	±0.9	0.0	±0.3	0.3	±0.5	0.5	±0.4	0.1	±0.8	±0.9
10	±0.9	−0.3	±0.2	0.0	±0.4	0.4	±0.3	0.0	±1.3	±1.0
9	±0.8	0.0	±0.3	0.2	±0.6	0.4	±0.4	0.1	±1.0	±1.3
8	±1.0	−0.1	±0.2	0.1	±0.5	0.2	±0.4	0.0	±0.9	±1.0
7	±0.8	0.0	±0.3	0.3	±0.5	0.3	±0.3	0.1	±1.3	±0.9
6	±0.9	−0.1	±0.2	0.1	±0.4	0.6	±0.4	0.0	±0.8	±0.9
5	±0.8	0.0	±0.3	0.3	±0.6	0.4	±0.3	0.1	±0.9	±0.8
4	±1.0	−0.1	±0.3	0.0	±0.5	0.5	±0.4	0.3	±0.9	±0.9
3	±0.9	0.0	±0.4	0.4	±0.6	0.5	±0.5	0.1	±0.9	±0.9
2	±1.0	−0.1	±0.4	0.0	±0.5	0.2	±0.4	0.1	±0.8	±1.0
1	±1.0	0.0	±0.5	0.7	±0.6	0.5	±0.2	0.4	±0.8	±0.9

[a] PRE-LAUNCH "IS GOLDEN TAPE" (5-198-10563, 16:14 30 AUG 83)

[b] AVERAGED (5-596-13285), (5-198-10563) AND (50005-16221)

Table 4-18

TM RADIOMETRIC VARIABILITY (IN DN)

	BAND 1	BAND 2	BAND 3	BAND 4	BAND 5	BAND 7
LANDSAT-4 TM/PF						
LOWEST NOISE						
SHUTTER rms	± 1.1	± 0.4	± 0.4	± 0.3	± 0.8	± 0.8
HIGHEST NOISE						
SHUTTER rms	± 1.5	± 1.0	± 1.3	± 0.6	± 1.1	± 2.0
SHIFT TYPE 4-1	2.0	—	0.3	0.2	−0.1	—
SHIFT TYPE 4-7	—	−0.2	0.6	—	0.6	0.9
32 KHz (3.2 mf)	2.6	0.3	1.6	0.8	[0.2]	[0.3]
6 KHz (18 mf)	0.4	0.2	0.5	0.3	[0.2]	[0.2]
LANDSAT-5 TM/F						
LOWEST NOISE						
SHUTTER rms	± 0.8	± 0.2	± 0.5	± 0.2	± 0.8	± 0.8
HIGHEST NOISE						
SHUTTER rms	± 1.0	± 0.5	± 0.7	± 0.5	± 1.3	± 1.3
SHIFT TYPE 5-3	−0.3	0.7	0.5	0.4	—	—

SECTION 5 - PROCESSING EFFECTS ON RADIOMETRY

In addition to the impact of innate sensor-induced uncertainties, information derived from TM imagery can also be affected by the processes used to calibrate the sensor, to apply the calibration to imagery, and to extract information. Procedures for radiometrically pre-processing of TM data used during the Scrounge-era are described elsewhere (Barker, Abrams et al., 1984b). The residual uncertainty associated with applying a single correction for gain and bias for each channel to a whole TM scene were discussed in Section 4 above. Some of the uncertainties of using the TM internal calibrator for absolute calibration in space were discussed in Section 3. This section focuses on additional uncertainties associated with:

- Existing and proposed procedures for calibration of individual channels with the TM internal calibrator
- Procedures for applying calibration to TM digital imagery
- Procedures for converting from radiance to reflectance
- Procedures for converting radiance or reflectance data into information

It is assumed that corrections to the raw data from sensor-related anomalies discussed previously have been performed prior to the processing procedures discussed here. However, repeated introduction of the $1/\sqrt{12}$ quantization error is to be avoided. Every time the digital numbers are changed, there is the potential for the introduction of additional error. Therefore, it is better to maintain corrected values in floating point notation, or in 16-bit bins, rather than their original 8-bit bins, through as many changes as possible; ideally, through to the finally derived information or value-added product.

5.1 CALIBRATION WITH INTERNAL CALIBRATOR

The random error associated with the use of the internal calibrator (IC) can be reduced by more than a factor of two by optimizing processing parameters. The random error can perhaps be reduced further by modeling trends. Factors which need to be examined for obtaining a high precision on the measurement of the calibration pulses include:

- Where in the data stream to measure background
- Whether or not to use net signals
- What portion of the calibration data to use as a collect window
- How to perform the calibration pulse integration step
- How to average the calibration pulses which are calculated for each line
- What regression strategy to use in terms of lamps and lamp configurations
- How to perform within-scene smoothing to correct for temperature-dependence of the pulse, odd-even shifts, and within/and between-band correlations
- How, or if, to smooth within a pass
- How, or whether, to model for between-date smoothing.

Data exist, or can be collected, to model these effects.

The radiometric stability of the TM sensor makes it likely that the reproducibility of the calibration can be improved by more than a factor of five once the above factors are understood and incorporated into improved ground-processing procedures. The increased precision from these improvements could become particularly important if procedures are developed for creating images of estimated at-surfaces reflectances for a whole pass by peeling off atmospheric effects.

Potential corrections and additional calculations using the calibration data are not likely to significantly impact the computer-processing time for applying the calibration to an image, as long as such calibrations require at least two passes over the raw TM digital data.

5.1.1 BACKGROUND CALCULATION

Proper background data are needed for calculation of net signal for both calibration data and image data. Whether background is considered as a variable to be calculated by line, or within a line, or whether the background is considered as a constant to be estimated from the shutter or a no-lamp-on 000 configuration, it is important to use an appropriate background. There have not been sufficient studies to date to definitively answer either key question, namely, where is the appropriate background, and how is it to be measured.

Current use by TIPS of lamp-state 000 values for background radiometric calibration is not sufficiently precise. Four reasons for this insufficiency are:

- Some high biasing of the background from negative DN values being stored in bin zero
- High values of background from an image-dependent light leak in part of the 148 mf collect window for Landsat-5 (Section 5.1.3)
- Insufficient data to make a line-by-line correction for scan-correlated shift (Section 4.5) or unrepresentative averaging for this shift over a whole scene from 40 consecutive scans of lamp-state 000
- Variations in background throughout the scene due to factors such as bright target saturation over clouds (Section 4.3).

TM was the first sensor in the Landsat series in which a positive non-zero offset of approximately 2 DN was used so that random variations about this mean would not result in values below this mean being stored collectively in bin zero. While this 2 DN offset was not large enough to prevent some negative values from occurring in Bands 1, 5 and 7 on TM/PF, nevertheless it may have prevented overestimating of background, except in a few particularly noisy channels; this effect can be quantitatively assessed. Use of uncorrected lamp-state 000 values introduces variability from scan-correlated shifts that is of the same order as the offset itself. Whether or not lamp-state 000 values, taken for 40 scans with the IC automatic sequencer, could provide appropriate backgrounds, after correction (Section 4), for all 360 scans in a repeating cycle remains to be determined from corrected data.

In any case, use of the shutter for some backgrounds will be necessary. First, it was always necessary for calibration of the emissive thermal IR Band, Band 6, since two points are necessary for calculating gain and bias; the black body temperature requires approximately 20 minutes to equilibrate and therefore has not been operated at more than one of its two temperatures during a single pass. Second, it is probably desirable to change the normal operating mode of the Mapper from automatic sequencer to manual use of a single lamp in order to preserve the absolute calibration on two of the three lamps, in which case a shutter value for background would be needed in order to avoid manually switching the settings back and forth from lamp-state 000 to one-lamp-on within a pass.

Verification of the region on the shutter to be measured for background remains to be done on both TM sensors. During the Scrounge-era, there was an initial collection of 52 mf from one region of the shutter before DC restoration in the forward scan and after DC restoration in the reverse scan. Final Scrounge-era calibration data tapes, CCT-ADDS, contained background collects from two regions on the shutter on both sides of expected DC restoration in each scan direction; each region was required to be a multiple of four minor frames, and to start with a minor frame containing the initial unrepeated value for Band 6. Currently TIPS-era processing is making only one 52 mf background (shutter) collect from the shutter region and it appears to be inside the region of DC restoration. Outlier rejection algorithms need to be used to remove severe noise and to see if systematic noise is present, such as from the resetting of the scan-line corrector (SLC).

An attempt was made to position these two 24 and 28 mf Scrounge-era collect windows before and after the period of electronic DC restoration, which occurs during obscuration of the optical axis by the shutter. This was necessary because the initial 52 mf background within the DC restore region was found to be changing in some bands, perhaps due to recovery from droop and bright-target saturation effects. It appears that some of these Scrounge-era collect windows may have incomplete obscuration because they were set too close to the edge of the shutter, especially in Band 6; this can be corrected by excluding some minor frames from the calculations, at the cost of a reduced precision in the mean value of the background. It is also possible to use regions within the 148 mf calibration collect window, immediately adjacent to the 40-50 mf calibration pulse. This possibility is more feasible in the TIPS-era now that calibration collects are set individually for each channel so as to put the peak in the center of the 148 mf window.

5.1.2 PULSE WINDOW LOCATIONS

During the Scrounge-era processing, the 148 mf collect windows of calibration data could not be adjusted for each channel. Pulse locations varied continuously from channel 1 through channel 16 for each reflective band, and the 50 mf wide pulses spread over all but about 20 mf of the collect window. Prior to December 1982, the collect window clipped part of some peaks of pulses in channels 1 through 4 of Band 1 (Barker, Abrams, et al. 1984). The processing algorithms did not adjust for this clipping and therefore the calculated gain for Band 1 Channel 1 was over estimated by about 5 percent. Clipping was also a problem in Band 6. Clipping is not as critical a problem in the TIPS-era because the peaks are individually centered for each channel, and therefore the margin for error in a priori knowledge of the peak location is approximately 50 mf, instead of 10 mf. Variations in line length are up to 10 mf.

5.1.3 PULSE INTEGRATION PARAMETERS

During the calibration of both TM/PF and TM/F, the IC pulse-integration methodology for pre-launch absolute radiometric calibration was a 31 mf "Hughes" algorithm. Various peak-location algorithms proved to be adequate to a precision of better than one minor frame. However, the IC pulses do not have flat tops, especially in the case of Landsat-5 TM/F (Figure 5-1). Therefore, the peak integration methodology affects the precision of the measurement.

A light leak in the shutter, which interferes with current procedures for pulse integration, has been observed as a secondary pulse in the calibration region on Landsat-5 TM/F (Figure 5-1, 2nd of 2). This leak has the following characteristics:

- Fixed Location. The center of the secondary peak is always a fixed distance from the center of the calibration pulse:

  +(53 ± 2) mf in forward scans

  -(53 ± 2) mf in reverse scans

- Always Present. A single secondary peak is always present, even in the 000 no-lamp-on state.

- Variable Intensity and Shape. Intensities and shape of the secondary peaks are a function of the light source being imaged along the optical axis during obscuration by the shutter. Actual values for radiant intensity are unknown since the imaging is 2 Km (reverse) or 20 Km (forward) outside the 180 Km field-of-view, except for

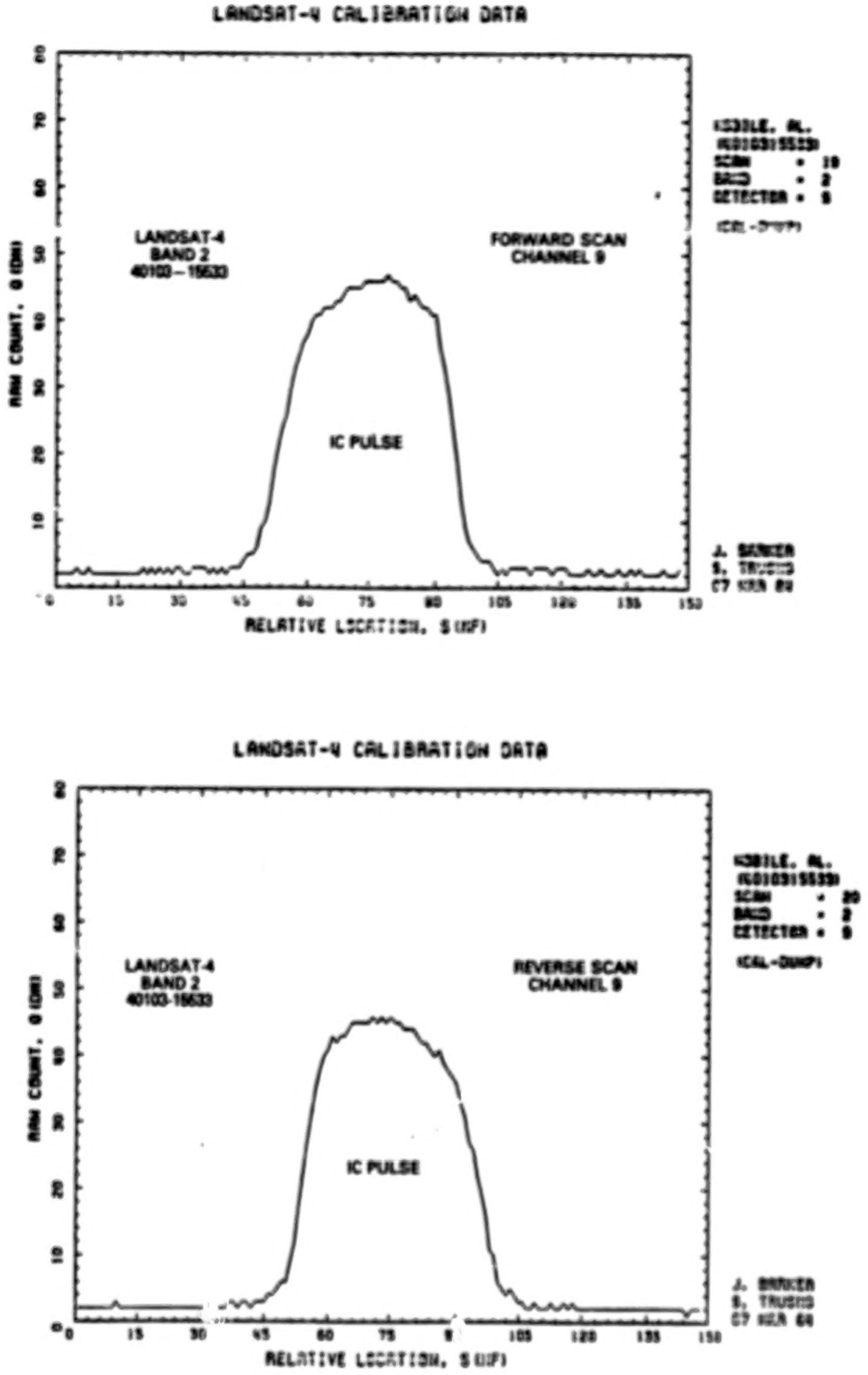

Figure 5-1. Landsat-4 and -5 Calibration Pulse and Light Leak (1 of 2)

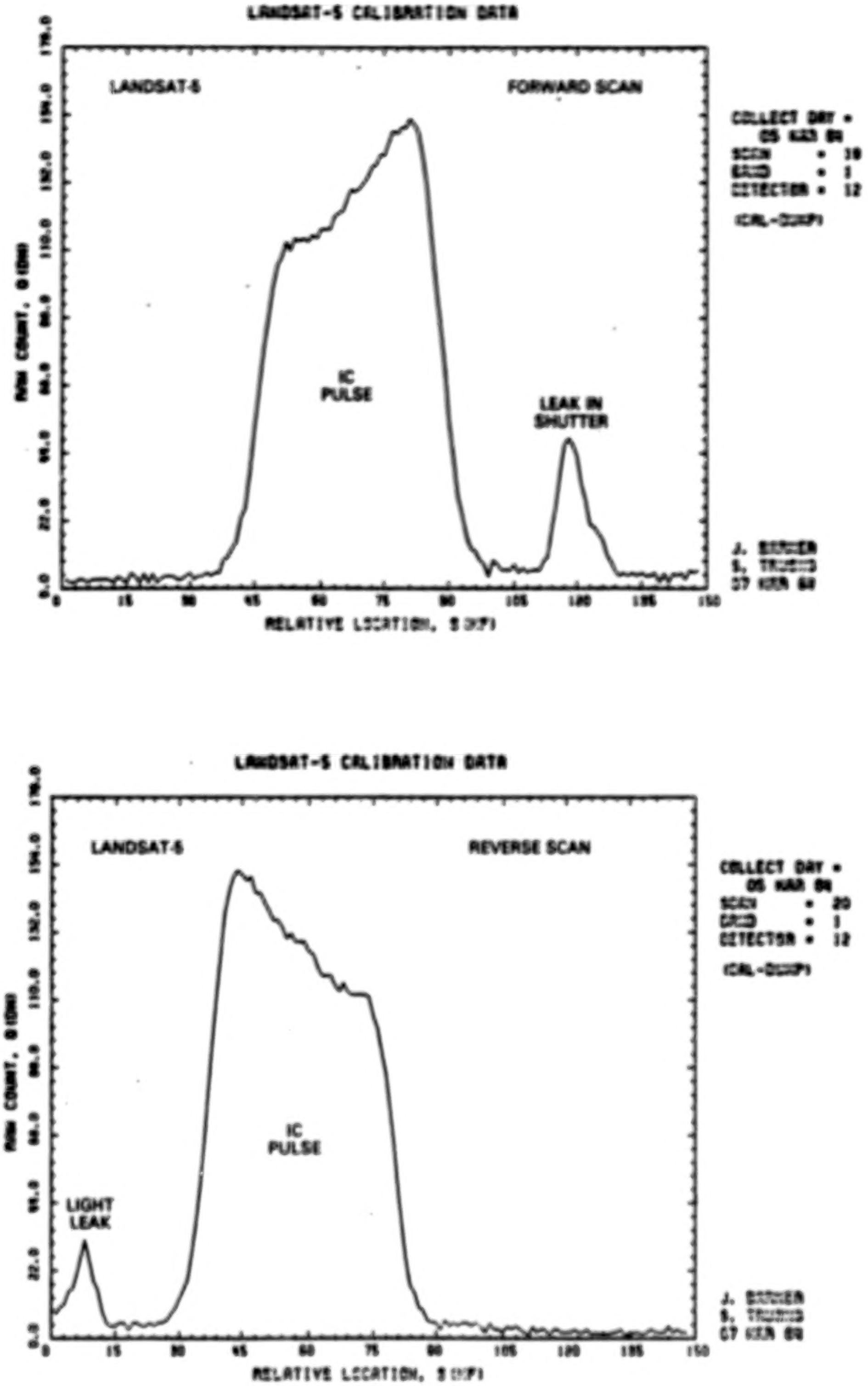

Figure 5-1. Landsat-4 and -5 Calibration Pulse and Light Leak (2 of 2)

the observed peaks when the scan mechanism was locked during "droop" tests. However, cloudy scenes have given the highest values in the PFP bands and clear scenes over land have given much lower secondary peaks. For a pre-launch flooding lamp test (9 Oct 82), the intensity of all secondary peaks differed by about a factor of two in the forward and reverse directions. The width of the secondary peak is as great as 24 mf in Band 5 and 16 mf in Band 4.

The origin of this light leak appears to be an incomplete masking of the lens on the shutter. Recommendations for reducing the impact of this light leak during TIPS processing are given in Section 6.3.2.

A few parametric studies on pulse integration width have been done. Results of a plot of σ_P versus pulse-integration width, w, is given in Figure 5-2 for one lamp state for one channel in each reflective band on TM/PF. A plot of the logarithm of $(100\sigma_P/P)$ versus w is given in Figure 5-3 for three channels in TM/F. Both plots illustrate the non-optimum nature of a $w = 31$ mf Hughes pulse-integration width. Severely non-flat IC pulses in Landsat-5 can result in this coefficient of variation (% error), CV, which is a factor of 2 to 4 higher than optimum for the current TIPS-era constant width of $w = 65$ mf.

The optimum pulse-integration width appears to be between 32 and 42 mf, before the slopes are reached on each side of the peak, and is channel dependent. A width of 39 mf is being used for both TM/PF and TM/F for current TRAPP processing. Parametric studies taken on different dates for all channels and for all lamp configurations need to wait until the largest systematic errors have been reduced, and the parametric analysis will be more sensitive.

5.1.4 PULSE AVERAGING PARAMETERS

Averaged pulse, $\bar{P}$, values are more precisely determined if the within-line pulse values, P, which are not too close to a change in lamp configuration are used to calculate the average. When the IC automatic sequencer is used, a set of pulses need to be chosen which show no trend with scan number. If there is a trend, it needs to be normalized out if it is characteristic of the IC system, or incorporated into a line-by-line calibration if it is a reflection of a real change in the gain and offset of the individual channels. Because of the slow cool down of the IC lamps in

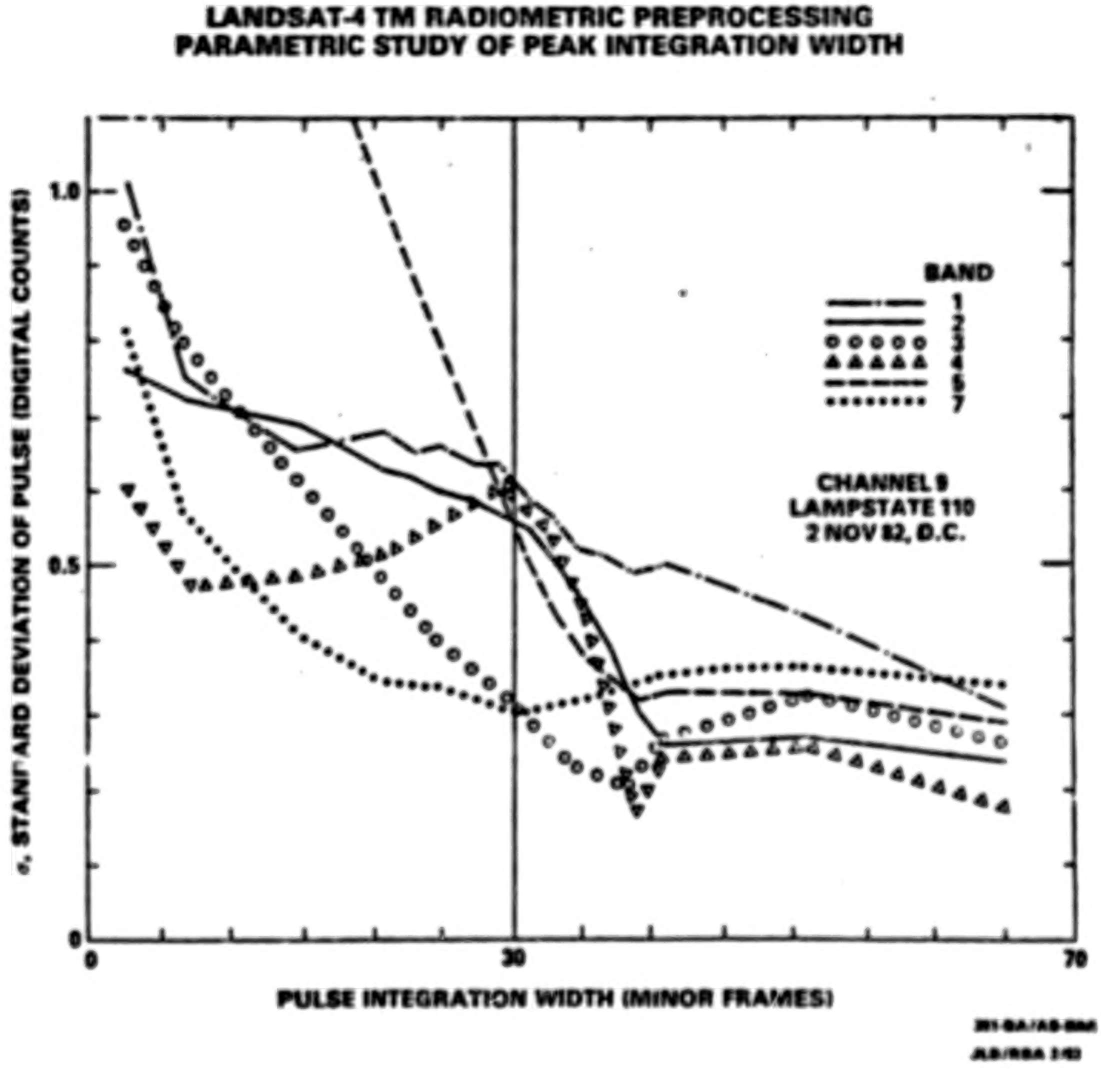

Figure 5-2. Parametric Study on Landsat-4 TM/PF Calibration-Pulse Integration Width

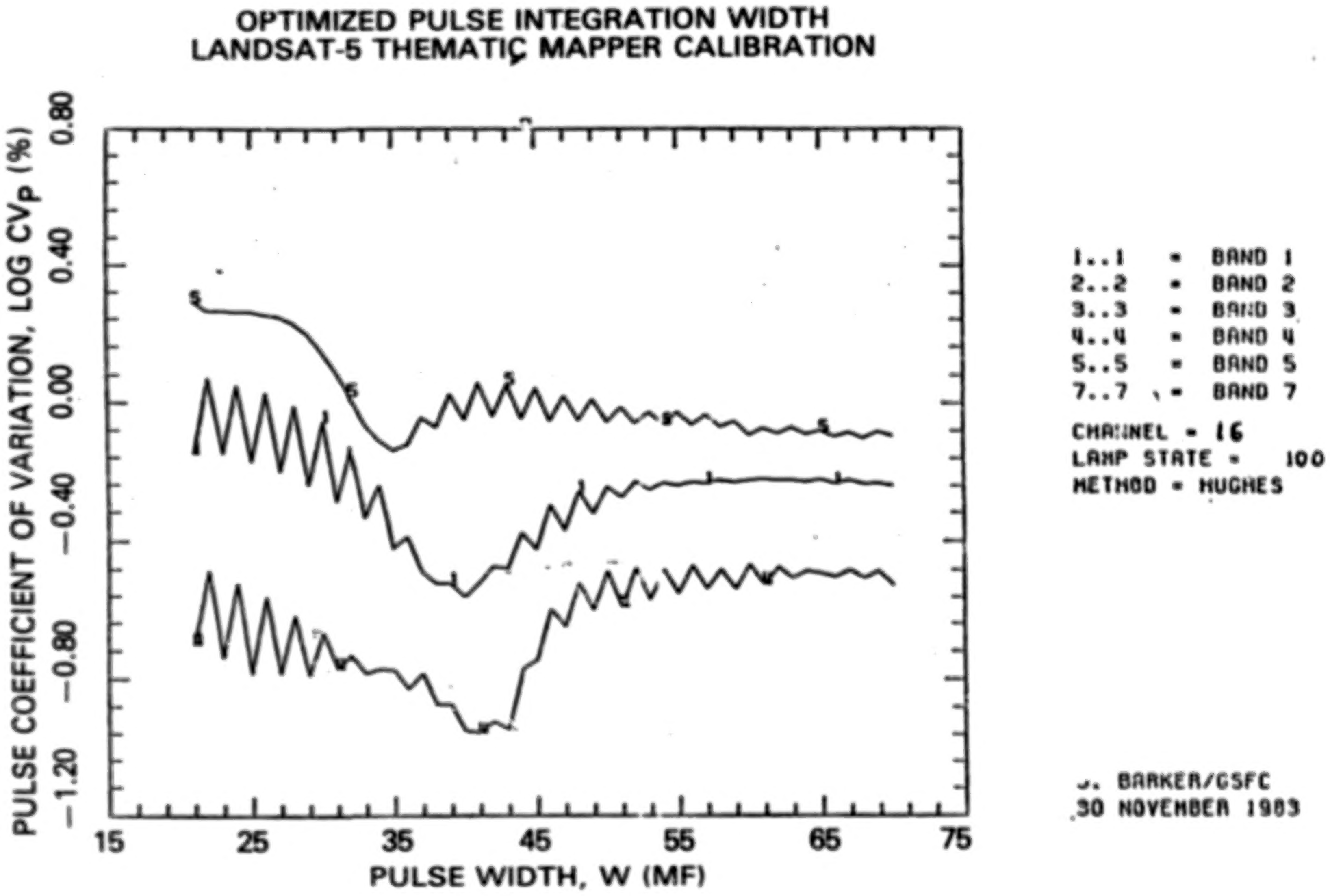

Figure 5-3. Parametric Study of Landsat-5 TM/F Calibration-Pulse Integration Width

the SWIR region, and the difficulty of identifying exactly where a lamp was turned on, parametric studies show that reduced errors resulted from omitting calibration-pulse data 4 scans before transitions and 10 scans after transitions between different lamp configurations. Dropping 4 scans preceding a transition improved precision for the SWIR bands by 35 percent. This has not been done during pre-launch or operational processing to date. Calibration needs to separate forward and reverse scans in order to avoid scene-dependence differences. Again, optimization of averaging parameters will be more efficient if it is done after reduction of the largest systematic errors.

5.1.5 REGRESSION STRATEGY

The choice of which IC lamp configurations to use in the regression of P versus L_λ^o can affect the uncertainty of the fitting parameters. In pre-launch calibration and in operational TM processing, all eight states have been used. This has resulted in a probable error in the calculation of the gain and effective spectral radiance when using lamp-state 111 for Band 4 (TM/PF) and Band 1 (TM/F), where maximum values of 255 were present, indicating that some signals may be in excess of the dynamic range of these channels. Values of gain calculated in Figures 2-1 and 2-2, by TRAPP, do not contain the 111 lamp-state. Self-consistency checks made in all TRAPP runs showed that the difference between the net 111 pulse and the sum of the net pulses of the individual lamp were always negative. DN values of 255 should not be used in calculations because they may represent higher unknown values. Furthermore, values of 255 cannot be removed as outliers without introducing a systematic under-estimate of P.

Selective use of different lamp states on different dates would also be likely to lead to systematic errors. Therefore, states that have the potential for saturation at any time should be excluded from all calculations, including the transfer of the absolute calibration from the integrating sphere to the lamps. Raw data exist on CCT tapes to permit this recalculation for Landsat-5 TM/F, but not for Landsat-4. Recalibration of the absolute radiometry from these integrating sphere tests would be better if it awaited development of correction procedures for the largest systematic errors and the optimization of pulse integration and pulse averaging parameters.

The IC lamp brightness values have not been constant with time. Test results indicate that TM/PF IC lamp 2 has changed its effective radiant output between pre-launch and in-orbit tests, as judged by comparisons with lamps 1 and 3. For any given band, the estimates of in-orbit changes of gain are the same to within 0.5 percent for all three lamps when compared to an in-orbit reference (2 NOV 82, ID 40109-15140). When pre-launch 9 March 1982 thermal-vacuum test data are used as a reference, lamps 1 and 3 have the same change to within 0.8 percent, while lamp 2 differs from lamp 1, on the average, by 2.2 percent. If this effect is real, it implies a change in something unique to that lamp, such as a change in the photodiode monitor system on that lamp or in the folding prism optics of the IC system prior to the point of merging the output of the three lamps; such a change might be the movement of the neutral-density filter on lamp 2, or in the sensitivity of the photodiode used to monitor the radiance of lamp 2.

One of the advantages of the three-lamp IC system is redundancy. It was designed to give 8 values for regression fitting. The observed linearity of the responses may allow for sufficient precision with fewer points for a regression. A comparison of single and multiple lamp regression fittings for a single scene indicates that, with appropriate independent calibration of manual-mode operation and corrections for background, single lamps could provide the necessary gains and offsets for routine calibration. This means that the two filtered lamps could be used as a monitor of long term, multi-year drift or change in spectral distribution of the unfiltered lamp. This would be particularly advantageous in an attempt to maintain absolute radiometric calibration. For monitoring of lamps, the automatic sequencer mode could be used about once a week. Furthermore, the presence of three lamps means that a discontinuous change in any one of them, such as noted above, can be considered as evidence of failure, and its values normalized to the pre-failure calibration. It appears that a 2-point fit with 7-point monitoring is preferred to the current 8-point regression fitting.

5.1.6 WITHIN-SCENE SMOOTHING

The redundancy associated with 100 channels of independently acquired calibration data on a single sensor offers unique opportunities for smoothing out random errors within and between bands. It also provides a built-in logic for isolating possible sources of discontinuous changes. The informational need for spectral transforms involving more than one band places a high value on the introduction of an explicit between-band step in the calibration process.

As one example of redundant information, odd and even channels have shown dissimilar changes in pulse values on

C-2

TM. It is currently assumed that these changes in odd/even channels are associated with how the six pencils of light from the edge of the IC shutter are played across the focal planes to produce the pulses, i.e., the pencils of light change position with changes of position or orientation of the shutter. Since movement of the shutter must affect all six IC lenses and the Band 6 mirror, this source of variability is subject to potential modeling by comparing multi-band data. To continue to calibrate each band in isolation of the others runs the risk of unnecessary loss of between-band calibration.

Another example of the potential for within-scene smoothing involves the temperature-dependence of the IC pulses. Pre-launch data on temperature-dependence were collected for TM/F PFP bands and only in ambient conditions at temperatures near 20°C, or 10°C above the conditions in space. This effect appears to be sufficiently linear that changes in the most sensitive channels could be used to make smaller changes in the effective spectral radiance for other, less sensitive channels. This might be desirable if the measurements of the appropriate temperature in the telemetry was less precise than the error associated with using the observed changes. This temperature-dependence needs to be measured in-orbit by sampling of 7-Band TM IC data from immediate turn-on through thermal shut down. Such an in-orbit calibration test (Section 6.2.2) might also empirically answer the question of which temperatures are related to this temperature-dependence.

5.1.7 WITHIN-PATH SMOOTHING

Original TIPS processing designs called for blending the calibration between scenes by creating segments and subsegments within a scene for separate transitional calibration. Initial attempts to do this to a scene during Scrounge-era processing produced demonstrably striped products. It appears that the TM sensor is sufficiently stable over a single scene that less error is introduced by assuming a constant set of calibration parameters for the whole scene than by blending. TM is a very stable radiometer. However, the possibility of multi-scene digital-image processing of a single pass (path) still calls for a search for trends. Examples of such trends are the temperature-dependence of the IC pulses, and multi-scan bright-target recovery of the background from exposure to solid fronts of clouds or snow. It is anticipated that such corrections for trends can be absorbed more continuously in a line-by-line calibration procedure rather than in segmented blending, if they are necessary at all.

5.1.8 BETWEEN-DATE SMOOTHING

Smoothly varying day-to-day trends in calibration parameters, as implied by Figures 2-1 and 2-2, perhaps from time-dependent vacuum-shift, can be corrected by modeling these trends and including them in the fitting required for calibration. It is desirable for radiometric accuracy to correct all known sources of systematic variation.

5.2 IMAGE CALIBRATION

Radiometric calibration of the raw digital imagery is computer-intensive. Calculation of the analytical expressions for the corrections discussed in Sections 4 and 5.1 are, for the most part, not computer-intensive. Exceptions include corrections that are image-dependent, such as bright-target saturation. This section discusses some of the uncertainties in the precision and accuracy of the radiometry that are associated with manipulating digital imagery. In particular, the following processes are discussed:

- Histogram equalization to reduce within-band striping by normalizing to a common mean and standard deviation for all channels in a band
- Replacement of bad channels
- Post-calibration dynamic-range options to retain a greater fraction of the acquired data
- Unbiased pixel calibration procedures for applying calculated corrections to individual pixels
- Geometric resampling of radiometrically-corrected imagery for registration to a reference image or rectification to a specific map projection.

5.2.1 HISTOGRAM EQUALIZATION

Scene-dependent normalization of channels to each other, such as histogram equalization or ratioing, is one method of radiometrically calibrating images from scanners. Scrounge-era and TIPS-era processing for Landsat-4 TM imagery have collected frequency histograms by DN level for each channel from the first pass through the raw high density tapes (HDT-RT). During the Scrounge-era, histograms were created from every fourth pixel (sample). Means and standard deviations derived from these histograms were used to bring all channels within a band to a common mean and standard deviation through application of a gain and bias for relative de-striping. Absolute radiometry was maintained by modifying this set further for the band-average apparent change in gain and offset based on the IC pulses. These were the radiometric corrections applied in Equation 1-1. Three assumptions are implicit in this calibration methodology:

- Within-scene variations in sensor characteristics are insignificant
- IC calibration is inadequate, since otherwise histogram equalization would not be needed
- Histogram equalization is more precise than IC calibration for destriping.

Neither IC nor histogram calibration currently correct for continuous or discontinuous within-scene variations or trends such as those outlined in Section 4. However, both methods can be used after reduction of systematic within-scene variations. Without these systematic corrections, phenomena such as between-scan striping will be inherent in the use of histogram equalization from raw data.

Pre-launch absolute calibration was based on the assumption that the individual channels are stable enough over a period of hours to a few days that they can be used as a transfer mechanism for calibrating the IC lamps from the known radiance of different levels of the integrating sphere. The use of histogram equalization implies that there was a significant imprecision in this transfer or that the effective radiance of the IC system has changed since it was calibrated, especially in regards to the relative gains and offsets of the channels in a single band. It is possible to examine this assumption quantitatively by measuring the residual between-channel standard deviation of a homogeneous scene after radiometric calibration using the IC data without histograming. Residual striping from IC calibration alone has not been quantitatively summarized.

The assumption that histogram equalization can and does produce less striping in a TM image than IC calibration has also not been evaluated quantitatively. Equalization techniques assume that each histogram has a sufficiently representative sample to be identical with that from other channels. This is dependent on the variability of scene content and will differ from scene to scene. Histogram equalization also assumes that the counts observed by each channel in a band cover the same dynamic range. This assumption can be evaluated from the range of gains and offsets in the absolute calibration of each channel, when combined with the histograms of the scene to be used for equalization. Histogram equalization also assumes a normal frequency distribution, which is not a good assumption, and is also scene-dependent. Finally, the use of histogram equalization on every scene assumes that the range of scene-dependent radiances is sufficiently great to provide the required sensitivity. Histogram equalization is used because it has worked on MSS digital imagery, it produces acceptable film products, and it has not yet been demonstrated that it does not work for analysis of TM digital imagery.

Iterative calibration algorithms have been suggested by Fischel (1984). The use of scene histograms to implement these equations means that the proposed iterative algorithm is subject to the same limitations as the direct use of histogram equalization.

The use of some type of iterative technique following systematic corrections such as those outlined in Section 4 may prove to be effective, assuming that a rapidly converging formulation can be made; ideally, it needs to be independent of scene content.

If histogram equalization continues to be used, it is probably better to use a weighted average based on observed variability for both histogram equalization and for the absolute calibration to the IC data. If this is not possible, then a reference to one or two quiet channels (Table 4-5) in both cases would be better than the reference to the band average, whose uncertainty is driven by the noisiest channels. If reliable full-scene error estimates could be made for both methods of calibration, then the best method would be to use an average weighted by the inverse of the variance for within-band destriping.

Inherent in the use of histogram equalization is the assumption that the TM sensor is stable during the period of data acquisition for histograms. If within-scene corrections are made for each channel, this appears to be a reasonable assumption to the extent that Figures 2-1 and 2-2 indicate a slowly-varying, smooth between-scene IC trend of band-averages with time. If a similar trend of histogram calibration constants, corrected for within-scene systematic errors, is found over many scenes, then the scene-dependent portion of histogram equalization can be taken out to any required level of statistical accuracy by calculating a functional relationship for within-band change with time.

This suggests a potentially powerful way of combining apparent within-band variations from separate IC calibration and histogram equalization or ratioing in order to reduce the random error in both. Changes with time might provide a means of modeling out systematic within-band trends associated with the IC system only. With sixteen-channel redundancy in every reflective band, histogram equalization may have some new applications for radiometric calibration when used as a slowly varying modifier with time on the internal calibrator system.

5.2.2 REPLACEMENT OF CHANNELS

A multichannel scanner, such as TM, requires replacement of channels that fail. Without replacement, the image would have a break every 16 lines (Barker, Gunther, et al., 1984 Figure 2-7). Failure can be of two types, complete or partial. Complete failure is a zero order effect (Table 4-8), i.e., data are missing from a dead channel, and the radiometric uncertainty in its correct value cannot be estimated. There is one such channel on Landsat-4 TM/PF, namely, Channel 3 of Band 5. Partial failure also implies partial success, therefore failures of this type are inherently different. Because of the potential for blurring boundaries, the out-of-specification modulation transfer function (MTF) of Channel 4 in Band 2 led to this channel being considered a failure on TM/PF. There are no failed channels on Landsat-5 TM/F.

During Scrounge-era and TIPS-era processing of Landsat-4 digital imagery, both bad channels were replaced by duplicating data from an adjacent channel (Barker, Guther, et al., 1984). In Band 5, Channel 3 was replaced with a duplicate line of Channel 4 data. In Band 2, Channel 4 was replaced by Channel 5. This is the simplest type of replacement.

A routine monitoring of Channel 4 of Band 2 by TRAPP has indicated that this channel has been as radiometrically stable as others in that band. It is therefore recommended that TIPS procedures be modified to stop replacing this channel. From a scientific point-of-view, it is better to use a partially-deficient channel than to not use it at all. This is especially true on the TM sensor where there is no significant overlap of the effective instantaneous field-of-view for adjacent channels.

Within-band algorithms for replacing bad channels are still being evaluated. In general, the trade-off is between the lower probability of an error by using as many neighbors as possible in an estimate and the increased computations inherent in multi-neighbor algorithms. The simplest strategy is one-for-one line replacement either by an adjacent line or by a more representative pattern such as alternating back and forth between the channels on either side of the dead channel. Averaging of two adjacent channels is the next easiest. Weighted averaging by position requires more intensive computation but allows for a nearly complete encirclement of the missing pixel with a probability of the radiance value being driven by the pixels which are geometrically closest to the one being replaced. For channels that have only partially failed, one has the additional possibility of a weighted average of the original pixel value itself and the value that would have been used if the channel had completely failed. For MTF deficiencies such as those in channel 4 of Band 2, the weighting could depend on the probable distance from a boundary, since the pure pixel value, while slightly averaged with its neighbors, will be best without additional averaging with data from other channels. Replacement algorithms can be evaluated by using several adjacent channels that have not failed to compare the proposed replacement value with either the observed value or the calculated partially-deficient value.

Between-band replacement algorithms, applied after radiometric calibration, are potentially better than within-band ones. They are better from a spatial perspective because they use imagery which is viewing the area that was missed by one band and from a radiometric perspective because there is a high degree of correlation between bands. Possible multi-band substitution algorithms also range from spatially simple single-pixel replacement to multi-neighbor resampling. Weighting algorithms for averaging within-band and between-band estimates of missing data could place higher weight on the spatial information from outside bands and on the radiometry from neighboring pixels within the band. If tests are run on the error in information content from alternative replacement algorithms, perhaps by optimizing the ratio of random error to computation cost, a likely replacement candidate is a single-pixel replacement where the new value is produced by calculations based upon correlation to another band.

Any replacement will lead to additional errors. For example, the sensitivity and accuracy of texture or contextual classifiers will be reduced by the implicit rather than explicit use of the same data in more than one pixel. To the extent that information of this type is important, it is desirable to limit the geometric extent of the pixels used for replacement and, if possible, to retain the ability to identify pixels that are calculated rather than observed. For TM imagery, tagging of replaced pixels is not warranted since, prior to geometric resampling, replaced data can be located by line number, and after resampling, especially after rotation of the image to north, all of the pixels are likely to contain some redundant data. One method to avoid the use of redundant data is to make the replacement step an inherent part of a non-uniform geometric resampling algorithm that behaves well in the presence of missing data.

Most applications of digital imagery of land place a high value on boundary location and/or mensuration. Both these requirements favor using some type of between-band replacement algorithm.

5.2.3 POST-CALIBRATION DYNAMIC RANGE

For a given and fixed resolution, such as TM's 8-bit radiometric precision, the total amount of information in digital imagery is reduced by radiometric calibration, since it either compresses data from more than one bin into a single inseparable bin, or it cuts off some data at the low or high ends of the post-calibration dynamic range. The graph of Band 5 gain versus time, Figure 2-2, illustrates that Scrounge-era processing did result in some loss of data by compression for those days when the raw channel gain was above the post-calibration gain. For TIPS-era processing after January 15, 1984, this post-calibration dynamic range has been raised, in part to avoid compressing data (Appendix 9.1).

Relative between-channel, between-band, and between-scene calibration is essential for information extraction. One data-intensive solution to this dilemma is to increase the radiometric resolution of the calibrated products. Another solution is to consider alternatives to the single gain options of the current calibration procedures.

A three-sectioned dynamic range is a possible future option for TIPS (Section 6.3.5). A small number of bins, perhaps b = 15, at both ends of the dynamic range would be calibrated separately from the central portion of (256 - 2b) bins. The dynamic range for the linear central portion would be a common range for both TM/PF and TM/F that would assure that, during the life-time of these sensors, calibration would result in information-retentive expansion in this, the most important part of the band. The overall dynamic range would be from a zero radiance to an upper limit of the most sensitive channel in a specific band. This would mean that one or both of these two less-important sections on either end would contain some compressed data.

The advantage of this three-section calibration scheme is that some out-of-range data (high radiance values from deserts, snow and clouds) would be retained in a less compressed manner. The fact that TM data are characterized by an absence of high radiance values means that shifting and expanding of the central portion will push very little data into the more compressed region at the top, while at the same time retaining the full range of data in those less frequent cases where there is saturation. Still more information would have been retained if these schemes could have been applied on the sensor to the selection of bits for transmission from the A/D converter. Calibration of these end sections could be linear, piece-wise linear, or use a more smoothly varying function for these regions. While it might be some time before users are able to demonstrate the utility of the less compressed data in these end regions, this three-section scheme would provide potential information that would otherwise be lost.

5.2.4 UNBIASED PIXEL CALIBRATION

Conventional calibration of a digital image introduces its own "nearest integer" striping. It can be made visible by differencing a TM image before and after radiometric calibration and noticing the stripes along lines on the resultant difference image (Barker and Gunther, 1983, Figure 9). This differencing of TM/PF images also makes the peaks of the coherent noise somewhat more visible every 3 and 17 pixels. The solid striping arises because of the additional discontinuous quantization error in converting from a raw 8-bit integer to a calibrated 8-bit integer. As Bernstein and Lotspiech (1983) have pointed out, this would occur even if the calibration step was a perfect inversion of the different responses that the channels have to a COMMON input radiance. Whether the radiometric corrections to the digital imagery are being applied by a conventional mainframe computer using a one-to-one replacement in a radiometric look-up table (RLUT) or by an array processor using calculations of a specific formula on many pixels in parallel, this "nearest integer" striping will occur.

Bernstein and Lotspiech (1983) have proposed a "probabilistic" approach to replace the "nearest integer" procedure. A modified version of that proposal would replace the RLUT generation, or parallel processing implementation of the corrected calibration from Equation 1-1:

$$\text{INT } L'_{cal} = \text{INT } \frac{L'_R - NB'_A}{NG'_A} \tag{5-1}$$

where INT = rounded integer value of its argument with a probabilistic choice between the nearest two integers,

$$\text{INT } L'_{cal} = \text{TRUN } L'_{cal} \tag{5-2}$$

with a probability of

$$p = 1 - [L'_{cal} - \text{TRUN } (L'_{cal})]$$

or (5-3)

$$\text{INT } L'_{cal} = 1 + \text{TRUN } L'_{cal}$$

with a probability of (1-p)

where TRUN = truncated integer value of its argument.

The advantages of this probabilistic approach are that visual striping is removed, and the accumulated error over all pixels is zero, i.e., it is an unbiased estimator of the correct value. The disadvantage is that the implicit quantization error has been entered explicitly as $1/\sqrt{12}$ salt-and-pepper noise into the imagery. This probabilistic approach could improve the radiometry sufficiently to produce less-biased estimates in multipixel information extraction algorithms such as boundary delineation, region growing, texture measures and contextural and textural classifiers. As with all radiometric corrections, a smaller error due to rounding will occur if this probabilistic approach is applied once and only once at the last geometric resampling required for "P" products. If separate "A" products are required, then this probabilistic approach could be used each time an 8-bit image is generated.

5.2.5 GEOMETRIC RESAMPLING

While several potential sources of radiometric error exist in the geometric pre-processing of TM data, Fischel (1984) has found that the "geometric correction algorithm for TM works exceedingly well". A quantitative comparison of the difference between alternative resampling algorithms remains to be done, partially because of the computational difficulty of implementing even a single resampling algorithm for TM digital imagery.

Between-scan fitting due to overlap or underlap between sweeps has not been a problem due to the excellent performance of the scan-line-corrector (SLC). The periscope-type mirrors of the SLC rotate to correct out the effect caused by the movement of the spacecraft during the period of a single scan. The SLC repositions the start of each scan relative to the end of the last scan (Engel, 1980). It is reset at the end of each sweep. Since the SLC is set for a specific altitude and latitude of operation, acquisitions at the current orbital altitude near the poles will result in as much as a three pixel overlap or underlap at the ends of lines 1 and 16 between sweeps. Landsat-4 TM/PF images of North America have shown less than a one pixel gap or overlap.

Rounding introduces some radiometric uncertainty during the geometric correction process. Procedures used during the Scrounge-era and current TIPS-era involve two steps:

1. Equal interval along-scan (within-scan) 4-point cubic convolution resampling

2. Unequal interval along-track (between-scan) 4-point cubic spline resampling, to create lines by "sweep extension" as necessary at the end of each sweep.

Fischel (1984) has recommended a single-pass resampling procedure to replace the current two-pass cubic spline in the second step in order to avoid the loss of as much as 40 DN levels from a bright pixel at the bottom of a scan. It is also desirable to change the current procedure and use raw data (HDT-RT) as input to this geometric process rather than radiometrically corrected data (HDT-AT); this could avoid one rounding error by applying radiometric and geometric corrections in the same process.

Smoothing of adjacent pixels is a characteristic of these resampling algorithms, and therefore there is an inherent loss of peaks and valleys. There is also a ringing from spatial filters that resample with the intention of maximizing the retension of extreme values. Appropriate scenes need to be identified for quantifying the extent of this smoothing or ringing by comparing the particular resampling algorithm to a nearest neighbor (NN) image which has the original DN values without smoothing by resampling.

Map compatibility for the TM digital imagery is a significant requirement for most applications. The utility of MSS imagery was directly related to the ease of rectifying the imagery to non-imagery data sets, such as maps. Satellite imagery over land has little utility as a stand-alone product. Canadian TM products can be resampled in their initial geometric processing to a projection which will directly overlay a north-pointing map projection for direct use in a geocoded data base (Murphy et al., 1984). Non-geodetic TIPS TM products are resampled by registration to a reference image, which means that an additional radiometric rounding error will be introduced if they are resampled again for rectification to a map.

5.3 RADIANCE-TO-REFLECTANCE CONVERSION

Conversion of TM radiance into reflectance could become a major scientific objective. Both within- and between-scene spectral "signature extension" was a major unobtained objective of remote-sensing scientists examining MSS digital imagery. The higher radiometric resolution, spectrally narrower bands, and new bands on the TM sensor, along with greater understanding of atmospheric models and spectral transforms, will probably lead to new attempts at TM signature extension. Radiance-to-reflectance conversion is a likely step in this objective because inferred bidirectional reflectance is closer to an innate characteristic of objects than observed at-satellite radiance. Two methods of deriving reflectances from at-satellite radiances are "irradiance normalization" and "atmospheric peeling".

5.3.1 IRRADIANCE NORMALIZATION

For some purposes, it may be sufficient to calculate the total apparent reflectance from both the atmosphere and the ground by dividing the observed radiance by a calculated solar irradiance. Exoatmospheric within-band solar irradiances can be calculated for a given TM scene from the following variables:

1. Average exoatmospheric solar irradiance spectrum

2. Time-of-year

3. Orbit of Earth

4. Solar zenith angle at time of scene acquisition, which depends on location

5. Individual relative spectral response (RSR) curves for the slightly different TM bands on Landsat-4 and -5 (Markham and Barker, 1984).

5.3.2 ATMOSPHERIC PEELING

For remote sensing of land, an atmosphere-free target bidirectional reflectance is more desirable than a total reflectance. The radiometric accuracy requirements for such an experiment are high. TM bands were selected to avoid parts of the electromagnetic spectrum with major water absorption, however, even "clear" scenes contain single photon reflections from the atmosphere and multiple reflections from the ground and the atmosphere. The smoothly varying nature of atmospheric scattering as a function of wavelength, the large and slowly moving nature of clouds and fronts, the redundancy of ground and atmospheric information in TM bands, and the stability of the TM sensor over a satellite path, suggest that atmospheric-radiance removal could be accomplished by acquisition and processing of full-pass multi-scene TM imagery. Initial test sets for demonstration of atmospheric correction feasibility might include:

- Long pass of TM imagery, to include extremes of homogeneous snow and water for atmospheric corrections, such as in the Arctic and over the Gulf of Mexico

- Automatic data collection platform (DCP) readout of atmospheric conditions at fixed points for periods up to the time of TM overpass, and afterwards, if possible

- Ground reflectance and atmospheric characteristics at several low and high reflectance regions in each pass, such as at White Sands, New Mexico

- Aircraft measurements of atmospheric conditions at time of TM overflight over large homogenous area, especially water

- Geosynchronous 4-Km weather-satellite imagery of whole pass, before and after TM acquisition

- NOAA-7 or -8 AVHRR polar orbiting 1- and 4-Km weather imagery before and after TM pass (early morning and early afternoon)
- Digitized terrain map of whole pass, including slope and aspect
- Regional weather maps of whole pass interpreted to time of overpass
- Selected full-pass TM imagery acquired with off-nadir viewing to develop and demonstrate atmospheric removal and terrain correction models.

Special ground processing could then "peel off" the atmospheric part of TM scene radiance on high-speed high capacity computers with specialized software by a series of steps to create the following intermediate type products:

- 16-bit 30m TM Full-Pass Radiance Data Base--With radiometric corrections (Sections 4 and 5)
- TM 30m Radiance Variance Data Base--For each pixel (Sections 4.1 and 4.8)
- Binary Boundary Masks--From individual TM full-scene passes and from merging with multi-date TM imagery and ancillary boundary maps
- Binary Cloud and Shadow Masks--From TM imagery
- 16-bit 1-Km TM Full-Pass Data Base--Created by resampling original radiometrically corrected 30m imagery to a grid common to the map projection for all the data sets, with radiance weighted by the inverse of the variance for cloud-free shadow-free non-boundary pixels
- 16-bit 1-Km GOES Data Base--Created by merging 4-Km GOES acquisitions before and after TM pass, resampled to common 1-Km map projection and interpolated to time of TM overpass with enhancement for early and late appearing atmospheric characteristics
- 16-bit 1-Km NOAA-7 or -8 Data Base--Created from low polar orbiting weather satellites in same manner as geosynchronous weather satellite imagery of TM region

- Digitized 1-Km Regional Weather Maps--interpolated to the time of TM overpass

- Digital 1-Km Grid Atmospheric Point Data Base--of known atmospheric conditions for selected pixels by merging aircraft, DCP and ground data bases interpolated to time of TM overpass with accompanying estimate of the error of each value

- Zero-Order 1-Km Atmospheric Seed Parameters Maps--For each required atmospheric parameter in removal model created by merging of GOES, NOAA-7, Weather and Point Data Bases and smoothing

- Zero-Order 1-Km TM Reflectance Data Base--Created by applying atmospheric removal model from seed maps to 16-bit 1-Km observed TM Pure Pixel Radiance Data Base, including solar irradiance view angle and topographic irradiance effects

- Zero-Order 1-Km TM Radiance Data Base--Calculated from Zero-order Reflectance and Atmospheric Seed Data Bases using known models from atmospheric spatial adjacency affects

- Zero-Order 1-Km TM Radiance Variance Data Base--Created from the difference of observed and calculated TM Radiance Data Bases

- Ith-Order 1-Km Atmospheric Parameter Data Base--Created by modifying previous atmospheric parameters based on previous calculated minus observed Radiance Variance Data Base

- Ith-Order 1-Km TM Reflectance Data Base--Calculated from Ith-order Atmospheric Parameter Data Base and 1-Km observed TM Pure Pixel Radiance Data Base

- Ith-Order 1-Km TM Radiance Data Base--Calculated from Ith order reflectance and Ith order Atmospheric Parameters Data Base

- Ith-Order 1-Km TM Radiance Variance Data Base--Created from the difference of observed and calculated TM Radiance Data Bases with iteration of last three products until the difference between observed and calculated TM radiances have been reduced to the desired level.

This final 1-Km TM reflectance image could be a scientifically valuable product because its pure-pixel characteristics are potentially related to innate properties of the target. Furthermore, the radiance variance can be used to create an estimated uncertainty for the reflectance in each of these pixels, thus providing the basis for statistical weighting by the inverse of the variance in multi-date models. The potential for multi-date modeling from TM data for global habitability is increased in this scheme by the factor of one thousand reduction in data volume in going from 30m to 1-Km imagery.

For scientific experiments requiring the full 30m spatial resolution of the original TM imagery, the ith-order 1-Km atmospheric parameters can be used with these atmospheric models to remove the atmospheric radiance from the 16-bit 30m TM radiance imagery. The model would use a 30m topographic terrain map of aspect and slope in place of the 1-Km terrain map in the iterations.

Here again, a comparison error plane can be calculated from the ith-order 1-Km Radiance Variance Data Base, known errors in the terrain map, and the 30m Radiance Variance Data Base. This compatible error data base provides the potential for statistical weighting by inverse variance in information extraction modeling.

This outline for a possible atmospheric-removal procedure is given to illustrate the potential for this type of correction with TM digital imagery. Feasibility for such an atmospheric-peeling experiment needs to be demonstrated. Implicit assumptions include hardware and software capability in data-base management systems and geographic information systems (GIS) that are in the research and testing phase but have not been applied to data sets as large as those involving full-pass TM imagery merged with other data sets. The critical radiometric requirements are that the errors of between-channel and between-band reproducibility and the errors of absolute radiance calibration are small relative to the errors introduced by the atmospheric peeling. This implies that the residual uncertainties in the bidirectional reflectances are small relative to the requirements for precision and accuracy in the information extraction processes. Quantitative radiometric requirements for atmospheric peeling in land remote sensing can be developed through modeling and simulation activities on TM imagery.

The TM sensor's correctable radiometry may represent a nearly unique opportunity for simulation and requirements definition over the next couple of decades to develop this capability for atmospheric peeling.

Another reason for discussing one approach to calculating atmosphere-free bidirectional reflectance in this section on processing effects on TM radiometry is that this type of procedure has almost no chance of success if attempted on single TM scenes, or if images have not been corrected for systematic radiometric trends discussed previously. Radiance-to-reflectance conversion by atmospheric peeling appears to require full-pass radiometric processing with at least some ancillary atmospheric information as a seed to an iterative model.

5.4 INFORMATION EXTRACTION

Optimization of radiometric and geometric processing parameters should ideally be based on their effect on the final information extracted from the digital data.

Optimization studies of this kind have not been extensively performed because of the absence of powerful low-error and quantitatively-reproducible information-extraction methodologies. Economic models of profit have been particularly subject to uncertainties in the assumptions of marketing conditions. Classification, as an information extraction procedure, has been operator- and category-dependent, i.e., the errors for classification procedures are not quantitatively reproducible. Therefore, near-term optimization studies will probably concentrate on the errors in inferred scientific variables that are continuous, rather than on discretely changing variables or on the uncertainties associated with predictions made using variables in decision-making or other models. Limitations on such parametric studies for scientific variables have been:

1. The absence of appropriate high-precision multi-date regionally sampled data sets with sufficient spectral, radiometric and spatial resolution to allow for interpolation rather than extrapolation.

2. The absence of hardware and software tools to handle both the remotely sensed imagery and the required ancillary data planes.

3. The absence of information extraction models for critical scientific variables.

Information extraction involving TM imagery can be usefully separated into three sensor-related mission-independent categories (Barker and Gunther, 1983):

1. Spectrometry
2. Radiometry
3. Geometry

Since these categories are not totally independent, uncertainties in the TM radiometry have effects on all three.

Scene radiance models are being created and evaluated for land remote sensing. There is the possibility of inverting some of these models. The most efficient way of doing this is still a matter of active research. Historically, the information-extraction processes have followed the preprocessing radiometric calibration and geometric correction processes both in time and place. The high data volumes associated with high spatial resolution may require introduction or addition of some information-extraction processes to the pre-distributed TM products.

The increasing personal-computer market suggests that distribution of TM data in a digital form usable by these computers may lead to development of new uses that would not be seen by centralized research groups. A highly distributed market requires a highly standardized product. One such product might be 5-inch 500-Megabyte read-only optical-base disks for standardized corrected and map-projectable 16-bit TM imagery of atmosphere-free reflectance with appropriate binary masks such as political and physical boundary data, infrastructure, pure pixels, clouds, and shadows. It could have ancillary planes of quantitative data such as radiance imagery, texture measures, atmospheric parameters, terrain, soil information, one or more standard unsupervised classifications of the imagery, and previous classifications of the image area. A widely distributed, inexpensive, timely, standardized product will create its own market among discipline scientists and others if there is minimal loss of information in the process of correction and standardization. Such a distribution of significant amounts of TM data would probably produce many more uses for the data than can be determined by a few hundred remote sensing scientists. This would test the useful information content and potentially provide a basis for optimizing procedures for correction and standardization based on maximizing a function such as the ratio of processing cost to rms error in required inferable or useful information.

Some spectral, radiometric, and geometric information-defining characteristics and needs, which are relevant to TM radiometric precision and accuracy and do not depend on how the information is used, are given below.

5.4.1 SPECTROMETRY

The number of spectral bands is one measure of information content of data. For the TM sensor, the reflective spectral regions from which between-band information can be drawn are limited to no more than 6 bands. Three of the spectral characteristics that can reduce the amount of this potential information are:

1. "Cross-talk" within and between bands due to electronic noise or a light leak
2. "Spectral striping" from spectral differences between channels in a band
3. Redundancy between the bands.

Pre-launch studies have quantitatively measured the extent of light leaks between PFP bands, apparently due to the openings between bands of detectors (Markham and Barker, 1984). This effect is less than a 5-percent-of-peak effect at 13 pixels from the peak and has not yet been observed in in-orbit data.

The potential for "spectral striping" between channels was not measured before launch because the homogenity of the filters was believed to be sufficient to assure no such effect. If differences existed between channels, then it would be impossible to correct this apparent radiometric striping because it would represent a real difference in what portion of the electromagnetic spectrum was observed. It is unlikely that large-enough homogeneous ground targets exist with sufficiently sharp changes in spectral reflectances at band edges to allow for an in-orbit check of possible spectral striping. It is also possible that the narrower spectral band widths on the TM sensors, compared to the 100 nm or larger band widths on the multispectral scanner system (MSS) sensors, are moving in the direction of reducing the potential for spectral striping to an insignificant point because the narrower bands have fewer independent physical phenomena reflected in them.

Redundancy in spectral data has been estimated primarily by the fraction of variance accounted for in principle component analysis (Gunther, 1982; Bernstein and Lotspiech, 1983; Anuta et al., 1983). This method of linearly combining fractions of each of six bands to account for the maximum amount of total variance is at the core of attempts to convert spectral axes into orthogonal informational axes via image-independent "spectral transforms". It is important to develop quantitative measures of how much useful information is in each of these transforms since it is desirable to reduce the TM dimensionality if this can be done without the loss of significant information. When principle component analysis has been applied to TM scenes, significant non-random non-noise patterns are visible in the sixth component, which accounts for less than a percent of the total variance of the six bands (Bernstein and Lotspiech, 1983). However, the mathematical linear orthogonality of this computation has not necessarily created informationally independent transformations. In particular, all six transforms of TM data reveal some similarity in spatial patterns. If the electronic, vibrational, rotational, and other energy transitions could be modeled from reflectance spectra of targets, then it might be possible to establish a physically meaningful functional form for an informational spectral transformation.

Any transform of independently measured radiances will have a larger associated error than the original observations. Current linear spectral transforms have the following form:

$$T_i = \sum_{B=1}^{6} E_i(B)\ L_{cal}(B) \qquad (5\text{-}4)$$

where $L_{cal}(B)$ = calibrated radiance in one of the six TM Bands, B, DN

$E_i(B)$ = factor for the ith transform for Band B

T_i = one of six TM spectral transforms.

Coefficients for one such set of spectral transforms are given in Table 5-1 (Crist and Cicone, 1984). The first three are called "brightness", "greenness", and "wetness" transforms, implying a relationship to physical variables. Some biophysically meaningful variables that might be inferable from such transforms include albedo, green biomass, soil moisture and canopy thickness. Some of these transforms increase the contrast as compared to the original single bands. Such increased separability can reduce the errors associated with single band "per pixel" classifiers and spatial correlation such as that required for ground

Table 5-1. Thematic Mapper Tasseled Cap Transformation Coefficients From In-Orbit Data (Crist and Cicone, 1984)

FEATURE	TM BAND					
	1	2	3	4	5	7
BRIGHTNESS	0.3037	0.2793	0.4743	0.5585	0.5082	0.1863
GREENNESS	−0.2848	−0.2435	−0.5436	0.7243	0.0840	−0.1800
WETNESS	0.1509	0.1973	0.3279	0.3406	−0.7112	−0.4572
FOURTH	−0.8242	0.0849	0.4392	−0.0580	0.2012	−0.2768
FIFTH	−0.3280	0.0549	0.1075	0.1855	−0.4357	0.8085
SIXTH	0.1084	−0.9022	0.4120	0.0573	−0.0251	0.0238

control point (GCP) registration of one image to a reference image. One reason for using spectral transforms rather than 6 bands is that they may lead more quickly to definitions of scientifically useful spectral information.

The variances of these transforms are:

$$\sigma_{T_i}^2 = \sum_{B=1}^{6} E_i(B)^2 \, \sigma_{L_{cal}}^2(B) \qquad (5\text{-}5)$$

where $\sigma_{L_{cal}}(B)$ = The rms error in the calibrated radiance in Band B, which has as it's minimum value the variability of the sensor.

The error in the spectral transform will usually be dominated by the largest errors in the individual bands. For the 6 TM bands, the uncorrected non-informational variance from the total noise background in the shutter region from Table 4-6 indicates that bands 1, 5, and 7 contribute approximately 80 percent of the variance. This suggests several alternative methods for reducing the errors associated with using spectral transforms:

1. Radiometric correction procedures could emphasize reduction in the largest uncertainties
2. Spectral transforms could be weighted by the inverse of the variance of their individual bands
3. Spectral transforms might be developed using only the low noise bands namely TM bands 2, 3 and 4.

These suggestions are particularly important in the use of spectral transforms, where all but the "brightness" component have mixed positive and negative terms, which can lead to larger errors in the calculated transforms. Since these spectral transforms appear to be informationally richer, or at least more focused, than the original bands, optimization of radiometric calibration parameters needs to minimize the variance in the spectral transforms.

5.4.2 RADIOMETRY

Entropy is one measure of the within-band informational content of discrete data such as 8-bit TM digital imagery. An advantage of using entropy is that it places a quantitative upper limit on the potential information that can be derived from the frequency and radiometric range of observed counts in a single band. Five limitations on the use of entropy as a measure of information include the absence of:

- Normalization for non-informational sensor variabilities (Section 4)
- Any measure of spatial information (Section 5.4.3)
- Subsets of useful information such as partitioning of atmospheric and terrestrial variability (Section 5.3.2)
- Potentially higher radiometric resolution information from the smaller bins of the bin-radiance variability (Section 4.1)
- Innate properties for associative or cumulative between-band aggregation without correction for factors discussed under spectrometry (Section 5.4.1).

Future radiometric calibration parameters could be derived by maximizing a per-pixel entropy-based correction for one or more of the above factors, especially the normalization for sensor variability. This radiometric optimization using entropy in processing steps might help in defining a three-sectioned post-calibration dynamic range (Section 5.2.3), or in definition of the dynamic range to be collected or transmitted from future land-observing satellite systems. One objective of such a formulation of per-pixel entropy would be to retain its thermodynamic property as a state function, which depends only on the state of the target, not on the path by which it was achieved.

5.4.3 GEOMETRY

Spatial information could be optimized in two steps. Radiometric parameters used for calibration could be optimized on unresampled corrected and radiometrically calibrated digital imagery. Parameters for geometric pre-processing could be optimized on spatially resampled data.

Texture is another measure of within-band information. Various measures of texture can be used to place upper limits on the combined radiometric and spatial information. If both the random and systematic contributions from the sensor variability can be removed from the measures of texture, then a figure-of-merit (FOM) could be calculated for the spatial information above by combining these normalized measures of texture with the normalized per-pixel entropy. Such a spatial FOM would still be an intensive property of the digital image and not an extensive property of the size of the image.

Intensive variables that quantify the point, line and regional spatial information of a digital image move closer to characterizing useful information than do total measures such as texture. Modified texture measures would then be used on binary masks of within-region "pure" pixels. It is likely that a "spatial stability theorem" will emerge from scientific and informational research in land remote sensing stating that pointed, linear, and areal features of two dimensional images remain invariant to spatial resolution. If this theorem is true, then research on information extraction techniques, which may involve artificial intelligence methodology, may separate the spectral and radiometric informational content of "pure pixels" from the spatial informational content of points, lines and regions on the whole scene for each specific sensor. Reproducible unsupervised methods using matrix filters are being developed for calculating these intensive spatial variables. Once such variables are found, they can be used to compare and optimize parameters in different resampling algorithms.

The geometric utility of digital imagery is related to two characteristics of a system's performance, the sensor's instantaneous-field-of-view (IFOV) for each pixel and the accuracy with which a resampled pixel can be located on a reference data set, usually a map. A more quantitative description of the nominal 30m IFOV for TM can be given in space as two line-spread functions, one along scan and one across scan, or as some other 2-dimensional spatial-distribution function. The nominal 30m IFOV for TM can be described in the time domain as frequency in a modulation transfer function (MTF) (Markham, 1984).

These measured spatial-distribution functions can be inverted to more accurately resample the original imagery. This is one method to reduce the loss of information during resampling. Such de-convolving will also provide more accurate resampling of imagery from different sensors to a common spatial data base.

SECTION 6 - RECOMMENDATIONS

The TM sensor is the most sensitive and best calibrated radiometer that has ever been flown for land remote sensing. If procedures can be developed and implemented for correcting its systematic radiometric variability (Section 4), then the TM sensor might contribute even more useful synoptic data. In addition to the improved utility of TM images over MSS images in agriculture (Pitts et al., 1983), natural resource mapping (Haas and Waltz, 1983), forestry (Hill, 1983), and geologic exploration (Everett et al., 1983), properly calibrated TM images could be used for modeling global habitability with a precision and accuracy unmatched by previous sensors. Some of the capabilities of the Landsat system suggest that the TM sensor might also be used experimentally to define requirements for future land observing satellite systems. A listing of the recommendations discussed below is provided in Appendix 9.13.

6.1 ENGINEERING CHARACTERIZATION

6.1.1 ABSOLUTE RADIOMETRIC CALIBRATION

Original specifications for absolute radiometric TM calibration required that the radiometric error be less than 10 percent. If the actual errors in the various bands had been this large, then a significant limitation would have existed on:

- The accuracy and precision of arithmetically and geometrically peeling off the atmospheric component of the at-satellite reflected radiance (Section 5.3.2)
- The between-band spectral transforms required for information extraction (Section 5.4.1)
- The ability to make precise and accurate comparisons to other sensors.

The slowly varying, or near-constancy, of radiometric gain with time (Sections 2 and 3), and the reproducibility of the absolute calibration with the external integrating sphere (Barker, Ball, et al., 1984), suggest that the TM sensor and the integrating sphere are stable enough to reduce the systematic errors of absolute calibration by more than a factor of two. This would be accomplished through recalibrating the integrating sphere against National Bureau of Standards (NBS) references.

The recommended experimental design for absolute radiometric recalibration involves three sets of cross-comparisons:

- Independent but co-ordinated spectral radiance measurements of the TM integrating sphere need to be made by the sensor's manufacturer, by the NASA calibration engineers, and by NBS scientists using absolute photon standards. These measurements need sufficient spectral resolution to avoid introducing errors when convolving them with the TM spectral response curves for each band. Errors resulting from variations across the aperture and with distance also have to be quantified.

- Recalibration of the two MSS integrating spheres for Landsat-4 and -5 by one or more of the above three groups calibrating the TM integrating sphere.

- Simultaneous calibration of one or more portable 8-Band Barnes Modular Multispectral Radiometer (MMR) TM field radiometers to serve as a radiometric transfer standard. The radiometers would be used in absolute radiometric calibration experiments at White Sands, New Mexico, and elsewhere. Accurate absolute calibration measurements taken from the ground on different dates provide one method for resolving whether the 8 percent cyclic behavior of the SWIR bands with time is a characteristic of the sensor only or of the internal calibration system (Section 2). This calibrated MMR would also be used at integrating sphere tests to measure the variability of sphere characteristics under different test conditions, as was done during the last set of pre-launch tests. Thermal band calibration needs to be done along with the reflective bands.

These recalibration data are needed for reprocessing of the pre-launch TM integrating sphere data for Landsat-5 TM/F after the tapes have been corrected for known sources of systematic variations. Such data on the TM and MSS integrating spheres will also enhance cross-comparisons of near-simultaneous acquisitions of MSS and TM digital imagery from Landsat-4 and -5.

6.1.2 RELATIVE RADIOMETRIC CALIBRATION

During pre-launch experiments using the TM sensors, it was not possible to record noise-free data on the 28-track tapes required as input to the TIPS system. Some 5-window collects were made on BRU tapes for Landsat-4 TM/PF, and a more extensive set was collected for Landsat-5 TM/F, especially during the special ambient tests at GE/Valley Forge, PA in August and September 1983.

Subsequent analysis has indicated a need for more data from the calibration region, especially from the shutter background. The raw data from these pre-launch collects are needed for within-scene correction prior to processing for absolute and relative recalibration of the detectors and the IC systems and to characterize the "double peak" in the calibration region of Landsat-5 TM/F. While corrections based on the absolute recalibrations recommended in Section 6.1.1 could be performed on the reduced data from the pre-launch "AC02" tests, a higher precision would be obtained if the raw data were used after correction for systematic variations.

Existing pre-launch 42-track HDTs, if noise free, need to be duplicated onto noise-free 28-track tapes for the critical pre-launch experiments on TM/PF and TM/F. 8-Window GPC are also needed on BRU tapes. Time needs to be made available on one of the TIPS strings to create appropriate "CALDUMP" tapes used as input to TRAPP processing, and to provide some specialized processing not available elsewhere. Computer resources are also needed for these recalibrations, especially for within-scene corrections as defined by analysis of in-orbit data and of the 1983 special collects.

6.1.3 MODELING OF SYSTEMATIC VARIABILITIES

Several types of systematic variations have been found during TM radiometric characterization (Section 4.8). The empirical corrections proposed for the systematic variations might be improved if the underlying causes could be identified and modeled. One way of identifying and quantifying these temperature-dependent causes would be to put heaters in specific locations on the existing engineering model of TM in order to run parametric sensitivity studies on temperature effects. Additional monitoring points for electronic noise isolation might also be required.

Specific engineering tasks are recommended to develop models for correcting systematic radiometric variations. These tasks might include obtaining quantitative explanations for the following:

- Vacuum shift (Section 2)
- Cyclic SWIR patterns (Section 2), apparent change in gain with time-in-orbit, presumably due to shutter position change

- IC pulse dependence on temperature, from a high change in Band 1 to a low change in Band 4

- Systematic changes of IC pulse values between dates, possibly due to thermal expansion of the primary focal plane from its one-sided line of attachment, as an additional or alternative cause of IC pulse temperature-dependence

- "Double peaks" in the calibration region of Landsat-5, apparently from incomplete obscuration of the optical path by the mask with a hole for the IC lens on the shutter

- Channel-correlated shifts

- Coherent noise

- Droop

- Bright-target saturation.

6.1.4 TM SENSOR REPORT

A report is recommended for the characterizing of the sensor performance from pre-launch engineering tests on TM/PF, TM/F and the engineering model of TM. This report needs to be prepared primarily by the sensor manufacturer and the TM system's engineer. The report needs to focus on the potential interpretation of digital imagery by scientists. The absence of such a single set of summarized volumes of test data and interpretation currently limits the ability to formulate quantitative algorithms for monitoring or correcting observations from the TM sensors. Examples of a few specific needs are:

- A schematic diagram of optical and electronic logic in order to build between-channel monitoring programs

- Prints of the exact locations of all the telemetry monitors, especially the temperature sensors

- A systematic summary of emissive band tests, characteristics, and scientific characterization

- A listing of optional tests that could be run in-orbit, such as the refocus of CFP relative to PFP.

A complete report on the spectral, radiometric, and geometric characterization of the TM sensor is needed from the engineers.

6.2 FLIGHT SEGMENT OPERATIONS

After the TM Research and Development (R&D) period ending in January 1985, or earlier, the operation of the Landsat satellites will be a NOAA responsibility. For scientific characterization, operational assistance, and experimentation, the following recommendations are made:

- Calibration and characterization tests need to be developed and performed prior to January 1985. The emphasis needs to be on possible changes in operational configuration and on implementing recommendations from the scientific investigations workshop in September, 1984.

- A memo-of-understanding (MOU) needs to be prepared between NASA and NOAA for NASA to provide technical and scientific assistance in the monitoring of Landsat normal performance and to help with potential problems. NOAA could provide operational time and access for occasional research experiments by NASA engineers and scientists. The NOAA/NASA MOU might include some compilation of conditions under which NOAA will turn back control of a Landsat satellite to NASA for possible de-boost since this might be an important time for higher-risk pre-defined calibration experiments (Section 6.4).

6.2.1 CHANGES IN OPERATIONAL PROCEDURES

Some options exist for changes in the configuration of the TM sensor during image acquisitions. Other options exist for changes in the operation of the MSS sensor and the spacecraft. Possible changes in the mission profile are suggested as scientific experiments in Section 6.2.4. This section recommends three changes in the current TM operations. Evaluation of TM data during its research and development (R&D) phase will probably lead to additional recommendations.

- Stop routine operation of the IC automatic sequencer, by operating the IC with only one of the lamps on, in order to preserve the pre-launch absolute radiometric characteristics of two of the three lamps throughout a possible multi-year mission. While each of the silicon photo-diodes, which monitor the three IC lamps, might keep the radiance output adjusted over long time periods by changes in the lamp temperature, the color balance between bands would be changed in this process. More than forty tests on Landsat-4 scenes using each of the one-lamp-on configurations individually in processing by TRAPP have demonstrated the feasibility of using one lamp state and the background from the shutter in place of the eight-lamp-state regression used for calculating gain and offset. The recommendation is that several seven-band test images be acquired at night to obtain the required data for modifying and testing the operational TIPS programs.

The automatic sequencer could be used once a week to monitor and possibly to correct changes in the characteristics of the single lamp. An alternative operating procedure would be to turn the automatic IC sequencer on for a short time at the beginning and end of each pass, in order to verify by interpolation that the single-lamp calibration was correct. A log needs to be kept of the total number of hours of operation of each lamp.

The linea[illegible]f the TM sensors and the redundancy supplied by the th[illegible]mp IC system provides a unique opportunity to monitor absolute radiometric calibration with time for changes such as clouding from filament evaporation and discontinuous filament movements.

- Change the operational procedure to alternate between black body temperatures "T2" and "T3" instead of always using "T3." Currently, there is no in-orbit test of linearity of gain with time for the emissive band. By alternating between two-point monitoring of the gain and offset with T3/shutter and T2/shutter, the degree of linearity can be evaluated quantitatively. Initial testing might involve use of T2 on a night scene. One long-pass test under constant operating conditions might involve bringing up T2 at the beginning of a pass, followed by switching to T3 with at least twenty minutes of subsequent IC data acquisition in order to determine whether the T3 temperature equilibrium had been reached and to measure the time needed for equilibration in space. These initial tests are also needed to verify whether the lower T2 temperature will provide sufficient sensitivity for calibration. Alternating use of T2 and T3 black-body temperature states would use the full TM calibration capability for Band 6.

- Establish a specific outgassing strategy for Band 6. A trade-off exists between loss of Band 6 sensitivity with time and the loss of all data from the CFP while it is outgassed and subsequently cooled down to restore the initial Band 6 sensitivity. Presumably, the criterion is the percentage loss in gain for Band 6; such loss might be acceptable until the gain drops between 20 and 30 percent.

6.2.2 IN-ORBIT CALIBRATION TESTS

Where possible, in-orbit calibration tests are desirable because:

- The pre-launch environmental test conditions are not exactly the same as those in space.
- Some characteristics of the sensor may have changed during launch.
- Some parameters may have been incompletely characterized prior to launch.

These radiometric-calibration tests place the emphasis on characterizing the normal operational mode of the sensor. Highest priority is needed on tests providing the required data for operational processing, or for modification of preprocessing or special-correction algorithms. Only one such test is currently recommended namely the calibration of the temperature-dependence of the IC pulses.

Calibration of the IC temperature-dependence is essential to the maintenance of absolute radiometry as well as to relative de-striping when scene histograms are not used. Ambient tests on Landsat-5 TM/F showed a 1 percent per °C change for some channels (Section 3). No tests were run for the IC temperature-dependence of the CFP, or during pre-launch thermal vacuum testing. Furthermore, temperatures of the TM shutter in space are up to 15°C cooler than during the 15°-25°C ambient IC calibration tests, calling for in-orbit calibration. This can be done by taking calibration data (CALDUMP) from the initial TM turn-on for as long a pass as possible to permit warming up of the TM. The most sensitive series of data would be obtained if TDRSS could be used to transmit TM data for more than one orbit without turning off the sensor.

In the absence of such a long pass, it is possible that a shorter 30-minute pass would work. These data could be acquired at night since no imagery is needed. The pass might be of some value in acquiring real imagery over Artic regions, which are not normally viewed by Landsat.

6.2.3 IN-ORBIT CHARACTERIZATION TESTS

For certain critical types of radiometric variability it may be possible to suggest alternative configurations of the TM sensor to verify the noise model, and perhaps to generate the necessary data for applying corrections during ground processing. Several suggestions are made for verification and characterization:

- Redundant Power Supply. Verify the constancy of IC pulses using the redundant power supply and compare the coherent noise of the two primary and redundant supplies on night scenes

- Manual IC Operation. Verify the agreement between IC pulses obtained with the automatic sequencer both on and off

- Back-up IC Operation. Verify the pre-launch relationship of "override" "constant-current" pulse values to normal "constant-radiance" IC pulses as a potential method for monitoring silicon photodiode performance with time

- Coherent Noise Phasing. Turn the midscan pulse on during a nighttime acquisition to look for the phasing relationship of coherent noise between scans. Midscan location information is always available in the Payload Correction Data (PCD), and therefore the midscan pulse is more of a convenience than a necessity.

6.2.4 IN-ORBIT SCIENTIFIC MISSION TESTS

Both the Landsat-4 and Landsat-5 spacecraft have mission capabilities that extend beyond the normal acquisition mode. Special tests have been and will be requested by the Landsat Science Office for sensor and image quality characterization. These tests gather representative normal nadir-looking data at night. In the daytime the tests gather data from homogeneous scenes of water, deserts, snow and clouds, and over selected calibration test sites, such as White Sands, New Mexico. In addition, several low-risk calibration and feasibility tests are proposed, which utilize additional capabilities of the TM sensor, or which provide between-sensor calibrations. Some higher risk experiments that test the extremes in TM capability are suggested elsewhere (Section 6.4).

Several characterization experiments for the TM sensor alone are recommended. They involve minimal changes in the mission profile, i.e., changes in configuration or pointing, but with no orbital adjusts.

They could be attempted on Landsat-4 TM/PF, and if successful, possibly used on Landsat-5.

- Subsampled Extension of Swath Width--By taking calibration data at the beginning and end of each pass and turning the internal IC shutter off, a 20 percent extension of imagery would be obtained to the east on forward scans and to the west on reverse scan, since the shutter would no longer be obscuring the optical axis at the end of each scan. Processing of such data would require special software because the scan-line-corrector resets during these acquisitions. One scientific use for such data might involve the creation of 40-percent larger swaths of lower spatial-resolution imagery for global monitoring of averaged biophysical variables, such as green biomass, temperature, and albedo. Obscuration by the resting shutter is a problem.

- Bidirectional Reflectance--By rotating the entire spacecraft to point the TM sensor off-nadir, either fore or aft, or to either side, bidirectional information could be collected over the same targets at different times. Such a data set could be used to test and/or modify radiance transfer models of the atmosphere and canopy models of specific sites.

- Intensive Single Site Acquisitions--Pointing the TM sensor from side-to-side could provide nearly daily coverage of a given path on the ground. Such an experimental set of acquisitions would help to define the mission requirements for overpass frequency, and demonstrate the limitations on the ability of Sun-synchronous satellites to monitor anomalous events, such as floods, for sites of various types of ground cover and with differing cloud-cover. Intensive sampling of several specific sites over several years could provide quantitative information on the feasibility of acquisition of cloud-free data by future-land observing satellite systems, and on the usefulness of such data.

- Single Sensor Stereo--Two ways to prepare stereo pictures from TM imagery are fore/aft pointing in the same pass or side-to-side pointing on different days. Both are technically feasible. The fore/aft is preferable because it provides nearly constant illumination.

Several in-orbit intercalibration and characterization experiments for comparing the TM sensor to other sensors are given below. They also appear to be within the operational capabilities of Landsat. By using known spectral response curves and assuming a flat spectral response within each band for the ground targets, atmospheric absorption, and scattering, radiometric calibration can be made for acquisitions at nearly the same time of overpass for:

- TM/F to TM/PF--This 7-band to 7-band comparison can be done by pointing both spacecraft. This creates a between-sensor stereo data set. Either a simultaneous TDRSS acquisition or an X-band acquisition for TM/F and a TDRSS relay for TM/PF could be used to acquire the data set. A test of this intercomparison was done on 15-16 March, 1984, when the CFP bands on Landsat-5 TM/F were being activated. This was a unique opportunity provided by adjustment of the Landsat-5 orbit to put it on the Landsat-4, -5 World Reference System (WRS). During these movements, Landsat-5 passed underneath Landsat-4

- TM/F to MSS/F (High Gain)--The high-gain MSS acquisition needs to be taken over a clear-water area like the Bahamas, where ground observations exist for comparing the capability of the sensors to produce bathymetric charts

- TM/F to GOES E/W to NOAA-7/8--GOES-East or -West could be used to transfer spectral data between TM and the NOAA-7 and -8 polar orbiting satellites since the latter do not go over a specific location at the same time as TM.

Experiments such as these might provide better intercomparisons of absolute radiometry than calculation from aircraft and ground measurements, which usually use single-photon scattering atmospheric models. Such models are prone to high errors, especially at low sun angles. Mixed-sensor data collections have potential utility in many scientific experiments in addition to radiometric calibration.

6.3 TIPS GROUND PROCESSING

The TM Image Processing System (TIPS) consists of two computer strings, TIPS-1 and TIPS-2, located at Goddard Space Flight Center. TIPS is scheduled to be turned over to NOAA in February, 1985. In the TM R&D period prior to turn-over, TIPS needs to be brought up to the highest level of performance possible. From a radiometric perspective, that would mean implementing corrections and changes suggested in the preceding sections. Realistically, the number of changes that can be tested and implemented is significantly smaller than desirable. Therefore, this section will focus on a subset of recommendations that seem most feasible, including updates of calibration parameters, several proposed changes in radiometric processing, changes in geometric processing, some new digital products, and R&D tasks for which TIPS is uniquely suited.

6.3.1 RADIOMETRIC CALIBRATION PARAMETERS

As a result of on-going research, a parameter file for TIPS processing is periodically updated. This was the mechanism for implementing a change in the post-calibration dynamic range on 15 January 1984. This change was a trade-off between the desire for recoverable raw data by use of expansion only during radiometric calibration and avoidance of pushing real high-radiance observations off-scale. Two further updates in calibrated dynamic range are scheduled. The first change is planned for late Spring, 1984, to assure a common range for in-orbit TM/PF and TM/F data. The second change is planned for the Fall, 1984, to implement any improved estimates of the absolute radiometric range from sources such as:

- Recalibration of the integrating spheres (Section 6.1.1)
- Sensor-to-sensor in-orbit cross comparisons (Section 6.2.4)
- Ground and aircraft absolute calibrations at the time of TM overpass over selected homogeneous areas.

Absolute radiometric calibrations from the ground using passive atmospheric sensing, rather than aircraft, are difficult. Repeated measurements over an area such as White Sands, NM under different atmospheric conditions will be needed to demonstrate greater reproducibility than pre-launch calibration tests.

It is also recommended that the absolute calibration parameters supplied to TIPS by NASA scientists and engineers be recalculated to separate effects of time and temperature during TM/IS calibration, and to remove as many sources as possible of systematic variability discussed in Sections 4 and 5.1.

The above discussion means that a capability has to be retained by TIPS for updating the following quantities:

- Post-calibration dynamic range for each band, RMIN (B) and RMAX (B) (Appendix 9.1)
- Pre-launch values for spectral radiance for each of the twenty-one integrating sphere levels, $L_{\lambda,IS}$ (Appendix 9.2)

- Pre-launch gain and offset for each channel calculated from the regression of raw radiance L_R against $L_{\lambda,IS}$ for the sphere levels inside the dynamic range of the detector (Appendix 9.3 and 9.4).

- Pre-launch average IC pulse values of each channel for each of the eight lamp configurations, ℓ; namely, P^o (ℓ, C).

An alternative to updating the pre-launch gain and offset of each channel, is to update the calculated nominal IC pulse, P_n (ℓ, C) in Equation 1-2. Still another alternative is to provide the effective spectral radiances, $L^o_\lambda(\ell)$, for each of the IC lamp configurations, ℓ, which are calculated from the observed pre-launch averaged IC pulse, $P^o(\ell)$, and the offset, O_{IS}, and gain, G_{IS}; this is Equation 1-3, solved for $L^o_\lambda(\ell)$. In any case, TIPS needs to retain the ability to calculate these values from improved estimates over the next several years, or to provide for a direct replacement of the critical values in its parameter file.

6.3.2 IC SYSTEMATIC RADIOMETRIC CORRECTIONS

It is recommended that TIPS-era radiometric processing be optimized for the minimum striping using stand-alone IC processing, without histograms. One reason for this is that any residual destriping from histogram equalization guarantees an increased between-channel variability in the absolute radiometric calibration, even if the correct reference histogram is applied. TIPS-specific recommendations, primarily from experience with Scrounge-era processing and analysis with TRAPP software, are given below for some of the corrections implied in Sections 4.0 and 5.1.

- Two-Background Shutter Collects. In the middle of Scrounge-era processing, the single 52mf background was replaced with a double background collect of 24mf and 28mf, in the stable regions before and after DC restoration (Section 5.1.1). The same needs to be done for TIPS-era processing until a better method of background estimation is determined, such as using regions directly adjacent to the pulse. In particular, the raw data collected for calibration and that used for engineering analysis (CALDUMP) should be taken from the same region. The Canadians have incorporated these two background collects into their TM preprocessing (Murphy et al., 1984).

- Within-Scene IC Corrections. As many of the systematic sources of variability as possible need to be removed from the raw calibration values before calculating relative gains and offsets (Section 4). This is an easier requirement for the pulse or average background calibration data for each line than for individual raw radiance values at each pixel location in the image.

- Background Outliers. Outliers need to be rejected by using a threshold on raw radiance values, or by using a lower thresholding on a traveling average, in the shutter region in order to avoid noise pulses from the sensor (e.g., scan-line correction reset, or incomplete obscuration), from transmission loss, or from tape drop-outs during processing (Section 5.1.1). Retention of high values in the background region will result in bias values which are too high. This background value will become essential to radiometric calibration of the reflective bands if a single lamp state is used, even though it is currently used only for band 6 calibration.

- "Pulse" from Light Leak. There is a secondary or double pulse in the calibration region due to a light leak around the IC shutter mask on Landsat-5 TM/F (Section 5.1.3). The algorithms in TIPS need to be examined to be sure that they will not be affected by this leak pulse, especially during the 000 no-lamps-on configuration. It is possible that this is contributing to the high 4-DN values for the IC-only relative bias in some PFP channels on TIPS, although the high initial values of bias in TIPS were probably from incomplete obscuration in the shutter collect window for the background. One possible method to remove the potential interference of the light leak is to take advantage of the observed reproducible location of a few mf for the pulse with time, the fixed 52 mf distance between the center of the pulse and the center of the leak, and use a subset of the 148 mf calibration region which always excludes the 24 mf wide leak, namely, a window less than 80 mf [2(52-(24/2))] centered at the calculated center of the pulse. The existing algorithms could then continue to be used on this 80 mf subset of the original 148 mf collect window. An implementation that has been verified, using TRAPP, is to restrict the acceptable region for the center of the pulse to a fixed subset, namely from 40 to 100 mf, of the 148 mf collect region. The location and size of this secondary peak needs to be monitored to be assured that there is no change with time.

- Pulse Integration. TIPS parameters should be modified to include a variable IC pulse-integration width for each channel in order to reduce the random error in the pulse by a factor of 2 (Section 5.1.3). It is also necessary to either recalculate the pulses used for absolute calibration the same way as TIPS, or to definitively demonstrate that a multiplication factor can be used for the conversion of a 31 mf to a 65 mf summation, in order to avoid additional error in absolute radiometric calibration.

- Pulse Averaging. The methodology used for averaging pulses in TIPS needs to be reviewed to assure that trends or transitional pulses between lamp state configurations are not included (Section 5.1.4). If a single lamp is used, then both calibration and trending errors can probably be reduced compared with the use of central pulses in the 40-scan periods of the IC automatic sequencer. An option is also needed for separate processing of forward and reverse scans.

- Lamp State Options. TIPS software needs to be modified to accept calibration data from any single lamp configuration, or from the automatic sequencer, instead of only from the automatic sequencer. The software also has to allow for omission of any particular lamp configurations in a "regression" with as few as one lamp state and the background from a shutter region (Section 5.1.5). TIPS currently uses a nine-state regression, i.e., the shutter background is used as a separate zero-level lamp-state configuration. Each of the nine states has an a priori inverse weighting factor which was set at maximum for shutter data on Landsat-4. The weighting factors are potentially valuable, although the current set of a priori "noise" could be reviewed in light of the known sources of variations (Section 4). These a priori weighting factors could be used as threshold defaults for comparison to observed "noise" on the corrected data.

- IC Temperature-Dependence. The temperature-dependence of the IC pulse is the single largest systematic error that needs to be quantified and normalized in order to preserve absolute radiometric calibration and to provide for relative within-band de-striping without histograms (Sections 5.1.6 and 6.2.2). Judging from a couple of twenty-plus scenes in a single pass for both Landsat-4 and -5, the rate of temperature increase with TM operating time is lower in space than it was in pre-lauch tests. This may mean that a single transformation to the temperature in space is all that is necessary to correct for the IC-temperature-dependence, i.e., within-pass smoothing may not be needed.

- Between-Channel Correlations. An algorithm needs to be developed to assure between-band absolute radiometric calibration for atmospheric correction and spectral transformation. In principle, the redundancy of the correlation of all 100 channels can be used if a method is developed which does not introduce significant additional error. A "shading factor" of the pulse value divided by the band average is one method for normalizing within-band correlations, which are often odd/even channel effects, that are presumably associated with characteristics of the IC system. This multiplicative gain-type shading factor correction has been used in pre-launch calculations. Correlation is a better method for between-band within-scene smoothing (5.1.6), because it can apply both an arithmetic and a multiplicative correction.

- Within-Pass Smoothing. Intervals of several scenes or a whole pass need to be smoothed to account for effects such as the continuous increase in the temperature along the path (Subsection 5.1.7). These effects need to be corrected in the floating point mode of calibration in order to avoid the addition of any rounding error associated with either segmentation or blending of subsegments.

- Between-Date Smoothing. If physical explanations can be used to reliably predict change with time, then provision could be made for utilizing this information during calculation of gains and biases (Section 5.1.8).

- Referencing or Weighting. Some channels are more noisy than others. When averages are used in calculations, it is desirable to use averages weighted by the inverse of the variance. If good estimates of the variance are not available, then it is better to use a quiet reference channel (Table 4-5) than an average.

- Quality Indices. Statistical measures of the uncertainty in the calculations, such as standard error of the estimate for regression, could be explicitly included in the TIPS reports as quality indices.

6.3.3 HISTOGRAM EQUALIZATION

It is recommended that histogram equalization by TIPS be used primarily as a quality control measure. The reasons for this are given in Section 5.2.1. Histogram equalization would be used for TIPS radiometric calibration if the striping, calculated after IC calibration by comparing the histograms of different channels, is above a threshold level, and then only as a slowly varying weighting with the gain and offset calculated from the IC system. Possible modifications to the TIPS processing, which appear to be appropriate to accomplish this recommendation, are given below.

- First Pass HDT-RT Histogram File. One option that would reduce the operational processing time is to drop histogramming from the first pass through the raw data on the HDT-RT. If this option is implemented operationally, a less frequently used engineering capacity is needed to calculate and retain a file for a histogram of each scene and for the cumulative pass. This engineering option for histogramming the HDT-RT would be used for creating files for the long term monitoring of the constancy of "bin-radiance dependence" and for monitoring the magnitude of the radiometric corrections by comparing the normalized gains and biases calculated from histogram equalization of this raw data to the actual normalized gains and biases that were calculated after applying a radiometric calibration.

- Calculation of Systematic Corrections. Normalized gains and biases need to be calculated for every line in the HDT-RT based on the corrections outlined in Section 6.3.2. The alternative of continuing to calculate a single RLUT for a whole scene, or segments of an interval, is almost unacceptable.

- Second Pass HDT-RT 11-Bit Histogram. An archival HDT-AT needs to be created, during the second pass through the raw HDT-RT, that is equivalent to the current HDT-AT with unity RLUT. The respective "relative" and "applied" gain and biases at the end of every line of the HDT-AT would be replaced, respectively, with systematically corrected normalized IC gains and biases, and normalized gains and biases calculated by histogram equalization. This histogram equalization would be calculated from a centrally defined common radiance region for all channels, presumably identical to the middle section of the three section dynamic range proposed in Section 6.3.5. The histogram used for this histogram equalization would be a cumulative 11-bit histogram of radiometrically corrected pixels from both the scene and the calibration region for all preceding scenes from this second pass through the HDT-RT. The 11-bit, rather than 8-bit, histogram is necessary to avoid loss of the accuracy gained by sub-DN systematic corrections. Some of the additional benefits of this proposed histogramming procedure include:

  Absolute radiometric calibration would be retained because the common radiance range for histogramming is chosen after radiometric calibration

- A higher sensitivity is obtained on low radiance scenes because a nearly full range of DN values can be guaranteed by the inclusion of IC data in the histogram

- The current HDT-AT format is unchanged

- Raw observations become routinely available to any investigator requesting either an HDT-AT or a CCT-AT. This is a high priority for scientific investigators, who are the principle users of non-P data

- Well averaged constants for both IC and histogram calibration become directly available from an -AT tape

● HDT-AT Histogram File. If the 11-bit scene histograms and the cumulative 11-bit histogram for all the scenes in a given pass are retained on a history file, as well as the normalized gains and offsets calculated from them, then it will be possible to systematically monitor the TM radiometric performance as a function of time, as required for making within-path or between date corrections (Sections 5.1.7 and 5.1.8). A history file of the systematically corrected IC normalized gains and offsets for each line, and an average for each scene and the whole pass, would provide the complementary data for monitoring and modeling the absolute radiometric performance of the TM internal calibrator.

● Histogram Reference. When the normalized gains and biases are calculated by histogram equalization, use the quietest channel in the band as the reference (Table 4-5), or the band-average weighted by the variance, in order to avoid the larger potential error in absolute radiometry associated with using the equally weighted band-average.

● Histogram Monitoring of IC Quality. Ideally, the residual striping will be sufficiently small, after appropriate calibration with the IC system alone, that there will be no justification for the use of histogram equalization. In that case, histogram equalization can be used as a monitor of residual striping, and only used if the striping is greater than some a priori value. This quality index could be calculated automatically in real-time just before geometric resampling.

● Weighting of IC and Histogram Constants. A less satisfactory procedure than using IC alone, but one that incorporates histogramming, is to calculate a set of weighting factors for the gains and offsets from the separate IC and histogram calculations and apply them in 16-bit or floating point calculations during the geometric resampling process. A set of weights could be calculated as the inverse of the square of the differences between the calculated gains and offsets and their values as predicted by an empirical fit of their slowly varying behavior with time. If it is not possible to modify TIPS to allow for radiometric calibration during the geometric resampling, then the raw values suggested above for the HDT-AT would have to be replaced with radiometrically calibrated values.

- HDT-PT Histogram File for Each Band. An 11-bit summary histogram for each band, for each scene and for the whole pass, from the geometrically resampled P-tapes, would provide the data necessary to monitor the overall operational radiometric performance of TIPS during P-processing by comparison to A-histograms for the same scene. P-histograms would also provide a research and development tool for quantitatively assessing the effect of difference resampling algorithms.

6.3.4 GEOMETRIC PROCESSING

In general, geometric processing on TIPS is excellent. Improvements would be useful in several areas, if possible.

- Single Pass Geodetic Product. At present, TIPS can not use its ground control points, GCPs, to produce a geodetically rectified image of the reference scene from which the GCPs are taken. This means that if there is only one cloud-free TM scene of an area, that it can not be geodetically rectified. A TIPS capability is needed for producing geodetically rectified scenes from a single TM pass.

- Map Compatibility by Rotation to North. A TIPS resampling option is needed for directly creating a north-pointing projection without resampling of the P-product, in order to provide greater compatibility to most maps, e.g., 1:24,000 scale USGS maps. The Canadians at CCRS are planning on providing this type of projection as a normal TM product, which will also be more easily compatible with information extraction procedures using GIS, Geographic Information Systems. An additional benefit of such a resampling is that residual channel-related striping remaining after radiometric calibration would be less visible. Since a UTM option exists in TIPS, a recommendation is made that all geodetic P products be in a UTM projection.

- Single Pass Cubic Spline Resampling. Fischel (1984) has suggested that it would be better to use a single pass, rather than a double pass, in the second part of the TIPS resampling procedure (see Section 5.2.5).

- Image Co-ordinates of GCPs. It would be useful to have the image co-ordinates (start line and sample) for each of the 33 by 33 pixel GCP chips that were used in a specific image.

- Relative GCPs. After the required geodetic accuracy has been achieved by use of map-referenceable GCPs, it is suggested that these cloud-free reference images be searched for additional "relative" 32 by 32 pixel GCP chips, even though they may represent features which are not present on current maps. Since many scenes are more than 50 percent cloud-covered, it is desirable to have two-to-four times as many GCP chips as are needed in a cloud-free scene. Excellent GCPs are being rejected by some operators in the current building of the TIPS GCP library because they can not be located on maps.

- GCP Methodology. Spectral transforms (Section 5.4.1) such as "greenness" and "brightness" are suggested as replacements for the two raw spectral bands, in order to provide potentially higher contrast in a one or two band correlation of the chip to the 128 by 128 pixel ground control point neighborhood. It is also recommended that these spectral transforms be examined for use, in conjunction with the thermal band, for automatic cloud cover assessment (ACCA). Up to four sets of GCPs are recommended for each scene so that the GCPs can be selected on the basis of season.

- Schedule for Global GCP Library Build. With the current TIPS methodology for building the GCP library, it will probably take one or two decades to complete it on a global scale, even if appropriate maps were available, which they are not. Therefore, it is recommended that an alternative methodology be proposed, perhaps using a factor of fifty fewer GCPs in the initial building of the library for each interval.

6.3.5 THREE-SECTIONED POST-CALIBRATION DYNAMIC RANGE

A proposal is requested for implementing the three-sectioned RLUT on TIPS in a manner similar to that discussed in Section 5.2.3. The Canadians at CCRS attempt to accomplish the same objective of retaining non-saturated data in all channels by widening the post-calibration dynamic range to include the lowest RMIN and the highest RMAX, with a linear fit in between. This single section procedure has the disadvantage, for a fixed 8-bit RLUT, of lowering the sensitivity for all channels, i.e., some data are compressed from two bins into one bin; this does not happen if the post-calibration radiometric resolution is increased, as CCRS accomplishes in intermediate steps by going to a 16-bit RLUT, or by dropping the most significant bit in the lower radiance scenes of the North and replacing it with one more bit in a shifted 8-bit RLUT.

Since DN values of 0 and 255 may represent values outside of the dynamic range, it is recommended that settings of the dynamic range be from DN values 1 through 254. DN values of 0 to 255 would then be used explicitly for values outside the post-calibration dynamic range.

6.3.6 IMAGE CALIBRATION

A TIPS procedure needs to be developed for replacing bad channels (Section 5.2.2), other than the current procedure of replacement with an adjacent channel. TIPS needs to retain, rather than replace, the imagery and calibration from Channel 4 of Band 2 in future processing of data from Landsat-4 TM/PF.

TIPS needs to implement an unbiased 8-bit probabilistic approach, using an individual bias and gain for each line, to replace the current 8-bit integer RLUT approach for the whole scene (Section 5.2.4). It is desirable to provide a mechanism for within-line calibration. The most desirable procedure to avoid quantization errors is to combine radiometric and geometric calibration and to use 16-bit arithmetic until the final stage of resampling, as CCRS will do. Here again, the final rounding can be done with zero bias by using the probabilistic approach.

6.3.7 PRODUCTS

TIPS, and other facilities with ground receiving stations or an ability to process high density tapes, are in a unique position to produce special, and potentially operational, products because they can start with raw data on an HDT-RT without introducing unnecessary additional quantization errors. The HDT-RT tapes are also the only source of raw calibration data. Some recommendations for current and future special products are given below.

- Semi-Weekly Tapes of Raw Calibration Data. A recommendation is made that raw TM data from the calibration region of the HDT-RT, which are used in TIPS processing, be made available as an optional part of an operational TIPS string. Currently, it is necessary to have dedicated use of a TIPS string to produce three files of data and an analysis file on an engineering tape, called CALDUMP. No changes in tape format are requested; what is needed is access to the raw calibration data from the background and calibration regions of the shutter (Section 5.1). It is recommended that it be possible to put any or all of the calibration collect files from a single TIPS processing interval of scenes onto such a CALDUMP tape. Such CALDUMP tapes are need approximately twice a week for TRAPP.

- Semi-Weekly "Unity" CCT-AT. An operational option is also needed to be able to produce a CCT-AT with "unity" RLUT to accompany the CALDUMP tape for input to TRAPP. This is the mechanism for accessing raw data and it needs to be part of the operational TIPS procedure. If the recommendation is accepted to normally use only one lamp (Section 6.2.1), whether the IC automatic sequencer is on or off, then it is anticipated that one monitoring tape a week would be with three lamps sequencing and one tape a week would be with only one lamp on.

- Special "Unity" CCT-AT. It is recommended that special collections of raw data on CCT tapes be occasionally accessible from anywhere on the HDT-RT, not just the current background collect regions. One method for implementing this request is to make a CCT-AT with a unity RLUT, with a different starting and ending minor frame; this worked in the Scrounge-era processing. It is not anticipated that these products would be standard products, they are viewed as necessary for engineering and scientific studies during the research and development period, and for subsequent monitoring and trouble-shooting by scientists in the Landsat Science Office.

- Reprocessed Internal Reference Scenes. A recommendation is made that ten 7-band reference scenes be chosen for both Landsat-4 TM/PF and Landsat-5 TM/F. When changes are made in the TIPS processing algorithms, it is recommended that the most appropriate reference scene be rerun and the following products submitted for examination to the Landsat Science Office: CALDUMP, unity CCT-AT, CCT-AT, CCT-PT, black and white prints of A-product in all bands, black and white prints of P-product if the resampling process was modified, and copies of appropriate quality assessment printouts. To the extent that such products are identical to previous submissions, they do no have to be resubmitted. These are also the scenes that need to be used for testing special processing options, such as nearest neighbor (NN) and different implementations of cubic convolution (CC) resampling.

- History Tapes of Calibration Constants. A recommendation is made that TIPS maintain a history file of calibration results for operational processing of TM imagery. Such a file would provide the data for trend analysis and possible smoothing (Sections 5.1.6, 5.1.7, and 5.1.8). Some of the suggested contents for a history file were outlined with recommendations for histogram equalization (Section 6.3.3). These files need to be made available periodically on tape to the Landsat Science Office for analysis. Possible contents for these files include tabulation by scene center and time of:

  - Average IC pulses
  - Average shutter background and standard deviation
  - 8-bit histograms of raw data
  - 11-bit radiometrically calibrated A-histograms
  - 11-bit P-histograms by band
  - IC offsets and gains
  - Applied offsets and gains
  - Corrections by type and channel
  - TIPS "TIG" Quality Assessment files
  - TIPS "TAG" Quality Assessment files.

- Selected HDT-RT Copies. If research efforts are started to separate information about the atmosphere and the land (Section 5.3.2), then it is assumed that copies of HDT-RT tapes will be needed as direct input to computers such as the MPP or Cyber. It is recommended that official intercomparisons of products from common HDT-RTs be made with other facilities, such as those in Canada and Italy.

- Extra Band(s) of Binary Data. Certain types of information that would increase the utility of TM imagery are extractable as part of the TIPS processing, especially the ground control-point geodetic resampling. Much of this type of information, such as boundary maps, can be summarized with single bit binary masks. Once a boundary map is prepared as part of the building of the GCP library, it can be used for all subsequent scenes at the same location. The addition of an 8th band to the TM digital imagery would permit the addition of eight such binary masks. It is recommended that a feasibility study be made of adding such a band with the following types of binary masks:

- Political boundaries from GCP maps
- "Infrastructure" of important features, such as roads and railroads, that are below the spatial resolution of the TM sensor
- Topographic boundaries for watersheds
- Boundaries for major ecosystems
- Clouds from ACCA
- Calculated edges of cloud shadows
- Outlines of locations of used and unused GCP chips
- Points and boundaries from texture analysis.

● Extra Bands of 8-Bit Data. Several types of 8-bit data are of potential value to users and are producible prior to quantization error during TIPS-type processing. It is recommended that the feasibility of preparing such registered P-products be examined for:

- Spectral transforms (Section 5.4.1)
- Texture measures
- Digital topographic maps
- Slope and aspect
- Irradiance
- Atmospheric variables
- Surface bidirectional reflectance.

● Tapes at Reduced Spatial Resolution. It is recommended that the feasibility of operational production of TM imagery at reduced spatial resolution be examined. Historically, it has been easier to acquire imagery from space than to analyze it. This proposal is designed to:

- Make the product less expensive to the user
- Take advantage of the multi-temporal synoptic strength of the Landsat system

  - Provide a maximum of cloud-free data by resampling only cloud-free pixels at resolutions of 120 m and 1 Km (Section 5.3.2)

  - Provide a reason for acquiring more imagery, both globally and at night, because of the presumed increase in the number of applications

  - Provide fewer bands, such as bands 3 and 4, and spectral transforms, such as brightness and greenness

  - Provide more multi-temporal data

  - Provide less data to process

  - Provide the user community with the opportunity to examine quantitative data, with the knowledge that if it proves useful, the full resolution of the TM data is available for exactly the same scene.

- Cloud-free Global TM Archive. It is recommended that a cloud-free archive of seasonal TM digital imagery be acquired and maintained on a medium, or with error correction capability, that can guarantee error-free recovery of this data over the next several decades.

6.3.8 RESEARCH AND DEVELOPMENT

Many of the proposed operational recommendations and suggestions in the preceding sections will require examination during the research and development period of TIPS. In addition, some effort needs to be made to examine other topics, such as:

- Within-line processing
- Band 6 processing
- Ingestion of foreign TM tapes
- Full interval radiometric processing
- Creation and processing of pre-launch 28-tracks
- Global Positioning System tests to reduce required control point neighborhood from 128 x 128.

6.4 CONTINGENCY EXPERIMENTS

It is recommended that a contingency plan of scientific and engineering experiments be prepared for acquisition of TM and MSS digital imagery when these sensors are not being used operationally. This requires agreement of NASA and NOAA on flight segment operation (Section 6.2). Advanced planning is important since opportunities for these experiments may be lost, or go unrecognized, if the need and feasibility are not understood. In the final stages of spacecraft operation, there may be very little time between loss of power, or some other failure, and the need to de-boost in order to attempt a recovery by a polar-orbiting shuttle mission at a lower altitude.

6.4.1 SCIENTIFIC EXPERIMENTS

Scientific needs are particularly great for space-acquired imagery to help define sensor and mission requirements for future land-observing satellite systems. Scientific experiments would be aimed at acquiring data that cannot be acquired in the normal modes or in the special in-orbit scientific mission tests (Section 6.2.4). Some experiments could be done with pointing or minor orbital adjusts while at current altitude, others could occur during or after de-boost to a lower altitude. Illustrative experiments include:

- Radiometric Calibration with Moon. The Landsat spacecraft is capable of pointing at the Moon, and this might provide a means of long-term multi-decade absolute radiometric calibration between sensors

- Stereo and Bidirectional Reflectance

- Time-of-Day Orbital Changes

- Revisit Frequency Requirements

- Utility of Mixed Spatial Resolution.

6.4.2 ENGINEERING EXPERIMENTS

Engineering experiments would be designed to characterize the best performance that could be achieved by the sensor, as a complement to the normal in-orbit calibration and characterization tests (Sections 6.2.2 and 6.2.3). Illustrative experiments might include:

- Band 6 Sensitivity at 70 Degrees Kelvin
- Focus Tests of Inchworms Over GCPs
- Tests of Global Positioning System Utility
- Tests of On-Board Computer Options
- Alternative Lamp and Power Supply Tests

SECTION 7 - ACKNOWLEDGMENTS

One of the reasons that a paper like this, which attempts to bridge part of the gap between the engineering and the scientific characterization of the TM sensor, can be written, is because of the initiative shown by key NASA engineers in inviting active participation of NASA scientists in the various phases of the Landsat program, especially in the pre-launch testing of both the MSS and TM sensors. Particular appreciation is expressed to Oscar Weinstein and Jon Busse, the instrument manager and the Project Manager, respectively, at the time of critical scientific involvement with the engineers. The complementary part of this successful working relationship was the encouragement from the Project Scientist, Vince Salomonson, to maintain a nearly full-time involvement with the engineers over a period of several years. The generous co-operation of many engineers at Santa Barbara Research Center (SBRC) and General Electric at Valley Forge (GE/VF), especially during on-site testing, was invaluable. Some of the engineers were: Jack Engel (SBRC), Jack Lansing (SBRC), Eric Beyer (GE/VF), and Nick Koepp-Baker (GE/VF). This was a marvelous opportunity to see first-hand the literally hundreds of people who, by personal dedication, have made the TM sensor on the Landsat spacecraft such a success. This co-operation between engineers and scientists has continued with the current Project Manager, Lou Gonzales, and the Mission Opeations Manager, Bill Webb.

Two teams of contractors have supported the computing and analysis efforts associated with this scientific characterization over the last three years, one from Computer Sciences Corporation (CSC) and the other, more recently, from Science Applications Research (SAR). Key scientists and analysts from these companies were Rochelle Abrams (CSC), Dave Ball (CSC), Fred Gunther (CSC), Yung Lee (SAR), and Son Truong (SAR). All of these people, and the supporting staff, have been extremely conscientious and devoted in designing, coding, maintaining and running the many versions of TRAPP software on the computers at Goddard Space Flight Center, and then assisting in the months of analysis of the library of TRAPP books upon which most of the conclusions in this paper are based.

A special note of appreciation goes to Fred Gunther who has assisted extensively in the preparation of this manuscript, and to those people who reviewed earlier versions of this paper, namely, Winona Barker, Jack Lansing, Yung Lee, Loren Linstrom, and Brian Markham.

A portion of data processing was performed under the National Oceanic and Atmospheric Administration, Contract Number NA-83-SAC-00600.

SECTION 8 - SELECTED BIBLIOGRAPHY

Anonymous, "Scrounge Interface Control Document," LANDSAT-D PROJECT, ADDS/LAS, Goddard Space Flight Center, Greenbelt, Maryland, February 1982

Anuta, P., L. Bartolucci, E. Dean, F. Lozano, E. Malaret, C. McGillen, J. Valdez and C. Valenzuela, "Landsat-4 data quality analysis,". PROCEEDINGS, PECORA 8 REMOTE SENSING SYMPOSIUM. Sioux Falls, South Dakota, 1983

Anuta, P. E., L. A. Bartolucci, M. E. Dean, D. F. Lozano, E. Malaret, C. D. McGillem, J. A. Valdez, and C. R. Valenzuela, "Landsat-4 MSS and Thematic Mapper data quality and information content analysis," IEEE TRANSACTIONS ON GEOSCIENCE AND REMOTE SENSING, Vol. GE-22, May 1984

Barker, John L., and Fred J. Gunther, "Landsat-4 sensor performance," PROCEEDINGS, PECORA 8 REMOTE SENSING SYMPOSIUM, Sioux Falls, South Dakota, 1983

Barker, J. L., R. B. Abrams, D. L. Ball, and K. C. Leung, "Characterization of radiometric calibration of Landsat-4 TM reflective bands," PROCEEDINGS, LANDSAT-4 SCIENTIFIC CHARACTERIZATION, EARLY RESULTS SYMPOSIUM, Greenbelt, Maryland, April 1984

Barker, J. L., R. B. Abrams, D. L. Ball, and K. C. Leung, "Radiometric calibration and processing procedure for reflective bands on Landsat-4 protoflight Thematic Mapper," PROCEEDINGS, LANDSAT-4 SCIENTIFIC CHARACTERIZATION, EARLY RESULTS SYMPOSIUM, Greenbelt, Maryland, April 1984

Barker, J. L. , D. L. Ball, K. C. Leung, and J. A. Walker, "Prelaunch absolute radiometric calibration of the reflective bands on the Landsat-4 protoflight Thematic Mapper," PROCEEDINGS, LANDSAT-4 SCIENTIFIC CHARACTERIZATION, EARLY RESULTS SYMPOSIUM, Greenbelt, Maryland, April 1984

Barker, J. L. F. J. Gunther, R. B. Abrams, and D. L. Ball, "TM digital image products for applications," PROCEEDINGS, LANDSAT-4 SCIENTIFIC CHARACTERIZATION, EARLY RESULTS SYMPOSIUM, Greenbelt, Maryland, April 1984

Bernstein, R., and J. B. Lotspiech, "Landsat-4 Thematic Mapper-results of advanced digital image processing experiments," PROCEEDINGS, PECORA 8 REMOTE SENSING SYMPOSIUM, Sioux Falls, South Dakota, 1983

Bernstein, R., J. B. Lotspiech, J. J. Myers, H. G. Kolsky, and R. D. Lees, "Analysis and processing of Landsat-4 data using advanced image processing techniques and technologies," IEEE TRANSACTIONS ON GEOSCIENCE AND REMOTE SENSING, Vol. GE-22, May 1984

Castle, K. R., R. G. Holm, C. J. Kastnev, J. M. Palmer, P. N. Slater, M. Dinguivard, C. E., Ezra, R. D. Jackson, and R. K. Savage, "In-flight absolute radiometric calibration of the Thematic Mapper," IEEE TRANSACTIONS ON GEOSCIENCE AND REMOTE SENSING, Vol. GE-22, May 1984

Chavez, P., Jr., S. C. Guptill, and J. Bowell, "Image processing techniques for Thematic Mapper data," TECHNICAL PAPERS OF THE 50TH ANNUAL MEETING OF THE AMERICAN SOCIETY OF PHOTOGRAMMETRY, Washington, D.C., 1984

Colvocoresses, A. P., "Mapping of Washington, D.C. and vicinity with the Landsat-4 Thematic Mapper," TECHNICAL PAPERS OF THE 50TH ANNUAL MEETING OF THE AMERICAN SOCIETY OF PHOTOGRAMMETRY, Washington, D.C., 1984

Engel, J. L., "Thematic Mapper: An interim report on anticipated performance," AIAA SYSTEMS FOR THE 80'S CONFERENCE, Colorado Springs, Colorado, 1980

Colwell, R. N. (Editor), "Manual of Remote Sensing," AMERICAN SOCIETY OF PHOTOGRAMMETRY, Falls Church, Virginia, 1983

Crist, E. P., and R. C. Cicone, "A physically-based transformation of Thematic Mapper Data - the TM Tasseled Cap," IEEE TRANSACTIONS ON GEOSCIENCE AND REMOTE SENSING, Vol. GE-22, May 1984

DeGloria, S. D., "Spectral variability of Landsat-4 Thematic Mapper and Multispectral Scanner data for selected crop and forest cover types," IEEE TRANSACTIONS ON GEOSCIENCE AND REMOTE SENSING, Vol. GE-22, May 1984

Dozier, J., "Snow reflectance from Landsat-4 Thematic Mapper," IEEE TRANSACTIONS ON GEOSCIENCE AND REMOTE SENSING, Vol. GE-22, May 1984

Engel, J. L., J. C. Lansing, Jr., D. G. Brandshaft, and B. J. Marks, "Radiometric performance of the Thematic Mapper," PROCEEDINGS, 17th INTERNATIONAL, ENVIRONMENTAL RESEARCH INSTITUTE OF MICHIGAN. Ann Arbor, Michigan, May 1983

Everett, J. R., J. D. Dykstra, and C. A. Sheffield, "The contribution of Landsat-4 Thematic Mapper data to geologic exploration," PECORA 8 REMOTE SENSING SYMPOSIUM. Sioux Falls, South Dakota, 1983

Fischel, D., "Validation of the Thematic Mapper radiometric and geometric correction algorithms," IEEE TRANSACTIONS ON GEOSCIENCE AND REMOTE SENSING, Vol. GE-22, May 1984

Fusco, L., "Thematic Mapper: The ESA-Earthnet ground segment and processing experience," IEEE TRANSACTIONS ON GEOSCIENCE AND REMOTE SENSING, Vol. GE-22, May 1984

Gunther, Fred J., "A new principal components procedure to aid the analysis of Landsat MSS digital data," PROCEEDINGS, 1982 CONFERENCE ON PATTERN RECOGNITION AND IMAGE PROCESSING IEEE Computer Society, Las Vegas, Nevada, 1982

Haas, R. H., and F. A. Waltz, "Evaluation of Thematic Mapper data for natural resource assessment," PECORA 8 REMOTE SENSING SYMPOSIUM, Sioux Falls, South Dakota, 1983

Hill, C. L. "Analysis of Landsat-4 Thematic Mapper data for classification of forest stands in Baldwin County, Alabama," PECORA 8 REMOTE SENSING SYMPOSIUM, Sioux Falls, South Dakota, 1983

Kogart, J., E. Larduinat, and M. Fitzgerald, "An Analysis of New Techniques for Radiometric Correction of Landsat-4 Thematic Mapper Images," Contractor Report, Contract No. NAS 5-27371, Research and Data Systems, Inc., Lanham, Maryland, October 1983

Malila, W. A., M.D. Metzler, D.P. Rice, and E. P. Crist, "Characterization of Landsat-4 MSS and TM digital image data," IEEE TRANSACTION ON GEOSCIENCE AND REMOTE SENSING, Vol. GE-22, May 1984

Masuoka, P. M., "Availability of Landsat-4 Thematic Mapper data," TECHNICAL PAPERS OF THE 50TH ANNUAL MEETING OF THE AMERICAN SOCIETY OF PHOTOGRAMMETRY, Washington, D.C., 1984

Murphy, J. M., T. Butlin, P. F. Duff, and A. J. Fitzgerald, "Revised radiometric calibration technique for Landsat-4 Thematic Mapper data," IEEE TRANSACTION ON GEOSCIENCE AND REMOTE SENSING, Vol. GE-22, May 1984

Palmer, J. M., "Effective bandwidths for Landsat-4 and Landsat-D' Multispectral Scanner and Thematic Mapper subsystems," IEEE TRANSACTIONS ON GEOSCIENCE AND REMOTE SENSING, Vol. GE-22, May 1984

Pitts, D. E., G. D. Bahhwar, D. R. Thompson, K. E. Henderson, S. Shen, C. Sorensen, and J. G. Carnes, "Evaluation of corn/soybeans separability using Thematic Mapper and Thematic Mapper simulator data," IEEE TRANSACTIONS ON GEOSCIENCE AND REMOTE SENSING, Vol. GE-22, May 1984

Price, J. C., "Comparison of the information content of data from the Landsat-4 Thematic Mapper and the Multispectral Scanner," IEEE TRANSACTIONS ON GEOSCIENCE AND REMOTE SENSING, Vol. GE-22, May 1984

Salomonson, V. V., and A. B. Park, "An Overview of the Landsat-D Project with Emphasis on the Flight Segment," PROCEEDINGS, 5th SYMPOSIUM ON MACHINE PROCESSING OF REMOTELY SENSED DATA, PURDUE UNIVERSITY, Lafayette, Indiana, June 1979

Salomonson, V. V., and R. Koffler, "An Overview of Landsat-4 status and results from Thematic Mapper data analysis," SUMMARIES, 17th INTERNATIONAL SYMPOSIUM ON REMOTE SENSING OF THE ENVIRONMENT, ENVIRONMENTAL RESEARCH INSTITUTE OF MICHIGAN, Ann Arbor, Michigan, May 1983

Salomonson, V. V., and H. Mannheimer, "An Overview of the evolution of Landsat-4," PECORA 8 REMOTE SENSING SYMPOSIUM, Sioux Falls, South Dakota, 1983

Sheffield, C., "Earthwatch - A Survey of the World from Space," MacMilan, New York, 1981, 160 pages

Short, N. M., P. D. Lowman, Jr., S. C. Freden, and W. A. Finch Jr., "Mission to Earth: Landsat Views the World," NASA Special Publication 360, Washington, D.C. 1976, 362 pages

Thompson, D. R. and K. E. Henderson, "Evaluation of Thematic Mapper for detecting soil properties under grassland vegetation," IEEE TRANSACTIONS ON GEOSCIENCE AND REMOTE SENSING, VOl. GE-22, May 1984

Walker, R. E., A. I. Zobrist, N. A. Bryant, B. Gohkman, S. Z. Friedman, and T. L. Logan, "An analysis of Landsat-4 Thematic Mapper geometric properties," IEEE TRANSACTIONS ON GEOSCIENCE AND REMOTE SENSING, Vol. GE-22, May 1984

Walker, R. E., A. I. Zobrist, N. A. Bryant, B. Gohkman, S. Z. Friedman, and T. L. Logan, "An assessment of the geometry of Thematic Mapper data," TECHNICAL PAPERS OF THE 50TH ANNUAL MEETING OF THE AMERICAN SOCIETY OF PHOTOGRAMMETRY, Washington, D.C., 1984

Welch, R. and E. Lynn Usery, "Cartographic accuracy of Landsat-4 MSS and TM image data," IEEE TRANSACTIONS ON GEOSCIENCE AND REMOTE SENSING, Vol. GE-22, May 1984

Williams, D. L., J. R. Irons, B. L. Markham, R. F. Nelson, D. L. Toll, R. S. Latty, and M. L. Stauffer, "A statistical evaluation of the advantages of Landsat Thematic Mapper data in comparison to Multispectral Scanner data," IEEE TRANSACTIONS ON GEOSCIENCE AND REMOTE SENSING, Vol. GE-22, May 1984

Williams, R. S., Jr., and W. D. Carter (Editors), "ERTS-1, A New Window on Our Planet," U.S. Geological Survey, Professional Paper 929, Washington, D.C., 1976, 362 pages

Wrigley, R. C., D. H. Card, C. A. Hlavka, J. R. Hall, F. C. Mertz, C. Archwamety, and R. A. Schowengerdt, "Thematic Mapper image quality: registration, noise and resolution," IEEE TRANSACTIONS ON GEOSCIENCE AND REMOTE SENSING, Vol. GE-22, May 1984

APPENDIX 9.1 - TIPS POST-CALIBRATION DYNAMIC RANGE

Copy of Memo that Established Significant Figures of Post-Calibration Dynamic Range Constants for TIPS Calibration, as of 20 January 1984.

January 20, 1984

TO: Distribution

FROM: 923/Landsat Associate Project Scientist/J. Barker

SUBJECT: Significant Figures for TM Dynamic Range Constants

At a working meeting on January 16, 1984 at Goddard Space Flight Center, it was agreed that the following specific and exact values shall be used for calibration of Landsat-4 and Landsat-5 Thematic Mapper (TM) image data:

Table 1) Spectral Radiance (in mWcm^{-2}ster^{-1}μm^{-1})

BAND	1	2	3	4	5	7
RMIN	-0.15	-0.28	-0.12	-0.15	-0.037	-0.015
RMAX	15.21	29.68	20.43	20.62	2.719	1.438

Table 2) TM Band-Width (in μm)

BAND	1	2	3	4	5	7
L-4	.066	.081	.069	.129	.216	.250
L-5	.066	.082	.067	.128	.217	.252

Table 3) In-Band Radiance for Landsat-4 (in mWcm^{-2}ster^{-1})

BAND	1	2	3	4	5	7
RMIN	-0.0099	-0.0227	-0.0083	-0.0194	-0.00799	-0.00375
RMAX	1.004	2.404	1.410	2.660	0.5873	0.3595

Table 4) In-Band Radiance for Landsat-5 (in $mWcm^{-2}ster^{-1}$)

BAND	1	2	3	4	5	7
RMIN	-0.0099	-0.0230	-0.0080	-0.0192	-0.00803	-0.00378
RMAX	1.004	2.434	1.369	2.639	0.5900	0.3624

It is the intention of this memo to provide the data necessary to assure that these particular numbers be explicitly entered into computer calibration programs as written and not be calculated from each other. The expectation is that these numbers will be used by TIPS until another recommendation is made, presumably after the launch of Landsat-5. By using these numbers, self-consistency and intercompariability of software or processed data will be more likely without differences due to significant digits, rounding or truncation on different computers.

The meeting was attend by J. Barker (GSFC, chair), F. Gunther (CSC), T. Keller (GE), Y. Lee (SAR) and S. Truong (SAR). The numbers agreed to at this meeting represent a slight change in a few numbers of the second table of the RMIN and RMAX in units of In-Band radiance included in the required CSC/GSFC delivery of Landsat-5 TM calibration constants to GE/VF on December 16, 1983. These recommendations do not change any numbers in the other twelve tables of spectral radiance, sphere radiance, channel gain, channel offset, or reference DN values for eight lamp configurations for all 96 channels.

John L. Barker

APPENDIX 9.2 - INTEGRATING SPHERE SPECTRAL RADIANCES

Integrating Sphere (IS) calibration data in spectral radiance, $L_{\lambda,IS}$ ($mWcm^{-2}ster^{-1}\mu m^{-1}$) for each IS lamp level, furnished by NASA/GSFC to GE/VF on 15 December 1983 for TIPS-era calibration of Landsat-5 TM/F instrument. These data were from a recalibration of the 48"IS in May, 1982.

LANDSAT-5
ABSOLUTE CALIBRATION
122cm INTEGRATING SPHERE RADIANCE LEVELS BY LAMP

LAMP STATE		SPECTRAL RADIANCE ($mWcm^{-2}ster^{-1}\mu m^{-1}$)					
STATE	WATTS	BAND 1	BAND 2	BAND 3	BAND 4	BAND 5	BAND 7
624	1500	11.4834	24.1872	37.5986	50.6061	20.1763	6.3701
524	1300	9.8813	20.8205	32.1692	43.7448	17.5040	5.5233
424	1100	8.2954	17.4969	27.1895	36.8790	14.7894	4.6894
324	900	6.7193	14.2517	22.1644	30.2746	12.1894	3.8490
224	700	5.1586	10.9343	17.1686	23.4835	9.5213	3.0056
224	700	5.1586	10.9343	17.1686	23.4835	9.5213	3.0056
214	600	4.4518	9.3815	14.6944	19.9793	8.0239	2.5277
124	500	3.7441	7.9530	12.4919	17.1592	6.9848	2.2071
114	400	3.0373	6.4002	10.0175	13.6547	5.4877	1.7296
024	300	2.1426	4.6344	7.3691	10.3740	4.3563	1.3797
023	275	1.9565	4.2449	6.7506	9.5372	4.0193	1.2723
022	250	1.7872	3.8795	6.1670	8.7236	3.6875	1.1680
014	200	1.4357	3.0817	4.8942	6.8696	2.8593	0.9021
012	150	0.0804	2.3267	3.6919	5.2192	2.1907	0.6903
011	125	0.9113	1.9641	3.1168	4.4225	1.8651	0.5881
010	100	0.7396	1.5924	2.5233	3.6058	1.5373	0.4912
004	100	0.6961	1.4898	2.3710	3.2634	1.3223	0.4109
003	75	0.5100	1.1003	1.7525	2.4264	0.9853	0.3036
002	50	0.3407	0.7348	1.1687	1.6134	0.6535	0.1991
001	25	0.1717	0.3722	0.5938	0.8164	0.3278	0.0970
000	0	0.0	0.0	0.0	0.0	0.0	0.0

APPENDIX 9.3 - TM/F GAINS

TM/F instrument calibration data (gain) are presented for each channel of each reflective band, as furnished by NASA/GSFC to GE/VF on 15 December 1983 for TIPS-era processing of Landsat-5 in-orbit image data. These pre-launch gains, G_{IS}, in units of DN per $mWcm^{-2}ster^{-1}\mu m^{-1}$ were calculated from the regression of averaged midscan counts in DN, L_R, against the known spectral radiance of the integrating sphere, $L_{\lambda,IS}$ (Appendix 9.2), in units of $mW\ cm^{-2}ster^{-1}\mu m^{-1}$: $L_R = O_{IS} + G_{IS} * L_{\lambda,IS}$.

CHANNEL	BAND					
	1	2	3	4	5	7
1	15.5973	7.8781	10.2083	10.8950	78.9797	147.5916
2	15.4837	7.8485	10.2852	10.8421	78.0460	146.2116
3	15.6616	7.8402	10.1852	10.7759	78.5030	147.3723
4	15.4738	7.8432	10.2747	10.7317	78.2444	146.5488
5	15.7131	7.8543	10.1887	10.8196	78.6471	148.8685
6	15.4406	7.8187	10.1612	10.8094	78.6875	146.3335
7	15.6139	7.8374	10.0438	10.7961	78.1700	148.4280
8	15.4797	7.9195	10.2459	10.8916	79.4837	147.9753
9	15.5082	7.8128	10.0956	10.7254	78.7218	147.6473
10	15.5686	7.8753	10.2281	10.9348	78.8279	147.3096
11	15.6141	7.8932	10.1053	10.8019	79.3421	148.6744
12	15.5868	7.9215	10.2798	10.8098	79.2062	148.4549
13	15.5822	7.8748	10.1573	10.7987	78.7834	148.4755
14	15.4218	7.8431	10.2711	10.8591	78.3314	148.3712
15	15.5370	7.9122	10.2169	10.7782	78.9255	147.4282
16	15.5579	7.7793	10.3020	10.8595	79.1123	147.8104

APPENDIX 9.4 - TM/F OFFSETS

TM/F instrument calibration data (offset) are presented for each channel of each reflective band, as furnished by NASA/GSFC to GE/VF on 15 December 1983 for TIPS-era processing of Landsat-5 in-orbit image data. These pre-launch offsets, O_{IS}, in DN were calculated from the regression of raw midscan radiance, $\overline{L}_R$, in DN, usually averaged over 25mF and 100 scans, L_R, against the twenty known settings of spectral radiance of the integrating sphere, $L_{\lambda,IS}$ (Appendix 9.2), in units of mWcm^{-2} ster^{-1} μm^{-1}. For each channel: $\overline{L}_R = O_{IS} + G_{IS} * L_{\lambda,IS}$.

CHANNEL	BAND					
	1	2	3	4	5	7
1	2.2965	2.2891	2.4569	2.6652	3.5727	3.8231
2	1.9313	1.5379	1.9920	2.1440	3.2601	3.2194
3	1.8734	1.8693	1.9709	2.4287	3.2736	3.3549
4	1.8895	1.5357	1.7282	1.9523	3.2701	3.2758
5	1.7628	1.5069	1.8442	2.2046	3.1314	3.1052
6	1.9744	1.8161	1.7437	2.3107	3.2506	3.2568
7	1.7435	1.5605	1.8571	2.5408	3.1252	3.0121
8	2.1147	1.7427	1.8852	2.2091	3.5024	3.2427
9	1.6412	1.7117	2.0105	2.1524	3.2843	3.1006
10	1.8049	1.5873	1.8130	2.0022	3.3784	3.1922
11	1.5761	1.8789	1.8650	2.4152	3.2440	3.1158
12	1.7649	1.6117	1.7688	2.0702	3.2882	3.0190
13	1.6324	1.5945	1.7462	2.1371	3.1520	3.0402
14	1.8487	1.5986	1.8063	2.1669	3.3691	3.2440
15	1.6416	1.6357	1.7881	2.1682	3.1806	3.1068
16	1.8337	1.5766	1.8836	2.1291	3.3460	3.2790

APPENDIX 9.5 - TM/PF APPARANT GAIN CHANGE WITH TIME

Landsat-4 TM/PF apparent gain changes with time, by band, under the assumption that the TM internal calibration (IC) has effective spectral radiances, L_λ^o, which do not change with time. Gain, G(c), in units of DN per $mWcm^{-2}ster^{-1}\ \mu m^{-1}$, is a measure of absolute radiometric sensitivity for each channel, C. These post-launch gains, G(C), were calculated from the regression of an averaged IC pulse, P (ℓ, C), in DN against the pre-launch values of L_λ^o (ℓ, C), in $mWcm^{-2}\ ster^{-1}\ \mu m^{-1}$. For each channel, the least squares values for O and G were calculated from data for the lowest seven lamp configurations, ℓ:

$$\overline{P}'(\ell) = O + G * L_\lambda^{\cdot}(\ell)$$

Averaged gains values for odd channels and even channels were averaged together to give G (B):

$$\overline{G}\ (B) = \frac{\overline{G}\ (odd) + \overline{G}\ (even)}{2}$$

O^o (B) and G^o (B) are the offset and gain after calibration to a common post-calibration dynamic range from RMIN to RMAX, for the Scrounge-era prior to August, 1983. Plots of apparant gain change with time are given in this appendix as follows:

9.5.1 Band 1
9.5.2 Band 2
9.5.3 Band 3
9.5.4 Band 4
9.5.5 Band 5
9.5.6 Band 7

Appendix 9.5.1

LANDSAT-4 TM RADIOMETRY, BAND 1

APPARENT GAIN CHANGE FROM INTERNAL CALIBRATION (IC) PULSES

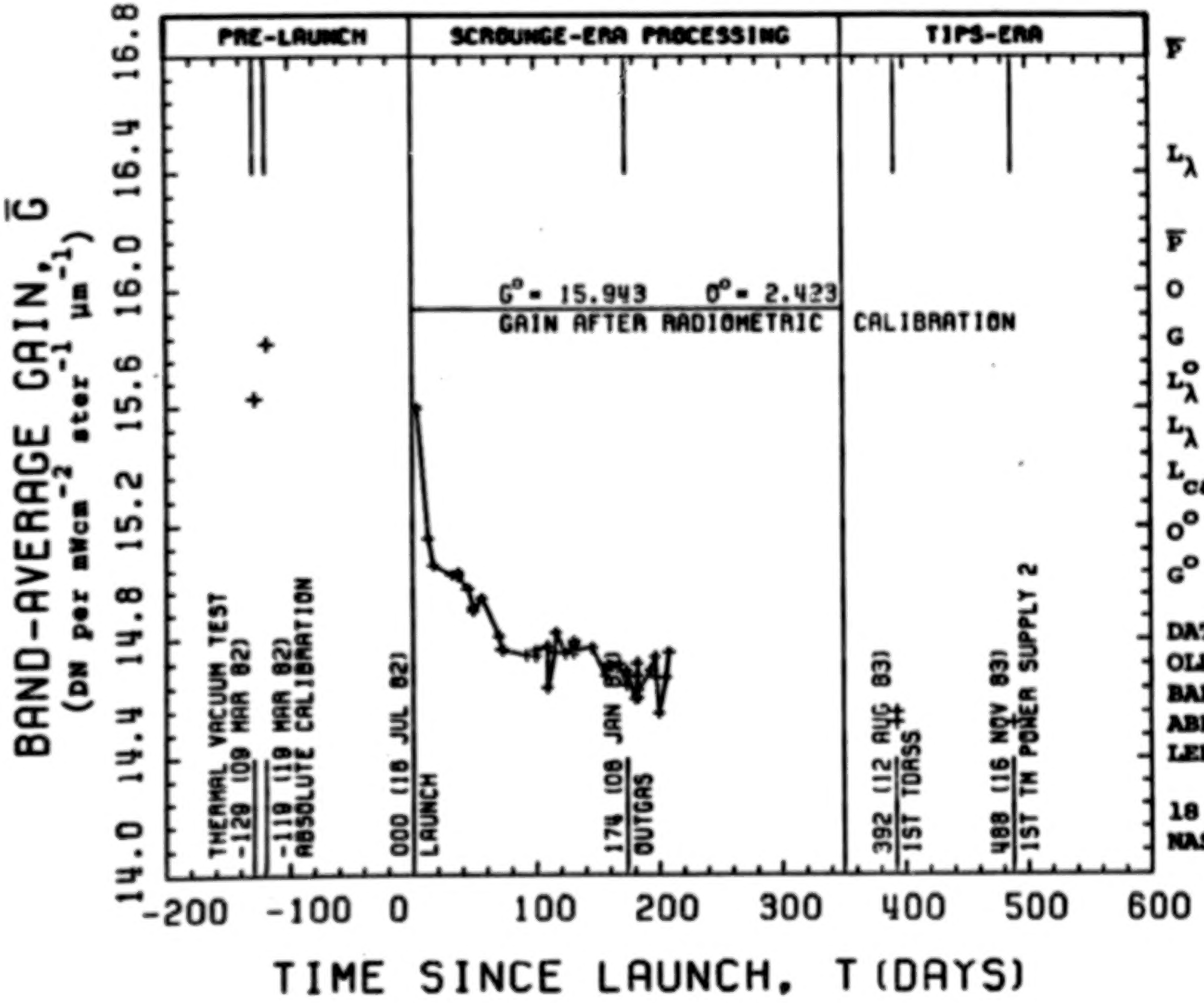

$\overline{F} = O + G^{*}L_{\lambda}^{o}$

$L_{\lambda} = \left[\frac{L_{cal} - O^{o}}{G^{o}}\right]$

$\overline{F}$ = OBS. TM IC PULSE

O = OFFSET BY FIT

G = GAIN BY FIT

L_{λ}^{o} = IC SPECTRAL RAD.

L_{λ} = CALC. SPECT. RAD.

L_{cal} = DIGITAL NUMBER (DN)

O^{o} = OFFSET AFTER CALIB.

G^{o} = GAIN AFTER CALIB.

DATA FROM "TRAPP"
OLD/NEW REF. DAY 70
BARKER
ABRAMS/GUNTHER
LEE/TRUONG

18 JAN 84
NASA/GODDARD

Appendix 9.5.2

LANDSAT-4 TM RADIOMETRY, BAND 2

APPARENT GAIN CHANGE FROM INTERNAL CALIBRATION (IC) PULSES

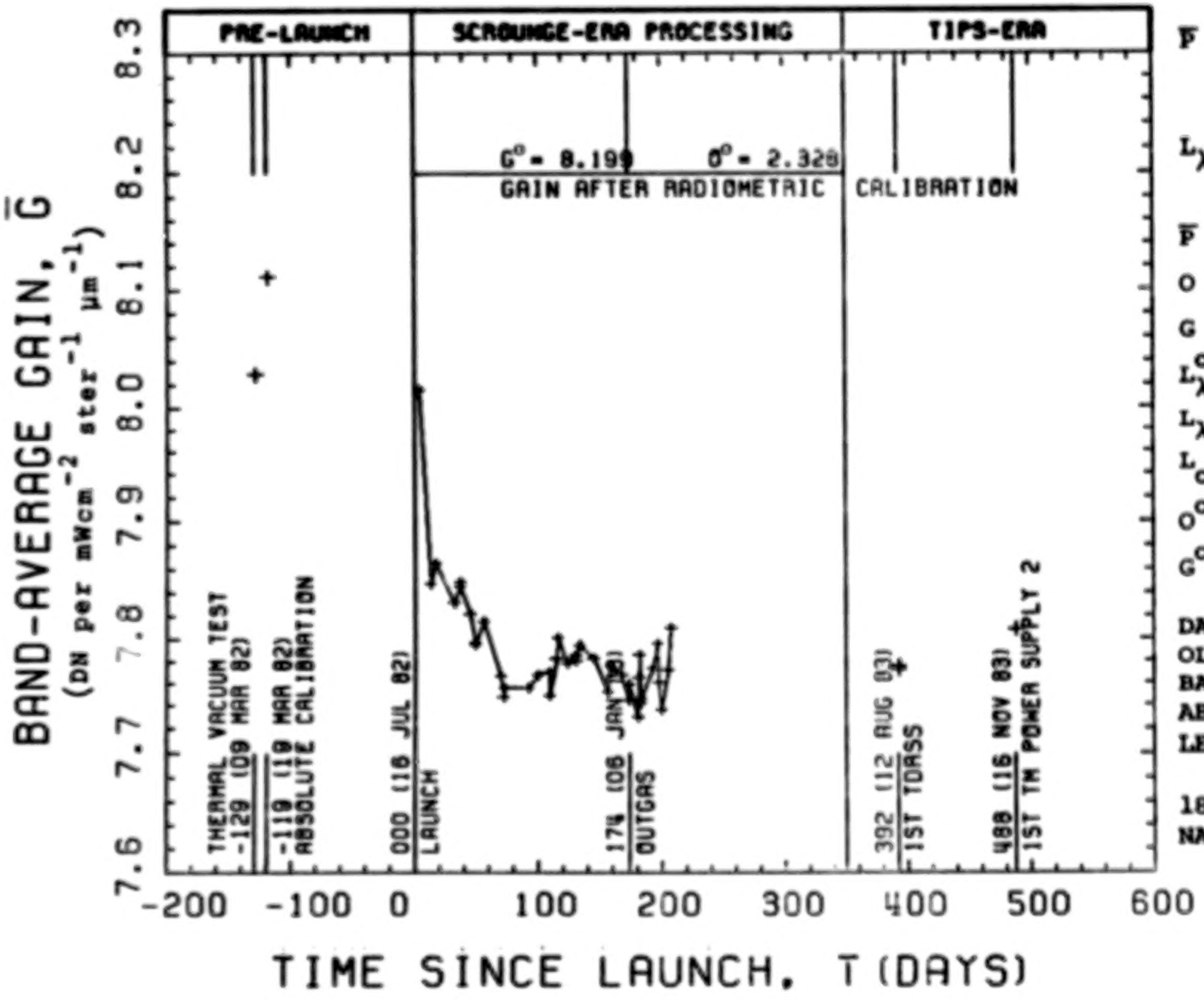

$\bar{F} = O + G^{*}L_{\lambda}^{o}$

$L_{\lambda} = \left[\frac{L_{cal} - O^{o}}{G^{o}}\right]$

$\bar{F}$ = OBS. TM IC PULSE
O = OFFSET BY FIT
G = GAIN BY FIT
L_{λ}^{o} = IC SPECTRAL RAD.
L_{λ} = CALC. SPECT. RAD.
L_{cal} = DIGITAL NUMBER (DN)
O^{o} = OFFSET AFTER CALIB.
G^{o} = GAIN AFTER CALIB.

DATA FROM "TRAPP"
OLD/NEW REF. DAY 70
BARKER
ABRAMS/GUNTHER
LEE/TRUONG

18 JAN 84
NASA/GODDARD

Appendix 9.5.3

LANDSAT-4 TM RADIOMETRY, BAND 3

APPARENT GAIN CHANGE FROM INTERNAL CALIBRATION (IC) PULSES

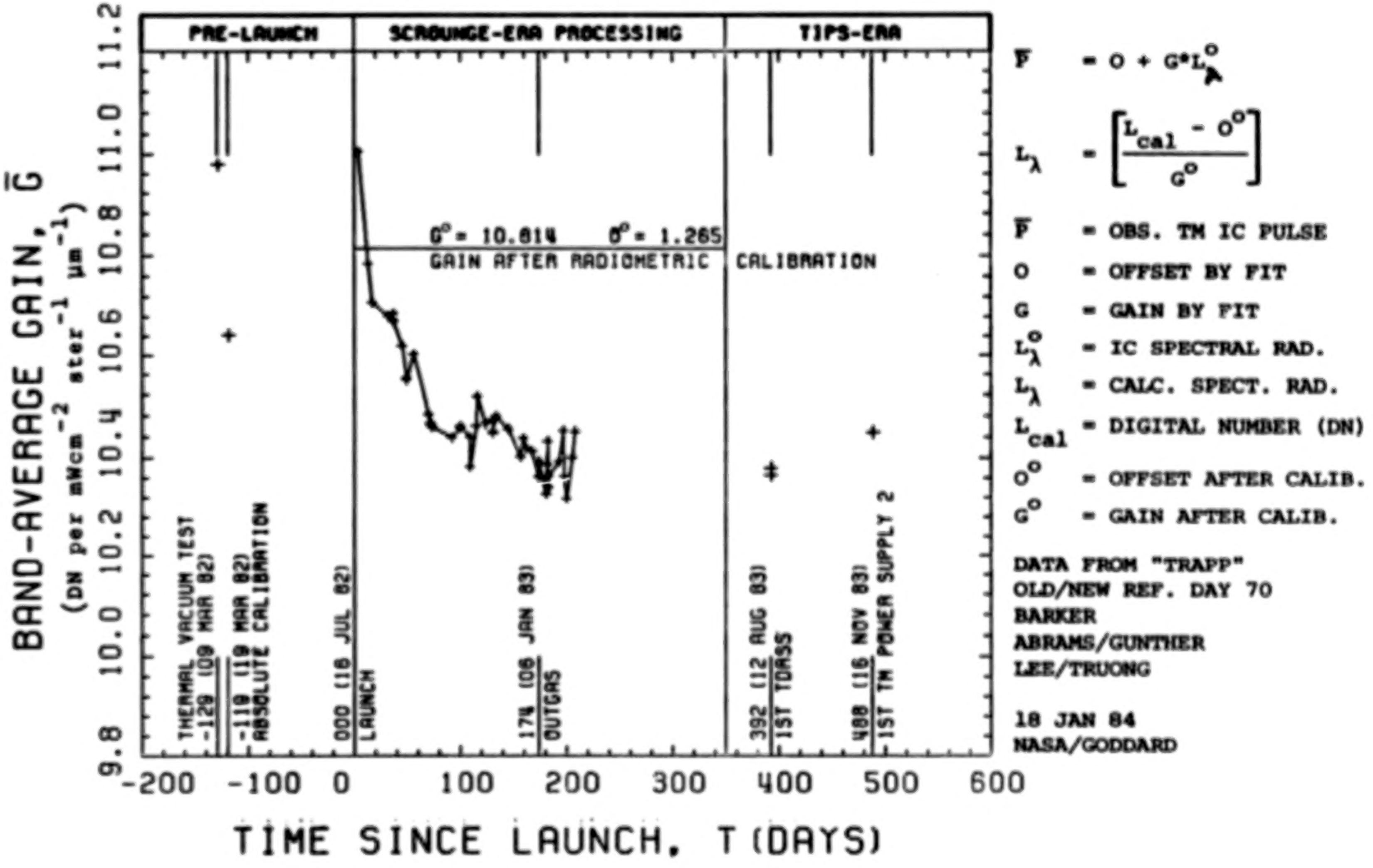

$\bar{F}$ = $O + G^{*}L^{o}_{\lambda}$

L_λ = $\left[\dfrac{L_{cal} - O^o}{G^o}\right]$

$\bar{F}$ = OBS. TM IC PULSE

O = OFFSET BY FIT

G = GAIN BY FIT

L^o_λ = IC SPECTRAL RAD.

L_λ = CALC. SPECT. RAD.

L_{cal} = DIGITAL NUMBER (DN)

O^o = OFFSET AFTER CALIB.

G^o = GAIN AFTER CALIB.

DATA FROM "TRAPP"
OLD/NEW REF. DAY 70
BARKER
ABRAMS/GUNTHER
LEE/TRUONG

18 JAN 84
NASA/GODDARD

Appendix 9.5.4

LANDSAT-4 TM RADIOMETRY, BAND 4

APPARENT GAIN CHANGE FROM INTERNAL CALIBRATION (IC) PULSES

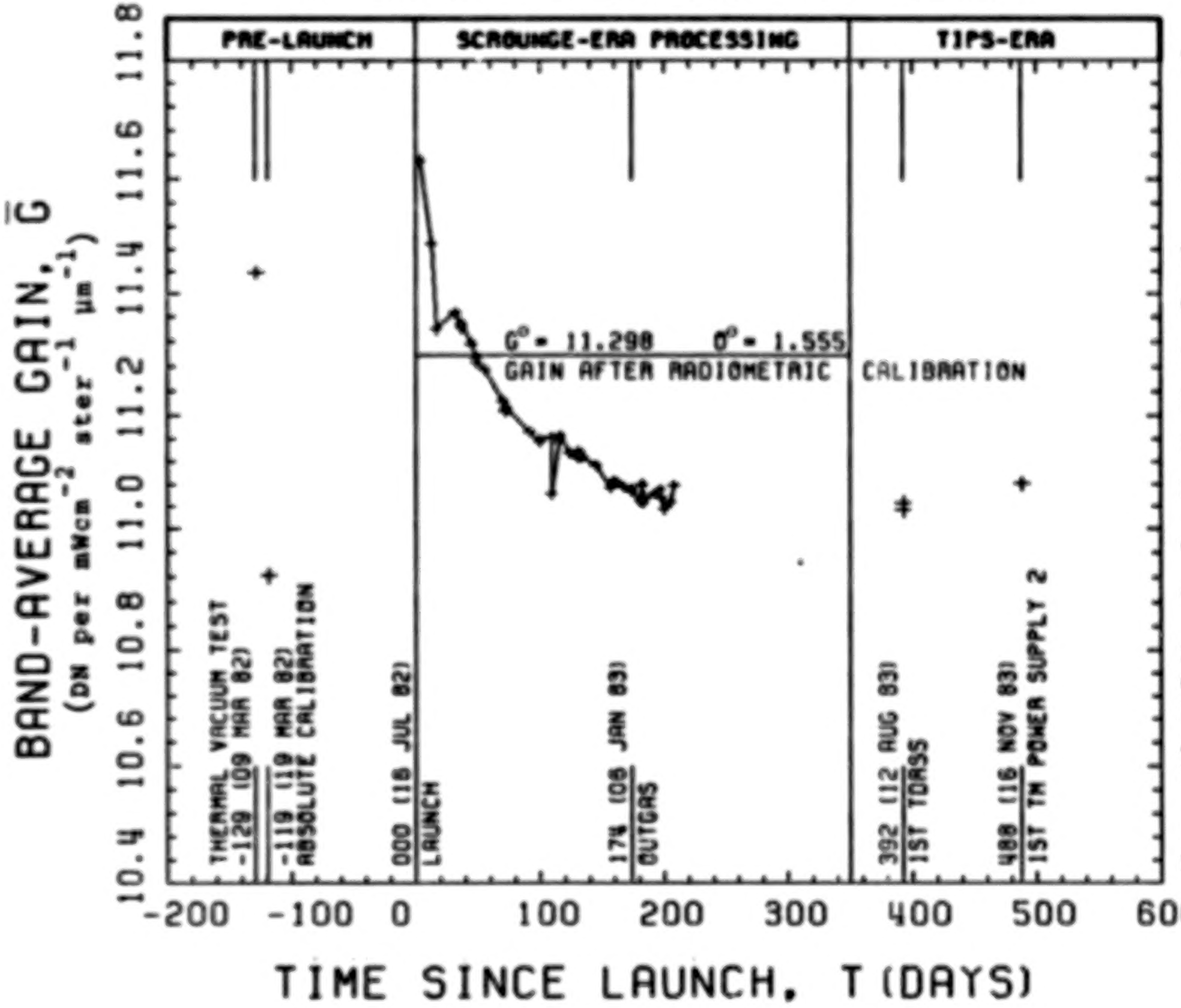

$\overline{F}$ = $O + G*L_\lambda^o$

L_λ = $\left[\frac{L_{cal} - O^o}{G^o}\right]$

$\overline{F}$ = OBS. TM IC PULSE

O = OFFSET BY FIT

G = GAIN BY FIT

L_λ^o = IC SPECTRAL RAD.

L_λ = CALC. SPECT. RAD.

L_{cal} = DIGITAL NUMBER (DN)

O^o = OFFSET AFTER CALIB.

G^o = GAIN AFTER CALIB.

DATA FROM "TRAPP"
OLD/NEW REF. DAY 70
BARKER
ABRAMS/GUNTHER
LEE/TRUONG

18 JAN 84
NASA/GODDARD

Appendix 9.5.5

LANDSAT-4 TM RADIOMETRY, BAND 5

APPARENT GAIN CHANGE FROM INTERNAL CALIBRATION (IC) PULSES

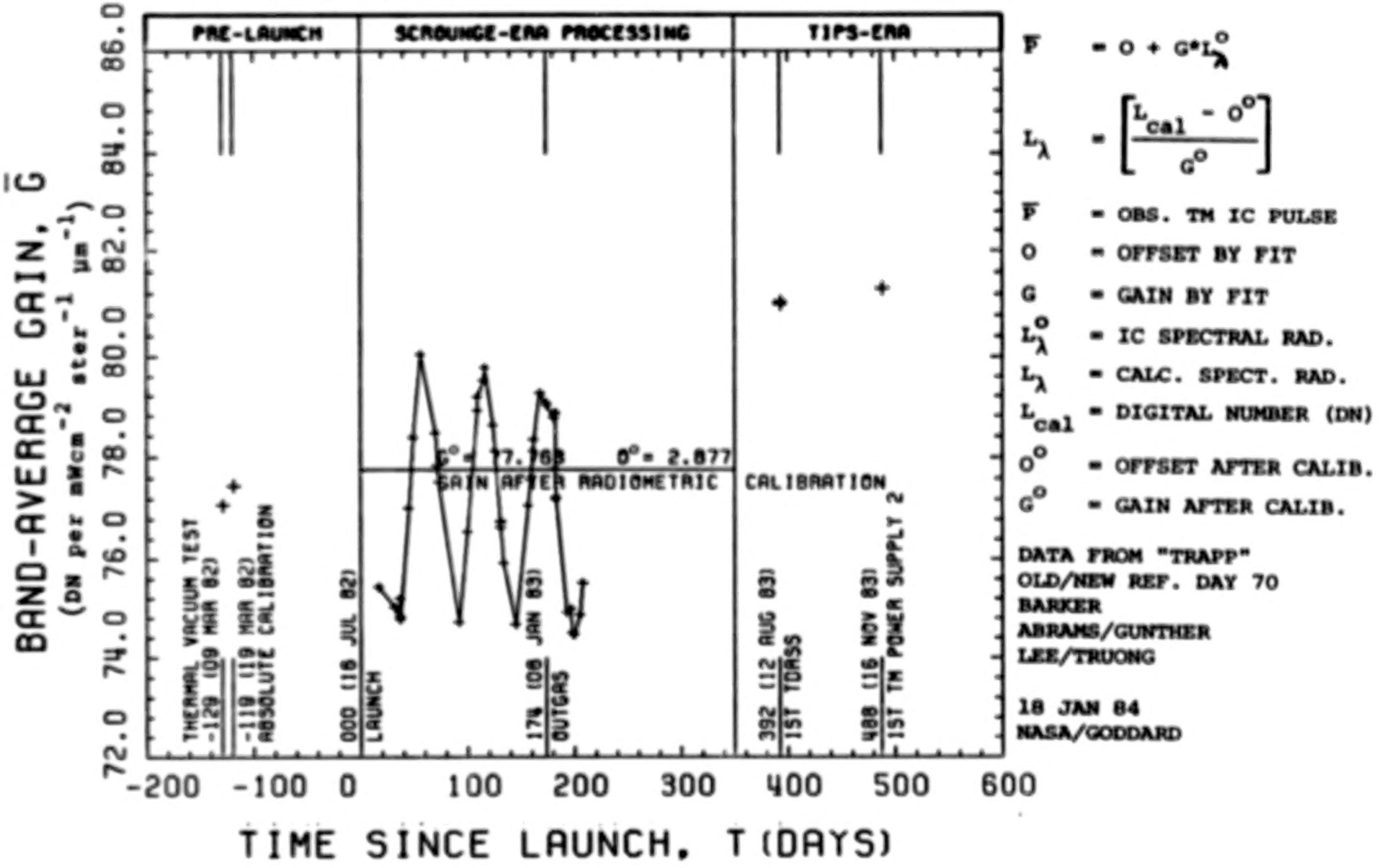

Appendix 9.5.6

LANDSAT-4 TM RADIOMETRY, BAND 7

APPARENT GAIN CHANGE FROM INTERNAL CALIBRATION (IC) PULSES

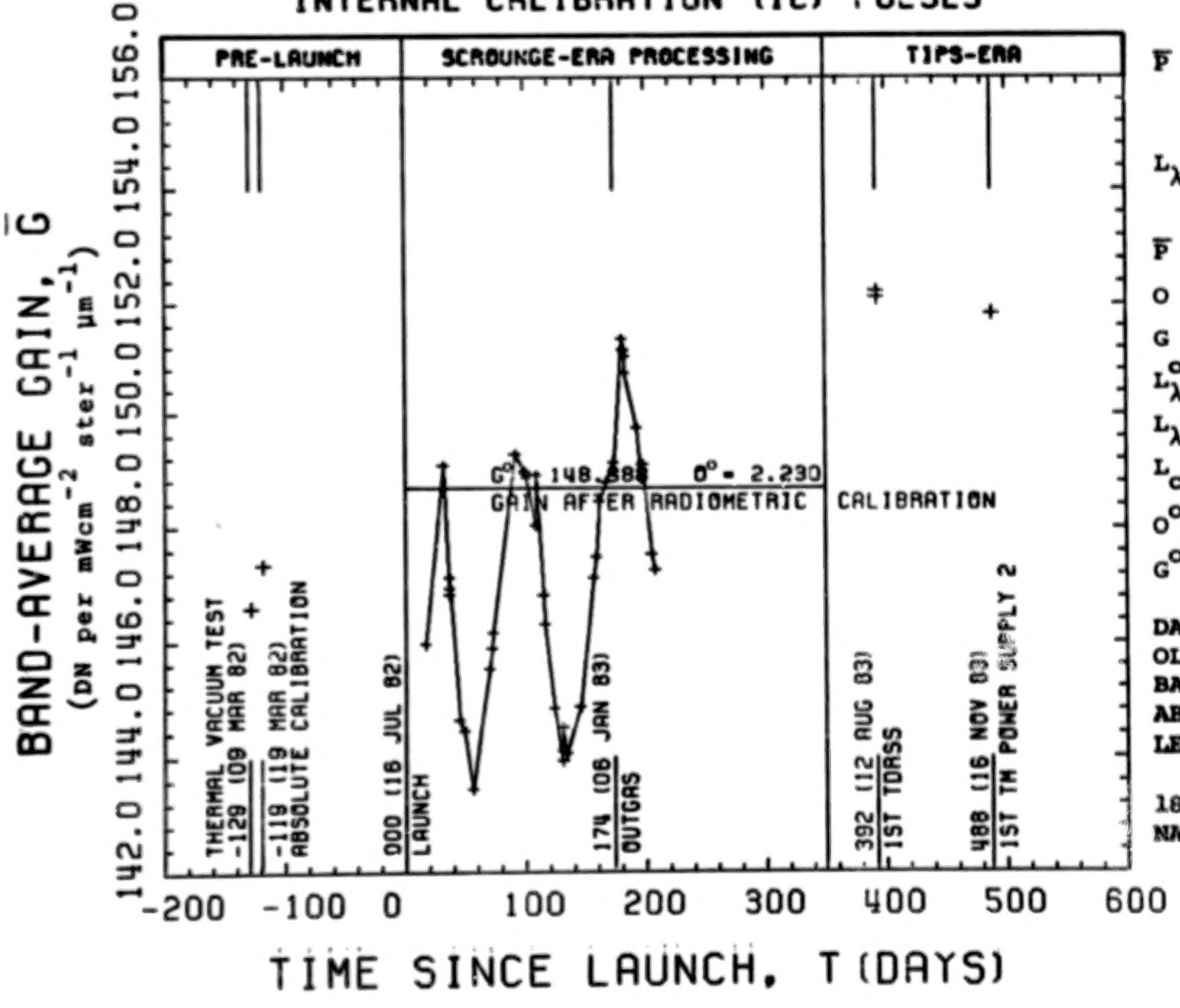

$\bar{F}$ = $O + G{*}L_\lambda^o$

L_λ = $\left[\frac{L_{cal} - O^o}{G^o}\right]$

$\bar{F}$ = OBS. TM IC PULSE

O = OFFSET BY FIT

G = GAIN BY FIT

L_λ^o = IC SPECTRAL RAD.

L_λ = CALC. SPECT. RAD.

L_{cal} = DIGITAL NUMBER (DN)

O^o = OFFSET AFTER CALIB.

G^o = GAIN AFTER CALIB.

DATA FROM "TRAPP"
OLD/NEW REF. DAY 70
BARKER
ABRAMS/GUNTHER
LEE/TRUONG

18 JAN 84
NASA/GODDARD

APPENDIX 9.6 - LANDSAT-4 IMAGES PROCESSED BY TRAPP

The catalog of Landsat-4 Images processed at Goddard Space Flight Center using the TM Radiative and Algorithm Performance Program (TRAPP) is provided herein.

Appendix 9-6
CATALOG OF LANDSAT-4 IMAGES PROCESSED BY TRAPP

WRS	SCENE	DATE	LOCATION
012031	4008014541	081082	BOSTON
012031	4008014541	081082	WATER OF BOSTON
028030	4004016321	082682	FT. DODGE, IOWA
015033	4010015140	110282	GODDARD
015033	4010015140	110282	WASH, DC
022039	4008216591	081682	NEW ORLEANS
W041028	4013117533	112482	HAMILTON MONTANA
W043034	4014518082	120882	MODESTO CALIF.
W015041	401571514	122082	FT. PIERCE
W017038	4015516282	121882	JACKSONVILLE, FLOR
W016028	4010015182	122482	OTTAWA, CANADA
W016028	4010015184	102482	KINGSTON CANADA
S030028	4007016442	082482	FORMAN, ND
W002002	4008016413	082582	DETROIT 2
W001001	4002515341	072082	DETROIT 3
W004025	4011018380	110882	VANCOUVER
W013038	4016015032	122282	CAPE HATTERAS
W014032	4002216001	080782	N.Y./PHILA
B016033	4001316125	072982	WASH, D.C.
W037288	4018317332	011583	LUKEVILLE ARIZONA
W004005	0012517405	111782	DEATH VALLEY CALIF.
J033038	UNKNOWN	010383	WHITE SANDS
J028031	4003216425	081782	TOLEDO, OH
J041033	4013117530	112482	KIMVERLY
J028030	4007216325	082082	N.W. IOWA
J016037	4007316400	082782	ATLANTA
J031025	4020520512	020083	WINNIPEG
J111213	4018802204	012283	WELLSBORO PENN.--PM
J041036	4013117504	112482	L.A., CAL
J112114	4003702243	082282	BUFFALO PM
J022040	4017416011	010683	TERREBONNE BAY, LOUISIANA
J119287	4018293073	011483	BIRMINGHAM, ALA. PM
J027027	4018316272	012583	GILBERT, MONTANA
J037036	4018317323	011583	CLARKDALE ARIZONA
J034036	4017817135	011083	QUEMADO, NM
J016032	4010015134	110282	HARRISBURG
J025039	4011516102	110882	LIBERTY, TEX
J034027	4016217004	122082	GRASSY BUTTE, ND
J014042	4018215125	010483	GRAND BAHAMA ISL
J044034	4020018152	020183	SAN FRANCISCO
K023035	4003716031	082282	N.E. ARK
J023029	4018110071	011383	BATON ROUGE
K046028	4010818251	013083	MT. ST. HELENS
J027030	4004016282	080382	N. CENTRAL IOWA
J014036	4007016004	082482	CAPE LOOKOUT NORTH CAROLINA
K028035	4038216385	081283	OKLAHOMA
K044034	4038218152	081283	SAN FRANCISCO
K027031	4008716273	112783	FT. DODGE IA
K014032	4013416082	112783	N.Y./PHILA
K028035	4048816382	111683	OKLAHOMA
K028034	4048816380	111683	WICHITA KANSAS
K028033	4048816353	111683	SALINA KANSAS
W033037	4017117180	010383	WHITE SANDS
P021039	4010316503	102782	MOBILE ALABAMA
P031025	4038216385	081283	WINNIPEG CANADA
P112211	4018702281	010883	WASH, D.C. PM
P024032	4008216082	101682	GALESBURG
P001001	4000416401	072082	DETROIT 1
P028035		030784	TULSA, OKL

0022051a*)/84

APPENDIX 9.7 - TM/F PLOTS OF SHIFTED BACKGROUND VERSUS SCAN

Landsat-4 TM/PF averaged shutter backgrounds before DC restoration are plotted versus scan number of illustrative reverse scans before and after being corrected (as described in Section 4.5) for scan-correlated shifts of type 4-1 (Landsat-4 Band 1, Channel 4) and type 4-7 (Landsat-4 Band 7, Channel 7) for San Francisco, 12 AUG 83 (Scene ID 40392-18152). Before-and-after-correction comparative plots are included in this Appendix as follows:

9.7.1 Band 1
9.7.2 Band 2
9.7.3 Band 3
9.7.4 Band 4
9.7.5 Band 5
9.7.6 Band 7
9.7.7 Band 6 (uncorrected).

Appendix 9.7.1

SCENE ID=40392-18152, BAND 1 (REVERSE)
SHUTTER BACKGROUND 1 SPECTRA BEFORE CORRECTION

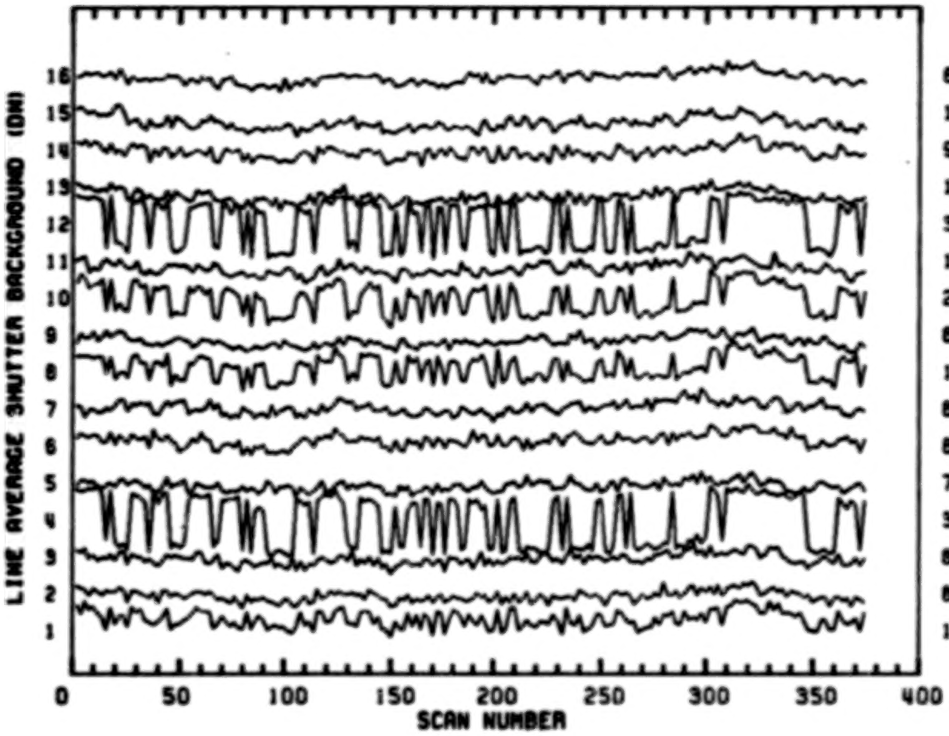

1000*CV	SHIFT1	SHIFT2
86	0.00	0.00
111	0.00	0.00
94	0.00	0.00
107	0.00	0.00
345	0.00	0.00
103	0.00	0.00
227	0.00	0.00
86	0.00	0.00
163	0.00	0.00
86	0.00	0.00
86	0.00	0.00
78	0.00	0.00
380	0.00	0.00
87	0.00	0.00
82	0.00	0.00
103	0.00	0.00

LEE/BARKER
6-MAR-84

SCENE ID=40392-18152, BAND 1 (REVERSE)
SHUTTER BACKGROUND 1 SPECTRA AFTER CORRECTION

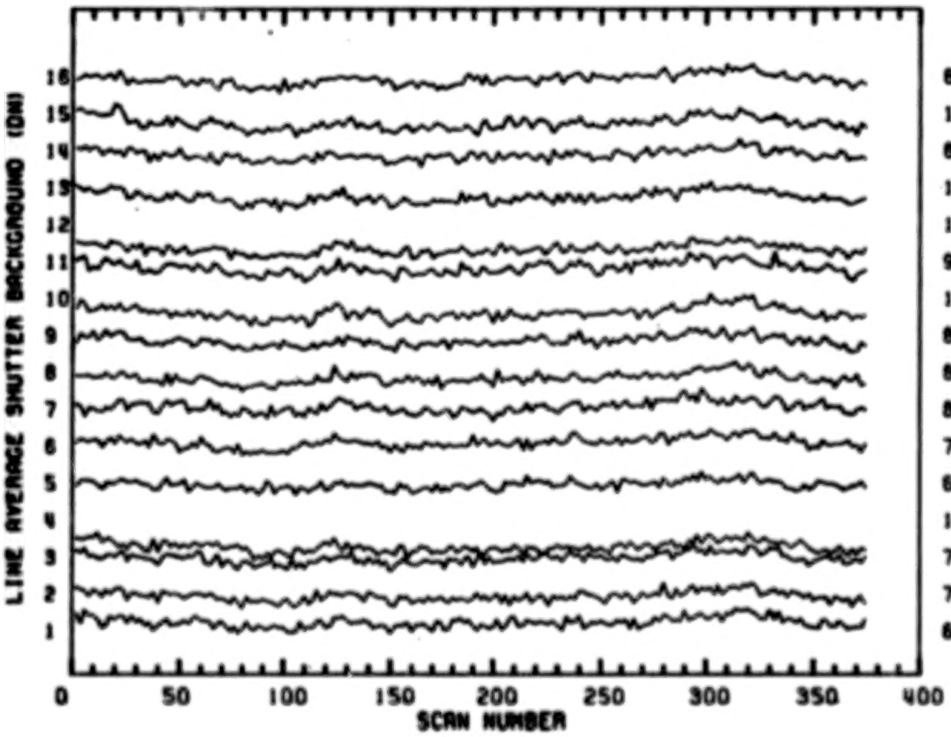

1000*CV	SHIFT1	SHIFT2
86	0.05	0.01
105	0.02	-0.08
80	0.19	-0.03
100	0.08	-0.08
111	1.83	-0.02
96	-0.02	-0.07
114	0.99	-0.03
84	-0.03	-0.02
87	0.79	-0.03
83	-0.02	-0.04
76	0.19	-0.01
67	-0.00	-0.11
128	1.95	-0.02
77	0.03	-0.12
76	0.07	-0.07
69	0.95	-0.14

LEE/BARKER
6-MAR-84

Appendix 9.7.2

SCENE ID=40392-18152, BAND 2 (REVERSE)
SHUTTER BACKGROUND 1 SPECTRA BEFORE CORRECTION

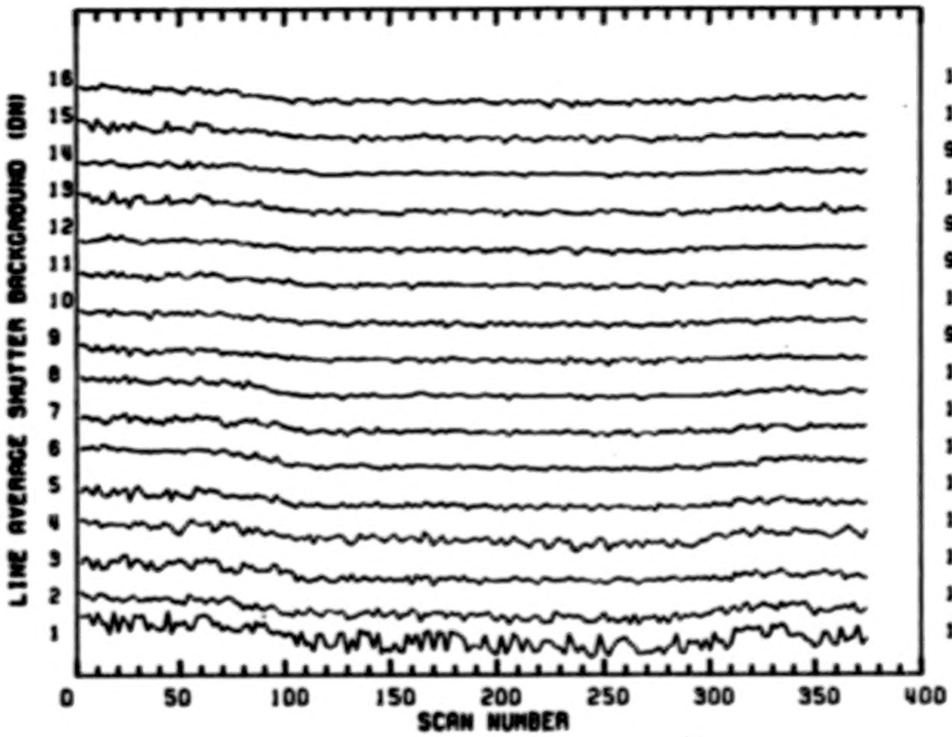

1000*CV	SHIFT1	SHIFT2
116	0.00	0.00
112	0.00	0.00
95	0.00	0.00
119	0.00	0.00
94	0.00	0.00
96	0.00	0.00
101	0.00	0.00
98	0.00	0.00
137	0.00	0.00
120	0.00	0.00
146	0.00	0.00
125	0.00	0.00
145	0.00	0.00
147	0.00	0.00
151	0.00	0.00
180	0.00	0.00

SCENE ID=40392-18152, BAND 2 (REVERSE)
SHUTTER BACKGROUND 1 SPECTRA AFTER CORRECTION

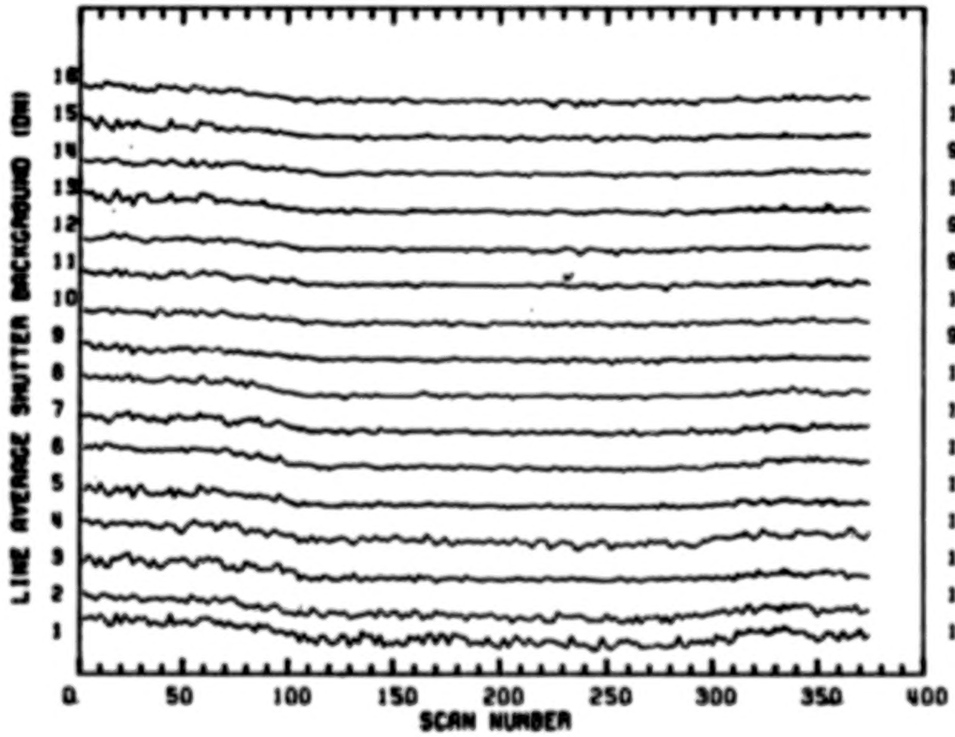

1000*CV	SHIFT1	SHIFT2
116	0.02	-0.00
108	0.02	-0.03
94	0.01	-0.00
118	0.01	-0.03
93	0.01	-0.01
94	0.01	-0.02
100	0.02	-0.01
96	0.01	-0.02
136	0.02	-0.01
117	0.01	-0.03
145	0.02	-0.00
120	0.02	-0.05
139	0.09	-0.01
140	0.01	-0.06
147	0.08	-0.01
143	0.13	-0.24

Appendix 9.7.3

SCENE ID=40392-18152, BAND 3 (REVERSE)
SHUTTER BACKGROUND 1 SPECTRA BEFORE CORRECTION

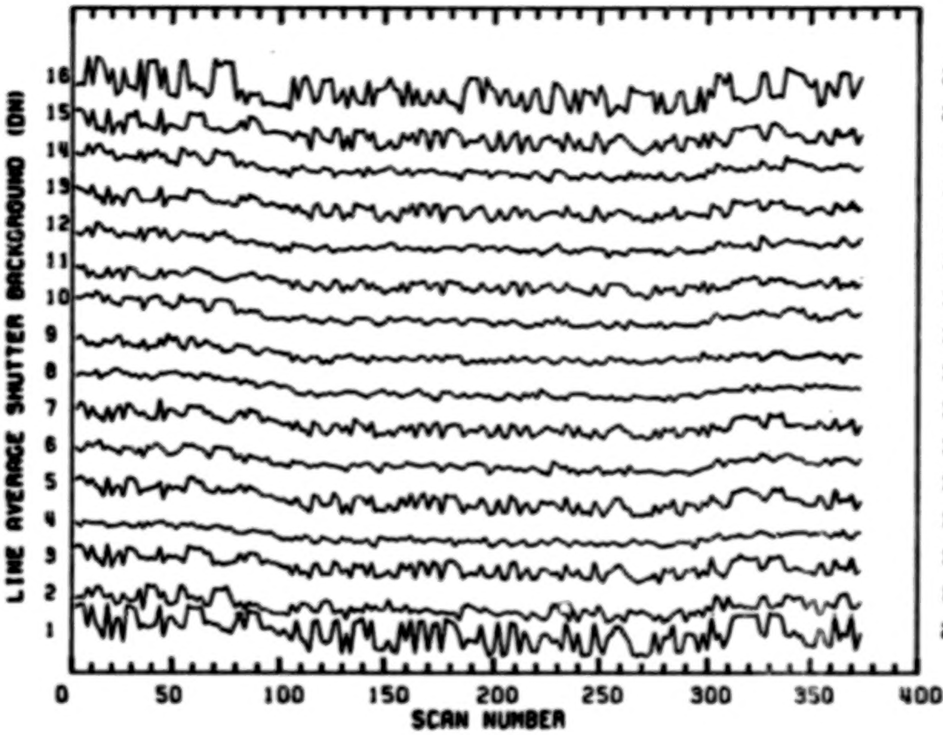

1000*CV	SHIFT1	SHIFT2
265	0.00	0.00
218	0.00	0.00
168	0.00	0.00
176	0.00	0.00
145	0.00	0.00
151	0.00	0.00
187	0.00	0.00
148	0.00	0.00
167	0.00	0.00
179	0.00	0.00
165	0.00	0.00
192	0.00	0.00
140	0.00	0.00
161	0.00	0.00
159	0.00	0.00
212	0.00	0.00

SCENE ID=40392-18152, BAND 3 (REVERSE)
SHUTTER BACKGROUND 1 SPECTRA AFTER CORRECTION

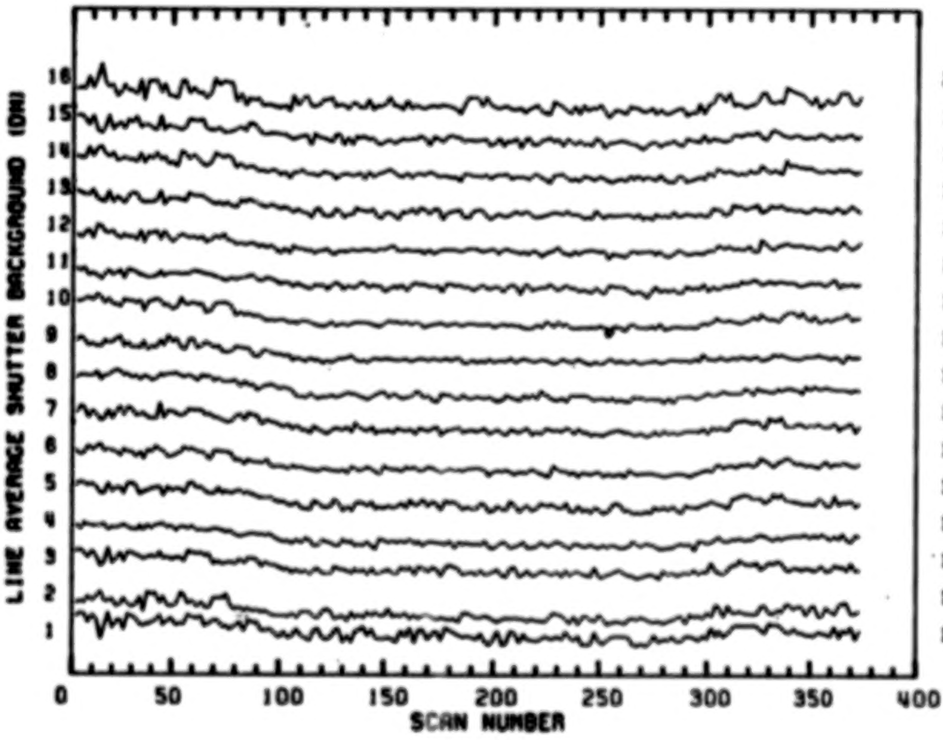

1000*CV	SHIFT1	SHIFT2
212	0.12	0.61
158	0.18	-0.25
166	0.06	0.03
146	0.12	-0.13
143	0.04	0.03
128	0.03	-0.14
183	0.09	-0.00
142	0.01	-0.05
167	0.01	-0.01
143	0.09	-0.17
160	0.09	0.00
154	0.15	-0.18
140	0.02	0.00
120	0.11	-0.24
146	0.13	0.13
114	0.29	-0.52

Appendix 9.7.4

SCENE ID=40392-18152, BAND 4 (REVERSE)
SHUTTER BACKGROUND 1 SPECTRA BEFORE CORRECTION

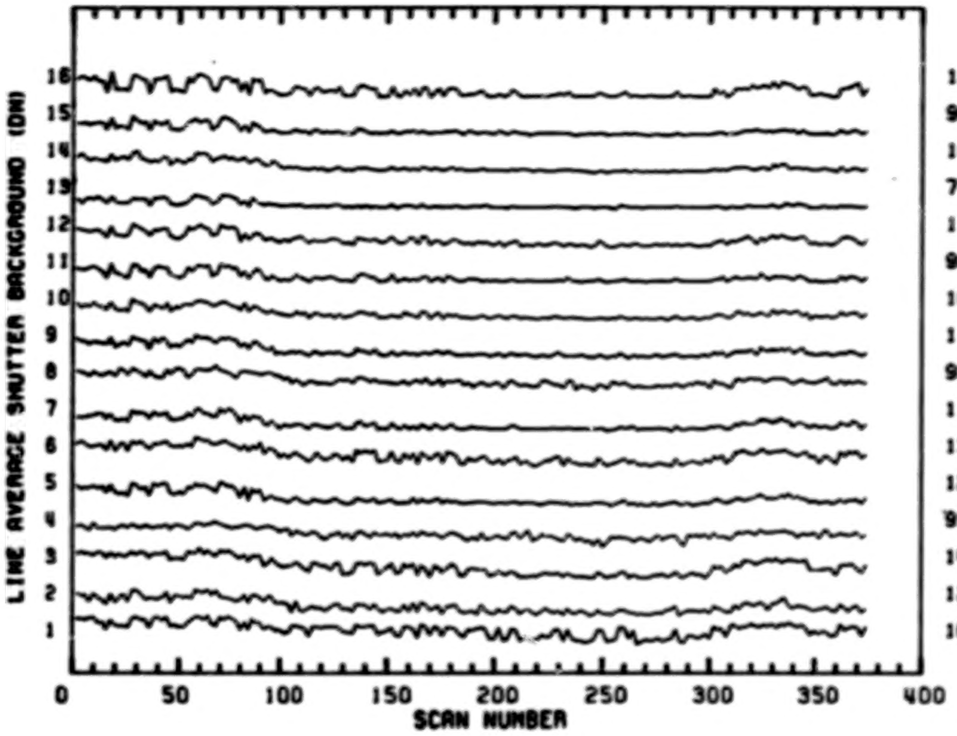

	1000*CV	SHIFT1	SHIFT2
16	126	0.00	0.00
15	94	0.00	0.00
14	109	0.00	0.00
13	71	0.00	0.00
12	114	0.00	0.00
11	98	0.00	0.00
10	104	0.00	0.00
9	119	0.00	0.00
8	96	0.00	0.00
7	113	0.00	0.00
6	132	0.00	0.00
5	127	0.00	0.00
4	99	0.00	0.00
3	149	0.00	0.00
2	126	0.00	0.00
1	103	0.00	0.00

SCENE ID=40392-18152, BAND 4 (REVERSE)
SHUTTER BACKGROUND 1 SPECTRA AFTER CORRECTION

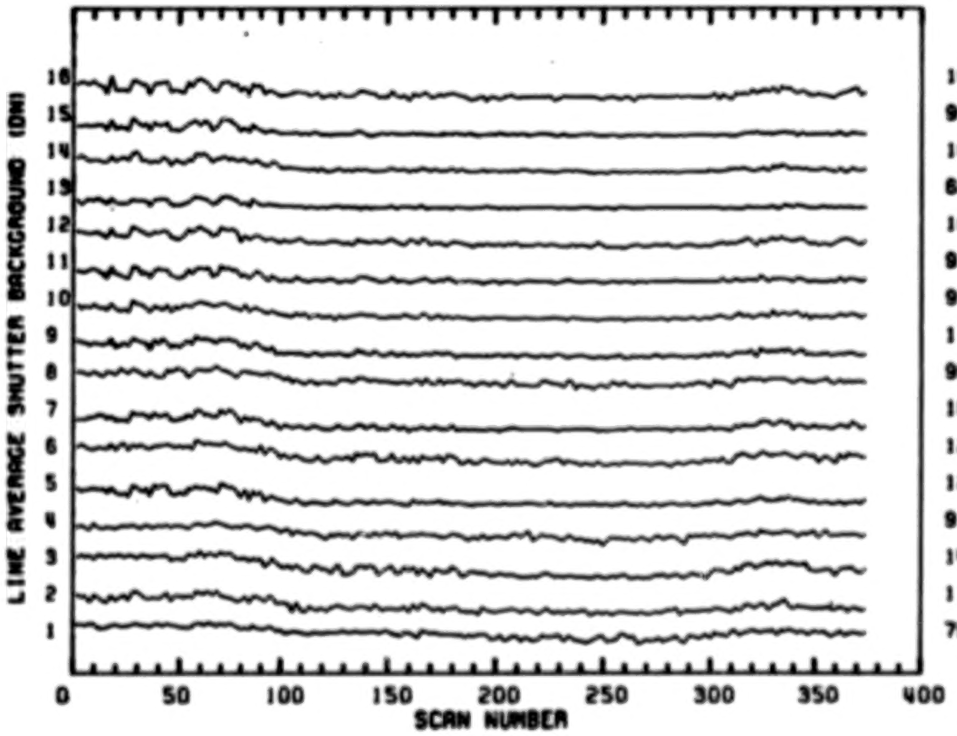

	1000*CV	SHIFT1	SHIFT2
16	106	0.18	-0.02
15	90	0.05	-0.01
14	108	0.02	-0.02
13	68	0.03	-0.00
12	107	0.08	-0.01
11	91	0.08	-0.01
10	99	0.05	-0.02
9	115	0.04	-0.01
8	90	0.01	-0.06
7	109	0.06	-0.01
6	121	0.12	-0.04
5	122	0.07	-0.01
4	91	0.01	-0.07
3	140	0.12	-0.02
2	116	0.05	-0.07
1	79	0.25	-0.02

Appendix 9.7.5

SCENE ID=40392-18152, BAND 5 (REVERSE)
SHUTTER BACKGROUND 1 SPECTRA BEFORE CORRECTION

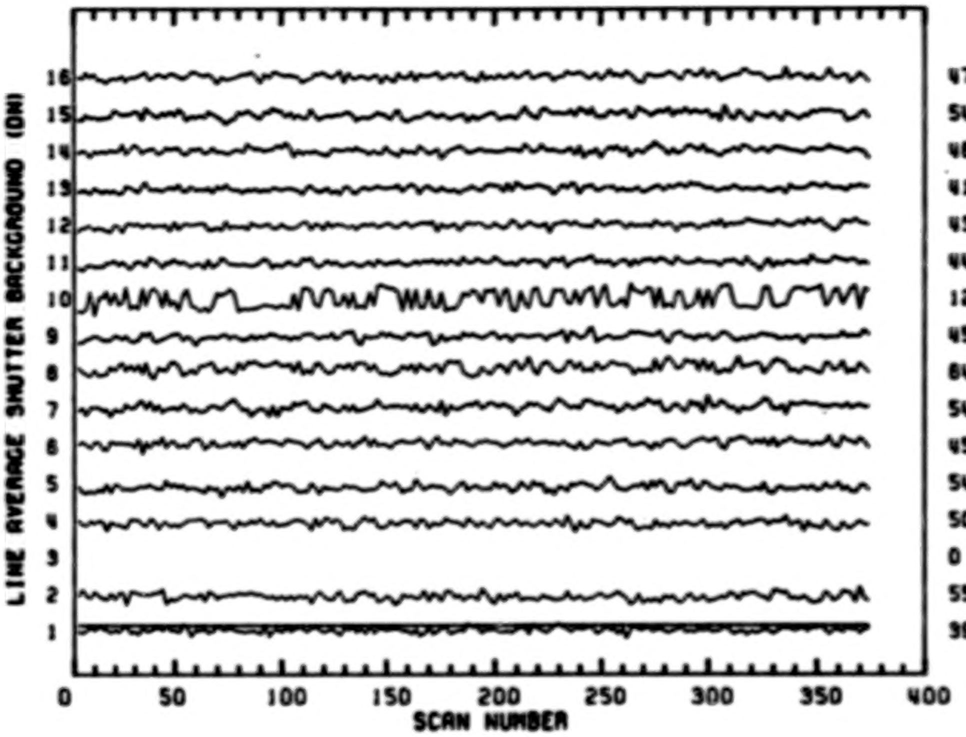

	1000*CV	SHIFT1	SHIFT2
16	47	0.00	0.00
15	54	0.00	0.00
14	48	0.00	0.00
13	41	0.00	0.00
12	43	0.00	0.00
11	44	0.00	0.00
10	129	0.00	0.00
9	45	0.00	0.00
8	84	0.00	0.00
7	54	0.00	0.00
6	45	0.00	0.00
5	54	0.00	0.00
4	50	0.00	0.00
3	0	0.00	0.00
2	55	0.00	0.00
1	39	0.00	0.00

LEE/BARKER
6-MAR-84

SCENE ID=40392-18152, BAND 5 (REVERSE)
SHUTTER BACKGROUND 1 SPECTRA AFTER CORRECTION

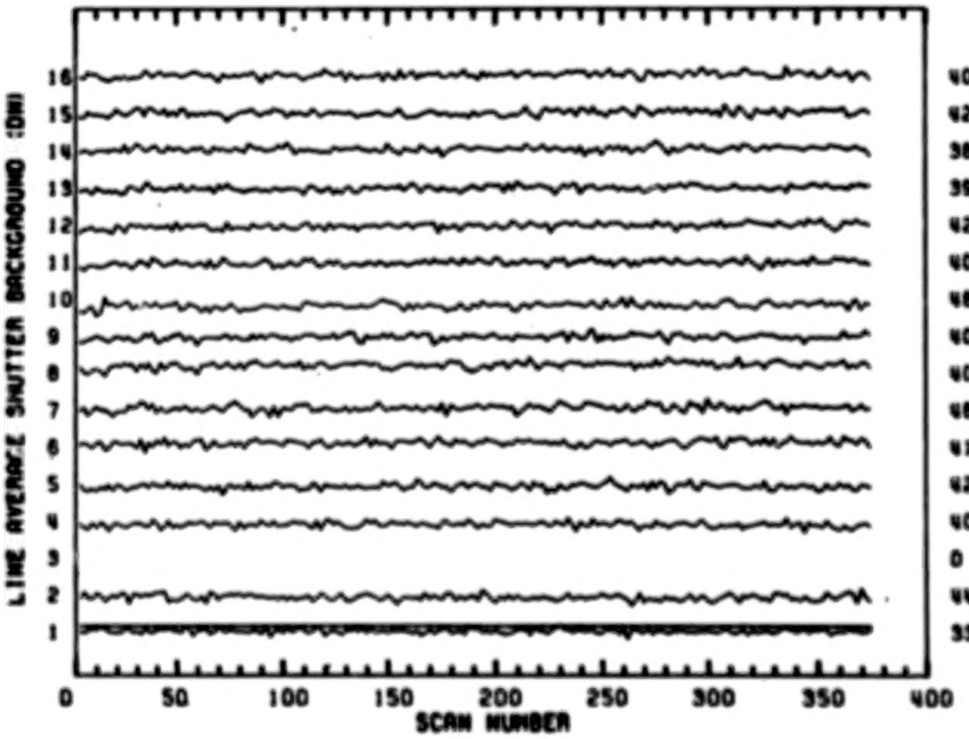

	1000*CV	SHIFT1	SHIFT2
16	40	-0.00	-0.09
15	42	-0.12	-0.01
14	38	-0.03	-0.08
13	39	-0.04	0.02
12	42	0.04	0.01
11	40	-0.04	0.04
10	48	-0.02	0.58
9	40	-0.04	0.05
8	40	-0.01	-0.22
7	48	-0.02	0.10
6	41	0.02	-0.06
5	42	-0.12	0.02
4	40	0.10	-0.06
3	0	0.00	0.00
2	44	0.07	-0.08
1	33	-0.02	0.08

LEE/BARKER
6-MAR-84

Appendix 9.7.6

SCENE ID=40392-18152, BAND 7 (REVERSE)
SHUTTER BACKGROUND 1 SPECTRA BEFORE CORRECTION

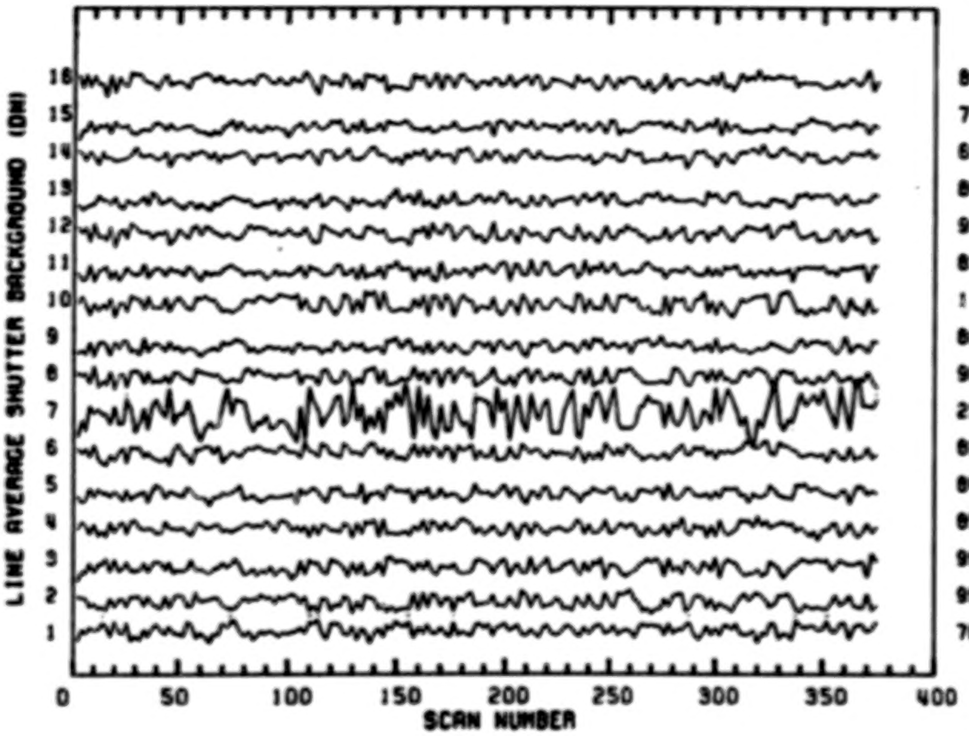

1000*CV	SHIFT1	SHIFT2
84	0.00	0.00
77	0.00	0.00
69	0.00	0.00
84	0.00	0.00
93	0.00	0.00
83	0.00	0.00
112	0.00	0.00
80	0.00	0.00
90	0.00	0.00
233	0.00	0.00
88	0.00	0.00
84	0.00	0.00
85	0.00	0.00
99	0.00	0.00
99	0.00	0.00
78	0.00	0.00

LEE/BARKER
6-MAR-84

SCENE ID=40392-18152, BAND 7 (REVERSE)
SHUTTER BACKGROUND 1 SPECTRA AFTER CORRECTION

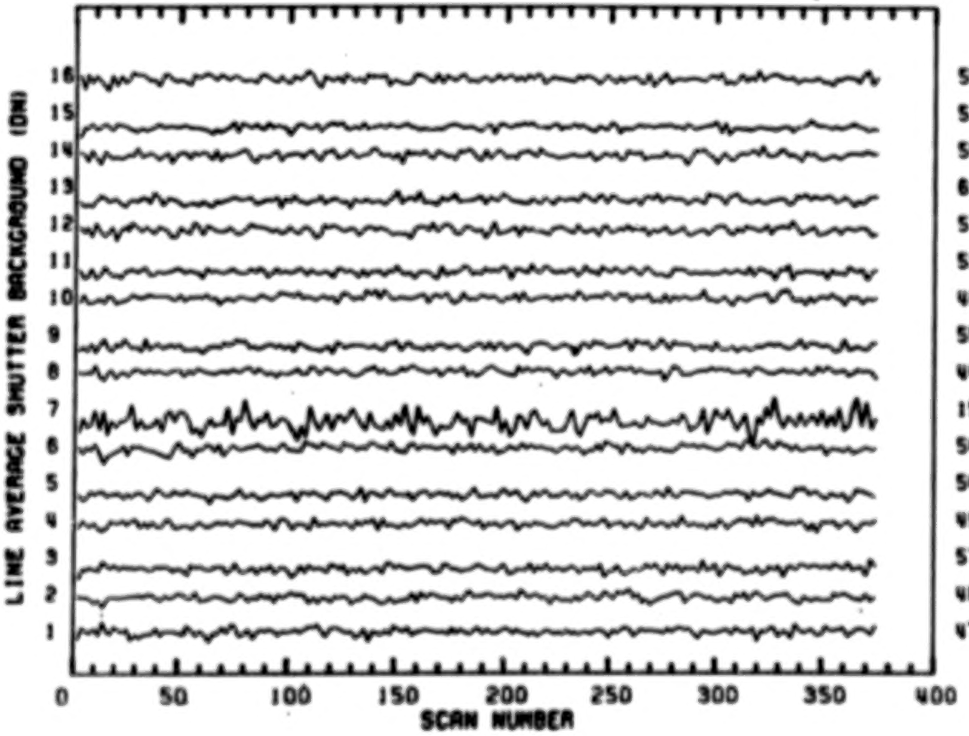

1000*CV	SHIFT1	SHIFT2
55	0.09	-0.19
51	-0.03	0.19
55	0.12	-0.08
61	-0.05	0.16
57	0.08	-0.21
53	-0.03	0.27
46	0.03	-0.42
55	-0.05	0.18
44	0.04	-0.33
154	-0.05	0.92
54	0.06	-0.25
54	-0.01	0.23
49	0.05	-0.26
57	-0.03	0.31
48	0.03	-0.32
47	-0.02	0.28

LEE/BARKER
6-MAR-84

Appendix 9.7.7

SCENE ID=40392-18152, BAND 6 (FORWARD)
SHUTTER BACKGROUND 1 SPECTRA BEFORE CORRECTION

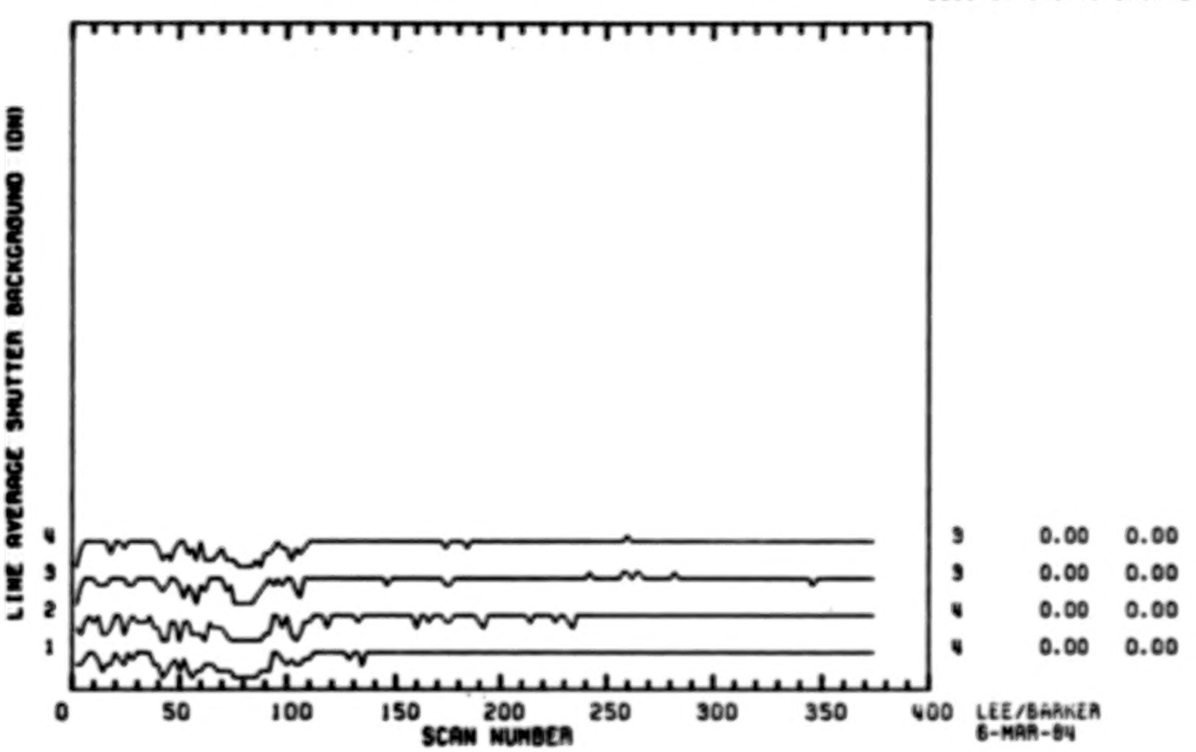

SCENE ID=40392-18152, BAND 6 (REVERSE)
SHUTTER BACKGROUND 1 SPECTRA BEFORE CORRECTION

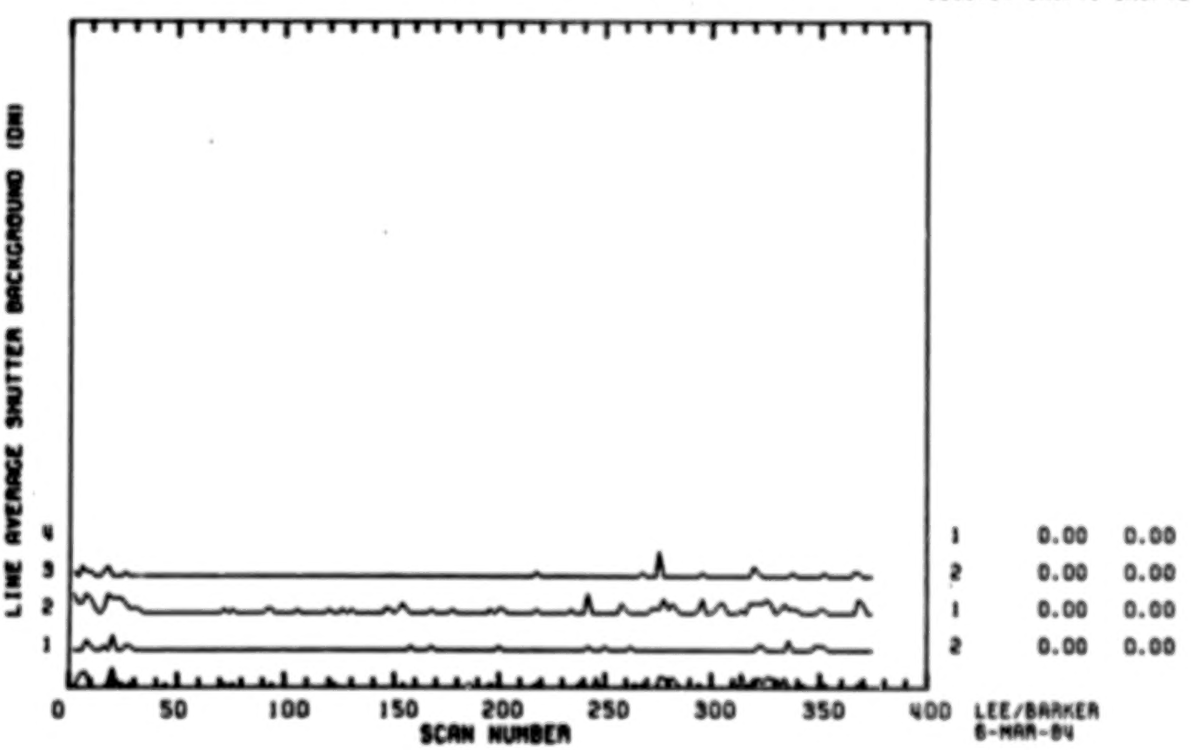

APPENDIX 9.8 - TM/PF TABLE OF SCAN-CORRELATED SHIFTS

Landsat-4 TM/PF within-scene tabulations (Section 4.5) of scan-correlated shifts by forward and reverse scans for type 4-1 (Landsat-4 Band 1, Channel 4) and type 4-7 (Landsat-4 Band 7, Channel 7) in shutter regions before and after DC restoration for San Francisco, 12 AUG 83 (Scene ID 40392-18152) and Buffalo PM, 26 SEP 82 (400037-02243) are included in this Appendix as follows:

9.8.1 TM/PF Band 1 Shifts (4-1, 4-7)
9.8.2 TM/PF Band 2 Shifts (4-1, 4-7)
9.8.3 TM/PF Band 3 Shifts (4-1, 4-7)
9.8.4 TM/PF Band 4 Shifts (4-1, 4-7)
9.8.5 TM/PF Band 5 Shifts (4-1, 4-7)
9.8.6 TM/PF Band 7 Shifts (4-1, 4-7).

Appendix 9.8.1

SCAN-CORRELATED SHIFTS (DN)
BAND 1 LANDSAT-4 TM/PF

	TYPE 4-1 NASA ID 40392-18152				TYPE 4-7 NASA ID 40037-02243				TYPE 4-7 NASA ID 40392-18152				
	SHUTTER 1		SHUTTER 2		SHUTTER 1		SHUTTER 2		SHUTTER 1		SHUTTER 2		
CH	FWD	REV	FWD	REV	FWD	REV	FWD	REV	FWD	REV	FWD	REV	CH
16	.05	.05	.04	.02	−.03	−.02	−.01	−.02	.03	.01	.01	−.02	16
15	.03	.02	.02	.02	−.06	−.08	−.14	−.10	−.02	−.08	−.07	−.04	15
14	.16	.19	.24	.11	−.05	−.05	−.05	−.05	−.01	−.03	−.01	−.03	14
13	.07	.08	.05	.03	−.05	−.08	−.10	−.05	−.02	−.08	−.04	−.04	13
12	1.62	1.83	1.88	1.52	−.03	−.03	−.04	−.02	−.02	−.02	−.02	−.04	12
11	.02	−.02	−.02	−.01	−.08	−.09	−.09	−.06	−.01	−.07	−.02	−.05	11
10	.93	.99	.09	.64	−.03	−.05	−.05	−.03	−.02	−.03	−.03	−.04	10
9	.01	−.03	−.02	−.02	.00	−.02	−.04	−.02	.02	−.02	.01	−.01	9
8	.75	.79	.84	.56	−.06	−.07	−.07	−.05	−.01	−.03	−.02	−.05	8
7	.01	−.02	−.01	.01	−.05	−.07	−.07	−.08	−.02	−.04	−.04	−.05	7
6	.17	.19	.18	.07	−.02	−.03	−.02	−.03	.02	−.01	.00	−.02	6
5	.04	−.00	.02	.01	−.12	−.13	−.12	−.14	−.03	−.11	−.13	−.07	5
4	1.70	1.95	2.05	1.50	.01	.01	−.01	.01	−.01	−.02	−.02	−.03	4
3	.03	.03	.03	.02	−.11	−.13	−.11	−.12	−.04	−.12	−.08	−.07	3
2	.07	.07	.06	.03	−.10	−.11	−.09	−.11	−.02	−.07	−.04	−.05	2
1	.33	.35	.38	.17	−.14	−.14	−.15	−.14	−.07	−.14	−.14	−.10	1

Appendix 9.8.2

SCAN-CORRELATED SHIFTS (DN)
BAND 2 LANDSAT-4 TM/PF

	TYPE 4-1 NASA ID 40392-18152				TYPE 4-7 NASA ID 40037-02243				TYPE 4-7 NASA ID 40392-18152				
	SHUTTER 1		SHUTTER 2		SHUTTER 1		SHUTTER 2		SHUTTER 1		SHUTTER 2		
CH	FWD	REV	FWD	REV	FWD	REV	FWD	REV	FWD	REV	FWD	REV	CH
16	−.00	.02	−.00	.01	.08	.09	.09	.05	−.00	−.00	.00	−.01	16
15	.00	.01	.01	.01	−.10	−.08	−.14	−.05	−.06	−.03	−.10	−.02	15
14	−.01	.01	−.00	.02	.01	.01	.02	.01	−.01	−.00	−.00	−.01	14
13	−.00	.01	.01	.01	−.12	−.06	−.11	−.08	−.04	−.03	−.07	−.01	13
12	−.01	.01	−.01	.01	.01	−.00	.01	.01	−.01	−.01	−.01	−.00	12
11	−.00	.01	.00	.01	−.08	−.07	−.10	−.05	−.03	−.02	−.05	−.02	11
10	−.01	.02	−.00	.02	.00	.00	.00	.01	−.01	−.01	−.00	−.01	10
9	−.00	.01	.00	.01	−.06	−.03	−.05	−.02	−.04	−.02	.05	−.01	9
8	−.00	.02	.00	.01	.01	−.01	.00	.01	−.01	−.01	−.01	−.01	8
7	−.01	.01	−.01	.02	−.10	−.09	−.09	−.06	−.03	−.03	−.05	−.03	7
6	−.00	.02	−.00	.02	.01	.01	.00	.01	−.01	−.00	.00	−.01	6
5	−.00	.02	.00	.03	−.12	−.12	−.14	−.09	−.04	−.05	−.08	−.04	5
4	.01	.09	.03	.06	.01	.03	.02	.02	−.01	−.01	−.01	−.01	4
3	−.01	.01	−.02	.01	**−.20**	**−.22**	**−.25**	**−.17**	−.06	−.06	−.09	−.06	3
2	.00	.08	.00	.03	.04	.02	.02	.02	−.01	−.01	−.00	−.01	2
1	.05	.13	.07	.10	**−.34**	**−.38**	**−.34**	**−.39**	**−.17**	**−.24**	**−.20**	**−.18**	1

Appendix 9.8.3

SCAN-CORRELATED SHIFTS (DN)
BAND 3 LANDSAT-4 TM/PF

	TYPE 4-1 NASA ID 40392-18152				TYPE 4-7 NASA ID 40037-02243				TYPE 4-7 NASA ID 40392-18152				
	SHUTTER 1		SHUTTER 2		SHUTTER 1		SHUTTER 2		SHUTTER 1		SHUTTER 2		
CH	FWD	REV	FWD	REV	FWD	REV	FWD	REV	FWD	REV	FWD	REV	CH
16	.03	.12	.06	.08	.78	.78	.81	.78	.41	.61	.15	.58	16
15	.09	.18	.12	.17	-.25	-.24	-.26	-.24	-.25	-.25	-.15	-.39	15
14	.00	.06	.05	.01	.15	.12	.13	.12	.01	.03	-.01	.03	14
13	.05	.12	.10	.09	-.17	-.15	-.18	-.14	-.11	-.13	-.09	-.18	13
12	-.00	.04	.02	-.00	.11	.09	.12	.08	.02	.03	-.01	.04	12
11	.01	.03	.03	.01	-.14	-.12	-.13	-.10	-.13	-.14	-.08	-.21	11
10	.01	.09	.03	.02	.03	.02	.03	.02	-.00	-.00	-.01	-.00	10
9	-.01	.01	.01	-.02	-.12	-.09	-.11	-.07	-.04	-.05	.02	-.04	9
8	-.02	.01	.01	-.02	-.05	-.02	-.04	-.03	-.01	-.01	-.01	-.01	8
7	.02	.09	.05	.03	-.21	-.20	-.21	-.19	-.12	-.17	-.10	-.17	7
6	.01	.09	.06	.02	.03	.04	.04	.03	.00	.00	-.01	.00	6
5	.06	.15	.10	.08	-.19	-.18	-.21	-.16	-.12	-.18	-.09	-.18	5
4	-.01	.02	.01	-.01	.01	.01	.01	.01	.00	.00	-.01	.00	4
3	.05	.11	.05	.09	-.30	-.32	-.32	-.27	-.20	-.24	-.12	-.28	3
2	.02	.13	.06	.04	.25	.23	.24	.18	.07	.13	.01	.13	2
1	.20	.29	.19	.27	-.54	-.59	-.59	-.53	-.41	.52	-.29	-.52	1

Appendix 9.8.4

SCAN-CORRELATED SHIFTS (DN)
BAND 4 LANDSAT-4 TM/PF

	TYPE 4-1 NASA ID 40392-18152				TYPE 4-7 NASA ID 40037-02243				TYPE 4-7 NASA ID 40392-18152				
	SHUTTER 1		SHUTTER 2		SHUTTER 1		SHUTTER 2		SHUTTER 1		SHUTTER 2		
CH	FWD	REV	FWD	REV	FWD	REV	FWD	REV	FWD	REV	FWD	REV	CH
16	.12	.18	.29	.17	.00	.00	−.00	−.00	−.03	−.02	−.03	−.02	16
15	.06	.05	.12	.07	−.01	−.00	−.01	−.00	−.02	−.01	−.01	−.01	15
14	−.01	.02	−.00	.03	−.02	−.00	−.01	−.00	−.03	−.02	−.04	−.02	14
13	.04	.03	.08	.03	−.01	−.00	−.00	−.00	−.01	−.00	−.01	−.01	13
12	.06	.06	.13	.06	.00	.01	.01	.00	−.02	−.01	−.01	−.02	12
11	.07	.08	.10	.04	−.01	−.00	−.01	−.00	−.02	−.01	−.02	−.01	11
10	.01	.05	.05	.04	−.01	−.01	−.01	−.01	−.03	−.02	−.03	−.03	10
9	.00	.04	.03	.03	−.02	−.00	−.01	−.00	−.01	−.01	−.01	−.01	9
8	−.01	.01	−.01	.01	−.07	−.07	−.09	−.06	−.05	−.06	−.05	−.04	8
7	.01	.06	.03	.02	−.01	−.00	−.01	−.00	−.02	−.01	−.01	−.01	7
6	.01	.12	.03	.01	−.05	−.05	−.06	−.04	−.02	−.04	−.04	−.02	6
5	.02	.07	.07	.04	−.02	−.01	−.02	−.00	−.02	−.01	−.02	−.01	5
4	−.01	.01	−.01	.02	−.06	−.07	−.07	−.05	−.04	−.07	−.10	−.04	4
3	.01	.12	.06	.03	−.02	−.02	−.05	−.02	−.02	−.02	−.02	−.02	3
2	−.00	.05	.01	.02	−.06	−.05	−.06	−.03	−.06	−.07	−.08	−.03	2
1	.10	.25	.17	.10	−.06	−.05	−.06	−.04	−.02	−.02	−.02	−.01	1

Appendix 9.8.5

SCAN-CORRELATED SHIFTS (DN)
BAND 5 LANDSAT-4 TM/PF

	TYPE 4-1 NASA ID 40392-18152				TYPE 4-7 NASA ID 40037-02243				TYPE 4-7 NASA ID 40392-18152				
	SHUTTER 1		SHUTTER 2		SHUTTER 1		SHUTTER 2		SHUTTER 1		SHUTTER 2		
CH	FWD	REV	FWD	REV	FWD	REV	FWD	REV	FWD	REV	FWD	REV	CH
16	.01	−.00	.01	.01	−.09	−.08	−.09	−.07	−.07	−.09	−.10	−.06	16
15	−.18	−.12	−.13	−.15	−.04	−.04	−.07	−.09	−.01	−.01	−.02	−.04	15
14	−.03	−.03	−.02	−.02	−.07	−.08	−.07	−.05	−.08	−.08	−.06	−.04	14
13	−.06	.04	.04	.02	.02	.01	.00	.02	−.00	−.01	.01	.01	13
12	.05	.04	.04	.02	.02	.01	.00	.02	−.00	−.01	−.01	−.01	12
11	−.04	−.04	−.01	−.04	.06	.06	.02	.04	.03	.04	.04	.02	11
10	−.04	−.02	−.03	−.04	.59	.63	.61	.59	.52	.58	.52	.60	10
9	−.05	−.04	−.02	−.04	.06	.05	.04	.02	.08	.05	.05	.00	9
8	−.02	−.01	−.01	−.05	−.17	−.20	−.20	−.13	−.19	−.22	−.17	−.13	8
7	−.01	−.02	.00	−.03	.10	.14	.08	.14	.10	.10	.10	.11	7
6	.03	.02	.03	.02	−.06	−.08	−.06	−.04	−.09	−.06	−.09	−.08	6
5	−.12	−.12	−.11	−.13	.01	−.02	−.01	−.01	.02	.02	.01	−.01	5
4	.06	.10	.07	.10	−.05	−.04	−.06	−.06	−.07	−.06	−.05	−.04	4
3	.00	.00	.00	.00	.00	.00	.00	.00	.00	.00	.00	.00	3
2	.07	.07	.10	.07	−.09	−.10	−.09	−.07	−.09	−.08	−.10	−.08	2
1	.00	−.02	−.01	−.02	.07	.04	.04	.04	.07	.08	.05	.04	1

Appendix 9.8.6

SCAN-CORRELATED SHIFTS (DN)
BAND 7 LANDSAT-4 TM/PF

	TYPE 4-1 NASA ID 40392-18152				TYPE 4-7 NASA ID 40037-02243				TYPE 4-7 NASA ID 40392-18152				
	SHUTTER 1		SHUTTER 2		SHUTTER 1		SHUTTER 2		SHUTTER 1		SHUTTER 2		
CH	FWD	REV	FWD	REV	FWD	REV	FWD	REV	FWD	REV	FWD	REV	CH
16	.03	.09	.11	.09	−.23	−.19	−.21	−.19	−.23	−.19	−.19	−.19	16
15	−.03	−.03	−.04	−.02	.20	.17	.17	.13	.18	.19	.16	.12	15
14	.10	.12	.13	.14	−.07	−.06	−.05	−.07	−.12	−.08	−.08	−.05	14
13	−.03	−.05	−.04	−.06	.15	.20	.21	.17	.26	.16	.20	.17	13
12	.07	.08	.09	.09	−.23	−.26	−.22	−.21	−.22	−.21	−.21	−.23	12
11	−.02	−.03	−.03	−.04	.21	.18	.17	.17	.23	.27	.21	.17	11
10	.04	.03	.07	.06	−.41	−.41	−.40	−.36	−.39	−.42	−.38	−.41	10
9	−.06	−.05	−.06	−.06	.14	.16	.18	.13	.17	.18	.21	.10	9
8	.03	.04	.04	.02	−.29	−.29	−.30	−.30	−.27	−.33	−.27	−.29	8
7	−.02	−.05	.09	−.07	1.03	1.07	.69	.80	1.09	.92	.76	.11	7
6	.06	.06	.07	.06	−.29	−.29	−.28	−.26	−.29	−.25	−.25	−.28	6
5	−.01	−.01	−.02	−.02	.23	.25	.22	.22	.23	.23	.24	.23	5
4	.04	.05	.06	.04	−.23	−.24	−.19	−.20	−.25	−.26	−.23	−.05	4
3	−.05	−.03	−.04	−.05	.30	.30	.31	.22	.28	.31	.34	.32	3
2	.04	.03	.03	.02	−.27	−.28	−.28	−.24	−.24	−.32	−.24	−.26	2
1	−.00	−.02	−.02	−.03	.28	.28	.26	.27	.25	.28	.30	.25	1

APPENDIX 9.9 - TM/PF PLOTS OF SHUTTER BACKGROUND VERSUS SCAN

Landsat-4 TM/PF averaged shutter backgrounds before and after DC restoration are plotted versus scan number for forward and reverse scans after being corrected (Section 4.5) for scan collerated shifts of type 4-1 (Landsat-4 Band 1, Channel 4) and type 4-7 (Landsat-4 Band 7, Channel 7) for 2 AUG 83 scene of San Francisco (NASA ID 40392-18152) in which lower half is cloud-covered. These plots are included as follows:

9.9.1 Band 1, Shutter 1
9.9.2 Band 1, Shutter 2
9.9.3 Band 2, Shutter 1
9.9.4 Band 2, Shutter 2
9.9.5 Band 3, Shutter 1
9.9.6 Band 3, Shutter 2
9.9.7 Band 4, Shutter 1
9.9.8 Band 4, Shutter 2
9.9.9 Band 5, Shutter 1
9.9.10 Band 5, Shutter 2
9.9.11 Band 7, Shutter 1
9.9.12 Band 7, Shutter 2.

Appendix 9.9.1

SCENE ID=40392-10152, BAND 1 (FORWARD)
SHUTTER BACKGROUND 1 SPECTRA AFTER CORRECTION

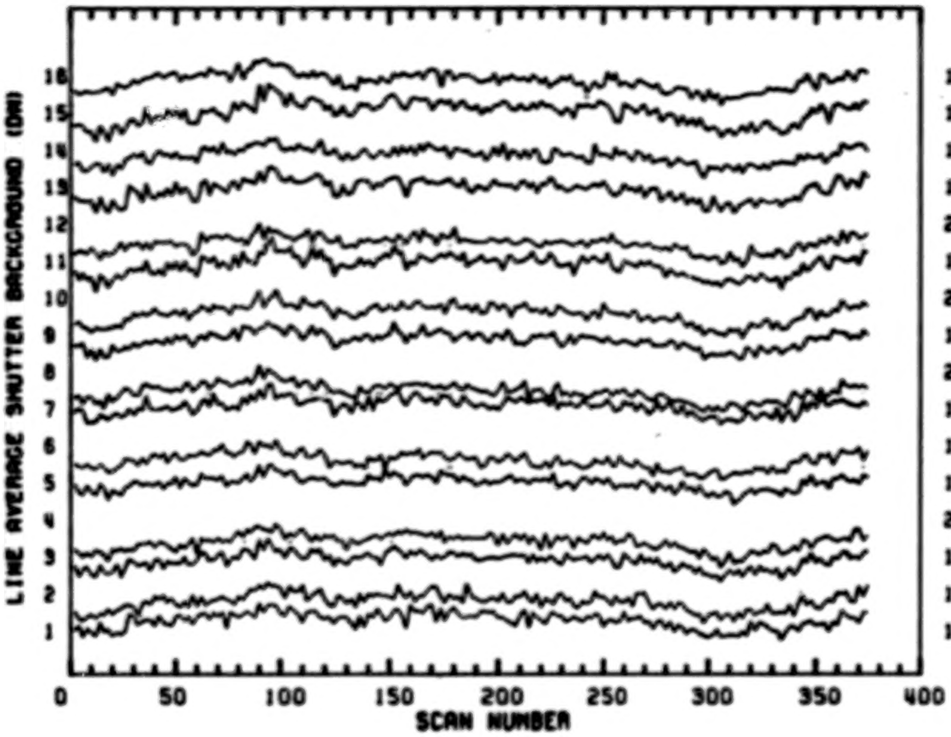

1000*CV	SHIFT1	SHIFT2
176	0.05	0.03
199	0.03	-0.02
158	0.16	-0.01
184	0.07	-0.02
213	1.62	-0.02
191	0.02	-0.01
230	0.93	-0.02
159	0.01	0.02
237	0.75	-0.01
195	0.01	-0.02
199	0.17	0.02
124	0.04	-0.03
244	1.70	-0.01
151	0.03	-0.04
178	0.07	-0.02
122	0.33	-0.07

LEE/BARKER
8-MAR-84

SCENE ID=40392-10152, BAND 1 (REVERSE)
SHUTTER BACKGROUND 1 SPECTRA AFTER CORRECTION

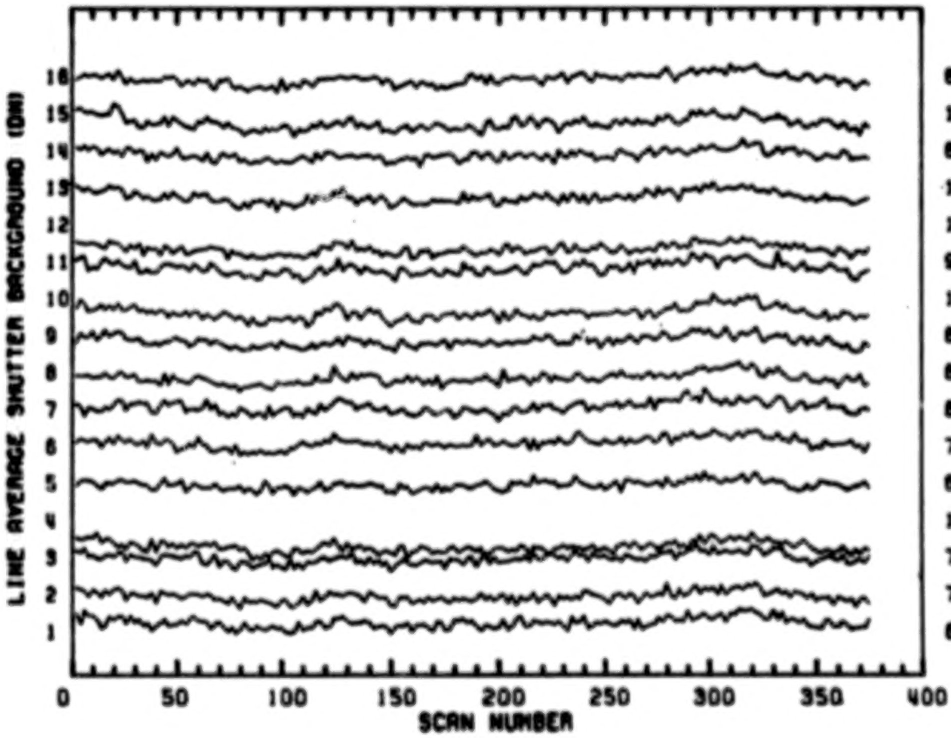

1000*CV	SHIFT1	SHIFT2
86	0.05	0.01
105	0.02	-0.08
80	0.19	-0.03
100	0.08	-0.08
111	1.83	-0.02
96	-0.02	-0.07
114	0.99	-0.03
84	-0.03	-0.02
87	0.79	-0.03
83	-0.02	-0.04
76	0.19	-0.01
67	-0.00	-0.11
128	1.95	-0.02
77	0.03	-0.12
76	0.07	-0.07
69	0.35	-0.14

LEE/BARKER
8-MAR-84

Appendix 9.9.2

SCENE ID=40392-18152, BAND 1 (FORWARD)
SHUTTER BACKGROUND 2 SPECTRA AFTER CORRECTION

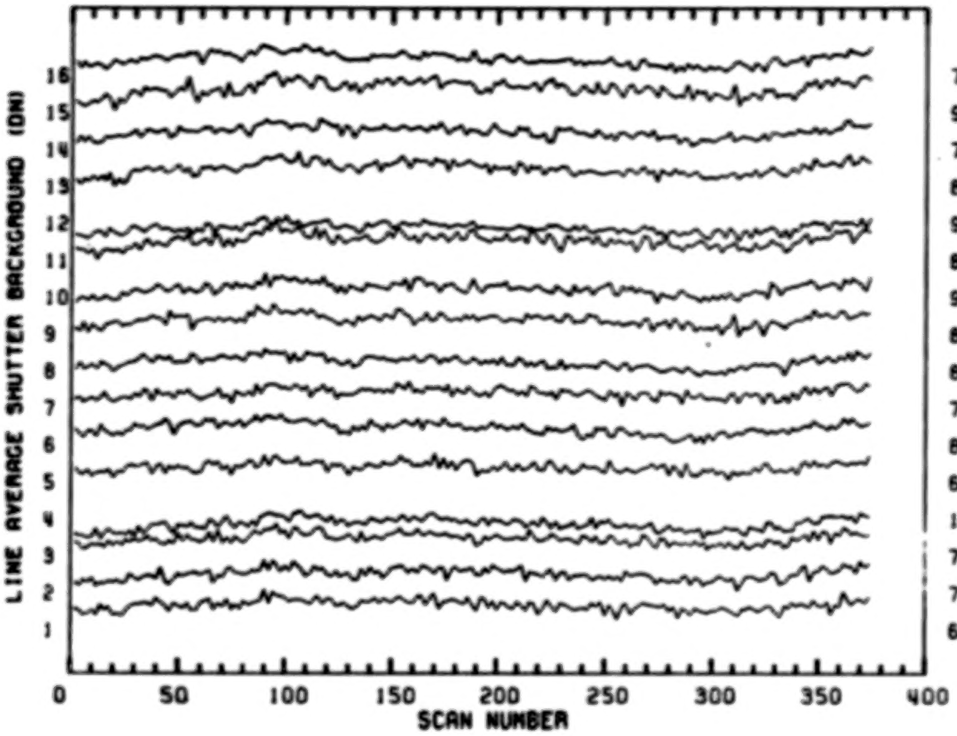

1000*CV	SHIFT B1/C4	SHIFT B7/C7
79	0.04	0.01
92	0.02	-0.07
74	0.24	-0.01
86	0.05	-0.04
93	1.99	-0.02
86	-0.02	-0.02
94	1.03	-0.03
80	-0.02	0.01
85	0.84	-0.02
70	-0.01	-0.04
80	0.18	0.00
67	0.02	-0.13
119	2.05	-0.02
72	0.03	-0.08
78	0.06	-0.04
66	0.38	-0.14

LEE/BARKER
6-MAR-84

SCENE ID=40392-18152, BAND 1 (REVERSE)
SHUTTER BACKGROUND 2 SPECTRA AFTER CORRECTION

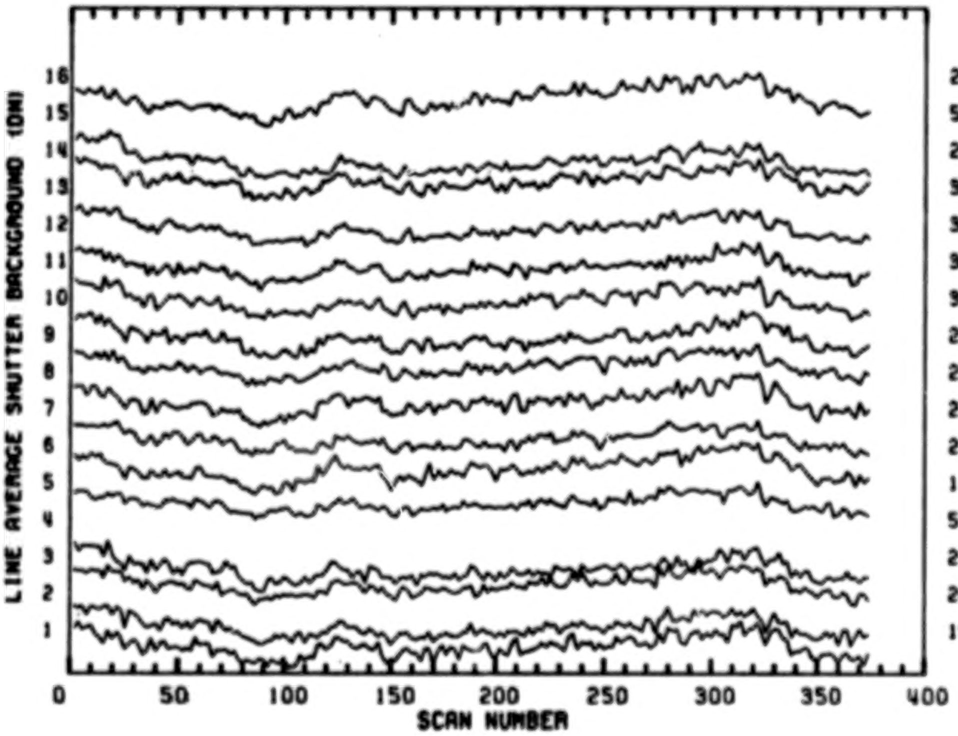

1000*CV	SHIFT B1/C4	SHIFT B7/C7
259	0.02	-0.02
553	0.02	-0.04
252	0.11	-0.03
361	0.03	-0.04
382	1.52	-0.04
358	-0.01	-0.05
385	0.64	-0.04
252	-0.02	-0.01
297	0.56	-0.05
229	0.01	-0.05
259	0.07	-0.02
162	0.01	-0.07
553	1.50	-0.03
237	0.02	-0.07
283	0.03	-0.05
199	0.17	-0.10

LEE/BARKER
6-MAR-84

Appendix 9.9.3

SCENE ID=40392-18152, BAND 2 (FORWARD)
SHUTTER BACKGROUND 1 SPECTRA AFTER CORRECTION

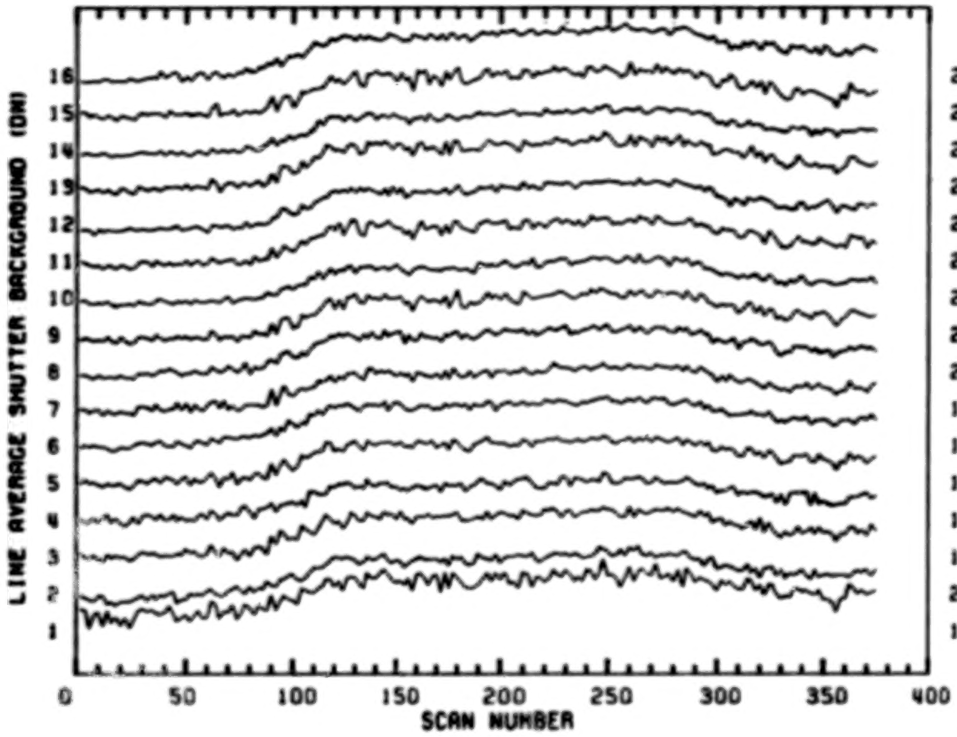

1000*CV	SHIFT1	SHIFT2
212	-0.00	-0.00
210	0.00	-0.06
204	-0.01	-0.01
219	-0.00	-0.04
219	-0.01	-0.01
207	-0.00	-0.03
206	-0.01	-0.01
217	-0.00	-0.04
205	-0.00	-0.01
193	-0.01	-0.03
193	-0.00	-0.01
192	-0.00	-0.04
178	0.01	-0.01
198	-0.01	-0.06
204	0.00	-0.01
165	0.05	-0.17

LEE/BARKER
6-MAR-84

SCENE ID=40392-18152, BAND 2 (REVERSE)
SHUTTER BACKGROUND 1 SPECTRA AFTER CORRECTION

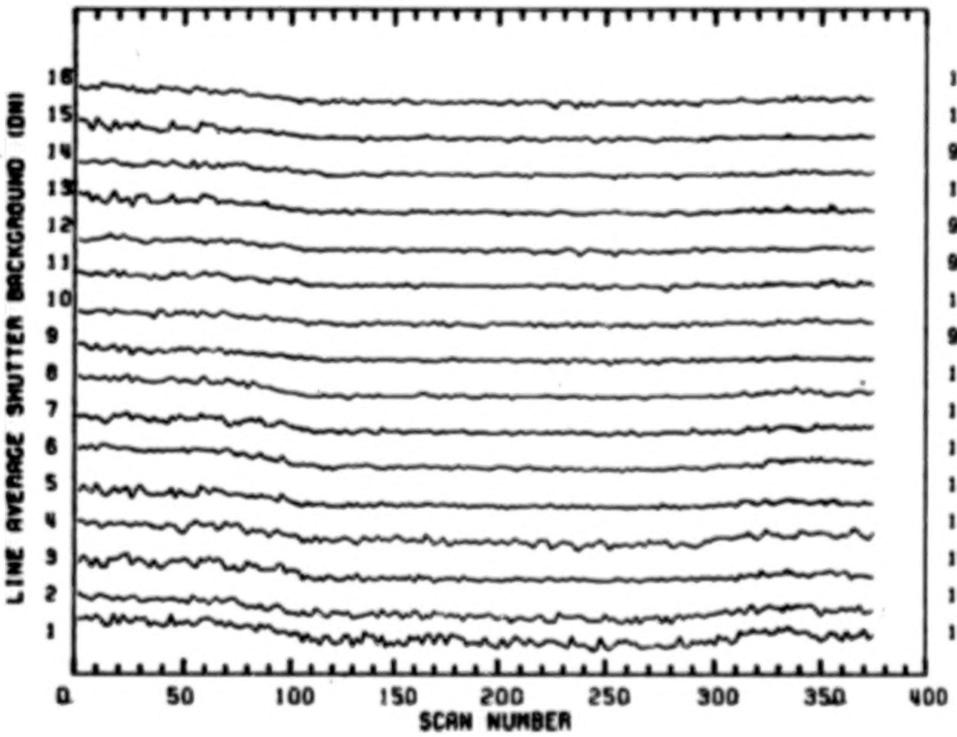

1000*CV	SHIFT1	SHIFT2
116	0.02	-0.00
108	0.02	-0.03
94	0.01	-0.00
118	0.01	-0.03
93	0.01	-0.01
94	0.01	-0.02
100	0.02	-0.01
96	0.01	-0.02
136	0.02	-0.01
117	0.01	-0.03
145	0.02	-0.00
120	0.02	-0.05
139	0.09	-0.01
140	0.01	-0.06
147	0.08	-0.01
143	0.13	-0.24

LEE/BARKER
6-MAR-84

Appendix 9.9.4

SCENE ID=40392-18152, BAND 2 (FORWARD)
SHUTTER BACKGROUND 2 SPECTRA AFTER CORRECTION

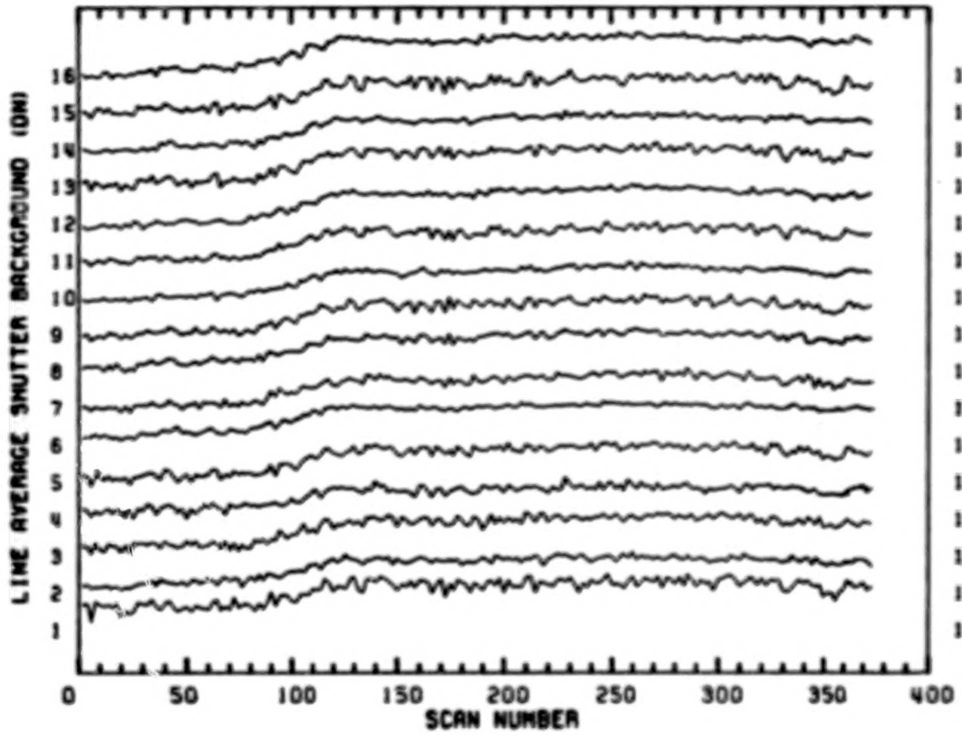

1000*CV	SHIFT B1/C4	SHIFT B7/C7
163	-0.00	0.00
163	0.01	-0.10
157	-0.00	-0.00
165	0.01	-0.07
173	-0.01	-0.01
162	0.00	-0.05
155	-0.00	-0.00
168	0.00	-0.05
145	0.00	-0.01
153	-0.01	-0.05
134	-0.00	-0.00
148	0.00	-0.08
120	0.03	-0.01
136	-0.02	-0.09
126	0.00	-0.00
113	0.07	-0.20

LEE/BARKER
6-MAR-84

SCENE ID=40392-18152, BAND 2 (REVERSE)
SHUTTER BACKGROUND 2 SPECTRA AFTER CORRECTION

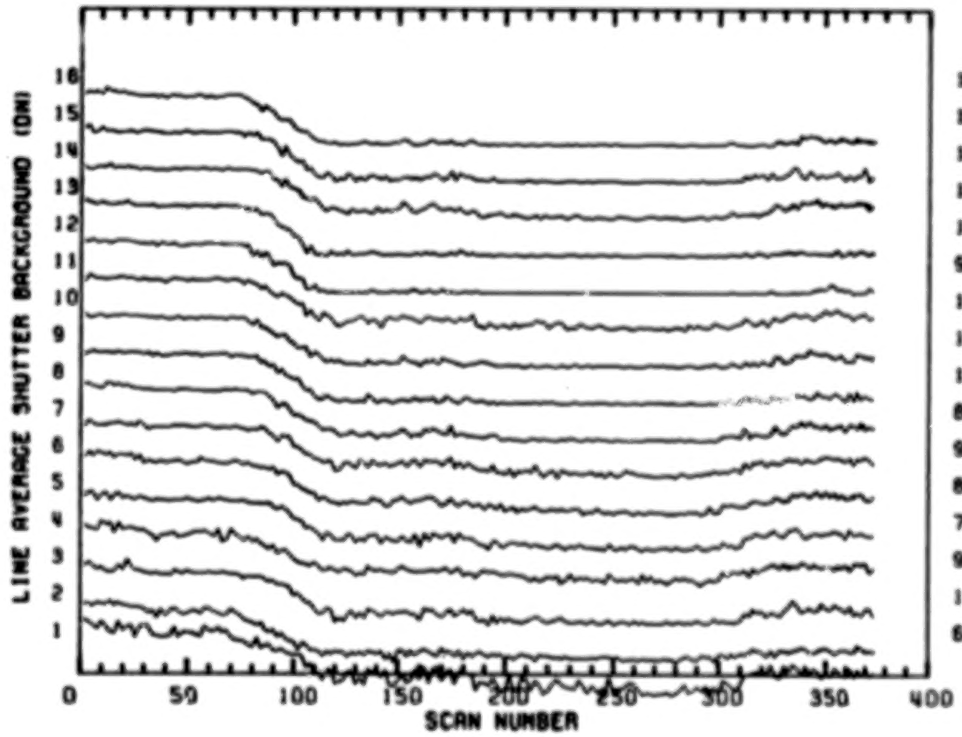

1000*CV	SHIFT B1/C4	SHIFT B7/C7
1463	0.01	-0.01
1306	0.01	-0.02
1065	0.02	-0.01
1518	0.01	-0.01
1584	0.01	-0.00
994	0.01	-0.02
1256	0.02	-0.01
1340	0.01	-0.01
1138	0.01	-0.01
876	0.02	-0.03
932	0.02	-0.01
880	0.03	-0.04
702	0.05	-0.01
961	0.01	-0.06
1021	0.03	-0.01
698	0.10	-0.18

LEE/BARKER
6-MAR-84

Appendix 9.9.5

SCENE ID=40392-18152, BAND 3 (FORWARD)
SHUTTER BACKGROUND 1 SPECTRA AFTER CORRECTION

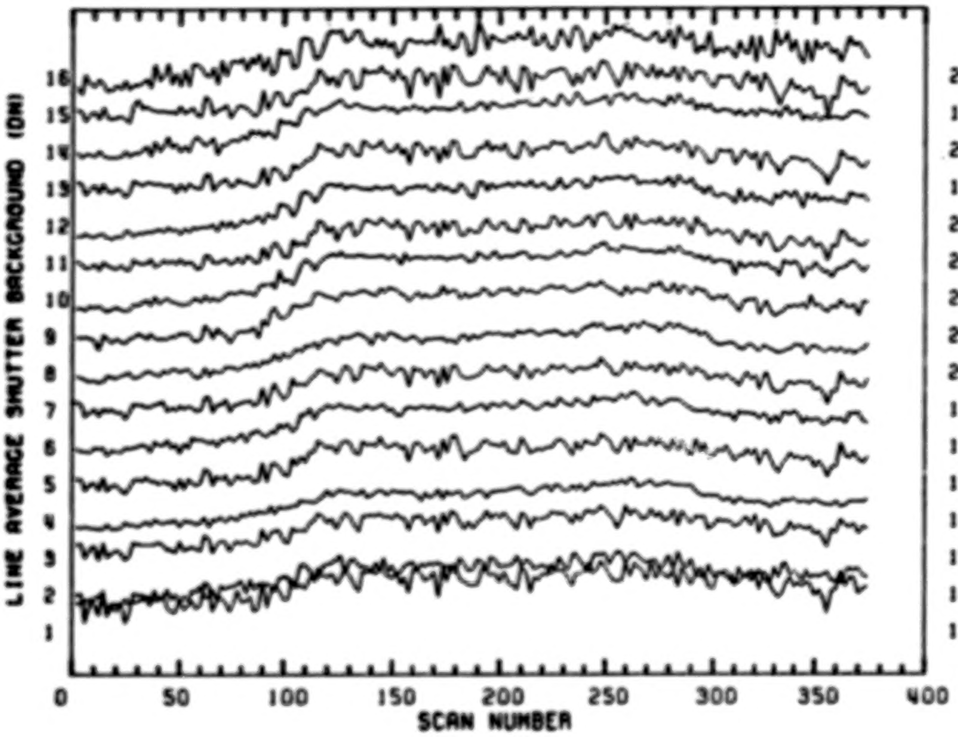

1000*CV	SHIFT1	SHIFT2
211	0.03	0.41
198	0.09	-0.25
202	0.00	0.01
196	0.05	-0.11
228	-0.00	0.02
206	0.01	-0.13
230	0.01	-0.00
217	-0.01	-0.04
203	-0.02	-0.01
189	0.02	-0.12
196	0.01	0.00
192	0.06	-0.12
182	-0.01	0.00
152	0.05	-0.20
188	0.02	0.07
134	0.20	-0.41

SCENE ID=40392-18152, BAND 3 (REVERSE)
SHUTTER BACKGROUND 1 SPECTRA AFTER CORRECTION

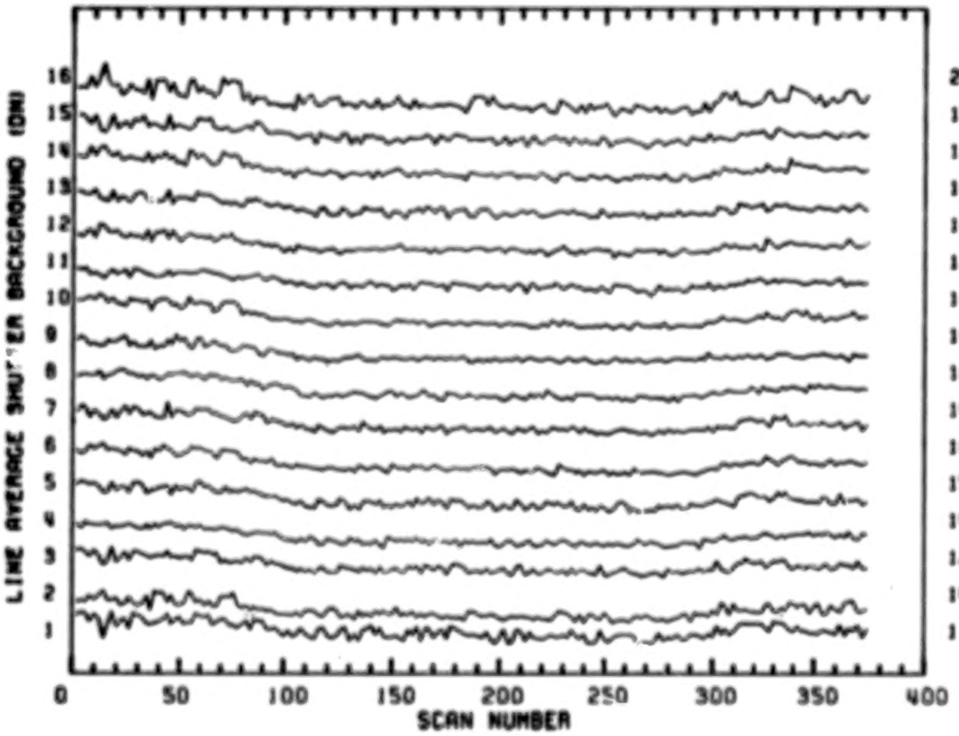

1000*CV	SHIFT1	SHIFT2
212	0.12	0.61
158	0.18	-0.25
166	0.06	0.03
146	0.12	-0.13
143	0.04	0.03
128	0.03	-0.14
183	0.09	-0.00
142	0.01	-0.05
167	0.01	-0.01
143	0.09	-0.17
160	0.09	0.00
154	0.15	-0.18
140	0.02	0.00
120	0.11	-0.24
146	0.13	0.13
114	0.29	-0.52

Appendix 9.9.6

SCENE ID=40392-18152, BAND 3 (FORWARD)
SHUTTER BACKGROUND 2 SPECTRA AFTER CORRECTION

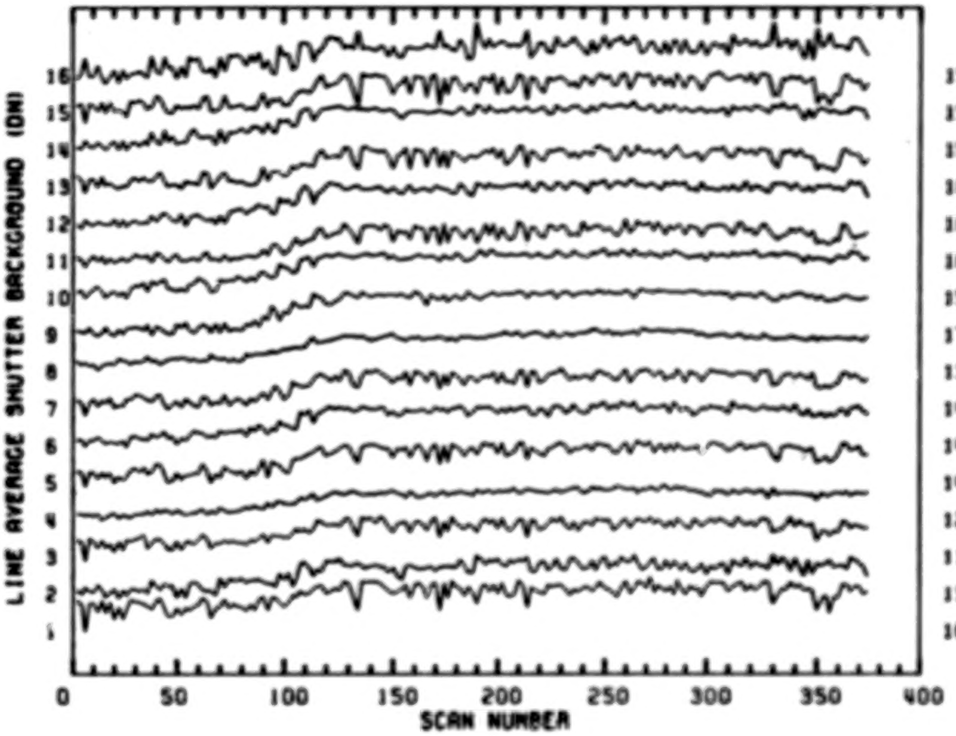

1000*CV	SHIFT B1/C4	SHIFT B7/C7
155	0.08	0.58
158	0.17	-0.39
152	0.01	0.03
161	0.09	-0.18
169	-0.00	0.04
164	0.01	-0.21
153	0.02	0.00
172	-0.02	-0.04
131	-0.02	-0.01
146	0.03	-0.17
147	0.02	0.00
141	0.08	-0.18
120	-0.01	0.00
112	0.09	-0.28
138	0.04	0.13
108	0.27	-0.52

LEE/BARKER
6-MAR-84

SCENE ID=40392-18152, BAND 3 (REVERSE)
SHUTTER BACKGROUND 2 SPECTRA AFTER CORRECTION

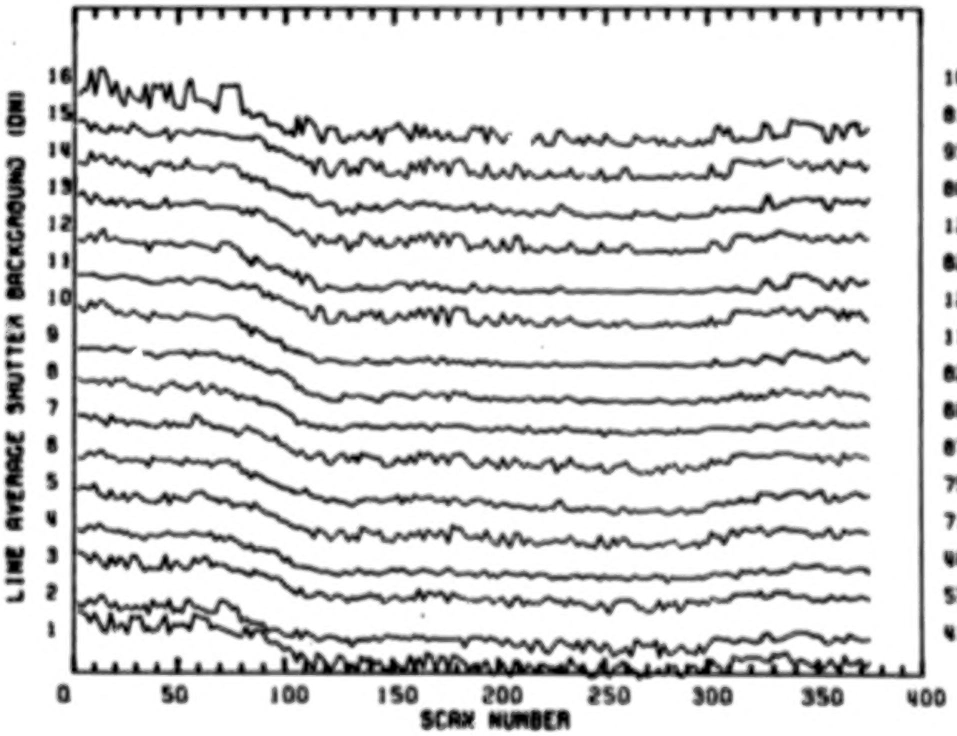

1000*CV	SHIFT B1/C4	SHIFT B7/C7
1016	0.06	0.15
814	0.12	-0.15
933	0.05	-0.01
804	0.10	-0.09
1264	0.02	-0.01
827	0.03	-0.08
1299	0.03	-0.01
1158	0.01	-0.02
820	0.01	-0.01
880	0.05	-0.10
873	0.06	-0.01
754	0.10	-0.09
711	0.01	-0.01
469	0.05	-0.12
550	0.06	0.01
417	0.19	-0.29

LEE/BARKER
6-MAR-84

Appendix 9.9.7

SCENE ID=40392-18152, BAND 4 (FORWARD)
SHUTTER BACKGROUND 1 SPECTRA AFTER CORRECTION

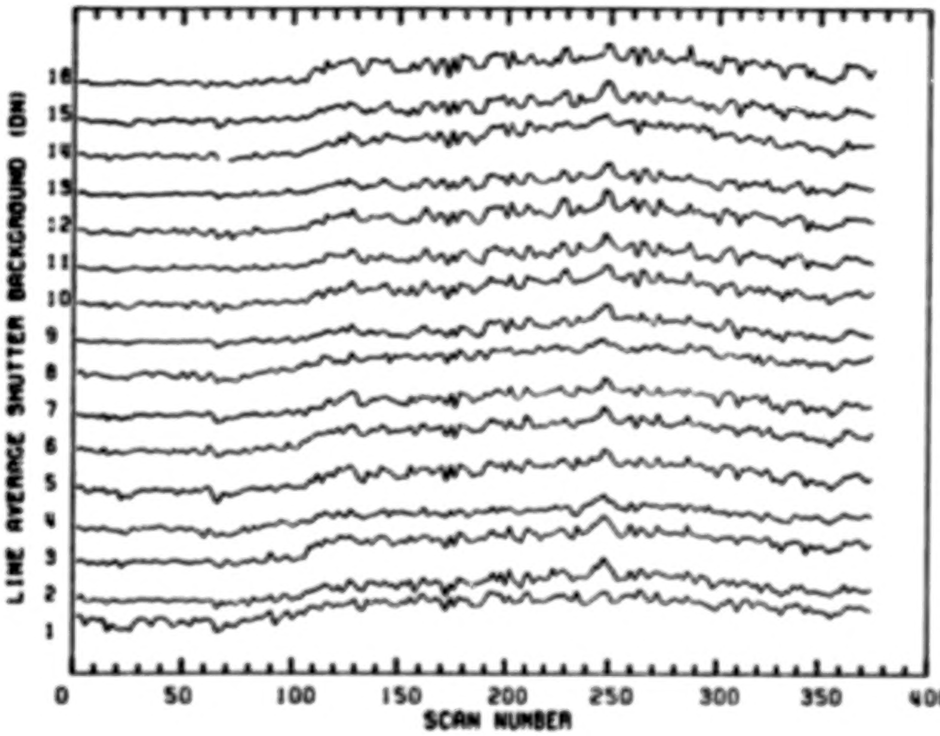

1000*CV	SHIFT1	SHIFT2
174	0.12	-0.03
158	0.06	-0.02
189	-0.01	-0.03
190	0.04	-0.01
186	0.05	-0.02
141	0.07	-0.02
171	0.01	-0.03
153	0.00	-0.01
180	-0.01	-0.05
188	0.01	-0.02
178	0.01	-0.02
187	0.02	-0.02
156	-0.01	-0.04
182	0.01	-0.02
170	-0.00	-0.06
129	0.10	-0.02

LEE/BARKER
8-MAR-84

SCENE ID=40392-18152, BAND 4 (REVERSE)
SHUTTER BACKGROUND 1 SPECTRA AFTER CORRECTION

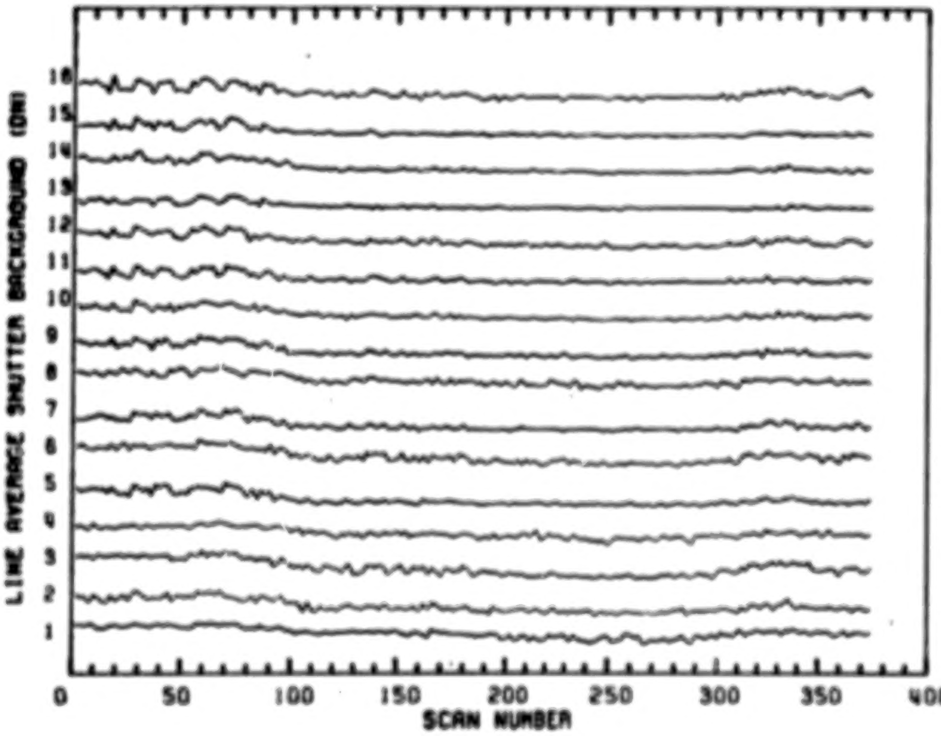

1000*CV	SHIFT1	SHIFT2
106	0.18	-0.02
90	0.05	-0.01
108	0.02	-0.02
88	0.03	-0.00
107	0.08	-0.01
81	0.08	-0.01
99	0.05	-0.02
115	0.04	-0.01
80	0.01	-0.08
109	0.06	-0.01
121	0.12	-0.04
122	0.07	-0.01
91	0.01	-0.07
140	0.12	-0.02
118	0.05	-0.07
79	0.25	-0.02

LEE/BARKER
8-MAR-84

Appendix 9.9.8

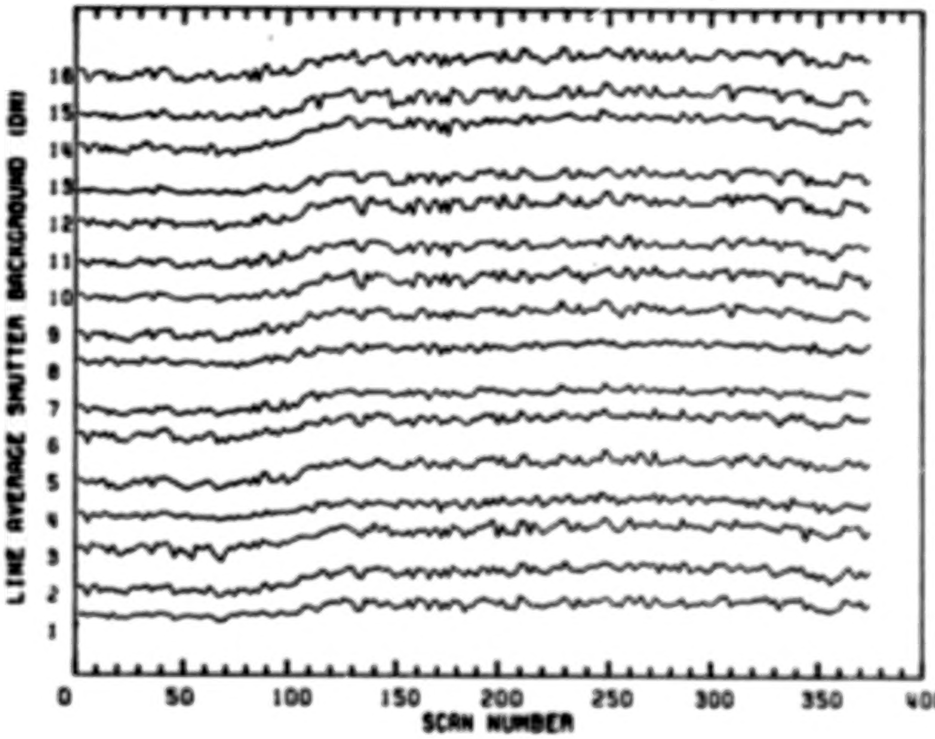
SCENE ID=40392-18152, BAND 4 (FORWARD)
SHUTTER BACKGROUND 2 SPECTRA AFTER CORRECTION

1000*CV	SHIFT B1/C4	SHIFT B7/C7
141	0.29	-0.03
180	0.12	-0.01
174	-0.00	-0.04
135	0.09	-0.01
151	0.13	-0.01
140	0.10	-0.02
149	0.05	-0.03
156	0.03	-0.01
107	-0.01	-0.06
136	0.03	-0.01
121	0.03	-0.04
148	0.07	-0.02
108	-0.01	-0.10
132	0.08	-0.02
134	0.01	-0.08
87	0.17	-0.02

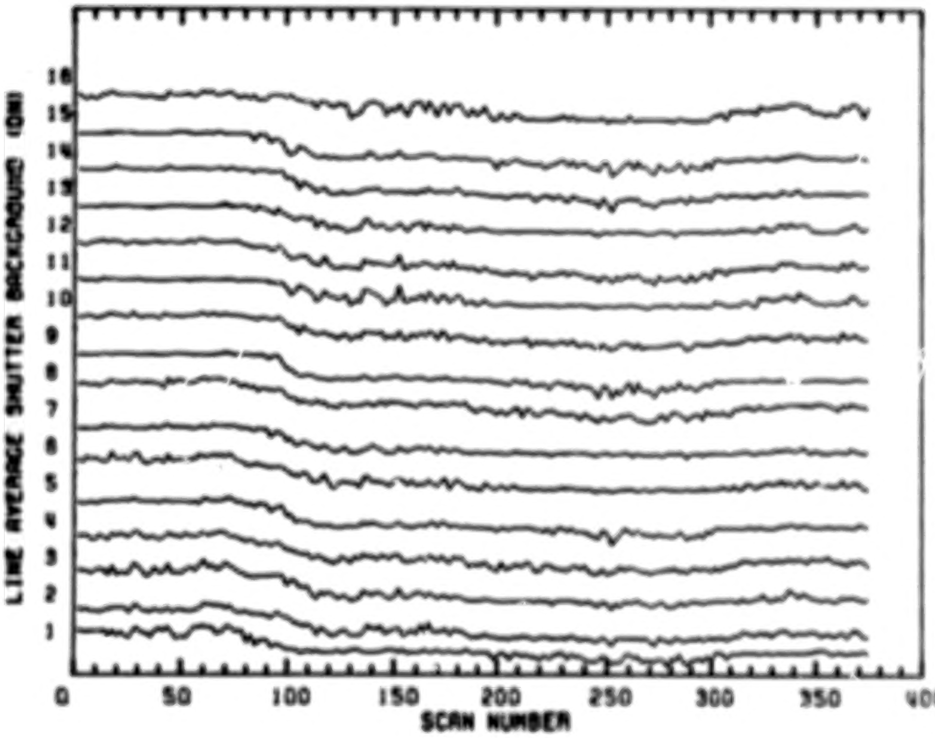
SCENE ID=40392-18152, BAND 4 (REVERSE)
SHUTTER BACKGROUND 2 SPECTRA AFTER CORRECTION

1000*CV	SHIFT B1/C4	SHIFT B7/C7
250	0.17	-0.02
426	0.07	-0.01
388	0.03	-0.02
308	0.03	-0.01
421	0.06	-0.02
286	0.04	-0.01
328	0.04	-0.03
429	0.03	-0.01
323	0.01	-0.04
330	0.02	-0.01
338	0.01	-0.02
402	0.04	-0.01
394	0.02	-0.04
383	0.03	-0.02
340	0.02	-0.03
188	0.10	-0.01

Appendix 9.9.9

SCENE ID=40392-18152, BAND 5 (FORWARD)
SHUTTER BACKGROUND 1 SPECTRA AFTER CORRECTION

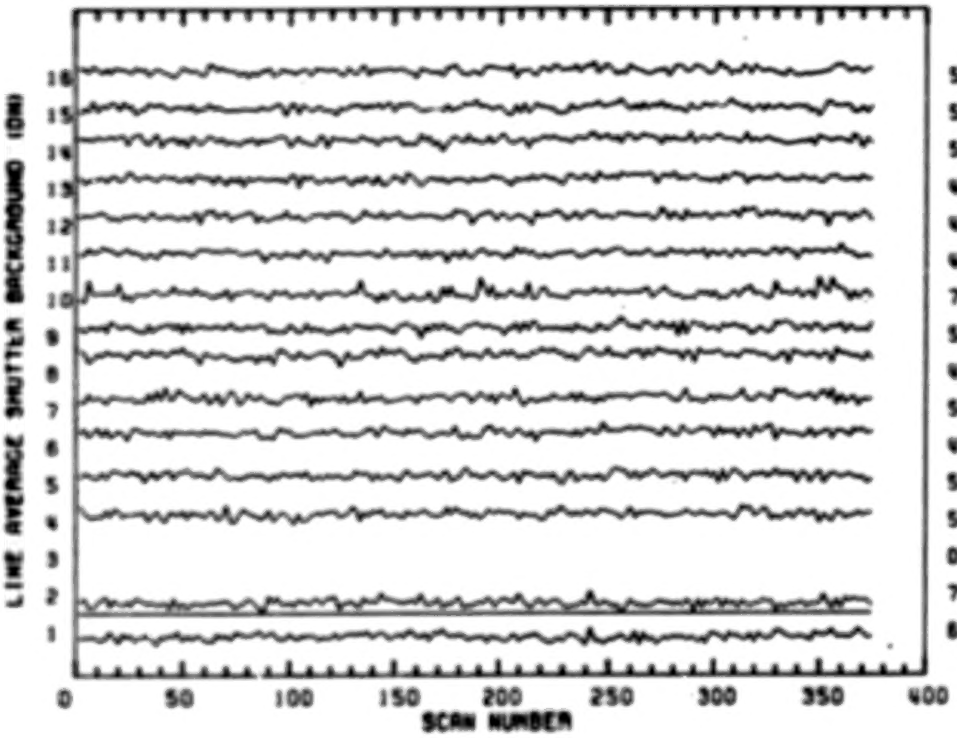

1000*CV	SHIFT1	SHIFT2
52	0.01	-0.07
54	-0.18	-0.01
50	-0.03	-0.08
48	-0.06	0.04
48	0.05	-0.00
46	-0.04	0.03
74	-0.04	0.52
53	-0.05	0.08
49	-0.02	-0.19
56	-0.01	0.10
45	0.03	-0.09
53	-0.13	0.02
56	0.06	-0.07
0	0.00	0.00
75	0.07	-0.09
63	0.00	0.07

LEE/BARKER
8-MAR-84

SCENE ID=40392-18152, BAND 5 (REVERSE)
SHUTTER BACKGROUND 1 SPECTRA AFTER CORRECTION

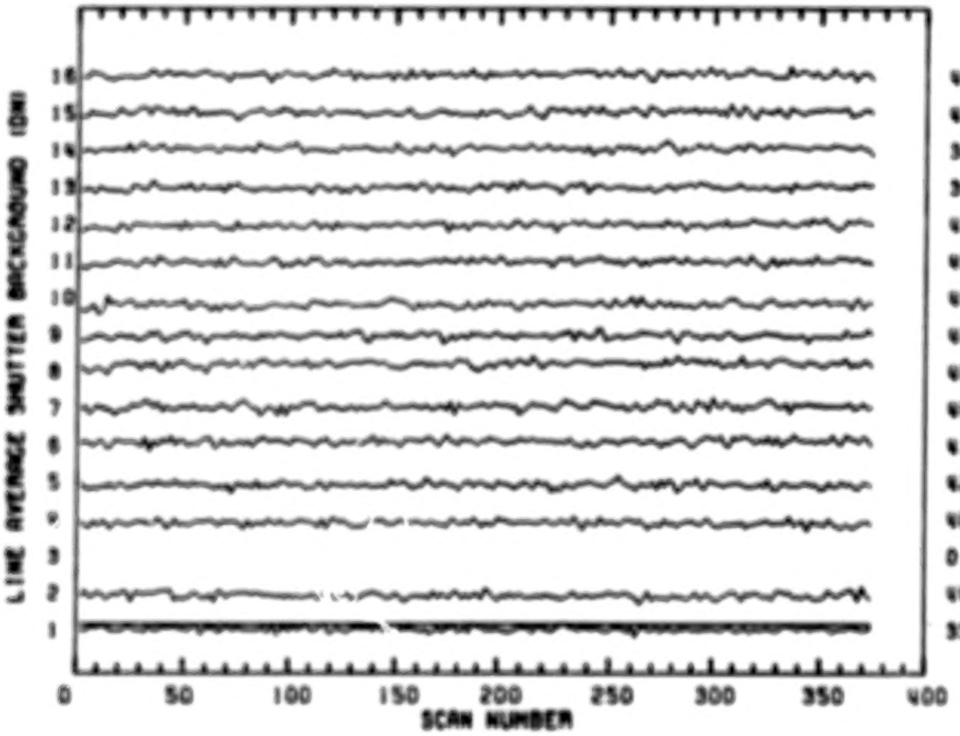

1000*CV	SHIFT1	SHIFT2
40	-0.00	-0.09
42	-0.12	-0.01
38	-0.03	-0.08
39	-0.04	0.02
42	0.04	0.01
40	-0.04	0.04
48	-0.02	0.58
40	-0.04	0.05
40	-0.01	-0.22
48	-0.02	0.10
41	0.02	-0.06
42	-0.12	0.02
40	0.10	-0.06
0	0.00	0.00
44	0.07	-0.08
33	-0.02	0.08

LEE/BARKER
8-MAR-84

Appendix 9.9.10

SCENE ID=40392-18152, BAND 5 (FORWARD)
SHUTTER BACKGROUND 2 SPECTRA AFTER CORRECTION

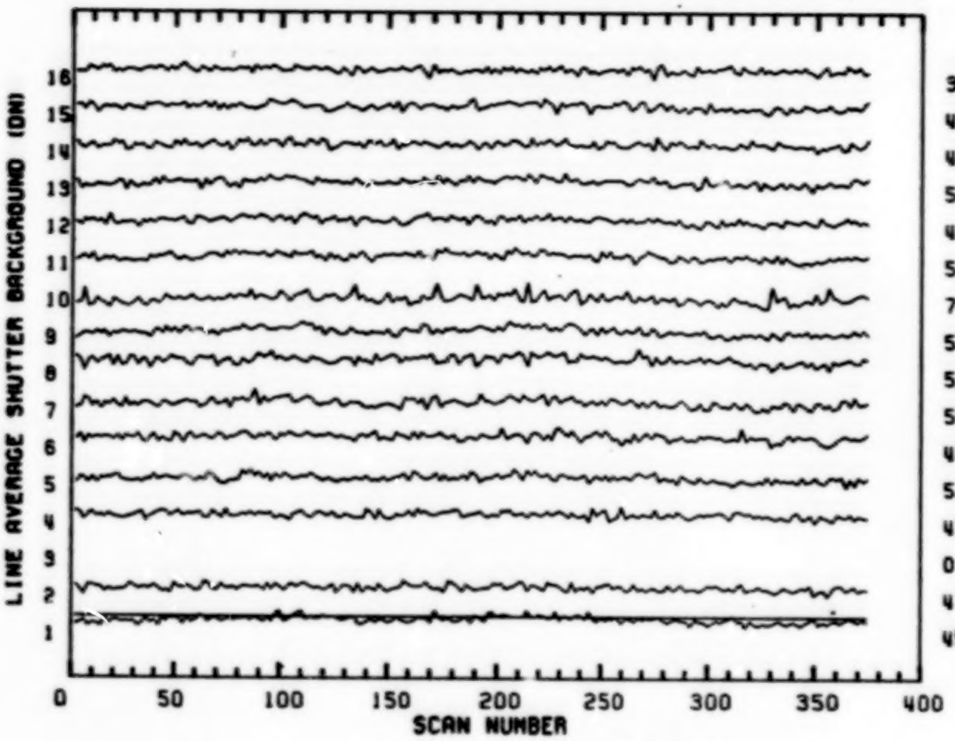

1000×CV	SHIFT B1/C4	SHIFT B7/C7
39	0.01	-0.10
46	-0.13	-0.02
44	-0.02	-0.06
50	-0.03	0.04
45	0.04	0.01
53	-0.01	0.04
78	-0.03	0.52
57	-0.02	0.05
52	-0.01	-0.17
56	0.00	0.10
46	0.03	-0.09
51	-0.11	0.01
43	0.07	-0.05
0	0.00	0.00
41	0.10	-0.10
45	-0.01	0.05

LEE/BARKER
6-MAR-84

SCENE ID=40392-18152, BAND 5 (REVERSE)
SHUTTER BACKGROUND 2 SPECTRA AFTER CORRECTION

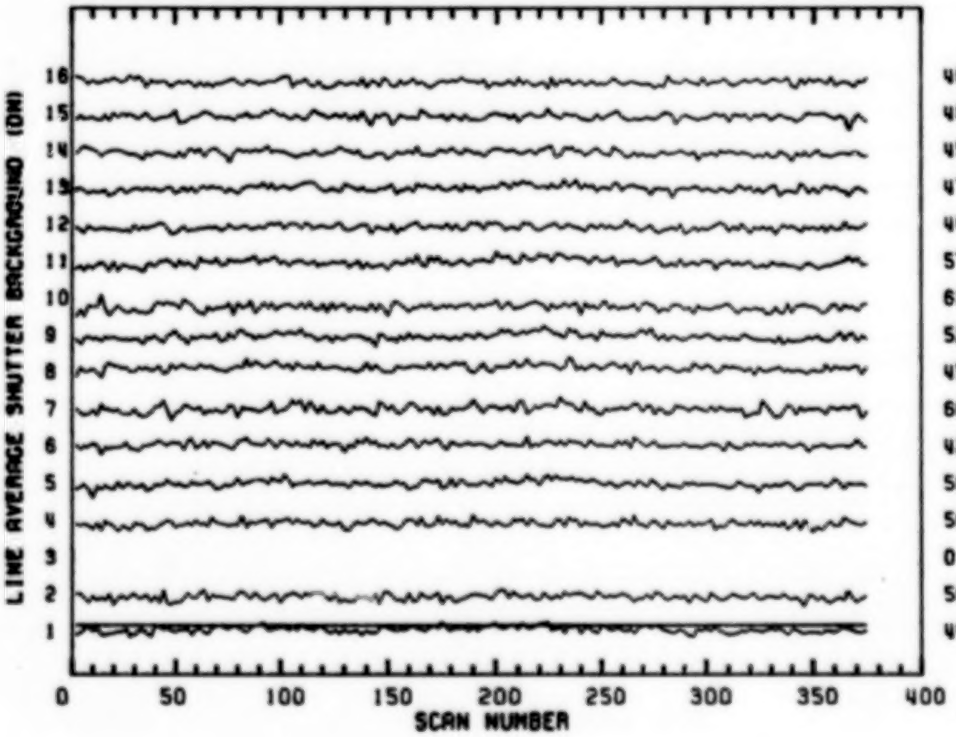

1000×CV	SHIFT B1/C4	SHIFT B7/C7
46	0.01	-0.06
48	-0.15	-0.04
45	-0.02	-0.04
47	-0.08	-0.00
44	0.02	0.01
57	-0.04	0.02
62	-0.04	0.60
52	-0.04	0.00
45	-0.05	-0.13
60	-0.03	0.11
42	0.02	-0.08
50	-0.13	-0.01
50	0.10	-0.04
0	0.00	0.00
50	0.07	-0.08
44	-0.02	0.04

LEE/BARKER
6-MAR-84

C-3

Appendix 9.9.11

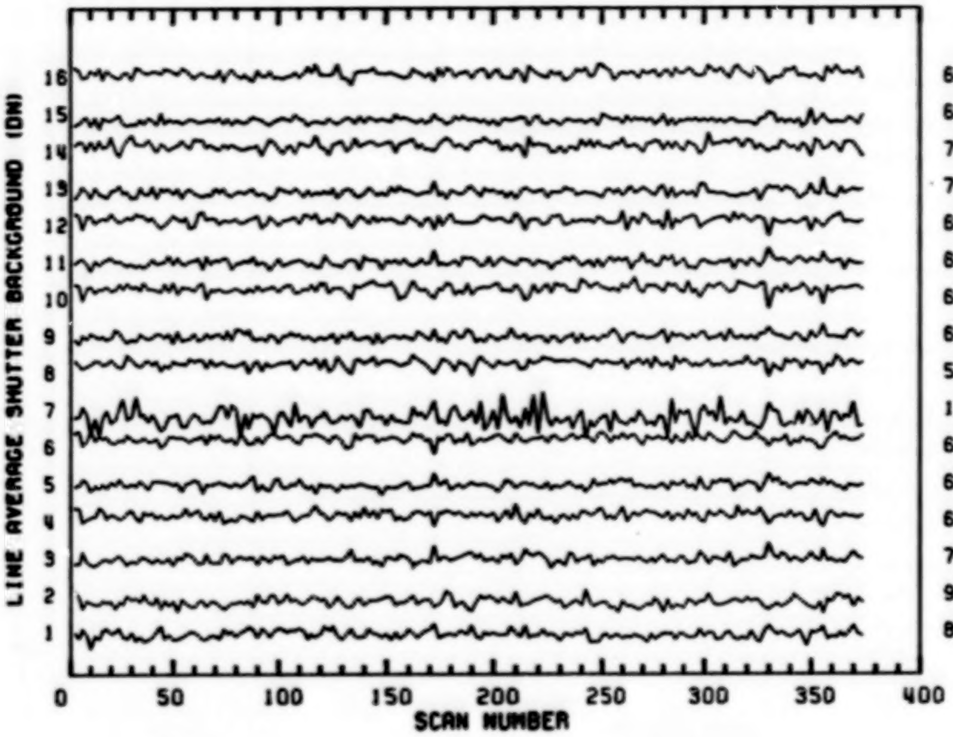

SCENE ID=40392-18152, BAND 7 (FORWARD)
SHUTTER BACKGROUND 1 SPECTRA AFTER CORRECTION

	1000*CV	SHIFT1	SHIFT2
16	68	0.08	-0.23
15	62	-0.03	0.18
14	72	0.10	-0.12
13	71	-0.03	0.26
12	68	0.07	-0.22
11	65	-0.02	0.23
10	67	0.04	-0.39
9	65	-0.06	0.17
8	59	0.03	-0.27
7	178	-0.02	1.09
6	60	0.06	-0.29
5	65	-0.01	0.23
4	67	0.04	-0.25
3	71	-0.05	0.28
2	91	0.04	-0.24
1	80	-0.00	0.25

LEE/BARKER
6-MAR-84

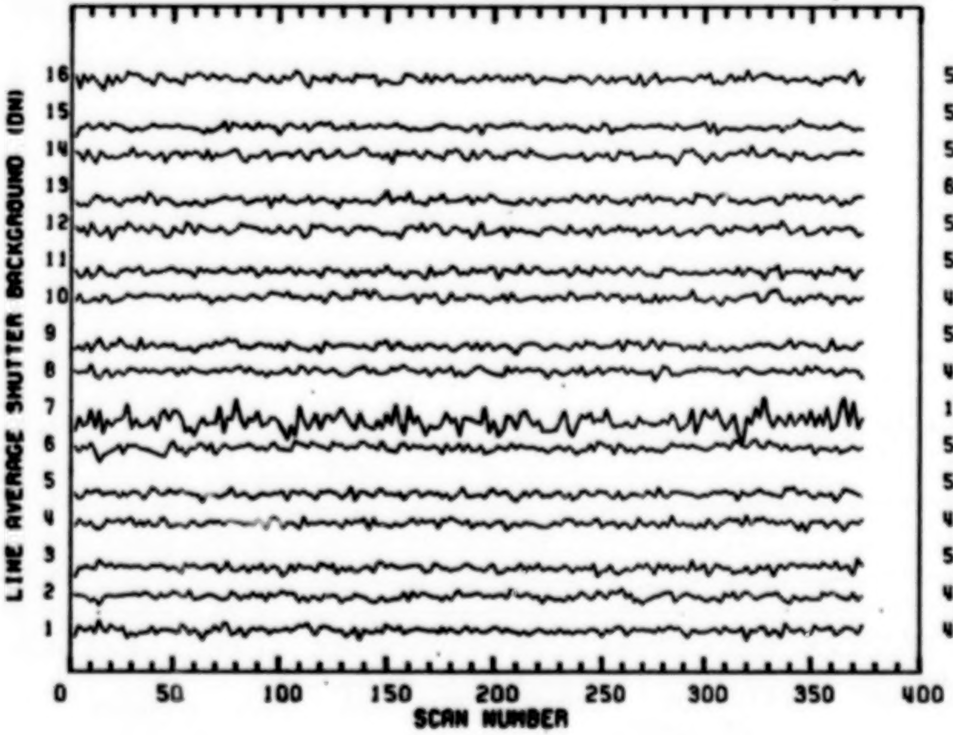

SCENE ID=40392-18152, BAND 7 (REVERSE)
SHUTTER BACKGROUND 1 SPECTRA AFTER CORRECTION

	1000*CV	SHIFT1	SHIFT2
16	55	0.09	-0.19
15	51	-0.03	0.19
14	55	0.12	-0.08
13	61	-0.05	0.16
12	57	0.08	-0.21
11	53	-0.03	0.27
10	46	0.03	-0.42
9	55	-0.05	0.18
8	44	0.04	-0.33
7	154	-0.05	0.92
6	54	0.06	-0.25
5	54	-0.01	0.23
4	49	0.05	-0.26
3	57	-0.03	0.31
2	48	0.03	-0.32
1	47	-0.02	0.28

LEE/BARKER
6-MAR-84

Appendix 9.9.12

SCENE ID=40392-18152, BAND 7 (FORWARD)
SHUTTER BACKGROUND 2 SPECTRA AFTER CORRECTION

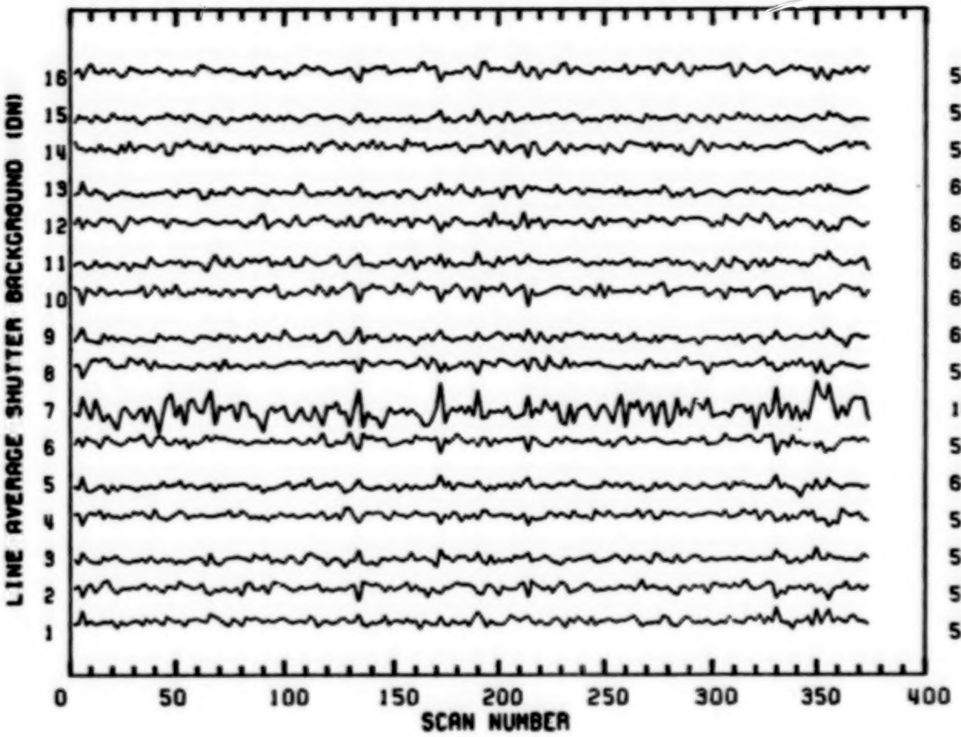

	1000×CV	SHIFT B1/C4	SHIFT B7/C7
16	54	0.11	-0.19
15	51	-0.04	0.16
14	57	0.13	-0.08
13	60	-0.04	0.20
12	62	0.09	-0.21
11	63	-0.03	0.21
10	62	0.07	-0.38
9	61	-0.06	0.21
8	54	0.04	-0.27
7	169	-0.09	0.84
6	59	0.07	-0.25
5	60	-0.02	0.24
4	53	0.06	-0.23
3	58	-0.04	0.34
2	58	0.03	-0.24
1	52	-0.02	0.30

LEE/BARKER
6-MAR-84

SCENE ID=40392-18152, BAND 7 (REVERSE)
SHUTTER BACKGROUND 2 SPECTRA AFTER CORRECTION

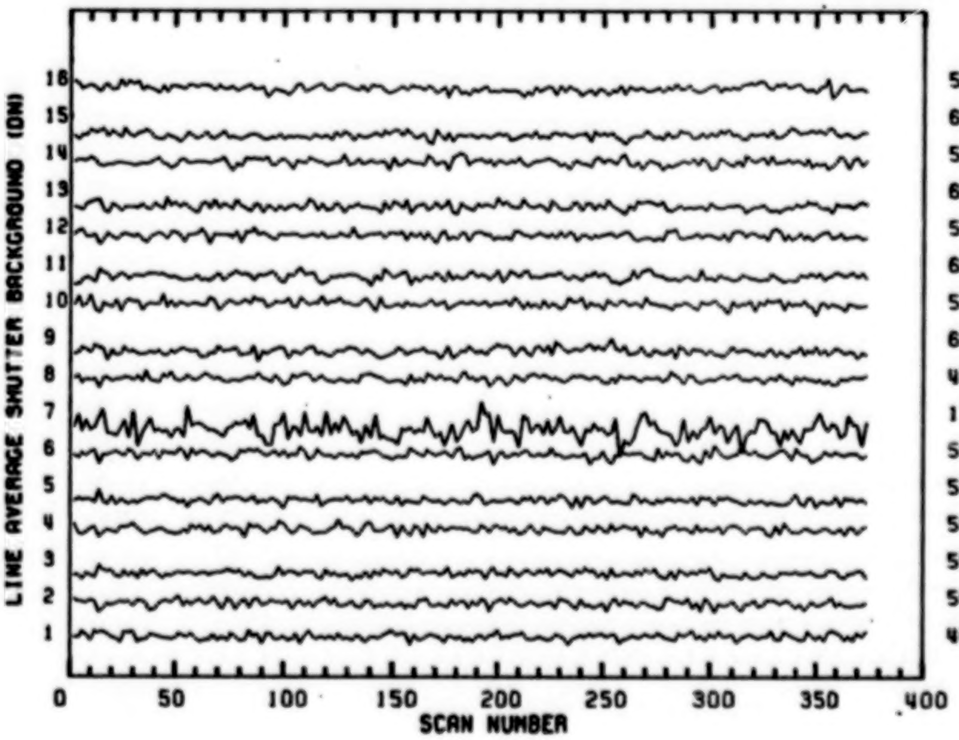

	1000×CV	SHIFT B1/C4	SHIFT B7/C7
16	57	0.09	-0.19
15	64	-0.02	0.12
14	56	0.14	-0.05
13	64	-0.06	0.17
12	53	0.09	-0.23
11	62	-0.04	0.17
10	53	0.06	-0.41
9	66	-0.06	0.10
8	45	0.02	-0.29
7	176	-0.07	0.76
6	56	0.06	-0.28
5	53	-0.02	0.23
4	54	0.04	-0.25
3	55	-0.05	0.32
2	54	0.02	-0.26
1	46	-0.03	0.25

LEE/BARKER
6-MAR-84

APPENDIX 9.10 - TM/F PLOTS OF "SHIFTED" BACKGROUND VERSUS SCAN

Landsat-5 TM/F averaged shutter backgrounds before DC restoration are plotted versus scan number for illustrative forward scans before and after being corrected (Section 4.5) for scan-correlated shifts of type 5-3 (Landsat-5 Band 3, Channel 1) for in-orbit data (NASA ID 50005-16221) and prelaunch data (5-596-13285). These plots are included as follows:

9.10.1 50005-16221 Band 1
9.10.2 50005-16221 Band 2
9.10.3 50005-16221 Band 3
9.10.4 50005-16221 Band 4
9.10.5 50005-16221 Band 5
9.10.6 5-596-13285 Band 5
9.10.7 5-596-13285 Band 7
9.10.8 5-596-13285 Band 6 (FWD/REV).

Appendix 9.10.1

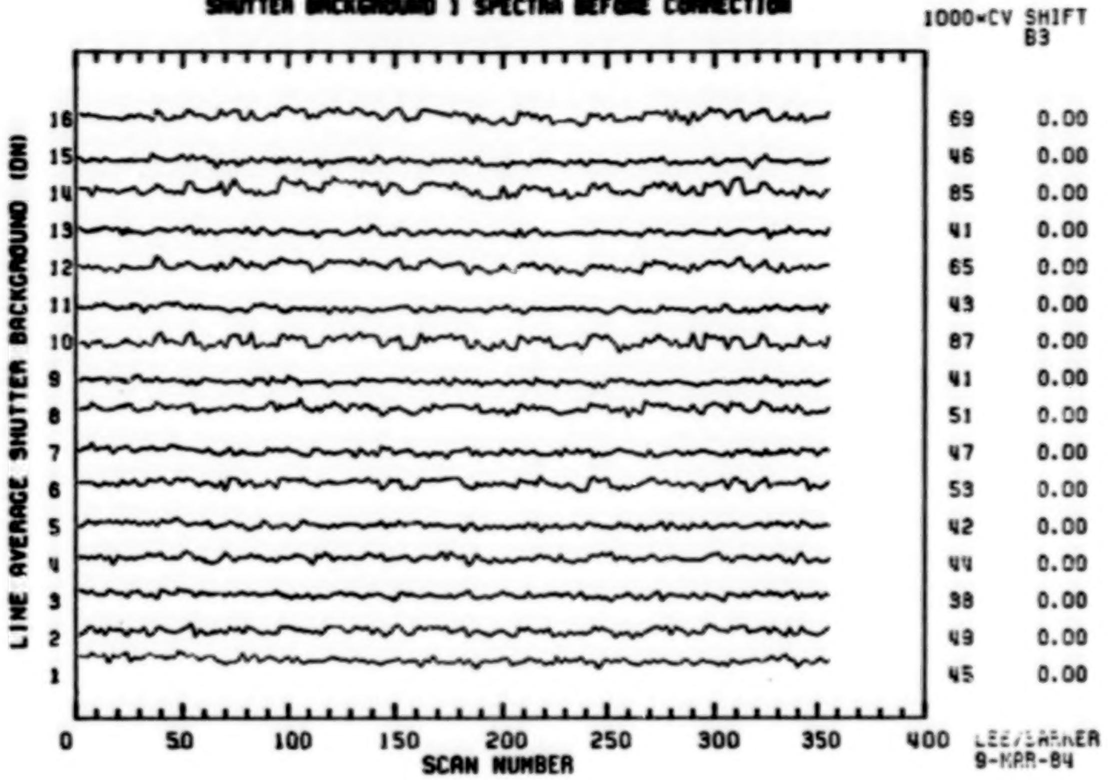

SCENE ID=50005-16221, BAND 1 (FORWARD)
SHUTTER BACKGROUND 1 SPECTRA BEFORE CORRECTION

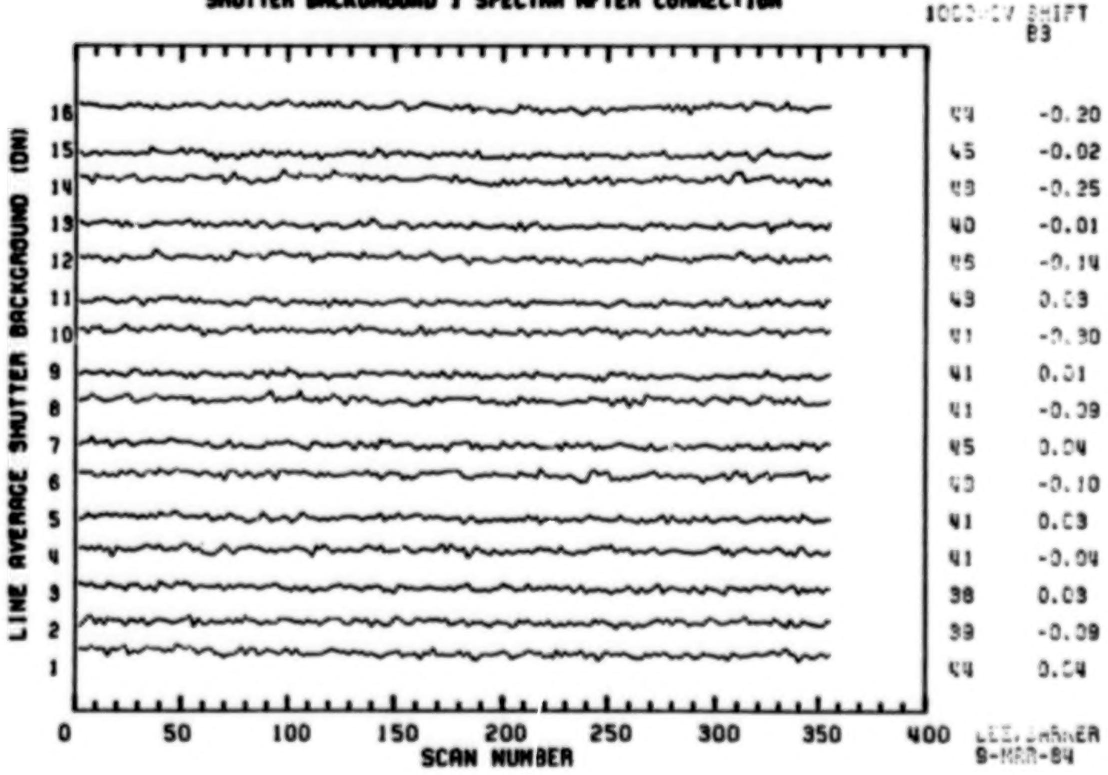

SCENE ID=50005-16221, BAND 1 (FORWARD)
SHUTTER BACKGROUND 1 SPECTRA AFTER CORRECTION

Appendix 9.10.2

SCENE ID=50005-16221, BAND 2 (FORWARD)
SHUTTER BACKGROUND 1 SPECTRA BEFORE CORRECTION

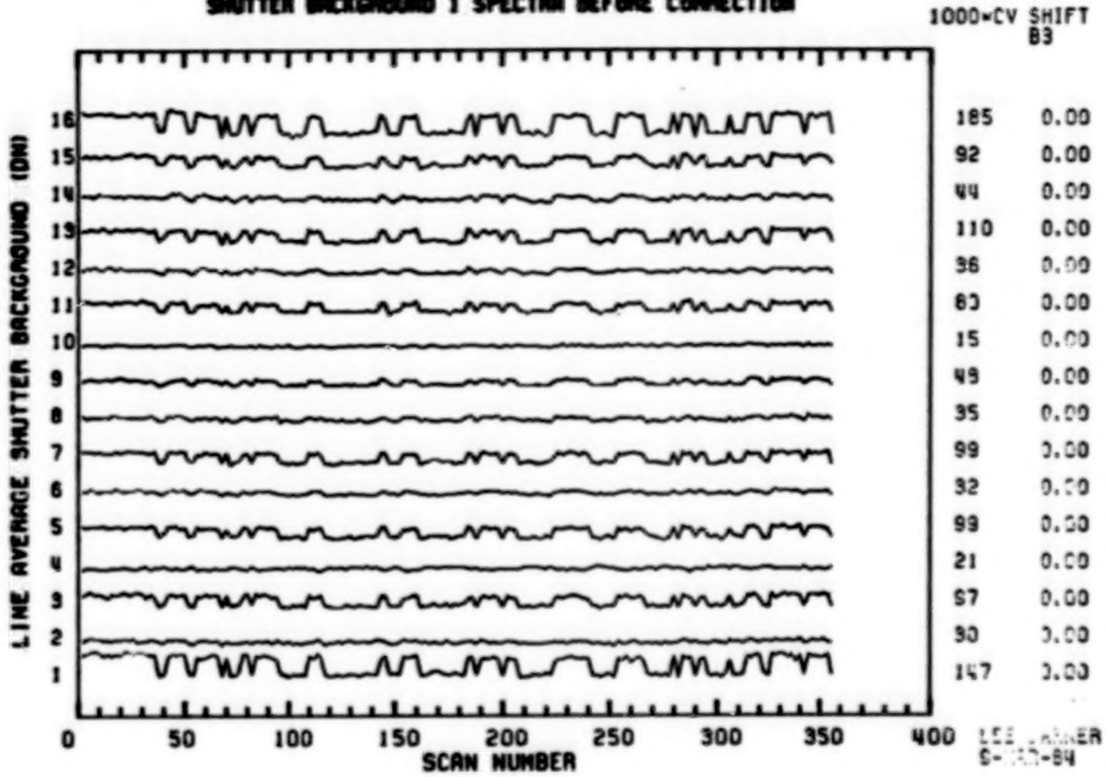

SCENE ID=50005-16221, BAND 2 (FORWARD)
SHUTTER BACKGROUND 1 SPECTRA AFTER CORRECTION

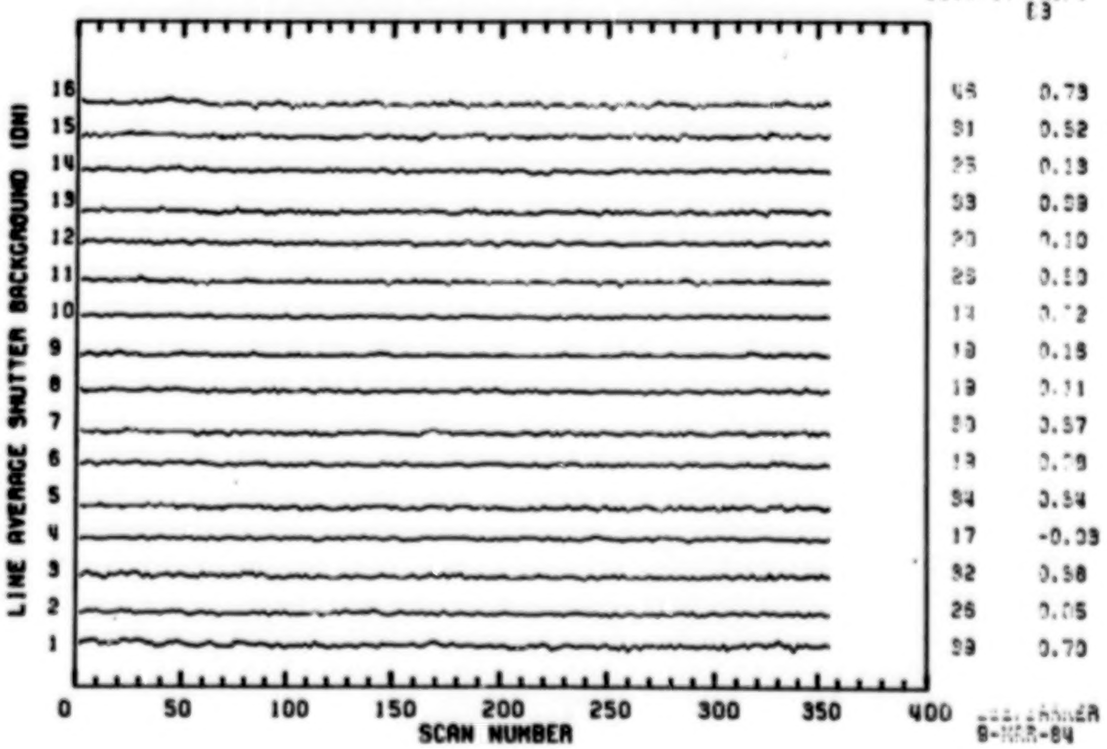

Appendix 9.10.3

SCENE ID=50005-16221, BAND 3 (FORWARD)
SHUTTER BACKGROUND 1 SPECTRA BEFORE CORRECTION

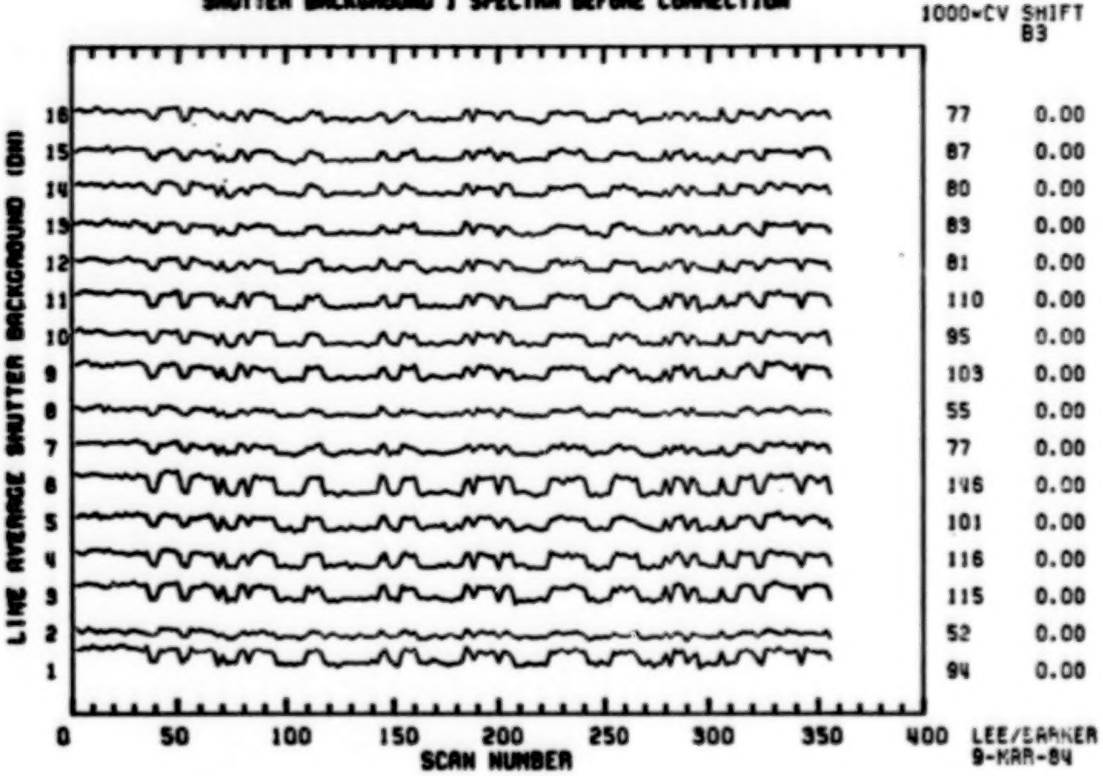

SCENE ID=50005-16221, BAND 3 (FORWARD)
SHUTTER BACKGROUND 1 SPECTRA AFTER CORRECTION

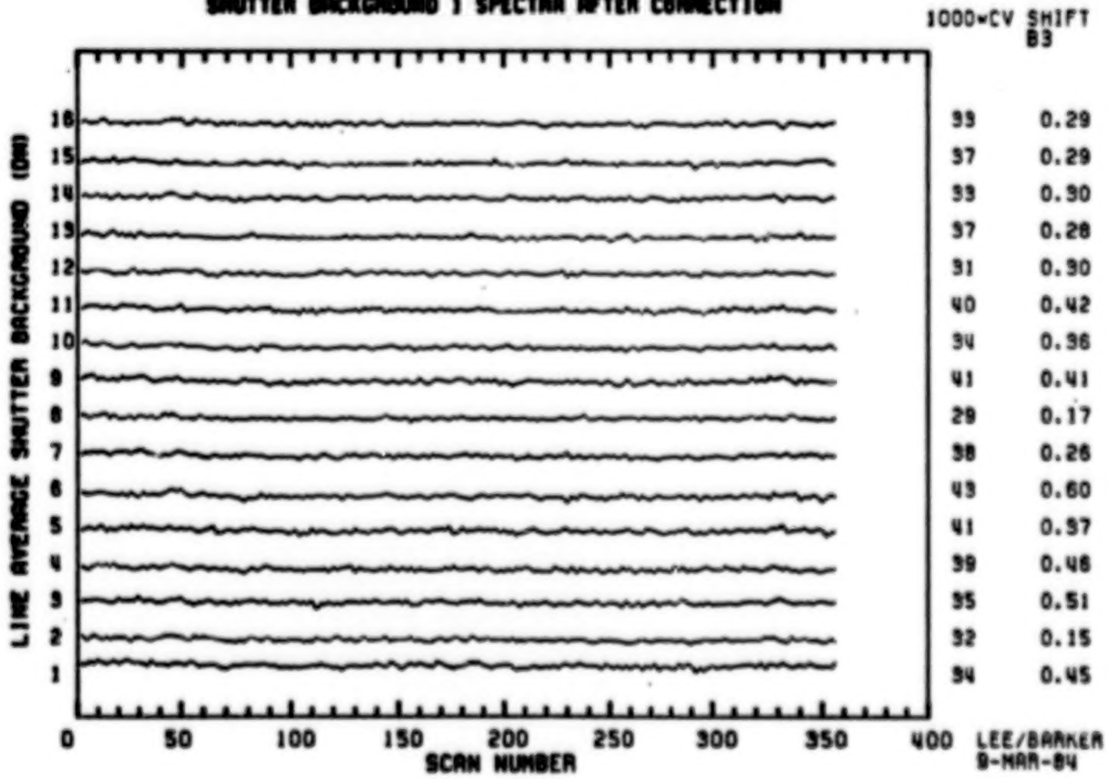

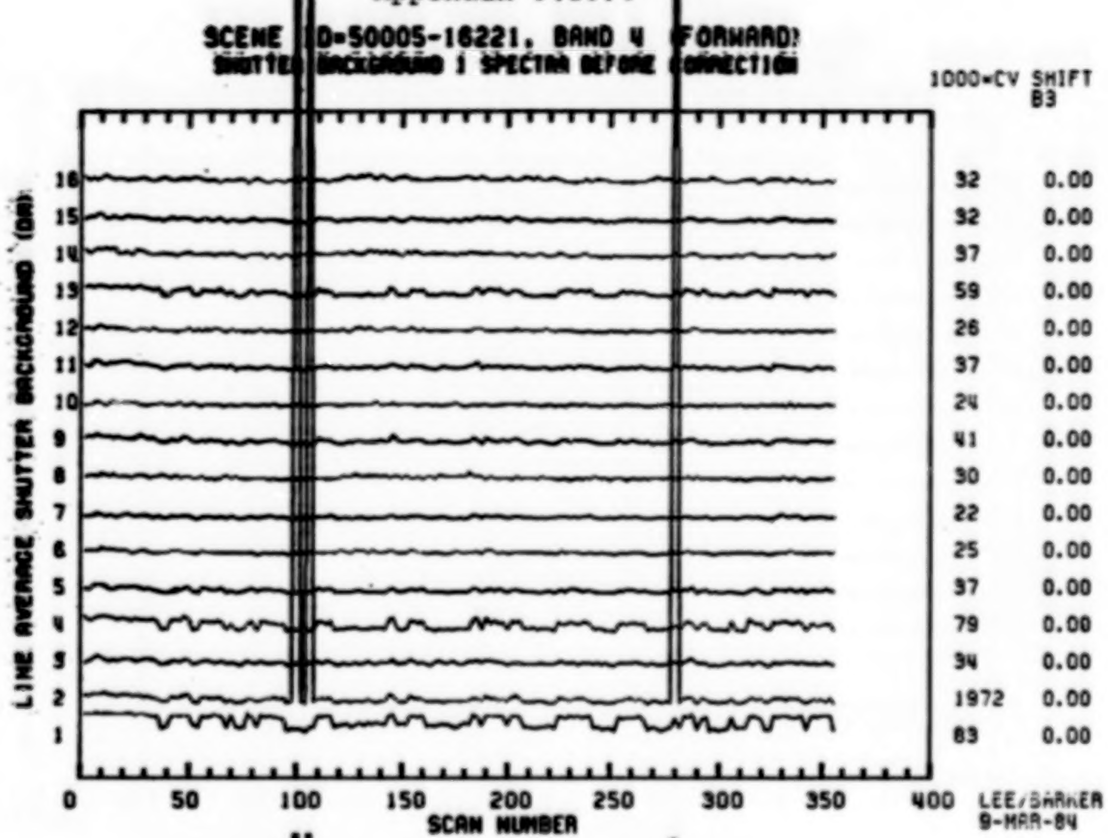

SCENE ID=50005-16221, BAND 4 (FORWARD)
SHUTTER BACKGROUND 1 SPECTRA BEFORE CORRECTION

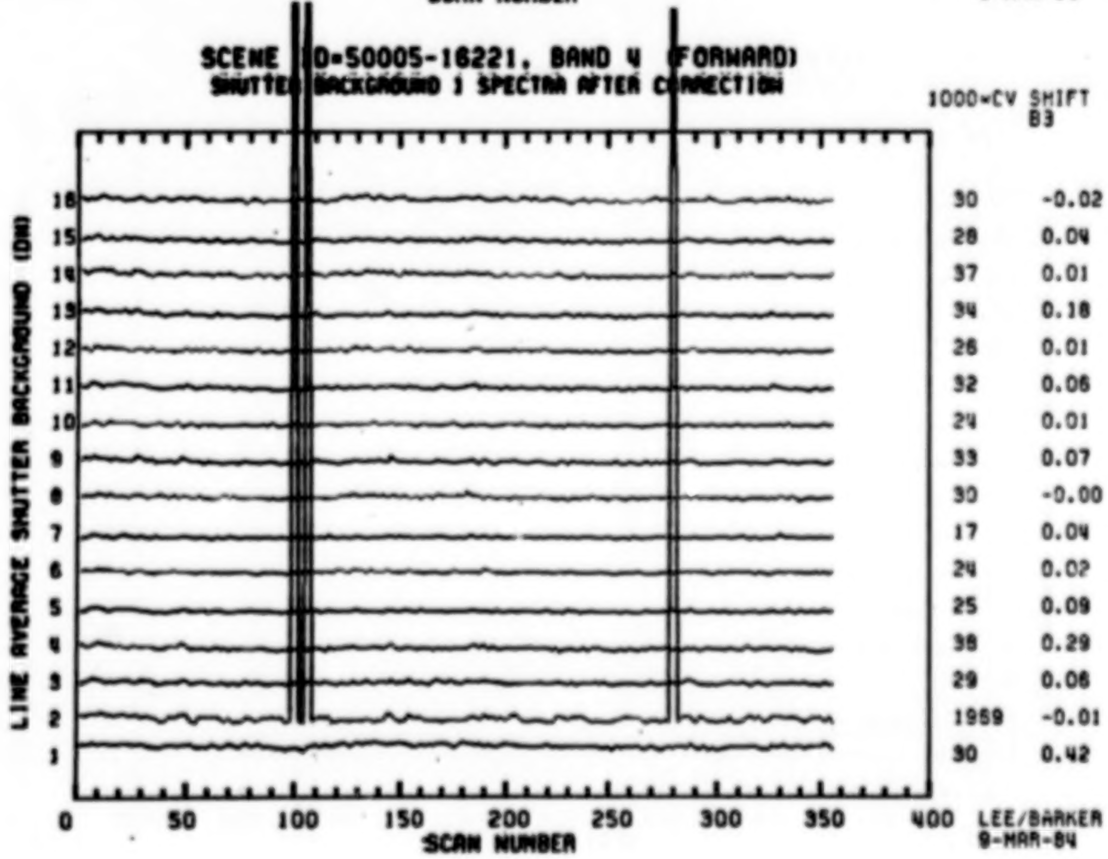

SCENE ID=50005-16221, BAND 4 (FORWARD)
SHUTTER BACKGROUND 1 SPECTRA AFTER CORRECTION

Appendix 9.10.5

SCENE ID=50005-16221, BAND 5 (FORWARD)
SHUTTER BACKGROUND 1 SPECTRA BEFORE CORRECTION

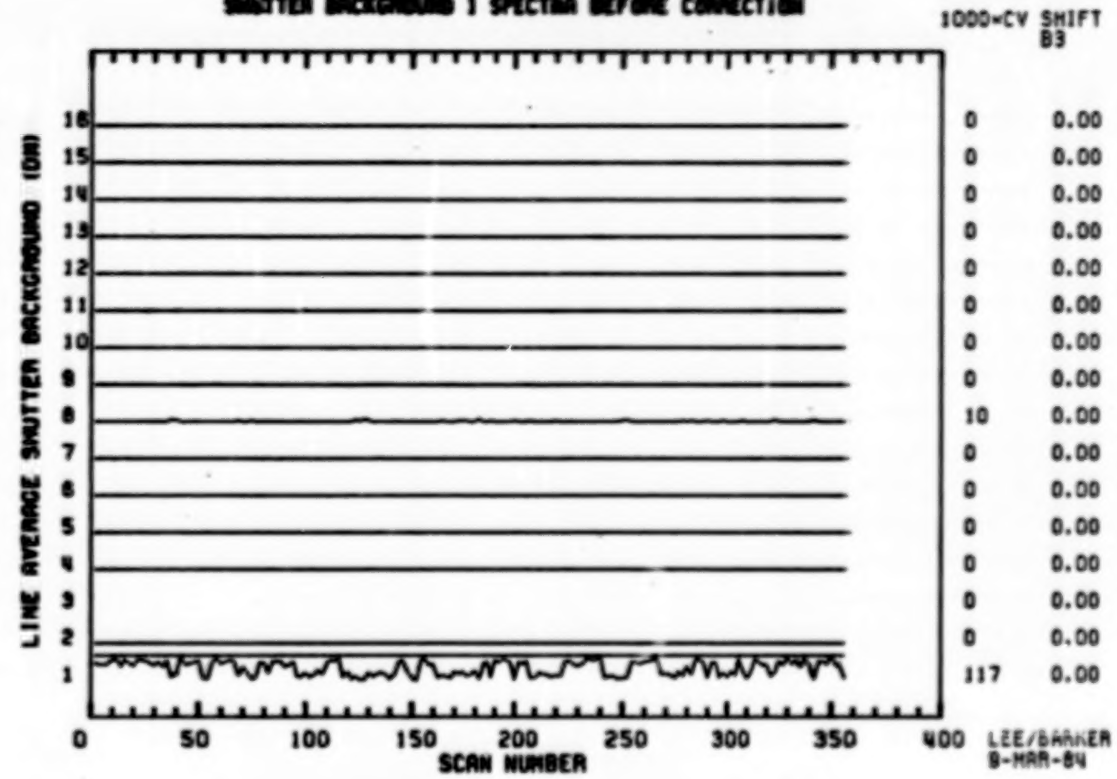

SCENE ID=50005-16221, BAND 5 (FORWARD)
SHUTTER BACKGROUND 1 SPECTRA AFTER CORRECTION

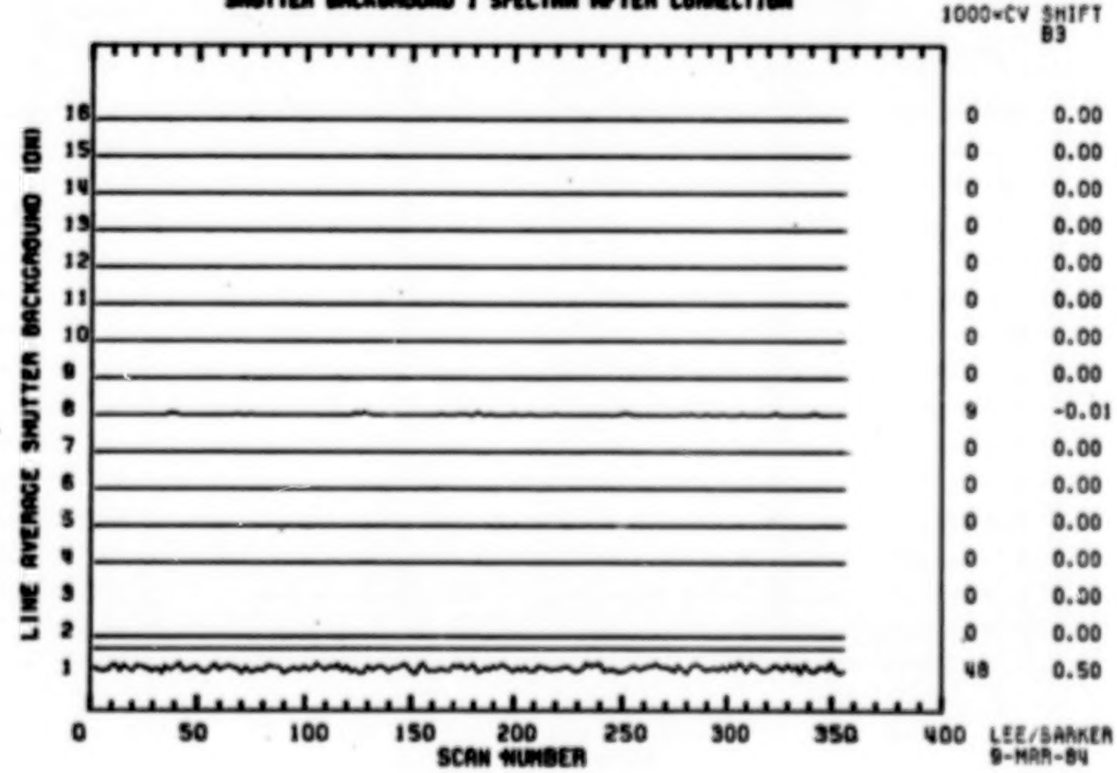

Appendix 9.10.6

SCENE ID=5-596-13205, BAND 5 (FORWARD)
SHUTTER BACKGROUND 1 SPECTRA BEFORE CORRECTION

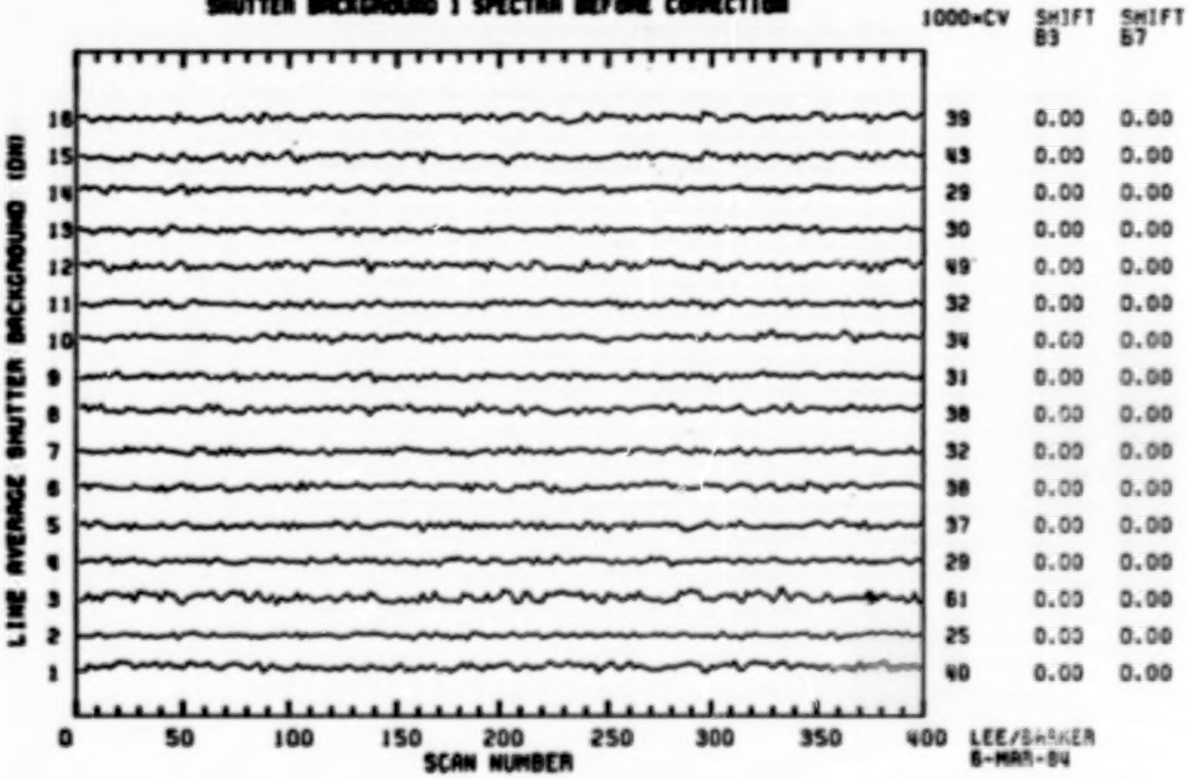

SCENE ID=5-596-13205, BAND 5 (FORWARD)
SHUTTER BACKGROUND 1 SPECTRA AFTER CORRECTION

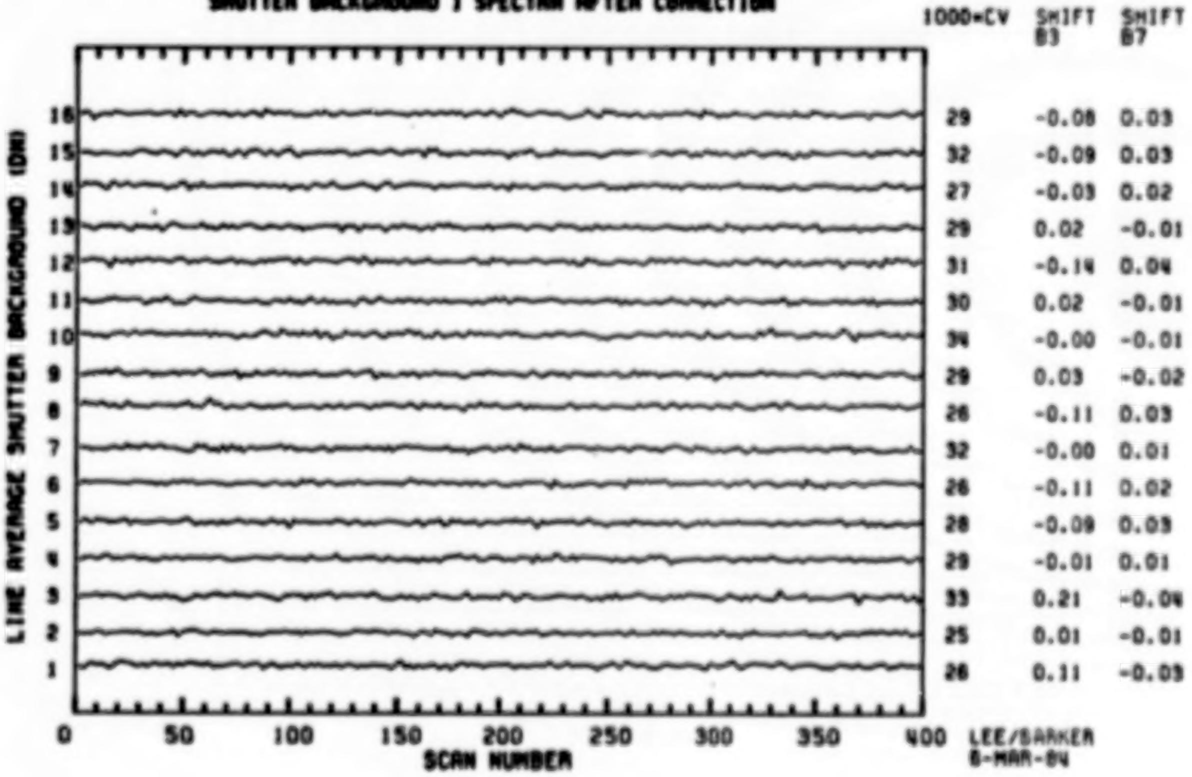

Appendix 9.10.7

SCENE ID=5-596-13205, BAND 7 (FORWARD)
SHUTTER BACKGROUND 1 SPECTRA BEFORE CORRECTION

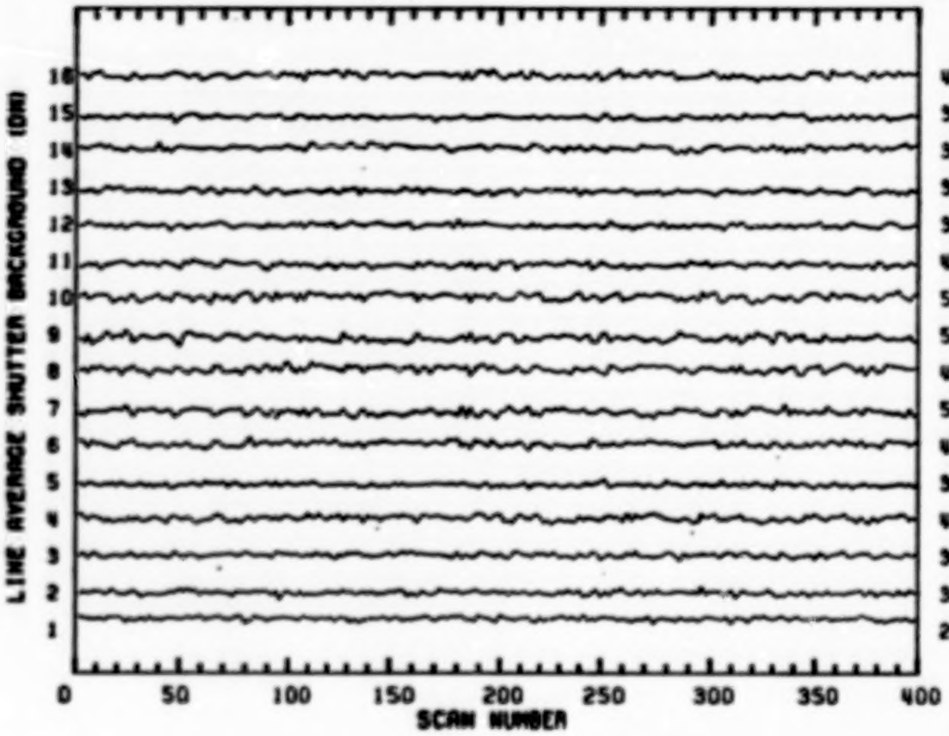

1000*CV	SHIFT B3	SHIFT B7
43	0.00	0.00
31	0.00	0.00
35	0.00	0.00
38	0.00	0.00
34	0.00	0.00
40	0.00	0.00
50	0.00	0.00
54	0.00	0.00
47	0.00	0.00
53	0.00	0.00
40	0.00	0.00
31	0.00	0.00
44	0.00	0.00
31	0.00	0.00
30	0.00	0.00
25	0.00	0.00

LEE/BARKER
6-MAR-84

SCENE ID=5-596-13205, BAND 7 (FORWARD)
SHUTTER BACKGROUND 1 SPECTRA AFTER CORRECTION

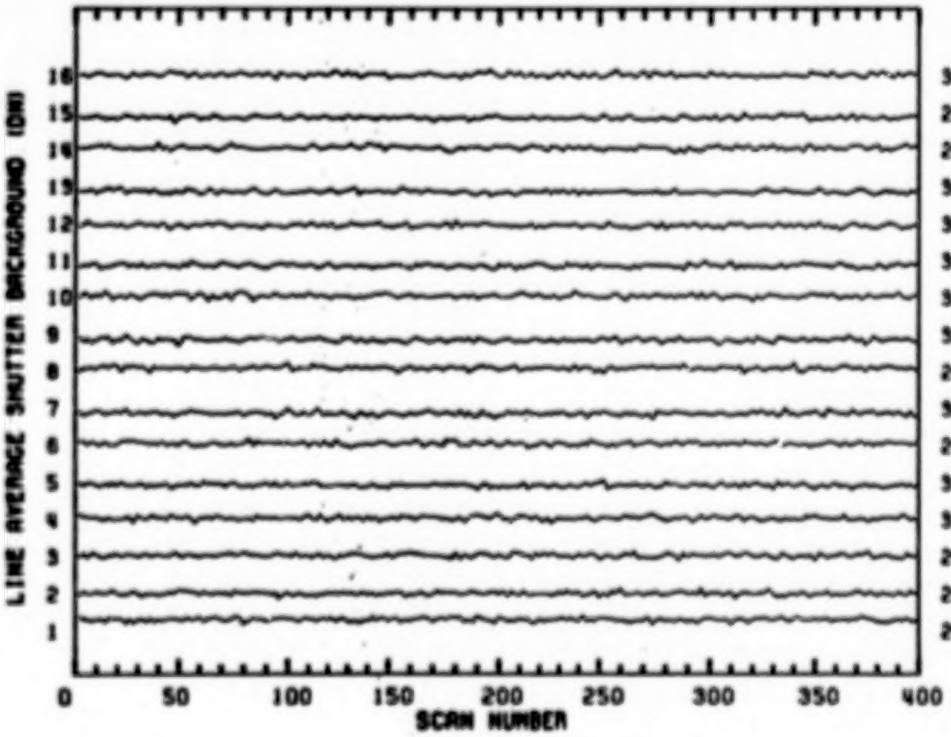

1000*CV	SHIFT B3	SHIFT B7
31	-0.10	0.04
29	0.03	-0.00
29	-0.05	0.04
31	0.06	-0.00
30	-0.04	0.04
31	0.10	-0.02
32	-0.12	0.05
35	0.18	-0.02
29	-0.14	0.04
38	0.13	-0.03
28	-0.10	0.04
31	0.00	0.01
31	-0.09	0.05
29	-0.03	0.02
29	-0.02	0.02
24	0.02	0.01

LEE/BARKER
6-MAR-84

Appendix 9.10.8

SCENE ID=5-596-13285, BAND 6 (FORWARD)
SHUTTER BACKGROUND 1 SPECTRA BEFORE CORRECTION

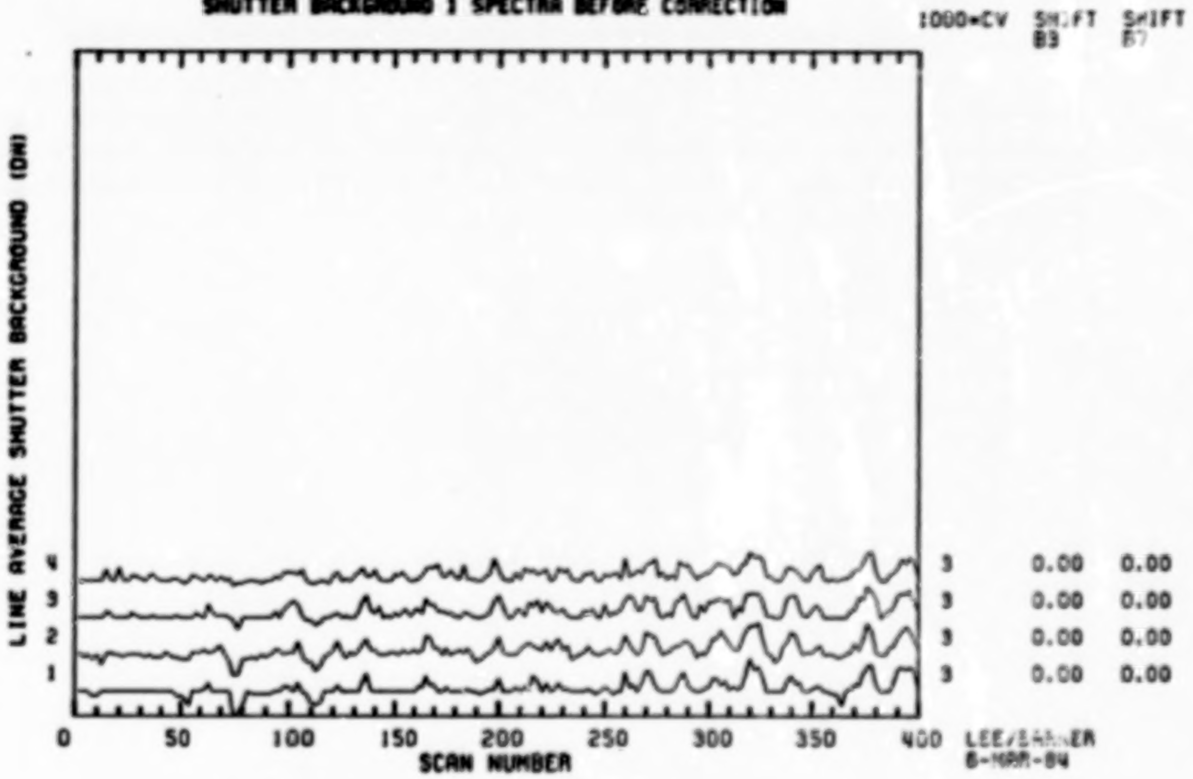

SCENE ID=5-596-13285, BAND 6 (REVERSE)
SHUTTER BACKGROUND 1 SPECTRA BEFORE CORRECTION

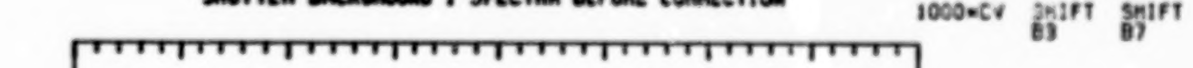

APPENDIX 9.11 - TM/F TABLES OF SCAN-CORRELATED SHIFTS

Landsat-5 TM/F within-scene tabulations (Section 4.5) of scan-correlated shifts by forward and reverse scans for type 5-3 (Landsat-5 Band 3, Channel 1) in Shutter regions before (shutter 1) and after (shutter 2) DC restoration for in-orbit data (NASA ID 50005-16221) and pre-launch tests (5-596-13285 and "golden tape" 5-198-10563) are included in this Appendix as follows:

9.11.1 TM/F Band 1 Shift 5-3
9.11.2 TM/F Band 2 Shift 5-3
9.11.3 TM/F Band 3 Shift 5-3
9.11.4 TM/F Band 4 Shift 5-3
9.11.5 TM/F Band 5 Shift 5-3
9.11.6 TM/F Band 7 Shift 5-3.

Appendix 9.11.1

TYPE 5-3 SCAN-CORRELATED SHIFTS
BAND 1 LANDSAT-5 TM/F

	PRE-LAUNCH 5-596-13285		PRE-LAUNCH 5-198-10563				IN-ORBIT 50005-16221		
	SHUTTER 1		SHUTTER 1		SHUTTER 2		SHUTTER 1		
CH	FWD	REV	FWD	REV	FWD	REV	FWD	REV	CH
16	−.13	−.21	−.21	−.20	−.17	−.18	−.20	−.23	16
15	−.05	−.07	−.01	−.01	−.00	−.02	−.02	−.02	15
14	−.20	−.20	−.25	−.24	−.23	−.20	−.25	−.31	14
13	−.03	−.04	−.01	−.01	−.00	−.02	−.01	−.03	13
12	−.22	−.25	−.20	−.18	−.17	−.19	−.14	−.20	12
11	.01	.00	.00	−.01	.01	.01	.03	.02	11
10	−.16	−.19	−.25	−.25	−.23	−.19	−.30	−.34	10
9	−.00	−.01	.02	.03	.01	.04	.01	−.01	9
8	−.13	−.10	−.12	−.16	−.15	−.10	−.09	−.09	8
7	.04	.04	.08	.05	.11	.08	.04	.02	7
6	−.19	−.17	−.20	−.19	−.17	−.16	−.10	−.13	6
5	−.02	−.02	.01	.00	.01	.02	.03	−.01	5
4	−.12	−.09	−.09	−.10	−.12	−.12	−.04	−.10	4
3	−.14	−.01	.04	.04	.04	.02	.03	.00	3
2	−.14	−.16	−.13	−.13	−.13	−.17	−.09	−.15	2
1	−.04	−.03	.03	.01	.02	.00	.04	−.01	1

Appendix 9.11.2

TYPE 5-3 SCAN-CORRELATED SHIFTS BAND 2 LANDSAT-5 TM/F

	PRE-LAUNCH 5-596-13285		PRE-LAUNCH 5-198-10563				IN-ORBIT 50005-16221		
	SHUTTER 1		SHUTTER 1		SHUTTER 2		SHUTTER 1		
CH	FWD	REV	FWD	REV	FWD	REV	FWD	REV	CH
16	.15	.16	.23	.21	.22	.23	.73	.75	16
15	.07	.07	.12	.13	.16	.12	.32	.37	15
14	.06	.07	.05	.05	.07	.07	.13	.20	14
13	.07	.08	.14	.14	.15	.12	.39	.41	13
12	−.02	−.02	.01	.00	.00	−.00	.10	.15	12
11	.05	.04	.10	.07	.11	.07	.30	.34	11
10	.00	.00	.00	.00	.00	.00	.02	.03	10
9	.03	.02	.07	.05	.07	.05	.16	.21	9
8	.03	.03	.04	.02	.03	.02	.11	.15	8
7	.09	.09	.13	.15	.16	.15	.37	.37	7
6	.04	.02	.04	.03	.04	.03	.08	.14	6
5	.12	.13	.17	.22	.20	.22	.34	.35	5
4	−.01	−.01	−.00	−.00	−.00	−.00	−.03	−.04	4
3	.18	.16	.23	.19	.23	.20	.38	.42	3
2	.02	.06	.06	.09	.06	.05	.05	.03	2
1	.55	.50	.54	.48	.55	.52	.70	.73	1

Appendix 9.11.3

TYPE 5-3 SCAN-CORRELATED SHIFTS
BAND 3 LANDSAT-5 TM/F

	PRE-LAUNCH 5-596-13285		PRE-LAUNCH 5-198-10563				IN-ORBIT 50005-16221		
	SHUTTER 1		SHUTTER 1		SHUTTER 2		SHUTTER 1		
CH	FWD	REV	FWD	REV	FWD	REV	FWD	REV	CH
16	.23	.22	.24	.25	.29	.23	.29	.32	16
15	.24	.24	.26	.30	.34	.27	.29	.39	15
14	.20	.20	.21	.24	.24	.20	.30	.36	14
13	.25	.24	.29	.35	.33	.28	.28	.33	13
12	.17	.19	.30	.31	.33	.32	.30	.30	12
11	.27	.22	.25	.32	.35	.24	.42	.49	11
10	.20	.21	.20	.24	.23	.18	.36	.42	10
9	.28	.28	.29	.30	.30	.25	.41	.47	9
8	.14	.14	.12	.13	.14	.09	.17	.22	8
7	.25	.20	.24	.27	.28	.25	.26	.30	7
6	.27	.26	.31	.35	.31	.31	.60	.65	6
5	.27	.24	.28	.29	.32	.26	.37	.42	5
4	.29	.28	.38	.41	.39	.38	.46	.50	4
3	.38	.39	.42	.45	.48	.45	.51	.52	3
2	.12	.14	.17	.20	.20	.15	.16	.18	2
1	.46	.46	.49	.50	.52	.44	.45	.45	1

Appendix 9.11.4

TYPE 5-3 SCAN-CORRELATED SHIFTS BAND 4 LANDSAT-5 TM/F

	PRE-LAUNCH 5-596-13285		PRE-LAUNCH 5-198-10563				IN-ORBIT 50005-16221		
	SHUTTER 1		SHUTTER 1		SHUTTER 2		SHUTTER 1		
CH	FWD	REV	FWD	REV	FWD	REV	FWD	REV	CH
16	.02	.01	.03	.01	.03	.02	−.02	−.03	16
15	.04	.03	.13	.05	.12	.07	.04	.07	15
14	.02	.03	.04	.02	.04	.03	.01	.02	14
13	.06	.10	.18	.09	.16	.09	.18	.27	13
12	.01	.01	.01	.00	.01	.02	.01	.00	12
11	.06	.06	.15	.10	.19	.12	.06	.06	11
10	.00	.00	.00	−.00	.01	.00	.01	.01	10
9	.03	.04	.11	.04	.12	.05	.07	.11	9
8	.00	.01	.01	.01	.01	.01	−.00	−.01	8
7	.00	.01	.03	.02	.03	.02	.04	.06	7
6	.01	.01	.03	.02	.04	.03	.02	.03	6
5	.01	.02	.06	.03	.06	.03	.09	.13	5
4	.11	.17	.26	.12	.23	.17	.29	.33	4
3	.10	.11	.21	.14	.20	.14	.06	.06	3
2	.08	.11	.21	.08	.18	.13	−.01	.16	2
1	.35	.32	.18	.31	.24	.29	.42	.34	1

Appendix 9.11.5

TYPE 5-3 SCAN-CORRELATED SHIFTS BAND 5 LANDSAT-5 TM/F

	PRE-LAUNCH 5-596-13285		PRE-LAUNCH 5-198-10563 (NOISY)				IN-ORBIT 50005-16221		
	SHUTTER 1		SHUTTER 1		SHUTTER 2		SHUTTER 1		
CH	FWD	REV	FWD	REV	FWD	REV	FWD	REV	CH
16	−.08	−.10	−.23	−.21	−.26	−.14	.00	.00	16
15	−.09	−.08	−.01	.01	.01	.08	.00	.00	15
14	−.03	−.04	−.23	−.24	−.25	−.16	.00	.00	14
13	.02	.01	.10	.11	.11	.18	.00	.00	13
12	−.14	−.13	−.29	−.29	−.29	−.20	.00	.00	12
11	−.00	.02	.16	.12	.16	.23	.00	.00	11
10	−.00	.02	−.21	.18	−.11	−.06	.00	.00	10
9	.03	.03	.24	.22	.23	.34	.00	.00	9
8	−.09	−.11	−.30	−.33	−.32	−.19	−.01	−.00	8
7	−.00	−.08	.25	.22	.23	.33	.00	.00	7
6	−.11	−.08	−.23	−.22	−.25	−.14	.00	.00	6
5	−.09	−.06	.07	.06	.06	.13	.00	.00	5
4	−.01	−.01	−.18	−.17	−.18	−.11	.00	.00	4
3	.21	.21	—	—	—	—	.00	.00	3
2	.01	.01	−.18	−.13	−.14	−.08	.00	.00	2
1	.11	.14	.14	.12	.16	.18	.50	.55	1

Appendix 9.11.6

TYPE 5-3 SCAN-CORRELATED SHIFTS
BAND 7 LANDSAT-5 TM/F

CH	PRE-LAUNCH 5-596-13285		PRE-LAUNCH 5-198-10563 (NOISY)			
	SHUTTER 1		SHUTTER 1		SHUTTER 2	
	FWD	REV	FWD	REV	FWD	REV
16	−.10	−.10	−.21	−.23	−.25	−.14
15	.03	.02	.09	.08	.09	.13
14	−.05	−.07	−.27	−.27	−.29	−.16
13	.06	.08	.11	.10	.11	.16
12	−.04	−.05	−.34	−.32	−.36	−.20
11	.10	.09	.13	.15	.13	.18
10	−.12	−.12	−.53	−.46	−.56	−.32
9	.18	.17	.16	.18	.16	.25
8	−.14	−.13	−.47	−.41	−.49	−.29
7	.13	.17	.16	.18	.17	.22
6	−.10	−.08	−.27	−.29	−.35	−.16
5	.00	.02	.09	.09	.09	.14
4	−.09	−.09	−.27	−.29	−.29	−.17
3	−.03	−.04	.05	.04	.04	.12
2	−.02	−.01	−.23	−.24	−.26	−.16
1	.02	.02	.09	.08	.09	.16

APPENDIX 9.12 - SHUTTER BACKGROUNDS

This appendix contains selected background counts in DN for the shutter region of both the TM/PF and TM/F sensors. These data are taken from runs of the TRAPP software on the following scenes:

APPEN-DIX	SENSOR	ID	DATE	LOCATION	BACK-GROUND
9.2.1	TM/PF	40109-15140	2 NOV 82	Washington, DC	BDC
9.2.2	TM/PF	40392-18152	12 AUG 82	San Francisco, CA	B-BC
9.2.3	TM/PF	40392-18152	12 AUG 82	San Francisco, CA	B-ADC
9.2.4	TM/F	5-596-13285	30 AUG 83	Pre-Launch, Ambient	B-BDC
9.2.5	TM/PF	40037-02243	22 AUG 82	Washington, D.C. PM	BDC.

Each page is from a TRAPP output. There are four sets of numbers and statistical summaries for the 96 reflective channels. These in-orbit scenes both have solid formations of could; the Washington scene has clouds on the eastern edge of the lower quarter of the scene, and this San Francisco scene has clouds on the western edge increasing to about 75% cloud cover. Bright-target for the saturation effects presumbably account for the non-zero differences in forward and reverse scans.

```
DATA COLLECT: 4010915140/ DCGFSC RUN ON DATE:  7-FEB-83 AT TIME: 17:30:27

                 SHUTTER AVERAGE                                              DIFFERENCE BETWEEN FORWARD AND REVERSE AVERAGES

  CHANNEL      BAND 1   BAND 2   BAND 3   BAND 4   BAND 5   BAND 7  CHANNEL      BAND 1   BAND 2   BAND 3   BAND 4   BAND 5   BAND 7
     1          2.830    2.858    2.897    2.792    2.676    2.725      1        -1.178   -0.326   -0.228   -0.125   -0.165   -0.104
     2          2.336    2.366    2.362    2.169    2.511    2.326      2        -1.195   -0.354   -0.273   -0.122   -0.165   -0.123
     3          2.306    2.355    2.479    2.359 -99999.0    2.315      3        -1.113   -0.342   -0.312   -0.186 -99999.0   -0.004
     4          2.340    2.432    2.337    2.161    2.544    2.336      4        -1.033   -0.225   -0.255   -0.104   -0.040   -0.025
     5          2.350    2.234    2.273    2.099    2.519    2.199      5        -0.835   -0.238   -0.327   -0.070   -0.025    0.002
     6          2.438    2.444    2.345    2.362    2.697    2.360      6        -1.193   -0.300   -0.282   -0.140   -0.018   -0.016
     7          2.214    2.167    2.230    2.068    2.613    2.446      7        -0.876   -0.198   -0.258   -0.049    0.012   -0.200
     8          2.405    2.236    2.403    2.418    2.703    2.437      8        -1.087   -0.271   -0.283   -0.074   -0.013   -0.037
     9          2.124    2.099    2.180    2.065    2.494    2.191      9        -0.982   -0.153   -0.261   -0.071   -0.018    0.000
    10          2.315    2.095    2.346    2.115    2.562    2.418     10        -1.054   -0.125   -0.343   -0.036   -0.007   -0.030
    11          2.069    2.138    2.053    2.069    2.512    2.227     11        -1.122   -0.178   -0.181   -0.054   -0.003    0.005
    12          2.421    2.146    2.210    2.181    2.538    2.333     12        -0.798   -0.207   -0.305   -0.033   -0.027   -0.038
    13          2.078    2.144    2.159    2.039    2.545    2.113     13        -1.078   -0.186   -0.236   -0.016   -0.019   -0.001
    14          2.446    2.151    2.386    2.077    2.560    2.399     14        -0.899   -0.152   -0.230   -0.014   -0.017   -0.023
    15          2.086    2.128    2.113    2.067    2.531    2.118     15        -1.168   -0.161   -0.240   -0.036   -0.087   -0.050
    16          2.428    2.230    2.523    2.215    2.581    2.426     16        -0.892   -0.184   -0.238   -0.020   -0.097   -0.093
 MEANODD        2.257    2.265    2.298    2.195    2.556    2.292 MEANODD     -1.044   -0.223   -0.255   -0.076   -0.044   -0.044
 MEANEVN        2.391    2.263    2.364    2.212    2.587    2.379 MEANEVN     -1.019   -0.227   -0.276   -0.068   -0.048   -0.048
 MEANALL        2.324    2.264    2.331    2.204    2.572    2.335 MEANALL     -1.031   -0.225   -0.266   -0.072   -0.046   -0.046
 MEANODD SD     0.255    0.253    0.274    0.262    0.065    0.206 MEANODD SD   0.132    0.073    0.047    0.055    0.062    0.074
 MEANEVN SD     0.052    0.135    0.087    0.118    0.073    0.046 MEANEVN SD   0.145    0.077    0.037    0.049    0.055    0.039
 MEANALL SD     0.191    0.196    0.199    0.197    0.069    0.151 MEANALL SD   0.134    0.073    0.042    0.050    0.056    0.057
 MEAN SPSD      0.048    0.049    0.050    0.049    0.018    0.038 MEAN SPSD    0.034    0.018    0.011    0.013    0.015    0.014
 MEANALL CV     8.212    8.650    8.537    8.934    2.672    6.470 MEANALL CV -13.020  -32.323  -15.840  -70.033 -122.384 -123.245

            STANDARD DEVIATION OF SHUTTER                                          MAXIMUM AND MINIMUM

  CHANNEL      BAND 1   BAND 2   BAND 3   BAND 4   BAND 5   BAND 7  CHANNEL     BAND 1    BAND 2    BAND 3    BAND 4    BAND 5    BAND 7
     1          1.289    0.503    0.790    0.472    0.805    0.985      1        8/  0     5/  2     5/  1     4/  2     5/  0     6/  0
     2          1.445    1.009    0.548    0.381    0.755    0.991      2        8/  0     6/  0     5/  1     4/  1     5/  0     6/  0
     3          1.195    0.490    0.578    0.481 -99999.0    0.854      3        7/  0     4/  1     4/  1     4/  2  *** /***     6/  0
     4          1.449    0.690    0.726    0.385    0.823    1.031      4        7/  0     5/  0     4/  1     3/  1     6/  0     6/  0
     5          1.084    0.432    0.534    0.305    0.878    0.916      5        6/  0     4/  1     4/  1     4/  1     6/  0     6/  0
     6          1.430    0.521    0.528    0.483    0.880    1.015      6        8/  0     4/  1     4/  1     4/  1     6/  0     6/  0
     7          1.264    0.376    0.496    0.259    1.084    1.945      7        8/  0     4/  1     4/  1     3/  1     8/  0    11/  0
     8          1.312    0.426    0.856    0.531    0.811    0.926      8        6/  0     4/  1     5/  1     4/  1     5/  0     6/  0
     9          1.093    0.308    0.452    0.247    0.852    0.960      9        6/  0     4/  1     4/  1     3/  1     6/  0     6/  0
    10          1.184    0.302    0.575    0.320    0.878    1.050     10        6/  0     4/  1     5/  1     4/  1     6/  0     7/  0
    11          1.242    0.352    0.393    0.254    0.912    0.935     11        6/  0     4/  1     4/  1     3/  1     6/  0     6/  0
    12          1.321    0.377    0.478    0.411    0.847    1.006     12        8/  0     4/  1     4/  1     4/  1     5/  0     6/  0
    13          1.149    0.359    0.521    0.202    0.830    0.809     13        6/  0     4/  1     4/  1     3/  1     6/  0     5/  0
    14          1.352    0.360    0.597    0.268    0.792    1.090     14        8/  0     4/  1     4/  1     3/  1     5/  0     7/  0
    15          1.260    0.340    0.517    0.255    0.824    0.786     15        6/  0     4/  1     4/  1     4/  1     6/  0     5/  0
    16          1.600    0.437    0.848    0.412    0.785    0.956     16        8/  0     4/  1     5/  1     4/  2     5/  0     6/  0
 MEANODD        1.197    0.395    0.535    0.310    0.884    1.024 MEANODD     6.63/.00 4.13/1.1 4.13/1.0 3.50/1.3 6.14/.00 6.38/.00
 MEANEVN        1.387    0.515    0.644    0.399    0.821    1.008 MEANEVN     7.38/.00 4.38/.75 4.50/1.0 3.75/1.1 5.38/.00 6.25/.00
 MEANALL        1.292    0.455    0.590    0.354    0.850    1.016 MEANALL     7.00/.00 4.25/0.9 4.31/1.0 3.63/1.2 5.73/.00 6.31/.00
 MEANODD SD     0.080    0.072    0.117    0.107    0.095    0.379 MEANODD SD 0.92/.00 .354/.35 .354/.00 .535/.46 .900/.00 1.92/.00
 MEANEVN SD     0.124    0.232    0.146    0.083    0.045    0.052 MEANEVN SD 0.92/.00 .744/.46 .535/.00 .463/.35 .518/.00 .463/.00
 MEANALL SD     0.140    0.177    0.140    0.103    0.077    0.261 MEANALL SD 0.97/.00 .577/.44 .479/.00 .500/.40 .799/.00 1.35/.00
 MEAN SPSD      0.035    0.044    0.035    0.026    0.020    0.065 MEAN SPSD  .242/.00 .144/.11 .120/.00 .125/.10 .206/.00 .338/.00
 MEANALL CV    10.863   38.949   23.729   29.211    9.050   25.723 MEANALL CV 13.8/*** 13.6/47. 11.1/.00 13.8/34. 13.9/*** 21.4/***
```

```
TRAPP PROGRAM:  IN-ORBIT  PATH/SCN/DATE: P044034/4039218152/12AUG83.18:15:12      RUNDATE:15-FEB-84  15:43:56                 151

                       SHUTTER1 AVERAGE                                            DIFFERENCE BETWEEN FORWARD AND REVERSE AVERAGES

   CHANNEL      BAND 1    BAND 2    BAND 3    BAND 4    BAND 5    BAND 7  CHANNEL       BAND 1    BAND 2    BAND 3    BAND 4    BAND 5    BAND 7
      1          3.053     3.140     3.322     2.986     2.487     2.538    1          -0.396     1.319     1.445     0.456    -0.727    -0.571
      2          2.361     2.605     2.617     2.343     2.327     2.171    2          -0.692     1.091     0.929     0.273    -0.722    -0.569
      3          2.418     2.661     2.823     2.527  -99999.0     2.321    3          -0.564     1.333     1.102     0.413  -99999.0    -0.073
      4          2.528     2.652     2.499     2.251     2.583     2.408    4          -0.471     1.117     1.006     0.191    -0.101    -0.063
      5          2.464     2.605     2.615     2.288     2.563     2.309    5          -0.386     1.344     1.227     0.469    -0.055    -0.047
      6          2.428     2.705     2.687     2.517     2.863     2.493    6          -1.259     1.289     1.364     0.364    -0.089    -0.046
      7          2.617     2.563     2.649     2.289     2.830     2.496    7          -0.448     1.232     1.224     0.410    -0.087    -0.246
      8          2.445     2.571     2.606     2.532     2.934     2.544    8          -1.082     1.291     1.249     0.311    -0.066    -0.062
      9          2.302     2.467     2.616     2.215     2.660     2.270    9          -0.458     1.303     1.522     0.320    -0.115    -0.061
     10          2.436     2.406     2.666     2.290     2.715     2.519   10          -0.598     1.196     1.444     0.442    -0.092    -0.019
     11          2.287     2.478     2.439     2.209     2.667     2.338   11          -0.369     1.273     1.329     0.344    -0.124    -0.049
     12          2.558     2.427     2.531     2.269     2.702     2.374   12          -0.432     1.293     1.378     0.397    -0.086    -0.025
     13          2.284     2.563     2.548     2.150     2.677     2.179   13          -0.198     1.452     1.426     0.366    -0.115    -0.055
     14          2.414     2.484     2.746     2.308     2.723     2.492   14          -0.564     1.237     1.606     0.590    -0.119    -0.058
     15          2.320     2.496     2.507     2.209     2.591     2.114   15          -0.060     1.330     1.411     0.442    -0.309    -0.162
     16          2.416     2.565     2.775     2.378     2.658     2.440   16          -0.591     1.477     1.344     0.478    -0.306    -0.228
  MEANODD        2.468     2.622     2.690     2.359     2.639     2.321 MEANODD       -0.360     1.323     1.336     0.402    -0.219    -0.158
  MEANEVN        2.448     2.552     2.641     2.361     2.688     2.430 MEANEVN       -0.711     1.249     1.290     0.381    -0.197    -0.134
  MEANALL        2.458     2.587     2.665     2.360     2.665     2.375 MEANALL       -0.536     1.286     1.313     0.392    -0.207    -0.146
  MEANODD SD     0.263     0.220     0.279     0.278     0.108     0.143 MEANODD SD     0.159     0.064     0.141     0.054     0.238     0.181
  MEANEVN SD     0.064     0.106     0.097     0.109     0.183     0.119 MEANEVN SD     0.298     0.121     0.225     0.125     0.225     0.188
  MEANALL SD     0.185     0.170     0.204     0.204     0.150     0.139 MEANALL SD     0.294     0.101     0.183     0.094     0.223     0.179
  MEAN SPSD      0.046     0.043     0.051     0.051     0.039     0.035 MEAN SPSD      0.073     0.025     0.046     0.024     0.058     0.045
  MEANALL CV     7.527     6.590     7.637     8.639     5.623     5.867 MEANALL CV   -54.830     7.865    13.913    24.019  -107.664  -122.500

                    STANDARD DEVIATION OF SHUTTER                                             MAXIMUM AND MINIMUM

   CHANNEL      BAND 1    BAND 2    BAND 3    BAND 4    BAND 5    BAND 7  CHANNEL       BAND 1    BAND 2    BAND 3    BAND 4    BAND 5    BAND 7
      1          1.365     1.253     1.718     0.722     0.919     1.041    1          10/  0    10/  0    14/  0     6/  0     6/  0     7/  0
      2          1.632     1.354     0.979     0.795     0.871     1.059    2          11/  0     9/  0     7/  0     6/  0     6/  0     6/  0
      3          1.225     1.113     1.238     0.732  -99999.0     0.879    3           8/  0     8/  0    10/  0     6/  0  *** /***     6/  0
      4          1.795     1.087     1.059     0.792     0.905     1.067    4          13/  0     6/  0     6/  0     6/  0     6/  0     8/  0
      5          1.154     1.045     1.243     0.690     0.941     0.958    5           8/  0     6/  0     9/  0     5/  0     6/  0     6/  0
      6          1.574     1.051     1.047     0.746     0.943     1.037    6           8/  0     7/  0     5/  0     6/  0     6/  0     6/  0
      7          1.355     1.000     1.179     0.633     1.103     1.825    7           9/  0     6/  0     9/  0     5/  0     7/  0    10/  0
      8          1.510     1.073     1.250     0.895     0.921     0.979    8           7/  0     8/  0     8/  0     6/  0     7/  0     6/  0
      9          1.200     1.043     1.252     0.592     0.930     1.003    9           9/  0     6/  0     9/  0     5/  0     8/  0     7/  0
     10          1.361     1.004     1.126     0.698     0.953     1.096   10           9/  0     6/  0     5/  0     6/  0     6/  0     9/  0
     11          1.395     1.029     1.227     0.592     0.950     0.972   11          11/  0     6/  0     9/  0     5/  0     6/  0     6/  0
     12          1.601     1.105     1.061     0.684     0.926     1.022   12          10/  0     8/  0     5/  0     6/  0     6/  0     6/  0
     13          1.368     1.191     1.325     0.579     0.924     0.863   13          11/  0     8/  0    10/  0     5/  0     6/  0     6/  0
     14          1.474     1.007     1.163     0.768     0.888     1.132   14           9/  0     6/  0     6/  0     6/  0     6/  0     6/  0
     15          1.513     1.134     1.410     0.652     0.887     0.814   15          12/  0     8/  0    11/  0     6/  0     6/  0     6/  0
     16          1.737     1.213     1.491     0.742     0.879     1.013   16           9/  0     9/  0    11/  0     6/  0     6/  0     6/  0
  MEANODD        1.322     1.101     1.324     0.649     0.951     1.044 MEANODD      9.8/.00  7.25/.00  10.1/.00  5.38/.00  6.43/.00  6.75/.00
  MEANEVN        1.586     1.112     1.147     0.765     0.911     1.051 MEANEVN      9.5/.00  7.38/.00  6.63/.00  6.00/.00  6.13/.00  6.63/.00
  MEANALL        1.454     1.106     1.236     0.707     0.929     1.048 MEANALL      9.6/.00  7.31/.00  8.38/.00  5.69/.00  6.27/.00  6.69/.00
  MEANODD SD     0.119     0.088     0.174     0.061     0.070     0.325 MEANODD SD  1.49/.00  1.49/.00  1.73/.00  .518/.00  .787/.00  1.39/.00
  MEANEVN SD     0.140     0.118     0.162     0.066     0.030     0.049 MEANEVN SD  1.85/.00  1.30/.00  2.07/.00  .000/.00  .354/.00  1.19/.00
  MEANALL SD     0.185     0.101     0.186     0.086     0.055     0.224 MEANALL SD  1.63/.00  1.35/.00  2.58/.00  .479/.00  .594/.00  1.25/.00
  MEAN SPSD      0.046     0.025     0.047     0.021     0.014     0.056 MEAN SPSD   .407/.00  .338/.00  .645/.00  .120/.00  .153/.00  .313/.00
  MEANALL CV    12.748     9.108    15.074    12.116     5.867    21.403 MEANALL CV  16.9/***  18.5/***  30.8/***  8.42/***   9.5/***  18.7/***
```

```
TRAPP PROGRAM:  IN-ORBIT  PATH/SCN/DATE: P044034/4039218152/12AUG83.18:15:12      RUNDATE:15-FEB-84  15:43:56            152

                      SHUTTER2 AVERAGE                                          DIFFRENCE BETWEEN FORWARD AND REVERSE AVERAGES

  CHANNEL       BAND 1   BAND 2   BAND 3   BAND 4   BAND 5   BAND 7  CHANNEL       BAND 1   BAND 2   BAND 3   BAND 4   BAND 5   BAND 7
     1           2.841    2.635    2.778    2.789    2.874    2.785     1           1.278    2.600    1.970    1.289    0.084    0.074
     2           2.287    2.160    2.296    2.269    2.676    2.417     2           1.680    2.613    2.092    1.654    0.073    0.079
     3           2.329    2.210    2.404    2.406 -99999.0    2.334     3           1.387    2.595    1.980    1.897 -99999.0    0.010
     4           2.428    2.258    2.141    2.123    2.649    2.404     4           1.638    2.234    2.202    1.550    0.013    0.020
     5           2.396    2.164    2.234    2.160    2.610    2.261     5           0.980    2.419    2.370    1.711   -0.053   -0.011
     6           2.507    2.311    2.267    2.414    2.777    2.422     6           1.229    2.668    2.568    1.801    0.001   -0.004
     7           2.227    2.094    2.203    2.114    2.757    2.465     7           1.392    2.321    2.265    1.488   -0.048    0.156
     8           2.504    2.158    2.259    2.408    2.846    2.498     8           1.278    2.672    2.558    1.608    0.009    0.043
     9           2.216    1.993    2.184    2.181    2.631    2.232     9           1.405    2.580    2.818    1.826   -0.056    0.001
    10           2.398    1.952    2.274    2.230    2.628    2.473    10           1.769    2.451    3.017    1.507   -0.033   -0.004
    11           2.170    2.041    2.039    2.157    2.650    2.311    11           1.983    2.404    2.289    1.406   -0.043    0.014
    12           2.499    1.965    2.140    2.203    2.620    2.354    12           1.311    2.673    2.813    1.763   -0.011    0.018
    13           2.114    2.054    2.161    2.045    2.645    2.150    13           1.968    2.707    2.341    1.308   -0.007    0.026
    14           2.403    2.077    2.327    2.291    2.616    2.454    14           1.568    2.484    2.742    1.921    0.016    0.029
    15           2.102    2.007    2.087    2.108    2.569    2.091    15           2.494    2.579    2.304    1.693    0.116    0.112
    16           2.454    2.100    2.309    2.376    2.570    2.436    16           1.152    2.850    2.653    1.446    0.167    0.184
 MEANODD         2.299    2.150    2.263    2.245    2.677    2.328 MEANODD        1.611    2.536    2.292    1.577   -0.001    0.048
 MEANEVN         2.434    2.123    2.252    2.289    2.673    2.432 MEANEVN        1.453    2.561    2.581    1.667    0.030    0.046
 MEANALL         2.367    2.136    2.257    2.267    2.675    2.380 MEANALL        1.532    2.558    2.437    1.622    0.015    0.047
 MEANODD SD      0.241    0.210    0.234    0.244    0.104    0.217 MEANODD SD     0.492    0.147    0.264    0.236    0.071    0.060
 MEANEVN SD      0.074    0.127    0.072    0.104    0.093    0.044 MEANEVN SD     0.236    0.187    0.307    0.152    0.063    0.062
 MEANALL SD      0.186    0.168    0.168    0.183    0.095    0.161 MEANALL SD     0.382    0.164    0.314    0.197    0.067    0.059
 MEAN SPSD       0.046    0.042    0.042    0.046    0.024    0.040 MEAN SPSD      0.095    0.041    0.079    0.049    0.017    0.015
 MEANALL CV      7.841    7.876    7.421    8.059    3.535    6.745 MEANALL CV    24.918    6.417   12.889   12.157  436.003  126.056

                STANDARD DEVIATION OF SHUTTER2                                           MAXIMUM AND MINIMUM

  CHANNEL       BAND 1   BAND 2   BAND 3   BAND 4   BAND 5   BAND 7  CHANNEL       BAND 1   BAND 2   BAND 3   BAND 4   BAND 5   BAND 7
     1           1.251    1.544    1.326    0.833    0.857    1.011     1          7/  0    5/  0    5/  0    4/  1    5/  0    6/  0
     2           1.610    1.679    1.264    1.031    0.817    0.988     2          8/  0    8/  0    5/  0    4/  0    5/  0    6/  0
     3           1.211    1.508    1.221    1.132 -99999.0    0.861     3          6/  0    5/  0    5/  0    4/  0 *** /***    5/  0
     4           1.568    1.438    1.399    1.023    0.874    1.029     4          8/  0    6/  0    5/  0    4/  0    5/  0    6/  0
     5           1.049    1.433    1.412    1.036    0.905    0.912     5          6/  0    5/  0    5/  0    4/  0    6/  0    5/  0
     6           1.513    1.538    1.494    1.086    0.907    1.016     6          7/  0    5/  0    5/  0    4/  0    6/  0    6/  0
     7           1.309    1.385    1.363    0.902    1.094    1.800     7          6/  0    4/  0    5/  0    4/  0    8/  0   10/  0
     8           1.490    1.536    1.591    1.101    0.843    0.939     8          7/  0    5/  0    5/  0    5/  0    6/  0    5/  0
     9           1.178    1.503    1.616    1.099    0.896    0.969     9          6/  0    5/  0    5/  0    4/  0    6/  0    6/  0
    10           1.438    1.437    1.708    1.036    0.898    1.069    10          7/  0    5/  0    5/  0    4/  0    5/  0    6/  0
    11           1.428    1.421    1.383    0.893    0.928    0.940    11          6/  0    4/  0    5/  0    4/  0    5/  0    6/  0
    12           1.430    1.546    1.608    1.120    0.885    1.004    12          6/  0    5/  0    5/  0    5/  0    5/  0    6/  0
    13           1.356    1.598    1.418    0.843    0.884    0.830    13          6/  0    5/  0    5/  0    4/  0    5/  0    5/  0
    14           1.537    1.460    1.587    1.167    0.862    1.096    14          7/  0    5/  0    5/  0    4/  0    5/  0    6/  0
    15           1.595    1.505    1.413    1.053    0.856    0.753    15          6/  0    5/  0    5/  0    4/  0    5/  0    5/  0
    16           1.716    1.625    1.615    0.940    0.817    0.967    16          7/  0    5/  0    5/  0    4/  0    5/  0    6/  0
 MEANODD         1.297    1.487    1.394    0.974    0.917    1.009 MEANODD     6.13/.00 4.75/.00 5.00/.00 4.00/.13 5.71/.00 6.00/.00
 MEANEVN         1.538    1.532    1.533    1.063    0.863    1.013 MEANEVN     7.13/.00 5.50/.00 5.00/.00 4.25/.00 5.25/.00 5.88/.00
 MEANALL         1.417    1.510    1.464    1.018    0.888    1.011 MEANALL     6.63/.00 5.13/.00 5.00/.00 4.13/.06 5.47/.00 5.94/.00
 MEANODD SD      0.167    0.070    0.111    0.119    0.082    0.330 MEANODD SD  .354/.00 .463/.00  000/.00 .000/.35 1.11/.00 1.69/.00
 MEANEVN SD      0.095    0.088    0.142    0.070    0.034    0.051 MEANEVN SD  .641/.00 1.07/.00 .000/.00 .463/.00 .463/.00 .354/.00
 MEANALL SD      0.181    0.080    0.143    0.105    0.065    0.228 MEANALL SD  .719/.00 .885/.00 .000/.00 .342/.25 .834/.00 1.18/.00
 MEAN SPSD       0.045    0.020    0.036    0.026    0.017    0.057 MEAN SPSD   .190/.00 .221/.00 .000/.00 .085/.06 .215/.00 .295/.00
 MEANALL CV     12.735    5.306    9.749   10.328    7.361   22.526 MEANALL CV  10.8/*** 17.3/*** .000/*** 8.28/*** 15.3/*** 19.9/***
```

```
TRAPP PROGRAM:  BRU  30AUG83.16:14:15G83 16:14:15.TM.FA       RUNDATE:31-MAR-84  11:35:09                                          127

                           SHUTTER1 AVERAGE                                              DIFFERENCE BETWEEN FORWARD AND REVERSE AVERAGES

   CHANNEL       BAND 1    BAND 2    BAND 3    BAND 4    BAND 5    BAND 7  CHANNEL        BAND 1    BAND 2    BAND 3    BAND 4    BAND 5    BAND 7
      1           2.868     2.589     2.836     2.955     2.729     3.019     1            0.089     0.206     0.081     0.018     0.229     0.268
      2           2.522     2.021     2.194     2.260     2.361     2.445     2            0.087     0.115     0.041     0.052     0.185     0.205
      3           2.434     2.175     2.400     2.309     2.440     2.502     3            0.021     0.132     0.063     0.041     0.197     0.194
      4           2.472     1.998     2.156     2.152     2.365     2.410     4            0.061     0.069     0.030     0.013     0.168     0.175
      5           2.330     1.962     2.237     2.102     2.254     2.340     5            0.069     0.081     0.065     0.018     0.166     0.158
      6           2.557     2.041     2.154     2.159     2.329     2.443     6            0.056     0.044     0.018     0.006     0.089     0.134
      7           2.269     1.992     2.226     2.137     2.266     2.280     7            0.034     0.061     0.058     0.015     0.124     0.118
      8           2.683     2.023     2.219     2.220     2.528     2.423     8            0.045     0.019     0.020    -0.014     0.088     0.083
      9           2.189     2.046     2.320     2.167     2.299     2.289     9            0.039     0.049     0.034     0.015     0.116     0.084
     10           2.302     2.017     2.170     2.124     2.377     2.352    10            0.030     0.015     0.010    -0.020     0.071     0.071
     11           2.143     2.008     2.193     2.191     2.288     2.271    11            0.034     0.036     0.009     0.010     0.048     0.054
     12           2.303     2.011     2.198     2.132     2.274     2.256    12            0.009     0.015    -0.008    -0.025     0.028     0.022
     13           2.202     1.985     2.122     2.096     2.207     2.180    13            0.018     0.022     0.016    -0.002     0.037    -0.008
     14           2.418     2.006     2.160     2.193     2.359     2.416    14            0.022     0.007    -0.014    -0.037    -0.004    -0.011
     15           2.129     2.020     2.108     2.136     2.167     2.163    15            0.011     0.027     0.008     0.010     0.000     0.005
     16           2.386     2.010     2.220     2.312     2.297     2.394    16            0.026     0.011     0.001    -0.045    -0.004    -0.008
 MEANODD          2.320     2.097     2.305     2.262     2.331     2.381 MEANODD          0.039     0.077     0.042     0.016     0.115     0.109
 MEANEVN          2.455     2.016     2.184     2.194     2.361     2.392 MEANEVN          0.042     0.037     0.012    -0.009     0.078     0.084
 MEANALL          2.388     2.056     2.245     2.228     2.346     2.386 MEANALL          0.041     0.057     0.027     0.003     0.096     0.097
 MEANODD SD       0.243     0.209     0.235     0.288     0.179     0.278 MEANODD SD       0.027     0.063     0.029     0.012     0.081     0.095
 MEANEVN SD       0.131     0.013     0.028     0.066     0.076     0.063 MEANEVN SD       0.025     0.038     0.019     0.031     0.072     0.082
 MEANALL SD       0.201     0.149     0.173     0.205     0.134     0.195 MEANALL SD       0.025     0.054     0.028     0.026     0.076     0.087
 MEAN SPSD        0.050     0.037     0.043     0.051     0.034     0.049 MEAN SPSD        0.006     0.014     0.007     0.007     0.019     0.022
 MEANALL CV       8.426     7.255     7.726     9.197     5.715     8.171 MEANALL CV      61.523    95.388   102.885   778.120    79.542    89.825

                       STANDARD DEVIATION OF SHUTTER                                                 MAXIMUM AND MINIMUM

   CHANNEL       BAND 1    BAND 2    BAND 3    BAND 4    BAND 5    BAND 7  CHANNEL        BAND 1    BAND 2    BAND 3    BAND 4    BAND 5    BAND 7
      1           0.973     0.524     0.645     0.240     0.820     0.906     1             6/  0     4/  1     5/  1     4/  2     6/  0     6/  0
      2           0.967     0.428     0.450     0.439     0.828     0.959     2             6/  0     4/  0     4/  1     3/  2     7/  0    35/  0
      3           0.940     0.409     0.587     0.462     0.916     0.893     3             6/  0     4/  1     5/  0     4/  1     7/  0    19/  0
      4           1.009     0.296     0.486     0.359     0.933     0.908     4             6/  0     4/  1     4/  1     3/  1     6/  0     5/  0
      5           0.846     0.321     0.559     0.303     0.869     0.835     5             5/  0     4/  1     4/  0     3/  2     6/  0     5/  0
      6           0.930     0.207     0.427     0.366     0.844     0.941     6             6/  0     3/  1     4/  1     3/  2     5/  0     5/  0
      7           0.829     0.295     0.506     0.344     1.265     0.862     7             5/  0     3/  1     4/  1     3/  2     6/  0     6/  0
      8           0.993     0.163     0.451     0.414     0.865     1.000     8             6/  0     4/  1     4/  1     4/  2     6/  0     6/  0
      9           0.772     0.267     0.571     0.373     1.036     1.263     9             5/  0     4/  1     5/  1     3/  2    78/  0   130/  0
     10           0.853     0.157     0.426     0.330     1.303     0.972    10             6/  0     3/  1     4/  1     3/  2     8/  0     6/  0
     11           0.854     0.329     0.453     0.393     0.825     0.882    11             5/  0     3/  1     4/  1     3/  2     6/  0     6/  0
     12           0.867     0.172     0.736     0.339     0.955     0.977    12             6/  0     3/  1     4/  0     3/  2     6/  0     6/  0
     13           0.811     0.294     0.484     0.295     0.855     0.772    13             5/  0     3/  1     4/  1     3/  2     6/  0     5/  0
     14           0.975     0.156     0.410     0.395     0.833     0.942    14             7/  0     3/  1     4/  1     3/  2     6/  0     6/  0
     15           0.762     0.308     0.433     0.343     0.815     0.787    15             6/  0     4/  1     4/  1     3/  2     5/  0     5/  0
     16           0.909     0.306     0.523     0.465     0.849     0.897    16             7/  0     4/  0     4/  1     4/  1     5/  0     5/  0
 MEANODD          0.849     0.343     0.530     0.344     0.925     0.900 MEANODD      5.38/.00 3.63/1.0 4.38/.75 3.25/1.9 15.0/.00 22.8/.00
 MEANEVN          0.938     0.236     0.488     0.388     0.926     0.949 MEANEVN      6.25/.00 3.50/.75 4.00/.88 3.25/1.8 6.13/.00  9.3/.00
 MEANALL          0.893     0.290     0.509     0.366     0.926     0.925 MEANALL      5.81/.00 3.56/.88 4.19/.81 3.25/1.8 10.6/.00 16.0/.00
 MEANODD SD       0.075     0.084     0.073     0.068     0.155     0.154 MEANODD SD   .518/.00 .518/.00 .518/.46 .463/.35 25.5/.00 43.6/.00
 MEANEVN SD       0.058     0.099     0.106     0.048     0.159     0.035 MEANEVN SD   .463/.00 .535/.46 .000/.35 .463/.46 0.99/.00 10.4/.00
 MEANALL SD       0.079     0.105     0.091     0.061     0.152     0.111 MEANALL SD   .655/.00 .512/.34 .403/.40 .447/.40 18.0/.00 31.4/.00
 MEAN SPSD        0.020     0.026     0.023     0.015     0.038     0.028 MEAN SPSD    .164/.00 .128/.09 .101/.10 .112/.10 4.50/.00 7.85/.00
 MEANALL CV       8.890    36.121    17.784    16.751    16.425    12.017 MEANALL CV   11.3/*** 14.4/39.  9.6/50. 13.8/22. 170./*** 196./***
```

```
TRAPP PROGRAM:  IN-ORBIT  PATH/SCN/DATE: K112114/4003702243/22AUG83.02:24:18      RUNDATE:11-JUL-83  09:33:30          66

                   SHUTTER AVERAGE                                               DIFFERENCE BETWEEN FORWARD AND REVERSE AVERAGES

  CHANNEL       BAND 1   BAND 2   BAND 3   BAND 4   BAND 5   BAND 7  CHANNEL       BAND 1   BAND 2   BAND 3   BAND 4   BAND 5   BAND 7
     1           2.921    2.858    2.847    2.739    2.820    2.763     1           0.224    0.156    0.259    0.114    0.024    0.005
     2           2.430    2.349    2.228    2.125    2.548    2.389     2           0.153    0.104    0.054    0.089    0.064    0.059
     3           2.483    2.477    2.486    2.310 -99999.0    2.365     3           0.212    0.171    0.171    0.193 -99999.0   -0.002
     4           1.596    2.378    2.329    2.177    2.580    2.351     4           0.166    0.056    0.067    0.105    0.037    0.040
     5           2.488    2.266    2.249    2.078    2.674    2.222     5           0.182    0.124    0.177    0.101   -0.038   -0.014
     6           2.502    2.449    2.241    2.224    2.757    2.346     6           0.143    0.108    0.050    0.130    0.018    0.031
     7           2.362    2.220    2.254    2.060    2.720    2.531     7           0.208    0.135    0.137    0.080   -0.032    0.044
     8           2.253    2.248    2.493    2.440    2.878    2.454     8           0.132    0.125    0.082    0.093    0.026    0.019
     9           2.288    2.134    2.304    2.055    2.632    2.249     9           0.234    0.118    0.197    0.079   -0.037   -0.034
    10           2.010    2.105    2.214    2.056    2.644    2.416    10           0.132    0.071    0.082    0.058    0.007    0.030
    11           2.250    2.232    2.098    2.046    2.617    2.269    11           0.299    0.138    0.139    0.073   -0.046   -0.008
    12           1.747    2.137    2.130    2.054    2.565    2.296    12           0.155    0.082    0.052    0.061    0.028    0.043
    13           2.216    2.188    2.137    2.032    2.659    2.166    13           0.332    0.149    0.186    0.059   -0.025    0.003
    14           2.462    2.137    2.268    2.048    2.660    2.363    14           0.111    0.079    0.042    0.065    0.015    0.038
    15           2.299    2.165    2.085    2.041    2.665    2.113    15           0.345    0.142    0.207    0.072    0.054    0.053
    16           2.496    2.200    2.279    2.029    2.614    2.363    16           0.091    0.095    0.133    0.043    0.100    0.122
 MEANODD         2.413    2.317    2.308    2.170    2.684    2.335 MEANODD        0.255    0.142    0.184    0.096   -0.014    0.006
 MEANEVN         2.187    2.250    2.273    2.144    2.656    2.374 MEANEVN        0.135    0.090    0.070    0.081    0.037    0.048
 MEANALL         2.300    2.284    2.290    2.157    2.669    2.354 MEANALL        0.195    0.116    0.127    0.089    0.013    0.027
 MEANODD SD      0.228    0.242    0.254    0.247    0.068    0.215 MEANODD SD     0.062    0.017    0.039    0.043    0.038    0.029
 MEANEVN SD      0.360    0.128    0.106    0.138    0.111    0.047 MEANEVN SD     0.025    0.022    0.029    0.029    0.031    0.032
 MEANALL SD      0.314    0.190    0.189    0.194    0.092    0.152 MEANALL SD     0.077    0.033    0.068    0.036    0.042    0.037
 MEAN SPSD       0.078    0.048    0.047    0.049    0.024    0.038 MEAN SPSD      0.019    0.008    0.017    0.009    0.011    0.009
 MEANALL CV     13.648    8.338    8.250    8.995    3.436    6.454 MEANALL CV    39.281   28.407   53.155   40.927  323.843  137.313

                   STANDARD DEVIATION OF SHUTTER                                          MAXIMUM AND MINIMUM

  CHANNEL       BAND 1   BAND 2   BAND 3   BAND 4   BAND 5   BAND 7  CHANNEL       BAND 1   BAND 2   BAND 3   BAND 4   BAND 5   BAND 7
     1           1.259    0.681    1.278    0.590    0.844    1.017     1           10/  0    7/  0   13/  0    6/  0    6/  0    6/  0
     2           1.326    0.985    0.587    0.440    0.768    1.022     2            8/  0    6/  0    5/  0    5/  1    6/  0    7/  0
     3           1.148    0.627    0.845    0.558 -99999.0    0.867     3            9/  0    6/  0    9/  0    5/  0 *** /***    6/  0
     4           1.155    0.680    0.706    0.493    0.847    1.055     4           11/  0    5/  0    5/  0    5/  0    6/  0    7/  0
     5           1.115    0.549    0.757    0.370    0.910    0.917     5            9/  0    5/  0    8/  0    5/  0    6/  0    5/  0
     6           1.290    0.553    0.468    0.493    0.913    1.010     6            6/  0    5/  1    4/  1    5/  1    7/  0    6/  0
     7           1.297    0.491    0.688    0.320    1.095    1.965     7           10/  0    5/  0    7/  0    5/  1    7/  0   11/  0
     8           1.152    0.523    0.877    0.594    0.890    0.951     8            6/  0    6/  1    5/  0    5/  1    8/  0    7/  0
     9           1.120    0.453    0.675    0.304    0.891    0.984     9            9/  0    5/  0    7/  0    5/  1    6/  0    6/  0
    10           0.960    0.392    0.468    0.318    0.913    1.065    10            8/  0    5/  0    4/  1    5/  1    6/  0    7/  0
    11           1.327    0.524    0.670    0.320    0.918    0.961    11           10/  0    5/  0    8/  0    5/  0    6/  0    6/  0
    12           1.121    0.472    0.381    0.285    0.889    0.989    12           11/  0    6/  0    4/  1    5/  1    6/  0    6/  0
    13           1.296    0.592    0.796    0.378    0.873    0.829    13           13/  0    6/  0    9/  0    5/  0    5/  0    5/  0
    14           1.268    0.387    0.546    0.335    0.873    1.091    14            6/  0    5/  1    5/  0    5/  1    6/  0    8/  0
    15           1.425    0.592    0.906    0.401    0.856    0.792    15           13/  0    6/  0    9/  0    5/  0    5/  0    5/  0
    16           1.553    0.461    0.988    0.277    0.828    0.961    16            9/  0    5/  0    9/  0    5/  1    6/  0    6/  0
 MEANODD         1.248    0.564    0.827    0.405    0.912    1.042 MEANODD      10.4/.00 5.63/.00 8.75/.00 5.13/.25 5.86/.00 6.25/.00
 MEANEVN         1.228    0.557    0.628    0.404    0.865    1.018 MEANEVN      8.13/.00 5.38/.38 5.13/.38 5.00/.88 6.38/.00 6.75/.00
 MEANALL         1.238    0.560    0.727    0.405    0.887    1.030 MEANALL       9.3/.00 5.50/.19 6.94/.19 5.06/.56 6.13/.00 6.50/.00
 MEANODD SD      0.111    0.074    0.201    0.110    0.085    0.381 MEANODD SD 1.69/.00 .744/.00 1.91/.00 .354/.46 .690/.00 1.98/.00
 MEANEVN SD      0.175    0.197    0.213    0.117    0.049    0.050 MEANEVN SD 2.10/.00 .518/.52 1.64/.52 .000/.35 .744/.00 .707/.00
 MEANALL SD      0.142    0.144    0.225    0.110    0.070    0.263 MEANALL SD 2.18/.00 .632/.40 2.54/.40 .250/.51 .743/.00 1.46/.00
 MEAN SPSD       0.036    0.036    0.056    0.027    0.018    0.066 MEAN SPSD  .544/.00 .158/.10 .636/.10 .063/.13 .192/.00 .365/.00
 MEANALL CV     11.485   25.701   30.953   27.077    7.888   25.524 MEANALL CV 23.5/*** 11.5/*** 36.6/*** 4.94/91. 12.1/*** 22.5/***
```

APPENDIX 9.13

RECOMMENDATIONS

TM RADIOMETRIC CHARACTERIZATION

6.1 ENGINEERING CHARACTERIZATION OF THE TM SENSOR

6.1.1 RECALIBRATE INTEGRATING SPHERE USED IN PRE-LAUNCH CALIBRATION

- ●.1 48" TM Integrating Sphere

    o.1 SBRC
    o.2 GSFC
    o.3 NBS

- ●.2 Two 30" MSS Spheres
- ●.3 MMR 8-Band Field Radiometer

6.1.2 ANALYZE RELATIVE RADIOMETRY OF PRE-LAUNCH DATA ON 42 TRACK TAPES

6.1.3 EMPLOY ENGINEERING MODEL TM TESTS TO INVESTIGATE SOURCE OF:

- ●.1 Bin-Radiance Dependence (Unequal Bins)
- ●.2 Coherent Noise (Stationary and Time-Dependent)
- ●.3 Within-Line Droop
- ●.4 Bright Target Saturation (Recovery)
- ●.5 Scan-Correlated Shifts
- ●.6 IC Pulse Temperature-Dependence
- ●.7 "Secondary" Light Pulse in Calibration Region
- ●.8 Apparent Gain Changes with Time

6.1.4 PRODUCE FINAL REPORT DESCRIBING TM PERFORMANCE CHARACTERISTICS

6.2 FLIGHT SEGMENT OPERATIONS

6.2.1 INSTITUTE CHANGES IN OPERATIONAL PROCEDURES

- ●.1 Stop Routine Operation of IC Automatic Sequencer

- .2 Alternate Black Body Temperatures "T2" and "T3"
- .3 Set Outgassing Strategy at 20% Band 6 Gain Loss

6.2.2 PERFORM IN-ORBIT CALIBRATION TESTS

- .1 Calibrate Temperature-Dependence of IC Pulses

6.2.3 PERFORM IN-ORBIT CHARACTERIZATION TESTS

- .1 Redundant Power Supply Noise
- .2 Manual IC Operation with Automatic Sequencer off
- .3 "Override" Back-Up IC Operation
- .4 Coherent Noise Phasing Relative to Midscan Pulse
- .5 Noise with DC Restoration off

6.2.4 PERFORM IN-ORBIT SCIENTIFIC MISSION TESTS

- .1 Subsampled Extension of Swath Width, No Shutter
- .2 Bidirectional Reflectance by Off-Nadir Pointing
- .3 Intensive Single Site Acquisition by Pointing
- .4 TM/F and TM/PF Stereo by Pointing
- .5 TM/F and MSS/F (High Gain) Bathymetry
- .6 TM Single S/C Stereo
  - o.1 Fore/Aft
  - o.2 Side-to-Side

6.3 TIPS GROUND PROCESSING

6.3.1 PROVIDE FOR FUTURE CHANGE IN RADIOMETRIC CALIBRATION PARAMETERS

- .1 Post-Calibration Dynamic Range (RMIN, RMAX)
- .2 Spectral Radiance for each IC Lamp level
- .3 Averaged Pulse for each IC Lamp Level
- .4 Pre-Launch Gains and Offsets
- .5 Calculated Pre-Launch Nominal IC Pulses

6.3.2 PROVIDE FOR CHANGES IN IC SYSTEMATIC RADIOMETRIC CORRECTION PROCEDURES INVOLVING:

●.1 Two Background Shutter Collects (avoid DC Restore)

●.2 Within-Scene Corrections

o.1 Bin-Radiance Dependence
o.2 Coherent Noise
o.3 Scan-Correlated Shifts

●.3 Background Outliers (Incomplete Obscuration)

●.4 "Secondary" Light Pulse in Calibration Region

o.1 Search 60 to 148 mf Collect Window

●.5 Pulse Integration Parameters

o.1 Optimize Integration Width (near 39 mf)

●.6 Pulse Averaging

o.1 Separate Forward and Reverse Scans

●.7 Lamp State Options

o.1 Reject 111 State for any Regression

o.2 Omit 000 State when possible

o.3 Omit Shutter Background when possible

o.4 Permit any States and Background

●.8 IC Pulse Temperature-Dependence

●.9 Between-Channel Correlations

o.1 Between-Band Absolute Radiometry

o.2 Quality Assurance Redundancy Check

●.10 Within-Pulse Smoothing

●.11 Between-Date Smoothing

●.12 Reference Channels or Variance Weighting

●.13 Statistical Quality Indices

6.3.3 MODIFY HISTOGRAM EQUALIZATION PROCEDURE TO PROVIDE FOR:

- .1 Optional 1st pass HDT-RT Histogram
- .2 Line-by-line Systematic Correction
- .3 2nd Pass HDT-RT 11-Bit Histogram
- .4 HDT-AT 11-Bit Histogram and File
- .5 Histogram Reference to "Quiet" Channel
- .6 Histogram Monitoring of IC Quality
- .7 Weighting of IC and Histogram Constants
- .8 HDT-PT Histogram File for each Band

6.3.4 MODIFY GEOMETRIC PROCESSING PROCEDURES TO PROVIDE FOR:

- .1 Single Pass Image Rectification (Geodetic) Product
- .2 Geocoded Map Compatibility
    - o.1 UTM Resampling as Standard
- .3 Single Pass Cubic Spline Resampling
- .4 Image Co-ordinate File for GCPs
- .5 Relative GCPs
- .6 Alternative Global GCP Library Build

6.3.5 PROVIDE THREE-SECTIONED POST-CALIBRATION DYNAMIC RANGE

6.3.6 MODIFY IMAGE CALIBRATION PROCEDURE TO PROVIDE FOR:

- .1 Non-Adjacent Channel Replacement Algorithm
- .2 Probabilistic Approach

6.3.7 PROVIDE THE FOLLOWING PRODUCTS

- ●.1 Semi-weekly Tapes of Raw Calibration Data
- ●.2 Semi-weekly "Unity" CCT-AT
- ●.3 Special "Unity" CCT-AT of Calibration Region
- ●.4 Reprocessed "Reference" Scenes
- ●.5 History Tapes Tapes of Calibration Constants
- ●.6 Selected HDT-RT Copies
- ●.7 Extra Band(s) of Binary Data
- ●.8 Extra Band(s) of 8-Bit Data
- ●.9 Tapes at Reduced Resolution
- ●.10 Cloud-free Global TM Archive by Season
- ●.11 "Unity" HDT-AT and CCT-AT as Standard, with PCD

6.3.8 RESEARCH AND DEVELOP PROCEDURES FOR:

- ●.1 Within-Line Processing
- ●.2 Band 6 Processing
- ●.3 Ingestion of Foreign TM Tapes
- ●.4 Full Interval Radiometric Processing
- ●.5 Creation and Processing of Pre-Launch Data
- ●.6 GPS Test to Reduce Control Point Neighborhood Size

6.4 DEVELOP PROCEDURES FOR POSSIBLE CONTINGENCY EXPERIMENTS

●.1 SCIENTIFIC EXPERIMENTS

- ●.1 Lunar Radiometric Calibration
- ●.2 Stero and Bidirectional Reflectance
- ●.3 Time-of-Day Orbital Changes
- ●.4 Revisit Frequency Requirements
- ●.5 Utility of Mixed Spatial Resolution

●.2 ENGINEERING EXPERIMENTS

●.1 Band 6 Sensitivity at70 K

●.2 Focus Test on Inchworms over GCPs

●.3 Tests of Global Position System Utility

●.4 Tests of On-Board Computer Options

●.5 Alternative Lamp and Power Supply Tests

●.6 Recalibration Before and After In-Orbit Repair

APPENDIX 9.14 - KEY WORDS

Absolute Radiometry

Apparent Gain Changes

Archival TM Imagery of Globe, Recommendation

Atmospheric Peeling

Automatic Sequencer

Background from Shutter

Between-Band Gain Changes

Between-Date TM Radiometry

Between-Date Smoothing, Recommendations

Between-Scan Shifts, see Scan-Correlated Shifts

Between-Scene Gain Changes

Bidrectional Reflectance, Recommendations

Bin-Radiance Dependence

Bright Target Saturation (Recovery)

Calibration

Calibrator, Internal (IC)

Channel-Correlated Shifts, see Scan-Correlated Shifts

Coherent Noise

Contingency Experiments for TM on Landsat, Recommendations

Dark Current Restoration (DC Restore)

DC Restoration

"Droop" within a Line of TM Imagery

Dynamic Range after TM Radiometric Calibration, Post-Calibration

Engineering Model of TM, Recommendations

Error Models

Extra Band, Recommendations

Flight Model of TM

Flight Segment Operations, Recommendations

Forward/Reverse Scan Differences

Gains from Radiometric Calibration

Gain Changes with Time

Geocoded Map Compatibility, Recommendations

Geometric Information Extraction

Geometric Processing, Recommendations

Ground Control Point (GCP) Recommendations

Ground Processing for Radiometric Calibration

Histogram Equalization, Recommendations

IC, Internal Calibrator

Image Calibration, Recommendations

In-Orbit Calibration Tests, Recommendations

In-Orbit Characterization Tests, Recommendations

In-Orbit Scientific Mission Tests, Recommendations

Information Extraction

Integrating Sphere Spectral Radiances

Intensive Single Site Acquisitions, Recommendation

Internal Calibrator (IC)

Interval Processing for Radiometry, Recommendation

Irradiance Normalization

Landsat-4 Thematic Mapper Radiometry (TM/PF)

Landsat-5 Thematic Mapper Radiometry (TM/F)

Lamp States of Internal Calibrator

Light Leak in Calibration Region

Line-by-Line Corrections

Lunar Radiometric Calibration, Recommendation

Manual IC Operation, Recommendation

Modeling of Systematic Variabilities

Moon for Between-Sensor Absolute Calibration, Recommendation

Noise within a Scene

Nominal Pre-Launch IC Pulses

Offsets from Radiometric Calibration

Operational Flight Segment Procedures, Recommendations

Outgassing of Cold Focal Plane, Recommendation

"Override" Back-Up IC Operation, Recommendation

Parametric Study of Pulse Integration Width

Peeling, Recommendation for Atmospheric Removal

Pointing of TM Sensor Off-Nadir, Recommendations

Point-Calibration Dynamic Range

Post-Launch, see In-Orbit

Pre-Launch Radiometric Calibration

Probabilistic Image Calibration, Recommendation

Products, Recommendations

Pulse from Internal Calibrator

Pulse Averaging

Pulse Integration

Pulse Location

Radiometric Information Extraction

Radiometry of Thematic Mapper

Radiance-to-Reflectance Conversion, Recommendation

Recommendations for TM Radiometric Calibration

Reduced Spatial Resolution of TM Products, Recommendation

Redundant Power Supply

Regression for Linear Radiometric Calibration

Relative Radiometric Calibration

Replacement Algorithms for Defective Channels, Recommendations

Scan-Correlated Shifts

Scan Direction, see Forward/Reverse-Scan Differences

"Secondary" Light Pulse in Calibration Region

Shifts of TM Background, Scan-Correlated

Spectral Information Extraction

Spectral Radiance

Stereo TM Imagery, Recommendation

Systematic Radiometric Corrections for TM Sensor

Temperature-Dependence of IC Pulse

Thematic Mapper (TM) Radiometric Calibration

Time-of-Day Orbital Experiments, Recommendations

TM Engineering Model, Recommendations

TM Flight Model (TM/F) on Landsat-5

TM Image Processing Facility (TIPS), Recommendations

TM Proto-Flight Model (TM/PF) on Landsat-4

TM Radiometry

Total Noise of TM Sensor

Unbiased Pixel Calibration, Probabilistic Approach

Variability in TM Radiometry

Within-Line Bright Target Saturation (Recovery)

Within-Line Droop

Within-Line Variability

Within-Scan Radiometry, see Within-Line

Within-Scene Error Models for TM Radiometric Variability

Within-Scene Variability of TM Radiometry

N85-21726

D2

EVALUATION OF THE RADIOMETRIC INTEGRITY OF LANDSAT 4 THEMATIC MAPPER BAND 6 DATA

John R. Schott
School of Photographic Arts & Sciences
Rochester Institute of Technology
One Lomb Memorial Drive
Rochester, New York 14623
(716)475-2783

Introduction and Background

The data from the thermal infrared channel (Band 6) aboard the thematic mapper represent the highest spatial resolution thermal information yet available from space. The radiometric response function of the thermal sensor must be carefully evaluated to permit proper interpretation of these unique data. Probably the most generally accepted method for processing radiometric data from space is to correct the observed radiance or apparent temperature to a surface radiance or temperature value using atmospheric propagation models. For example using radiosonde data from the study area at the time of an overpass the atmospheric transmission and path radiance terms (τ and W_A) can be computed using AFCRL's LOWTRAN code (Ref. 1) or NASA's RADTRA code (Ref. 2). These terms can be used to compute the surface radiance from

$$W_S = (W - W_A)/\tau. \qquad (1)$$

Where; W is the observed radiance and W_S is the surface radiance which can be associated with an equivalent black body temperature (T_S).

As part of NASA's Heat Capacity Mapping Mission (HCMM) experiment the atmospheric propagation models were used in reverse in an attempt to evaluate the post launch radiometric response of the Heat Capacity Mapping Radiometer (HCMR). Bohse et al 1979, describe how surface radiometric readings were used in conjunction with radiosonde data to predict the radiance at the top of the atmosphere using atmospheric propagation models. Surface data taken with a point radiometer viewing a lake were averaged to define W_S and the atmospheric propagation models were used to define and W_A at the time of the overpass. Therefore the radiance observed by

Original photography may be purchased
from EROS Data Center
Sioux Falls, SD 57198

PAGE III-220 INTENTIONALLY BLANK

PRECEDING PAGE BLANK NOT FILMED

the spacecraft sensor W' and the radiance calculated from the model ($W = \tau W_S + W_A$) should be identical. In fact for the five dates studied the difference in observed and predicted values ranged from 4.15 to 6.14°C with an average difference of 5.24°C (radiance values have been converted to equivalent blackbody temperatures). As a result of these analysis, NASA offset the prelaunch calibration values for the sensor by -5.5°C and applied this offset to all standard HCMM products (Ref. 4).

This offset was based on the assumption that the sensor response and/or the calibration standard had somehow changed since the prelaunch calibration. Subsequent studies five months later conducted in an identical fashion indicated that the offset should be moved back toward the original value by 3.3 to 7.7°C (Ref 5). This would essentially nullify the original offset. If we accept the initial premise of a shift in the HCMR response function we must now speculate on the possibility of long term drift in the sensor calibration. An alternative and perhaps more acceptable hypothesis is that the atmospheric propagation models are inadequate and part or all of the variance is associated with changes in the atmosphere insufficiently accounted for by the models.

Whether the sensor or the models were at fault - the fact remains that - the radiometric calibration of the data was seriously in question. Both the actual radiance reaching the sensor and surface radiance values generated by processing the raw data were in doubt.

Lest these same doubts plaque the thermal data from Landsat 4, it is imperative that the radiometric response function of the sensor be carefully evaluated after launch using reliable experimental data. Since nearly all users have a requirement for surface radiance data it is also essential that the atmospheric propagation models be more carefully evaluated and refined as preprocessing algorithms. This paper describes a program to experimentally evaluate the radiometric calibration of the Landsat 4 band 6 data. This approach draws on a method employed by Schott and Schimminger, 1981 as part of the HCMM experiment to radiometrically calibrate the HCMR data. Schott and Schimminger 1981 successfully utilized an approach to radiometric calibration of HCMR data that involved underflying the satellite with an infrared line scanner. This approach enabled calibration of the satellite sensor to within 1°C of surface temperature values. By extending this technology to higher altitudes experimental radiance data suitable for radiometric calibration of the TM band 6 sensor can be generated. Repetition of this experiment will permit evaluation of long term drift in the sensor and provide a data base for the second phase of the program.

The second phase of the experiment involves evaluation of the atmospheric propagation models for radiation transfer. Along with the underflight data from phase one, radiosonde data (suitable for input to the propagation models) will be available. The propagation models can be used to predict atmospheric transmission and path radiance values as a function of altitude and at slant paths to the satellite. These same values are derivable from the empirical data gathered during the underflight. By comparing these values it should be possible to begin to evaluate any systematic errors in the models. During this phase modifications to the models based on systematic errors and/or additional surface truth data will be evaluated. If sufficiently accurate models can be defined then underflight data would not be required for continued evaluation of sensor performance. In addition satellite data could be preprocessed to produce direct surface radiance or equivalent temperature images.

TECHNICAL DISCUSSION

Data collection for this effort involves an extension of techniques successfully used to radiometrically calibrate the HCMM sensor. We will briefly describe the HCMM experiment and use this as a base for describing the evaluation of the TM band 6 sensor. To account for atmospheric effects we utilized a model involving collection of ground truth simultaneously with satellite data collection. Great care must be taken to insure that ground truth data for a satellite sensor represents the true integrated surface radiance or temperature over the entire projected instantaneous field of view (IFOV) of the sensor. To accomplish this large areas of uniform temperature are employed -- usually water bodies. However most water bodies have significant variation in them such that integration of the temperature or radiance pattern observed is often desirable. To accomplish this on the HCMM experiment the satellite sensor was underflown with an infrared line scanner to image large areas at different temperatures. Fractions of the imaged areas could then be registered with satellite pixels and integrated to provide corresponding radiance fields (cf., Figure 1). These radiance data however are degraded by the atmosphere between the aircraft and the ground. These atmospheric effects are accounted for by a method described by Schott 1979 which involved flying the aircraft at a series of altitudes over the same target areas. This method yields the atmospheric transmission term "τ" and the path radiance term "W_A" at flight altitude and therefore permits computation of the surface radiance W_S or equivalent temperature T_S for any target imaged at the flight altitude. This method was extensively tested in blindfold experiments which showed a standard error of 0.4°C between the temperature predicted from the aircraft data and independently observed at the surface. By employing this method the true surface temperature or equivalent surface radiance of an area imaged by the aircraft and the satellite was defined by analysis of the apparent temperature observed by the aircraft. By regressing the observed radiance at the spacecraft against the true surface radiance the atmospheric transmission and path radiance terms affecting satellite data can be determined from

$$W_0 = \tau W_S + W_A. \qquad (2)$$

Where W_0 is the observed radiance at the satellite. In practice a range of targets largely separated in temperature provide the best fit to equation 2. The spring thermal bar in the Laurention Great Lakes provides this temperature range admirably with large areas of the lake surface (tens of km^2) differing by as much as 10 to 12°C.

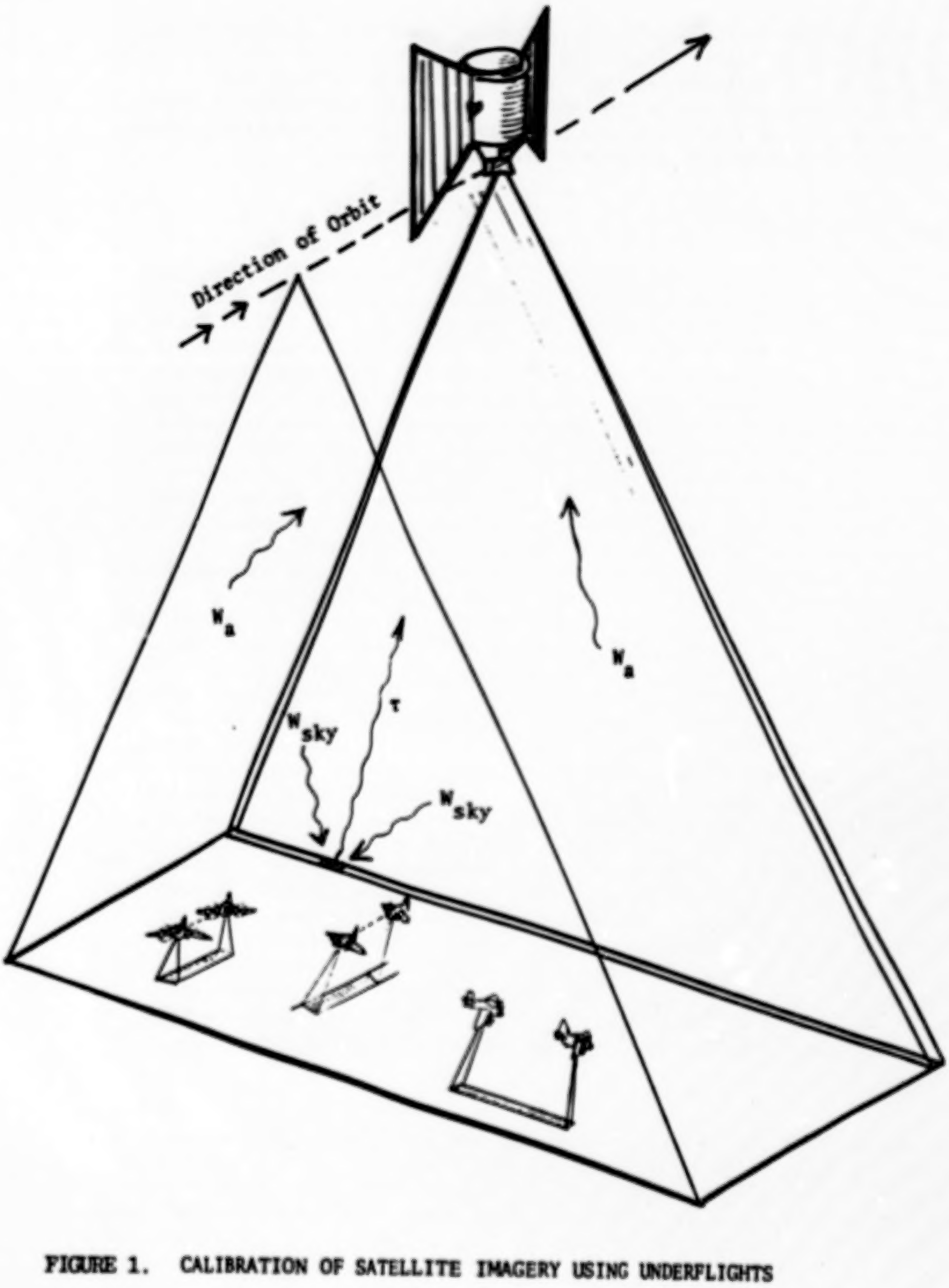
Direction of Orbit
W_a
W_a
τ
W_{sky}
W_{sky}

FIGURE 1. CALIBRATION OF SATELLITE IMAGERY USING UNDERFLIGHTS

The approach described above was applied to the thermal infrared data from the HCMR. In addition radiosonde data were used to run the LOWTRAN and RADTRA models and predict surface temperatures. Figure 2 is a graphic display of the results of these analyses. This figure illustrates that the experimental underflight method checks against itself as expected but that neither of the atmospheric propagation models very effectively predicted surface temperature values. This experiment yields a suitable means of absolute calibration of a satellite thermal infrared sensor when appropriate underflight data are available. It does not however provide insight into whether the satellite response calibration or the propagation models or both are at fault in the LOWTRAN and RADTRA approaches. (N.B., Because the underflight method employs ground truth it does not require a calibrated sensor, only a linear response function; i.e., it only requires that observed radiance be linear with true radiance).

The method described above can be modified to permit empirical analysis of the radiance reaching the spacecraft. The airborne sensor has been filtered to match the spectral response of the TM band 6 sensors. Therefore the atmospheric transmission and path radiance terms computed for each altitude are the same terms that affect the satellite data. By flying the aerial sensor at several altitudes up to or approaching the top of the atmosphere the effective propagation terms can be directly measured or simply extrapolated with the aid of radiosonde data (cf., Figure 3). Previous studies over the target area indicated that nearly all the atmospheric effects took place below 7 Km.. This is within the range of the turbo charged Aztec C which is being used for data collection. With the atmospheric propagation terms defined in this manner the radiance reaching the satellite can be defined for any targets imaged both by the satellite and the aircraft. The satellite sensors post launch performance can then be evaluated by comparing the observed satellite radiance to the radiance values known to be incident on the sensor. Through repetitive measurements the presence of drift or the existence of any systematic shift in system performance will be verified. Since many points are available for comparison between the satellite and the aerial images the functional relationship between the radiance recorded by the satellite and the actual radiance should be definable. Thus any corrections required to affect post launch shifts in system response will be defined.

Radiosonde data collected in the study area will be accessed for each underflight. These data are used to generate atmospheric propagation terms using the models sited above. The propagation terms generated by the models and the experimentally derived terms will be evaluated to determine if the models are adequate for sensor evaluation and preprocessing of radiometric data.

As necessary, further effort will be directed at defining and developing corrections to the atmospheric propagation models to bring them into agreement with experimental data. If these models can be sufficiently improved then the method used in the attempt at validating the HCMM calibration could be used for TM band 6 verification. In addition the models could be used to preprocess TM band 6 data to provide actual surface radiance or surface temperature images.

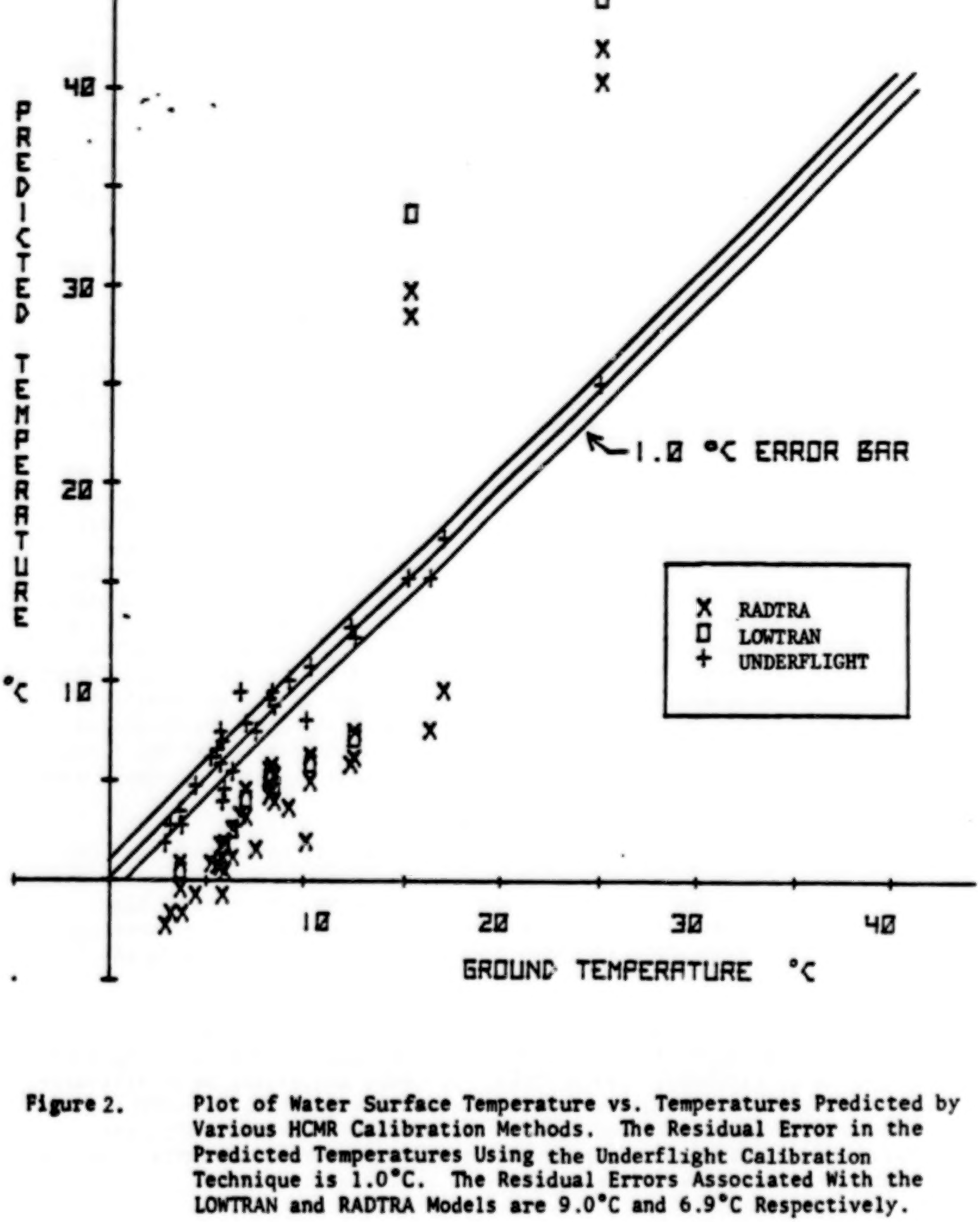

Figure 2. Plot of Water Surface Temperature vs. Temperatures Predicted by Various HCMR Calibration Methods. The Residual Error in the Predicted Temperatures Using the Underflight Calibration Technique is 1.0°C. The Residual Errors Associated With the LOWTRAN and RADTRA Models are 9.0°C and 6.9°C Respectively.

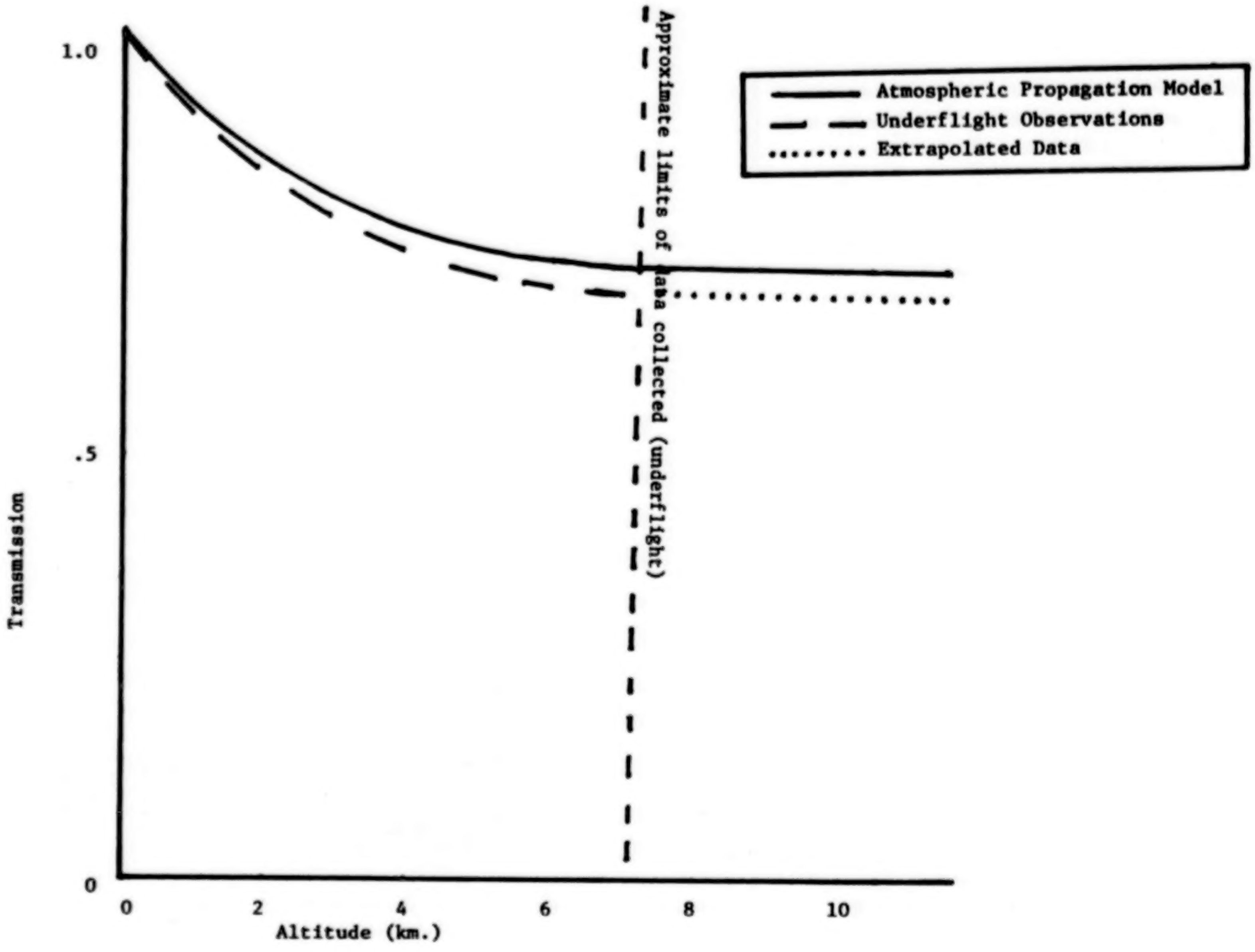

Figure 3. Idealized Plot of Atmospheric Transmission as a Function of Altitude

The models will be evaluated using the underflight data. The underflight data can be used to observe the atmospheric transmission (τ) and path radiance (W_A) at each altitude sampled. In addition by interpolation through the models described by Schott 1979 the transmission and path radiance terms to any altitude and at various angles can be computed. The atmospheric propagation models are also capable of interpolating within the radiosonde data to provide transmission and path radiance data as a function of altitude and view angle. Therefore, an extensive data base will be developed for comparing the data derived from the atmospheric propagation models to the empirical data. Through statistical analysis of these data, corrections to the propagation models can be inferred. Analyses of the various underflight data sets obtained will provide information on the effects of varying atmospheric conditions on the model performance. This added dimension will enable us to look for a systematic pattern to the statistical corrections derived for an individual data set. Using these data we will attempt to develop corrections to the models either in the form of corrections to the model's coefficients or refinements to the theoretical approach. The systematic corrections developed in this manner will be applied to the satellite data and compared to the known surface radiance values derived from the underflight data. Again, these results will be analyzed to determine if the revised models are suitable for evaluation of the radiometric calibration of TM band 6 and also therefore suitable for preprocessing of the band 6 data.

To date, efforts have concentrated on modification of the infrared line scanner to match the spectral response of the TM band 6 sensor. In addition, the LOWTRAN code corresponding to a satellite overpass of September 1982 has been run to yield a plot of transmission and path radiance as a function of altitude as shown in Figure 4. When underflight data is available, the empirically observed values would be compared to these modeled values. The computed values of transmission and path radiance (0.6293, 6.005$wm^{-2}sr^{-1}$) were used to compute water surface temperature for Lake Ontario assuming unit emissivity. Figure 5 is a black and white image of the lake which has been color coded to temperature in approximately one degree steps. A quick comparison with lake wide water temperature values available for lakes Erie and Ontario indicates several degree centigrade temperature differences using this approach. A more detailed analysis on specific point temperature readings will be required to properly evaluate the potential for direct use of LOWTRAN for accurate surface temperature measurements and further evaluation of the absolute radiometric calibration of the Landsat band 6 sensor package. Future efforts will incorporate correlation with underflight empirical measurements and corrections for the emissivity and reflected sky radiance of the water. The major data collection thrust is scheduled for the spring of 1983 when the large temperature gradients in the Laurention Great Lakes will insure the availability of properly dispersed data.

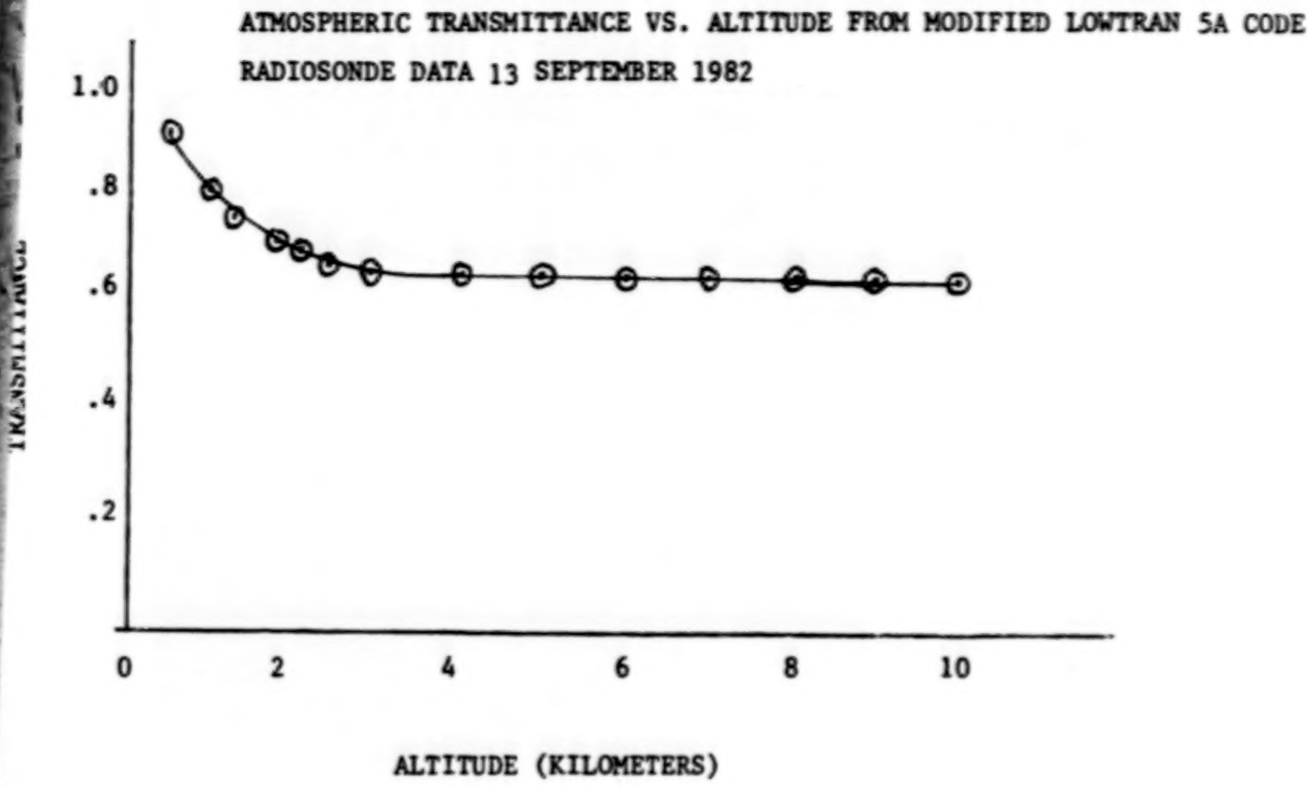

ATMOSPHERIC TRANSMITTANCE VS. ALTITUDE FROM MODIFIED LOWTRAN 5A CODE
RADIOSONDE DATA 13 SEPTEMBER 1982

****

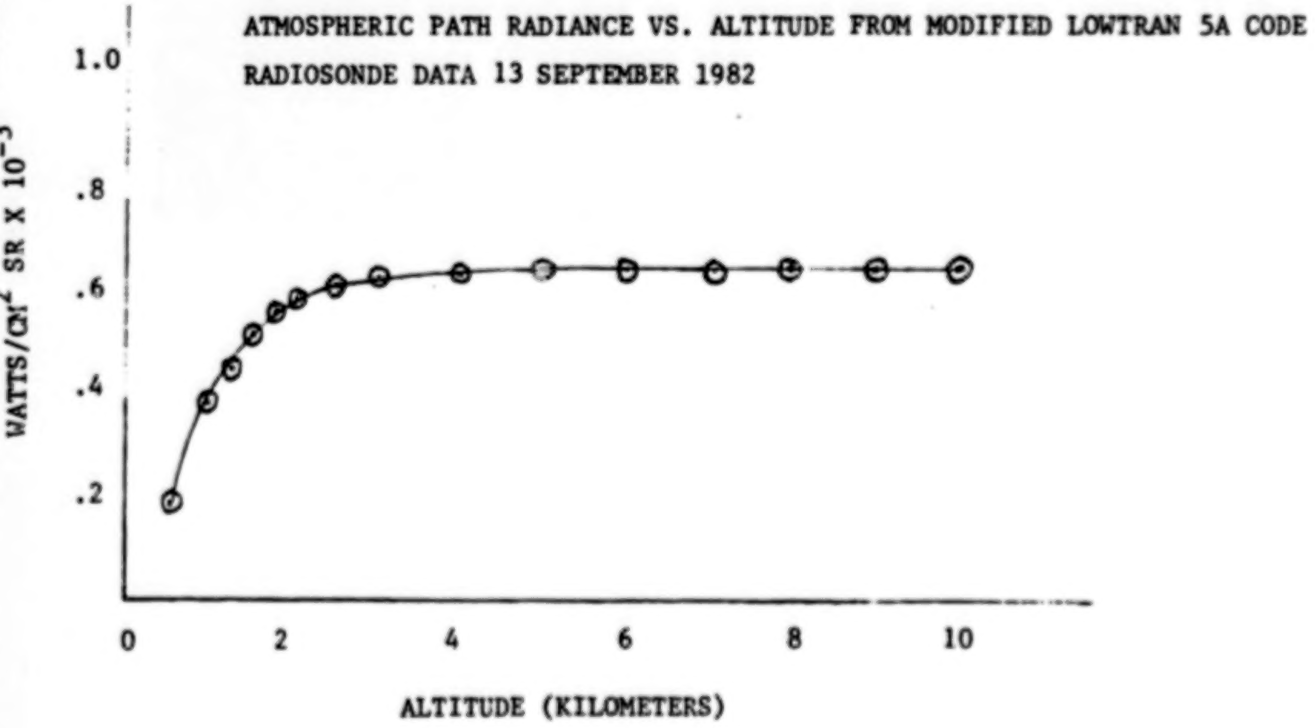

ATMOSPHERIC PATH RADIANCE VS. ALTITUDE FROM MODIFIED LOWTRAN 5A CODE
RADIOSONDE DATA 13 SEPTEMBER 1982

FIGURE 4. PREDICTED TRANSMISSION AND PATH RADIANCE VALUES FROM LOWTRAN CODE

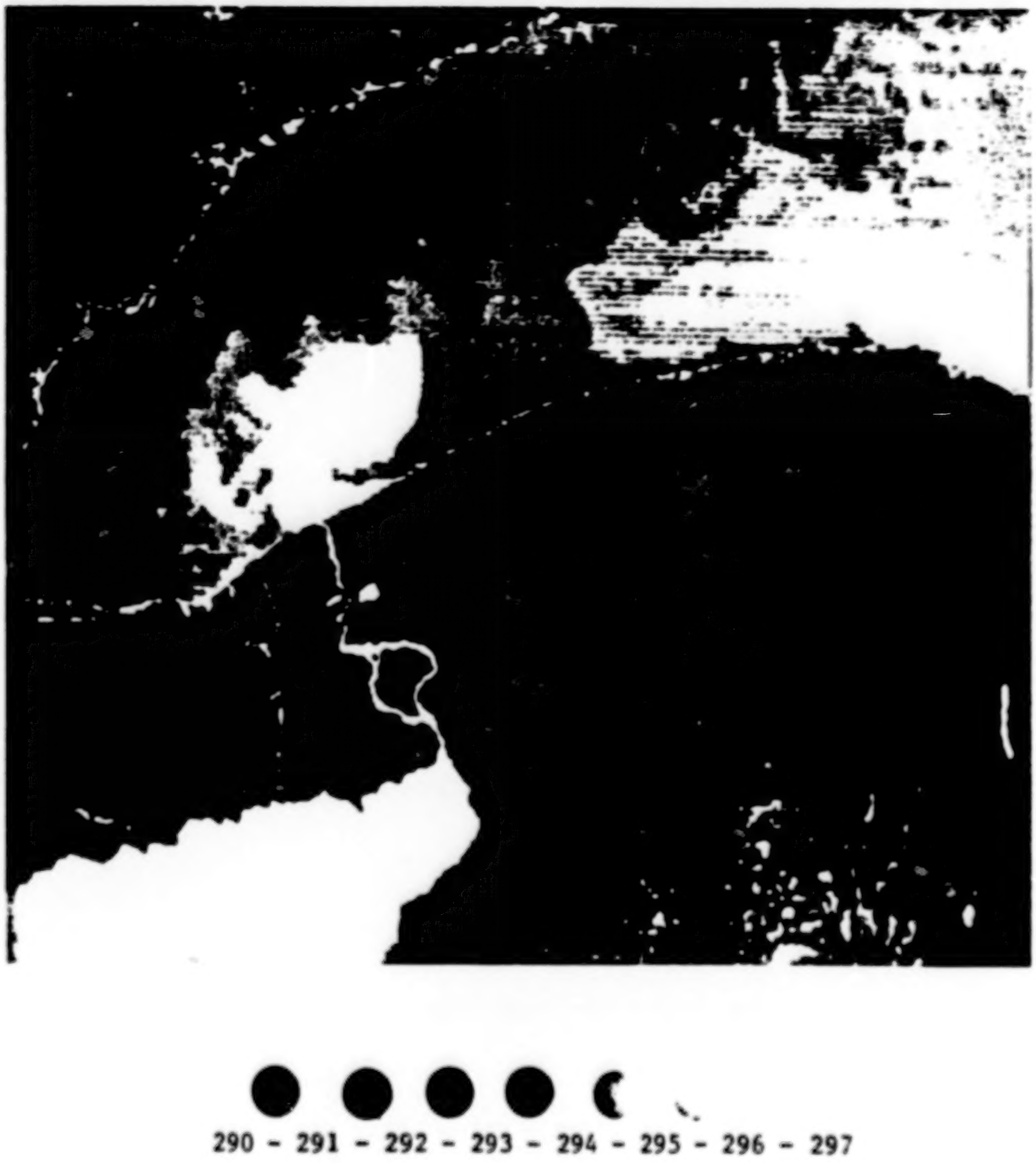
290 - 291 - 292 - 293 - 294 - 295 - 296 - 297
CORRECTED TEMPERATURE (°K)

FIGURE 5. THERMAL IMAGE OF LAKE ONTARIO FROM LANDSAT 4

ORIGINAL PAGE IS
OF POOR QUALITY

REFERENCES

1. Selby et al, 1978. "Atmospheric Transmittance". Radiance Computer Code Lowtran 4, AFGL-TR-78-0053.

2. Rangaswamg, S., Subbaragudu, J. 1978. RADTRA Program developed under contract NAS 5-2-4272.

3. Bohse, J.R., Bewtra, M. and Barnes, W.L. 1979. "Heat Capacity Mapping Radiometer (HCMR) Data Processing Algorith, Calibration, and Flight Performance Evaluation". NASA Technical Memorandum 80258.

4. . 1980. Heat Capacity Mapping Mission (HCMM) Data Usery Handbook prepared by NASA Goddard.

5. Subbarayudu, J. 1979. "Heat Capacity Mapping Mission (HCMM) Validation Study". Systems and Applied Sciences Corporation Report #R-SAG-3/79-01 to NASA Goddard.

6. Schott, J.R. and Schimminger, E.W. 1981. "Data Use Investigations For Applications Explorer Mission A (HCMM)". CAL #6175-M-1, NASA Accession #E81-10079.

7. Schott, J.R. 1979. "Temperature Measurement of Cooling Water Discharged from Power Plants". Photogrammetric Engineering and Remote Sensing, Vol. 45,NO6.

N85-21727

D3

THERMAL BAND CHARACTERIZATION OF THE LANDSAT-4 THEMATIC MAPPER

Jack C. Lansing, Santa Barbara Research Center
and
John L. Barker, Goddard Space Flight Center

Original photography may be purchased from
EROS Data Center
Sioux Falls, SD 57198

An initial characterization of the Thematic Mapper (TM) thermal band has been done and is reported here, including gain stability, gain relation to internal calibration, corrections for channel-to-channel and scan direction differences, an approximate comparison to ground truth, and a calculation of noise equivalent temperature difference. In addition, updated calibration information is presented, and is put at the start of this paper to provide definitions of terms used later.

CALIBRATION

Effective Radiance

The effective radiance at the TM aperture is defined as

$$L(T) = \int_0^\infty L_b(\lambda,T)R(\lambda,T_f)d\lambda/[\int_0^\infty R(\lambda,T_f)d\lambda] \qquad (1)^*$$

where $L_b(\lambda,T)$ is the spectral radiance of an ideal blackbody at temperature T and $R(\lambda,T_f)$ is the spectral response of the TM at cold focal plane temperature T_f. This expression was evaluated for several blackbody temperatures at each of the three T_f control points. Equations in power series form were fitted to these results which are convenient for rapid computation of L for any T and T for any L.[1]

In addition, an equation simplified from the Planck function was fitted which uses fewer constants and thus is more convenient for hand calculators where the computation time difference is not as noticeable. The equations, shown in Table 1, agree with Eq. (1) within about 0.2%. The coefficients in the table vary with focal plane temperature because the detector spectral response changes. This response was measured at 95K

---

*Symbols are summarized in a separate listing at the end of this paper.

Table 1

EQUATIONS FOR EFFECTIVE RADIANCE
IN mW cm^{-2} sr^{-1} μm^{-1} AND
TEMPERATURE IN KELVINS

$$L = a' + b'T + c'T^2 \tag{2}$$

$$T = a'' + b''L + c''L^2 + d''L^3 \tag{3}$$

$$L = K_1/(e^{K_2/T} - 1) \tag{4}$$

$$T = K_2/[\ln(K_1/L + 1)] \tag{5}$$

Focal Plane Temperature	90K	95K	105K
a'	1.771	1.827	1.950
b'	-1.916×10^{-2}	-1.965×10^{-2}	-2.071×10^{-2}
c'	5.4656×10^{-5}	5.5708×10^{-5}	5.798×10^{-5}
a"	194.06	194.89	195.39
b"	169.25	168.08	165.56
c"	-77.99	-79.21	-75.84
d"	18.927	20.05	18.15
K_1	67.162	69.527	74.571
K_2	1284.3	1293.1	1311.1

and responses at the other temperatures were estimated using typical data for the detector material. The long-wave 50% response points for the TM, including optics, are 11.95 μm, 11.75 μm, and 11.3 μm for 90K, 95K, and 105K focal plane temperatures. The short-wave 50% response point remains at 10.42 μm over the temperature range.

Calibration at Launch

Equation (6) in Table 2 represents the calibration installed at launch. Notice that the calibration is in terms of radiance at the TM aperture, thus does not include atmospheric effects, which are discussed below.

Table 2

THERMAL BAND CALIBRATION AT LAUNCH

$$L = (Q_{sc} - Q_{sh} + k_c)/G_c \qquad \text{(Q in counts)} \tag{6}$$

$$k_c = (0.9L_{sh} - 0.19)G_i \tag{7}$$

$$G_i = (Q_{cb} - Q_{sh})/(L_{cb} - L_{sh}) \tag{8}$$

$$L_{sh} = 0.4 + 0.004\,Q_{sh} \tag{9}$$

$$G_c = f_{rv}G_i \tag{10}$$

$$f_{rv} = 0.725 \tag{11}$$

Later Calibration Items

More complete reduction of thermal vacuum data after the calibration above was assembled produced additional useful information, summarized in Table 3. Equation (13) is a fit to the TM thermal vacuum test data, where two blackbodies were used as scene sources so that the time between data points could be minimized, allowing accurate determination of the shutter radiance in scene terms.

Item 2 of Table 3 is the ratio of external gain to internal gain, the variability of which may be due to slight shifts in the internal shutter position. If this is the case, greater stability would be expected in orbit, and it would be possible to estimate the value of f_{rv} from ground truth data.

Table 3

LATER CALIBRATION ITEMS

1. Effective spectral radiance at TM ($mW\ cm^{-2}\ sr^{-1}\ \mu m^{-1}$)

$$L = (Q_{sc} - Q_{sh})/G_c + L_{esh} \quad \text{(Q in counts)} \qquad (12)$$

Shutter scene-equivalent radiance

$$L_{esh} = a + bT_{sh}' \text{ (in °C)} \qquad (13)$$

Channel	1	2	3	4
a	0.516	0.497	0.502	0.498
b	0.01380	0.01512	0.01490	0.01472

2. f_{rv} varied over the range 0.69 to 0.78 in test
3. Shutter counts as a function of shutter temperature (°C)

$$Q_{sh} = 53.27 + 3.05T_{sh}' \qquad (14)$$

ORBITAL DATA STUDIES

A raw data tape of a night scene centered near Buffalo, NY, Scene ID No. 4003702243, local time 21:24, 21 August 1982, and a calibration tape of the same scene were furnished by GSFC. A digital image of the raw data had a striped appearance (as expected) because there is some difference in channel gains, but there was also a banded appearance discernible where the band size corresponded to four channel widths. This was interpreted as an amplitude difference in signal between forward and reverse scans.

Histogram Studies

Frequency histograms of quantity of pixels versus quantum level counts were made of portions of the scene. The raw scene and some lines delineating portions of it are shown in Fig. 1. The regions labeled 1000 samples use the minor frame sample rate, where thermal band data for a channel appear once in four samples. The data start at the south side for night scenes, opposite to the usual daytime scene.

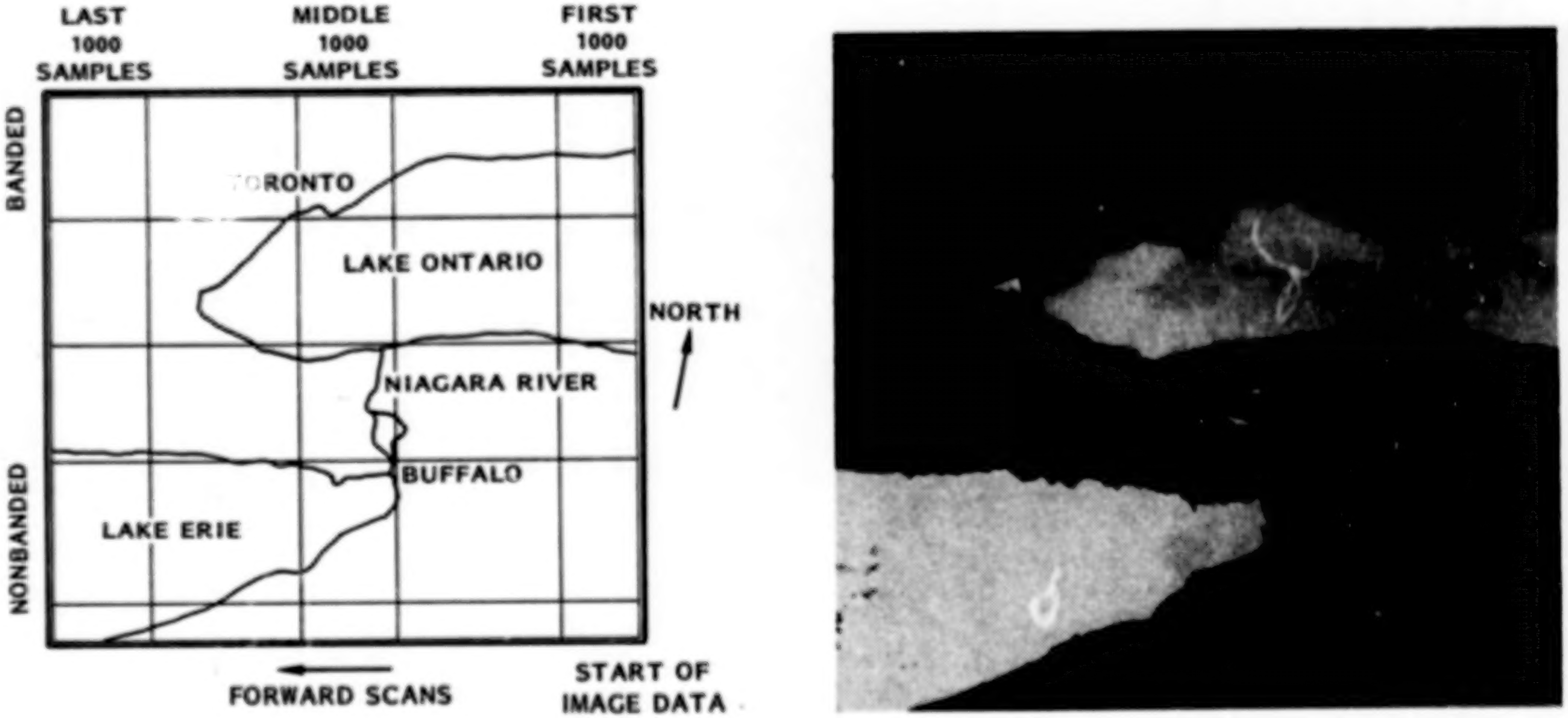
LAST
1000
SAMPLES
MIDDLE
1000
SAMPLES
FIRST
1000
SAMPLES
BANDED
NONBANDED
TORONTO
LAKE ONTARIO
NORTH
NIAGARA RIVER
BUFFALO
LAKE ERIE
FORWARD SCANS
START OF
IMAGE DATA

Fig. 1 Raw Data Image and Image Orientation Diagram. Image Data Amplitude is Stretched to 75 Counts.

ORIGINAL PAGE IS
OF POOR QUALITY

Two histograms of the region, labeled "banded" across the upper portion of the image, appear in Figs. 2 and 3. The histograms are fitted with cubic spline curves as a visual aid. The curves insert some spurious effects, such as occasional negative values in some histograms, but are useful in perceiving the pattern of the data points. Channels 1 and 4 are shown; 2 is very similar to 4, and 3 to 1.

Several effects are apparent in these figures:

1. There is a ripple from count to count. This is attributed to the fact that the switch points between levels in the quantizer are not equally spaced with regard to input analog signal level; wider spacing between two switch points will produce a greater number of samples than will a narrow spacing.

2. Reverse scans tend toward higher quantum levels than forward scans do, which could produce the banding effect.

3. Channel 4 tends toward higher quantum levels than channel 1, because of differences in gain and/or offset.

Figs. 4 and 5 show histograms for the same channels, but in the area which appeared nonbanded. These histograms are each in two sections because of the spread in quantum levels. The narrow peak near 120 counts is from Lake Erie, very warm and uniform compared to other portions of the image. In this nonbanded region there is also some tendency for reverse scans to be higher level than the forward scans, as in the banded region.

To the eye, the banding in the raw data image was brighter for forward scans than reverse, in image areas where the eye could follow the band to the serrated edge of the image and thus identify scan direction. This apparent anomaly was studied by forming histograms of subdivisions of the banded and unbanded regions, located as shown in Fig. 1, the first (for forward scans), middle, and last 1000 sample subdivisions of the regions, all four channels added together.

The results (using nonbanded as an example) in Figs. 6, 7, and 8 show a tendency for the first subdivision to have forward scan higher, but reverse scan higher in the middle and last subdivisions. A similar pattern was observed in the banded region and also in the two regions marked off in Fig. 1 between the banded and nonbanded. It so happens that the image areas where the eye could identify the direction of brighter scans were at the first of the scene, thus resolving this anomaly.

Another view of the banding pattern was formed by subtracting the signals in two succeeding scans (forward minus reverse) for each channel, averaging the differences in groups along scan and for each horizontal portion as shown in Fig. 1. The results, shown in Fig. 9, indicate some similarity in shape, but obviously other effects must be involved also.

Scene correction estimates were made of the magnitudes of differences in quantum levels between channels and between forward and reverse scans in

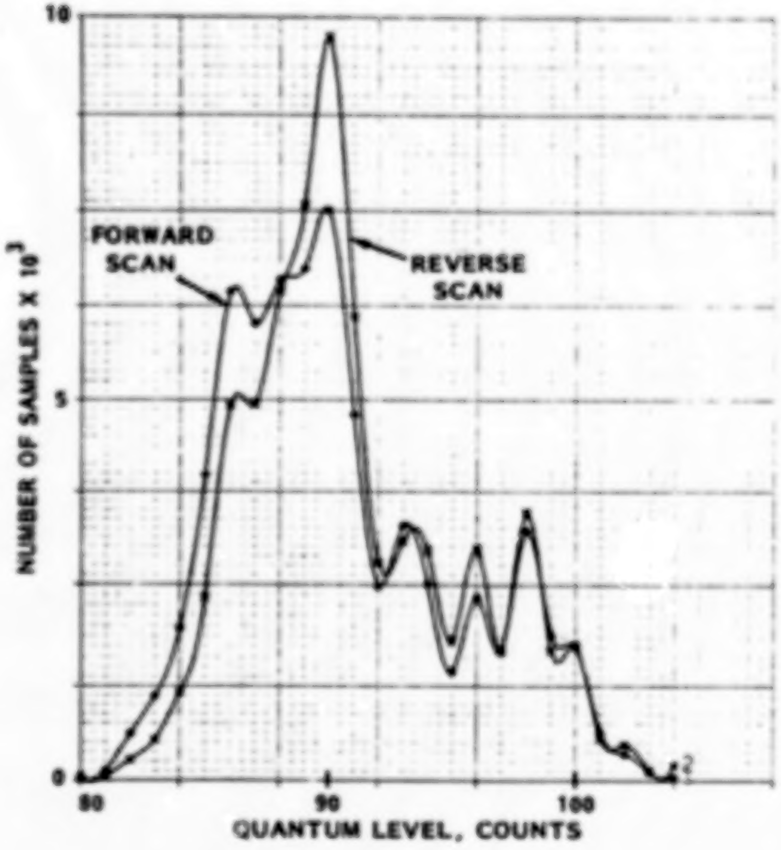

Fig. 2 Frequency Histogram, Banded Portion, Channel 1

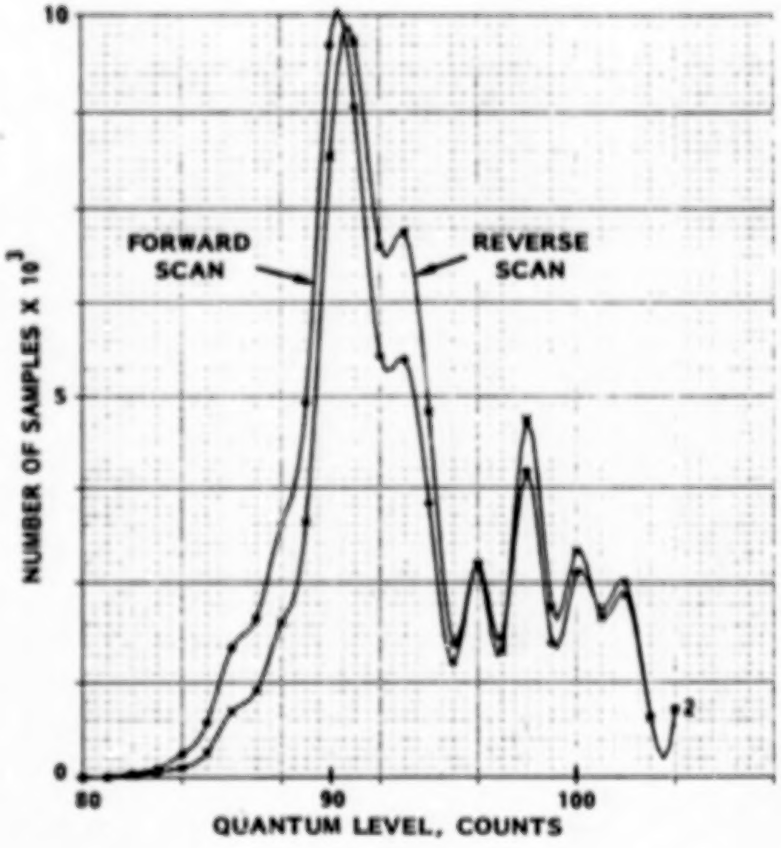

Fig. 3 Frequency Histogram, Banded Portion, Channel 4

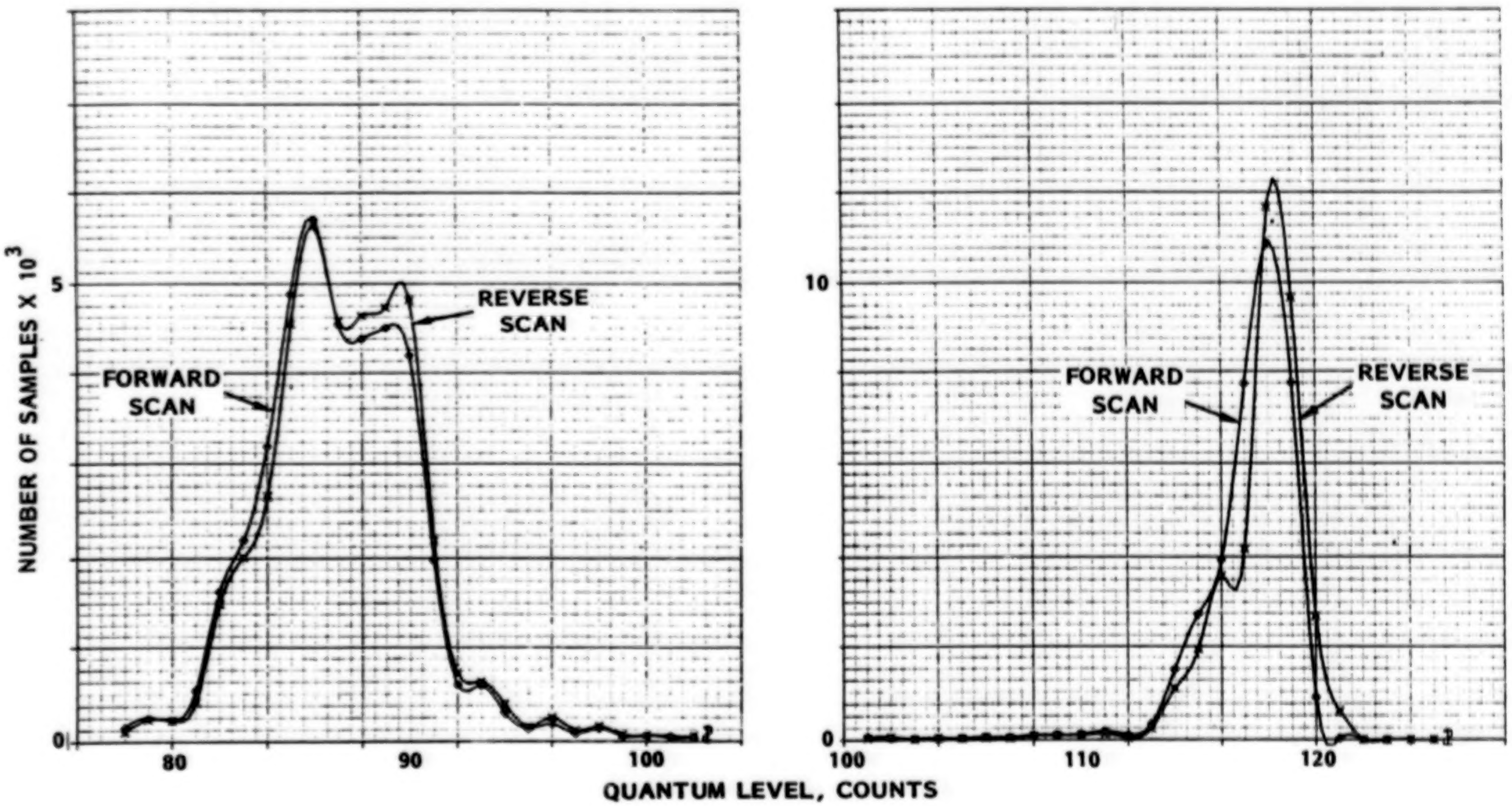

Fig. 4 Frequency Histogram, Nonbanded Portion, Channel 1

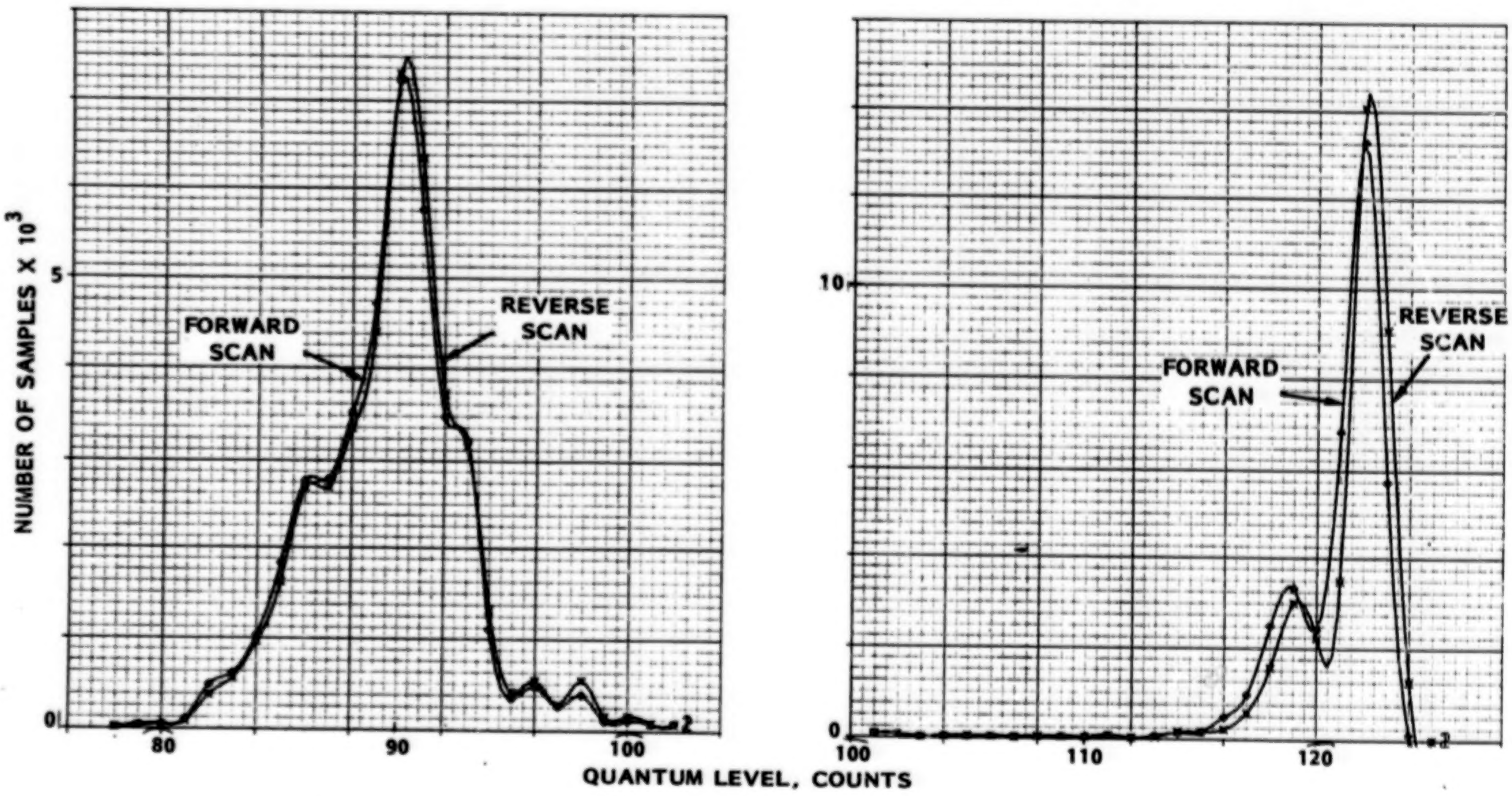

Fig. 5 Frequency Histogram, Nonbanded Portion, Channel 4

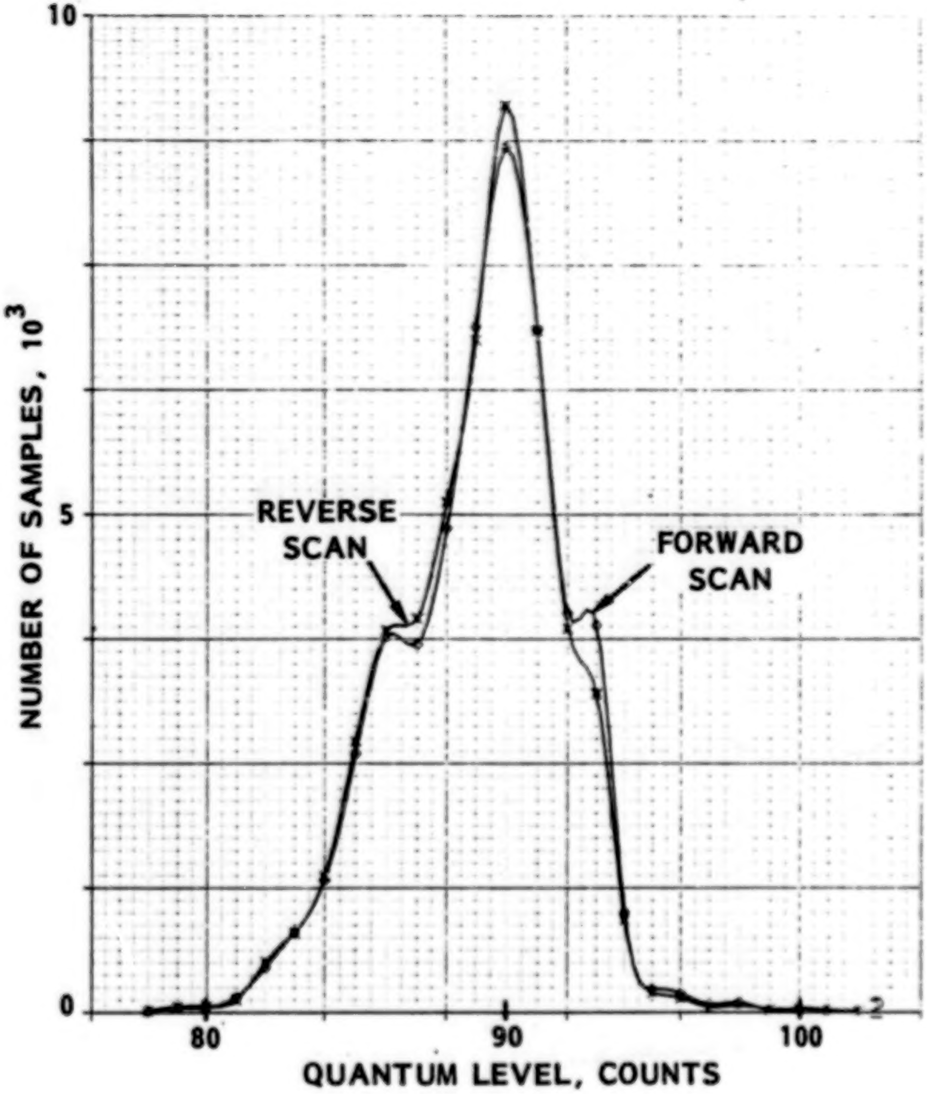

Fig. 6 Frequency Histogram, First 1000 Samples, Nonbanded Portion, All Channels

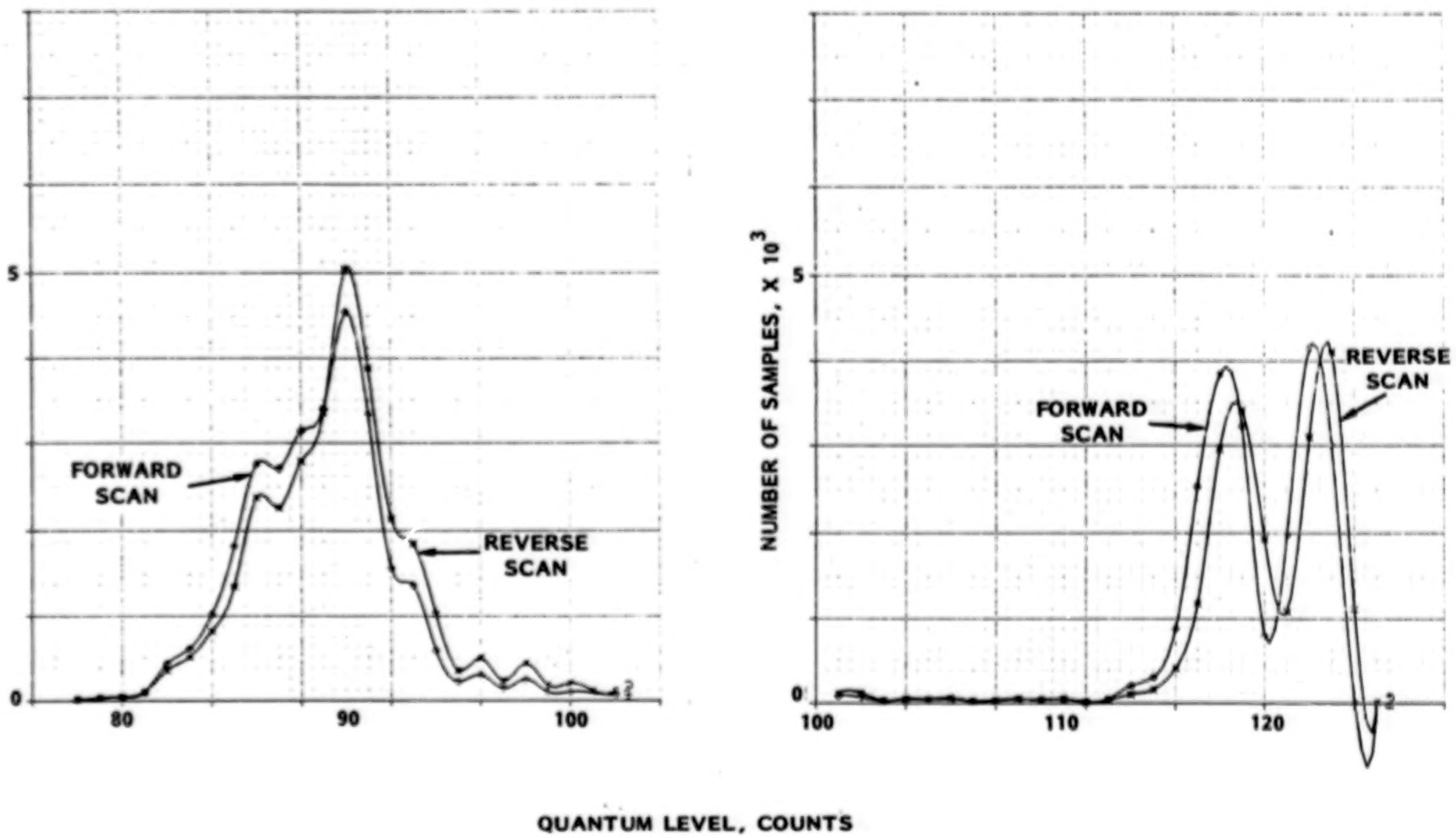

Fig. 7 Frequency Histogram, Middle 1000 Samples, Nonbanded Portion, All Channels

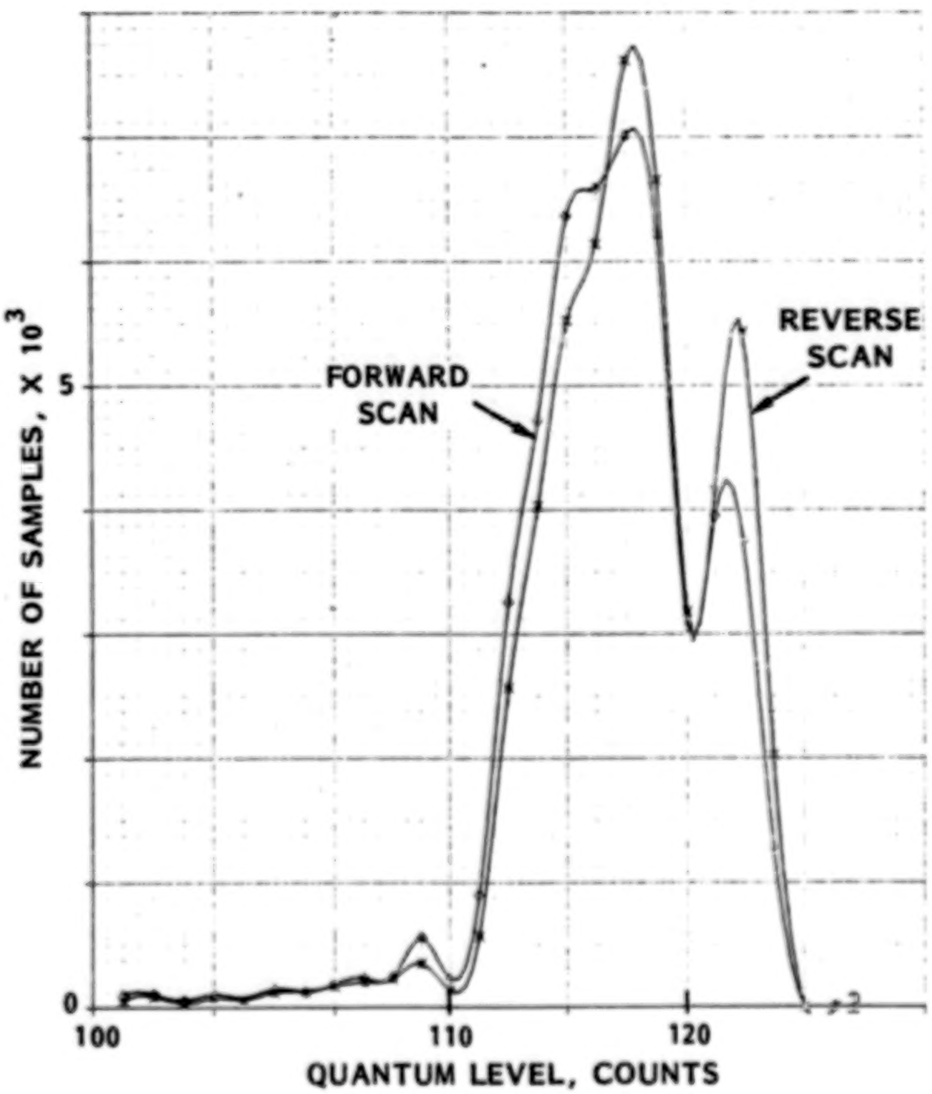

Fig. 8 Frequency Histogram, Last 1000 Samples of Nonbanded Region, All Channels

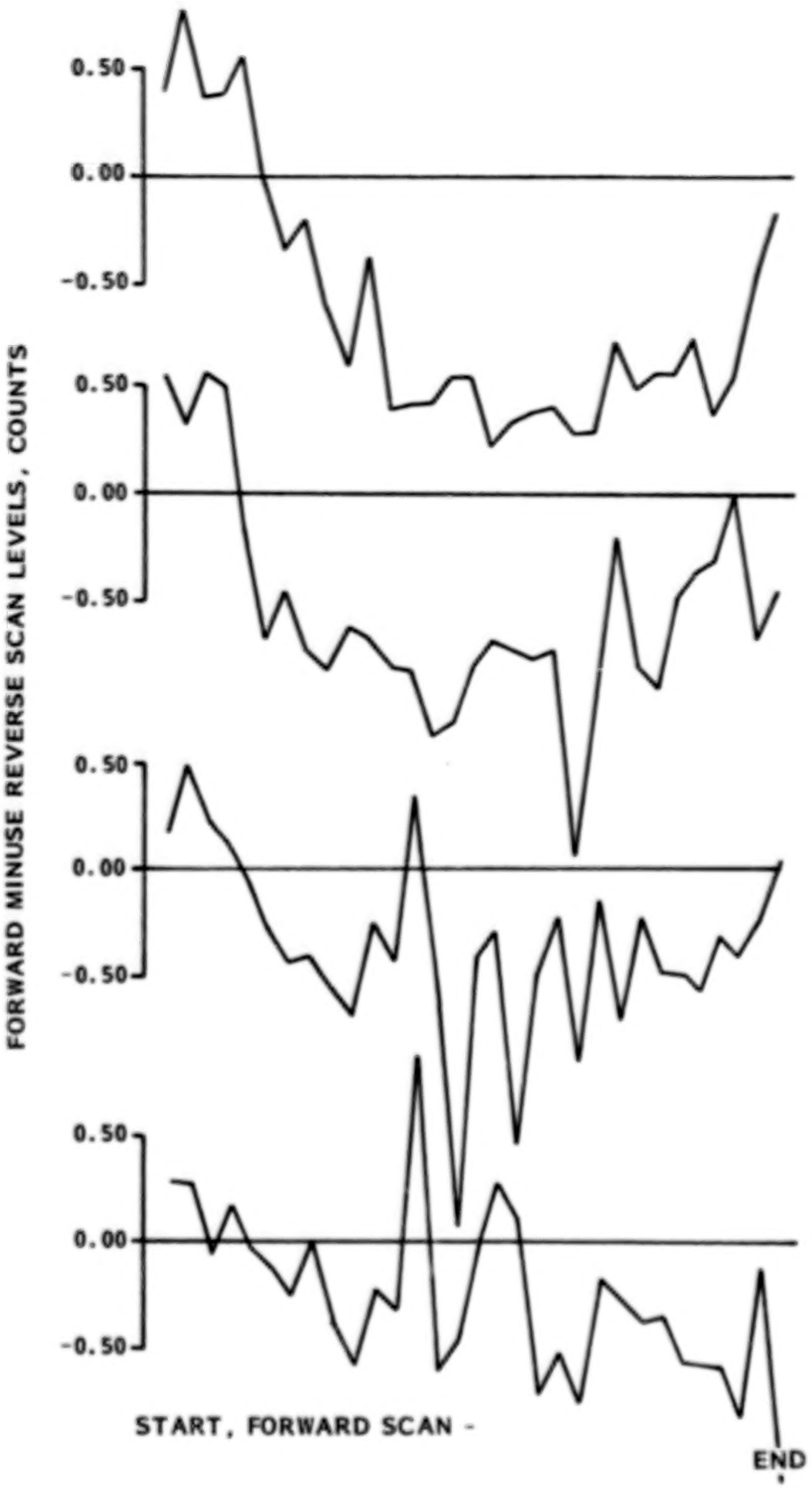

Fig. 9 Forward-Minus-Reverse Levels versus Scan Location, 200 Minor Frame Averages. Top Plot is Banded Region at North of Picture; Others are Succeeding Regions as Indicated in Fig. 1.

the various regions. The channel difference values were applied as gain and offset corrections to the raw data. The forward-reverse differences were used to estimate a fixed offset to be applied to the first 1000 pixels in all forward scans, and another fixed offset to be applied to all pixels after 1200 of all forward scans. A digital image of the data thus operated on showed a need for small changes in the corrections. A few iterations of the process led to the set of gains, offsets, and forward-reverse corrections shown in Table 4, and to the image of Fig. 10.

Table 4

EMPIRICAL CORRECTIONS FOR BUFFALO SCENE

Step 1. For Each Pixel

Corrected scene counts

$$Q_{scc} = (Q_{sc} - Q_{sh})/G_{rel} - Q_{of} + Q_{ref}$$

Approximate mean shutter counts

$$Q_{ref} = 78$$

Channel	1	2	3	4
G_{rel}	0.989	1.002	0.966	1.008
Q_{of}	-1.2	+1.6	-0.7	+1.5

Step 2. For Forward Scans Only

First 1000 pixels:	subtract 0.7 count
All pixels after 1600:	add 0.3 count

SCENE RADIANCE CALCULATIONS

Calculations of ground radiance in the Buffalo night scene were done based on the updated calibration with adjustment for the channel-to-channel differences obtained in the studies of striping just described. The atmosphere, which has a strong variable influence in this spectral region, was estimated from rawinsonde data taken within 3 hours of the TM data, at Buffalo.

Gain and Offset

The gain of the channels was calculated using Eq. (8) and (10) and the results are shown in Table 5. Quantities are shown for the two extreme values of f_{rv} observed in test. The average of gain G_c over the four channels was multiplied by relative gain G_{rel} as determined from the Buffalo scene (Table 4) to obtain the renormalized gain G_c'. The ratio of this value to G_i is the renormalized f_{rv}'.

The offset was calculated by first calculating the scene-equivalent effective spectral radiance of the shutter L_{esh} from Eq. (13). Then the offset in counts estimated from the Buffalo scene (shown in Table 4) was divided by the renormalized gain G_c' to put the offset in radiance units, which was then added to L_{esh} averaged over the channels to give renormalized L_{esh}'.

ORIGINAL PAGE IS
OF POOR QUALITY

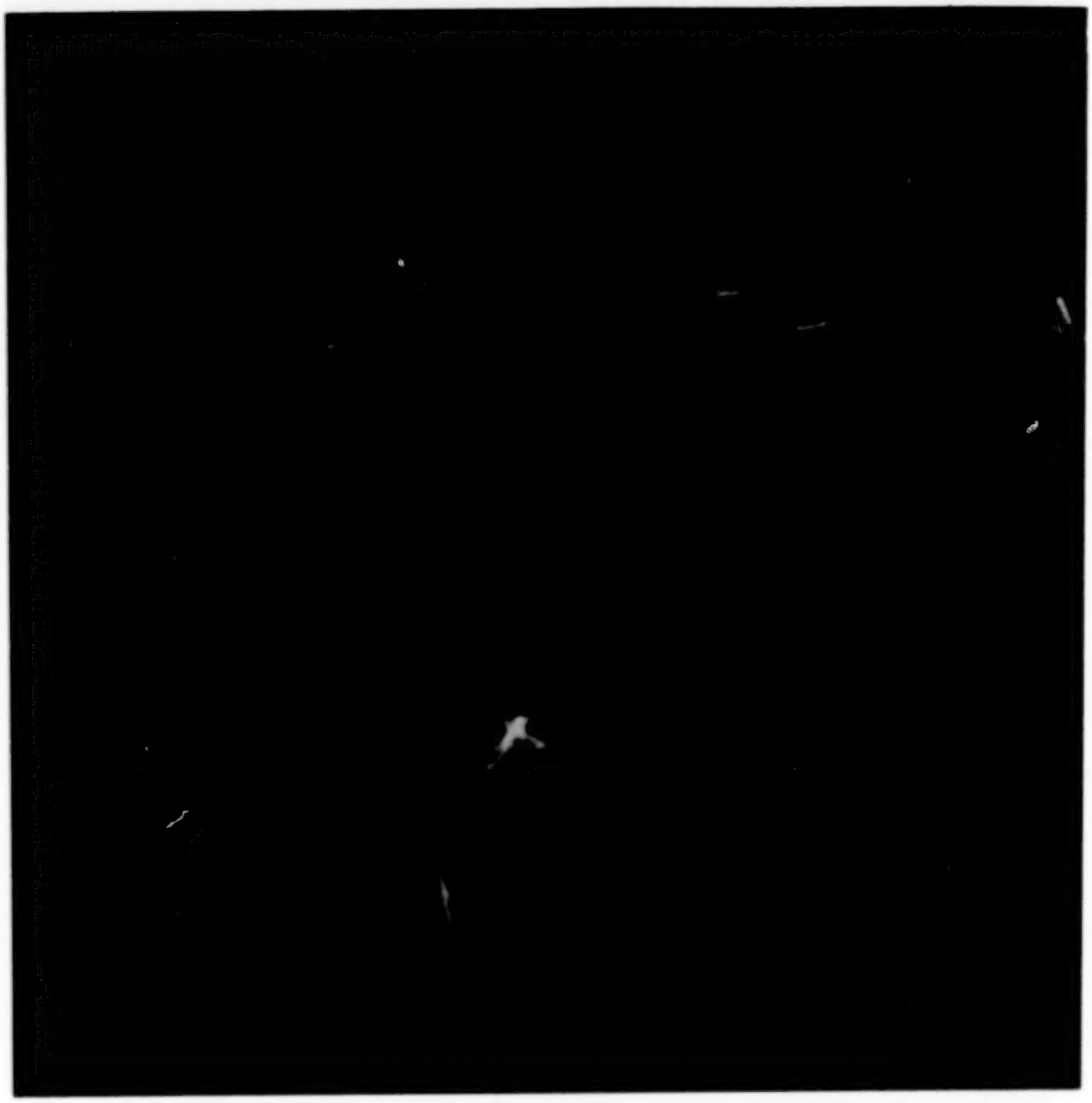

Fig. 10 Buffalo Scene with Correction

Table 5

GAIN AND OFFSET CALCULATIONS FOR BUFFALO SCENE; Q IN COUNTS, L IN mW cm^{-2} sr^{-1} μm^{-1}

Channel	1	2	3	4
$Q_{cb} - Q_{sh}$	94.7	96.5	92.6	98.1
L_{cb} (34.7°C)	← 1.052 →			
L_{sh} (8.2°C)	← 0.707 →			
G_i	274.5	279.7	268.4	284.3
f_{rv}	← 0.78/0.69 →			
G_c	214.1/189.4	218.2/193.0	209.4/185.2	221.8/196.2
G_{rel}	0.989	1.002	0.966	1.008
Renormalized				
G_c'	213.5/188.8	216.3/191.3	208.5/184.5	217.6/192.5
f_{rv}'	0.778/0.688	0.773/0.684	0.777/0.687	0.765/0.677
L_{esh}	0.629	0.620	0.624	0.619
Q_{of}/G_c'	0.006/0.006	-0.007/-0.008	0.003/0.004	-0.007/-0.008
L_{esh}'	0.629/0.629	0.616/0.615	0.626/0.627	0.616/0.615

The G_c' and L_{esh}' values, together with the shutter count, Q_{sh}, can be used to generate graphs of output quantum level counts versus scene effective spectral radiance, shown in Fig. 11. These graphs show that there is more than adequate margin within the 0 to 255 count available range for the specified 260K to 320K temperature range.

Atmosphere Considerations

The variability of the atmosphere in this spectral band can be illustrated by the typical examples shown in Ref. 2, computed with LOWTRAN 5. The vertical transmittance from earth to space covers a range from 0.5 to 0.9 and the atmospheric radiance is from 0.02 to 0.5 mW cm^{-2} sr^{-1} μm^{-1}. LOWTRAN 5 was used to compute transmittance and radiance from rawinsonde data. Since those data did not include an aerosol model, cases were run with high and low aerosol standard models, namely 5 km visibility and 23 km visibility maritime models. The visibility at Rochester, NY, just east of this scene, was 20 km at this time, suggesting low aerosol for Buffalo.

Lake Erie Temperature Estimates

The quantum level counts at the higher temperature peaks in the histograms of this area (nonbanded), together with the gains and offsets in Table 5, yield radiances at the TM aperture. (See Table 6.) Subtracting atmospheric radiance and dividing by transmittance gives radiance at the surface. Equation (2) gives the corresponding temperature. The results

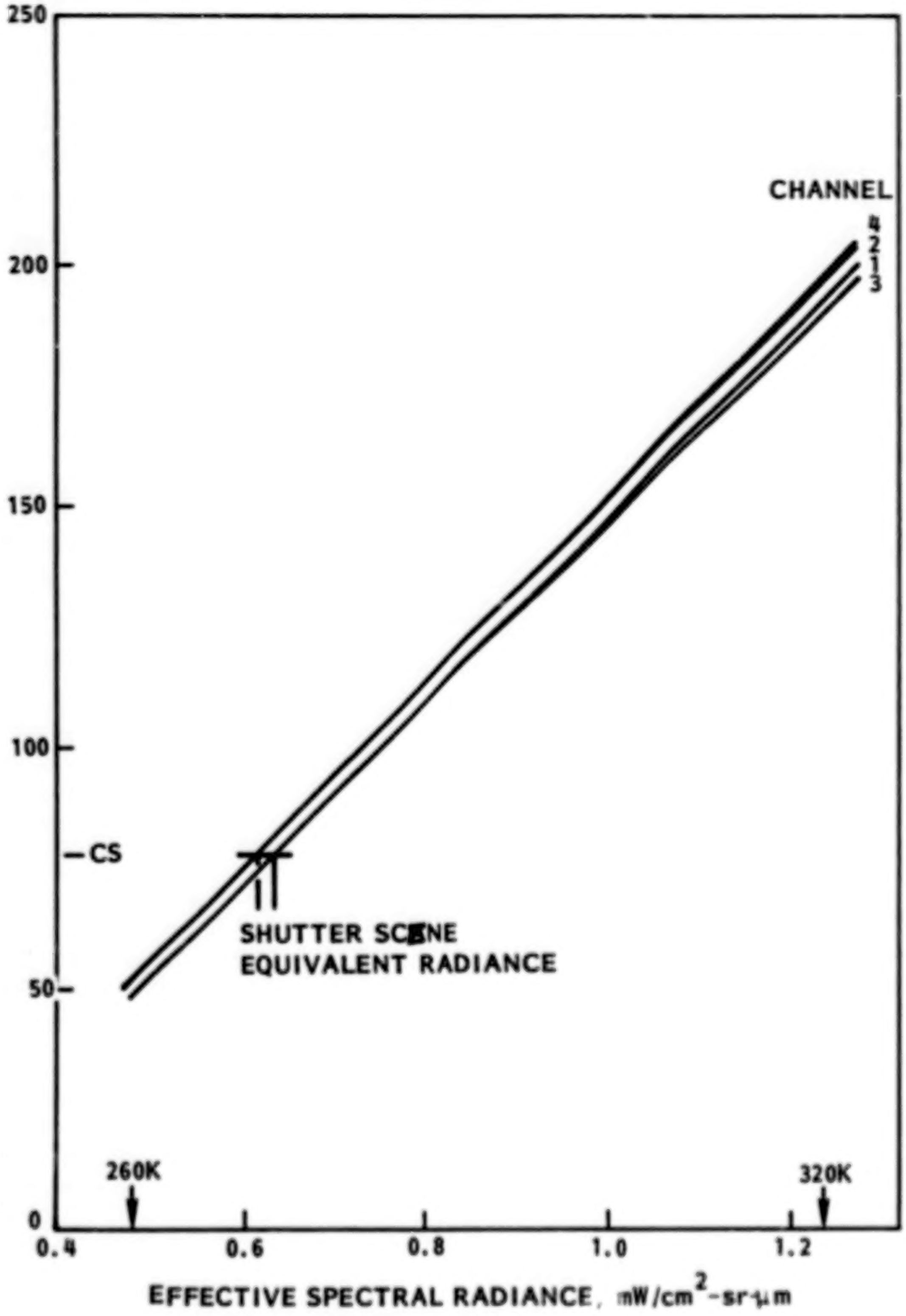

Fig. 11 Thermal Band Output versus Input Estimated from Calibration Data with Channel-to-Channel Adjustments from Buffalo Scene

Table 6

LAKE ERIE TEMPERATURE ESTIMATE; Q IN COUNTS, L IN mW cm^{-2} sr^{-1} µm^{-1}

Channel	1	2	3	4
Q_{sc}	118.2	122.0	117.7	122.0
L_{sc} at TM	0.817/0.842	0.819/0.845	0.816/0.842	0.818/0.844
High Aerosol Atmosphere Transmittance	← 0.765 →			
L_a	← 0.122 →			
L_{sc} at Surface	0.908/0.941	0.911/0.945	0.907/0.941	0.910/0.944
Calculated Temperature, °C	24.3/26.8	24.6/27.1	24.3/26.8	24.5/27.0
Low Aerosol Atmosphere Transmittance	← 0.823 →			
L_a	← 0.106 →			
L_{sc} at Surface	0.864/0.894	0.866/0.898	0.863/0.894	0.865/0.897
Calculated Temperature, °C	21.0/23.3	21.2/23.6	20.9/23.3	21.1/23.5
Surface Records Temperature, °C	21			

as shown in Table 6 are in the range from equal to the lake temperature, according to surface records, to 6°C higher. A provisional conclusion is that the value of f_{ry} to be used should be that producing the lower temperature, or 0.778, 0.773, 0.777, and 0.765 for channels 1 through 4.

Comparison to Other Scenes

Some data were collected from several other scenes, identified in Table 7, which can be compared to the Buffalo scene results. The relative internal gain is shown in Table 8. The first entry in Table 8 is prelaunch data from spacecraft thermal vacuum test, and the second is the Buffalo night scene. The post-launch data are also shown in graph form in Fig. 12 with least squares lines fitted. A definite time dependence is indicated. A comparison of frequency histograms from several scenes appears in Fig. 13 and is intended to simply indicate the variety of patterns encountered.

GAIN STABILITY

The thermal band gains decrease with time, as summarized in Table 9 and Fig. 14. An outgassing cycle was performed between 7 January and 13

Table 7
LANDSAT-4 TM SCENE IDENTIFICATION

Acquisition Date	Scene ID	WRS Path/Row	Area
22 Aug 82	40037-02243	030/017	Buffalo, NY
22 Aug 82	40037-16031	023/035	NE Arkansas
25 Aug 82	40040-16321	028/030	Ft. Dodge, IA
10 Sep 82	40056-14541	012/031	Boston, MA
24 Sep 82	40070-16442	030/028	Forman, ND
24 Oct 82	40100-15182	016/028	Ottawa, Canada
24 Oct 82	40100-15184	016/029	Kingston, Canada
2 Nov 82	40109-15140	015/033	Washington, D.C.
24 Nov 82	40131-17533	041/028	Mt. Hamilton, MT
8 Dec 82	40145-18082	043/034	Modesto, CA
20 Dec 82	40157-15174	013/041	Ft. Pierce, FL

Table 8
THERMAL BAND RELATIVE GAIN

Relative Internal Gain* $(CB/CS)/\overline{CB-CS}$

Scene ID	CH 4	CH 3	CH 2	CH 1
9 Mar 82 (68512)	1.055	0.973	1.004	0.969
40037-02243	1.027	0.970	1.011	0.992
40037-16031	1.027	0.971	1.012	0.990
40040-16321	1.025	0.971	1.013	0.991
40056-14541	1.025	0.970	1.013	0.992
40070-16442	1.021	0.972	1.013	0.994
40100-15182	1.022	0.976	1.010	1.000
40100-15184	1.022	0.968	1.011	1.000
40109-15140	1.020	0.974	1.011	0.996
40131-17533	1.017	0.975	1.011	1.008
40157-15174	1.009	0.972	1.009	1.011

*Current labels of channels 1, 2, 3, and 4 for ADDS calibration data have been reversed to 4, 3, 2, and 1, respectively, in apparent conformity to prelaunch thermal vacuum data on 9 March 1982.

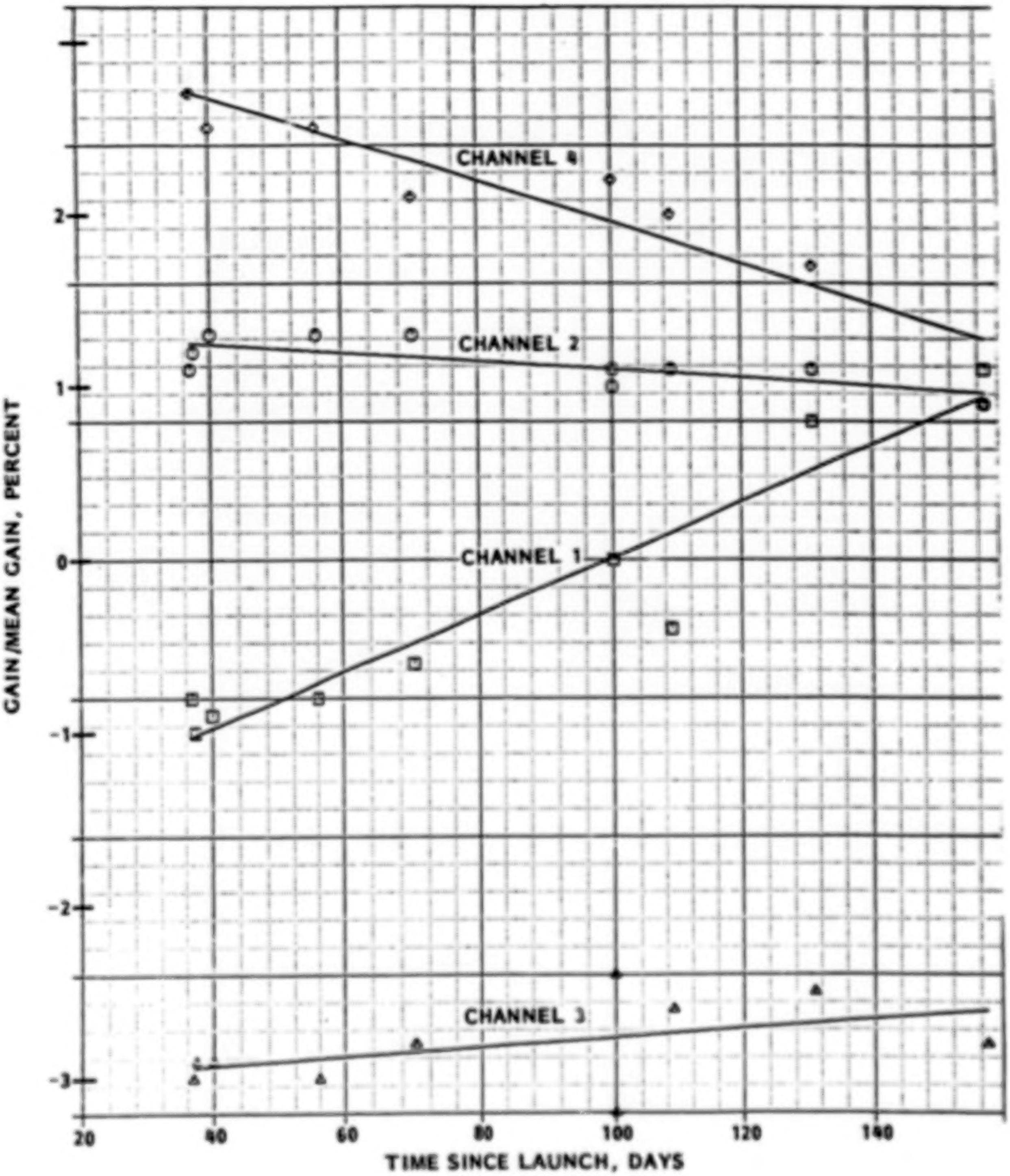

Fig. 12 Relative Internal Gain versus Time

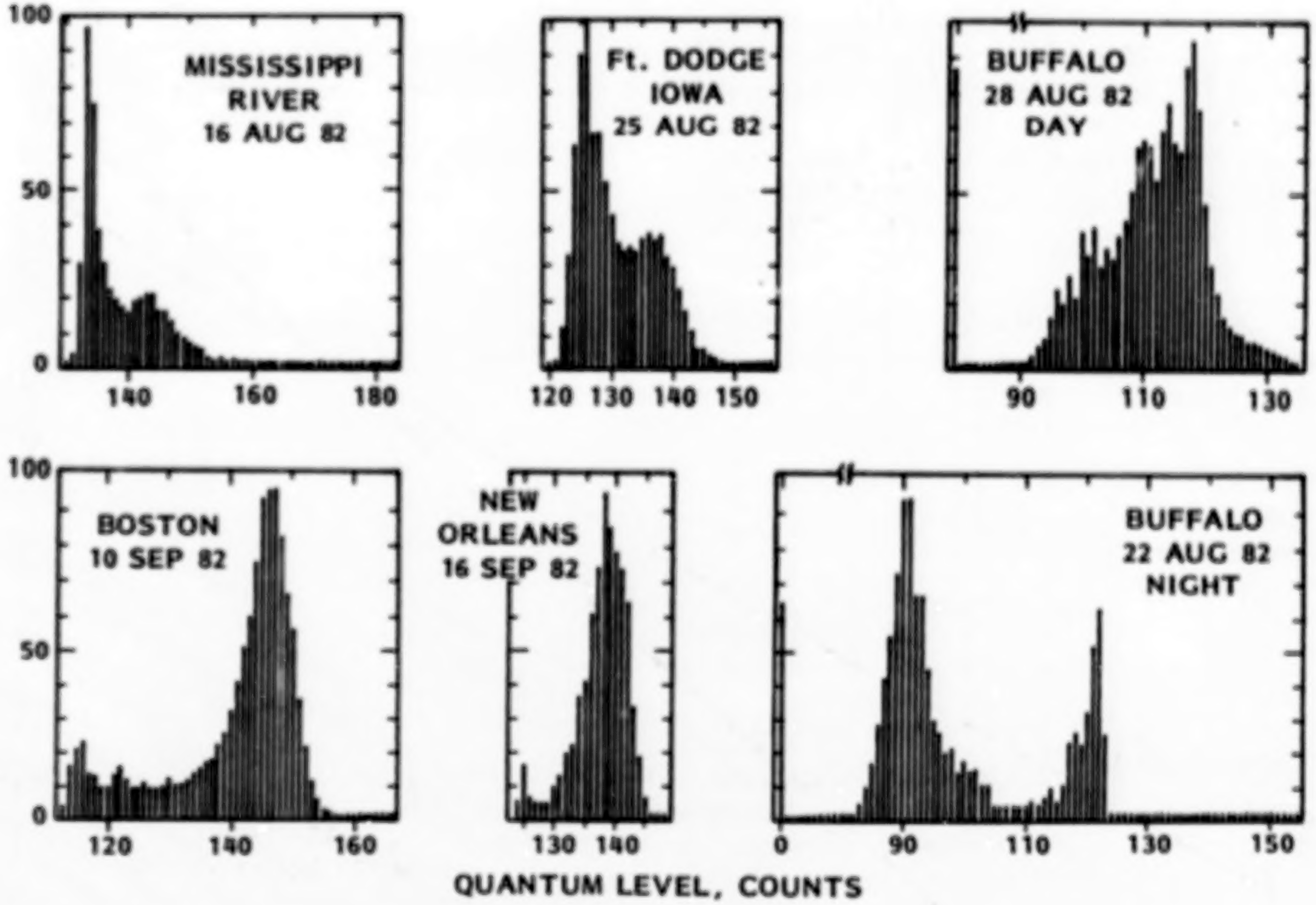

Fig. 13 Frequency Histograms from Thermal Band for Several Scenes

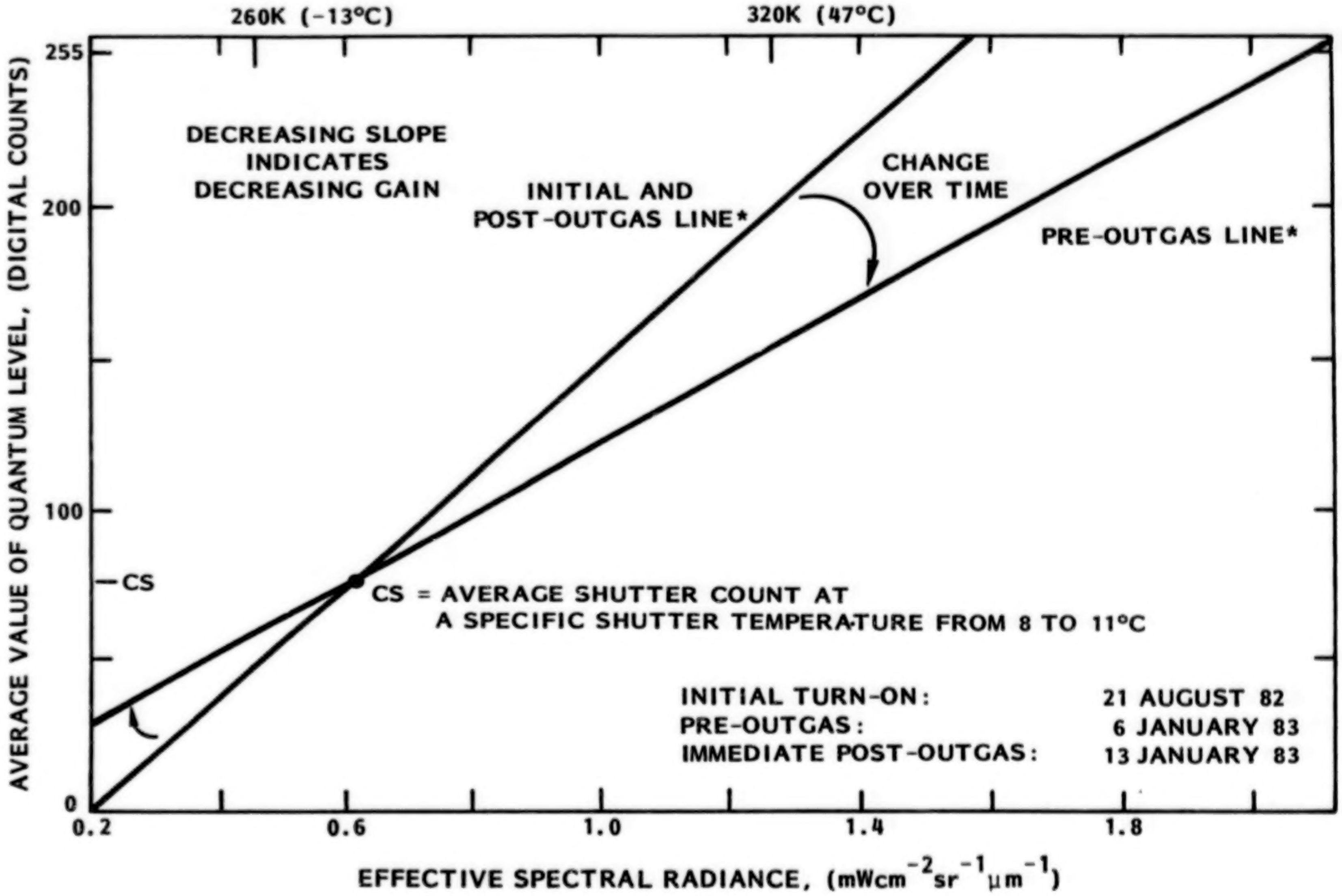

Fig. 14 Thermal Band Gain Change with Time

January 1983 to restore the gains to initial levels. Since the data were estimated to the nearest 0.1 cm amplitude on an oscilloscope, the gain as calculated from the difference between blackbody and shutter has a resolution of approximately 3%. The gain decrease is attributed to water vapor collecting on a window surface in the radiative cooler.

Table 9

LANDSAT-4 TM BAND 6 GAIN LOSS

Observed Data (On Spacecraft Control Monitor, L. Linstrom)

Day	Channel 1		Channel 2		Channel 3		Channel 4		Flag
	SH CM	BB CM	SH CM	BB CM	SH CM	BB CM	SH CM	BB CM	Temp Deg
22 Aug 82	3.1	6.9	3.1	7.0	3.1	6.8	3.1	7.8	8.2
7 Jan 83	3.4	5.9	3.4	5.9	3.5	5.8	3.5	5.8	10.7
13 Jan 83	3.4	7.2	3.4	7.2	3.4	7.0	3.4	7.3	10.7
25 Jan 83	3.2	6.9	3.2	7.0	3.2	6.9	3.2	7.0	9.5

Calculated Internal Gain (Counts per Spectral Radiance Unit)

Day	Channel 1	Channel 2	Channel 3	Channel 4
22 Aug 82	281	289	274	296
7 Jan 83	202	202	186	186
13 Jan 83	308	308	291	316
25 Jan 83	287	294	279	294

The estimated data were also used in an attempt to establish the trend of relative internal gain through the outgas time because the more precise data, as shown in Table 8, were not available after the outgas period. Each value shown is the average of 9 or 10 sets of observations. The results, shown in Table 10, indicate that the relative gains return to approximately the startup values after outgassing.

Table 10

RELATIVE INTERNAL GAIN TREND ESTIMATED FROM OSCILLOSCOPE READINGS

Period	Number of Data Sets	Time Since Startup Days	Average Relative Internal Gain			
			Chan 1	Chan 2	Chan 3	Chan 4
Startup	10	0-10	0.991	1.018	0.973	1.018
Pre-Outgas	10	90-143	1.010	1.014	0.970	1.006
Post-Outgas	9	148-177	0.994	1.015	0.970	1.021

NOISE EQUIVALENT TEMPERATURE DIFFERENCE

The noise equivalent temperature difference was calculated from an area of Lake Erie of rather uniform appearance. The boundaries of the area were selected to give equal representation to each channel and each direction of scan. The data used were a preliminary attempt at channel relative gain and forward to reverse scan corrections, so the standard deviation was computed independently for each channel and scan direction. (See Table 11.) Each of these 8 sets contains 75 data samples. The root mean square of the 8 sets is used to calculate noise equivalent temperature difference as shown in Table 11.

Table 11

NOISE CALCULATION, UNIFORM AREA OF LAKE ERIE
STANDARD DEVIATION, CT

Channel	1	2	3	4
Forward Scan	0.356	0	0.162	0.162
Reverse Scan	0.226	0.327	0.464	0.197
RMS Standard Deviation		0.272		

Noise Equivalent Temperature Difference

NETD = Std Dev/(G_c x $\partial N/\partial T$) = 0.11K (at 300K)

$\partial N/\partial T$ = Partial Derivative of Radiance with Temperature
= 0.0136 mW cm^{-2} sr^{-1} μm^{-1} K^{-1} (at 300K)

NOTATION

L	Effective spectral radiance, mW cm^{-2} sr^{-1} μm^{-1}
T	Temperature, K
T'	Temperature, °C
λ	Wavelength, μm
R	Responsivity
Q	Quantized output, counts (ct)
G	Gain, ct/(mW cm^{-2} sr^{-1} μm^{-1})
f_{rv}	Gain factor G_c/G_i
k	A constant

Subscripts

b	Ideal blackbody	i	Internal
cb	Internal calibrator blackbody	e	Scene equivalent
sh	Calibrating shutter	rel	Relative
sc	Scene	ref	Reference
f	Cold focal plane	of	Offset
c	Channel or corrected	a	Atmosphere

REFERENCES

1. L. Linstrom, unpublished draft.

2. F.X. Kneizys, et al., "Atmospheric Transmittance/Radiance; Computer Code LOWTRAN 5," Air Force Geophysics Laboratory, 21 February 1980.

N85-21728 D4

A PRELIMINARY ASSESSMENT OF LANDSAT-4 THEMATIC MAPPER DATA

D.G. Goodenough,
E.A. Fleming and
K. Dickinson
Department of Energy, Mines and Resources
Canada

INTRODUCTION

The geometric errors for image to map rectification of one Thematic Mapper (TM) scene of an area near Windsor, Ontario were studied. The scene had been produced on computer compatible tape by NASA and contained radiometric and system corrections for geometric distortions.

The role of the LANDSAT MSS and RBV sensors has been well-established for topographic map revision in Canada. (Fleming, 1981; Moore, 1982) and it is fully anticipated that satellite-derived information for map revision and change detection will form an ever-increasing part of map revision programs of the future. At present resolution levels this information is suited to the revision of 1:250,000 maps and change detection in 1:50,000 maps over approximately 30% of the country. With the increased resolution promised by the Thematic Mapper and eventually SPOT, it is hoped to increase the area of information reliability using satellite sources to between 60% and 100% of the country.

Two images from the Thematic Mapper have been examined for cartographic content. Both images fall within geographic zones that are currently classified as not suitable for the application of satellite techniques for revision purposes, one in the urban-rural area south of Windsor, Canada, and one in the prairie region of Medicine Hat.

The extraction of information relating to ground cover from digital imagery requires that the data be radiometrically as well as accurately geometrically corrected. It is essential to be able to assess the quality of these corrections before the data are analyzed. As a first step, a preliminary study of Thematic Mapper detector response has been carried out. Raw TM scenes of Vancouver Island and the sea off California were used. These scenes were received by the Prince Albert Satellite Station and transcribed to computer compatible tapes at the Canada Centre for Remote Sensing.

OBSERVATIONS

A. GEOMETRIC CORRECTION OF NASA TM DATA

A computer compatible tape was received from NASA-GSFC containing Thematic Mapper data of Windsor-Detroit (WRS track 37, row 34) imaged by LANDSAT-4 on July 20, 1982. The scene had been previously geometrically and radiometrically corrected on the LANDSAT-D Assessment System (LAS) of NASA-GSFC.

Using the CCRS Image Analysis System (CIAS) (Goodenough, 1979), we selected 27 map ground control point (GCP)-image GCP pairs spanning a 1000 by 1000 pixel area of the scene near Windsor. The scale of the map sheets was 1:50,000. GCPs were usually road intersections. An affine transformation of the image to map was derived. The root-mean-square (rms) error in the across-track direction was 32.0 m and in the along-track direction, 40.6 m. We noted a systematic effect; namely, that errors along track were consistently greater than position errors across track.

This NASA product had only geometric corrections for system errors (without GCPs) applied. It was most impressive how good a relative geometric correction had been made with LAS. It is clear that such images of flat terrain can be rectified to have errors less than 41 m. However, multitdate classification requires that these errors be less than 0.5 IFOV or 15 m for Thematic Mapper data if classification accuracy is to be improved with the additional information.

B. CARTOGRAPHIC POTENTIAL OF NASA TM DATA

1. Geometric Accuracy

Band 5 of a scene of the Medicine Hat area, imaged on November 10, 1982 (E40117-17392) was used for this study.

During the revision tests using photographic TM imagery, we found that the fit of the imagery to the map base was much better than when system corrected MSS imagery is used. In an effort to quantify the overall geometry of the Medicine Hat image relative to a U.T.M. map grid, map-based control points were identified on the photograph and their positions measured using a Wild STK-1 stereocomparator.

Thirty control points were selected, and although coordinate position determinations to within 20 m could be made from 1:50,000 maps, larger uncertainties in position result from the fact that the water levels are variable in this region and 21 of the selected points were on water-related features. Although some road intersections were better defined on band 7, band 5 provided the best overall source for control points and all identifications and measurements were made on this band.

The result of the transformation of image coordinates to map coordinates is given in Table 1.

A slight improvement in fit is noted when the affine transformation is used. However, since most people using imagery are scaling to a map using simple enlargement procedures, the residual displacements for the points after a similarity transformation to 5 points (#2 in table) is shown graphically in Figure 1. The area of large displacements in the north-west portion of the image was characteristic of all the transformations.

2. Map Information Content

Two scenes were examined for cartographic content: Band 3 of the Windsor-Detroit scene imaged on July 20, 1982 (track 37, row 34) and bands 1-7 of the Medicine Hat scene described in the previous subsection.

The image quality and cartographic information content of the Windsor area image approached that of a Skylab 190B photograph of the same area. All the road patterns mapped at a scale of 1:250,000 were clearly visible in both the semi-urban and rural areas, railways were not discernible and the land-water interface was not well-defined. Although individual rural buildings were not resolved, the difference between roads having houses or built-up areas and those on which no development had taken place, was quite obvious. Wooded areas were poorly defined.

The total topographic map content of the image with respect to cultural details fell somewhere between that contained on 1:250,000 maps and that contained on 1:50,000 maps. Such images would provide road revision information for both scales and excellent change detection capability for 1:50,000 revision planning.

About 5% of the country has similar cultural patterns to that of the Windsor area, and is a category in which LANDSAT MSS is not currently considered useful for revision purposes. Thus the availability of Thematic Mapper data would increase the boundaries of where satellite data is useful into these urban-rural areas.

The Medicine Hat images supplied in transparency form by NASA were too dense for use on the projection equipment used in revision work and it was necessary to make secondary negatives and positives, increasing by two the number of generations removed from the original image. Interpretations were confirmed by reference to the original images.

It was established that band 3 (0.63-0.69 μm), band 5 (1.55-1.75 μm) and band 7 (2.03-2.35 μm) contained cartographic information. Band 4 (0.76-0.90 μm) which should have provided a good land-water interface was lacking in contrast and did not provide any useful information.

The area covered by this photograph is prairie and rangeland dotted with numerous intermittent lakes and water storage areas. This is a geographic zone in which LANDSAT MSS is not a useful source of revision information. Detailed study of the three potentially best bands of the Thematic Mapper would lead to a similar conclusion for this sensor.

Roads and railroads were best delineated on band 5, but they were fragmentary and did not include all road classes mapped at 1:250,000. Some roads through range-land were clearer in band 7. The airport at Medicine Hat showed most clearly on band 3 but other cultural features showed up poorly. Water details were best rendered on band 5.

The determination of changes to road pattern is probably the primary consideration in evaluating revision sources for 1:250,000 mapping. If this basic requirement is not met from a satellite sensor then it is more advantageous to get all revision information from other sources. In this area of the prairies the cultivation pattern of the fields dominates, over-riding any road pattern. LANDSAT MSS fails as a revision tool for this reason and it would appear that the Thematic Mapper would likewise fail.

C. RADIOMETRIC CORRECTION OF RAW TM DATA

The scene used for this analysis was of the Vancouver Island area, imaged on November 9, 1982 (track 48, frame 26). The solar azimuth and elevation with respect to the frame centre were 158.1° and 22° respectively.

Relative gains and offsets were calculated using the method described by Strome and Vishnubhatla (1973). The calculations were based on the following equations:

$$G_K = \sqrt{\left(\frac{Q_L - P_L^2}{Q_K - P_K^2}\right)} \quad , \quad O_K = P_L - P_K G_K$$

where G_K = Relative gain of detector K

O_K = Offset of detector K

$$P_K = \frac{1}{N_K} \sum_{I=1}^{N_K} I_K\,(I)$$

$$Q_K = \frac{1}{N_K} \sum_{I=1}^{N_K} [I_K(I)]^2$$

and $G_L = 1$ = Gain of reference detector

$O_L = 0$ = Offset of reference detector

$I_K\,(I)$ = Intensity of Ith pixel for detector K

N_K = Number of pixels in sample for detector K

Throughout this paper, the G_K's are referred to as relative gains. In actual fact, G_K is the relative gain of detector L relative to detector K (or relative attenuation of detector K relative to detector L). O_K is the offset that must be added to detector K so that its zero level will correspond to detector L. Note that we use the expression in the form calibrated output is a function of uncalibrated input. This is the reverse of NASA representation, so the gains in this paper are the inverse of those in NASA papers.

The relative gains and offsets were calculated for the forward and reverse scan directions separately and detector 16 (forward scan) was used as the reference detector.

First of all, the calculations were performed on the full scene for bands 1,2,3,4,5 and 7. The results for the reverse scan direction were seen to be correlated with those of the forward direction for each band. The forward direction gains were greater than the reverse for the lower numbered detectors but smaller for the higher numbered detectors. The actual cross-over point depended on the band as follows:

- Detectors 1-6, Bands 1-4:	Forward Gain > Reverse Gain
Detectors 7-16, Bands 1-4:	Forward Gain < Reverse Gain
- Detectors 1-7, Band 5:	Forward Gain > Reverse Gain
(Detector 3 of Band 5 was dead in this scene and therefore was not included in the analysis)	
Detectors 8-16, Band 5	Forward Gain < Reverse Gain
- Detectors 1-10, Band 7:	Forward Gain > Reverse Gain
Detectors 11-16, Band 7:	Forward Gain < Reverse Gain

Figure 2 shows the results for band 4.

The same calculations were performed on subscenes of the image formed by dividing the scene into 11 non-overlapping horizontal swaths, each 500 lines deep. The number of pixels contributing to the calculation of each gain and offset was at least 82,500. An area of bad data was found to extend from line 4913 to 4927. The swath containing these lines was excluded from the analysis. The results were analyzed for bands 1 and 4.

The amount of variation of gain with swath was found to be a factor of typically 2 and 3 times greater than for LANDSAT-1 MSS, as reported by Shlien and Goodenough (1974), allowing for the difference in dynamic range between the TM and MSS sensors. The same algorithm for calculating gains and offsets was used in each case.

The amount of variation in the gain of a given detector over the scene was found to depend on the distance of the detector from its nearest reference detector in the image. As the distance from a reference detector increased, so did the amount of variation in the gain. This is shown in Figure 3 which is a plot of relative gain versus swath start line number for a subset of detectors from band 1.

A convenient way to observe this effect is to plot the range of gain for each detector versus the relative detector position, as shown in Figure 4 for band 1. The range of gain is defined to be the difference between the largest and the smallest gains obtained from the calculations for the different swaths. The relative detector position is the position of a detector relative to its nearest reference detector in the image. Thus, the relative detector positions of detectors 16 to 1 in the forward scan direction are 0 to 15 when detector 16 is the reference detector. The relative detector positions of detectors 16 to 1 in the reverse scan direction are 16 to 1 because they are closer to the next line imaged by the reference detector rather than the previous one.

The swath size was then halved; i.e. the image was divided into 22 swaths each 250 lines deep. A plot of range of gain versus relative to detector position for band 1 was generated from these results for the forward scan direction. Its shape was similar to the 500 line swath case but the spread of values of the range increased by approximately 40%, indicating considerable sensitivity in the correction algorithm for the scene content in this image.

The scene was also divided into 11 non-overlapping vertical strips, each 500 pixels wide. The number of pixels contributing to the calculation of each gain and offset was at least 85,500. The results of the gain and offset calculations were examined for bands 1 and 4. A tendency of the range of gain to increase with relative detector position was again observed. The mean intensity was also calculated for each detector and each vertical strip. The variation of mean intensity across the image was similar for each detector: a typical example is shown in Figure 5.

A comparison was made between this method for calculating gains and offsets and that used by J. Murphy (1983). The gains calculated for the same TM data were closely correlated, although those calculated by the present method tended to be shifted to higher values. It should be noted that it was necessary to invert one set of gains before the comparison could be made.

Some of the above analysis was repeated on another scene of TM data. The second scene was of California (track 42, frame 36), and had much less intensity variation than the Vancouver Island scene. The gains were calculated over the full scene for bands 1-5 and 7. The forward and reverse scan direction results showed strong correlation for each band. The forward direction gains were smaller than the reverse for all detectors; i.e.

- Detectors 1-16, Bands 1-5,7: Forward Gain < Reverse Gain

Figure 6 shows the results for band 4. Detector 10 can be seen to have significantly lower gain than the other detectors in both scenes. The dependence of the amount of variation in the gain on the distance to the nearest reference detector was not observed in this second scene. This implies that the observed variation is a scene-dependent effect.

CONCLUDING REMARKS

The geometric properties of TM photographic imagery permitted very good fitting to map detail using simple scaling techniques to localized areas and, using simple scaling, the overall geometry remained within 500 metres or 0.4 mm at the image scale of 1:1,141,600. An affine transformation, permitting differential scaling, slightly improves the fit to about 400 metres or 0.35 mm at image scale.

The imagery shows promise of having the needed additional resolution and spectral discrimination to provide map revision information in urban-rural areas where the MSS sensor is now considered inadequate. The late-season prairie image, however, did not hold such promise, and judgement must be reserved until images are acquired at other seasons in this particular geographic area.

The relative gains and offsets of TM detectors calculated over two full scenes of raw data showed correlations between the forward and reverse scan directions. It was noted that for the bands studied in one scene (bands 1-5 and 7), the forward gain was always greater than the corresponding reverse gain for detectors 1 to 6 but always less than the corresponding reverse gain for detectors 11 to 16. In a second scene studied, the forward and reverse scan direction gains again showed correlation. In this case, the forward gain was less than the corresponding reverse gain for all detectors.

The amount of variation of gain over the Vancouver Island scene was found to be larger than that for LANDSAT-1 MSS by a factor of 2 to 3, allowing for the difference in dynamic range.

The amount of variation in the gain of a given detector over the scene was found to depend on its distance from the nearest reference detector in the image. However, this effect was not observed in a second scene; one which contained considerably less intensity variation. The relative radiometric correction algorithm may be inadequate for TM scenes with large intensity variations across them.

Future work in this area includes the study of the variation in detector response with time over many scenes. The approach described in this paper must be tested by using the relative gains and offsets to radiometrically correct the data and then re-analyzing the corrected scenes. In addition, the absolute calibration of TM detectors will be studied.

REFERENCES

Fleming, E.A., "Monitoring revision requirements for Canadian maps". Proceedings of the 7th Canadian Symposium on Remote Sensing, Winnipeg, 1981.

Goodenough, D.G., "The Image Analysis System (CIAS) at the Canada Centre for Remote Sensing," Canadian Journal of Remote Sensing, 5, 3-17, 1979.

Moore, H.D., "LANDSAT increases efficiency of topographic map revision". CIS Proceedings, Centennial Convention Vol. 2, Ottawa, Canada, April 1982.

Murphy, J., W. Park and G. Fitzgerald, "Preliminary evaluation of radiometric calibration of LANDSAT-4 Thematic Mapper data by the Canada Centre for Remote Sensing". Proceedings of the LIDQA Symposium, February 22-24, 1983.

Shlien, S. and D.G. Goodenough, "Quantitative methods of processing the information content of ERTS imagery for terrain classification". Proceedings of the 2nd Canadian Symposium on Remote Sensing, Guelph, 1974.

Strome, M. and S. Vishnubhatla, "A system for improving the radiometric corrections for ERTS-1 MSS data". Proceedings, XXIV International Astronautical Congress, Baku, USSR, 1973.

TABLES

TABLE 1 Residual Displacements from UTM Control in TM Image E40117-17392(5)

FIGURES

FIGURE 1 Residual Displacements at Check Points After a Similarity Transformation to UTM Control

FIGURE 2 Gains for Band 4 Relative to Detector 16 - Vancouver Scene

FIGURE 3 Gains for Band 1 Relative to Detector 16 - Forward Scans

FIGURE 4 Range of Gain for Band 1 vs. Detector Position Relative to Reference Detector

FIGURE 5 Mean Intensity for Band 4 vs. Pixel Number for Detector 16

FIGURE 6 Gains for Band 4 Relative to Detector 16 - California Scene

TABLE 1

RESIDUAL DISPLACEMENTS FROM UTM CONTROL IN TM IMAGE E40117-17392(5)

(1:1,141,600)

TRANSFORMATION	No. of Points		RMS (X) M	RMS (Y) M	RMS (XY) M
	USED	CHECK			
1. Similarity	27		422	324	532
2. Similarity	5		394	308	501
		22	430	327	540
3. Affine	27		318	206	379
4. Affine	5		212	36	216
		22	352	256	436

RESIDUAL DISPLACEMENTS AT CHECK POINTS AFTER A SIMILARITY TRANSFORMATION TO UTM CONTROL

Landsat Thematic Mapper E-40117-17392 band 5 Medicine Hat, Alberta

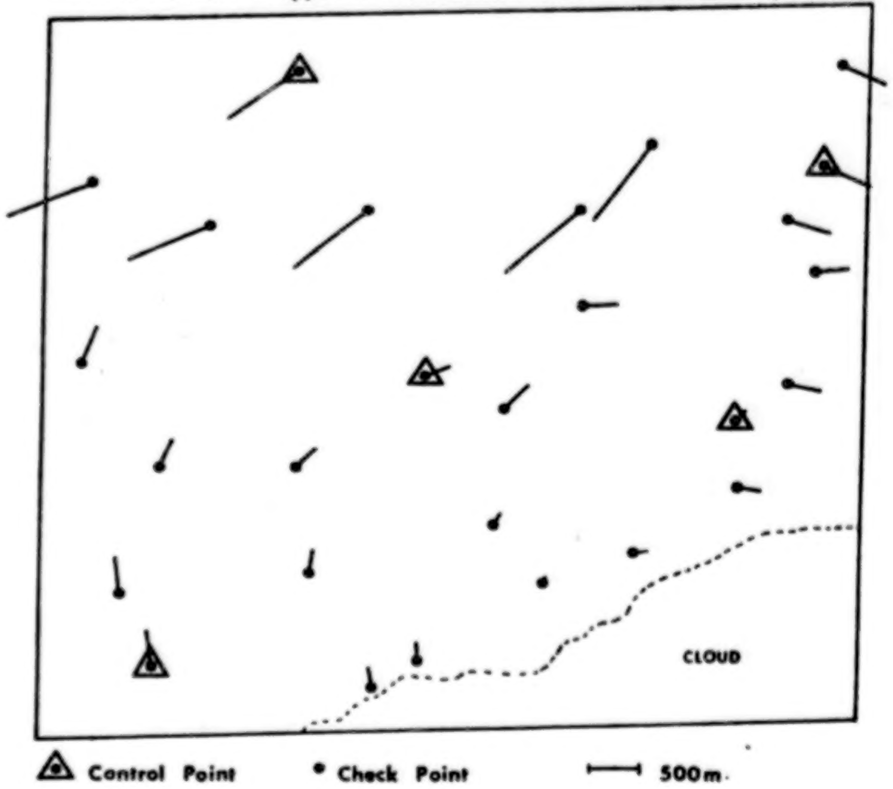
CLOUD
Control Point
Check Point
500m

Figure 1

GAINS FOR BAND 4 RELATIVE TO DETECTOR 16

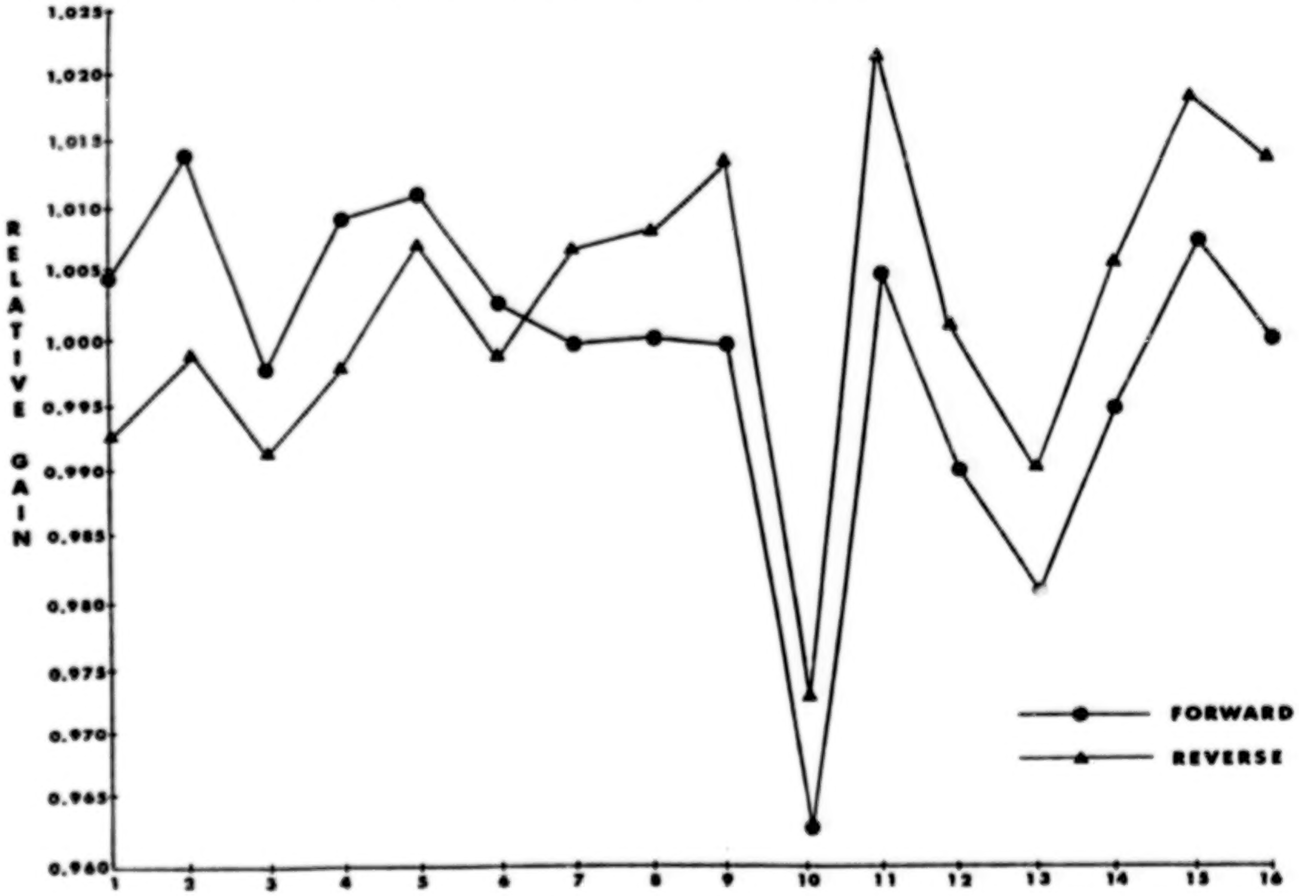

Figure 2

Vancouver Scene

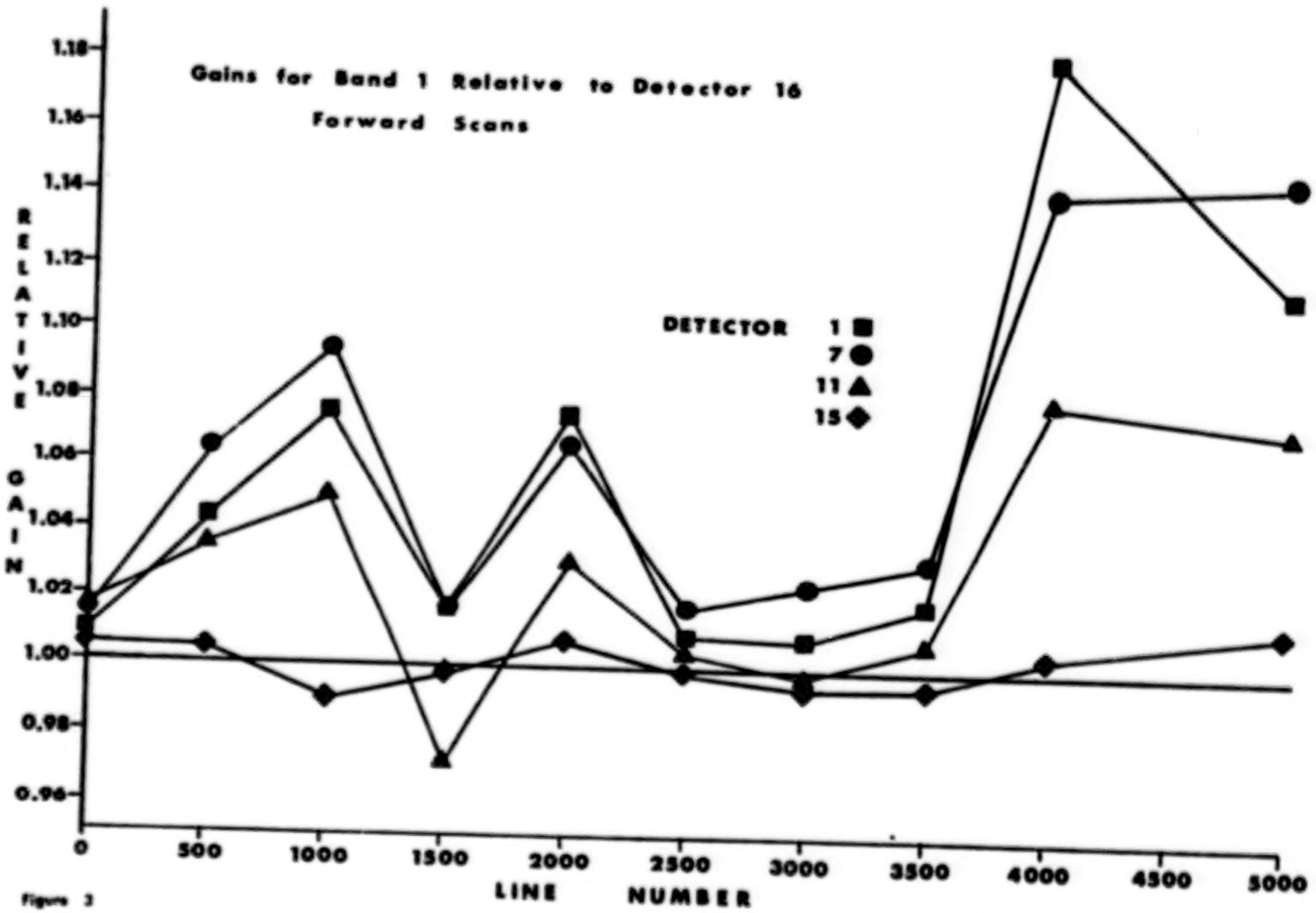
Gains for Band 1 Relative to Detector 16
Forward Scans

Figure 3

Vancouver Scene

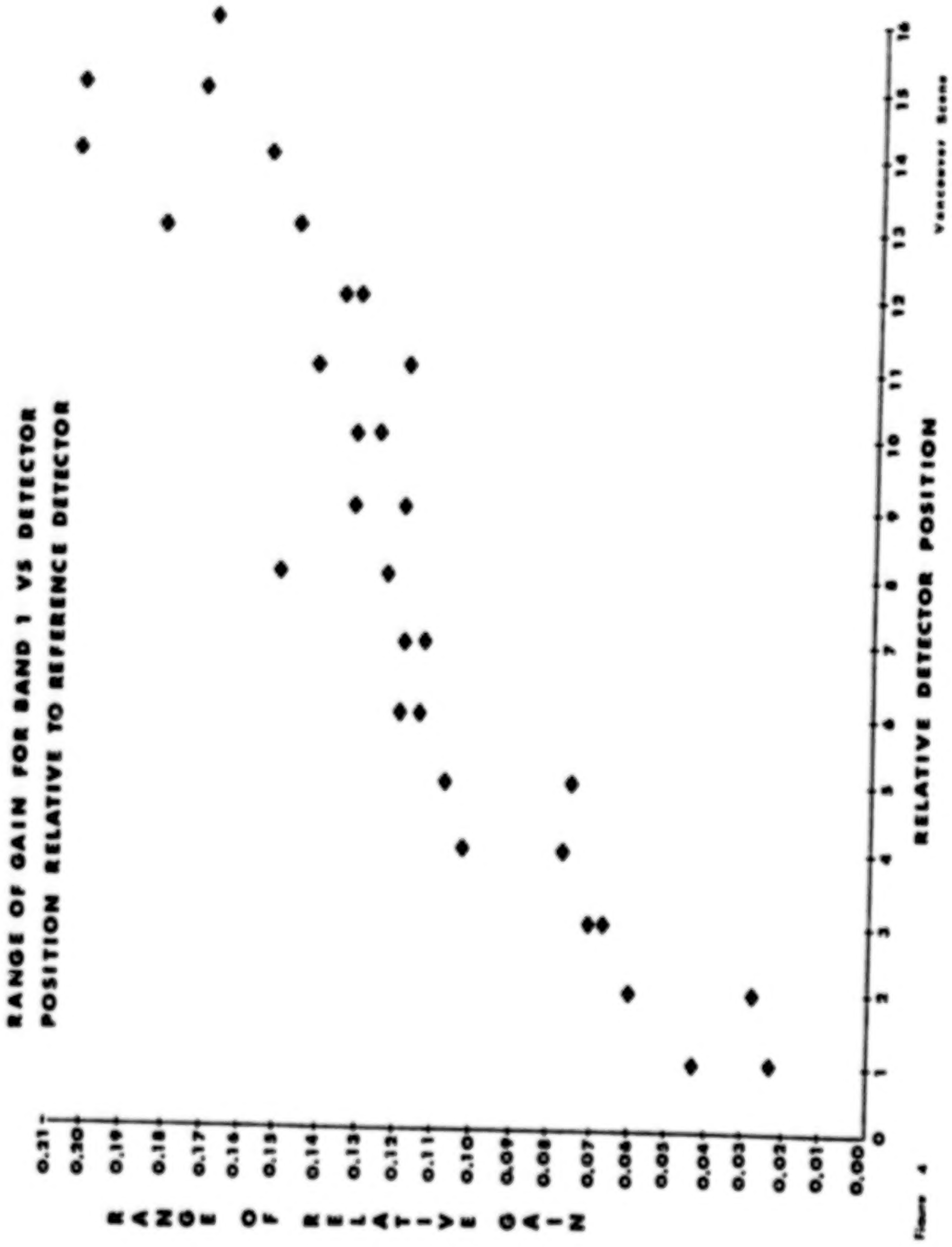

Figure 4

RANGE OF GAIN FOR BAND 1 VS DETECTOR POSITION RELATIVE TO REFERENCE DETECTOR

MEAN INTENSITY FOR BAND 4 VS PIXEL NUMBER FOR DETECTOR 16

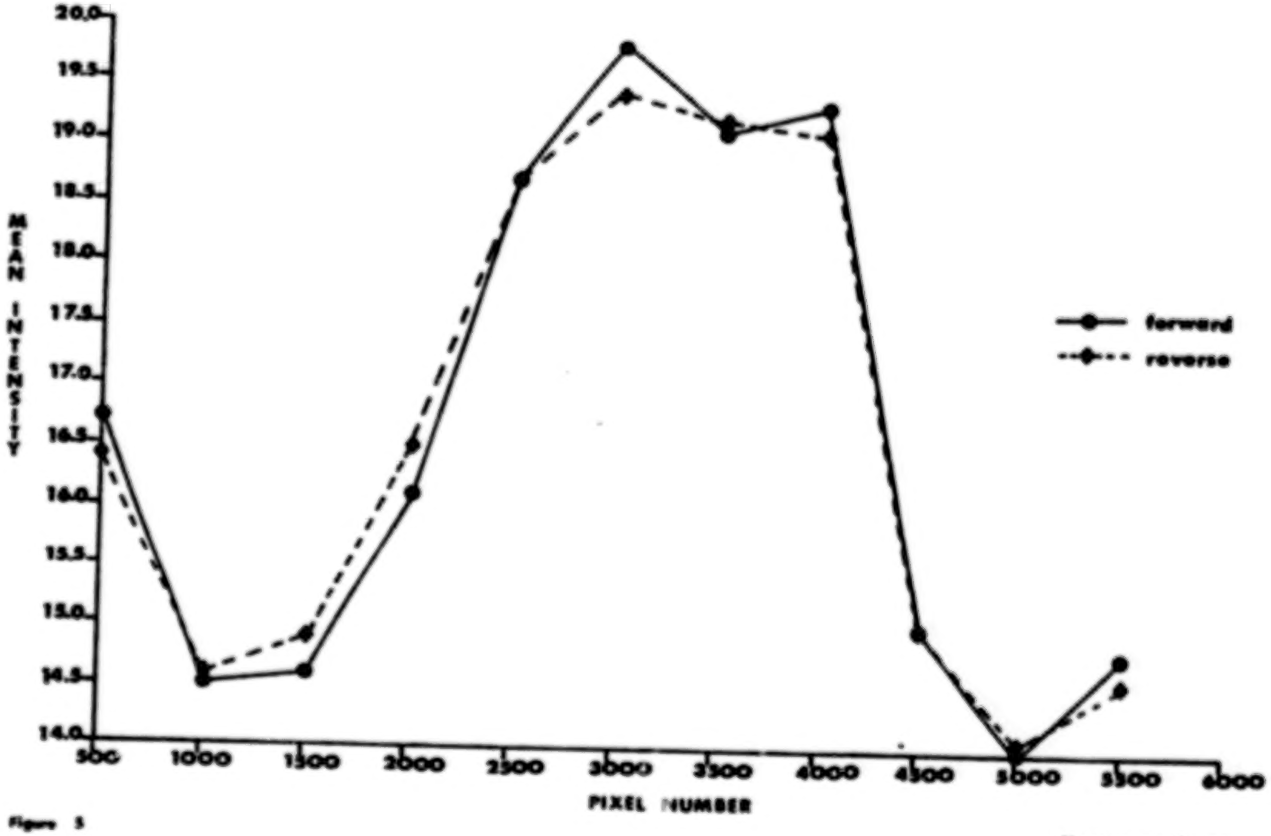

Figure 5

Vancouver Scene

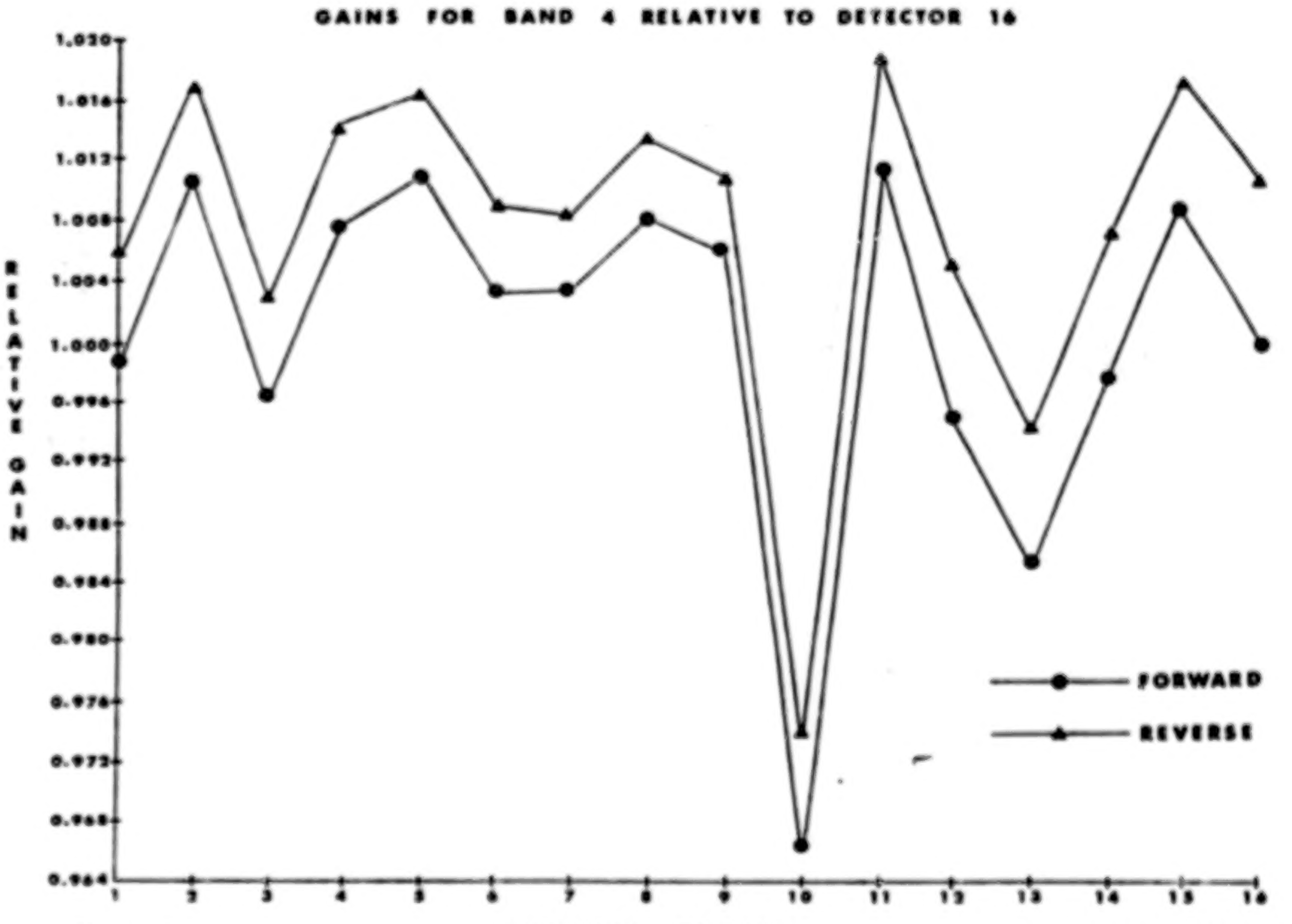
GAINS FOR BAND 4 RELATIVE TO DETECTOR 16
RELATIVE GAIN
1.020
1.016
1.012
1.008
1.004
1.000
0.996
0.992
0.988
0.984
0.980
0.976
0.972
0.968
0.964
1
2
3
4
5
6
7
8
9
10
11
12
13
14
15
16
FORWARD
REVERSE
DETECTOR NUMBER
CALIFORNIA SCENE

Figure 6

N85-21729 35

PRELIMINARY EVALUATION OF THE RADIOMETRIC CALIBRATION OF LANDSAT-4 THEMATIC MAPPER DATA BY THE CANADA CENTRE FOR REMOTE SENSING

J. Murphy,
W. Park and
A. Fitzgerald
Canada Centre for Remote Sensing

1.0 AVAILABILITY OF RAW TM DATA AT CCRS

The Canada Centre for Remote Sensing (CCRS) began recording data from the LANDSAT-4 Thematic Mapper (TM) at the Prince Albert Station in October, 1982. Development of a low throughput system (Butlin, 1983) is being completed in order to transcribe the TM imagery from high density tapes to Computer Compatible Tapes (CCT). It is providing early access to the data for the development of radiometric and geometric correction algorithms and for TM evaluation. The first raw CCTs were generated early in January 1983 and were used for this study.

The capabilities of the transcription system include the recording of either half or full scan lines of TM data on CCTs, from one or more of the seven bands in any combination. In this way, either quadrant products, or segments of scenes varying in size from a few scan lines to a full Worldwide Reference System (WRS) scene may be generated for use in developing and evaluating processing algorithms.

The transcription system lines up the start of line code on the forward scan with the end of line code from the previous reverse scan. The system also applies the detector offsets to account for detector displacement and sampling delays, such that all detectors within all the spectral bands are nominally registered within plus or minus one pixel. Band 6 pixels and lines are replicated four times such that all spectral bands have the same pixel spacing. After this nominal alignment process, only those pixels corresponding to ground areas observed by all detectors are retained in order to align the edges of the seven bands.

In order for geometric correction algorithms to be developed using raw data from the transcription system, all the original line length information together with a count of the number of pixels in each scan line both before and after correction is retained with the imagery data.

On the early CCTs the DC restore value, immediately preceeding or following the raw imagery data, and the radiometric calibration samples were not recorded. In the study reported here, the emphasis is therefore placed on the development of destriping algorithms rather than on an absolute calibration of TM data.

PAGE III-274 INTENTIONALLY BLANK

PRECEDING PAGE BLANK NOT FILMED

2.0 RAW DATA OBSERVATIONS

In this study three scenes have been used for the early testing of radiometric processing procedures. The first two are winter scenes acquired over Vancouver, British Columbia (path 48, row 26, November 11, 1982) and Ottawa, Ontario (path 16, row 28, December 12, 1982), respectively. The third, recorded over the coast of California (path 42, row 36, November 15, 1982) in the same time period was included in the test set in order to provide a greater dynamic range of raw TM data.

2.1 DETECTOR REPLACEMENT

The raw data has been examined in some detail to determine the signal-to-noise ratio of individual detectors within the seven bands. This forms part of an on-going study to determine the most appropriate replacement or smoothing techniques for dead or excessively noisy detectors. In the study reported here, the data from detector 3 of band 5 has simply been replaced with the data from detector 4 of band 5. Band 6 pixels and lines are replicated four times. For all other detectors, there is no data modification.

3.0 RADIOMETRIC CORRECTION METHOD

The radiometric correction process being evaluated for LANDSAT-4 TM data may be divided into three stages.

a) A reference detector is chosen for each spectral band, and the corrections required to place the data from this detector on an absolute scale are calculated, using in-flight calibration data, pre-launch calibration data and the maximum and minimum radiance values associated with the response of the band.

b) The relative differences between all other detectors in each band and the reference detector are calculated, using the means and standard deviations of the raw data values as calculated from the sums and the sums of the squares of the scene data values.

c) Finally, the absolute calibration of the reference detector for each band is combined with the relative calibration of the other detectors within the same band to provide an absolute calibration of all one hundred detectors.

Inherent in the technique is the assumption that the response of each detector is linear, that is, the voltage output varies in a linear fashion with the radiance input. Hence the calibration process may be represented by the equation:

$$V' = (V - a)/b \qquad (1)$$

where V' is the calibrated digital value,
V is the uncalibrated digital value,
b is the gain
and a is the offset.

The b's and a's are referred to as gains and offsets in Tables 3.1 and 3.6.

3.1 ABSOLUTE CALIBRATION

In the absence of calibration data, an arbitrary choice of reference detector, namely, detector 1 for each band, was initially chosen. The gain and offset of each of these reference detectors were arbitrarily set to 1 and 0 respectively.

3.2 RELATIVE RADIOMETRIC CALIBRATION ALGORITHM

The relative radiometric correction of the individual detectors within each band is performed using information from the scene being viewed by the sensor. It has been shown (Strome et al, 1975) that the gain of one detector relative to the gain of another, chosen as a reference detector, is equal to the ratio of the standard deviations of the data acquired with these detectors. Similarly, the difference in zero offset is equal to the difference between the mean of the data values acquired with one detector and the mean of the data values acquired with the reference detector. The mean and standard deviation can be calculated from the sum and the sum of the squares of the scene data values, which in turn, are usually calculated from the histogram of the raw data values.

In order to ensure that the histograms correspond only to pixels with radiance values for which the response of each detector is linear, all those pixels which saturate any one detector within a band are removed from the histogram of each detector within that band. The procedure is repeated for each band in turn. This technique was shown by Murphy (1981) to reduce residual striping in LANDSAT MSS scenes containing very bright snow and clouds.

3.3 RELATIVE GAIN AND OFFSET CALIBRATION

The histograms of the raw data for the Californian test scene were accumulated for all detectors of all bands, treating the forward scans and reverse scans separately. The histograms for all detectors of all bands for the first 1600 scan lines of the forward scans only are shown in Figures 3.1 to 3.7 for bands 1 to 7 respectively. The histograms for the forward and reverse sweeps were also combined, yielding one histogram for each detector of each band. These two sets of histograms were used to generate three different sets of relative gains and offsets, using the method outlined in Section 3.2. Firstly, the forward scans and reverse scans were treated independently, choosing a reference detector in each band for EACH scan direction, and setting its gain and offset to 1 and 0 respectively. These relative gains and offsets are shown in Table 3.1 for the forward scans and in Table 3.2 for the reverse scans. Secondly, the histograms for the forward scans and the reverse scans were added together, and the resulting relative gains and offsets, to be applied equally to the forward scans and reverse scans, are shown in Table 3.3. Thirdly, the forward scans and reverse scans were treated independently, but a reference detector in each band was chosen ONLY for the forward scan. The resulting relative gains and offsets are shown in Table 3.4 for the forward scans and in Table 3.5 for the reverse scans. Finally, the relative gains and offsets, assuming a reference detector number 1 for each band, were derived from the NASA pre-launch gains and offsets, and are shown in Table 3.6.

3.4 RELATIVE GAIN AND OFFSET OBSERVATIONS

Within each band, the largest variation in relative gain is seen to be 5%, with a maximum relative offset variation of approximately 1%. Comparison of Tables 3.1 and 3.2 shows that the relative intra-band calibration for the forward and reverse scans for all bands is almost identical. This factor is also reflected in the similarity between the relative intra-band calibration for either scan direction independently and for both scan directions combined. However, for the Californian test scene, the gain of the reverse scans relative to the gain of the forward scans is seen, from Table 3.5, to be [illegible]% higher for bands 1, 2 and 3 and 1% higher for bands 4, 5, 6 and 7. Offsets are measured on a scale of 0-255.

The relative gains and offsets calculated from the NASA pre-launch calibration data indicate a similar relationship in the relative calibration of the detectors within each band, although the spread in relative gains is closer to 3% rather than to 5% as calculated from the histograms.

4.0 RESIDUAL RADIOMETRIC STRIPING

A simple method of assessing the radiometric striping in TM images consists of selecting arbitrary subscenes, and for each band plotting as a function of the line (or detector) number the radiometric intensity values averaged over a fixed number of pixels. In such profiles, the residual striping appears as a repetitive pattern with a period of sixteen lines which is added to the scene content. Because the scene data is averaged over a number of pixels, (for example 100 pixels), variations from line to line due to scene content tend to be small and gradual, particularly over uniform areas such as large water bodies. A detailed discussion and evaluation of this striping assessment method is given by Murphy (1981).

Figures 4.1 to 4.7 show the striping profiles for bands 1 to 7 respectively, on a 256 digital count scale, for a subscene extracted from a large ocean area in the Californian test scene. The striping both before and after calibration is shown for all bands using a 64-line by 50-pixel subscene.

For each band, a total of 5 graphs are shown, and they are identified as shown in Table 4.1.

TITLE	EXPLANATION
RAW	Raw data, before calibration.
METHOD 1	Forward and reverse scans corrected independently.
METHOD 2	Forward and reverse scans corrected using the same prelaunch gains and offsets.
METHOD 3	Forward and reverse scans corrected using one lookup table derived from combined forward and reverse histograms.
METHOD 4	Forward and reverse scans corrected independently, reference detector only in forward scan.

TABLE 4.1 SUMMARY OF DESTRIPING METHODS

For bands 2, 3, 4, 5 and 7, the striping before any corrections is seen to be less than 2 levels, and is reduced by all relative calibration procedures. For band 6, the striping is reduced from 3 levels to less than 1 level. In the uncorrected image for band 1, the striping is difficult to distinguish from the scene content. However, after corrections, the residual striping appears by this method to be between 1 and 2 levels.

5.0 RESULTS

Observations based on the residual striping estimates for a large ocean area in the Californian test scene using four different methods of relative calibration have shown no clear superiority of one method over the others. This indicates the need to quantify in more detail the differences between the radiometry of the forward and reverse scans as a function of line number within a full scene, using histograms of the raw data. An effective means of dealing with those detectors having significantly different singal-to-noise characteristics from the other detectors in the same band is required.

Observations of the histograms of the radiometrically corrected data show the necessity of choosing as reference detectors those which have the highest gain within a band. This will prevent the mapping of more than one raw digital level into the same output digital level. Discussion at the LANDSAT-4 Scientific Characterization Early Results Symposium focussed attention on the existence of "empty bins" and of "overpopulated bins" in the histograms of the corrected data from various sensors. This is to be expected with any system which quantizes analogue data and then performs digital intensity corrections. If the shape of the histograms is important in an analysis procedure, then the histogram should be used to estimate a probability density function. Strome (1980) discussed alternative methods for dealing with this problem for radiometrically corrected MSS data.

6.0 CONCLUSION

CCRS has initiated a study into the radiometric characteristics of the LANDSAT-4 TM sensor, with a view to developing absolute and relative radiometric calibration procedures. This early report has discussed the preliminary results from several different approaches to the relative correction of all detectors within each band. Further areas for study related to intra-band relative corrections have been outlined, and absolute calibration procedures will be developed using the internal calibration system.

C-4

REFERENCES

Butlin, T., Murphy, J. (1983) Early Processing of Thematic Mapper Data by the Canada Centre for Remote Sensing, Seventeenth International Symposium on Remote Sensing of Environment, Ann Arbor.

Murphy, J. (1981) A Refined Destriping Procedure for LANDSAT MSS Data Products, 7th Canadian Symposium on Remote Sensing, Winnipeg, pp. 454-470.

NASA (1982) Third LANDSAT Technical Working Group Meeting (LTWG), October.

Strome, W.M. et al. (1975) Format Specifications for Canadian LANDSAT MSS System Corrected Computer Compatible Tape, CCRS Research Report 75-3.

Strome, W.M., (1980) Histogram Estimation for Multiple Detector Sensors, 6th Canadian Symposium on Remote Sensing, Halifax.

DETECTOR	BAND 1		BAND 2		BAND 3		BAND 4	
	GAIN	OFFSET	GAIN	OFFSET	GAIN	OFFSET	GAIN	OFFSET
1	1.0000	0.0000	1.0000	0.0000	1.0000	0.0000	1.0000	0.0000
2	1.0039	−0.6416	0.9686	0.0320	0.9804	−0.3950	0.9934	−0.9306
3	1.0171	−0.9148	0.9861	−0.7299	0.9873	−0.4417	1.0060	−0.5541
4	1.0139	−0.4417	0.9382	1.2030	0.9901	−1.0224	0.9989	−1.1325
5	1.0086	−1.0367	1.0140	−0.8926	1.0020	−0.9082	0.9940	−0.9847
6	1.0062	−1.0608	1.0065	−0.7763	1.0035	−0.9386	1.0048	−0.7736
7	1.0002	−1.4956	0.9962	−0.9986	0.9927	−0.9398	0.9999	−0.7847
8	1.0145	−1.4110	0.9974	−0.9919	0.9888	−0.9576	1.0036	−1.0330
9	1.0130	−1.9947	1.0058	−1.1820	1.0099	−1.3618	0.9996	−0.8654
10	1.0224	−1.4132	1.0003	−1.2268	0.9969	−0.9437	1.0377	−0.8744
11	1.0228	−2.3670	0.9999	−1.2037	0.9985	−1.4286	0.9913	−0.7320
12	1.0257	−1.3593	0.9936	−1.1430	1.0096	−1.1606	1.0093	−1.0941
13	1.0289	−2.2193	1.0209	−1.3010	1.0145	−1.3821	1.0193	−1.1426
14	1.0354	−2.4720	1.0170	−1.3211	1.0101	−0.9705	1.0031	−0.8770
15	1.0509	−3.0255	1.0379	−1.4728	1.0247	−1.4142	0.9985	−1.2094
16	1.0548	−2.8177	0.9989	−1.2146	0.9959	−0.9282	1.0013	−0.8034

DETECTOR	BAND 5		BAND 6		BAND 7		NOTES
	GAIN	OFFSET	GAIN**	OFFSET**	GAIN	OFFSET	
1	1.0000	0.0000	1.0000	0.0000	1.0000	0.0000	*Failed detector replaced by adjacent detector
2	0.9914	0.3457	1.0000	0.0000	0.9827	−0.1742	
3	0.9912*	0.3048*	1.0000	0.0000	0.9884	−0.1938	
4	0.9912	0.3048	1.0000	0.0000	0.9864	−0.1994	
5	0.9886	−0.2571	1.0078	1.3885	0.9713	−0.2827	**Replicated 4 times
6	1.0039	0.0575	1.0078	1.3885	0.9710	0.1022	
7	1.0136	0.0706	1.0078	1.3885	0.9870	−0.4106	
8	1.0101	0.3444	1.0078	1.3885	0.9520	0.0874	
9	1.0094	−0.2120	0.9694	2.7018	0.9864	−0.2858	
10	0.9923	0.0063	0.9694	2.7018	0.9662	−0.0536	
11	1.0288	−0.2332	0.9694	2.7018	0.9820	−0.2553	
12	1.0303	−0.0892	0.9694	2.7018	0.9887	−0.0302	
13	1.0195	−0.3601	1.0232	−0.4413	0.9766	−0.3438	
14	1.0133	−0.1651	1.0232	−0.4413	0.9780	−0.1559	
15	1.0047	−0.5183	1.0232	−0.4413	0.9634	−0.3696	
16	1.0201	−0.1233	1.0232	−0.4413	0.9939	−0.0507	

RELATIVE GAINS AND OFFSETS, USING HISTOGRAMS
CALIFORNIA SCENE
FORWARD SCAN

TABLE 3.1

DETECTOR	BAND 1		BAND 2		BAND 3		BAND 4	
	GAIN	OFFSET	GAIN	OFFSET	GAIN	OFFSET	GAIN	OFFSET
1	1.0000	0.0000	1.0000	0.0000	1.0000	0.0000	1.0000	0.0000
2	1.0051	-0.7881	0.9696	-0.0001	0.9808	-0.4033	0.9946	-1.0195
3	1.0147	-0.7633	0.9819	-0.6206	0.9837	-0.3435	1.0043	-0.5271
4	1.0132	-0.3259	0.9345	1.3503	0.9845	-0.8598	0.9990	-1.2205
5	1.0084	-0.9733	1.0064	-0.6684	0.9963	-0.7476	0.9926	-1.0335
6	1.0030	-0.8576	0.9939	-0.3946	0.9937	-0.6218	1.0024	-0.7828
7	0.9924	-0.9355	0.9787	-0.4762	0.9780	-0.4821	0.9933	-0.6278
8	1.0078	-0.9192	0.9782	-0.3961	0.9726	-0.4312	0.9969	-0.8669
9	1.0081	-1.5715	0.9892	-0.6510	0.9952	-0.8642	0.9925	-0.6424
10	1.0207	-1.2342	0.9888	-0.8439	0.9877	-0.6047	1.0345	-0.7959
11	1.0204	-2.1188	0.9889	-0.8172	0.9897	-1.0820	0.9859	-0.5398
12	1.0268	-1.2495	0.9847	-0.8172	1.0018	-0.8314	1.0045	-0.8770
13	1.0276	-2.0676	1.0101	-0.9393	1.0056	-1.0515	1.0126	-0.8800
14	1.0330	-2.2611	1.0048	-0.9155	1.0007	-0.6141	0.9966	-0.6112
15	1.0483	-2.7819	1.0251	-1.0311	1.0146	-1.0272	0.9896	-0.8195
16	1.0562	-2.8072	0.9917	-0.9283	0.9907	-0.6496	0.9980	-0.6104

DETECTOR	BAND 5		BAND 6		BAND 7	
	GAIN	OFFSET	GAIN**	OFFSET**	GAIN	OFFSET
1	1.0000	0.0000	1.0000	0.0000	1.0000	0.0000
2	0.9903	0.3304	1.0000	0.0000	0.9805	-0.1691
3	0.9946*	-0.0969*	1.0000	0.0000	0.9884	-0.2418
4	0.9946	-0.0969	1.0000	0.0000	0.9894	-0.3812
5	0.9949	-0.8718	1.0072	1.4032	0.9787	-0.5731
6	1.0112	-0.5493	1.0072	1.4032	0.9797	-0.2085
7	1.0204	-0.4570	1.0072	1.4032	0.9940	-0.6022
8	1.0171	-0.1845	1.0072	1.4032	0.9607	-0.1861
9	1.0155	-0.6614	0.9717	2.4665	0.9949	-0.5222
10	0.9971	-0.2960	0.9717	2.4665	0.9757	-0.3183
11	1.0356	-0.5915	0.9717	2.4665	0.9917	-0.4579
12	1.0363	-0.3753	0.9717	2.4665	0.9979	-0.2246
13	1.0241	-0.6168	1.0222	-0.2998	0.9844	-0.5178
14	1.0161	-0.3217	1.0222	-0.2998	0.9842	-0.2943
15	1.0091	-0.7547	1.0222	-0.2998	0.9707	-0.5193
16	1.0267	-0.4893	1.0222	-0.2998	1.0033	-0.2799

*Failed detector replaced by adjacent detector

**Replicated 4 times

RELATIVE GAINS AND OFFSETS,

USING HISTOGRAMS, REVERSE SCAN ONLY, CALIFORNIA SCENE

TABLE 3.2

DETECTOR	BAND 1		BAND 2		BAND 3		BAND 4	
	GAIN	OFFSET	GAIN	OFFSET	GAIN	OFFSET	GAIN	OFFSET
1	1.0000	0.0000	1.0000	0.0000	1.0000	0.0000	1.0000	0.0000
2	1.0045	-0.7146	0.9691	0.0155	0.9806	-0.3993	0.9940	-0.9749
3	1.0159	-0.8359	0.9839	-0.6734	0.9854	-0.3910	1.0051	-0.5397
4	1.0135	-0.3818	0.9363	1.2778	0.9872	-0.9388	0.9989	-1.1757
5	1.0085	-1.0015	1.0101	-0.7776	0.9990	-0.8256	0.9933	-1.0078
6	1.0044	-0.9454	1.0000	-0.5810	0.9985	-0.7767	1.0036	-0.7766
7	0.9959	-1.1934	0.9873	-0.7314	0.9851	-0.7059	0.9965	-0.7037
8	1.0108	-1.1398	0.9875	-0.6877	0.9805	-0.6891	1.0002	-0.9471
9	1.0103	-1.7662	0.9973	-0.9111	1.0024	-1.1083	0.9960	-0.7516
10	1.0214	-1.3140	0.9944	-1.0314	0.9922	-0.7713	1.0360	-0.8338
11	1.0215	-2.2356	0.9943	-1.0069	0.9940	-1.2526	0.9886	-0.6344
12	1.0263	-1.3055	0.9890	-0.9773	1.0056	-0.9939	1.0068	-0.9847
13	1.0282	-2.1404	1.0154	-1.1165	1.0099	-1.2140	1.0159	-1.0097
14	1.0341	-2.3633	1.0107	-1.1142	1.0053	-0.7894	0.9998	-0.7426
15	1.0496	-2.8998	1.0313	-1.2478	1.0195	-1.2177	0.9940	-1.0129
16	1.0555	-2.8126	0.9952	-1.0694	0.9933	-0.7880	0.9996	-0.7068

DETECTOR	BAND 5		BAND 6		BAND 7	
	GAIN	OFFSET	GAIN**	OFFSET**	GAIN	OFFSET
1	1.0000	0.0000	1.0000	0.0000	1.0000	0.0000
2	0.9908	0.3386	1.0000	0.0000	0.9816	-0.1712
3	0.9929	0.1047*	1.0000	0.0000	0.9884	-0.2175
4	0.9929	0.1047	1.0000	0.0000	0.9879	-0.2899
5	0.9918	-0.5638	1.0075	1.3948	0.9750	-0.4281
6	1.0075	-0.2455	1.0075	1.3948	0.9754	-0.0536
7	1.0170	-0.1931	1.0075	1.3948	0.9905	-0.5071
8	1.0136	0.0799	1.0075	1.3948	0.9564	-0.0500
9	1.0125	-0.4368	0.9706	2.5818	0.9907	-0.4048
10	0.9947	-0.1456	0.9706	2.5818	0.9710	-0.1869
11	1.0322	-0.4138	0.9706	2.5818	0.9869	-0.3581
12	1.0333	-0.2334	0.9706	2.5818	0.9934	-0.1288
13	1.0218	-0.4981	1.0227	-0.3685	0.9806	-0.4318
14	1.0147	-0.2437	1.0227	-0.3685	0.9812	-0.2259
15	1.0069	-0.6370	1.0227	-0.3685	0.9671	-0.4455
16	1.0234	-0.3072	1.0227	-0.3685	0.9987	-0.1664

* Failed detector replaced by adjacent detector

** Replicated 4 times

RELATIVE GAINS AND OFFSETS,

USING HISTOGRAMS, COMBINED SCANS, CALIFORNIA SCENE

TABLE 3.3

DETECTOR	BAND 1		BAND 2		BAND 3		BAND 4	
	GAIN	OFFSET	GAIN	OFFSET	GAIN	OFFSET	GAIN	OFFSET
1	1.0000	0.0000	1.0000	0.0000	1.0000	0.0000	1.0000	0.0000
2	1.0039	−0.6416	0.9686	0.0320	0.9804	−0.3950	0.9934	−0.9306
3	1.0171	−0.9148	0.9861	−0.7299	0.9873	−0.4417	1.0060	−0.5541
4	1.0139	−0.4417	0.9382	1.2030	0.9901	−1.0224	0.9989	−1.1325
5	1.0086	−1.0367	1.0140	−0.8926	1.0020	−0.9082	0.9940	−0.9847
6	1.0062	−1.0608	1.0065	−0.7763	1.0035	−0.9386	1.0048	−0.7736
7	1.0002	−1.4956	0.9962	−0.9986	0.9927	−0.9398	0.9999	−0.7847
8	1.0145	−1.4110	0.9974	−0.9919	0.9888	−0.9576	1.0036	−1.0330
9	1.0130	−1.9947	1.0058	−1.1820	1.0099	−1.3618	0.9996	−0.8654
10	1.0224	−1.4132	1.0003	−1.2268	0.9969	−0.9437	1.0377	−0.8744
11	1.0228	−2.3670	0.9999	−1.2037	0.9985	−1.4286	0.9913	−0.7320
12	1.0257	−1.3593	0.9936	−1.1430	1.0096	−1.1606	1.0093	−1.0941
13	1.0289	−2.2193	1.0209	−1.3010	1.0145	−1.3821	1.0193	−1.1426
14	1.0354	−2.4720	1.0170	−1.3211	1.0101	−0.9705	1.0031	−0.8770
15	1.0509	−3.0255	1.0379	−1.4728	1.0247	−1.4142	0.9985	−1.2094
16	1.0548	−2.8177	0.9989	−1.2146	0.9959	−0.9282	1.0013	−0.8034

DETECTOR	BAND 5		BAND 6		BAND 7		NOTES
	GAIN	OFFSET	GAIN**	OFFSET**	GAIN	OFFSET	
1	1.0000	0.0000	1.0000	0.0000	1.0000	0.0000	*Failed detector replaced by adjacent detector
2	0.9914	0.3457	1.0000	0.0000	0.9827	−0.1742	
3	0.9912*	0.3048*	1.0000	0.0000	0.9884	−0.1938	
4	0.9912	0.3048	1.0000	0.0000	0.9864	−0.1994	
5	0.9886	−0.2571	1.0078	1.3885	0.9713	−0.2827	**Replicated 4 times
6	1.0039	0.0575	1.0078	1.3885	0.9710	0.1022	
7	1.0136	0.0706	1.0078	1.3885	0.9870	−0.4106	
8	1.0101	0.3444	1.0078	1.3885	0.9520	0.0874	
9	1.0094	−0.2120	0.9694	2.7018	0.9864	−0.2858	
10	0.9923	0.0063	0.9694	2.7018	0.9662	−0.0536	
11	1.0288	−0.2332	0.9694	2.7018	0.9820	−0.2553	
12	1.0303	−0.0892	0.9694	2.7018	0.9887	−0.0302	
13	1.0195	−0.3601	1.0232	−0.4413	0.9766	−0.3438	
14	1.0133	−0.1651	1.0232	−0.4413	0.9780	−0.1559	
15	1.0047	−0.5183	1.0232	−0.4413	0.9634	−0.3696	
16	1.0201	−0.1233	1.0232	−0.4413	0.9939	−0.0507	

RELATIVE GAINS AND OFFSETS, USING HISTOGRAMS
CALIFORNIA SCENE
FORWARD SCAN

TABLE 3.4

DETECTOR	BAND 1		BAND 2		BAND 3		BAND 4	
	GAIN	OFFSET	GAIN	OFFSET	GAIN	OFFSET	GAIN	OFFSET
1	1.0360	-2.6076	1.0295	-0.9411	1.0273	-0.9541	1.0156	-0.6614
2	1.0413	-3.4089	0.9982	-0.9126	1.0075	-1.3390	1.0101	-1.6773
3	1.0513	-3.4093	1.0108	-1.5446	1.0105	-1.2820	1.0199	-1.1914
4	1.0497	-2.9679	0.9620	0.4709	1.0114	-1.7991	1.0145	-1.8813
5	1.0447	-3.6028	1.0361	-1.6155	1.0234	-1.6981	1.0081	-1.6900
6	1.0391	-3.4730	1.0232	-1.3299	1.0208	-1.5699	1.0180	-1.4458
7	1.0281	-3.5232	1.0076	-1.3973	1.0046	-1.4151	1.0088	-1.2848
8	1.0441	-3.5471	1.0070	-1.3166	0.9991	-1.3592	1.0124	-1.5254
9	1.0444	-4.2001	1.0184	-1.5819	1.0223	-1.8137	1.0079	-1.2988
10	1.0575	-3.8958	1.0180	-1.7744	1.0147	-1.5471	1.0506	-1.4801
11	1.0572	-4.7797	1.0181	-1.7478	1.0166	-2.0262	1.0013	-1.1919
12	1.0638	-3.9269	1.0137	-1.7439	1.0291	-1.7872	1.0201	-1.5414
13	1.0646	-4.7472	1.0399	-1.8898	1.0330	-2.0109	1.0284	-1.5497
14	1.0702	-4.9548	1.0344	-1.8610	1.0279	-1.5688	1.0121	-1.2704
15	1.0861	-5.5155	1.0553	-1.9958	1.0422	-1.9952	1.0051	-1.4741
16	1.0942	-5.5613	1.0210	-1.8616	1.0177	-1.5948	1.0136	-1.2705

DETECTOR	BAND 5		BAND 6		BAND 7		NOTES
	GAIN	OFFSET	GAIN**	OFFSET**	GAIN	OFFSET	
1	1.0067	-0.3869	1.0130	-1.2717	1.0095	-0.2692	* Failed detector replaced by adjacent detector
2	0.9970	-0.0528	1.0130	-1.2717	0.9898	-0.4331	
3	1.0013	-0.4817*	1.0130	-1.2717	0.9978	-0.5079	
4	1.0013	-0.4817	1.0130	-1.2717	0.9988	-0.6476	
5	1.0016	-1.2567	1.0203	0.1223	0.9879	-0.8366	** Replicated 4 times
6	1.0180	-0.9405	1.0203	0.1223	0.9890	-0.4723	
7	1.0272	-0.8518	1.0203	0.1223	1.0034	-0.8699	
8	1.0239	-0.5781	1.0203	0.1223	0.9698	-0.4448	
9	1.0224	-1.0544	0.9843	1.2309	1.0043	-0.7901	
10	1.0038	-0.6819	0.9843	1.2309	0.9849	-0.5810	
11	1.0425	-0.9922	0.9843	1.2309	1.0011	-0.7249	
12	1.0433	-0.7763	0.9843	1.2309	1.0074	-0.4933	
13	1.0310	-1.0131	1.0355	-1.5997	0.9938	-0.7828	
14	1.0229	-0.7148	1.0355	-1.5997	0.9936	-0.5593	
15	1.0159	-1.1452	1.0355	-1.5997	0.9799	-0.7807	
16	1.0336	-0.8866	1.0355	-1.5997	1.0129	-0.5500	

**RELATIVE GAINS AND OFFSETS,
USING HISTOGRAMS, REVERSE SCAN ONLY, USING DETECTOR 1
OF FORWARD SCAN AS REFERENCE DETECTOR,
CALIFORNIA SCENE**

TABLE 3.5

DETECTOR	BAND 1		BAND 2		BAND 3		BAND 4	
	GAIN	OFFSET	GAIN	OFFSET	GAIN	OFFSET	GAIN	OFFSET
1	1.0000	0.0000	1.0000	0.0000	1.0000	0.0000	1.0000	0.0000
2	1.0074	−0.8103	0.9930	−0.6475	0.9837	−0.5143	0.9858	−0.5562
3	1.0180	−0.5904	0.9804	−0.5280	0.9826	−0.1937	1.0042	−0.5830
4	1.0180	−0.6555	0.9963	−0.5436	0.9771	−0.6168	0.9871	−0.6763
5	1.0104	−0.5451	1.0026	−0.5762	0.9858	−0.5055	0.9854	−0.7374
6	1.0055	−0.6889	1.0010	−0.4559	0.9894	−0.4837	0.9964	−0.5694
7	1.0025	−0.6104	0.9856	−0.6341	0.9818	−0.5371	0.9856	−0.2803
8	1.0069	−0.6458	0.9883	−0.4457	0.9766	−0.5423	0.9914	−0.6800
9	1.0113	−0.5840	0.9879	−0.5755	0.9877	−0.5629	0.9898	−0.6195
10	1.0136	−0.7535	0.9900	−0.6215	0.9804	−0.5935	1.0290	−0.8721
11	1.0025	−0.6632	0.9784	−0.5685	0.9780	−0.6064	0.9800	−0.5527
12	1.0108	−0.7104	0.9803	−0.6049	0.9875	−0.6048	0.9935	−0.7284
13	1.0030	−0.6319	0.9926	−0.5970	0.9914	−0.6661	1.0076	−0.8815
14	1.0071	−0.7707	0.9959	−0.5134	0.9872	−0.4352	0.9944	−0.6032
15	1.0086	−0.6271	1.0025	−0.6274	0.9992	−0.5922	0.9816	−0.7929
16	1.0144	−0.8593	0.9761	−0.4990	0.9728	−0.4316	0.9869	−0.5022

DETECTOR	BAND 5		BAND 6		BAND 7		
	GAIN	OFFSET	GAIN	OFFSET	GAIN	OFFSET	NOTES
1	1.0000	0.0000			1.0000	0.0000	
2	1.0034	−0.3471	NO DATA		0.9901	−0.5524	*Failed detector
3	1.0148*	−0.4737*			0.9963	−0.5657	replaced by
4	1.0148	−0.4737	AVAILABLE		0.9965	−0.5138	adjacent detector
5	1.0031	−0.2859			0.9966	−0.6725	
6	1.0042	−0.2630			0.9896	−0.4596	
7	1.0110	−0.3060			0.9972	−0.6603	
8	1.0078	−0.1602			0.9805	−0.5138	
9	1.0052	−0.2702			0.9978	−0.6028	
10	1.0051	−0.3712			0.9765	−0.4286	
11	1.0143	−0.2866			0.9915	−0.6133	
12	1.0155	−0.4462			0.9980	−0.4515	
13	1.0129	−0.2138			0.9859	−0.7494	
14	1.0090	−0.3577			0.9968	−0.3641	
15	1.0097	−0.1654			0.9863	−0.7546	
16	1.0153	−0.3540			1.0017	−0.3848	

RELATIVE GAINS AND OFFSETS, USING NASA PRELAUNCH CALIBRATION DATA

TABLE 3.6

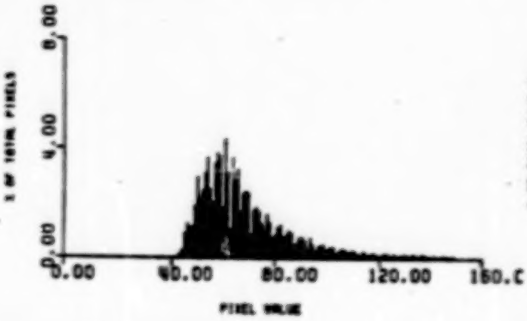

END OF PLOT FOR BAND 1 DETECTOR 1

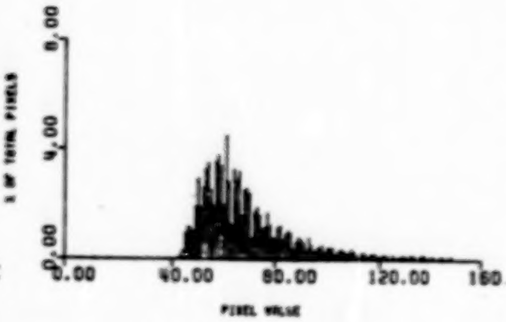

END OF PLOT FOR BAND 1 DETECTOR 3

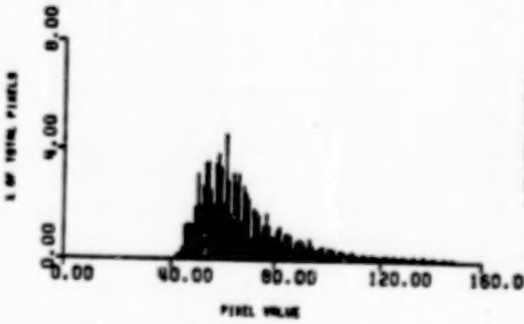

END OF PLOT FOR BAND 1 DETECTOR 2

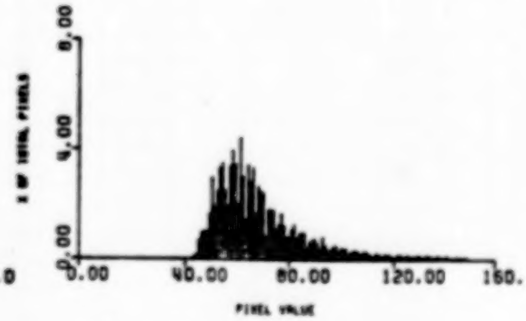

END OF PLOT FOR BAND 1 DETECTOR 4

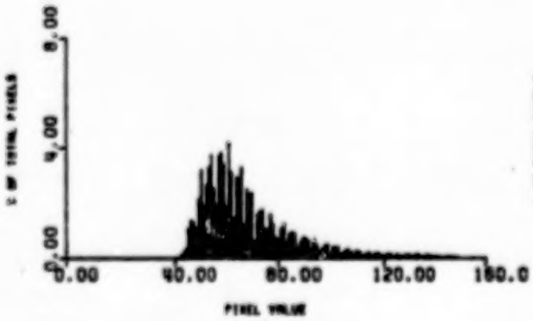

END OF PLOT FOR BAND 1 DETECTOR 5

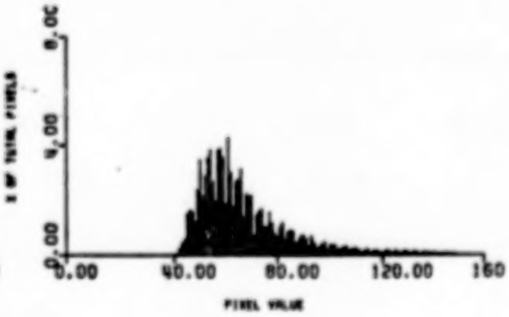

END OF PLOT FOR BAND 1 DETECTOR 7

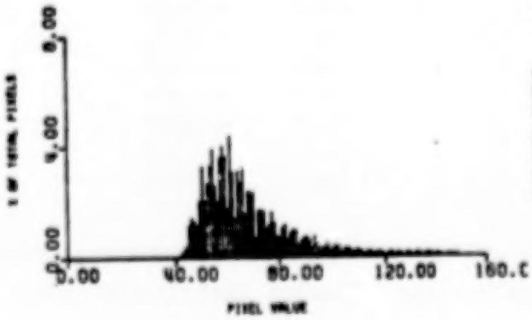

END OF PLOT FOR BAND 1 DETECTOR 6

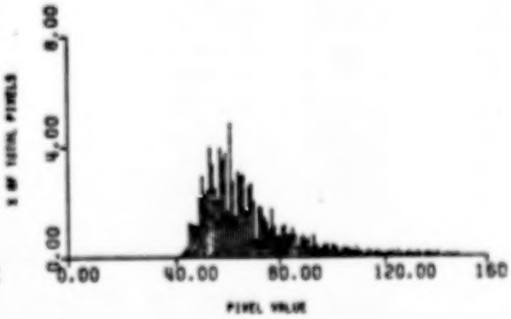

END OF PLOT FOR BAND 1 DETECTOR 8

FIGURE 3.1 BAND 1 HISTOGRAMS

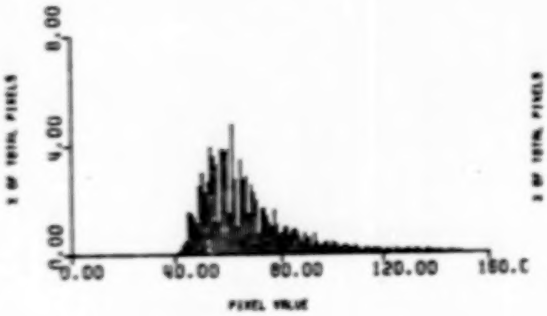

END OF PLOT FOR BAND 1 DETECTOR 9

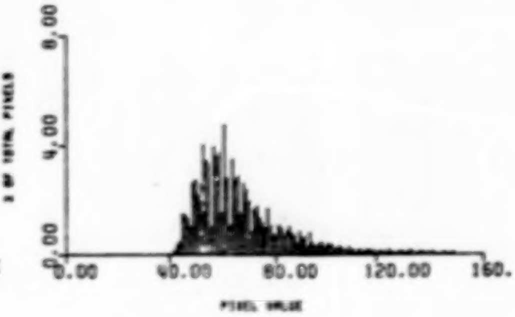

END OF PLOT FOR BAND 1 DETECTOR 11

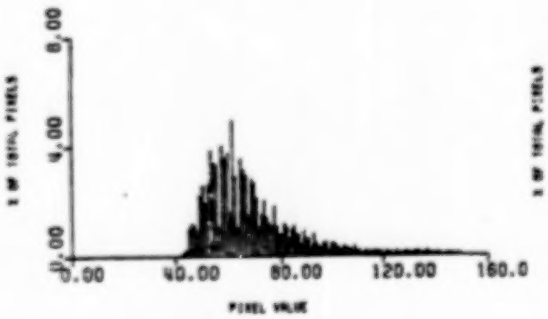

END OF PLOT FOR BAND 1 DETECTOR 10

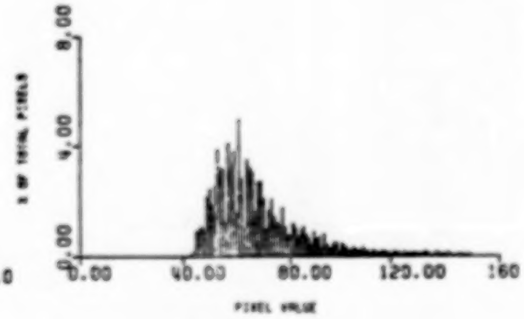

END OF PLOT FOR BAND 1 DETECTOR 12

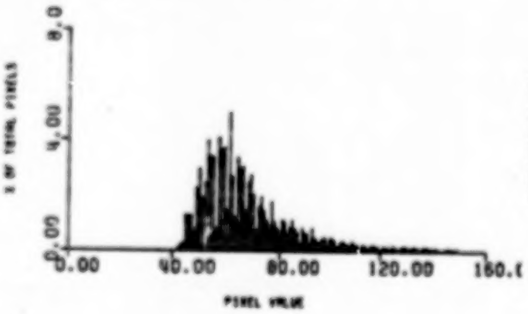

END OF PLOT FOR BAND 1 DETECTOR 13

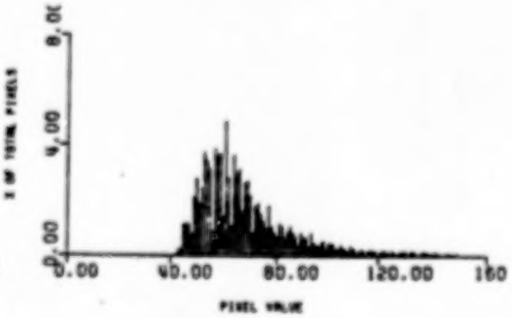

END OF PLOT FOR BAND 1 DETECTOR 15

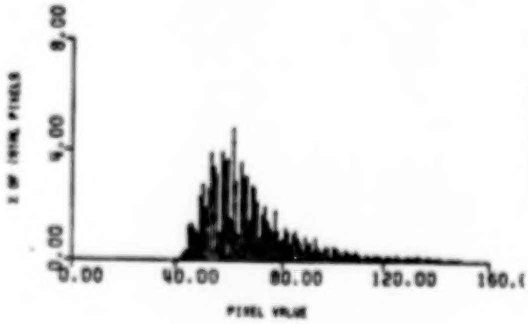

END OF PLOT FOR BAND 1 DETECTOR 14

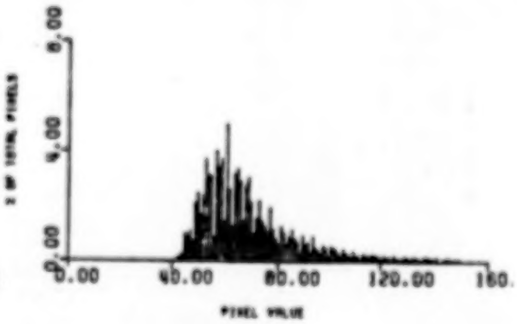

END OF PLOT FOR BAND 1 DETECTOR 16

FIGURE 3.1 (CONT) BAND 1 HISTOGRAMS

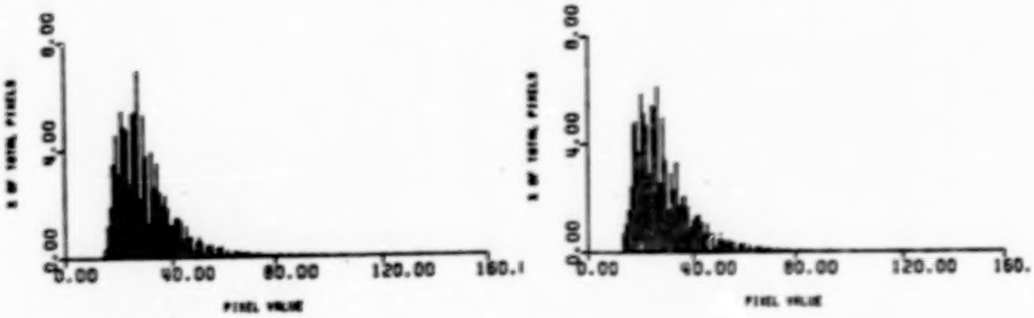

END OF PLOT FOR BAND 2 DETECTOR 1

END OF PLOT FOR BAND 2 DETECTOR 3

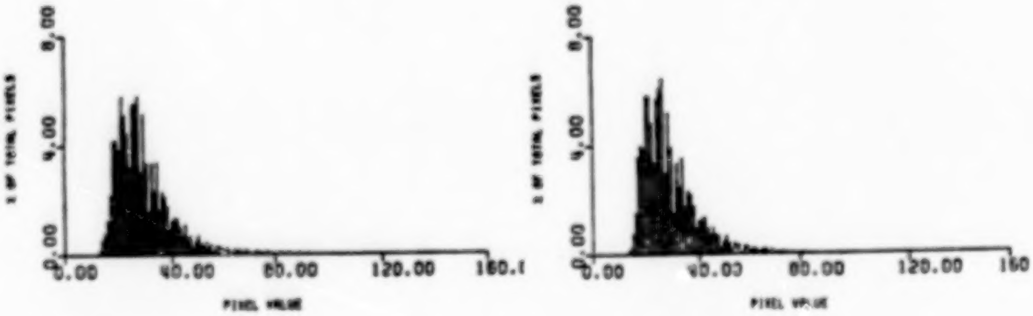

END OF PLOT FOR BAND 2 DETECTOR 2

END OF PLOT FOR BAND 2 DETECTOR 4

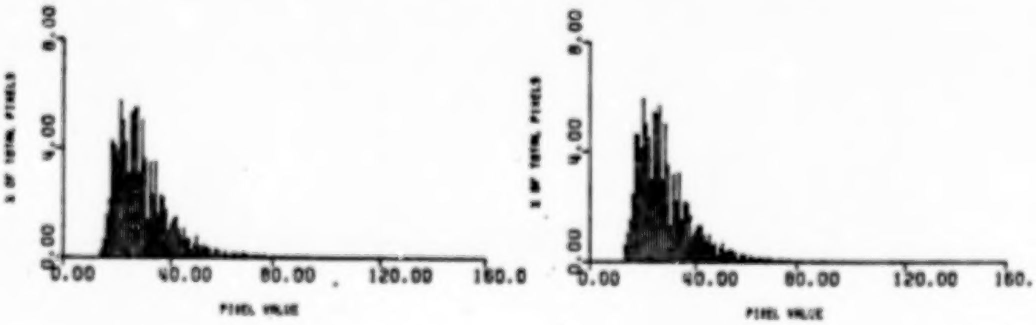

END OF PLOT FOR BAND 2 DETECTOR 5

END OF PLOT FOR BAND 2 DETECTOR 7

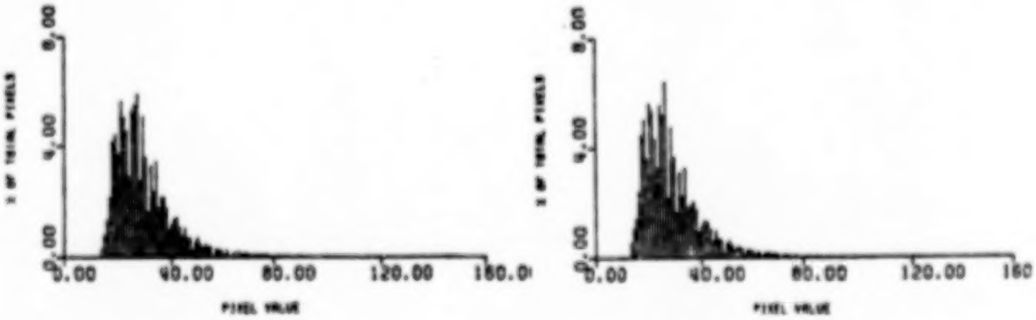

END OF PLOT FOR BAND 2 DETECTOR 6

END OF PLOT FOR BAND 2 DETECTOR 8

FIGURE 3.2 BAND 2 HISTOGRAMS

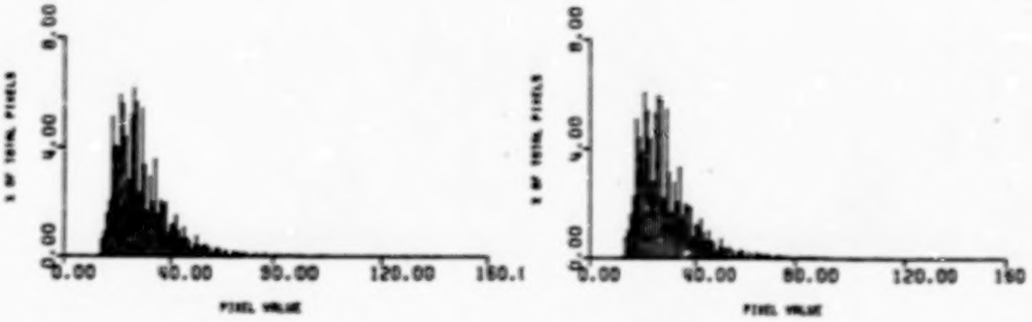

END OF PLOT FOR BAND 2 DETECTOR 9

END OF PLOT FOR BAND 2 DETECTOR 11

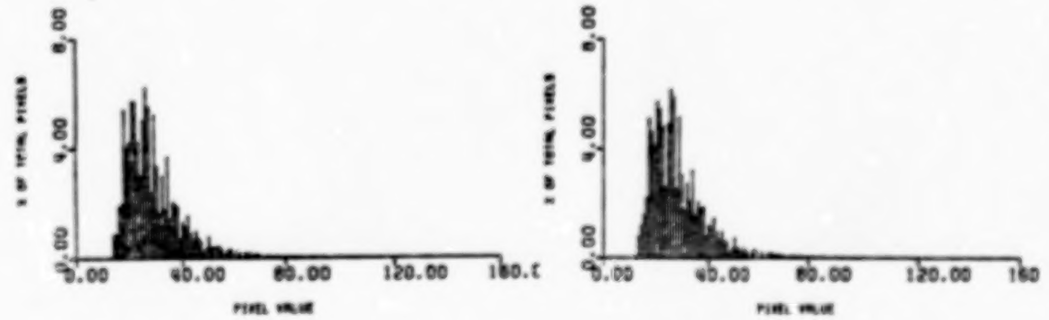

END OF PLOT FOR BAND 2 DETECTOR 10

END OF PLOT FOR BAND 2 DETECTOR 12

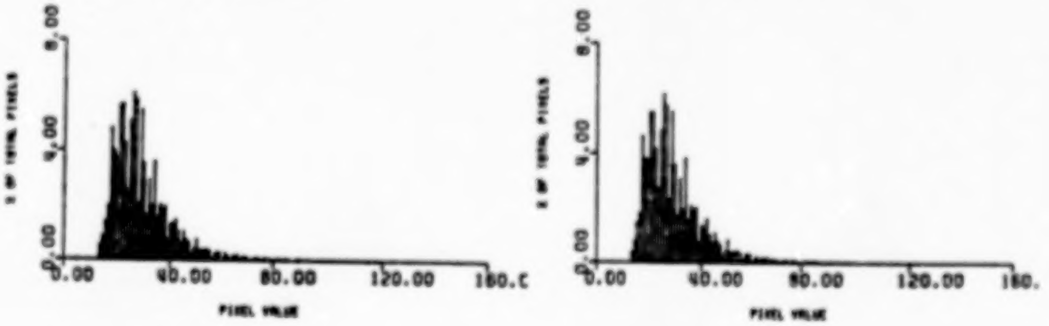

END OF PLOT FOR BAND 2 DETECTOR 13

END OF PLOT FOR BAND 2 DETECTOR 15

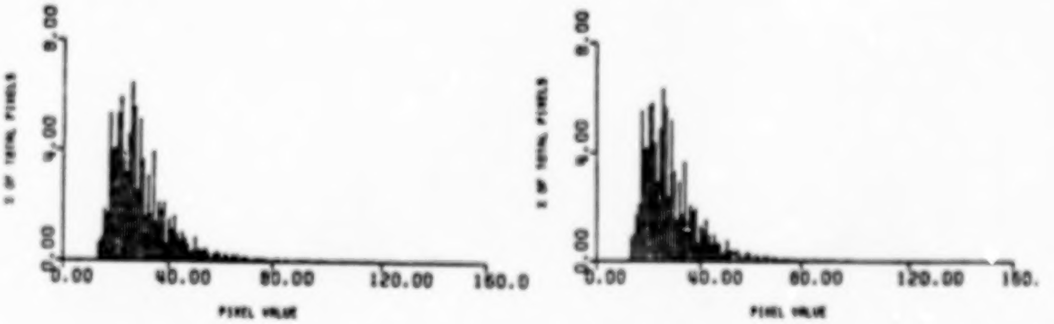

END OF PLOT FOR BAND 2 DETECTOR 14

END OF PLOT FOR BAND 2 DETECTOR 16

FIGURE 3.2 (CONT) BAND 2 HISTOGRAMS

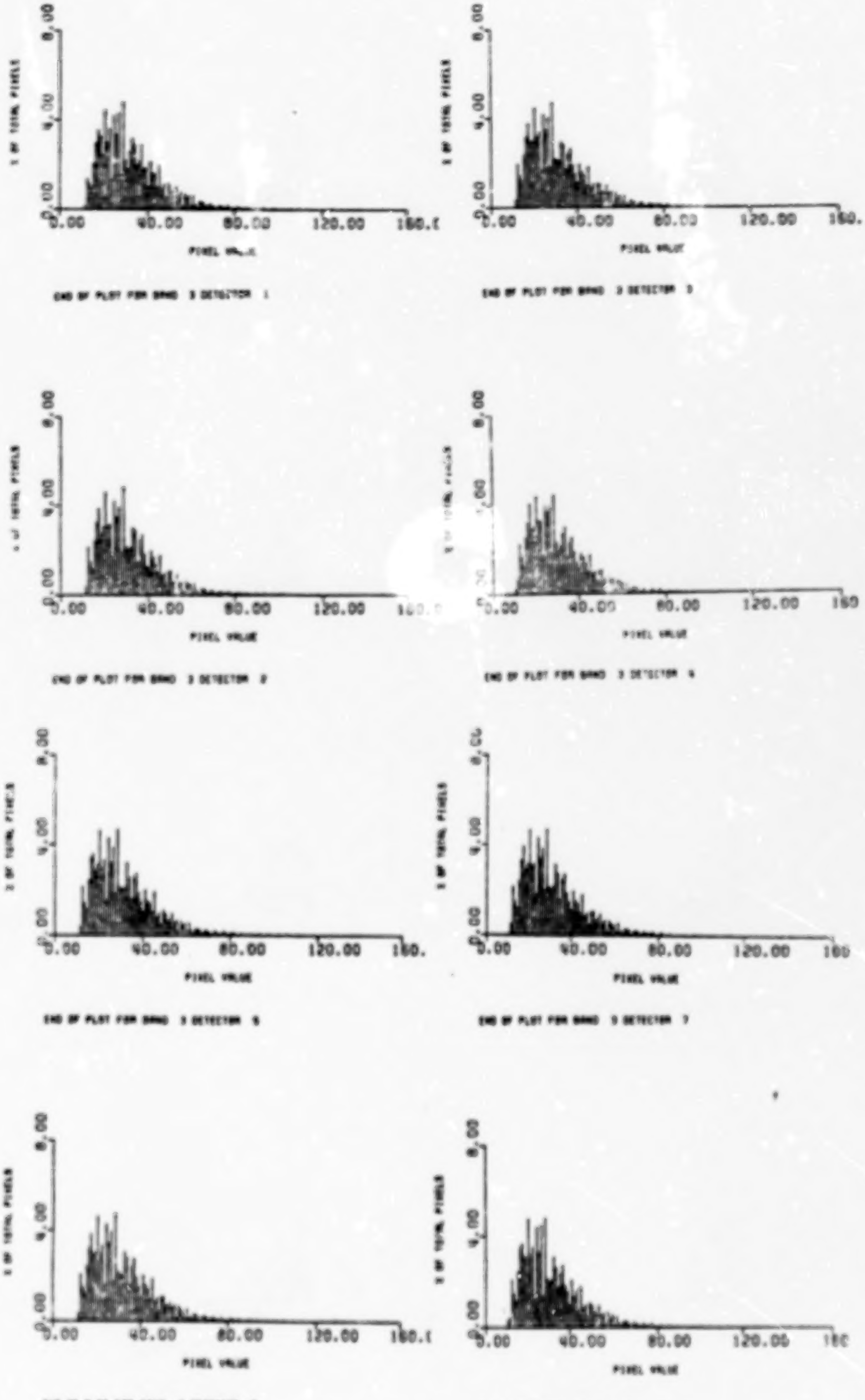

FIGURE 3.3 BAND 3 HISTOGRAMS

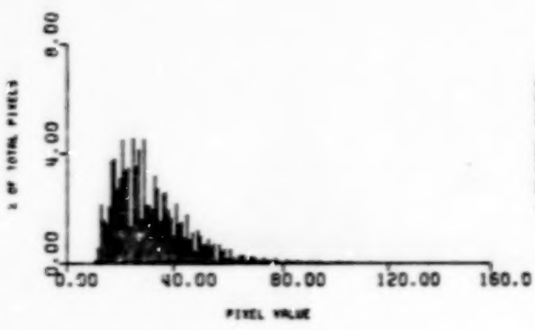

END OF PLOT FOR BAND 3 DETECTOR 9

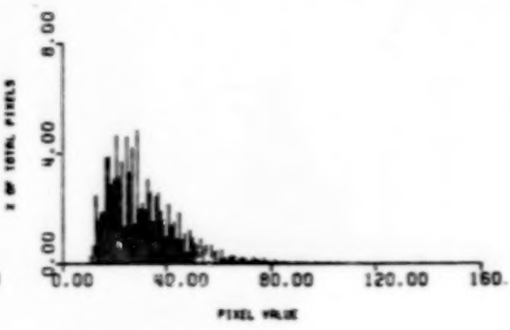

END OF PLOT FOR BAND 3 DETECTOR 11

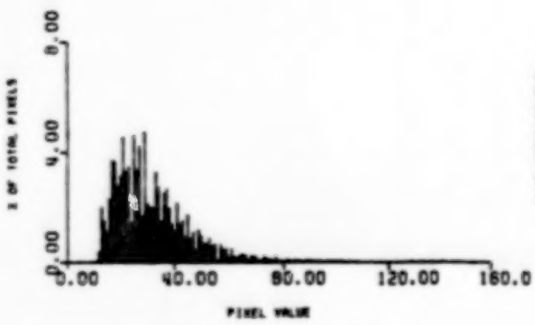

END OF PLOT FOR BAND 3 DETECTOR 10

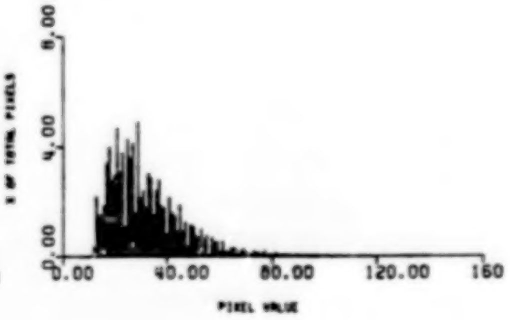

END OF PLOT FOR BAND 3 DETECTOR 12

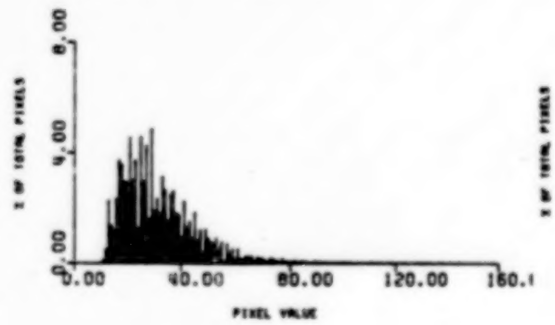

END OF PLOT FOR BAND 3 DETECTOR 13

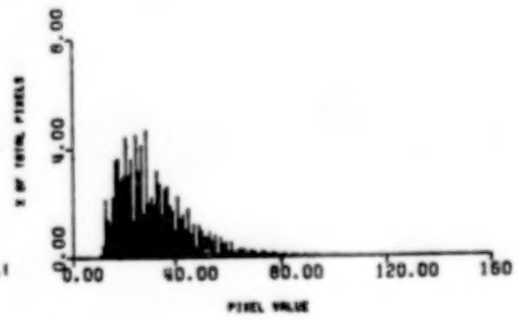

END OF PLOT FOR BAND 3 DETECTOR 15

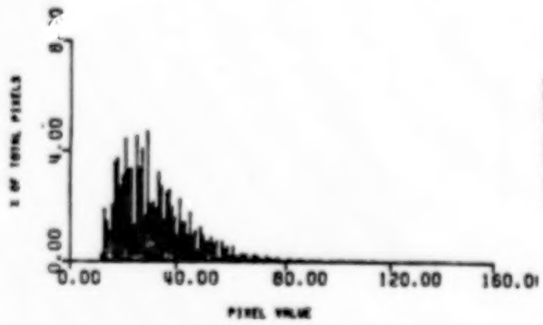

END OF PLOT FOR BAND 3 DETECTOR 14

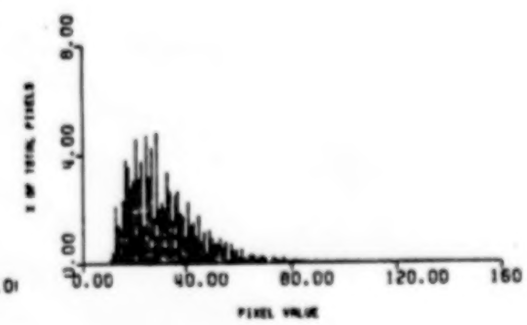

END OF PLOT FOR BAND 3 DETECTOR 16

FIGURE 3.3 (CONT) BAND 3 HISTOGRAMS

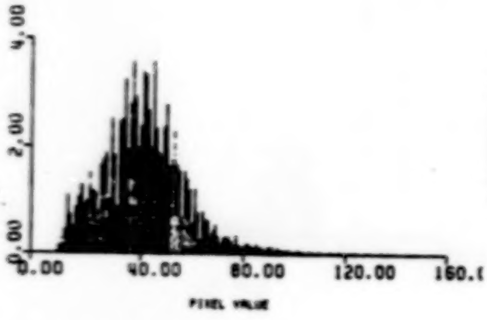

END OF PLOT FOR BAND 4 DETECTOR 1

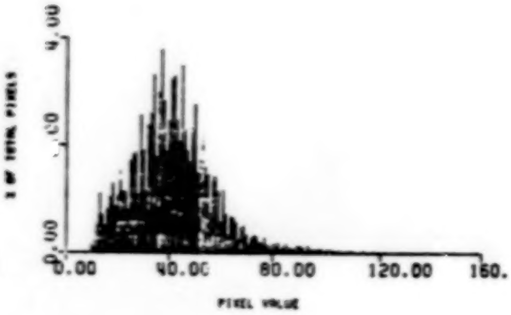

END OF PLOT FOR BAND 4 DETECTOR 3

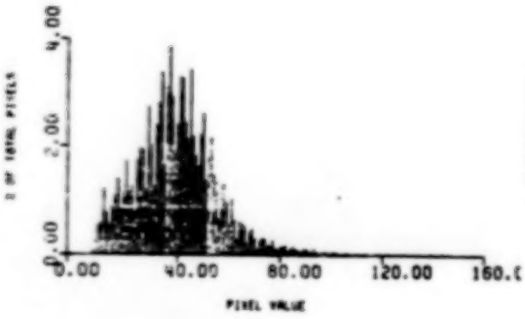

END OF PLOT FOR BAND 4 DETECTOR 2

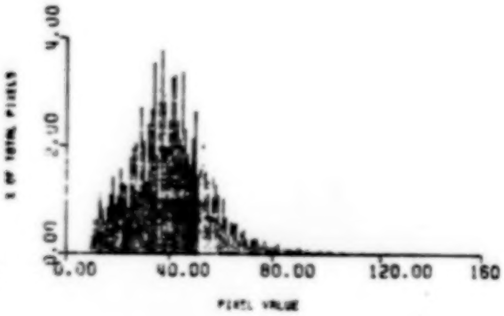

END OF PLOT FOR BAND 4 DETECTOR 4

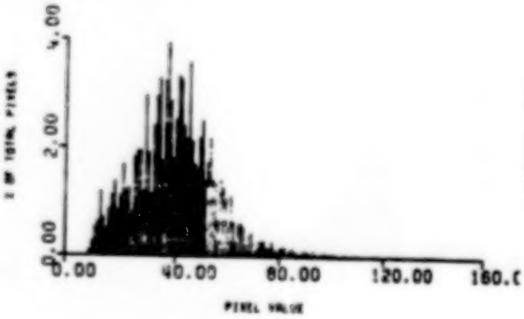

END OF PLOT FOR BAND 4 DETECTOR 5

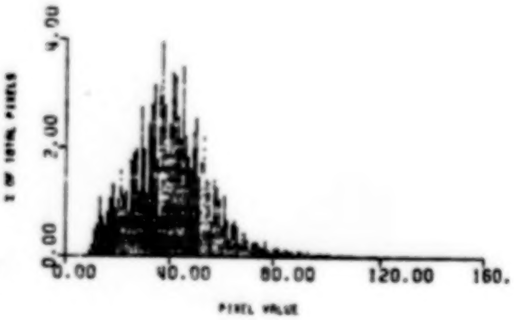

END OF PLOT FOR BAND 4 DETECTOR 7

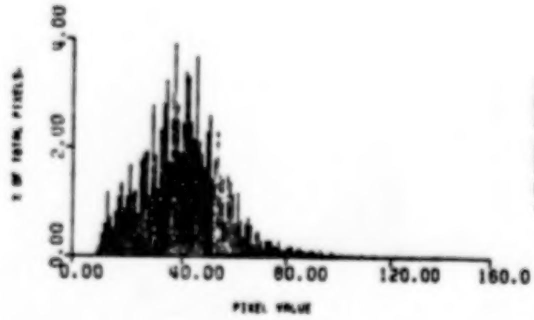

END OF PLOT FOR BAND 4 DETECTOR 6

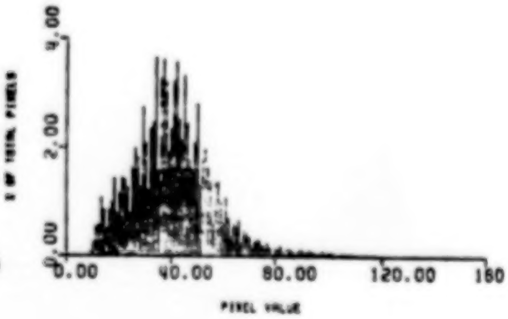

END OF PLOT FOR BAND 4 DETECTOR 8

FIGURE 3.4 BAND 4 HISTOGRAMS

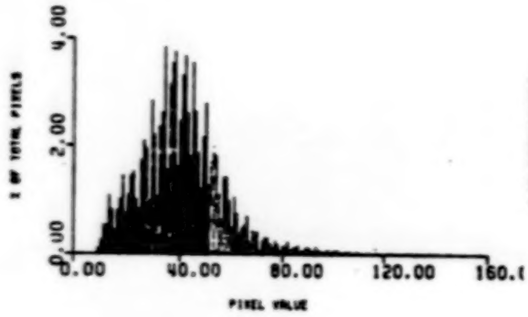

END OF PLOT FOR BAND 4 DETECTOR 9

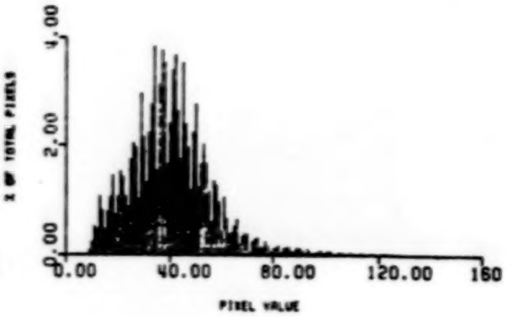

END OF PLOT FOR BAND 4 DETECTOR 11

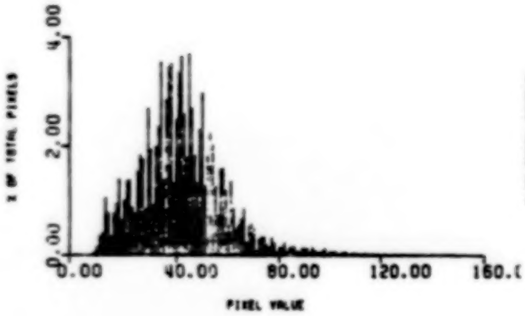

END OF PLOT FOR BAND 4 DETECTOR 10

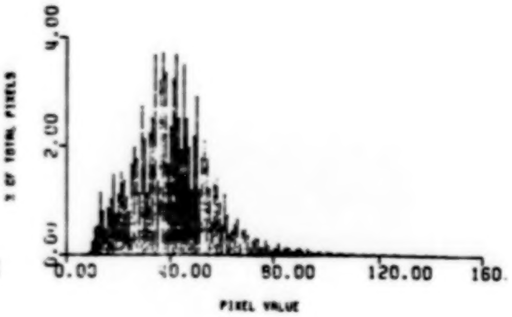

END OF PLOT FOR BAND 4 DETECTOR 12

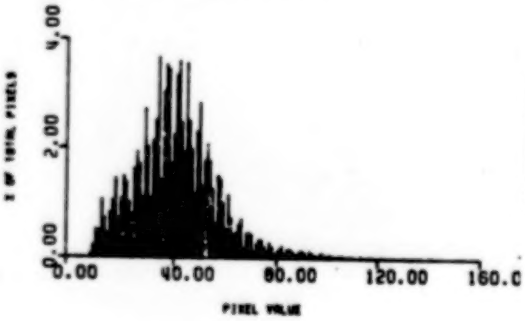

END OF PLOT FOR BAND 4 DETECTOR 13

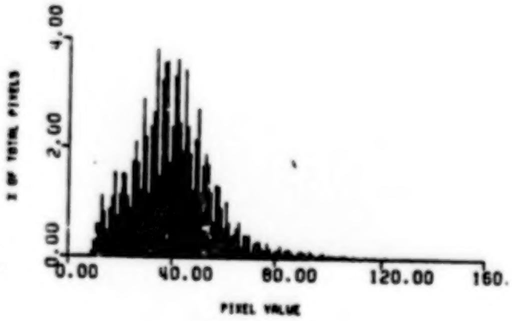

END OF PLOT FOR BAND 4 DETECTOR 15

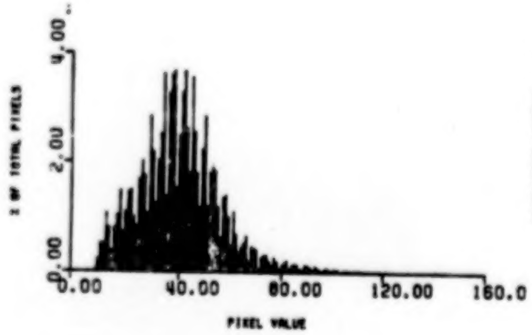

END OF PLOT FOR BAND 4 DETECTOR 14

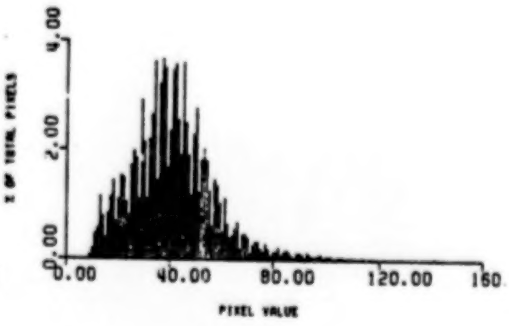

END OF PLOT FOR BAND 4 DETECTOR 16

FIGURE 3.4 (CONT) BAND 4 HISTOGRAMS

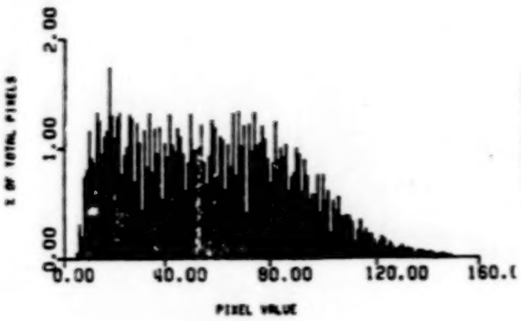

END OF PLOT FOR BAND 5 DETECTOR 1

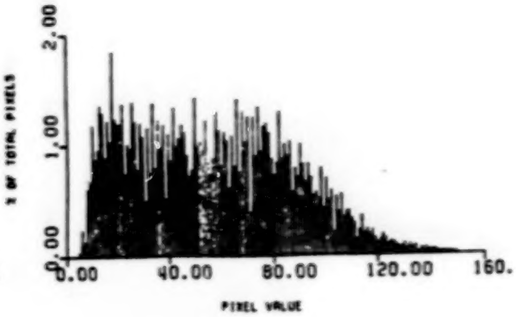

END OF PLOT FOR BAND 5 DETECTOR 3

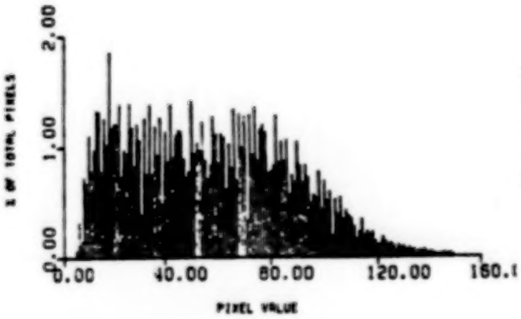

END OF PLOT FOR BAND 5 DETECTOR 2

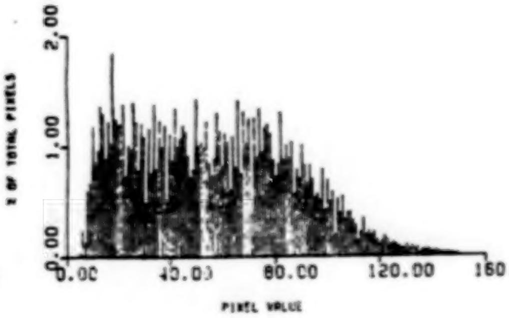

END OF PLOT FOR BAND 5 DETECTOR 4

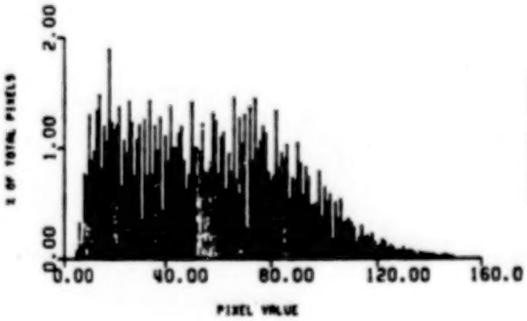

END OF PLOT FOR BAND 5 DETECTOR 5

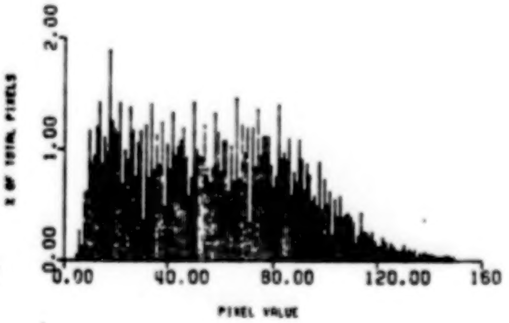

END OF PLOT FOR BAND 5 DETECTOR 7

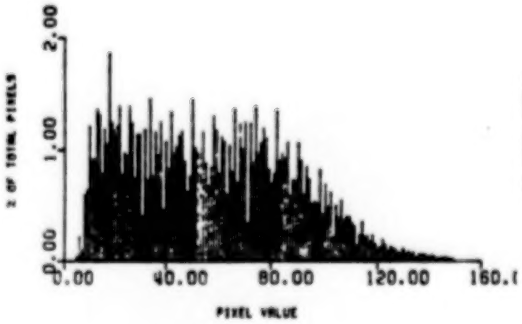

END OF PLOT FOR BAND 5 DETECTOR 6

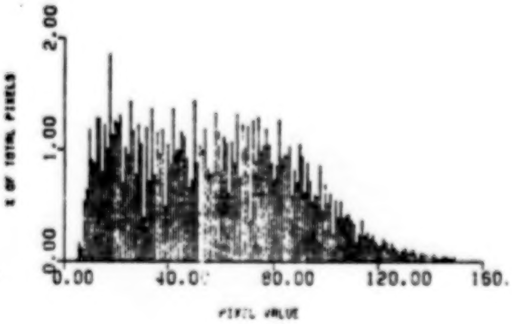

END OF PLOT FOR BAND 5 DETECTOR 8

FIGURE 3.5 BAND 5 HISTOGRAMS

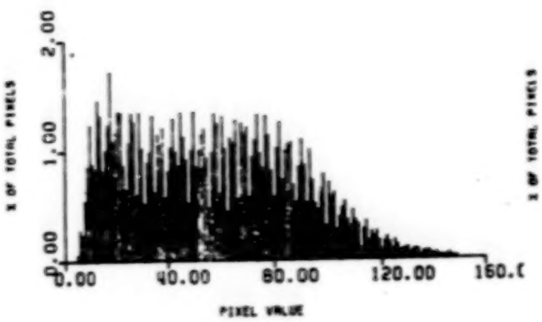

END OF PLOT FOR BAND 5 DETECTOR 9

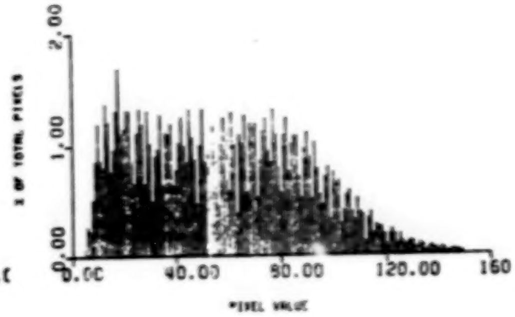

END OF PLOT FOR BAND 5 DETECTOR 11

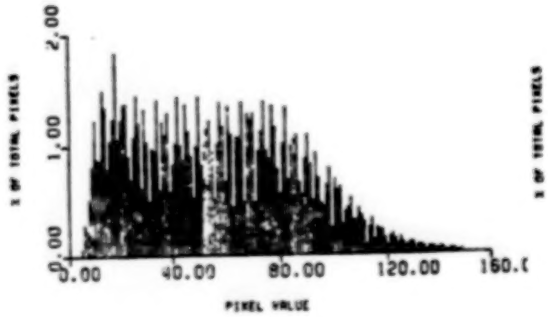

END OF PLOT FOR BAND 5 DETECTOR 10

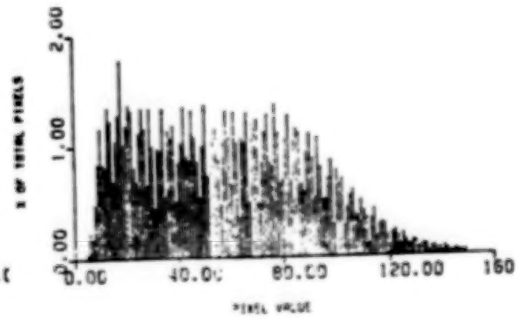

END OF PLOT FOR BAND 5 DETECTOR 12

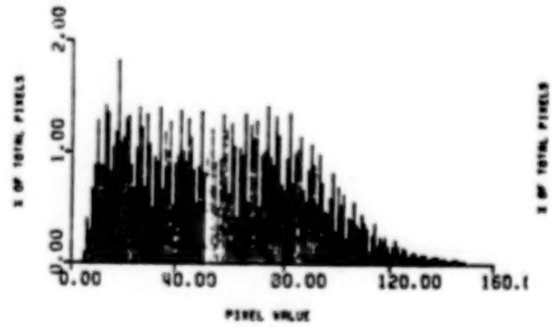

END OF PLOT FOR BAND 5 DETECTOR 15

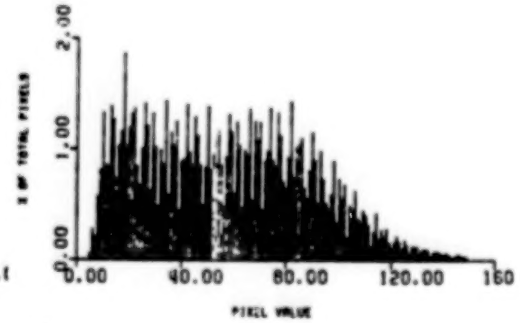

END OF PLOT FOR BAND 5 DETECTOR 13

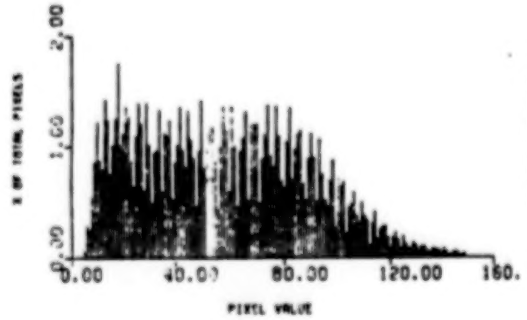

END OF PLOT FOR BAND 5 DETECTOR 16

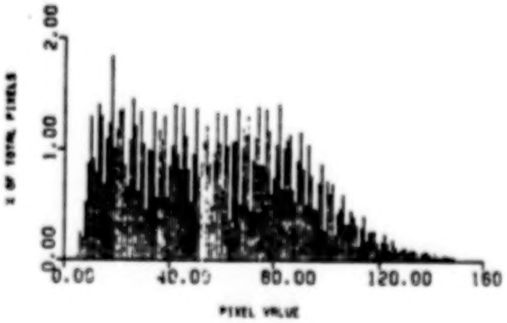

END OF PLOT FOR BAND 5 DETECTOR 14

FIGURE 3.5 (CONT) BAND 5 HISTOGRAMS

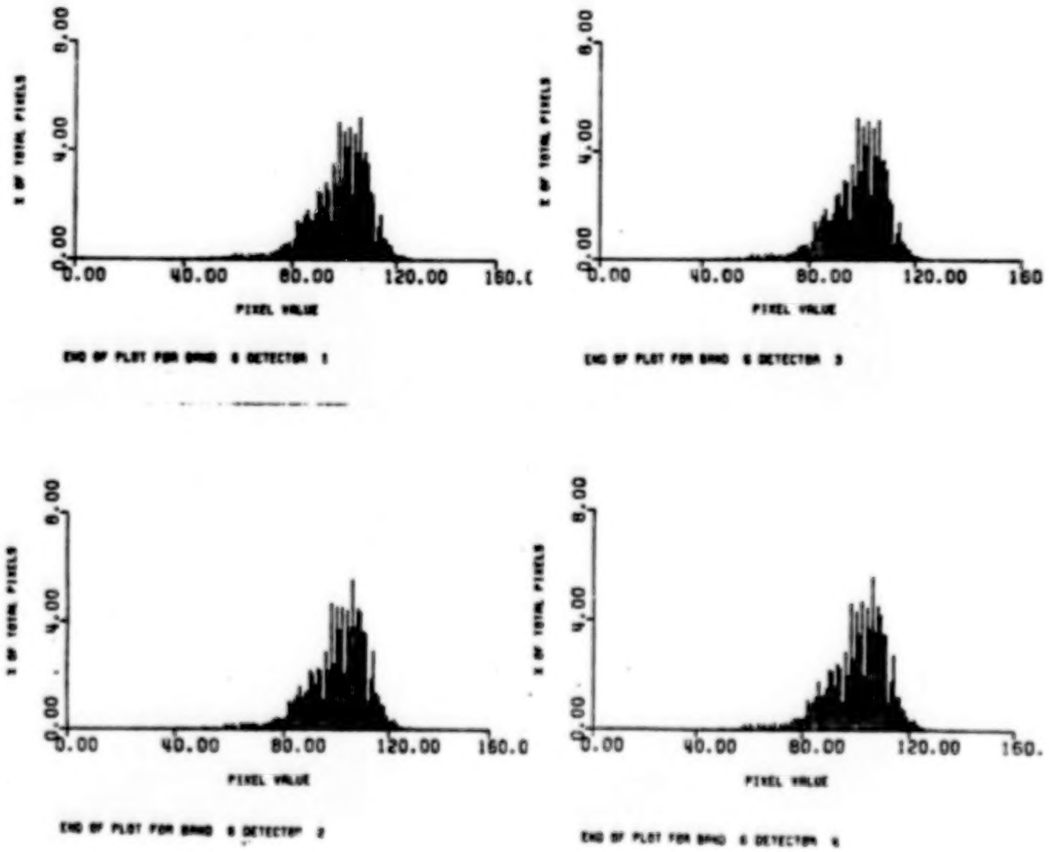

END OF PLOT FOR BAND 6 DETECTOR 1

END OF PLOT FOR BAND 6 DETECTOR 3

END OF PLOT FOR BAND 6 DETECTOR 2

END OF PLOT FOR BAND 6 DETECTOR 4

FIGURE 3.6 BAND 6 HISTOGRAMS

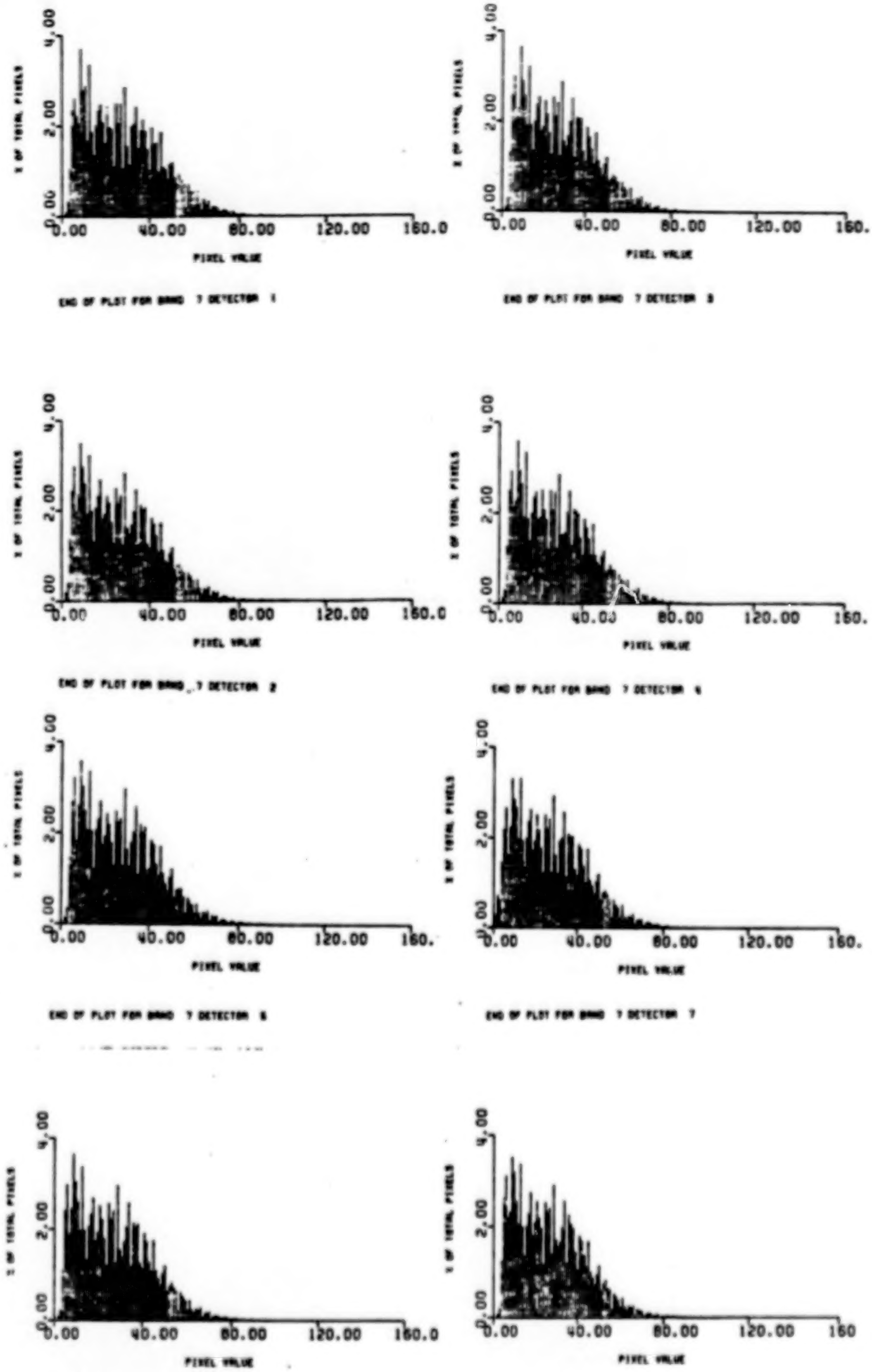

END OF PLOT FOR BAND 7 DETECTOR 1

END OF PLOT FOR BAND 7 DETECTOR 3

END OF PLOT FOR BAND 7 DETECTOR 2

END OF PLOT FOR BAND 7 DETECTOR 4

END OF PLOT FOR BAND 7 DETECTOR 5

END OF PLOT FOR BAND 7 DETECTOR 7

END OF PLOT FOR BAND 7 DETECTOR 6

END OF PLOT FOR BAND 7 DETECTOR 8

FIGURE 3.7 BAND 7 HISTOGRAMS

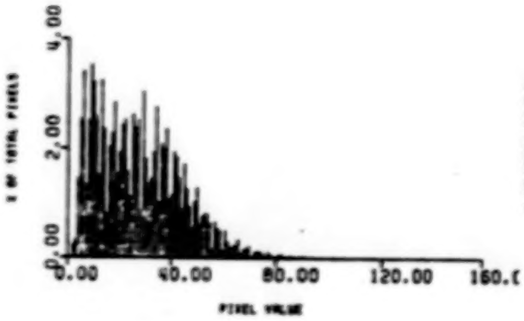

END OF PLOT FOR BAND 7 DETECTOR 9

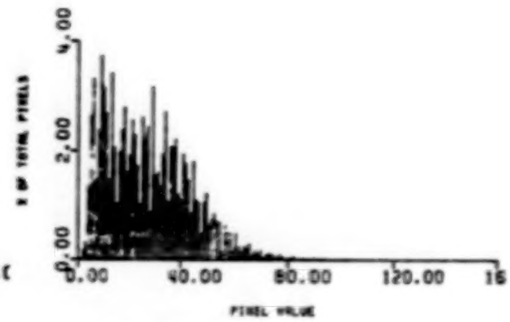

END OF PLOT FOR BAND 7 DETECTOR 11

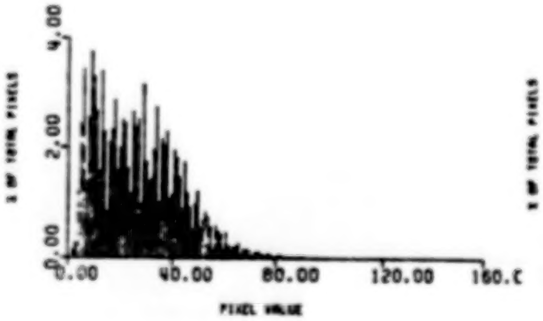

END OF PLOT FOR BAND 7 DETECTOR 10

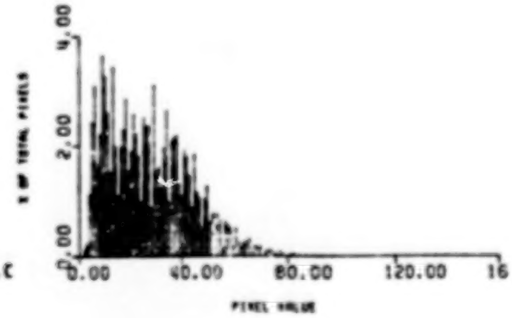

END OF PLOT FOR BAND 7 DETECTOR 12

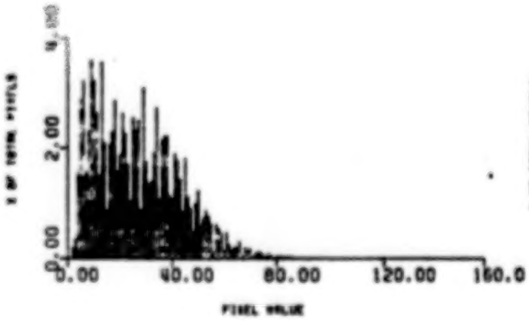

END OF PLOT FOR BAND 7 DETECTOR 13

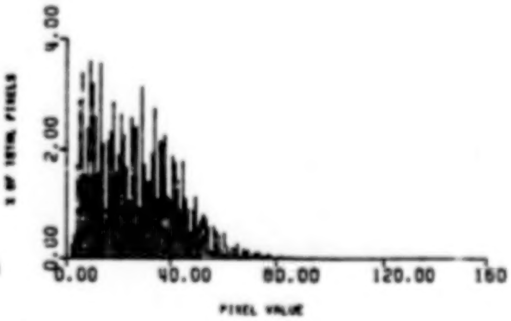

END OF PLOT FOR BAND 7 DETECTOR 15

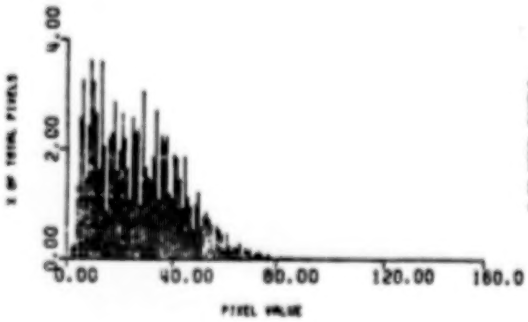

END OF PLOT FOR BAND 7 DETECTOR 14

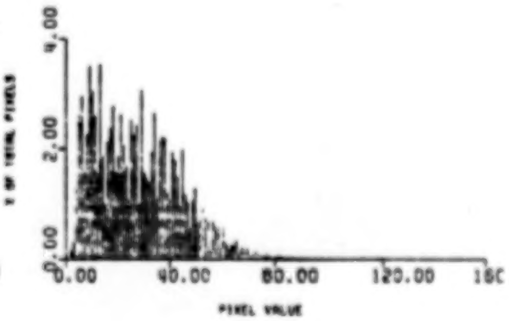

END OF PLOT FOR BAND 7 DETECTOR 16

FIGURE 3.7 (CONT) BAND 7 HISTOGRAMS

FIGURE 4.1 (Cont) Residual Striping Over Water - Band 1

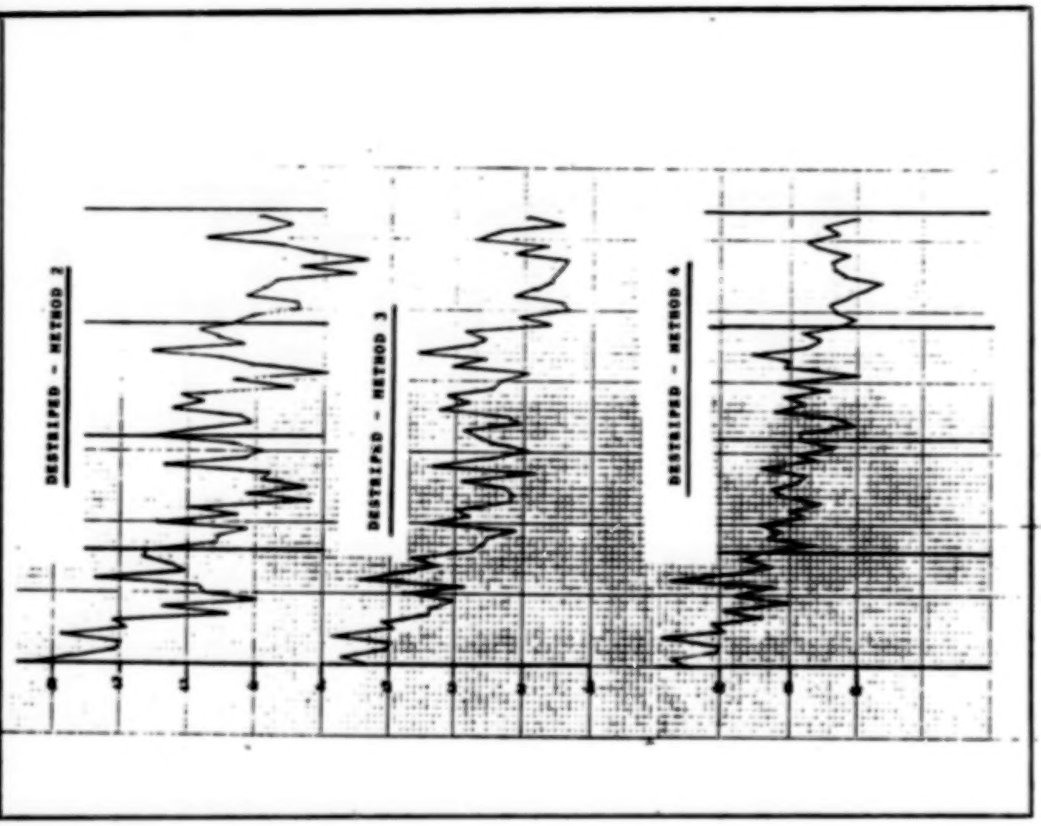

FIGURE 4.1 Residual Striping Over Water - Band 1

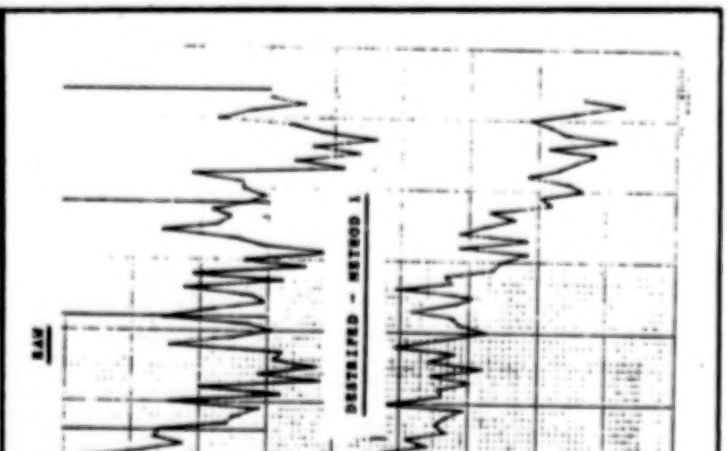

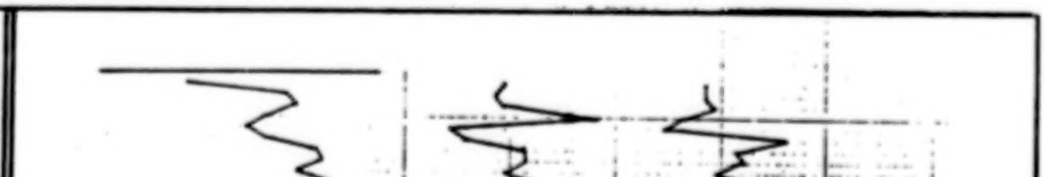

FIGURE 4.2 Residual Striping Over Water - Band 2

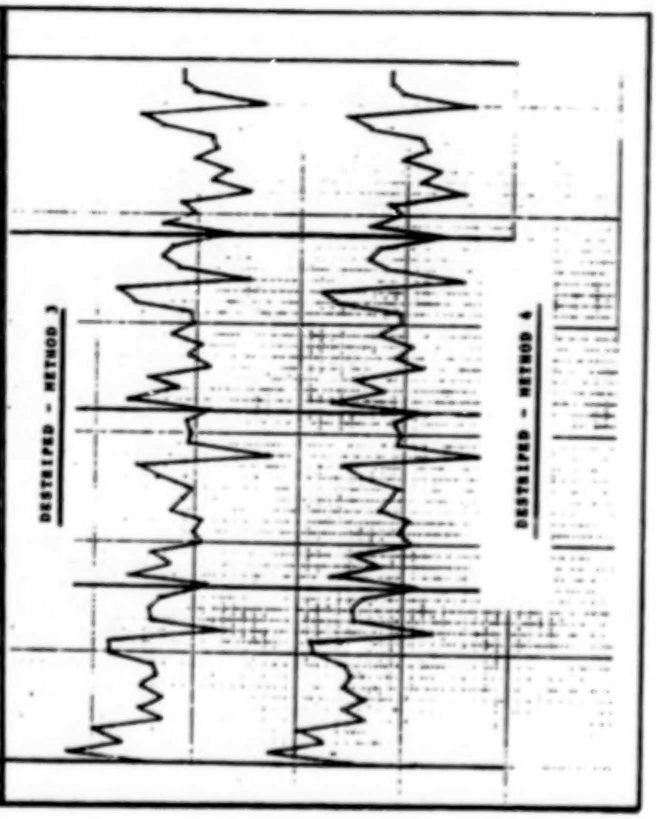

FIGURE 4.2 (Cont) Residual Striping Over Water - Band 2

FIGURE 4.3 Residual Striping Over Water - Band 3

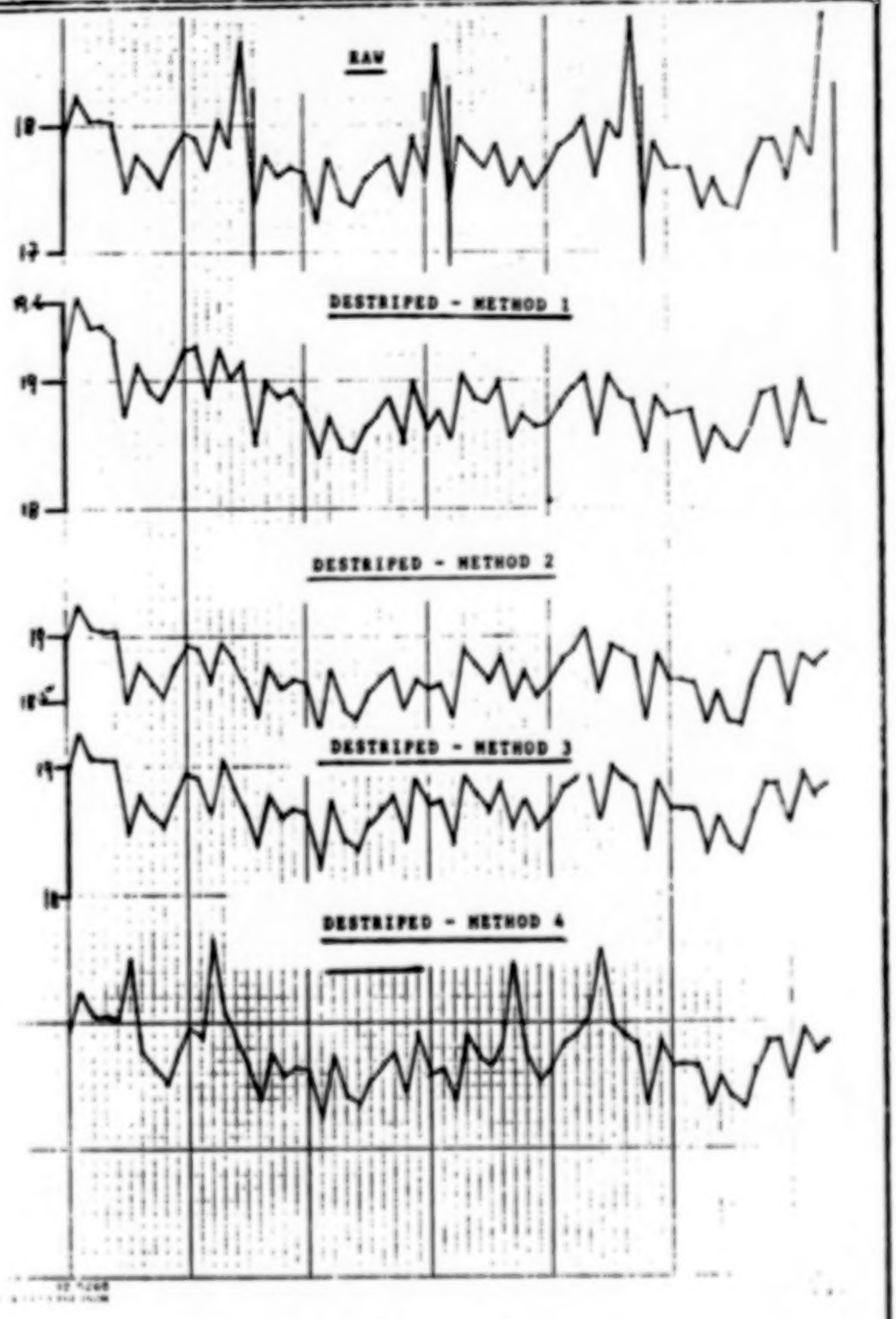

FIGURE 4.4 Residual Striping Over Water - Band 4

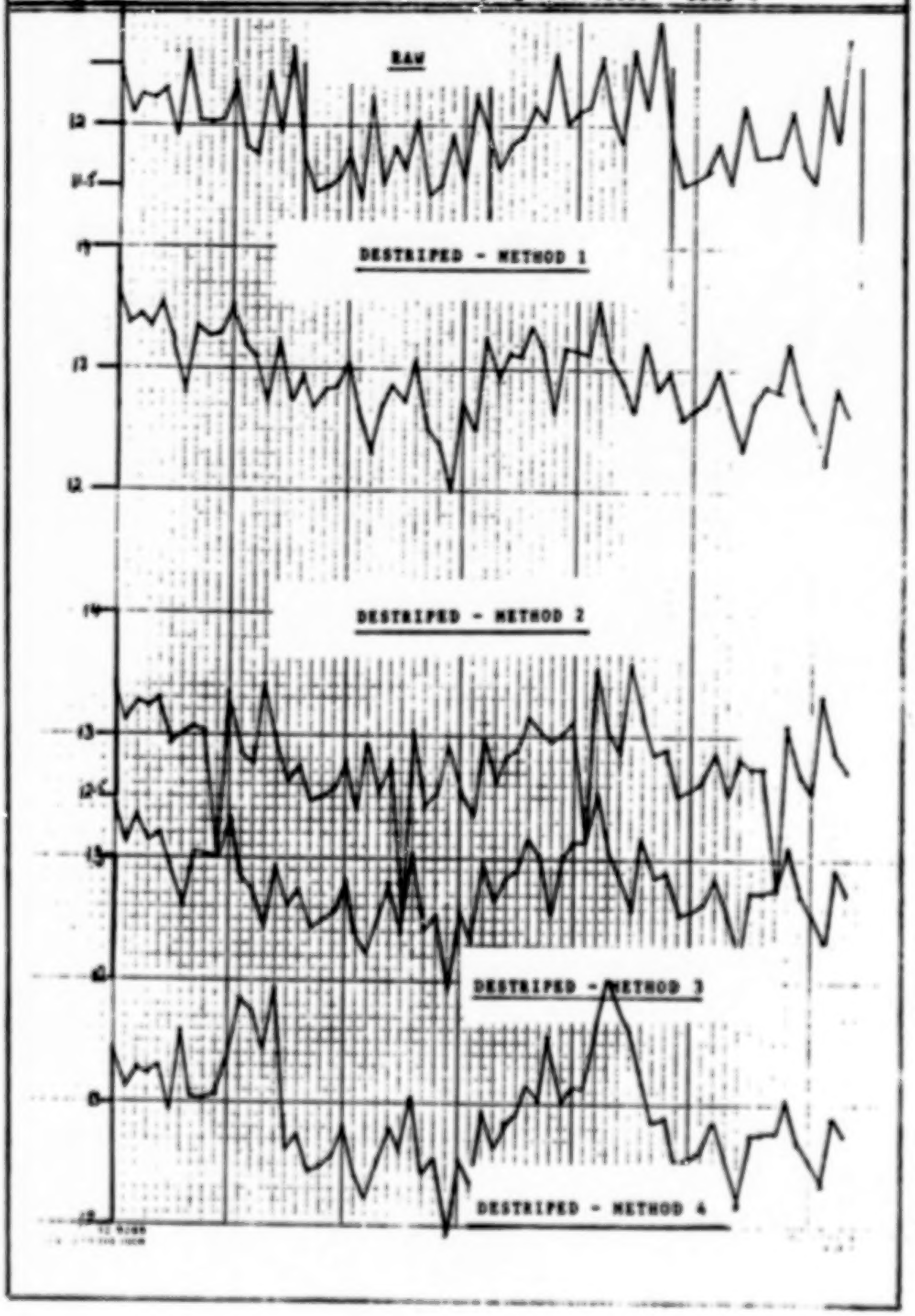

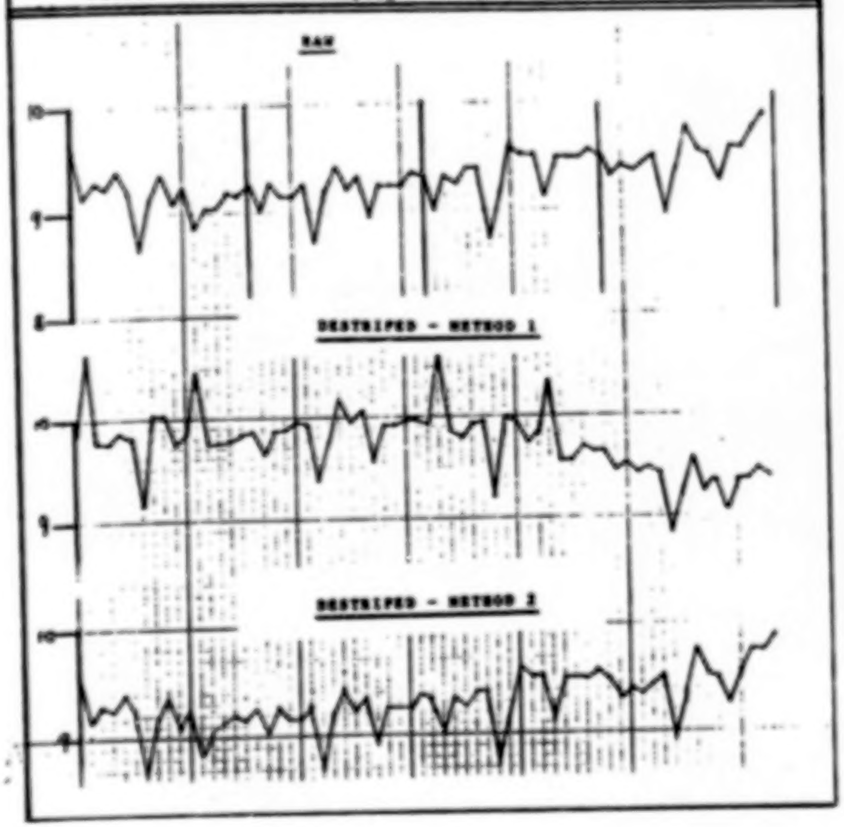
FIGURE 4.5 Residual Striping Over Water - Band 5

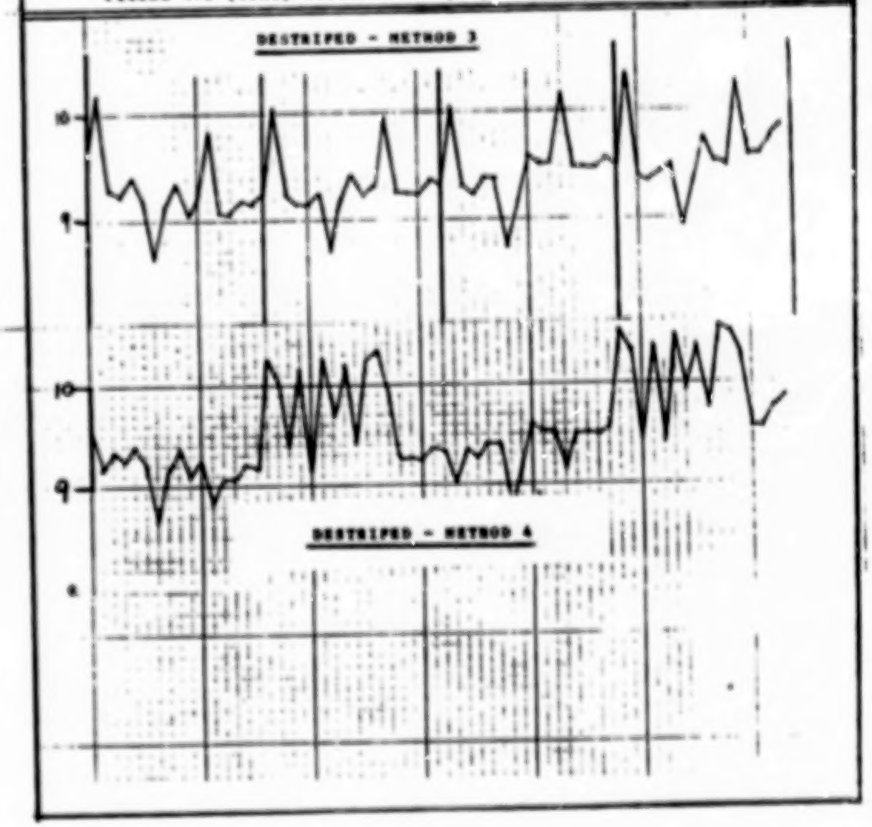
FIGURE 4.5 (Cont) Residual Striping Over Water - Band 5

ORIGINAL PAGE IS
OF POOR QUALITY

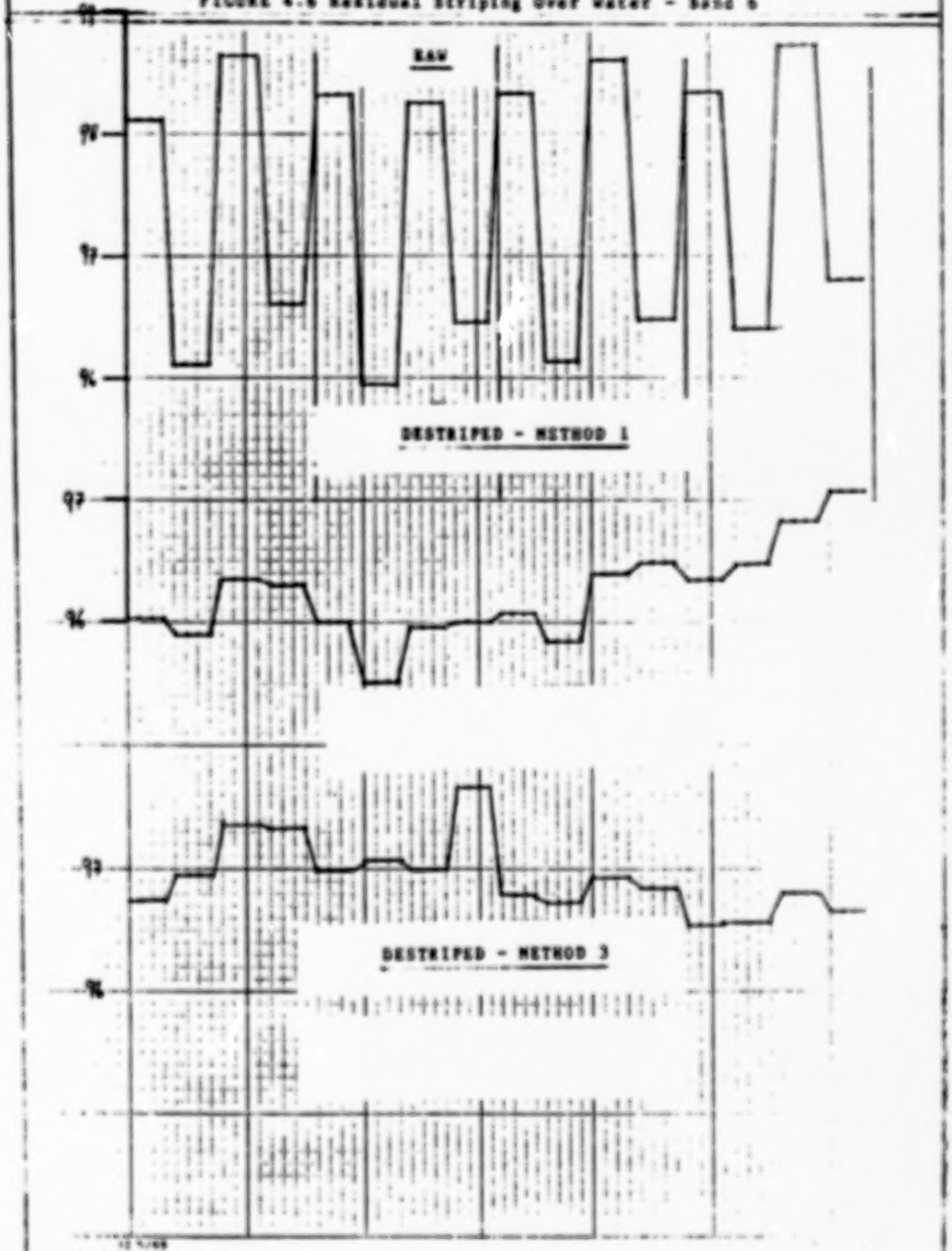

FIGURE 4.6 Residual Striping Over Water - Band 6

ORIGINAL PAGE IS
OF POOR QUALITY

FIGURE 4.7 Residual Striping Over Water - Band 7

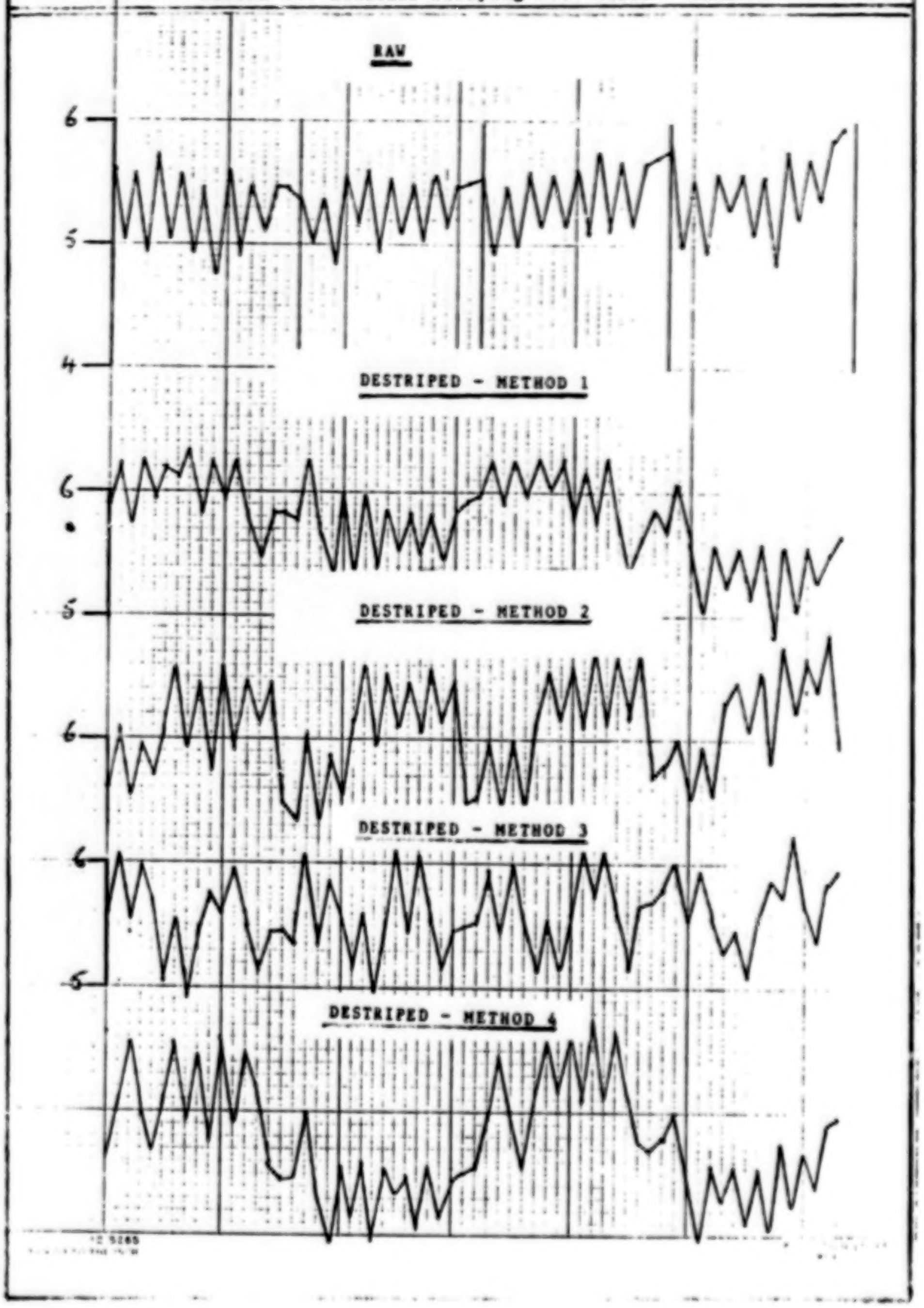

N85-21730

D6

A PRELIMINARY ANALYSIS OF LANDSAT-4 THEMATIC MAPPER RADIOMETRIC PERFORMANCE

C. Justice, ESA/EPO, Frascati, Italy
L. Fusco, ESA/EPO, Frascati, Italy
W. Mehl, CEC/JRC, Ispra, Italy

Original photography may be purchased
from EROS Data Center
Sioux Falls, SD 57198

INTRODUCTION

Analysis was performed to characterize the radiometry of three Thematic Mapper (TM) digital products of a scene acquired on August 22, 1982 of Arkansas, USA (Track 23, Frame 35). The three digital products examined were the NASA raw (BT) product, the radiometrically corrected (AT) product and the radiometrically and geometrically corrected (PT) product. The scene was one of the first seven band images made available for analysis as part of the Landsat Image Data Quality Assessment (LIDQA) program. The objective of the analysis was to examine the frequency distribution of the digital data; the statistical correlation between the bands; and the variability between the detectors within a band.* The analyses were performed on a series of image subsets from the full scene. The results presented in this paper are from one 1024 x 1024 pixel subset of Realfoot Lake, Tennessee which displayed a representative range of ground conditions and cover types occurring within the full frame image. Bands 1, 2 and 5 of the sample area are presented as Fig. 1, 2, and 3 respectively. The subsets were extracted from the three digital data products to cover the same geographic area. The following analysis was undertaken within the first few weeks of obtaining the TM data and provides the first step towards a full appraisal of the TM radiometry being performed as part of the ESA/CEC contribution to the NASA/LIDQA program.

CHARACTERIZATION OF THE DATA DISTRIBUTION

The mean, standard deviation and mode values were calculated for each of the spectral bands for the three data products and are presented as Fig. 4 (a,b,c). The mean values for the raw (BT) data were higher by two counts in Band 4 than the mean value for the same band of the radiometrically processed (AT) data. The mean values for the radiometrically and geometrically processed (PT) data were higher than the mean BT values in all channels by as much as four counts

---

*NB The band notation used in this paper refers to Band 6 as 10.4 - 12.5 μm and Band 7 as 2.08 - 2.35 μm.

PAGE III-308 INTENTIONALLY BLANK

PRECEDING PAGE BLANK NOT FILMED

(4.6) in Band 4 and two counts (6.8%) in Band 5. The highest standard deviations were calculated for Bands 4 and 5 which had markedly polymodal distributions for the selected study area. The frequency histograms of the seven bands of the PT data are presented as Figure 5.

BAND-TO-BAND CORRELATION

Pearsons Product Moment Correlation Coefficient (r^2) were calculated for the three TM data sets and are presented as Fig. 6 (a, b, c). High correlations *(>.9) were calculated between Bands 1, 2 and 3 for the particular sample scene. Lowest correlations (<.05) were calculated between Bands 1 and 5, 3 and 5, 4 and 6. A negative relationship was calculated between Band 4 and Bands 1, 2 and 3 for all data sets. The relationships between Bands 5/3, 6/4 were inverted for the BT and PT correlations. Both increases and decreases in correlation coefficients were observed when comparing the BT and PT correlations.

DETECTOR VARIABILITY

Statistical analyses were undertaken to examine the variability between the 16 detectors in each band. The results for the raw (BT) data are summarized by Fig. 7 where different measures are used to quantify the within band detector variability. A wide range in mean values between the different detectors was observed for Bands 4 and 6. During the analysis Detector 3 of Band 5 was found to be defective and was replaced within the analysis by the previous detector values. Detector 4 of Band 2 was found to have an atypical mean and variance for that band. Examination of the radiometrically corrected (AT) data revealed a decrease in the range of mean values for each detector but still showed considerable variation between the detectors after correction (Fig. 8). The greatest remaining range in detector mean values of 1.16 digital counts was found for Band 1.

Visual examination of the raw data revealed a marked striping effect with a 16 line modulus due to the difference in the gain and offset values for detectors 1 and 16. This swath interface striping was quantified and is summarized in Fig. 9(a). Differences of more than one pixel level between the means of detector 16 and detector 1 were observed for Bands 2, 3 and 4. This effect was substantially reduced in the radiometrically corrected data Fig. 9(b).

FORWARD AND REVERSE DETECTOR ANALYSIS

One possible source of the apparent variation between the detectors is a difference between the response in the forward and reverse scan direction which is not compensated for within the radiometric correction procedure. Analysis of the data revealed substantial differences between the forward and reverse scan detector responses. The mean and variance for the forward and reverse detector responses for the BT and AT data are presented in Fig. 10 (a-d). The maximum difference of .8 of a digital count were observed between forward and reverse detector means.* Standard deviations were consistently higher for forward than for reverse scans.

STATISTICAL ANALYSIS OF WATER SURFACE RESPONSE

As a preliminary to assessing the performance of the sensors over areas of relatively uniform response, analysis was performed to examine the first order statistics for three selected water classes. Polygons were delineated interactively for major river and lake areas. In addition all values in Band 5 of less than 15 digital counts were taken as a seperate general water class. Mean and standard deviation values were calculated for the three classes and are presented in Fig. 11a. Considerable differences can be seen between the lake and water classes. Correlation coefficients for the lake and river classes are presented in Fig. 11b. Highest correlations were observed between Bands 2 and 3.

---

*Striping is visually apparent where mean difference between detectors is >.5.

CONCLUSIONS

From this cursory examination of one of the first seven channel TM data sets it would appear that the radiometric performance of the system is most satisfactory and largely meets pre-launch specifications. Problems were noted with Band 5 Detector 3 and Band 2 Detector 4. A suitable algorithm needs to be developed to overcome the visual problems associated with failed or noisey detectors. Differences were observed between forward and reverse scan detector responses both for the BT and AT products. Further analysis is required to assess whether alternative correction procedures are required to compensate for forward and reverse scan effects in the different channels. No systemmatic variations were observed between odd and even detectors.

Further analysis is required to provide a comprehensive assessment of the radiometric performance of the system for a variety of surface reflectances and illumination conditions.

ORIGINAL PAGE IS
OF POOR QUALITY

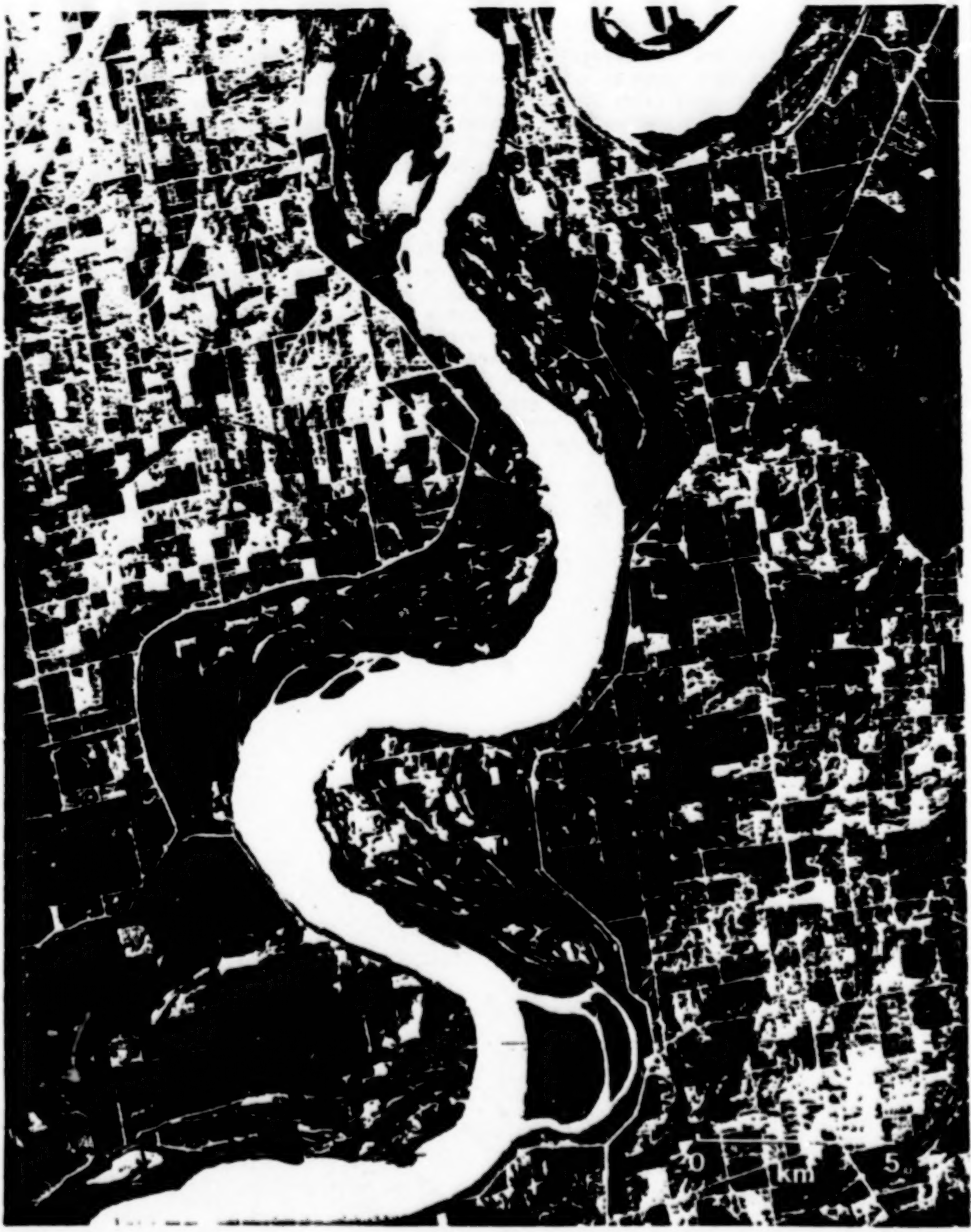

Fig 1. Thematic Mapper Band 1. Reelfoot Lake Tennessee. 1024 x 1024 pixels.
(Tr. 23, Fr. 25) 22.06.82.

ORIGINAL PAGE IS
OF POOR QUALITY

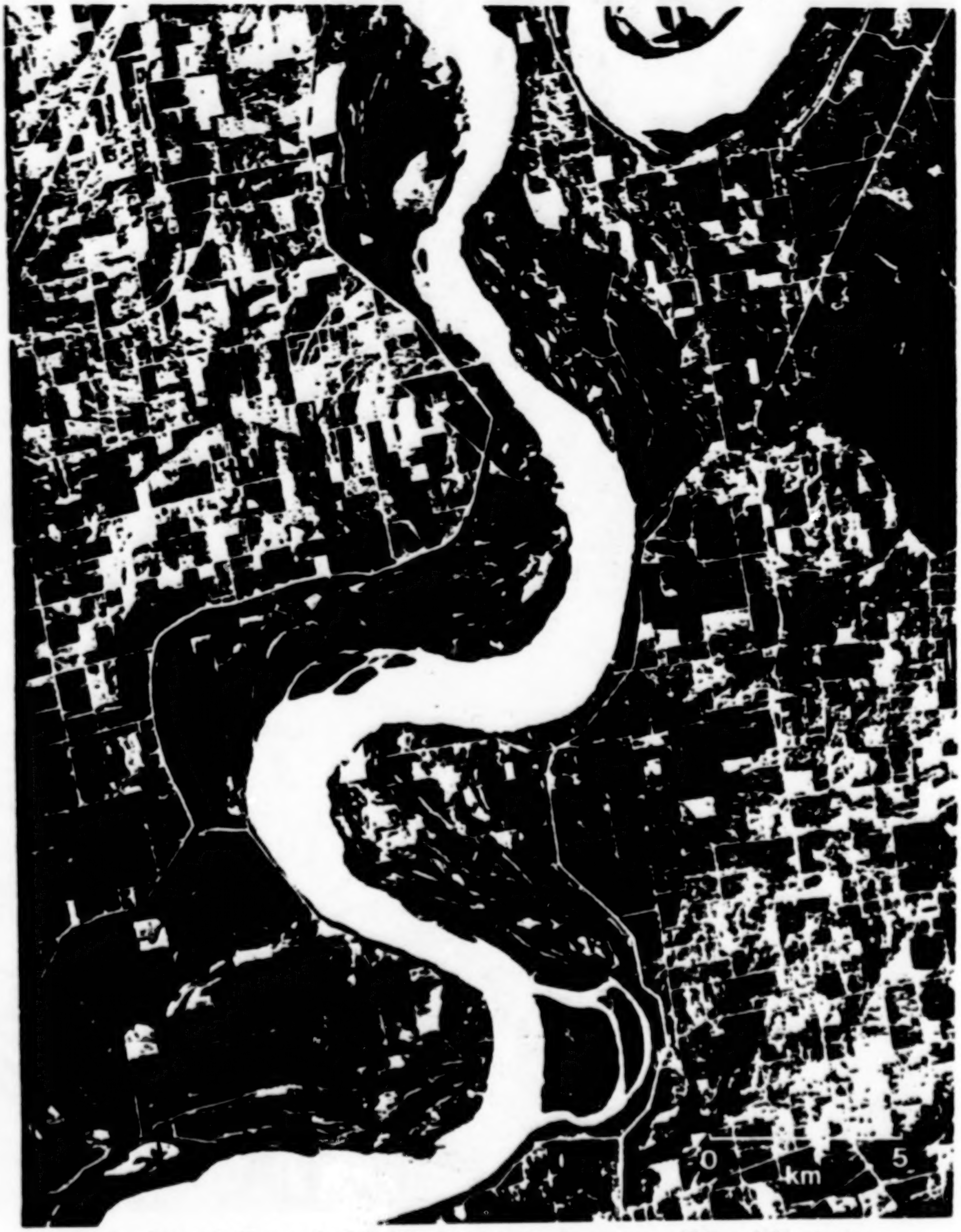

Fig 2. Thematic Mapper Band 2. Realfoot Lake, Tennessee. 1024 x 1024 pixels. (Tr. 23, FR. 25) 22.08.82.

ORIGINAL PAGE IS
OF POOR QUALITY

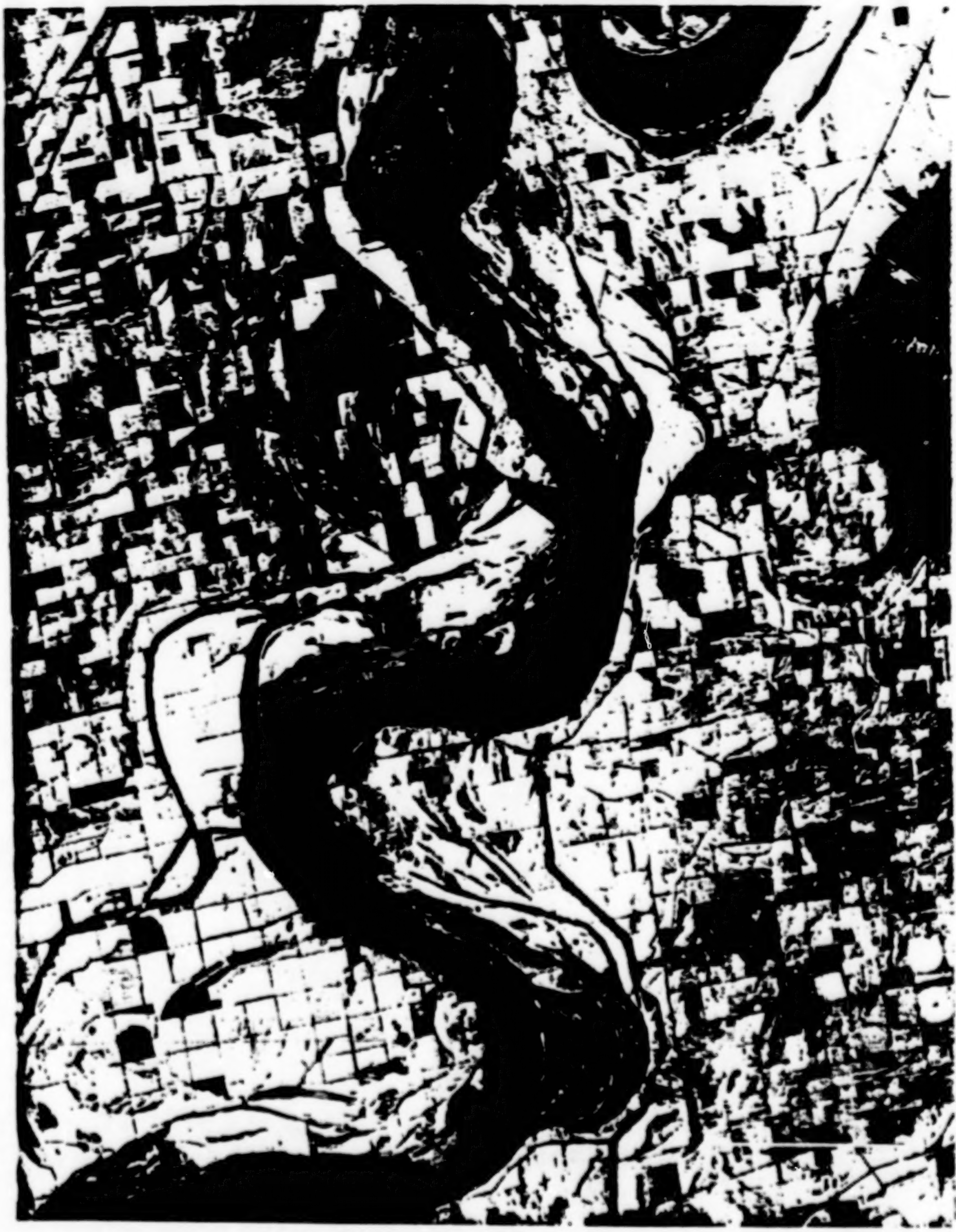

Fig 3. Thematic Mapper Band 5. Realfoot Lake, Tennessee. 1024 x 1024 pixels. (Tr. 23, Fr. 25) 22.08.82.

BAND	MEAN	δ	MODE 1	2	3
1	75.3	8.0	70/10/7%	86/2.2%	-
2	31.9	5.6	28/12/8%	-	-
3	28.5	9.5	21/14.2%	45/2.6%	-
4	99.5	34.2	41/1.72%	96/1.64%	18/1.44%
5	70.0	27.8	78/3.44%	6/2.58%	-
6	137.3	6.1	134/10.74%	-	-
7	25.7	13.7	25/6.37%	5/3.55%	-

Fig 4a. Statistical Description of the Raw Data (BT) Distribution.

BAND	MEAN	δ	MODE 1	2	3
1	74.9	7.8	70/11.4%	86/2.4%	-
2	31.2	5.2	27/15.3%	29/12.6%	-
3	28.5	9.3	21/14.0%	45/3.4%	-
4	97.3	33.1	93/1.97%	38/1.73%	18/1.62%
5	68.8	27.1	82/4.38%	6/2.56%	-
6	137.3	5.7	134/11.4%	-	-
7	25.6	13.4	25/8.07%	4/3.66%	-

Fig 4b. Statistical Description of the Radiometrically Processed Data (AT) Distribution.

BAND	MEAN	δ	MODE 1	2	3
1	76.09	7.8	70/8.7%	86/2.3%	-
2	32.38	5.3	28/11.6%	-	-
3	29.36	9.6	21/11.8%	45/2.8%	-
4	101.78	33.07	93/1.30%	39/1.98%	-
5	72.55	28.10	83/3.39%	6/2.2%	-
6	139.68	5.98	134/11.3%	-	-
7	27.35	14.01	25/6.47%	4/3.4%	-

Fig 4c. Statistical Description of the Processed Data (PT) Distribution.

BANDS	1	2	3	4	5	6
2	.943					
3	.953	.948				
4	-.401	-.305	-.485			
5	.063	.143	.007	.652		
6	.355	.405	.341	-.039	.497	
7	.413	.478	.385	.273	.877	.649

Fig 6(a) Correlation Coefficients (r^2) for the Raw (BT) Data Bands.

BANDS	1	2	3	4	5	6
2	↓.908					
3	.955	↓.909				
4	-.397	↓-.331	-.480			
5	.064	.141	.006	.656		
6						
7	.416	↓.462	.384	.275	.876	

Fig 6(b) Correlation Coefficients (r^2) for the Radiometrically Corrected (AT) Data Bands.

BANDS	1	2	3	4	5	6
2	↑.951					
3	↑.962	↑.952				
4	↓.495	↓.442	↓.577			
5	↓.022	↓.106	↓-.042	↓.597		
6	↓.282	↓.329	↓.259	↑.032	↑.597	
7	↓.410	.478	↓.370	↓.210	↓.842	↓.627

Fig 6(c) Correlation Coefficients (r^2) for the Processed (PT) Data Bands

↓↑ Indicates increase or decrease with respect to the raw data coefficients.

BAND	$\bar{x}$	δ	RANGE $\bar{x}_i$	RANGE δ_i	δ OF MEANS	$\frac{\delta \text{ OF MEANS}}{x} \times 100$
1	74.9	7.83	2.20	.399	.593	.792
2	31.2	5.21	1.49	.762	.398	1.28
3	28.5	9.31	1.42	.377	.305	1.07
4	97.3	33.10	4.27	.947	1.131	1.16
5	68.8	27.1	2.90	1.33	.798	1.15
6	137.3	5.69	4.65	.363	2.191	1.59
7	25.6	13.41	1.43	.736	3.48	1.35

Fig 7. Detector Variability Within Different Bands for the Raw (BT) Data, taking the Mean Values and Statistics for a Line Modulus of 16.

BAND	$\bar{x}$	δ	RANGE $\bar{x}_i$	RANGE δ_i	δ OF MEANS	$\frac{\delta \text{ OF MEANS}}{x} \times 100$
1	75.3	7.97	1.16	0.755	.288	.382
2	31.9	5.54	0.93	0.578	.215	.674
3	28.5	9.45	0.50	0.699	.124	.434
4	99.5	34.16	0.71	0.881	.499	.502
5	70.0	27.77	1.13	0.812	.279	.399
6	-	-	-	-	-	-
7	25.7	13.67	1.13	0.707	.226	.879

Fig 8. Detector Variability within Different Bands for the Radiometrically Corrected (AT) Data, taking the Mean Values and Statistics for a Line Modulus of 32.

BAND	DIFFERENCE BETWEEN $\bar{x}$ OF DETECTORS 16 AND 1	DIFFERENCE BETWEEN σ OF DETECTORS 1 AND 16
1	.987	.022
2	1.366	.278
3	1.098	.400
4	1.584	.505
5	.878	.510
6	-	-
7	.444	.444

Fig 9(a). Difference Between the Mean and Standard Deviations of Detectors 1 and 16 showing the Swath Interface Striping for the Raw (BT) Data.

BAND	DIFFERENCE BETWEEN $\bar{x}$ OF DETECTORS 16 AND 1	DIFFERENCE BETWEEN σ OF DETECTORS 1 AND 16
1	0.676	-0.308
2	0.014	0.044
3	0.316	0.614
4	0.131	0.264
5	0.274	0.268
6	-	-
7	1.079	0.369

Fig 9(a) Difference Between the Mean and Standard Deviations of Detectors 1 and 16 Showing the Swath Interface Striping for the Radiometrically Corrected (AT) Data.

					BANDS			
		1	2	3	4	5	6	7
	$F\bar{x}$	74.79	31.17	28.54	96.88	69.9	-	25.70
	$R\bar{x}$	75.10	31.23	28.53	97.67	68.6	-	25.50
(R - F)	$\Delta\bar{x}$	+.310	+.060	-.001	+.789	-.265	-	-.201

Fig 10(a) Mean Values and Difference for Forward and Reverse Scan Lines for Raw (BT) Data Bands.

					BANDS			
		1	2	3	4	5	6	7
	$F\bar{x}$	75.11	31.87	28.49	99.07	70.11	-	25.83
	$R\bar{x}$	75.43	31.89	28.49	99.87	69.85	-	25.63
(R - F)	$\Delta\bar{x}$	+.32	+0.18	-0.02	+.808	-.256	-	-.195

Fig 10(b) Mean Values and Difference for Forward and Reverse Scan Lines for the Radiometrically Corrected (AT) Data Bands.

					BANDS			
		1	2	3	4	5	6	7
	$F\sigma$	7.89	5.29	9.401	33.21	27.23	-	13.54
	$R\sigma$	7.704	5.16	9.226	33.02	27.02	-	13.29
(R - F)	$\Delta\sigma$	-.285	-.069	-.175	0.196	-.213	-	-.254

Fig 10(c) Standard Deviations and Differences for Forward and Reverse Scan Lines for the Raw (BT) Data Bands.

				BANDS			
	1	2	3	4	5	6	7
$F\sigma$	8.12	5.89	9.53	34.26	27.87	-	13.79
$R\sigma$	7.84	5.33	9.37	34.06	27.68	-	13.55
$\Delta\sigma$	-0.282	-0.560	-0.166	-0.194	-0.187	-	-0.235

Fig 10(d) Standard Deviations and Differences for Forward and Reverse Scan Lines for the Radiometrically Corrected (AT) Data Bands.

BAND		RIVER POLYGON N = 4004	LAKE POLYGON N = 17,644	SLICED AT CH 5 > 15 VALUES N = 119,681
1	$\bar{x}$	88.0	71.4	82.0
	δ	2.1	2.0	7.6
2	$\bar{x}$	38.5	27.3	34.9
	δ	1.1	1.0	5.1
3	$\bar{x}$	46.2	22.1	38.4
	δ	1.3	1.0	10.7
4	$\bar{x}$	39.6	18.2	32.89
	δ	1.3	0.7	9.5
5	$\bar{x}$	9.4	6.4	8.0
	δ	1.5	1.2	2.0
6	$\bar{x}$	132.2	133.3	132.5
	δ	2.7	2.4	1.7
7	$\bar{x}$	5.4	4.0	4.6
	δ	1.3	1.2	1.4

Fig 11(a) Mean and Standard Deviation for Three Water Classes of the Raw (BT) Data.

LAKE AREA (N = 17.644)

BANDS	1	2	3	4	5	6
2	.286					
3	.407	.513				
4	.270	.376	.412			
5	.285	.158	.331	.186		
6	-.097	-.010	-.095	-.078	-.094	
7	.188	.112	.220	.112	.248	-.055

RIVER AREA (N = 4004)

BANDS	1	2	3	4	5	6
2	.369					
3	.412	.616				
4	.243	.185	.243			
5	.241	.263	.330	.203		
6	-.051	.039	-.105	.039		
7	.187	.213	.263	.146	.408	-.018

Fig 11(b) Correlation Coefficients for Lake and River Polygons of the Raw (BT) Data.

N85-21731

~~D6~~ D7

EVALUATION OF THE RADIOMETRIC QUALITY OF THE TM DATA USING CLUSTERING, LINEAR TRANSFORMATIONS AND MULTISPECTRAL DISTANCE MEASURES

by

L.A. Bartolucci[1], M.E. Dean[2] and P.E. Anuta[3]
Laboratory for Applications of Remote Sensing
Purdue University

INTRODUCTION

For the past ten years the remote sensing research community and users of space-acquired multispectral scanner data have developed and applied successfully a variety of digital techniques to extract useful information from the Landsat MSS data for mapping, inventorying, monitoring, and managing the earth resources.

Now with the availability of the Thematic Mapper (TM) data, different analysis techniques will be required to deal with the improved spatial and spectral resolutions, and with the higher dimensionality and sensitivity of the TM data.

The primary objective of this investigation was to evaluate the radiometric quality of the TM data for classification and identification of earth surface features utilizing clustering, data compression (linear transformations), multispectral distance measures, and hierarchical classification techniques.

COMPARISON BETWEEN "A"-TAPE AND "P"-TAPE TM DATA

For this investigation, the three different types of TM data tapes were requested, i.e. B-tapes (raw data), A-tapes (radiometrically corrected data), and P-tapes (geometrically corrected data) for a number of different test sites. To date, however, only A-tapes and P-tapes were received for the Chicago, Illinois and Webster Co., Iowa test sites. The identification information for the TM and MSS data sets used in this investigation is shown in Table 1.

Original photography may be purchased
from EROS Data Center
Sioux Falls, SD 57198

---

[1] Technical Director, Technology Transfer Programs
[2] Graduate Research Assistant
[3] Associate Program Leader, Data Processing and Analysis Research Programs

Table 1. TM and MSS Data Sets (A and P tapes)

Scene ID	Data	Location
40049-16264	9/03/82	Iowa
40101-16025	10/25/82	Illinois

In order to determine the effect of the geometric correction process (resampling - gray level interpretation) on the radiometry of the new resampled pixels when converting the data from an A-tape (30m x 30m pixels) to a P-tape (28.5m x 28.5m pixels) format, the means and standard deviation for homogeneous and heterogeneous areas on the ground were calculated using the data from both the A and P-tapes. A comparison of both sets of statistics, illustrated in Tables 2 and 3, demonstrate that there has not been a significant change (radiometric degradation) caused by the non-zero-order (cubic convolution) interpolation process.

Furthermore, in order to determine whether the cubic convolution interpolation had affected the structure of the data in feature space, a set of data from the A and P-tapes for the same area on the ground were clustered (Ref. 14) into 16 cluster classes. Then, the resulting 16 cluster classes from the A and P data sets were merged together into a single 32 class file. Subsequently, the pair-wise spectral separability for the 32 classes was computed using a Transformed Divergence algorithm (Ref. 12). Table 4 shows the transformed divergence (D_T) measures for all the pairs of corresponding classes from the A and P-tape data sets. For example, the transformed divergence between the second cluster class from the TM A-tape (symbol B) and the corresponding second cluster class from the TM P-tape (symbol R) is 53, and since the transformed measure ranges from zero to 2000 (Ref. 13); where a value of 2000 indicates that the two classes in question are completely separable (different), and any D_T value between zero and 500 indicates that the pair of classes are not separable (very similar), it may be concluded that the 16 cluster classes obtained from the A and P tapes are essentially equivalent. Thus these results corroborate the previously stated conclusion that the radiometry of the resampled pixels from the P-tape have not been significantly affected by the geometric correction process, consequently meeting the GSFC specifications for the Landsat-D system, i.e. 'resampling shall not introduce radiometric degradation of more than 1 quantum level' (Ref. 9). Based on these findings, the rest of the results reported in this paper deal with only the TM P-tape data.

NOTE: Thoughout this paper band 6 refers to the 2.08-2.35 μm band, and band 7 refers to the TM thermal infrared band.

Table 2.

MEANS AND STANDARD DEVIATIONS FOR HOMOGENEOUS AREAS IN THE TM "A" AND "P" DATA SETS
(Scene ID: 40049-16264)

Bright Homogeneous Target

TM A-Tape

Band	1	2	3	4	5	6	7
Mean	72.64	33.75	37.93	64.59	119.95	57.23	136.77
St. Dev.	2.27	1.45	2.85	2.49	6.37	3.28	3.74

TM P-Tape

Band	1	2	3	4	5	6	7
Mean	72.88	33.95	38.30	64.34	120.80	*	137.75
St. Dev.	2.18	1.42	2.83	2.52	6.54	*	3.46

---

* LARS band 6 (2.08-2.35 μm) had not arrived at the time these calculations were performed.

Table 3.

MEANS AND STANDARD DEVIATIONS FOR HETEROGENEOUS AREAS IN THE TM "A" AND "P" DATA SETS
(Scene ID: 40049-16264)

Heterogeneous Area

TM A-Tape

Band	1	2	3	4	5	6	7
Mean	68.31	29.56	26.94	89.58	75.75	27.94	127.78
St. Dev.	15.31	8.91	13.12	21.30	16.35	12.62	4.53

TM P-Tape

Band	1	2	3	4	5	6	7
Mean	68.28	29.56	26.90	89.77	75.92	*	127.83
St. Dev.	15.36	8.94	13.10	21.80	16.42	*	4.65

---

* LARS band 6 (2.08-2.35 μm) had not arrived at the time these calculations were performed.

Table 4.

SEPARABILITY FOR THE MERGED TM "A" AND "P" TAPE CLUSTER CLASSES

CLASS SYMBOLS				CLASS PAIRS	D_T*
"A" Tape	A	"P" Tape	Q	AQ	59
	B		R	BR	53
	C		S	CS	164
	D		T	DT	85
	E		U	EV	35
	F		V	FU	150
	G		W	GW	60
	H		X	HX	99
	I		Y	IY	108
	J		Z	JZ	262
	K		$	K$	63
	L		+	L+	62
	M		=	M=	22
	N		/	N/	37
	O		-	O-	168
	P		.	P.	75

---

* D_T = Transformed Divergence
(Ranges from 0 to 2000)

PRINCIPAL COMPONENT ANALYSIS

Comparison of A and P-Tape MSS Results

As shown in Tables 5 and 6 the statistics generated from every fifth line and fifth column from the same area in the Chicago frame for both the A and P tapes are essentially identical. In addition, the resulting eigenvalues and eigenvectors from these statistics (i.e. covariance matrices) are also identical. This further corroborates the fact that the A and P tapes are radiometrically identical and that the cubic convolution process had little effect on the radiometry of the data.

Comparison of TM and MSS P-Tape Results

A. Significant Dimensionality

One of the major advantages of using orthogonal linear transformations such as the Principal Component or Karhunen-Loeve transformation is in their ability to compress overall data variance in a multifeature space onto a relatively few number of transformed orthogonal axes. This essentially separates non-random variance (information content) from random variance (noise), while, concurrently, uncorrelating the transformed axes in such a way that any information redundancy (due to interband correlation) is eliminated. Such transformations therefore allow a compression of the data into a fewer number of dimensions while retaining a maximum amount of significant information content and removing much of the random variance or noise from the data.

Principal components were generated for this part of the analysis for both the MSS and TM P-Tape data sets from the Chicago O'Hare test site. Figs. 1 through 4 show the images of the Landsat MSS four spectral bands of the Chicago O'Hare test site, and Figs. 5 through 8 show the Landsat MSS four ordered principal components of this test site. Also, Figs. 9 through 15 show the images of the Landsat TM seven spectral bands of the Chicago O'Hare test site, and Figs. 16 through 22 show the seven ordered principal components of this test site. Statistics used in calculating these principal components were generated from data samples of the original MSS and TM data sets from every fifth line and fifth column. Tables 6 and 7 show the statistics for the MSS and TM data sets, respectively. Since the sum of the eigenvalues is equal to the trace of the original covariance matrix, i.e. the total variance, the importance or percent of total variance explained by eigenvector(λ_i) is given by:

$$\frac{\alpha_i}{\text{tr } S}$$

where

α_i = eigenvalue i or characteristic root of the ith component

tr S = trace of covariance matrix S or total variance.

Table 5.

STATISTICS FOR THE MSS 'A' TAPE FOR THE CHICAGO O'HARE TEST SITE

(Scene ID: 40101-10625)

Covariance Matrix Diagonal

16.7	29.6	32.1	23.7

Correlation Matrix

1.00			
0.92	1.00		
0.56	0.55	1.00	
0.15	0.13	0.82	1.00

Table 6.

STATISTICS FOR THE MSS 'P' TAPE FOR THE CHICAGO O'HARE TEST SITE

Covariance Matrix Diagonal

17.5	30.0	32.4	25.5

Correlation Matrix

1.00			
0.93	1.00		
0.54	0.53	1.00	
0.11	0.11	0.83	1.00

ORIGINAL PAGE IS
OF POOR QUALITY

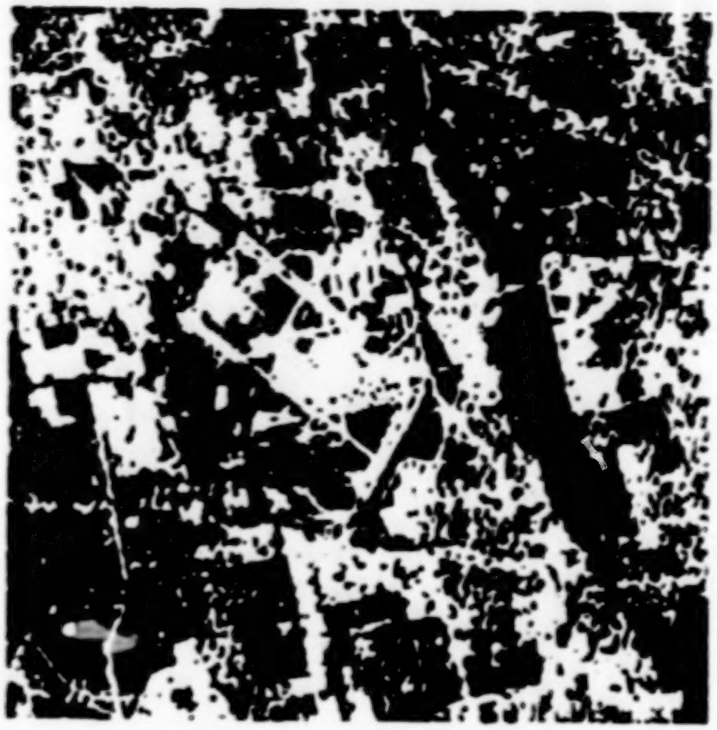

Fig. 1 Image of Band 1 (0.50 - 0.60μm) of Landsat IV MSS of the Chicago O'Hare Test Site.

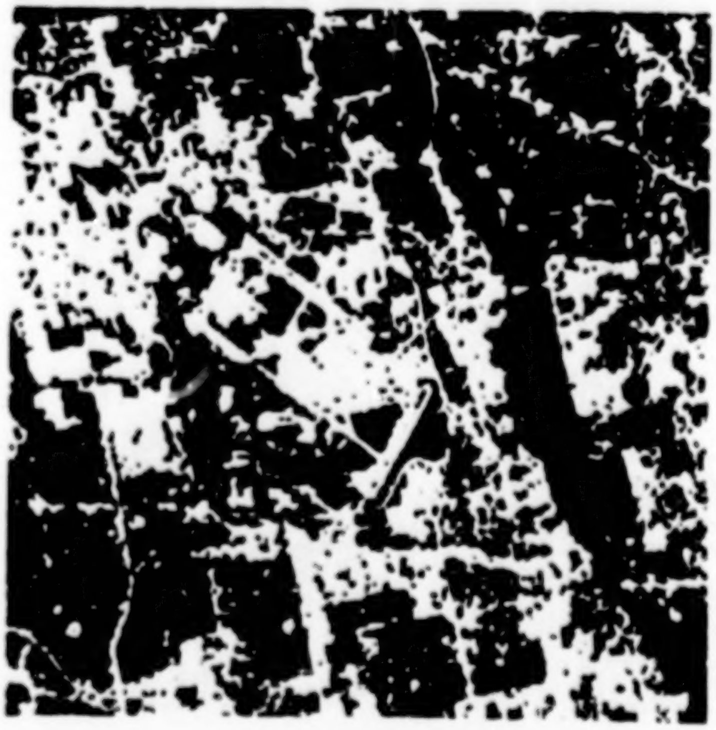

Fig. 2 Image of Band 2 (0.60 - 0.70μm) of Landsat IV MSS of the Chicago O'Hare Test Site.

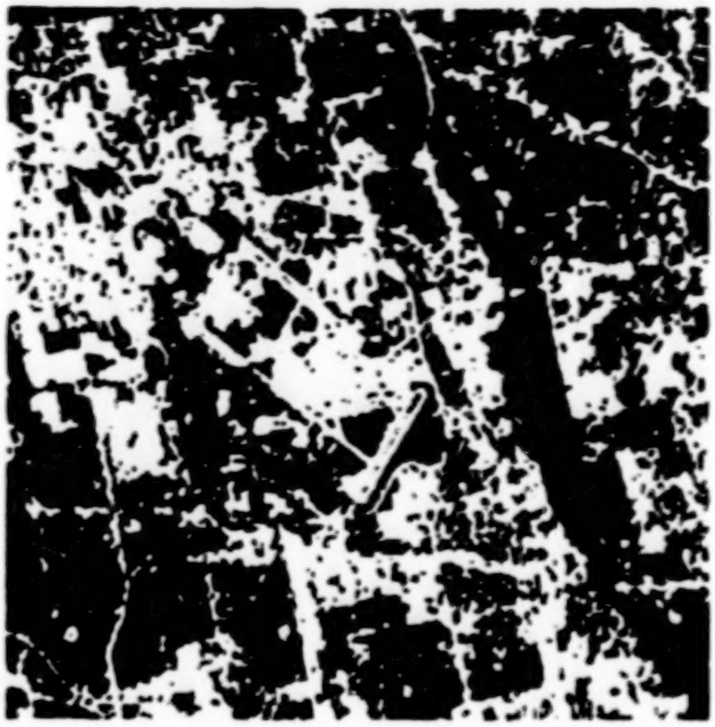

Fig. 3 Image of Band 3 (0.70 - 0.80μm) of Landsat IV MSS of the Chicago O'Hare Test Site.

ORIGINAL PAGE IS
OF POOR QUALITY

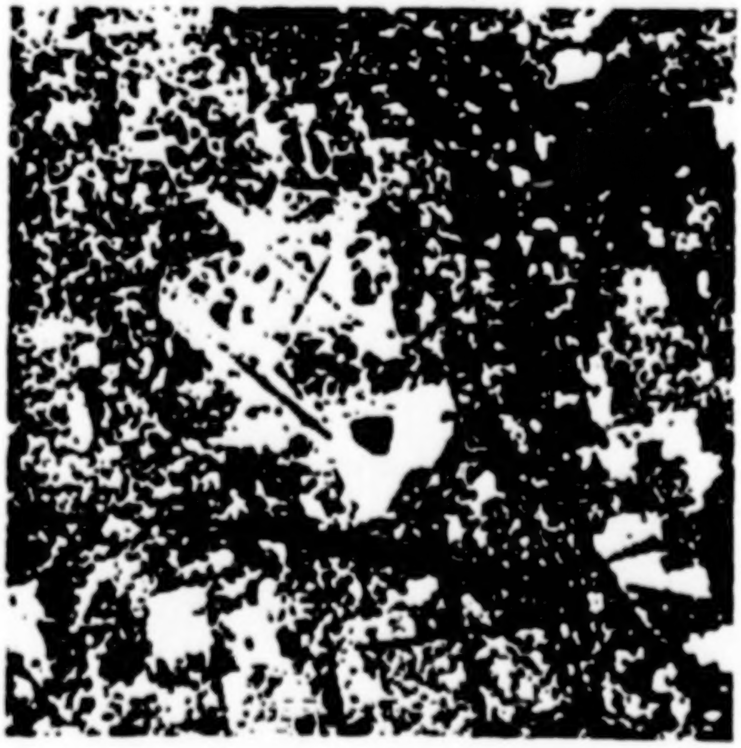

Fig. 4 Image of Band 4 (0.80 - 1.10μm) of Landsat IV MSS of the Chicago O'Hare Test Site.

ORIGINAL PAGE IS
OF POOR QUALITY

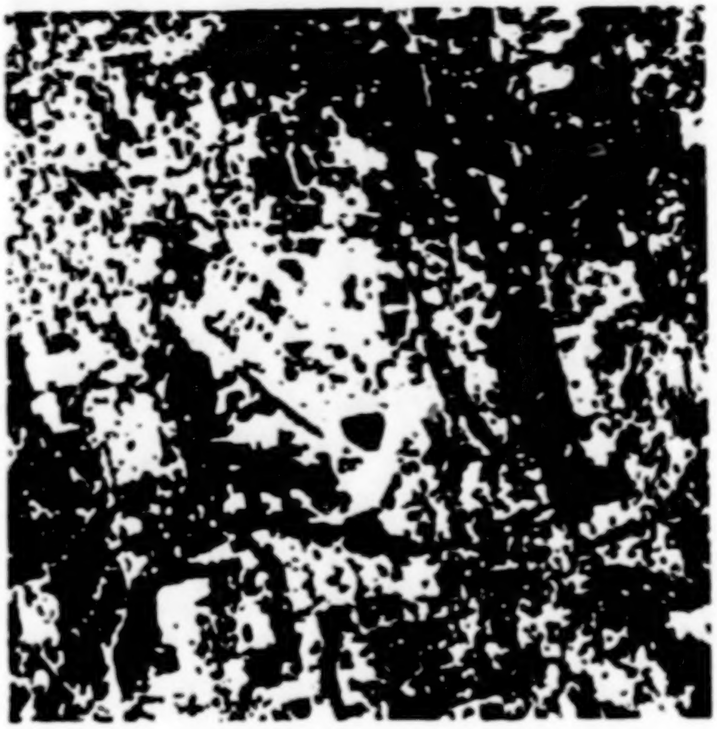

Fig. 5 Image of Principal Component 1 of Landsat IV MSS of the Chicago O'Hare Test Site.

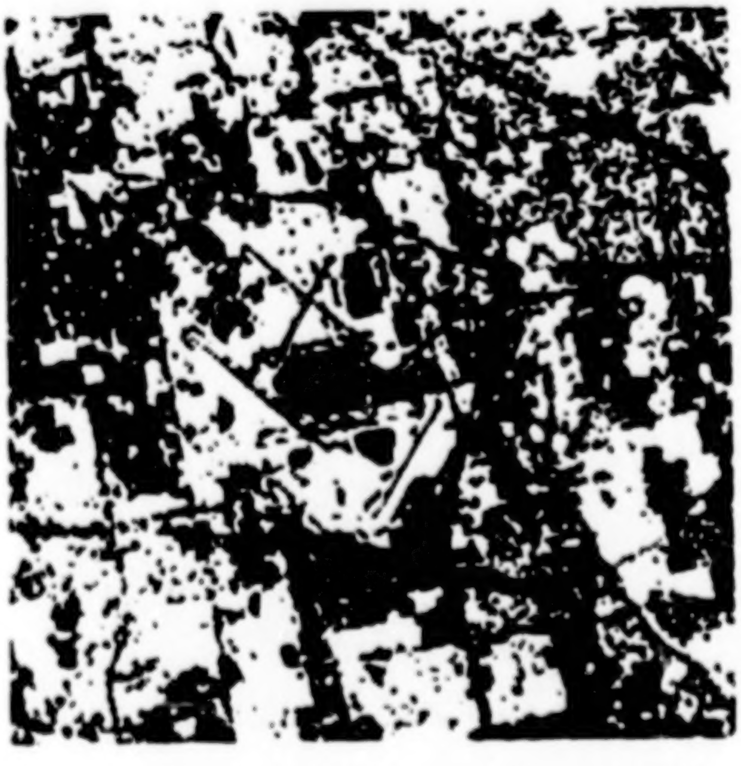

Fig. 6 Image of Principal Component 2 of Landsat IV MSS of the Chicago O'Hare Test Site.

ORIGINAL PAGE IS
OF POOR QUALITY

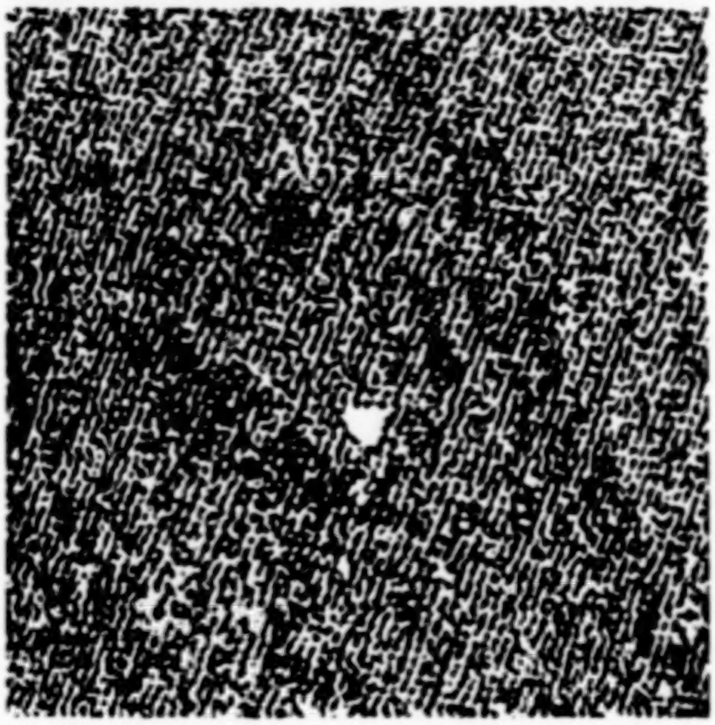

Fig. 7 Image of Principal Component 3 of Landsat IV MSS of the Chicago O'Hare Test Site.

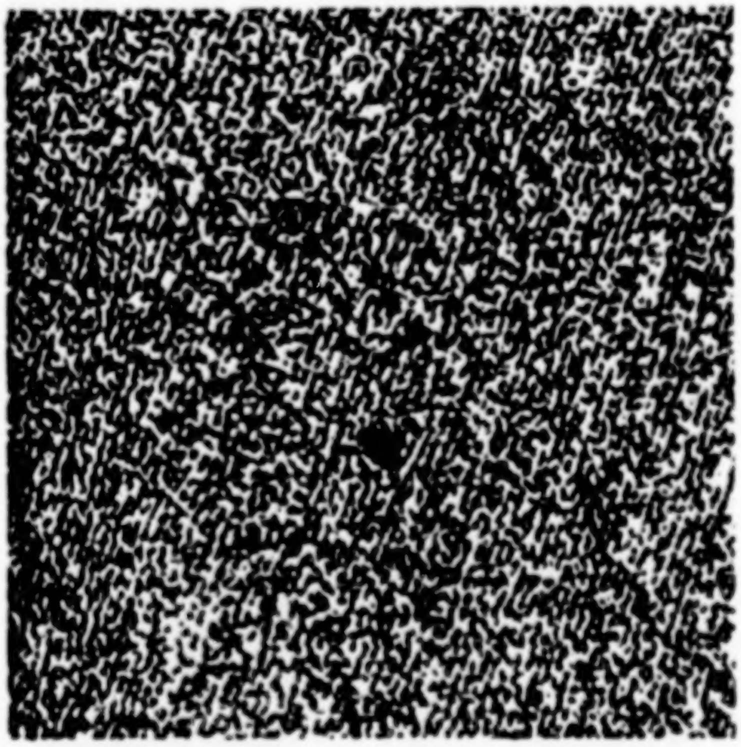

Fig. 8 Image of Principal Component 4 of Landsat IV MSS of the Chicago O'Hare Test Site.

ORIGINAL PAGE IS
OF POOR QUALITY

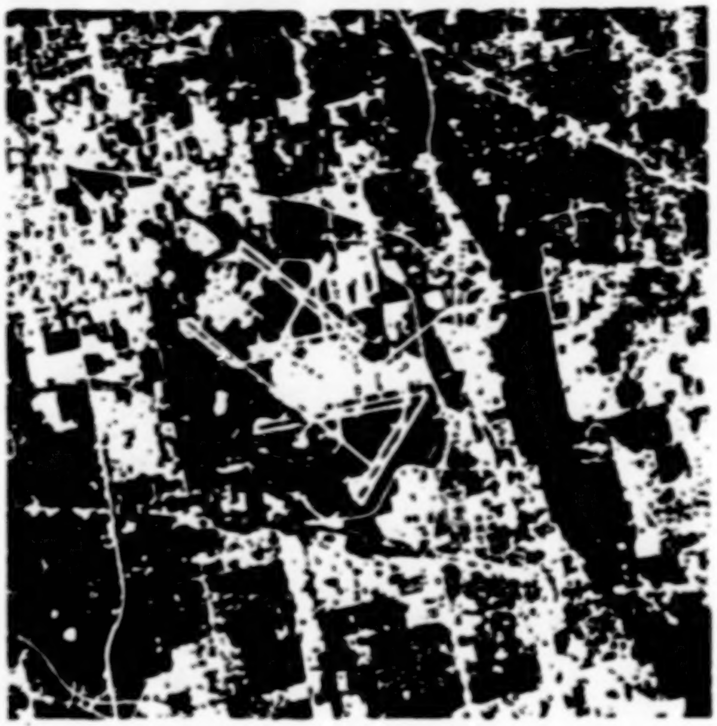

Fig. 9 Image of Band 1 (0.45 - 0.52μm) of Landsat IV TM of the Chicago O'Hare Test Site.

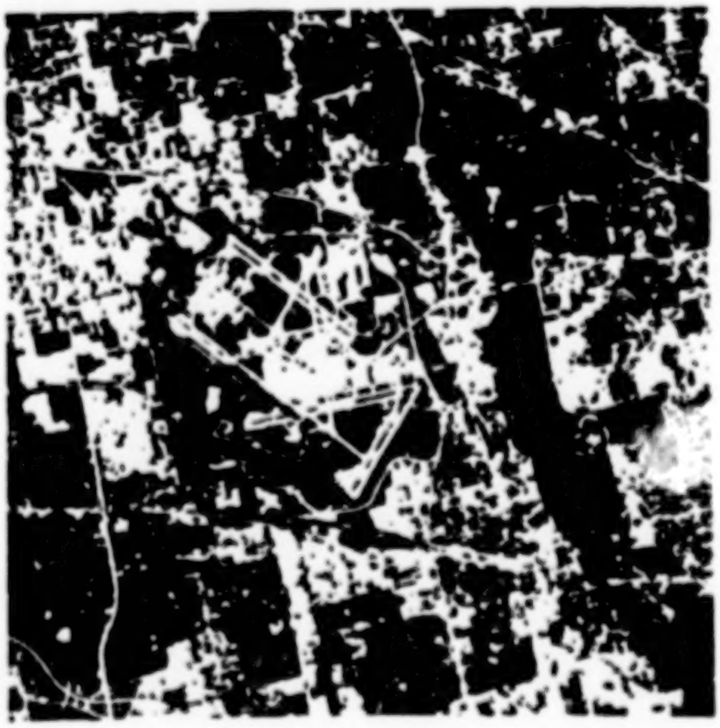

Fig. 10 Image of Band 2 (0.52 - 0.60μm) of Landsat IV TM of the Chicago O'Hare Test Site.

ORIGINAL PAGE IS
OF POOR QUALITY

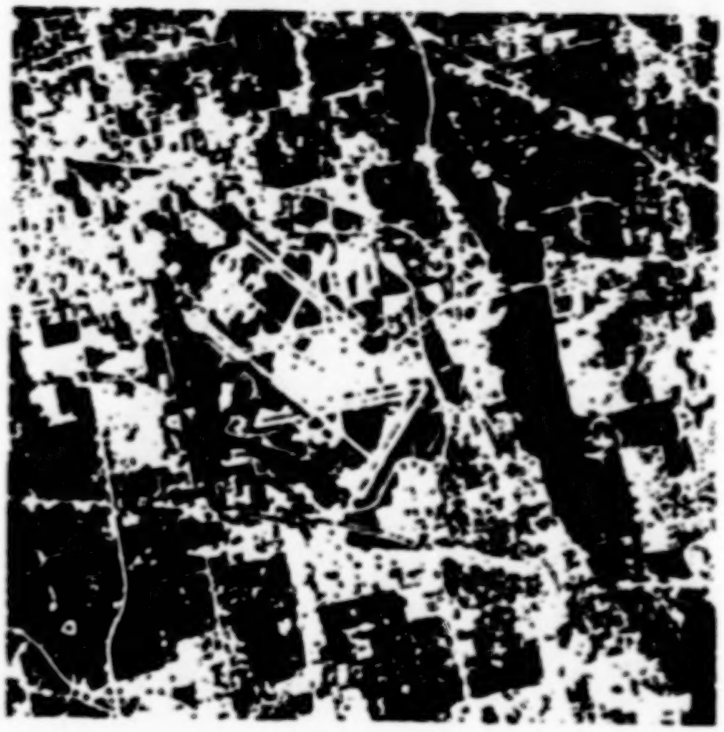

Fig. 11 Image of Band 3 (0.63 - 0.69μm) of Landsat IV TM of the Chicago O'Hare Test Site.

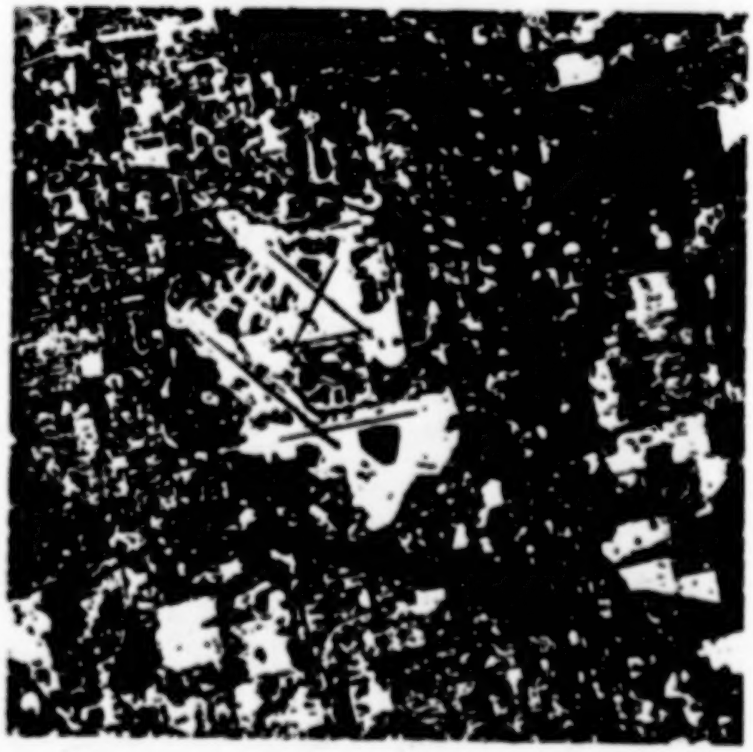

Fig. 12 Image of Band 4 (0.76 - 0.90μm) of Landsat IV TM of the Chicago O'Hare Test Site.

ORIGINAL PAGE IS
OF POOR QUALITY

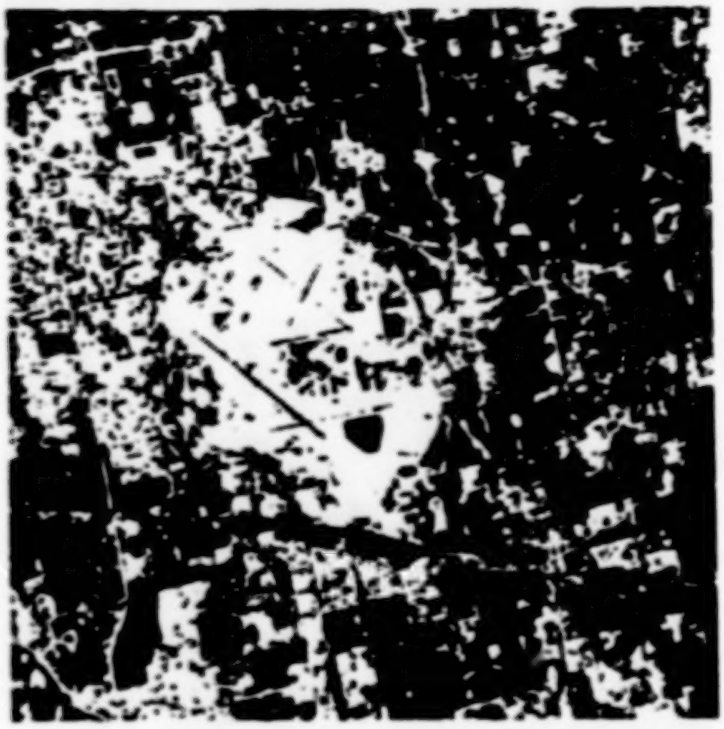

Fig. 13 Image of Band 5 (1.55 - 1.75μm) of Landsat IV TM of the Chicago O'Hare Test Site.

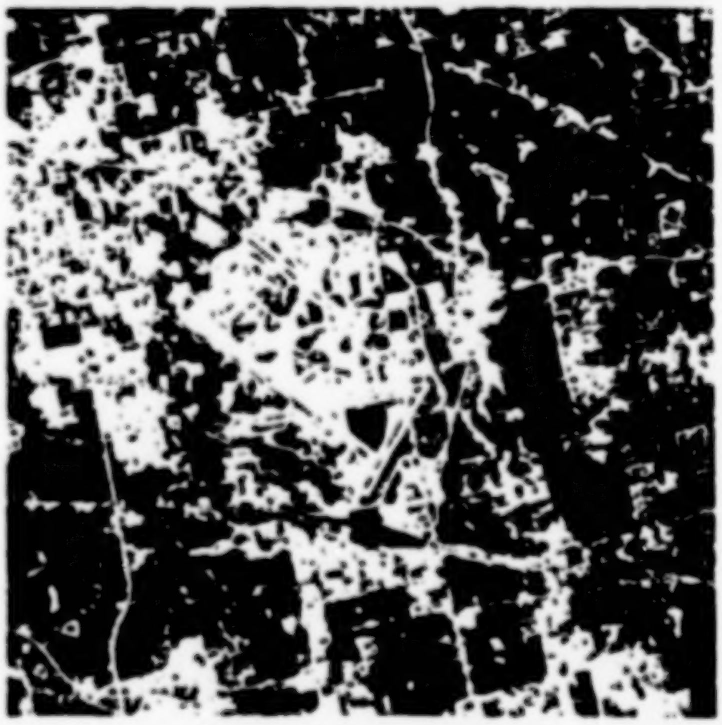

Fig. 14 Image of Band 6 (2.08 - 2.35μm) of Landsat IV TM of the Chicago O'Hare Test Site.

ORIGINAL PAGE IS
OF POOR QUALITY

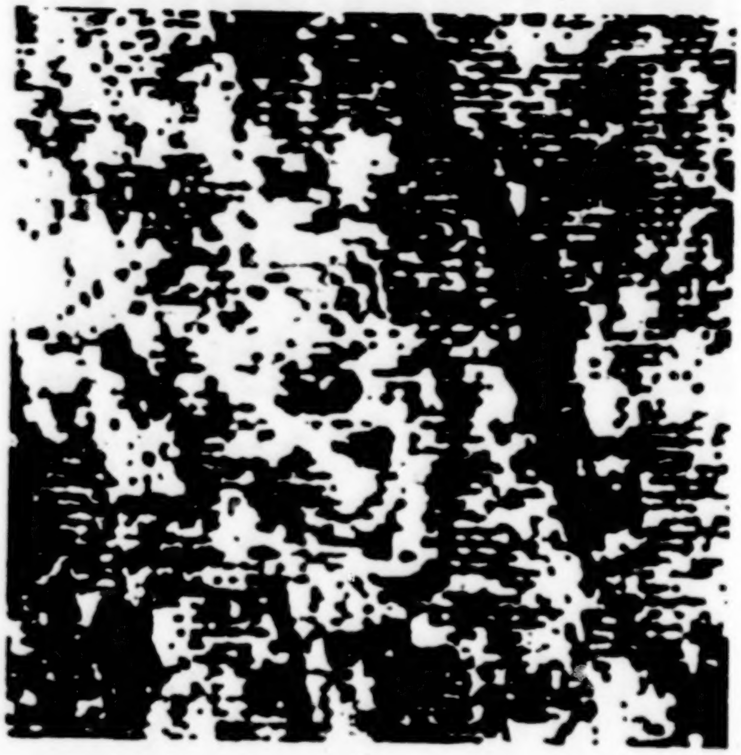

Fig. 15 Image of Band 7 (10.4 - 12.5μm) of Landsat IV TM of the Chicago O'Hare Test Site.

ORIGINAL PAGE IS
OF POOR QUALITY

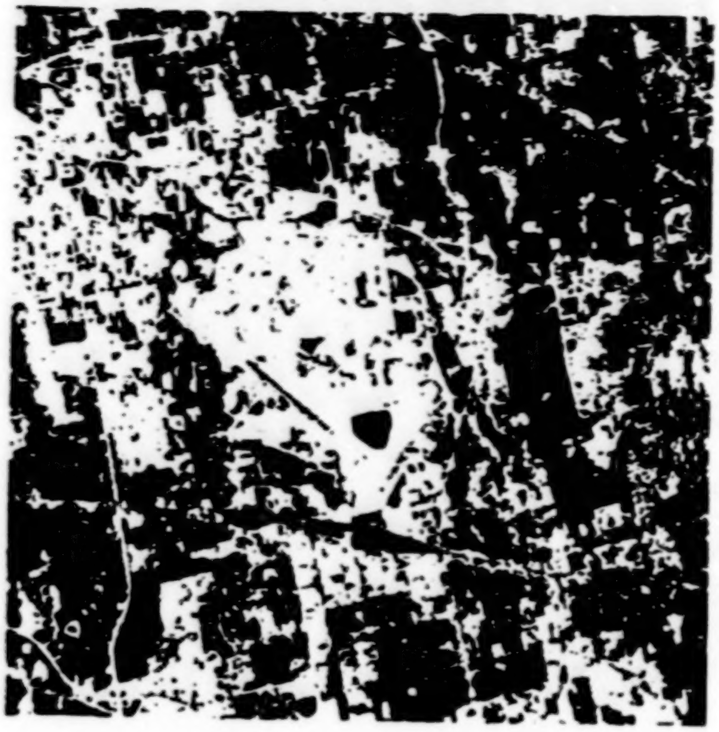

Fig. 16 Image of Principal Component 1 of Landsat IV TM of the Chicago O'Hare Test Site.

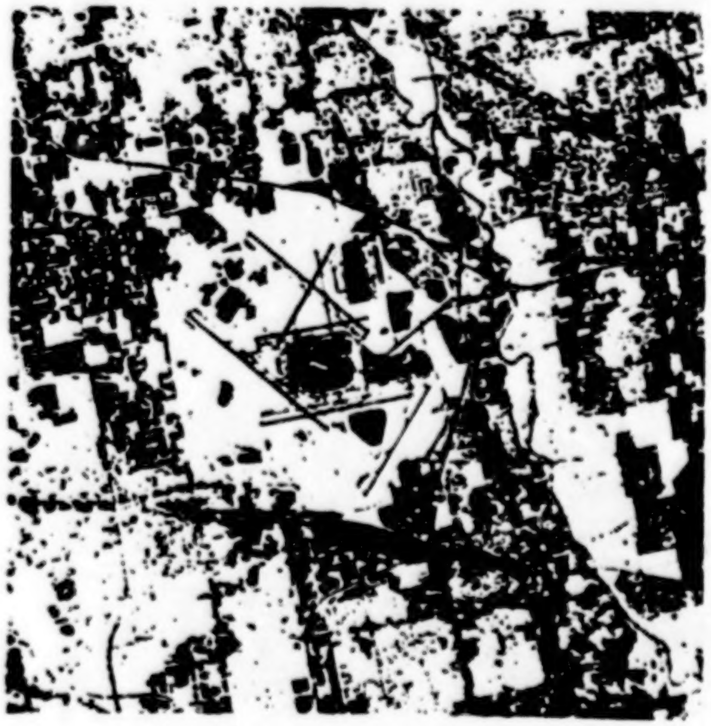

Fig. 17 Image of Principal Component 2 of Landsat IV TM of the Chicago O'Hare Test Site.

ORIGINAL PAGE IS
OF POOR QUALITY

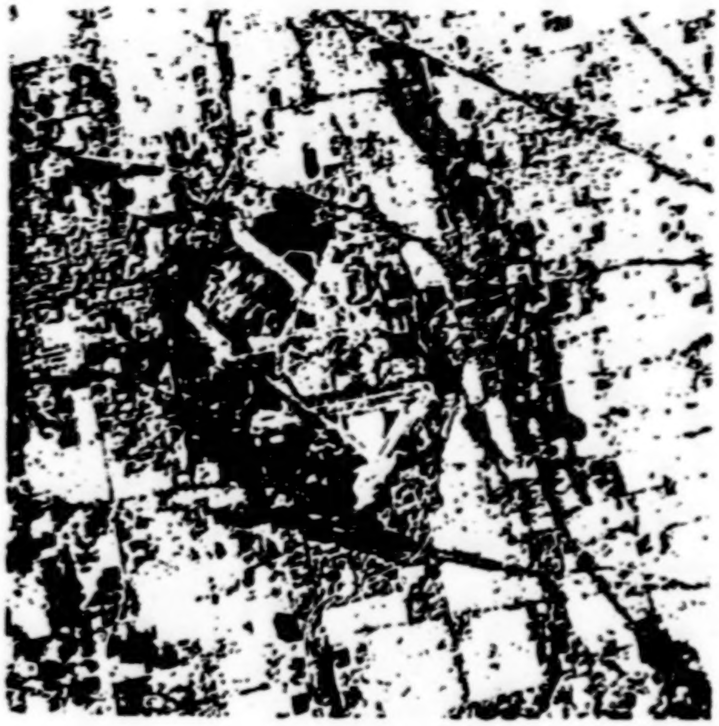

Fig. 18 Image of Principal Component 3 of Landsat IV TM of the Chicago O'Hare Test Site.

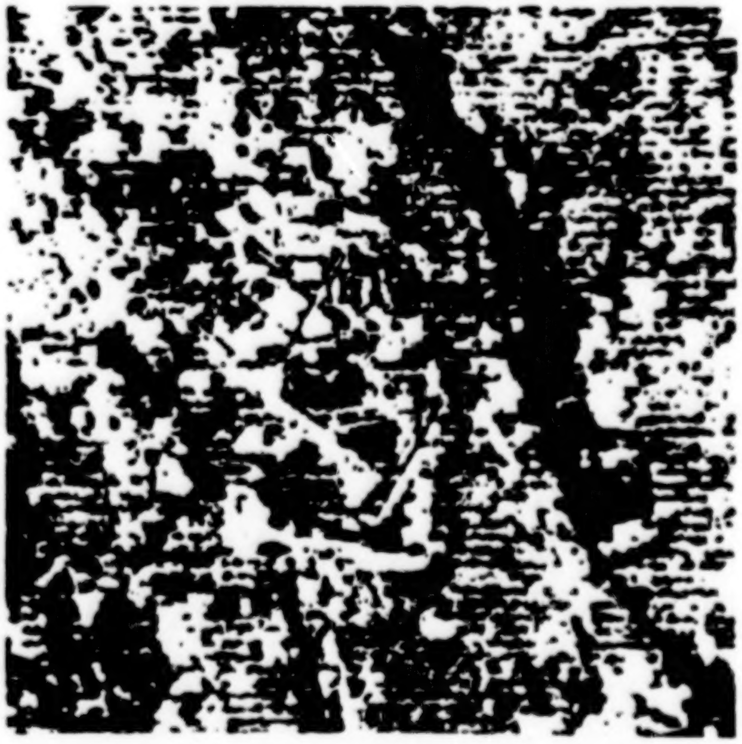

Fig. 19 Image of Principal Component 4 of Landsat IV TM of the Chicago O'Hare Test Site.

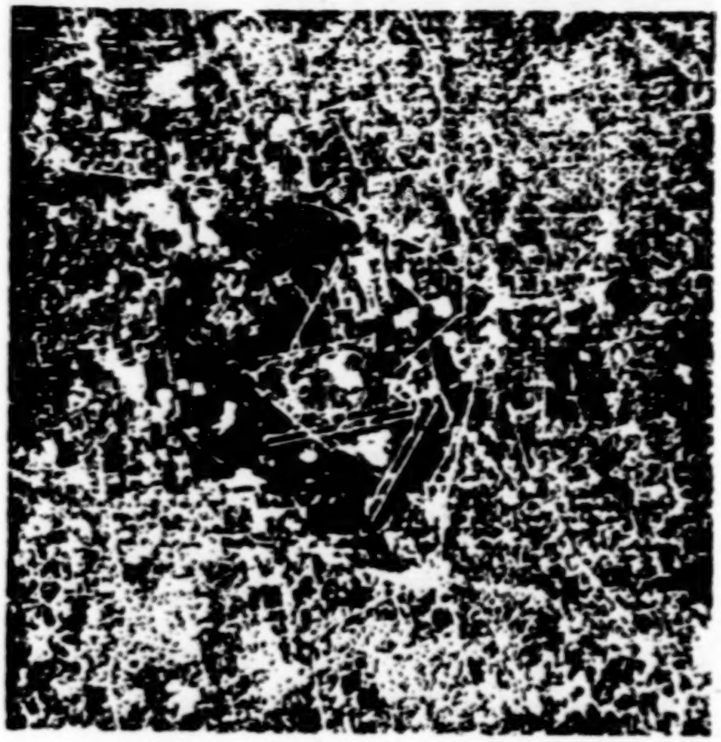

ORIGINAL PAGE IS
OF POOR QUALITY

Fig. 20 Image of Principal Component 5 of Landsat IV TM of the Chicago O'Hare Test Site.

Fig. 21 Image of Principal Component 6 of Landsat IV TM of the Chicago O'Hare Test Site.

ORIGINAL PAGE IS
OF POOR QUALITY

Fig. 22 Image of Principal Component 7 of Landsat IV TM of the Chicago O'Hare Test Site.

Table 7

STATISTICS FOR THE TM 'P' TAPE
FOR THE CHICAGO O'HARE TEST SITE
(Scene ID: 40101-16025)

Covariance Matrix Diagonal

90.9	35.6	72.5	80.5	194.5	80.1	6.7

Correlation Matrix

1.00						
0.96	1.00					
0.96	0.97	1.00				
0.19	0.27	0.24	1.00			
0.54	0.62	0.65	0.59	1.00		
0.77	0.82	0.85	0.30	0.86	1.00	
0.34	0.36	0.35	0.15	0.30	0.36	1.00

Therefore, each of the eigenvalues of the ordered components divided by the sum of the eigenvalues represents the amount of total data variance or information content accounted for by each eigenvector. Tables 8 and 9 list the eigenvalues and the corresponding amount of data variance that is accounted for by their respective eigenvectors, for both the MSS and the TM data sets. As shown in these tables, the first two principal components of the MSS P-tape account for almost 97% of the total data variance. This is also evident from the images of the ordered MSS principal components. The first two components contain a significant amount of scene contrast and data structure, while the last two MSS components contain mostly random noise.

In the TM data set, the first two ordered components together account for 90% of the data variance, the first three account for 97.45% and the first four components almost 99% of the data variance. The images of the TM principal components again show that the first four components contain a significant amount of scene contrast with a sequential decrease in this scene contrast in the lower ordered components. Figs. 23 and 24 graphically show the percent variance of the ordered components. From these it is readily apparent that a significant amount of the variance is accounted for by the first ordered principal components.

From both the listed eigenvalues and the images of the ordered components of the MSS and TM data sets, it is possible to conclude that the first two components of the MSS and the first four components of the TM data sets contain a maximum amount of significant information. It could be possible, therefore, to conclude that for this data set of the Chicago O'Hare area, the TM data contains more significant information, i.e. a higher significant dimensionality, than the corresponding MSS data set. The significant dimensionalities as defined by a principal component analysis may be substantially different for other data sets and other ground cover types. However, these results do imply that for the same area, the TM may contain more significant information than the corresponding MSS.

Table 8.

TABLE OF EIGENVECTORS (PRINCIPAL COMPONENTS) AND EIGENVALUES OF THE MSS 'P' TAPE DATA FOR THE CHICAGO O'HARE TEST SITE
(Scene ID: 40101-10625)

Matrix of Eigenvectors

	Principal Component (Eigenvector)			
Wavelength Band	1	2	3	4
1	0.39291	-0.41975	0.36717	0.73117
2	0.51763	-0.57144	-0.54223	-0.33392
3	0.64029	0.31652	0.54675	-0.43693
4	0.40951	0.63015	-0.52176	0.40371

Eigenvector	Eigenvalue	Percent Variance	Cumulative Percentage
1	68.83	65.30%	65.30%
2	33.18	31.48%	96.78%
3	1.98	1.88%	98.66%
4	1.42	1.34%	100.00%

B. Comparison of Principal Component Loadings

It is possible to qualitatively describe the relative importance of the original variables (spectral bands) to a particular eigenvector using their respective coefficients, as long as the original variables are fairly commensurable, such as is the case with both the MSS and the TM spectral bands. In this situation, the larger the coefficient of a given variable, the more importance or weight that variable is given in that particular eigenvector. The coefficients are sometimes referred to as 'loadings' and can be used to describe qualitatively the relative importance of the original bands to the data set in general. This is especially true with the higher ordered eigenvectors which contain most of the important information; i.e. it can be inferred that those variables or spectral bands which have relatively high coefficients in one or more of the first ordered components, are also more important in the original data set.

Tables 25 and 26 show graphically the coefficients or loadings of the original bands of the MSS and the TM data sets in each of the ordered eigenvectors or principal components. The first eigenvector or component of the TM shows a relatively high weighting of band 5 and, to a lesser degree, of band 6. This may be due to the relatively high correlation between bands 5 and 6 (Table 7) rather than a significant amount of contribution from both. Pictorially the importance of band 5 can be observed in the first Principal Component image when compared with the original image of band 5. Furthermore, band 5 was consistently selected by a transformed divergence (spectral separability) criterion as being the best single band for separating 12, 16, and 20 cluster classes of the Chicago O'Hare test area. It is interesting to note that component 4, although it accounts for only about 1% of the data variance (Table 9), its image shows that it still has clearly recognizable image content. In this case, the thermal band has the highest loading on component 4 which is readily apparent from a comparison of the two images, i.e. component 4 and the original band 7 (thermal IR). It is also important to note that the information content of the principal component 4 is strikingly similar to the thermal IR image, but it shows a higher spatial resolution. This is probably a result of the contributions from the other reflective bands of higher spatial resolution.

C. Scaling Effects

Since the Principal Component transformation is a linear orthogonal transformation which constructs a new set of uncorrelated axes from an original set of correlated axes. It constructs the new variables from the eigenvectors and eigenvalues of either a variance-covariance matrix or a correlation matrix. The new axes have directions as determined by the ordered eigenvectors of this matrix with length proportional to the square root of their respective eigenvalues. In multidimensional space, such transformations will not alter the Euclidean distance between data points (Ref. 8). However, if the resulting components are given some relative magnitude or length other than values which are proportional to the square roots of their respective eigenvalues, then the Euclidean distance between data points will be altered. Clustering algorithms are often highly sensitive to such movements or changes in position of data points with respect to each other. Therefore, it is important for clustering and classification purposes that the resulting transformed components of such

Table 9

TABLE OF EIGENVECTORS (PRINCIPAL COMPONENTS) AND EIGENVALUES OF THE TM "P" TAPE DATA FOR THE CHICAGO O'HARE TEST SITE

(Scene ID: 40101-10625)

	Principal Component (Eigenvector)						
Wavelength Band	1	2	3	4	5	6	7
1	0.38933	-0.48411	0.33460	-0.10358	-0.21253	-0.66554	-0.05709
2	0.25827	-0.24404	0.18937	-0.00917	-0.02399	0.36076	0.84078
3	0.37575	-0.35741	0.17324	-0.06512	-0.05095	0.63914	-0.53453
4	0.23126	0.59933	0.72770	0.07013	0.22440	-0.01326	-0.04812
5	0.63867	0.45624	-0.43559	-0.15732	-0.40970	-0.02462	0.03150
6	0.42059	-0.10269	-0.32059	0.25366	0.79236	-0.13257	-0.00453
7	0.04739	-0.02105	0.00999	0.94389	-0.32497	0.00707	-0.02493

Eigenvector	Eigenvalue	Percent Variance	Cumulative Percentage
1	402.90	71.84%	71.84%
2	102.29	18.24%	90.07%
3	41.37	7.38%	97.45%
4	5.90	1.05%	98.50%
5	4.96	0.88%	99.39%
6	2.20	0.39%	99.78%
7	1.24	0.22%	100.00%

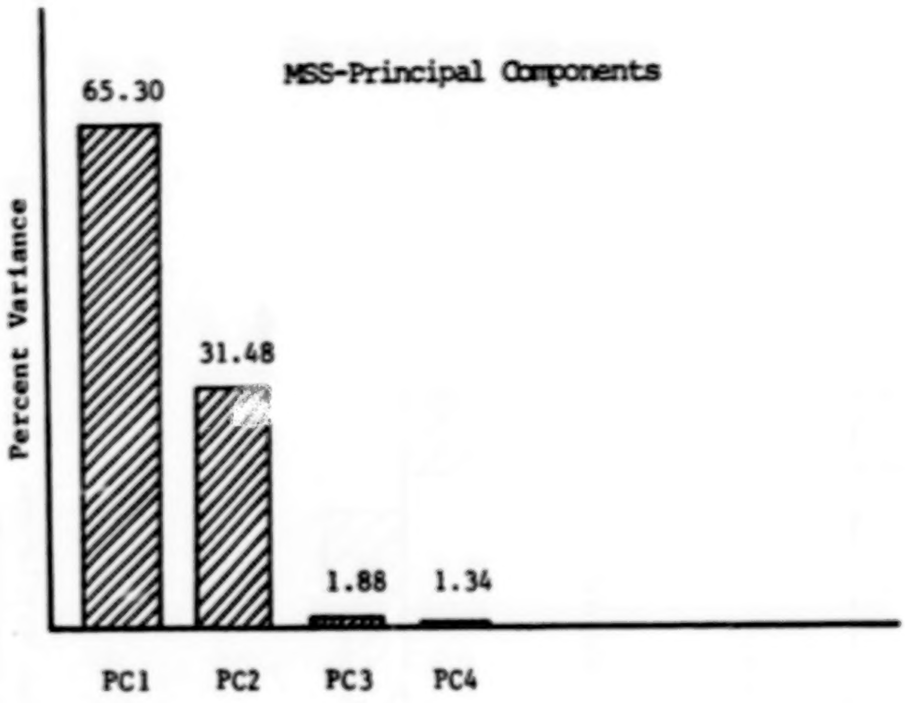

Fig. 23 Percent of Total Data Variance Accounted for by Each of the Ordered MSS Principal Components.

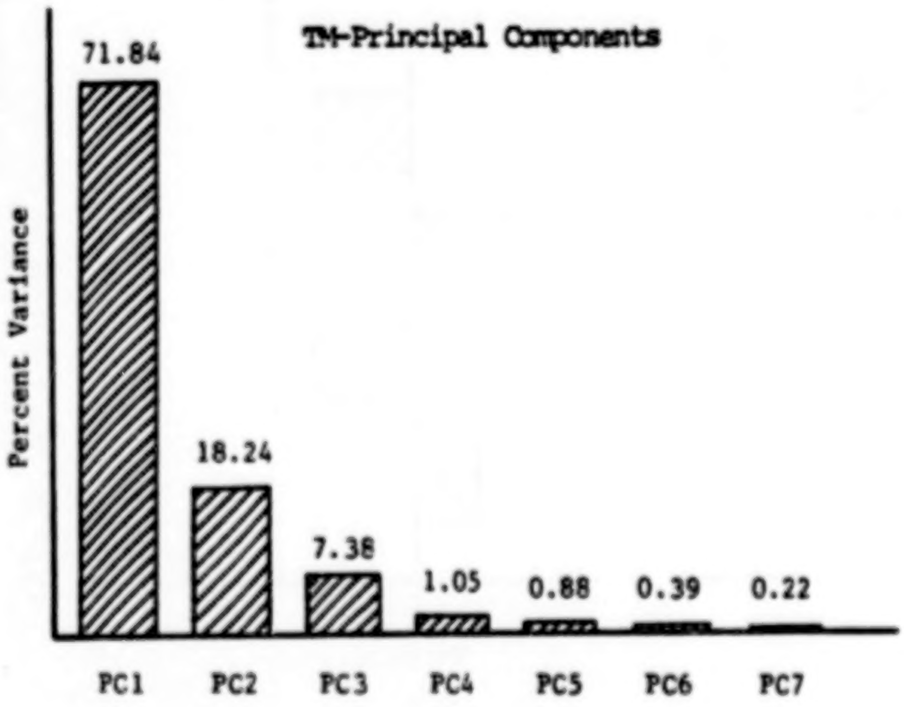

Fig. 24 Percent of Total Data Variance Accounted for by Each of the Ordered TM Principal Components.

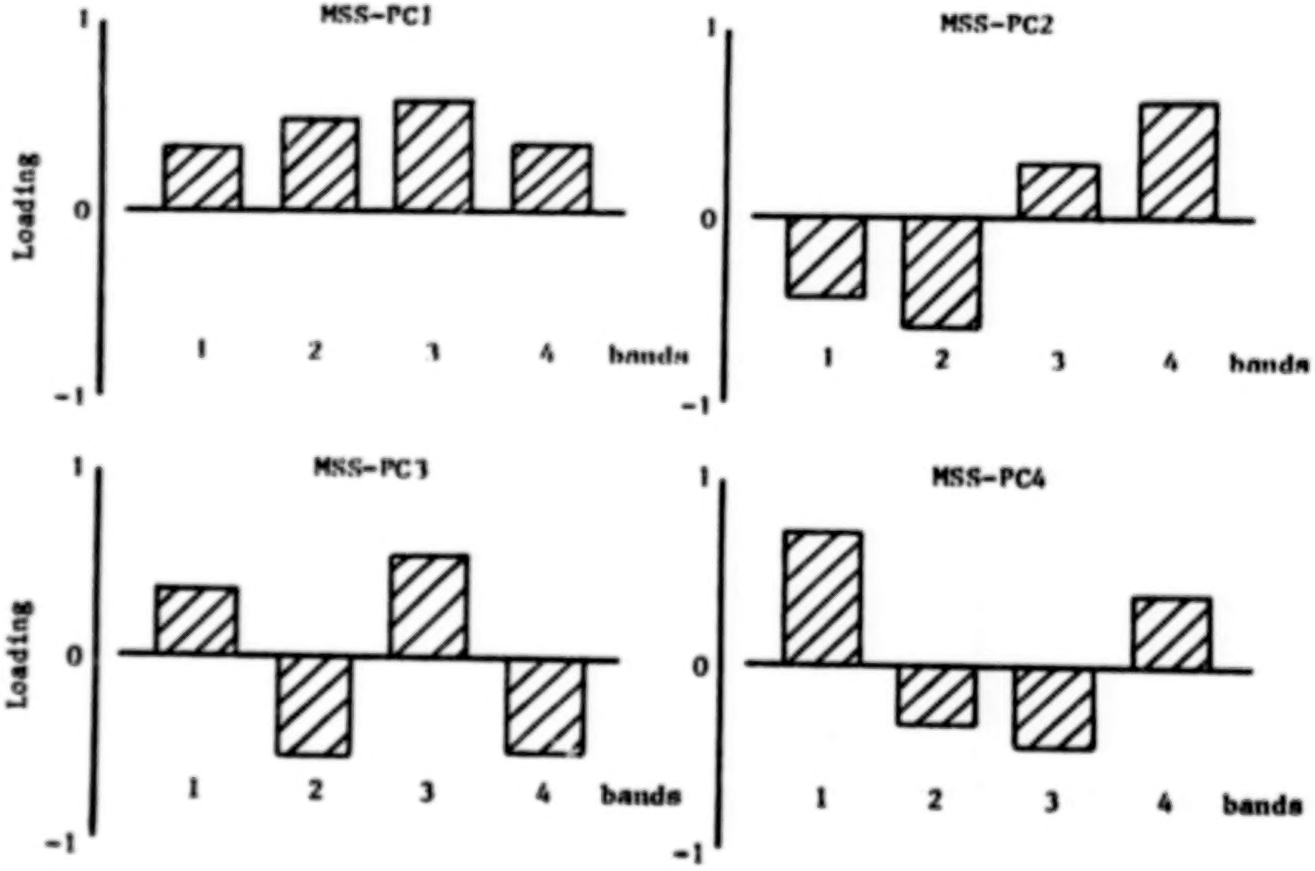

Fig. 25 The Loadings or Coefficients of the Original Wavelength Bands on Each of the Ordered MSS Principal Components.

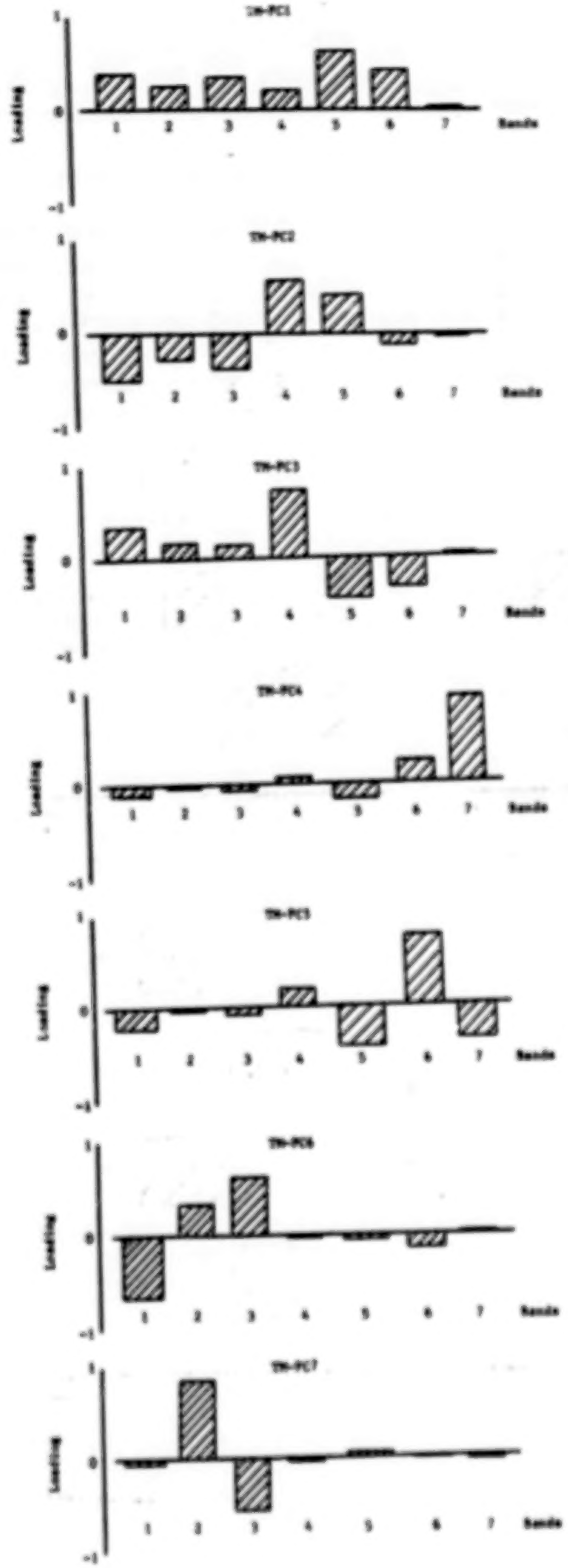

ORIGINAL PAGE IS
OF POOR QUALITY

Fig. 26 The Loadings or Coefficients of the Original Wavelength Bands on Each of the Ordered TM Principal Components.

orthogonal transformations be correctly scaled. Previous experience has demonstrated little or no correlation between cluster classes from an incorrectly, e.g. contrast stretched, principal component data set with actual spectral clusters of the original, untransformed data.

D. Clustering of the Original and Transformed TM data

Both the original and a Principal Component transformed TM P-tape data set from the Chicago O'Hare test site were each clustered separately into 16 cluster classes. With the original TM data all 7 bands were used for clustering while for the transformed data set, three unique sets of 16 clusters were generated using only the first three, four and all seven components, respectively. Both a minimum transformed divergence value (D_T(Min)) and an average transformed divergence value (D_T(Ave)) for each waveband and principal component set are given in Tables 10 and 11.

Table 10.

SEPARABILITY OF 16 CLUSTER CLASSES FOR THE
'BEST' TWO AND MORE WAVELENGTH BAND COMBINATIONS
OF THE TM DATA FROM THE CHICAGO O'HARE TEST SITE
(Scene ID: 40101-16025)

Wavelength Band Combination	D_T(Min)	D_T(Ave)
(3,5)	68	1859
(3,4,5)	1281	1929
(3,4,5,6)	1312	1937
(1,3,4,5,6)	1322	1944
(1,3,4,5,6,7)	1347	1947
(1,2,3,4,5,6,7)	1361	1950

Table 11.

SEPARABILITY OF 16 CLUSTER CLASSES FOR THE COMBINATIONS OF
THE FIRST 3,4 AND ALL 7 ORDERED PRINCIPAL COMPONENTS
OF THE TM DATA FROM THE CHICAGO O'HARE TEST SITE
(Scene ID: 40101-16025)

Principal Components	D_T(Min)	D_T(Ave)
(1,2,3)	1261	1934
(1,2,3,4)	1257	1934
(1,2,3,4,5,6,7)	1322	1946

The clusters produced from the 7 bands of the original data set were very similar to those produced from the 7 components of the transformed data. Furthermore, the clusters generated from the first three and the first four principal components were almost identical to those generated from the 7 components. Both the original and the transformed data set separabilities indicate that a dimensionality of three is required for optimum separability with little increase in separability beyond three dimensions. These results indicate that identical cluster groupings are likely to be obtained with a subset of the higher ordered components as those obtained with all 7 components and using a fraction of the computer time. Three components in this case produced an optimum cluster grouping using only 1/3 of the CPU time required for clustering with all 7 components.

TEMPERATURE MAPPING OF A COOLING POND AND THERMAL PLUME FROM A NUCLEAR POWER PLANT

The use of thermal infrared (IR) data in conjunction with reflective multispectral data, obtained from aircraft altitudes, has been proven to be an effective means for increasing the classification accuracy of earth surface features (Ref.s 7, and 11).

Also it has been demonstrated that radiometrically calibrated thermal IR data obtained from airborne platforms can be used to produce accurate temperature maps of water bodies (Ref.s 1,3,4, and 10).

Accurate temperature maps of water bodies have been obtained also from calibrated thermal IR data gathered in 1973 by the SKYLAB SL-2 S192 scanner system (Ref. 6). However, for almost ten years the remote sensing data users have not had available high spatial resolution thermal IR data (in contrast to the coarse spatial resolution data gathered by meteorological satellites) acquired from spaceborne platforms, until the TM thermal data were recently collected.

In order to determine the radiometric quality of the TM thermal data for temperature mapping of surface water, a test site was selected within the area covered by the TM scene (Scene ID: 40101-16025) gathered over Illinois. This site was chosen because it includes a surface water body with a large range of temperatures, i.e. a cooling pond for the Dresden nuclear power plant and the junction of two rivers: the Kankakee and the Des Plaines rivers which once merged form the Illinois river.

The Dresden power generating station is located approximately 50 miles southwest of Chicago near Morris, Illinois. The station houses three nuclear reactors which together have a maximum nameplate generating capacity of 1,656,630 Kw. The water which is taken from the Kankakee river and is used to cool the steam condensers is channeled into a man-made lake which is designed to dissipate heat. This 1300 acre lake has a dike in its center which directs the water flow up, around and down the lake in an eight-mile loop that takes two-and-a-half days to complete. During its course the water is cooled by natural evaporation and is either recycled back through the station or discharged into the Illinois river. A schematic diagram of the power plant, channels, cooling lake, and the three rivers is shown in Fig. 27.

Because the radiant temperature of the various cover types in the test site is a function not only of the kinetic temperature of the materials, but it is also a function of the intrinsic emissive properties (emissivity) of the objects, and to avoid differential emissivity complications, it was decided to perform the calibration of the TM thermal IR data corresponding to only those pixels representing water, which has an emissivity close to that of a perfect radiator or blackbody.

To accomplish the thermal calibration of water only, a heirarchical classification of the TM data had to be performed, i.e. one of the middle IR (1.55 - 1.75 μm) band was utilized to discriminate the water pixels from all the other cover types using the LARSYS layered classifier (Ref.s 3,5,15), and once all the water pixels were separated from everything else, their thermal IR response (relative digital count) was converted to radiant temperatures. Fig. 28 shows the decision tree utilized to carry out the heirarchical or layered classification and calibration of the water bodies present in the test site, and Figs. 29 and 30 show the images of the test site corresponding to the 1.55-1.75μm and 10.4-12.5μm bands respectively.

The conversion of the relative thermal IR responses into radiant temperature measurements was accomplished using a 'non-linear' calibration function derived specifically for the TM thermal IR band and the range of temperatures of the two internal calibration reference blackbodies.

The 'non-linear' calibration function was derived through the integration of Planck's equation for a spectral band covering the 10.4-12.5μm spectral range, and for a range of temperatures between 260 K and 320 K (Ref. 2) at increments of 0.1 K. The resulting in-band radiances (in Watts/cm^2-sr) were then plotted versus the corresponding temperatures as illustrated in Fig. 31. Note in this figure that if one assumes a linear relationship between the emitted energy from a blackbody and its temperature for a range of temperatures in excess of 10 K (the range between the cold and hot internal calibration sources of the TM system is 60 K), errors on the order of 4 K (4°C) would be introduced.

The non-linear calibration function is given by Equation 1 below:

$$T(^{\circ}C) = -12.5809 + 0.2917D - 0.000233D^2 \tag{1}$$

where: T = temperature in degrees Celsius
D = relative digital counts for the TM thermal IR band

If a linear interpolation was performed, the linear calibration function would be represented by Equation 2:

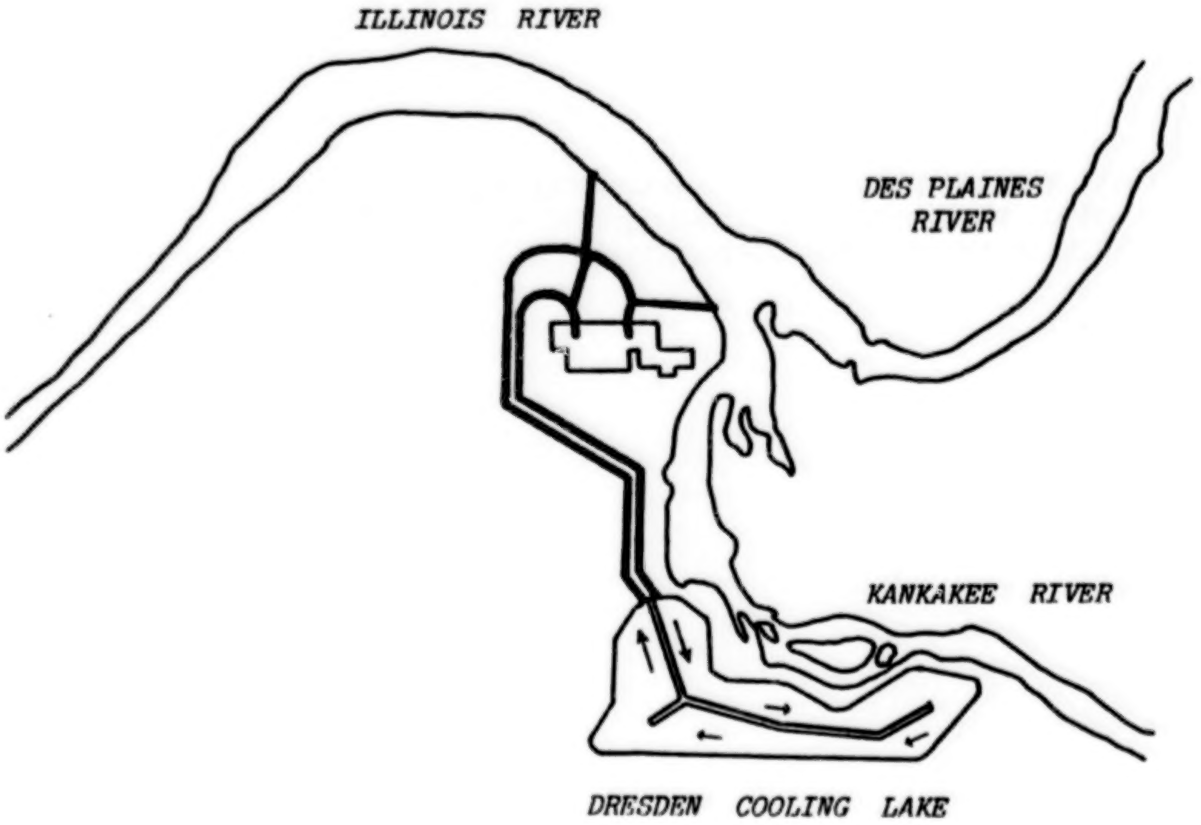
ILLINOIS RIVER
DES PLAINES RIVER
KANKAKEE RIVER
DRESDEN COOLING LAKE

Fig. 27 Schematic Diagram of the Dresden Nuclear Power Plant, Channels, Cooling Lake and the Kankakee, Des Plaines and Illionois Rivers.

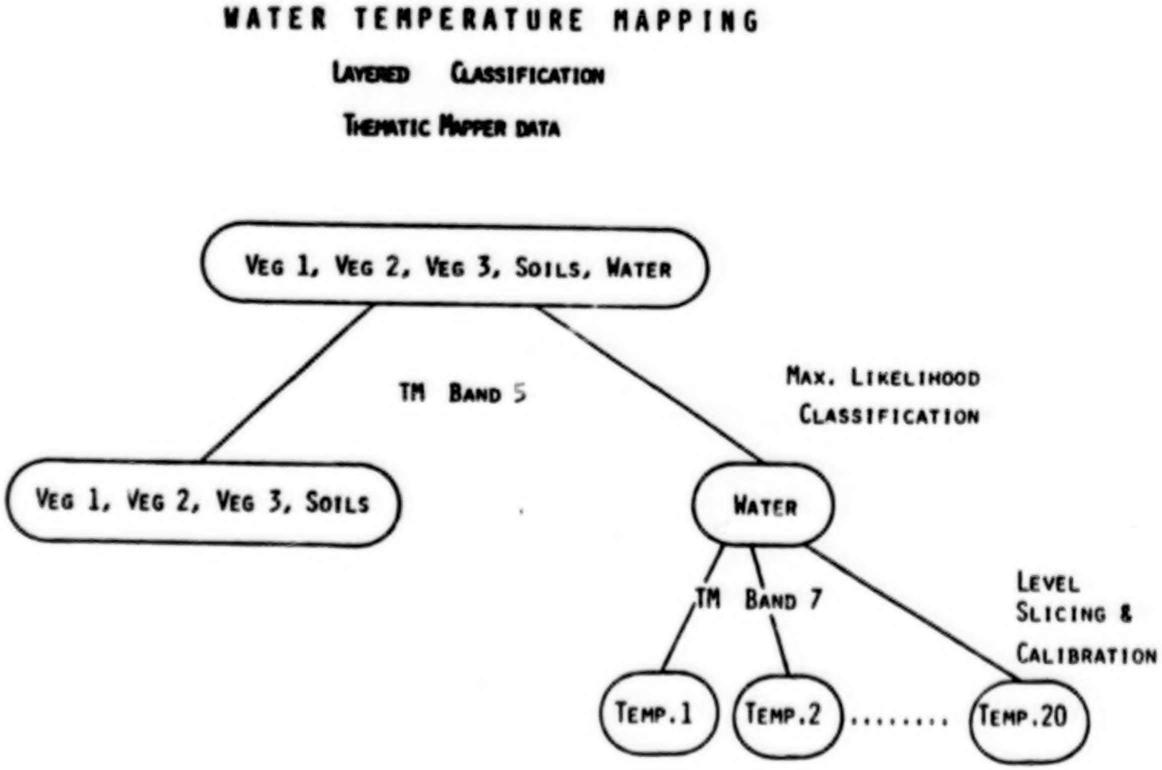
WATER TEMPERATURE MAPPING
LAYERED CLASSIFICATION
THEMATIC MAPPER DATA
VEG 1, VEG 2, VEG 3, SOILS, WATER
TM BAND 5
MAX. LIKELIHOOD CLASSIFICATION
VEG 1, VEG 2, VEG 3, SOILS
WATER
TM BAND 7
LEVEL SLICING & CALIBRATION
TEMP.1
TEMP.2
....
TEMP.20

Fig. 28 Decision Tree Utilized to Carry out the Heirarchical Classification and Calibration of the Water Bodies Present in the Dresden Nuclear Power Plant Test Site.

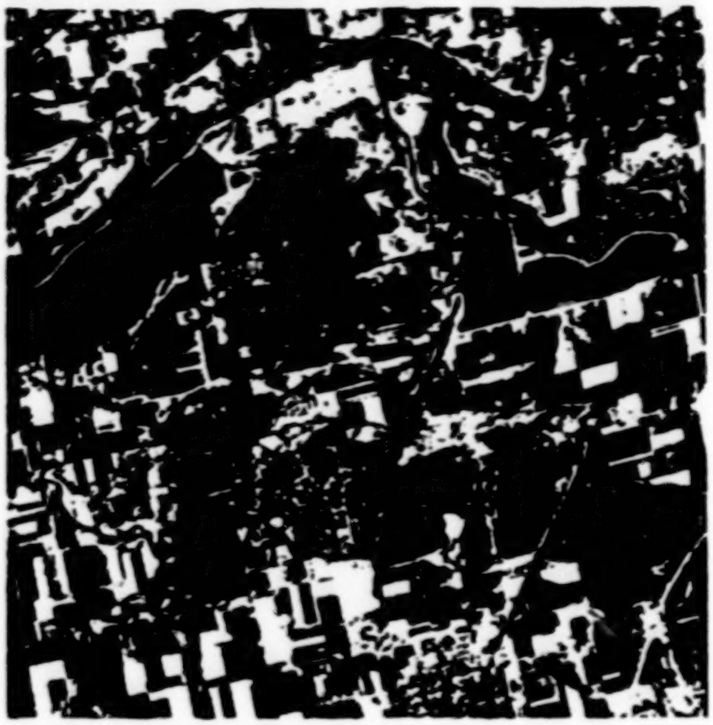

ORIGINAL PAGE IS OF POOR QUALITY

Fig. 29 Image of Band 5 (1.55 - 1.75μm) of Landsat IV TM of the Dresden Power Plant Test Site.

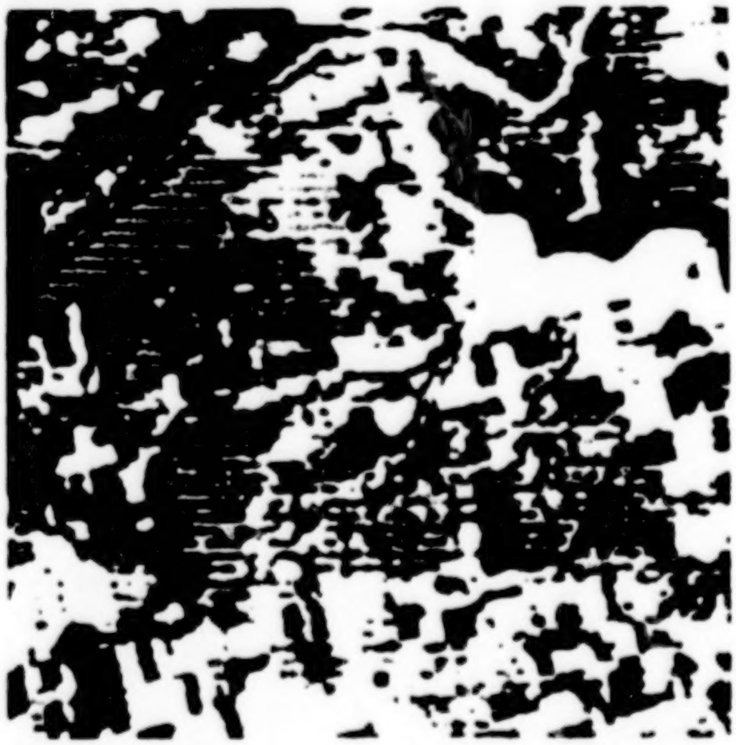

Fig. 30 Image of Band 7 (10.4 - 12.5μm) of Landsat IV TM of the Dresden Power Plant Test Site.

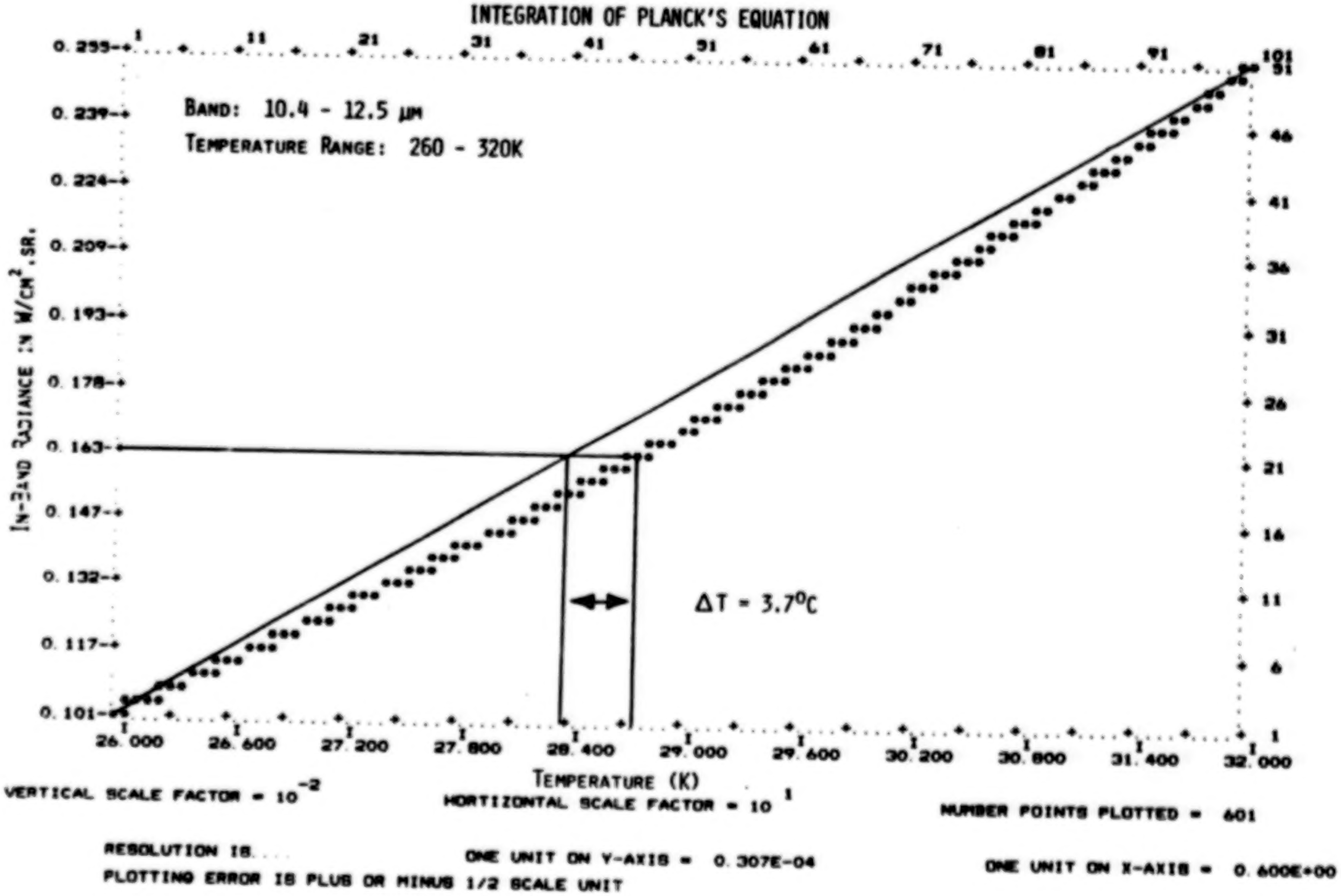

Fig. 31 Integration of Planck's Equation for a Spectral Band Covering the 10.4 - 12.5µm Spectral Range, and for a Range of Temperatures Between 260°K and 320°K at 0.1°K increments.

ORIGINAL PAGE IS
OF POOR QUALITY

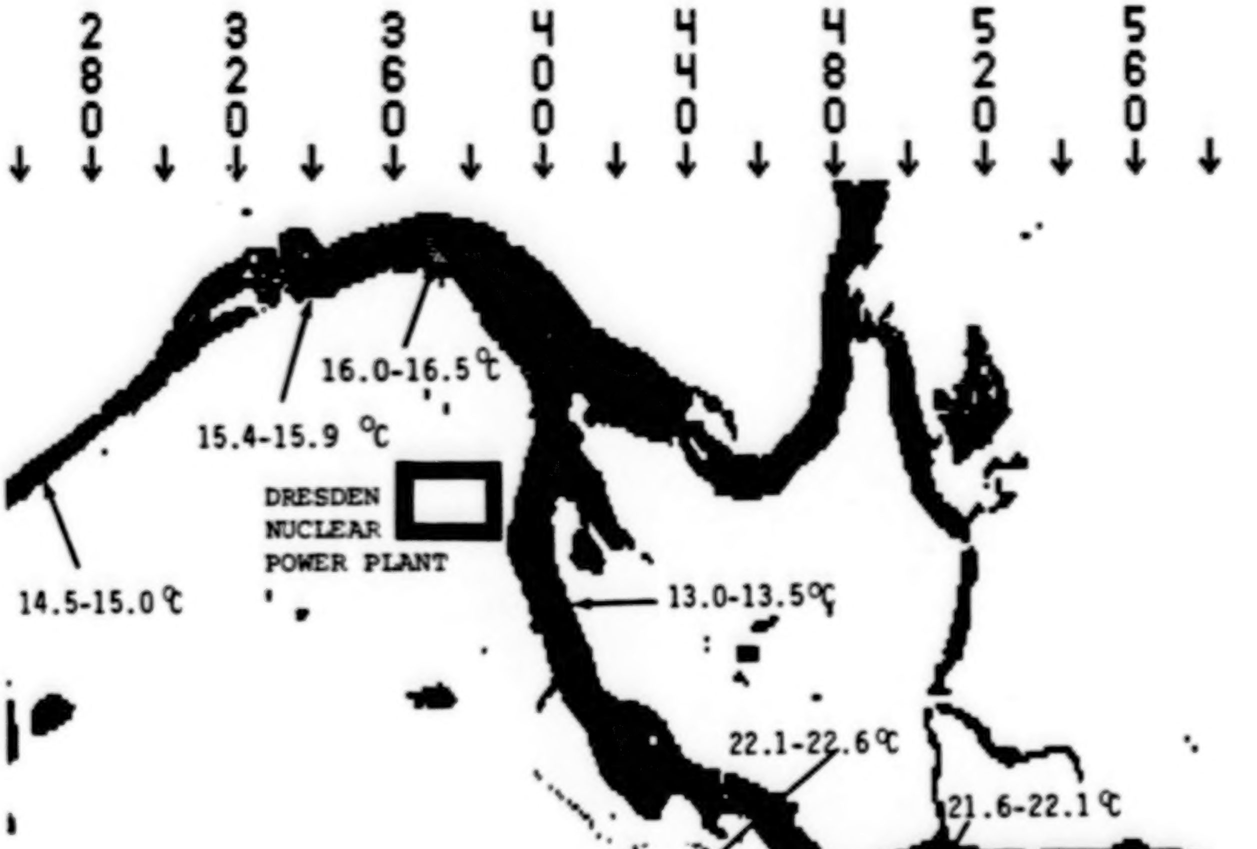
280
320
360
400
440
480
520
560
16.0-16.5 °C
15.4-15.9 °C
DRESDEN
NUCLEAR
POWER PLANT
14.5-15.0 °C
13.0-13.5 °C
22.1-22.6 °C
21.6-22.1 °C
18.3-18.7 °C
20.3-20.7 °C
18.8-19.3 °C
19.8-20.2 °C
280
320
360
400
440
480
520
560
1 MILE

Fig. 32 Temperature Map of the Dresden Nuclear Power Plant Test Site Derived from the Landsat-4 TM Data.

$$T(^{\circ}C) = -13 + 0.23529D \quad (2)$$

The pixels of water at the intake (Kankakee River) have a relative thermal IR response equal to 95 digital counts, and those corresponding to the water at the entrance of the cooling pond equal to 135 digital counts. If these two relative thermal responses (digital counts) are substituted in Equation 1, one obtains the following radiant temperatures:

Digital Count	Radiant Temperature
95	13.1°C
135	22.6°C

Since at the time the TM data were recorded (October 25, 1982 at 16:02 GMT) reference (ground truth) data were not being collected, it was not possible to assess reliably the accuracy of the radiant temperatures derived from the TM thermal IR data. However, the personnel from the Dresden nuclear power plant keep a record of the temperature of the water at the entrance to the cooling lake. The temperature recorded for that date was 71°F or 21.7°C, which is a difference of approximately 1°C with respect to the radiant temperature derived from the TM thermal IR data. Fig. 32 shows a temperature map of the Dresden power plant test site.

Although neither the temperature of the water recorded at the power plant nor the precise temperature of the internal calibration reference blackbodies in the TM system were reliable, the results obtained during this preliminary assessment of the TM radiometric data quality are very encouraging.

CONCLUSIONS

The results of the preliminary evaluation of the Landsat-4 MSS and TM data presented in this paper indicate that:

a. The radiometric quality of the MSS and TM P-Tape data meets the specifications for the system, i.e. the resampling-graylevel interpolation process has not degraded the radiometric quality of the resampled pixels.

b. The Principal Components analysis of the TM data shows that the combined first four ordered eigenvectors account for almost 99% of the total data variance, i.e. 'four' is the significant dimensionality of the data. However, although the last three ordered eigenvectors combined account for only one percent of the data variance, the images of the 5th and 6th TM eigenvectors show a certain amount of information content. These results are in contrast with these obtained from the MSS data, in which the images for the last two ordered MSS eigenvectors contain only random variations or noise.

c. The 4th ordered principal component (eigenvector 4) from the TM data is primarily loaded by information originating in the thermal IR band, as illustrated in Table 9 and the comparison of the images included in Figures 15 and 19. It is very interesting to note that the image of the 4th ordered TM principal component is extremely similar to that of the TM thermal IR band, but it contains also higher spatial resolution information than the original thermal IR band.

d. The TM thermal IR data, when properly processed, could be effectively utilized to produce temperature maps of water bodies.

REFERENCES

1. Atwell, B.H., R.B. MacDonald, and L.A. Bartolucci, 'Thermal Mapping of Streams from Airborn Radiometric Scanning," Water Resources Bulletin, Journal of the American Water Resources Association, Vol. &, No. 2, Urbana, Illinois, April 1971.

2. Barker, T.L., 'TM Sensor Description and Status,' First European Landsat-4 Workshop, ESA/EARTHNET Program, Frascati, Italy, November 1982.

3. Bartolucci, L.A., R.M. Hoffer, and T.R. West, 'Computer-Aided Processing of Remotely-Sensed Data for Temperature Mapping of Surface Water from Aircraft Altitudes,' LARS Information Note 042373, Laboratory for Applications of Remote Sensing, Purdue University, West Lafayette, Indiana, April 1973.

4. Bartolucci, L.A., R.M. Hoffer, and J.R. Gammon, 'Effects of Altitude and Wavelength Band Selection on Remote Measurements of Water Temperature,' Proceedings of the First PanAmerican Symposium on Remote Sensing, Panama City, Panama, May 1973.

5. Bartolucci, L.A., P.H. Swain, and C.L. Wu, 'Selective Radiant Temperature Mapping Using a Layered Classifier,' Journal of the IEEE Geoscience Electronics, Bol. GE-14, No. 2, April 1976. Also Available as LARS Information Note 111175, 1975.

6. Bartolucci, L.A., 'Hydrologic Features Survey,' Chapter 4, LARS Information Note 121275, Laboratory for Applications of Remote Sensing, Purdue University, West Lafayette, Indiana, 1975.

7. Bauer, M.E., P.H. Swain, R.P. Mroczynski, P.E. Anuta, and R.B. MacDonald, 'Detection of Southern Corn Leaf Blight by Remote Sensing Techniques,' Proceedings of the Seventh International Symposium on Remote Sensing of the Environment, Vol.1, May 17-21, 1971, pp.693-704.

8. Duda, R.O. and P.E. Hart, Pattern Classification and Scene Analysis, John Wiley and Sons, New York, 1973.

9. Goddard Space Flight Center Specifications for the Landsat-D System, Revision C, March 1981, Greenbelt, Maryland, pp:3-88.

10. Hoffer, R.M. and L.A. Bartolucci, 'Remote Sensing Techniques for Measurements of Water Temperature,' LARS Information Note 111671, Laboratory for Applications of Remote Sensing, Purdue University, West Lafayette, Indiana, 1971.

11. Kumar, R. and L.F. Silva, 'Emission and Reflectance from Healthy and Stressed Natural Targets with Computer Analysis of Spectroradiometric and Multispectral Scanner Data,' LARS Information Note 072473, Laboratory for Applications of Remote Sensing, Purdue University, West Lafayette, Indiana, July 1973.

12. Swain, P.H., T.V. Robertson, and A.G. Wacker, 'Comparison of the Divergence and B-Distance in Feature Selection,' LARS Information Note 020871, Laboratory for Applications of Remote Sensing, Purdue University, West Lafayette, Indiana, February 1971.

13. Swain, P.H. and R.C. King, 'Two Effective Feature Selection Criteria for Multispectral Remote Sensing,' LARS Information Note 042673, Laboratory for Applications of Remote Sensing, Purdue University, West Lafayette, Indiana, April 1973.

14. Wacker, A., 'A Cluster Approach to Finding Spatial Boundaries in Multispectral Imagery,' LARS Information Note 122969, Laboratory for Applications of Remote Sensing, Purdue University, West Lafayette, Indiana, December 1969.

15. Wu, C.L., D.A. Landgrebe, and P.H. Swain, 'The Decision Tree Approach to Classification,' LARS Information Note 090174, Laboratory for Applications of Remote Sensing, Purdue University, West lafayette, Indiana, September 1974.

N85-21732

TM GEOMETRIC PERFORMANCE : LINE TO LINE DISPLACEMENT ANALYSIS (LIDA)

L. Fusco European Space Agency - Earthnet, Frascati (I)
W. Mehl Commission of the European Communities - JRC, Ispra (I)

1. Introduction

This paper describes the early results of ESA-Earthnet, Frascati and CEC-JRC, Ispra contribution to the LIDQA programme. It is worthwhile to mention that Earthnet is currently operating two Landsat-4 acquisition and processing stations (Ref. 1) for both the MSS and TM instruments and a third, TM processing system, is under development at EPO - Earthnet Programme Office, Frascati (Italy), with the main role of a Quality Assessment System (QAS). The QAS (Fig. 1) uses a Perkin-Elmer 3252 as a central unit with 2M bytes memory, supported by an AP120B. Its peripherals include : 3 x 300M bytes disc units; a 42 track high density tape recorder with special interfaces to the AP array processor;an I2S image display system. The HDTR has a direct output on a Quick-look moving window display.

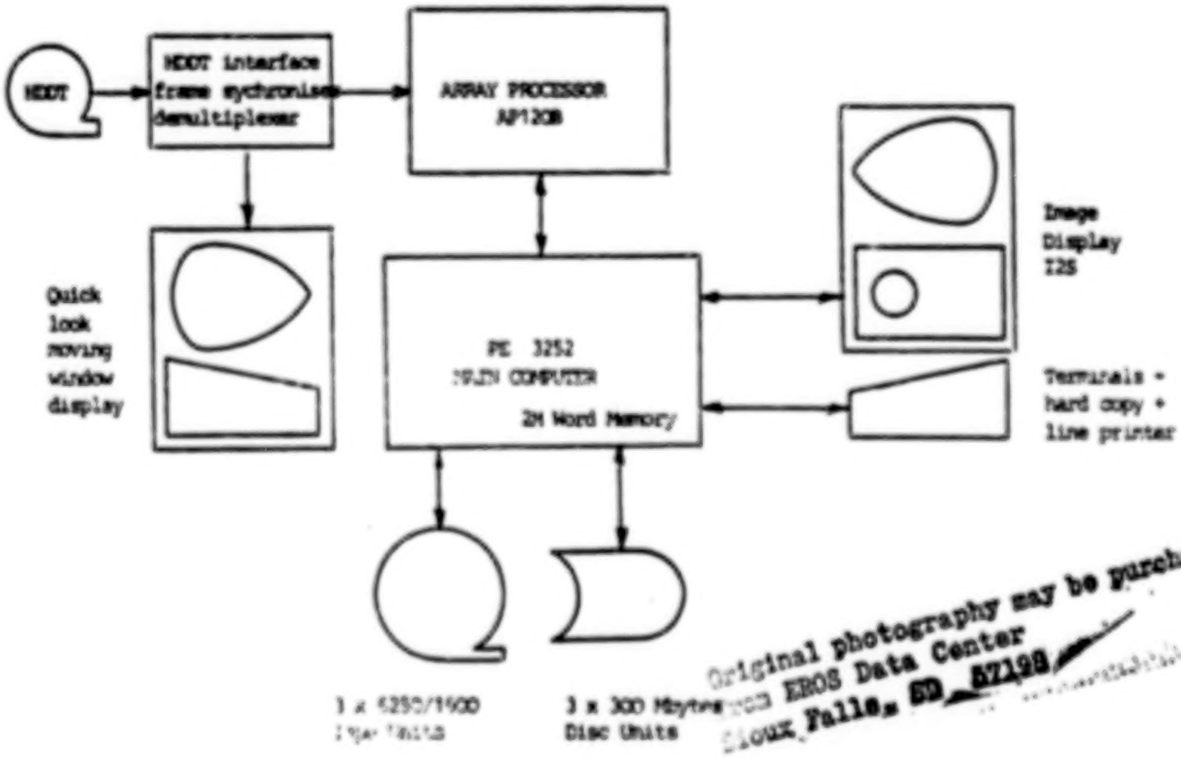
HDDT
HDDT interface
frame sychroniser
demultiplexer
ARRAY PROCESSOR
AP120B
Image
Display
I2S
Quick
look
moving
window
display
PE 3252
MAIN COMPUTER
2M Word Memory
Terminals +
hard copy +
line printer
1 x 6250/1600
Tape Units
3 x 300 Mbytes
Disc Units

Original photography may be purchased from EROS Data Center
Sioux Falls, SD 57198

Fig. 1 EPO - TM Quality Assessment System Configuration

PAGE III-358 INTENTIONALLY BLANK

PRECEDING PAGE BLANK NOT FILMED

The EPO/JRC contribution to the Landsat Image Data Quality Assessment Program is somewhat unique in that :

a) EPO is setting-up the QAS system whose objectives are in line the purposes of the LIDQA program;

b) EPO is operating Landsat acquisition and processing stations, and therefore an adequate knowledge of the system performance is mandatory.

Although the EPO/JRC TM data quality assessment programme goes far beyond the content of the present paper, in the first phase we have been mainly concentrating on the TM geometric performances, including :

- across scan jitter,
- along scan jitter and scan profile non-linearity,
- detector to detector and band to band displacement,

which will be detailed in the following sections. The description of the Thematic Mapper instrument can be found in Ref.2 and 3. It must be pointed out that TM system performances described in this paper have been measured without any knowledge of the PCD payload correction data which are sensed during image data collection and are used to correct the system errors.

2. LLDA : The Line to Line Displacement Analysis Method

The basic tool utilised for assessing the geometric performances of the TM instrument is the correlation between two Thematic Mapper image lines. This section describes how the correlation technique has been used to extract significant information from the TM image data.

Generally speaking, the correlation between any two TM adjacent lines (within the same scan) of the same band is very high, as shown in Fig. 2. The correlation increases as the dynamic range of the image data increases and more structure (i.e. larger standard deviation) is present in the image data. If the correlation is computed at different lags between the two lines, the correlation maximum will be located at the position where most of corresponding "structures" will be aligned. The value of the correlation maximum and the shape of the correlation profile will indicate how well the two lines have "aligned structures".
The deviation from the expected position may be used to measure TM instrumental behaviour.

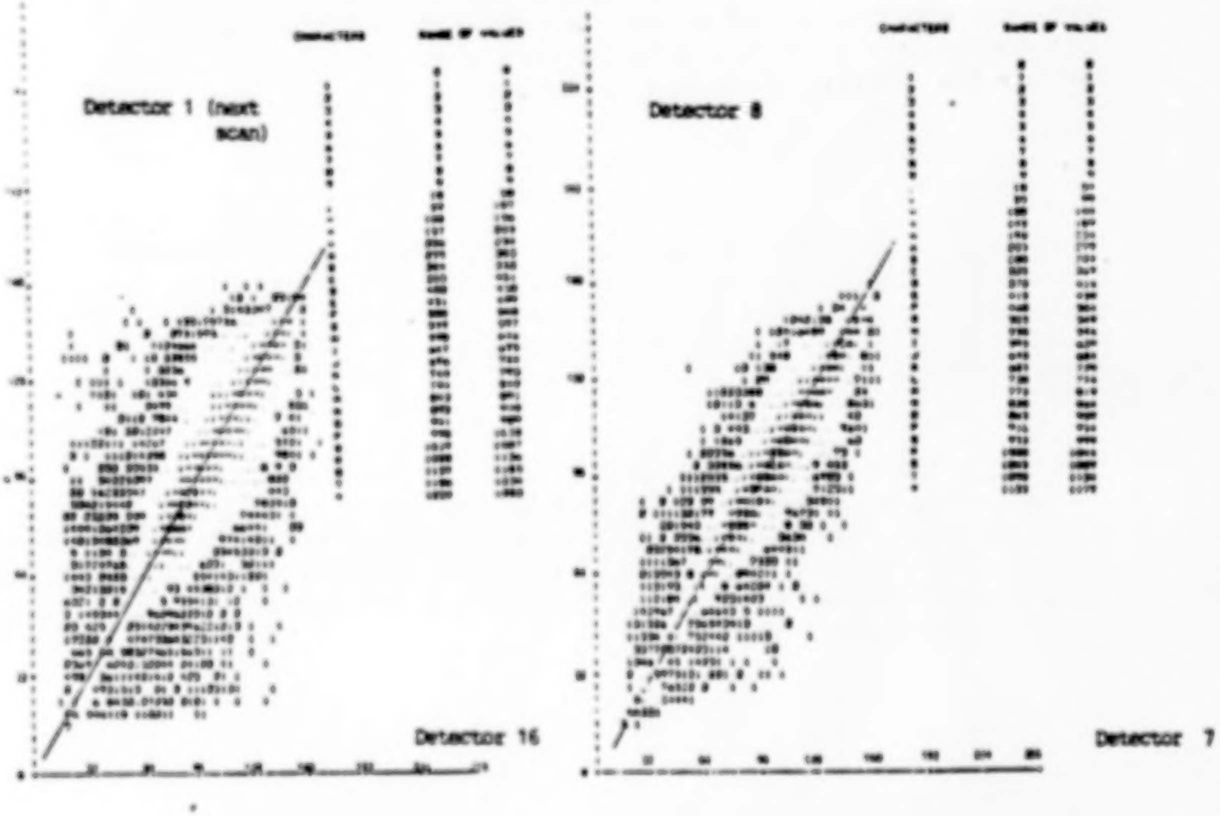

Fig. 2 2 Dim. spread diagram for 31 K pixels using successive lines (successive detectors). Data taken from TM frame 35 track 23 (22 August 1982) band 4. The diagram visually shows the high correlation between successive TM lines.

The size of the image line windows used in the correlation computation will influence the correlation profile in two different ways :

a) larger windows will have correlation with more stable shape and better statistics; therefore large windows may be used to analyse low frequency behaviour of the TM instrument;

b) smaller windows will align better local structures although the correlation will be more sensitive to noise; small windows may be be used to get information on high frequency behaviour of the TM TM instrument.

In the present analysis, although several correlation techniques (euclidean norm, cross products, etc.) have been tested, the use of the conservative solution has been preferred in using the standard correlation co-efficient calculated from :

where x, y, $\overline{x}$, $\overline{y}$ indicate respectively the generic pixel value for the two lines and their averaged pixel value, and the sum is performed for all N_p pixels in the window. The value is computed for N_s different lag position of the two windows, to generate the correlation profile.

Typically, the value of N_p is chosen close to 1000 and the value for N_s never been experienced larger than 25 for the correlation of lines in two consecutive scans.The displacement of the correlation maximum from the zero position will be used as a line to line misalignment indicator and it is processed as indicated in the following sections.

As the correlation is computed at discrete positions to achieve a more accurate correlation maximum location, the correlation profile is interpolated between the discrete integer positions (Fig. 3) :

- with a quadratic shape around the highest computed correlation co-efficient
- with a linear fit at any other position.

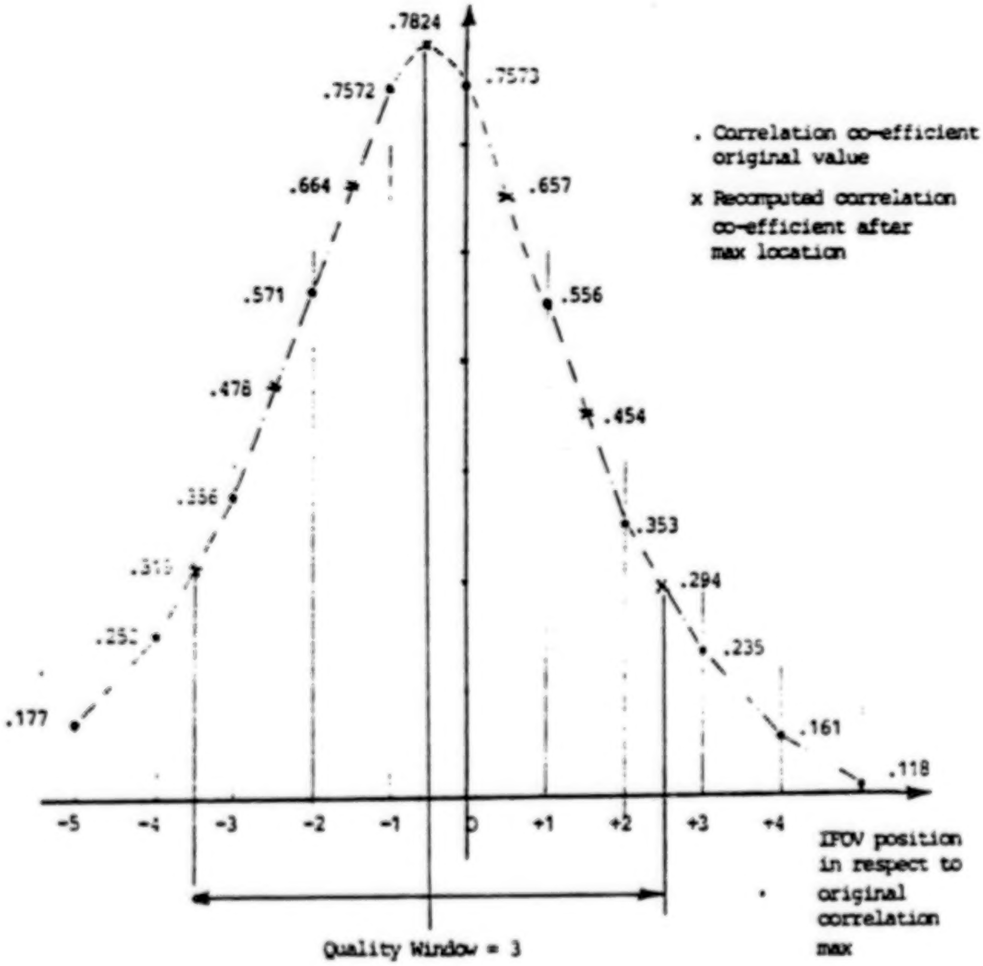

Final correlation max computed in .7824 at position -.499

Quality average/max = 0.579
Quality falloff/max = 0.392
Quality symmetry/max = 0.033

Fig. 3 Example of line to line correlation quality check

As already indicated the correlation shape and maximum value are checked to eliminate spurious cases. In the present analysis four quality criteria have been used. They refer to a quality window, i.e. the window of a given size (typically 3 pixels) centered on the computed correlation maximum, where the following quality parameters are tested against user defined thresholds (typical values are indicated) :

- flatness : the correlation profile in the quality window should verify :

$$\frac{\text{window correlation mean value}}{\text{correlation max}} < \text{threshold (.92)}$$

- fall-off : the correlation value of at the quality window extremes should verify :

$$\frac{\text{correlation window extremes mean}}{\text{correlation max}} < \text{threshold (.85)}$$

- symmetry : the correlation profile should be symmetrical in respect to maximum value :

$$\frac{\text{window correlation extreme absolute difference}}{\text{correlation max}} < \text{threshold (.35)}$$

- monotony : the correlation profile should decrease as the distance increases from the correlation maximum in the quality window

All precaution so far described will try to isolate good from bad results considering only the statistical properties of image data.

As we know, the correlation technique is sensitive to high gradient structures and we are interested in evaluating local geometric errors by measuring the deviation from the correct alignment local structure. When we do try to measure this displacement, we have to make sure that diagonal linear structure are kept aligned. Therefore it is necessary to filter the low components in the north/south direction of the correlation maximum displacement.

A user defined parameter will allow this filtering operation (see Fig. 4). Typically the HP parameter is defined as 2 lines.

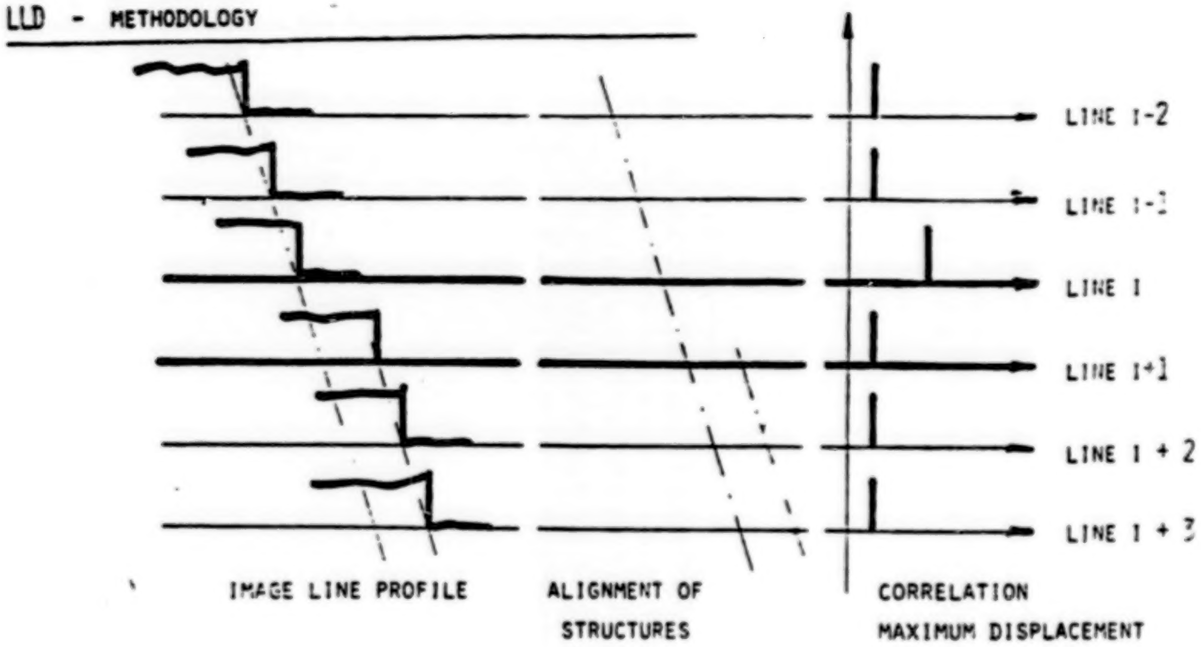
LLD - METHODOLOGY
LINE I-2
LINE I-1
LINE I
LINE I+1
LINE I + 2
LINE I + 3
IMAGE LINE PROFILE
ALIGNMENT OF STRUCTURES
CORRELATION MAXIMUM DISPLACEMENT

FIG. 4 - THE SCENE DEPENDENCE IS REMOVED BY FILTERING THE CORRELATION MAXIMA DISPLACEMENT WITH AN HIGH PASS FILTER :

$$CMD_{HPI} = CMD_I - \frac{1}{2}(CMD_{I-K} + CMD_{I+1+K}) \qquad K = \text{HP PARAMETER}$$

Most of the measurements are reduced to significant performance parameters by means of a statistical analysis on a large number of cases. The developed software programs will report (see Fig. 5) on the simple statistical analysis (σ, μ , regression) performed on the measured correlation maximum displacements.

```
*** INPUT  FILE IMAGE      DR1 B4 IMA

LINE (FIRST.LAST.SAMPLE)            48  5985    32
CORREL (WIND CEN .SIZE.STEPS)     3072  3000     7
CORREL MEASURE. HP LINE OFFS.     COR1     2
NR., DIST. WINDOWS.                  1  4000
QUALITY WINDOW EXT.                3.0   3.0   3.0
REJECT THRESHOLDS               0.920 0.920 2.000 3.000

*** OUTPUT FILE IMAGE

LINE

                                  ------------------- CMD
                                  |
                                      59 654--------- REGRESSION COEFFICI
                                            ---------- CUMULATIVE CMD
  48                             2.16.0  2.16.0
  80                             2.99.0  5.16.0
 112                             0.31.0  5.46.0
 144                             2.03.0  7.49.0
 176                             2.93.0 10.42.0
 208                             1.97.0 12.39.0
 240                             1.69.0 14.08.0
 272                             2.34.0 16.43.0
 304                             2.85.0 19.28.0
 336                             1.11.0 20.39.0
 368                             1.50.0 21.89.0
 400                             3.37.0 25.26.0
 432                             1.50.0 26.76.0
 464                             0.90.0 27.66.0
 496                             2.26.0 29.93.0
 528                             2.22.0 32.14.0
 560                             1.31.0 33.46.0
 592                             1.11.0 34.57.0
 624                             3.04.0 37.61.0
 656                             1.92.0 39.53.0
 688                             0.64.0 40.17.0
 720                             2.60.0 42.77.0
 752                             2.64.0 45.41.0
 784                             1.34.0 46.76.0
 816                             1.63.0 48.56.0
 848                             2.77.0 51.35.0
 880                             2.09.0 53.44.0
 912                             0.95.0 54.39.0
 944                             2.04.0 56.44.0
 976                             3.08.0 59.51.0
1008                             0.90.0 60.42.0 <==   QUALITY FLAGS
1040                             1.21.0 61.63.0
1072                             2.79.0 64.42.0
1104                             1.46.0 65.87.0
1136                             1.39.0 67.27.0
1168                             1.73.0 69.00.0
1200                             3.14.0 72.14.0
1232                             1.10.0 73.24.0
```

Fig. 5 Example of Line to Line Displacement Printout

3. TM Geometric Performance Analysis

The TM Arkansas scene acquired on 22 August 1982 (track 23, frame 35) has been processed to assess TM geometric performances. The raw data (B-tape) and the processed data (P-tape) have been used for the present analysis. Most of the described performance parameters have been measured from the analysis of the whole scene (whenever possible band 4 was selected as its radiometric distribution has the largest standard deviation). A detailed comparison on a small area (1024 x 1024 pixels) between our reprocessed B-tape and the P-tape was performed to validate the results of the present analysis, shown in figs. 6a - 6e.

As no information was available at the time, the alignment of the and the reverse scans in the B-tape was performed by a fixed shift of 45 pixels (instead of 46 as afterwards described). This error does not affect any of the reported analysis.

In the following sections the results of detailed investigations are reported.

3.1 Scan to scan analysis

Objective	Identify the low frequency (period 2 scan time) components of the TM geometric distortion.
Method	Full line to line correlation (window of 6000 pixels) using the last line in a scan (detector #16) and the first line of the next scan (detector #1).
Definition	Scan to scan jitter is defined by the sum of distortion along scan (line length, TM attitude) which is measurable from misalignment of across scan structures.

ORIGINAL PAGE IS
OF POOR QUALITY

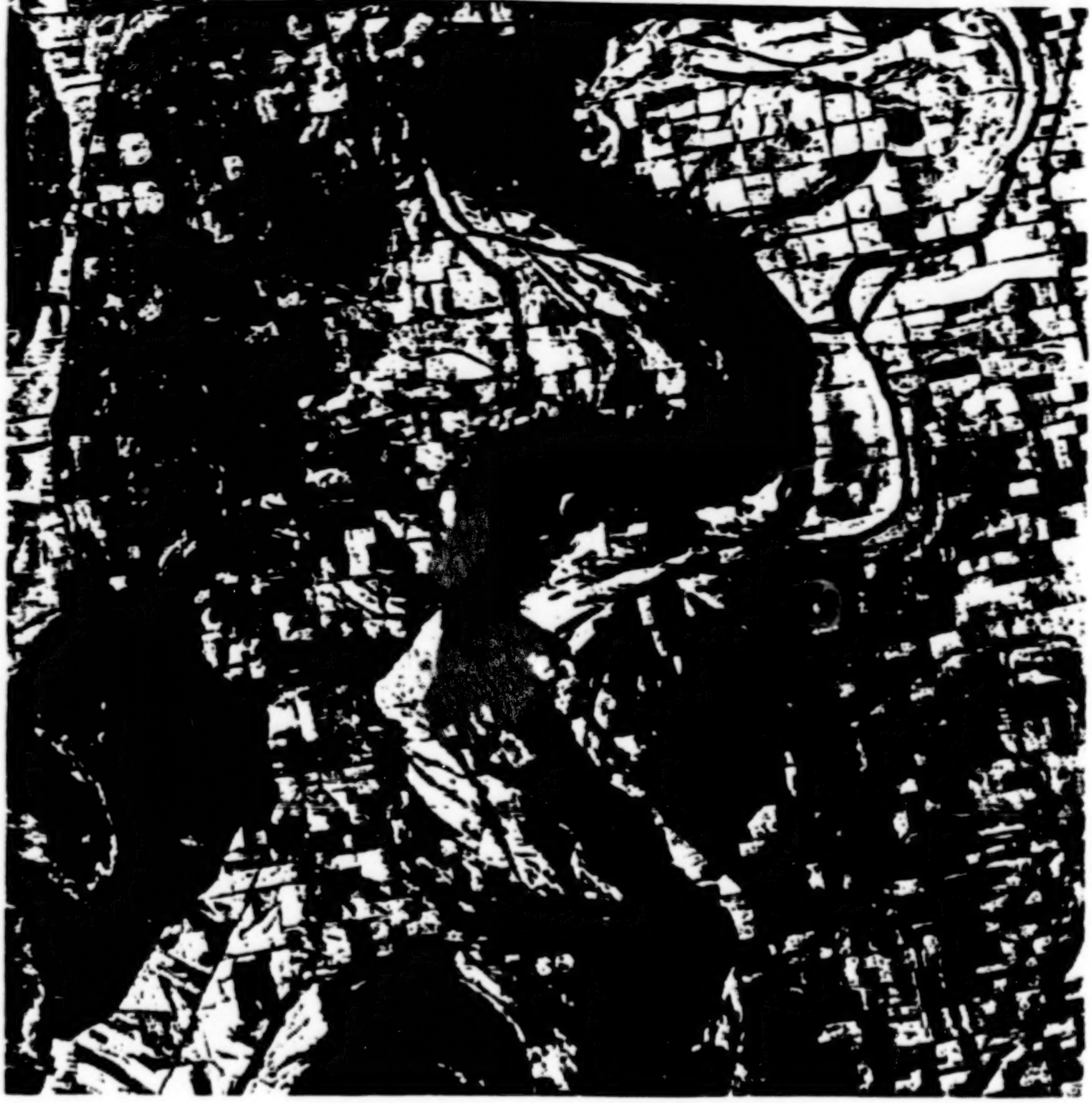

Fig. 6a Original Arkansas Raw Data (1024 x 1024 Pixels)

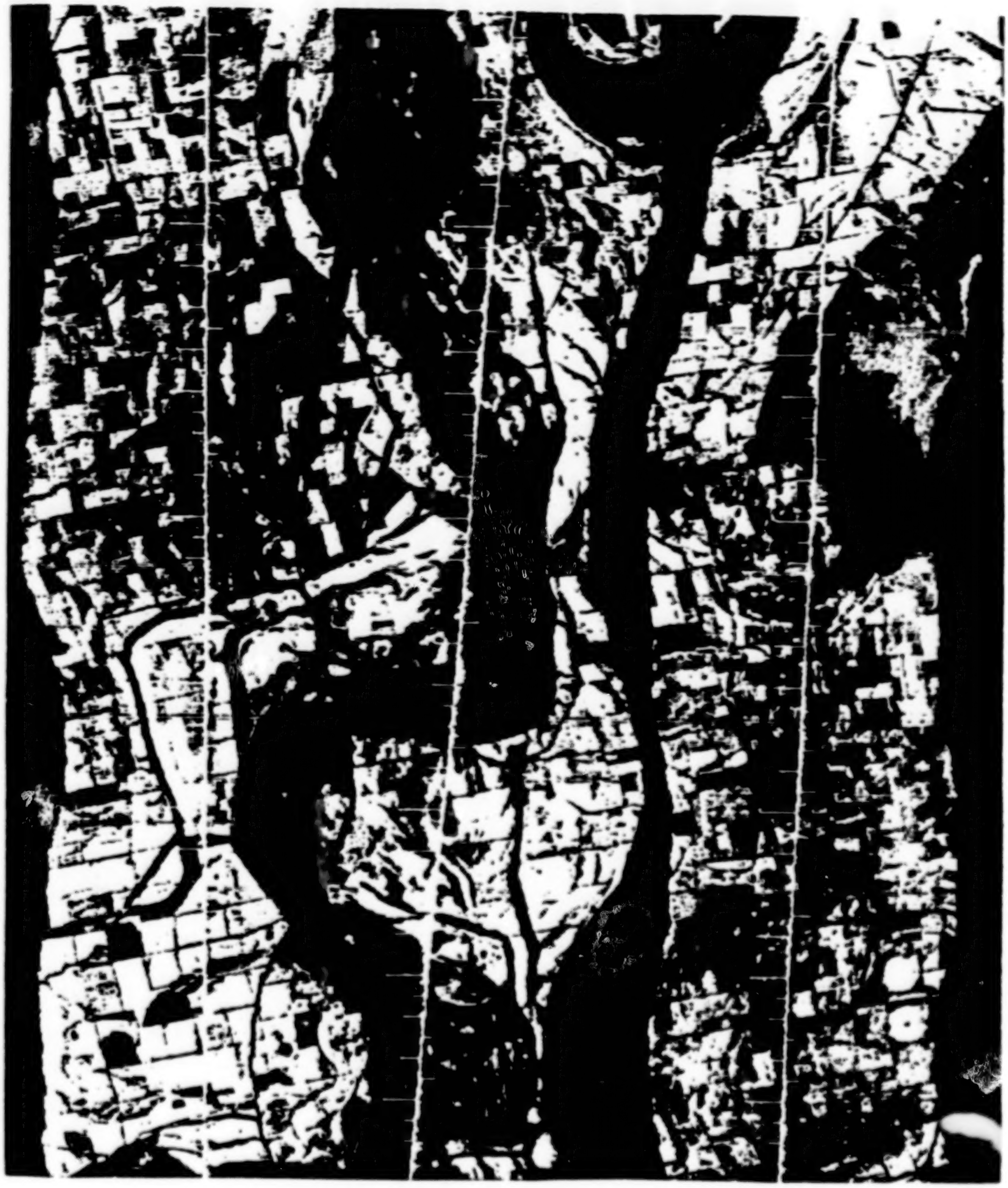

Fig. 6b Processed 6a data using 3 windows and no scene dependance corrections. The 3 white lines show the line to line displacement correction performed on each window (all lines processed).

ORIGINAL PAGE IS
OF POOR QUALITY

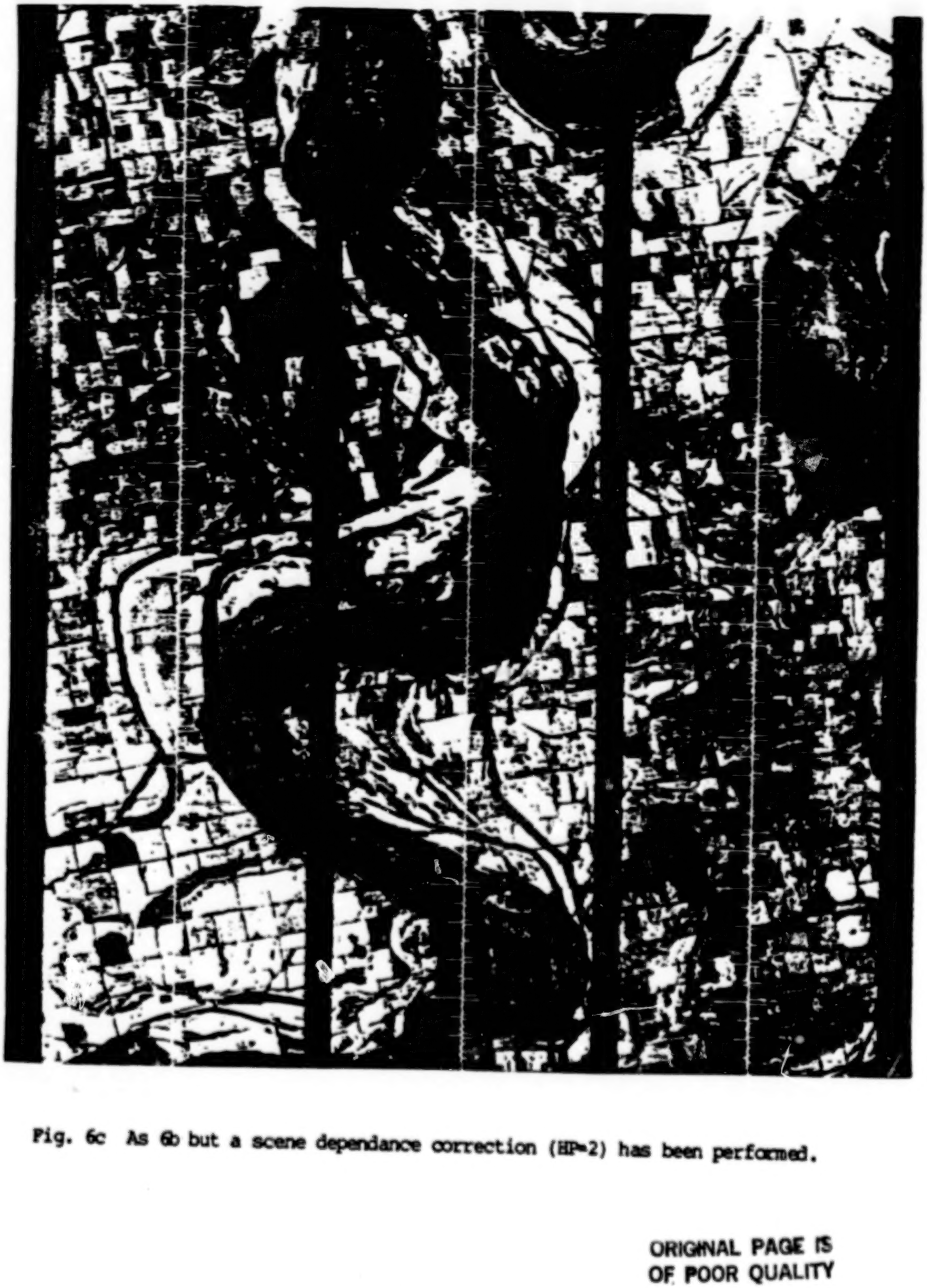

Fig. 6c As 6b but a scene dependance correction (HP=2) has been performed.

ORIGINAL PAGE IS
OF POOR QUALITY

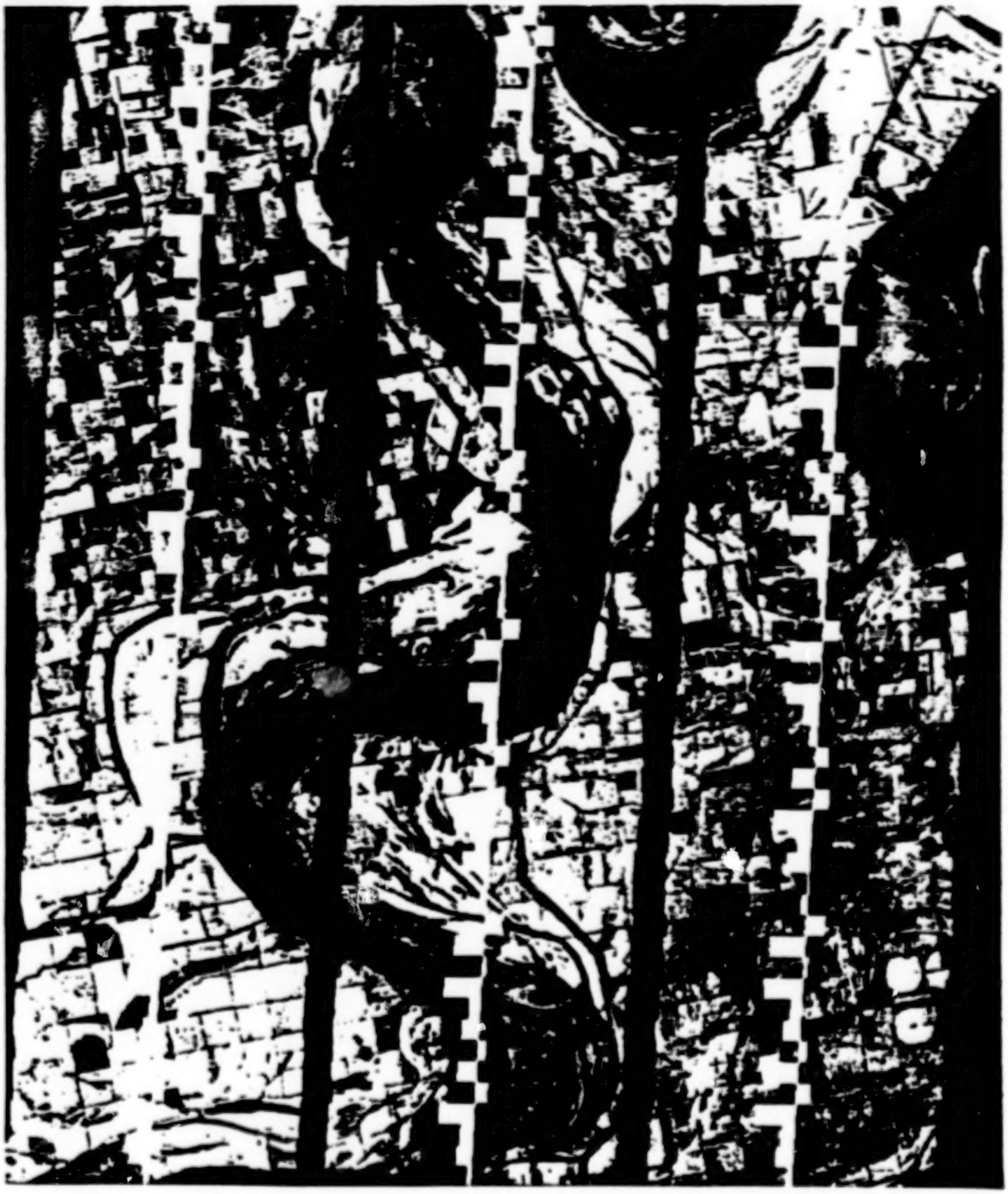

Fig. 6d As 6c but the same correction is applied to the 16 detectors in the same scan.

ORIGINAL PAGE IS
OF POOR QUALITY

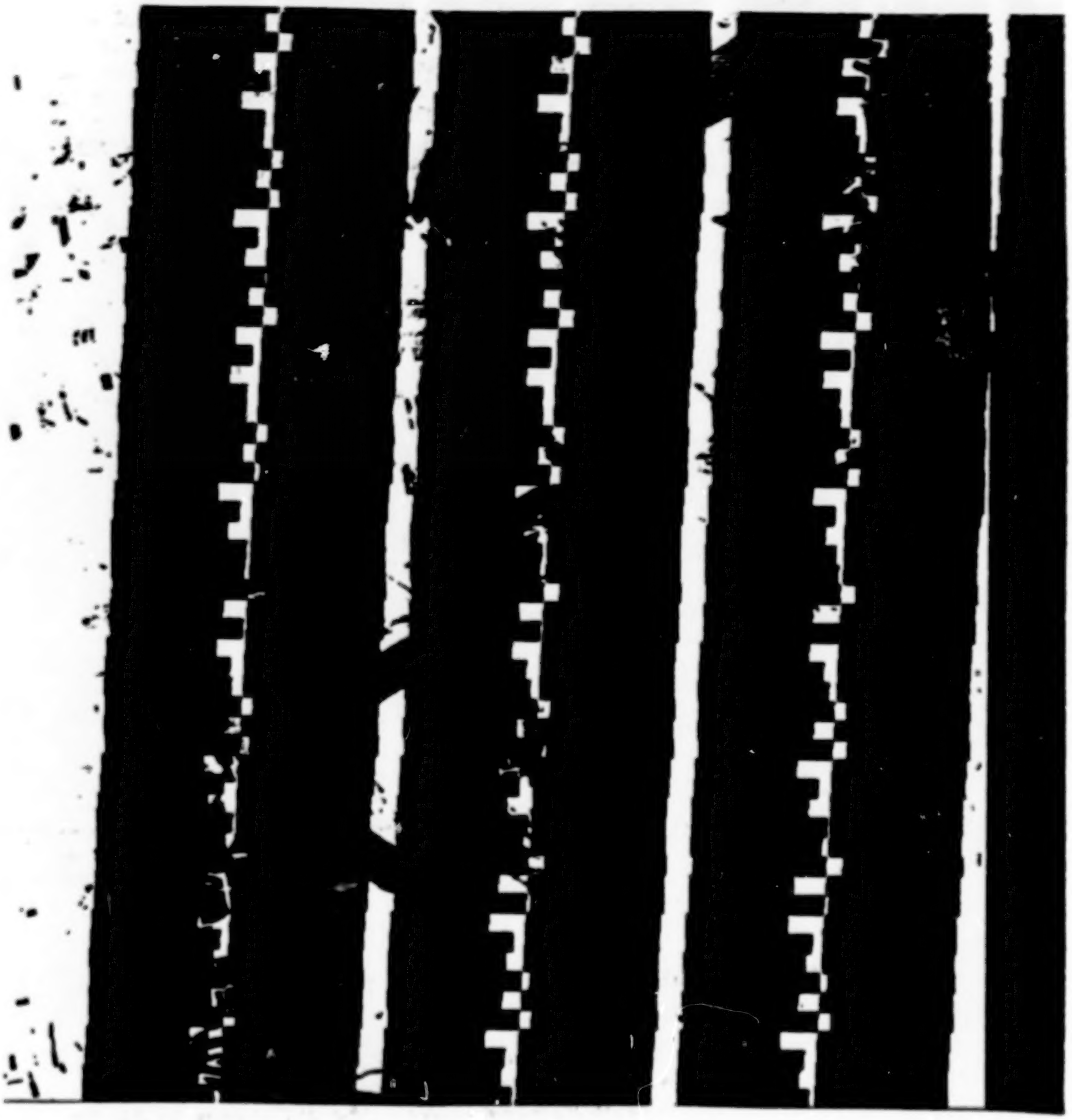

Fig. 6e Difference between 6d and NASA processed Ptape data re-scaled at original pixel resolution. The comparison shows a very good along line distortion correction.

ORIGINAL PAGE IS OF POOR QUALITY

Result 1 The earth's rotation will produce a constant value scan to scan distortion (scan to scan skew), which must be taken into account. The scan to scan skew has been computed from a linear regression analysis of the correlation maximum displacements (CMD) results in 0.8125 pixels/scan. Fig. 7 shows the cumulative CMD computed for the first 320 scenes of the B-tape.

ORIGINAL PAGE IS
OF POOR QUALITY

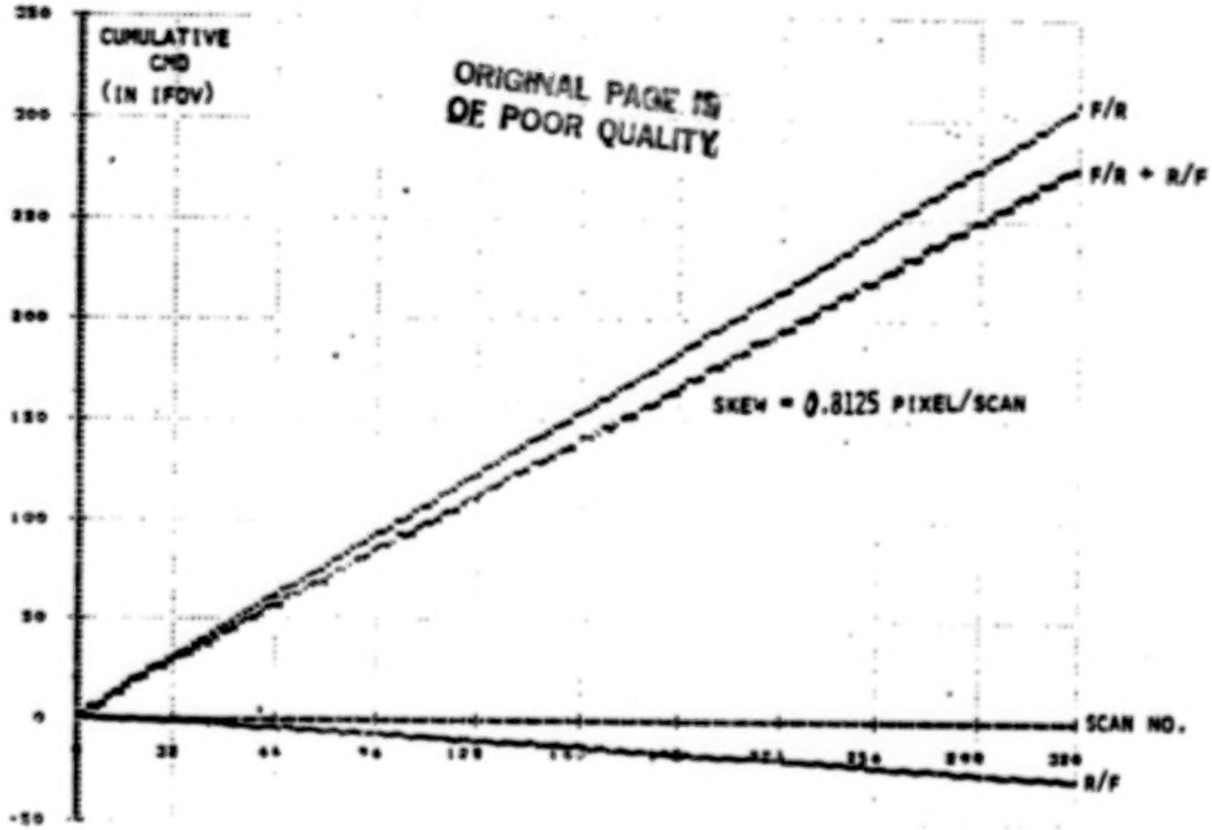

Fig. 7 Cumulative CMD computed for first 320 scenes

It is shown separately the analysis of the CMD in the Forward/Reverse (F/R) scan interaction and in the Reverse/Forward (R/F). The difference is due to the wrongly assumed 45 (instead of 46) pixel shift necessary to align Forward and Reverse scans.

Result 2 As is shown in Fig. 8, the scan to scan displacement, after considering the skew correction, has a peak to peak magnitude of about 2.4 and a period of about 7 scans (2 Hz).

ORIGINAL PAGE IS
OF POOR QUALITY

In more recent Earthnet acquired TM images, a peak to peak magnitude has been measured of about 10 IFOV (track 191, 20 Jan. '83; track 198, 23 Jan. '83; track 202, 19 Jan. '83) with the same frequency of about 2 Hz.

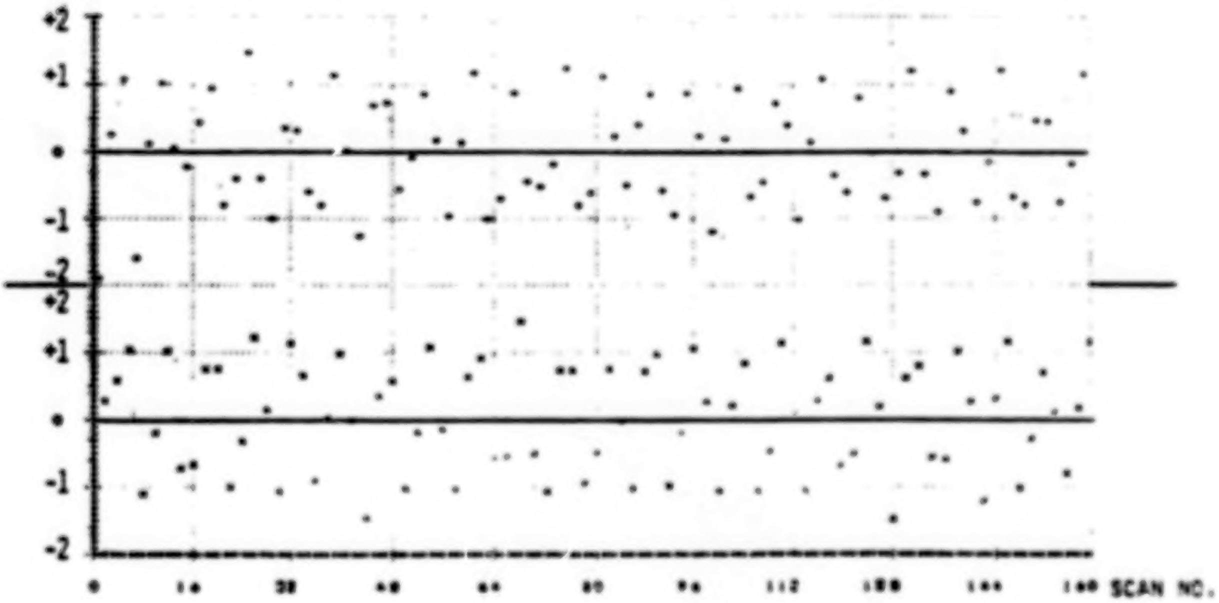

FORWARD/REVERSE (+) and REVERSE/FORWARD CMD after Correction.
Units are in IFOV.
Note the good fit with a sinus function with period of 7 scans.

Fig. 8

3.2 Scan to scan profile non-linearity

Objective Identify systematic errors in the TM scan profile.

Method Line to line correlation (window of 960 pixels) at different positions in the line (every 512 pixels) using the last line in a scan (detector #16) and the first line in the next scan (detector #1). Fig. 9 displays the F/R and R/F scan to scan displacement computed at 512 pixel distances within the scan, for the first 48 scans.

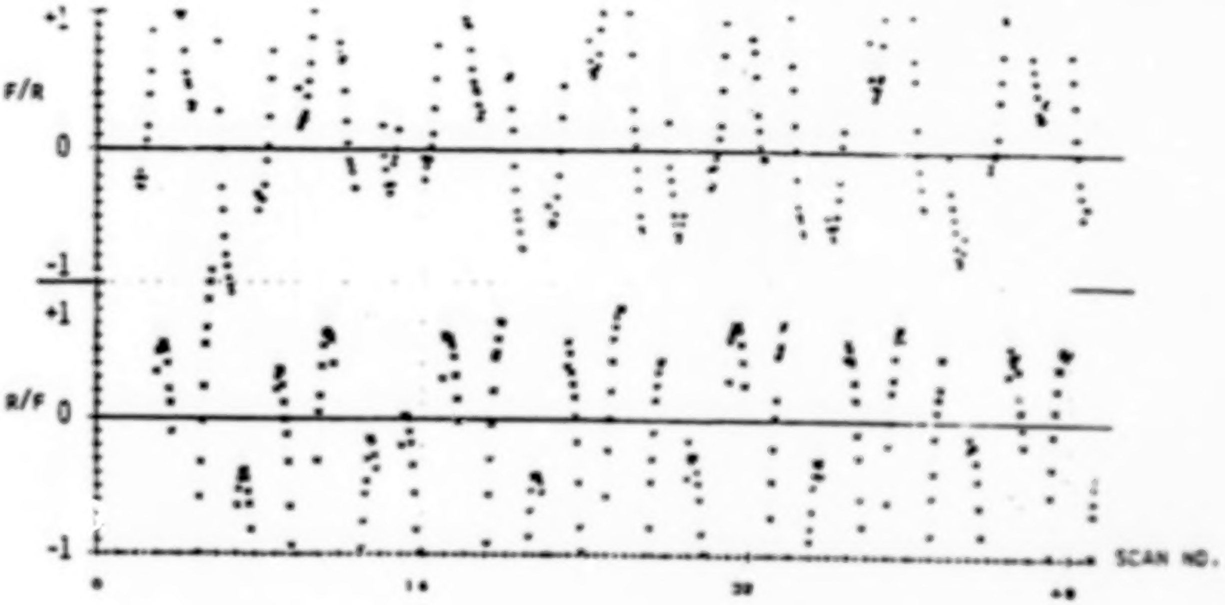

F/R and R/F (X) scan-to-scan displacement computed using windows of 960 pixels centered every 512 pixels. Values (in IFOV) are corrected for the skew only.

Fig. 9

Results Fig. 10a and 10b show the measured difference between forward and reverse scan profile non-linearity as measured from the image itself. The averaged residuals give an indication of the residual errors of the measurements. It must be noted that a wrong value of the skew influences the plotted scan profile non-linearity.

3.3 Along scan medium frequency jitter

Objective Identify and quantify along scan non systematic errors.

Method As for the scan profile non-linearity (section 3.2) but using the non systematic contribution in the correlation maximum displacement.

ORIGINAL PAGE IS
OF POOR QUALITY

	FULL IMAGE*	-2560	-2048	window** center -1536	-1024	-512	MID SCAN	+512	+1024	+1536	+2048	+2560
Regression F/R scan displacement	1.909	2.69	2.50	2.32	2.07	1.87	1.74	1.71	1.77	.85	1.96	2.15
Skew relative to mid-scan		+.56	+.45	+.34	+.22	+.11	-	-.11	-.22	-.34	-.45	-.56
Residual F/R		.22	.14	.07	-.06	-.15	-.17	-.09	-.08	.28	.50	.80
Regression R/F scan displacement	-.284	-1.31	-.95	-.65	-.36	-.16	-.06	-.02	-.07	-.17	-.28	-.50
Skew relative to mid-scan		-.56	-.45	-.34	-.22	-.11	-	+.11	+.22	+.34	+.45	+.56
Residual R/F		-.47	-.22	-.03	+.14	+.23	+.22	+.15	-.01	-.23	-.45	-.78
Averaged Residual		-.13	-.04	+.02	+.04	+.04	+.03	+.03	+.04	+.03	+.03	+.01

* windows of 6000 pixels centered at pixel (FORWARD) 3072 (mid-scan)

UNITS are IFOV

All results were filtered for scene dependence

** windows of 960 pixels

Fig. 10a FORWARD/REVERSE Scan Non-Linearity - TM Image of 22/08/82

Scan to Scan Displacement Analysis

ORIGINAL PAGE IS
OF POOR QUALITY

C-5

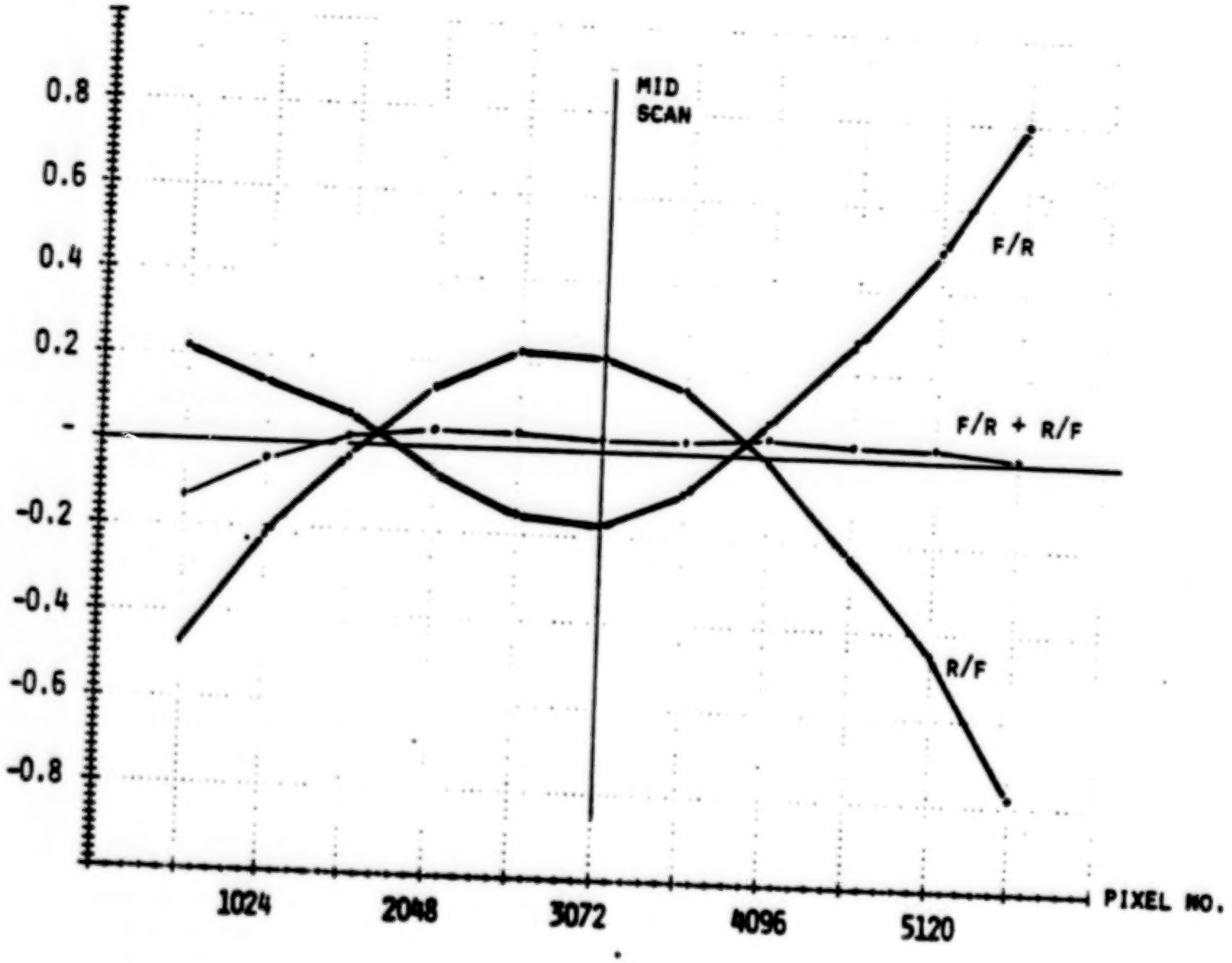

Fig. 10b F/R and R/F Scan Non-Linearity (Units in IFOV)

Results Fig. 11 shows the variation of CMD, a 512 pixel distance in a time sequence, computed from F/R and R/F scans. The plotted values have been corrected for the skew contribution which is different in F/R and in R/F. The low frequence components (2Hz) described in section 3.1 have not been removed.

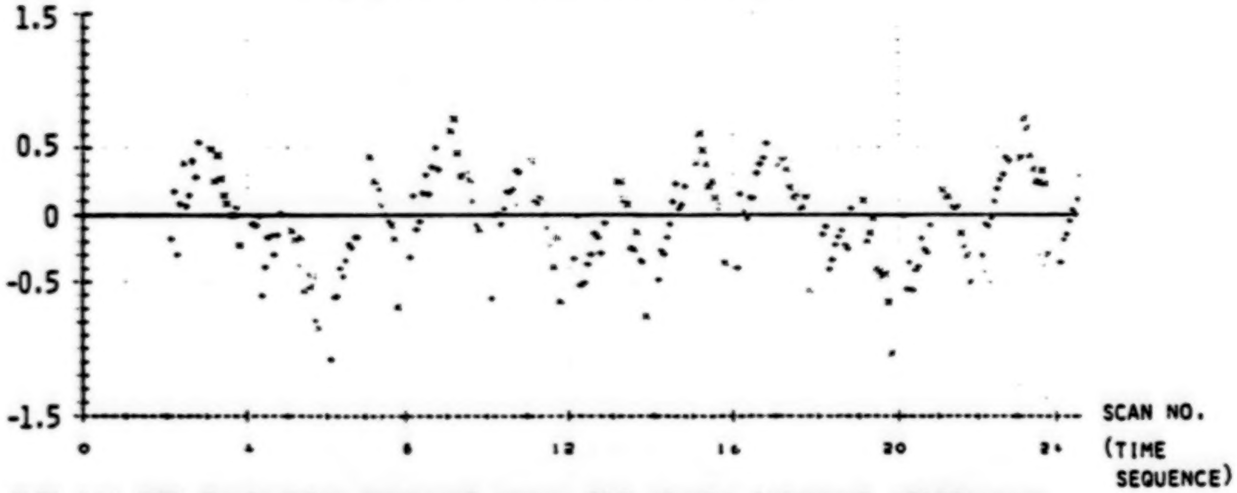

F/R (+) CMD derivative measured every 512 pixels interval (difference between two successive measurements of previous plot). Data in IFOV are plotted in time sequence, i.e. R/F measuremnts are inverted in the plot.

Fig. 11

3.4 Odd/even detectors displacement

Objective Identify and measure odd/even detector displacement due to delays in data sampling from image data.

Method Although the detectors are on a fixed position on the two focal planes, the electronic circuitry is different for each single detector. Some delays in the electronics will result in small but constant delays between two adjacent image lines. It is assumed that the correlation technique will be capable to detect small delays between lines, especially if a large number of cases are studied. The method chosen for this analysis consists in measuring the correlation maximum and displacement of two adjacent lines (odd/even or even/odd) belonging to the same scan. Foward and Reverse scans are processed separately. The correlation windows were centered at mid scan (pixel 3072) and a window size of 6000 pixels was used. The method will allow measurement only along scan displacement.

Results Fig. 12 shows the displacement for each detector in respect to the next, averaged on all Forward and Reverse scans in the scene. Bands 4,5 and 7 were processed. The averaged distance (or delay) between odd/even (ΔOE) and and even/odd (ΔEO) detector is different for Forward and Reverse scans, as indicated in Fig. 12.

Results The standard deviation in some cases (Band 5) is too large, meaning that there is a large variability of detector behaviour.
The OE, EO measurements are combined to generate a sort of physical model of the displacement of the detectors. In respect to expected reference location of odd/even detectors after some systematic delays (2 or 3 pixels, respectively, in the Forward and Reverse scan), Fig. 13 shows the mid-location and the apparent inclination in respect to scan detection.

3.5 Band to band displacement

Objective Identify and measure the band to band displacement due to displacement of focal planes and to different delays in data sampling.

Method To achieve good results, the band to band correlation has been performed on band pairs which have a good overall correlation, as is the case of Band 1/Band 3, B3/B7, B3/B5, B5/B7.

The line of two bands corresponding to the same detector number were correlated, using a window of 1000 pixels centered at pixel 1024,3072 and 5120. The measurements were averaged over the total number of available scans. Forward and Reverse scans were processed separately.

	B4				B5				B7			
	F		R		F		R		F		R	
	O/E	E/O	O/E	E/O	O/E	E/O	O/E	E/O	O/E	E/O	O/E	E/O
1	-0.41		.008		-.059		+.156		+.139		+.052	
2		-.010		-.061		-.006		-.196		-.160		-.045
3	-.025		-.018		-0.29		+.085		+.121		+0.18	
4		-.076		-.005		-.087		-.102		-.151		-.038
5	-.010		-.026		+.018		+.027		+.126		+.016	
6		-.035		-.035		-.097		-.086		-.128		-.054
7	-.008		-.043		+.005		+.048		+.065		+.053	
8		-.050		-.019		+.023		-.237		-.066		-.121
9	-.042		-.003		-.150		+.220		+.087		+.025	
10		-.036		-.031		+.013		-.212		-.143		-.042
11	-.024		-.021		-.053		+.102		+.082		+.032	
12		-.025		-.045		-.084		-.115		-.120		-.061
13	-.034		-.013						+.064		+.063	
14		-.031		-.028						-.097		-.112
15	-.012		-.035		.064		+.028		+.090		+.089	
μ OE	-.024		-.020		-.029		+.095		+.097		+.043	
μ EO		-.037		-.032		-.040		-.158		-.124		-.068
σ	.013	.019	.014	.018	.064	.050	.066	.140	.026	.030	.026	.032
OE sensor distance $\frac{1}{2}(\mu OE - \mu EO)$	+.007		+.006		+.006		+.127		+.111		+.056	
OE sensors slope $\frac{1}{2}(\mu OE + \mu EO)$	-.030		-.026		-.035		-.031		-.013		-.012	

Fig. 12. LLD : Sensor to Sensor Displacements within Band (measurements in RFOV)

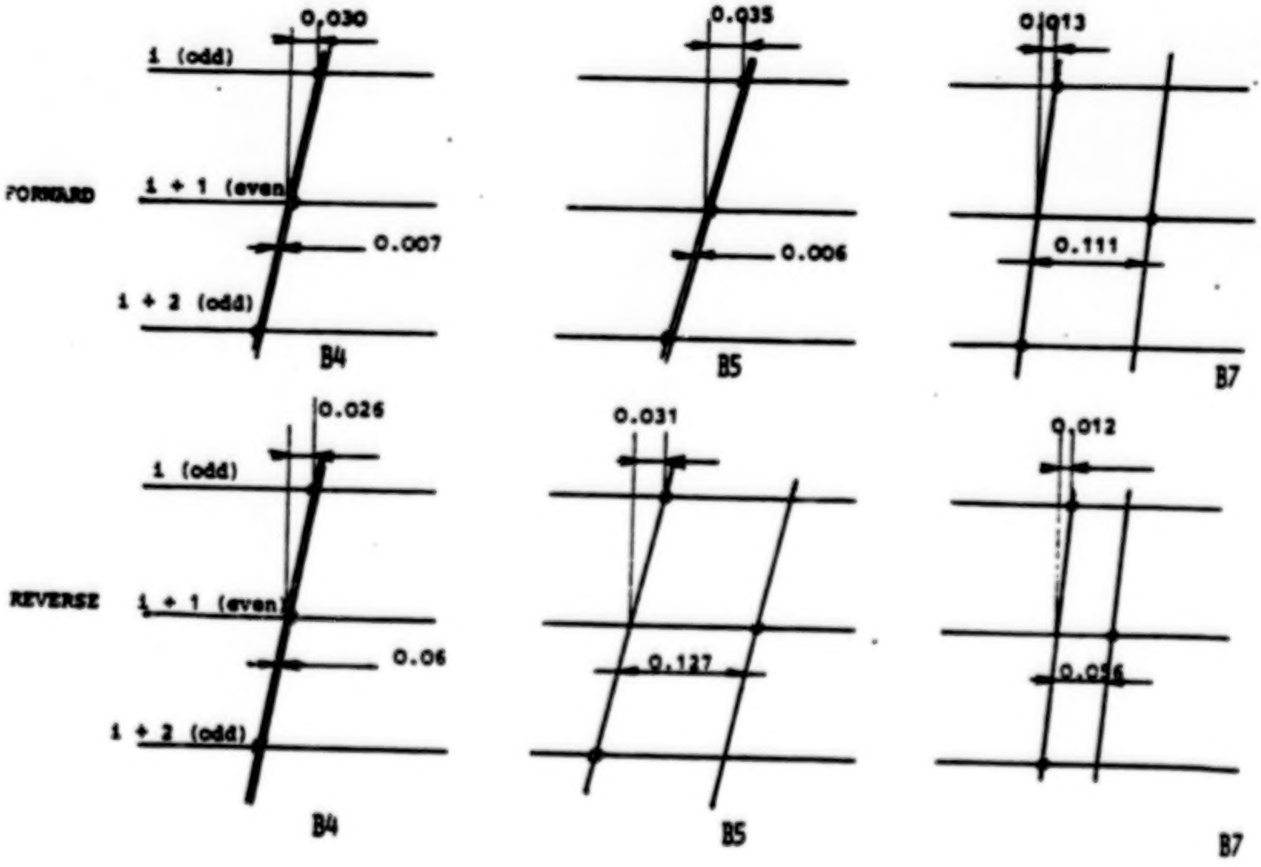
0.030
i (odd)
FORWARD
i + 1 (even)
0.007
i + 2 (odd)
B4
0.035
0.006
B5
0.013
0.111
B7
0.026
i (odd)
REVERSE
i + 1 (even)
0.06
i + 2 (odd)
B4
0.031
0.127
B5
0.012
0.056
B7

Fig. 13 Sensor to Sensor Displacement within Band (measurements in RFOV)

Results

Fig. 14a reproduces the list of all performed measurements. A summary table is given Fig. 14b.

It must be noted that :

a) The two focal planes have an averaged displacement of .50 pixels, which is outside pre-flight specifications.

b) The Forward scan band to band measured are slightly different from Reverse scans.

c) The band to band displacement changes with the pixel position. The physical distance between the different band detector (B1-B5 distance is about 151 pixels) is not negligible and the mirror speed changes with the pixel position within the line.

sensor /scan	B1-B3			B1-B7			B3-B7			B3-B5			B7-B5		
	1024	3072	5120	1024	3072	5120	1024	3072	5120	1024	3072	5120	1024	3072	5120
1F	.06	.04	.03					.36		.59	.51	.44	.08	.07	.06
2F	.10	.07	.06					.67		.57	.46	.38	-.08	-.09	-.10
3F	.10	.07	.06	.66	.53	.47		.35		.59	.49	.41	.08	.07	.06
4F	.02	.00	-.01	.78	.70	.65		.68		.68	.62	.52	-.03	-.04	-.05
5F	.09	.06	.05	.64	.51	.45		.38		.55	.46	.39	.05	.04	.03
6F								.74							
7F								.55							
8F	.00	-.02	-.03					.75		.77	.72	.66	-.02	-.03	-.04
9F	.16	.13	.12					.35		.74	.69	.62	.09	.08	.07
10F	.05	.03	.02					.75		.72	.52	.46	-.11	-.12	-.13
11F								.48							
12F								.73							
13F								.59							
14F								.71							
15F								.59							
16F	.03	.00	-.01					.73		.77	.71	.65	-.00	-.01	-.02
1R	.05	.00	-.03					.38		.35	.23	.16	-.08	-.09	-.11
2R	.07	.03	.01					.45		.62	.46	.35	.03	.01	.00
3R	.06	.02	-.01	.69	.49	.35		.41		.38	.27	.17	-.08	-.09	-.12
4R	.13	.08	.05	.76	.59	.45		.42		.53	.35	.27	-.00	-.02	-.04
5R	.10	.05	.03	.74	.56	.41		.44		.48	.32	.23	-.04	-.06	-.08
6R								.37							
7R								.31							
8R	.15	.10	.08					.38		.50	.34	.25	-.00	-.02	-.04
9R	.10	.07	.04					.35		.33	.22	.15	-.08	-.09	-.12
10R	.09	.05	.03					.42		.71	.57	.44	.08	.07	.05
11R								.42							
12R								.48							
13R								.35							
14R								.54							
15R								.34							
16R	.14	.09	.07	.81	.79	.76		.57		.68	.55	.41	-.00	-.02	-.04

Values are in RFOV in respect to nominal band to band displacements.
Window centers are indicated.

Fig. 14a LLD : Band to Band Displacement Measurements (all results)

LLD BAND TO BAND DISPLACEMENT : RESULT SUMMARY

Band to Band		B1-B3	B1-B7	B3-B7	B3-B5	B7-B5
Number of processed sensors		9	3/4	16	9	9
Average	F1024	.07	.69	.65	.65	.01
	F3072	.04	.58	.60	.58	.00
	F5120	.03	.52	.55	.50	-.01
	R1024	.10	.75	.55	.51	-.02
	R3072	.05	.61	.42	.37	-.03
	R5120	.03	.50	.32	.27	-.06
	F ODD	.08	.54	.48	.55	+.06
	FEVEN	.02	.71	.71	.61	-.06
	R ODD	.04	.54	.38	.27	-.09
	REVEN	.08	.69	.45	.47	.00
	F ALL	.05	.62	.59	.58	.00
	R ALL	.06	.62	.42	.37	-.04
	ODD	.06	.54	.43	.41	-.02
	EVEN	.05	.70	.58	.54	-.03
	TOTAL	.05	.62	.50	.47	-.02

Fig. 14b

4. Conclusions

The results so far achieved using the LLDA indicates that this method is adequate for evaluating TM geometric performances from image data.

Although most of the results are consistent with themselves, there are cases where they are not, due to the limitation of the method which expects well contrasted/correlated data sets.

Overall, the geometric performance of the TM instrument is so good that a simple correction method can be derived from the reported analysis.

We have been experimenting with this on a certain amount of cases, as for the frame illustrated in Fig. 15 (track 193, frame 31 of 20 Jan. 1983 - image received at ESA's Fucino station, Italy).

Additional data sets will be processed to complete the reported analysis.

ORIGINAL PAGE IS
OF POOR QUALITY

REFERENCES

1. L. Marelli, "Earthnet Prepares for Landsat-D", ESA Bulletin No. 32, Nov. 1982

2. J.L. Engel, "Thematic Mapper - An interim report on anticipated performances", Encl. 5 to NASA Application Notice for participating in LIDQA Program, Oct. 23, 1981.

3. NASA, Landsat-D Investigation Workshop, May 13-14, 1982,GSFC, Washington, D.C.

N85-21733

~~D8~~
D9

IN-PROGRESS ABSOLUTE RADIOMETRIC INFLIGHT CALIBRATION OF THE LANDSAT-4 SENSORS

K. R. Castle(1), M. Dinguirard(2), C. E. Ezra(3), R. G. Holm(1), R. D. Jackson(3),
C. J. Kastner(1), J. M. Palmer(1), R. Savage(4), and P. N. Slater(1)

(1) Optical Sciences Center, University of Arizona.
(2) Centre d'Etudes et de Recherches de Toulouse.
(3) Agriculture Research Service, USDA, Phoenix.
(4) Atmospheric Sciences Laboratory, White Sands Missile Range.

INTRODUCTION

In this project we are planning to calibrate, radiometrically in an absolute sense, the sensors on Landsat-4, particularly the Thematic Mapper (TM), on several occasions by reference to selected instrumented areas at White Sands Missile Range (WSMR), New Mexico. WSMR was chosen because it includes extensive, flat, diffuse, uniform areas of different reflectances. Each of these attributes is of importance for the following reasons. Atmospheric adjacency effects are minimial because of the large areas of the reference sites. The flatness and uniformity of the sites simplifies the mapping of residual spatial nonuniformities in their reflectance. The diffuse or near-lambertian nature of the ground reflectance means that only small corrections may be necessary for BRDF effects, in relating the ground measurements to the space measurements. The advantage of having areas of different reflectance is that they provide more than one point on the calibration curve. Actually the internal TM calibration is a sufficient check on linearity, and this last advantage is perhaps a more useful check on the consistency of our approach than on the calibration of the TM itself.

Two series of optical measurements are made concurrently during the morning of a TM overpass. In one, the radiances of selected large ground areas ~120 x 120 m in size are measured in the spectral bandpasses of the TM. In the other, the total optical thickness of the atmosphere is measured in nine narrow spectral intervals (~10 nm) between 0.4 and 1.0 μm using the well-known Langley plot technique. The Rayleigh optical thickness can be determined simply from a knowledge of the ground atmospheric pressure at the time of the overflight. Subtracting the Rayleigh from the measured total optical thickness of the atmosphere provides the aerosol optical thickness as a function of wavelength except in regions of O_3 and H_2O absorption. The O_3 optical thickness in the Chappuis band can be determined either by measurements at the

PRECEDING PAGE BLANK NOT FILMED

PAGE III-388 INTENTIONALLY BLANK

edge of high O_3 absorption near 0.3 μm (the long wavelength cut-off of the Hartley-Huggins bands), or by fitting a curve of aerosol optical thickness versus wavelength through the entire spectral range 0.4 to 1.0 μm referring only to points outside the Chappuis band; the difference in the Chappuis band between the measured total optical thickness and the sum of the Rayleigh and aerosol optical thicknesses provides the O_3 optical thickness as a function of wavelength.

A description of the instrumentation to be built for this project and the initial results of a measurement sensitivity analysis has been previously reported.(1)

PROGRESS TO DATE WITH FIELD MEASUREMENTS

We are tentatively planning to use three sites at White Sands Missile Range on this project, however, we may add or substitute others for those mentioned here. The reason for this indecisiveness is that, because of weather conditions that have prevented helicopter flights and the lack of aerial photography and TM imagery, we have not been able to study the vast area available to us in any detail. Our present sites are the so-called Cherry site, near the southern end of the Northrup strip, which is extremely convenient because of the presence of two large temperature-controlled trailers with electricity, telephones, storage space, and meteorological instrumentation; the Coconut site (so named by Ray Jackson because shredded coconut accurately describes the appearance of the crystallized gypsum there); and the Parker site. The Coconut site is about a kilometer west of the Cherry site and the reflectances of the two sites are about the same. The Coconut site was chosen mainly because it provides a second reference and it is nearer the vegetated area surrounding the alkali flats and could thus provide a measure of any residual adjacency effect. The Parker site has not yet been examined, but is reported to be a large graded circular area of desert of a yellow-orange color. It is used as the impact zone for the Multiple Launch Rocket System and is graded to facilitate the determination of the spatial dispersal of the dummy warheads.

The weather this winter in the Southwest has been unusually poor. Precipitation since the start of the year has been 2.5 times normal. TM overpasses occurred on December 18, 1982; January 3 and 19, 1983; and February 4, 1983. Only on January 3 was the sky clear enough for the solar radiometer to be used and data from these measurements are shown in Figures 1-4. (Even on that occasion there were a few high thin cirrus clouds present, as can be seen from the outlier points in Figures 1-3.).

Barnes and Exotech radiometer data were collected on December 16 (pre TM overpass) of the gypsum which was damp due to rain and frost, and on January 3 of the 80 mm thick snow layer that covered the area. Graphs showing the results of the laboratory and in-situ reflectance measurements of gypsum and the in-situ measurements of the snow are shown in Figures 5-8. Note that the non-lambertian reflectance properties of our $BaSO_4$ reference panel have not yet been determined and are thus not accounted for here.

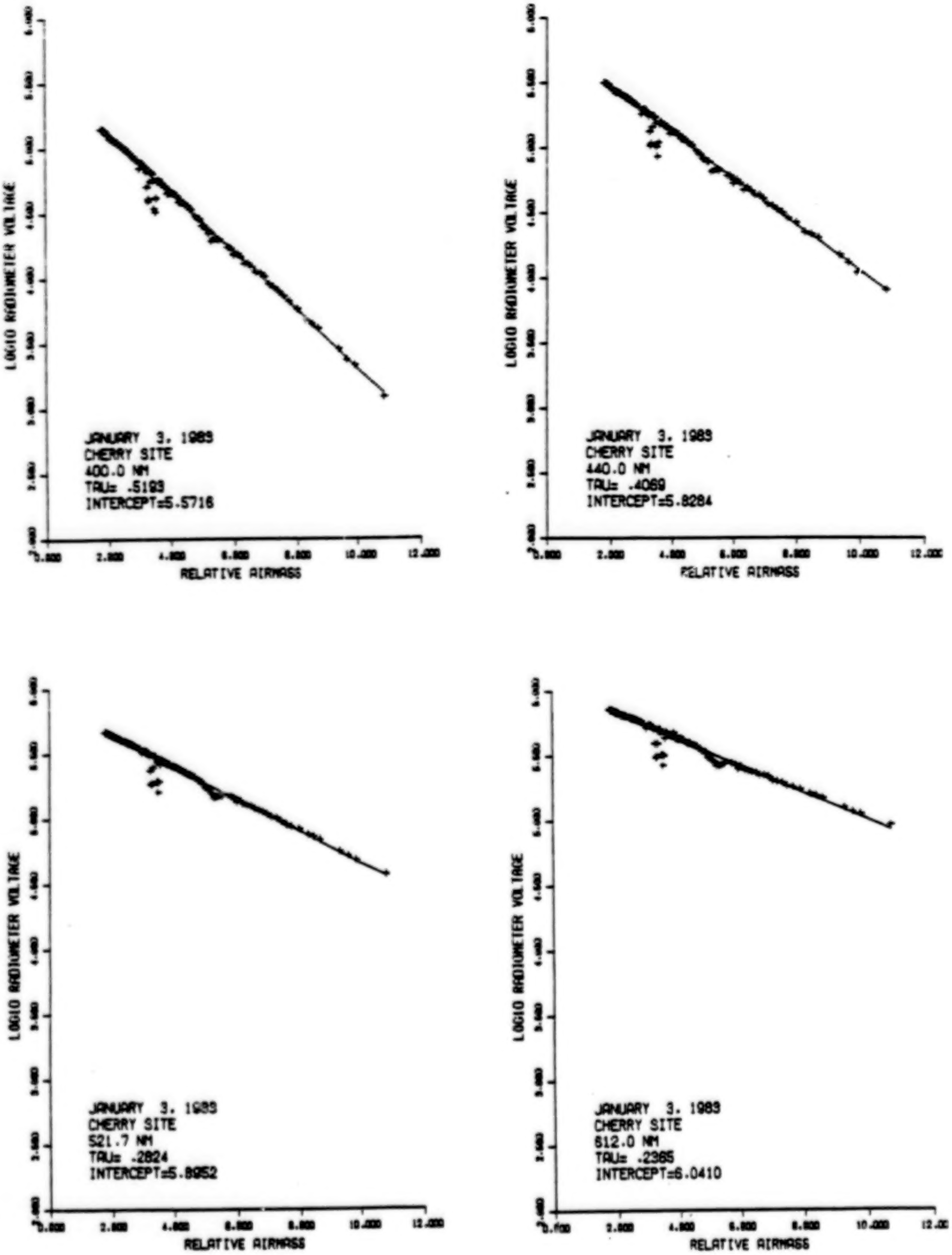

Figure 1. Langley plots for 400, 440, 521.7 and 612 nm.

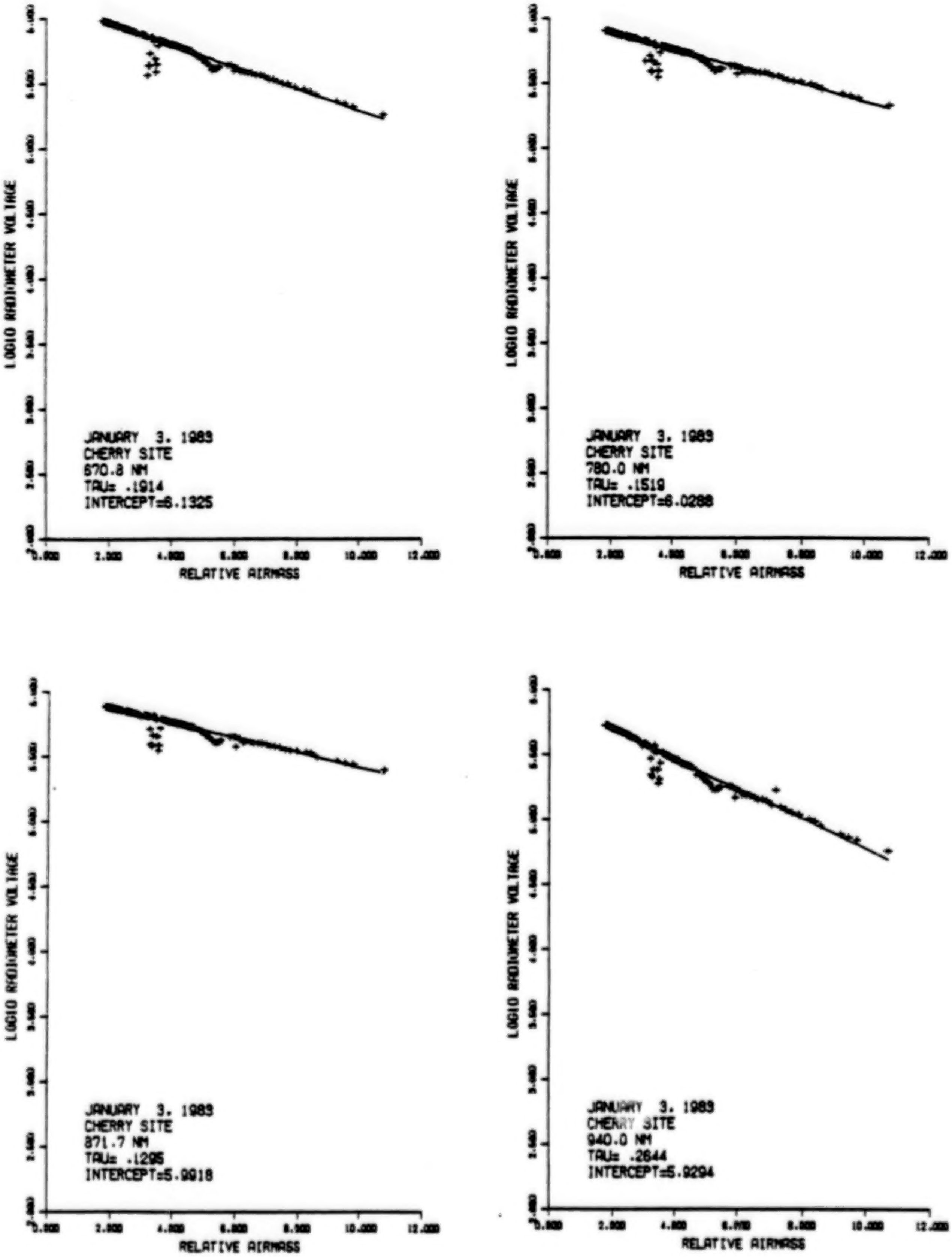

Figure 2. Langley plots for 670.8, 780, 871.7 and 940 nm.

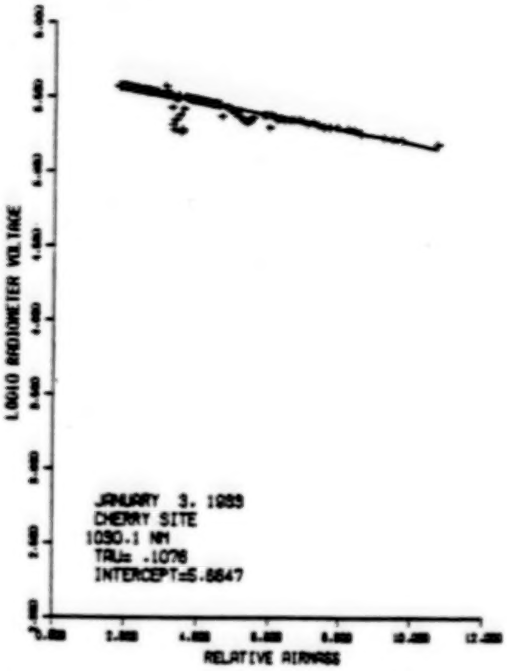

Figure 3. Langley plot for 1030.1 nm.

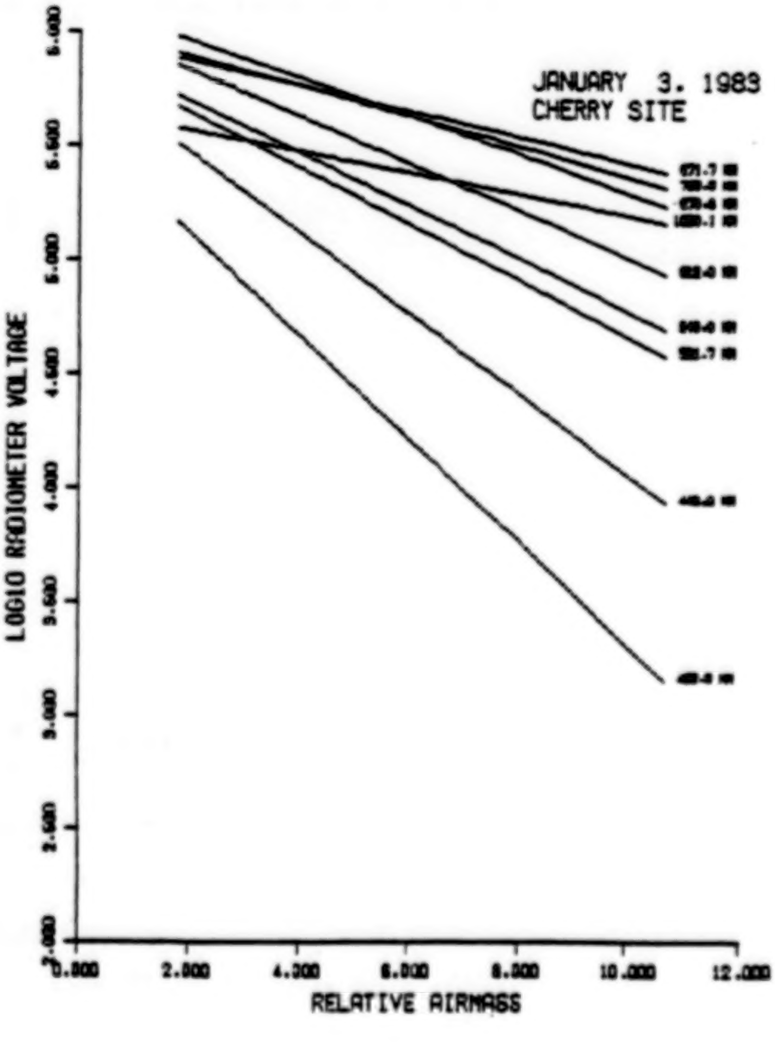

Figure 4. Langley plots for all solar radiometer wavelengths.

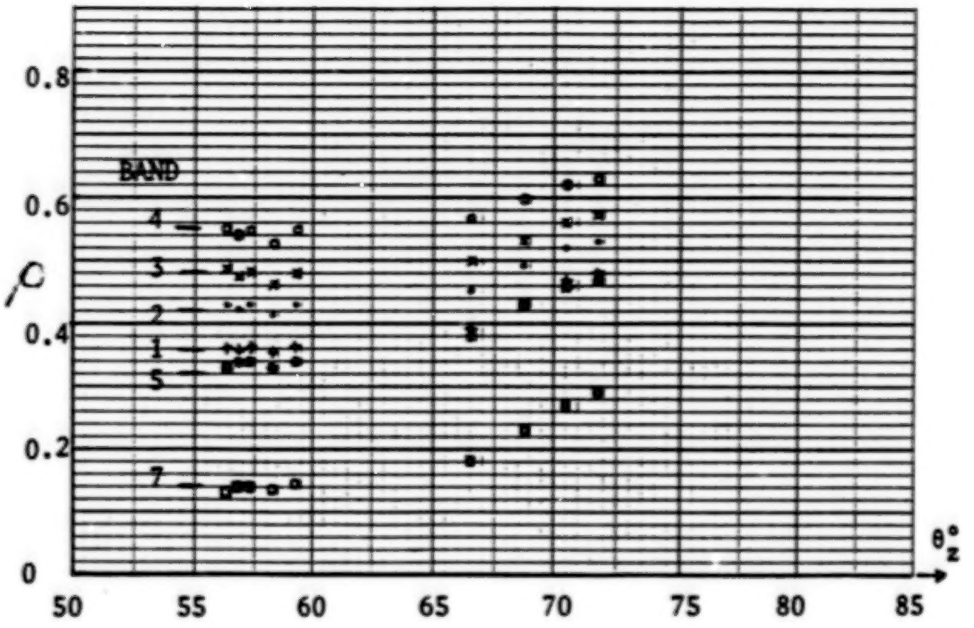

Figure 5. Measurements of TM band reflectances for gypsum at the Cherry site, versus solar zenith angle θ_z, December 16, 1982.

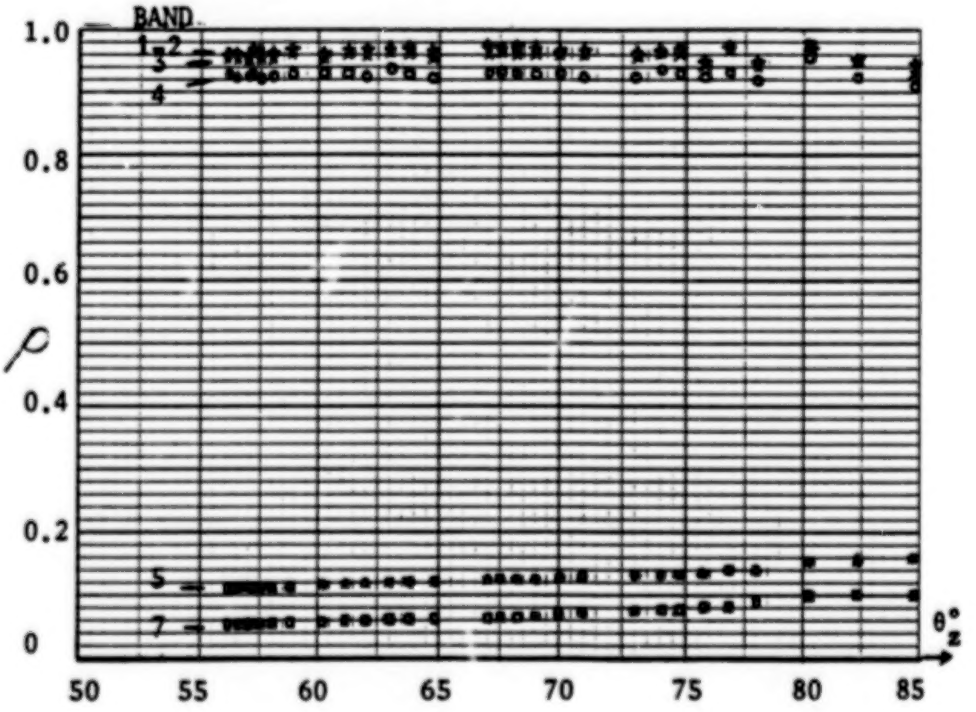

Figure 6. Measurements of TM band reflectances for snow at the Cherry site, versus solar zenith angle θ_z, January 3, 1983.

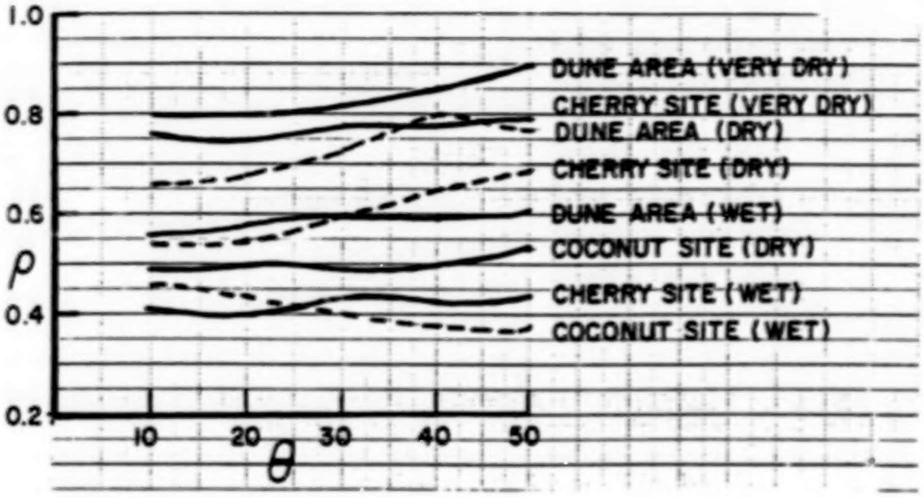

Figure 7. Laboratory reflectance data at 750 nm as a function of observation angle θ, source vertical.

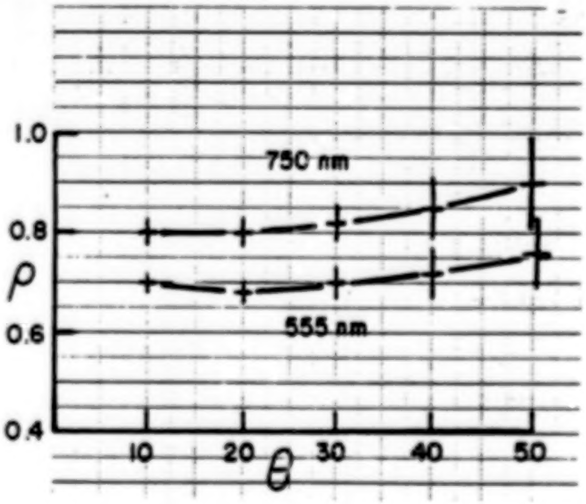

Figure 8. Laboratory reflectance data of dune gypsum as a function of observation angle θ, for 750 nm and 555 nm, source vertical.

It is interesting to note that a wide variety of reflectances can be encountered depending on the dampness of the gypsum. Contrary to our initial assumption, the extensive alkali flat region of gypsum at White Sands is damp for long periods of the year, because the water table is close to the surface. This will enable us to calibrate sensors over a longer period of the year than we had anticipated, before the detectors become saturated.

The in-situ measurements of the variation of gypsum reflectance with solar zenith angle in Figure 5 show an increase with high zenith angles. We believe the increase is due mainly to a light layer of frost on the damp gypsum that gradually melted during the morning.

The reflectance data for snow shown in Figure 6 are interesting because they indicate that the snow has exactly the same non-lambertian reflectance properties as $BaSO_4$.

The next important steps in our measurement program are to accurately check the reflectance and determine the non-lambertian reflectance characteristics of the $BaSO_4$ panel used at White Sands. When we receive the CCT-BT from Goddard Space Flight Center for the 3 January 1983 overflight of White Sands, we will then be in a position to run an atmospheric radiative transfer calculation to determine the relation between digital counts and entrance pupil radiance for the visible, near and short wave infrared bands of the Thematic Mapper.

MODEL CALCULATIONS TO DETERMINE TM SATURATION CONDITIONS AT WHITE SANDS

Considerable effort has been spent on familiarization with available atmospheric radiative transfer computer codes. In particular we have worked with the Turner code and a version of the Herman code that does not account for polarization. (Work on the polarization version is about to begin.) One useful output of these studies, described briefly in the following, has been concerned with predicting the reflectance threshold conditions at White Sands below which the TM and MSS bands will not be saturated.

In order to minimize computer expense, the effective center wavelength of each TM band was determined using one of the methods described by Stair.(2) In this method the system spectral response is weighted by the source spectral distribution before the effective center wavelength is determined. In the case shown in Figure 9, Labs and Neckel exo-atmospheric solar irradiance data were used at 1 nm intervals through the TM band 2 response.

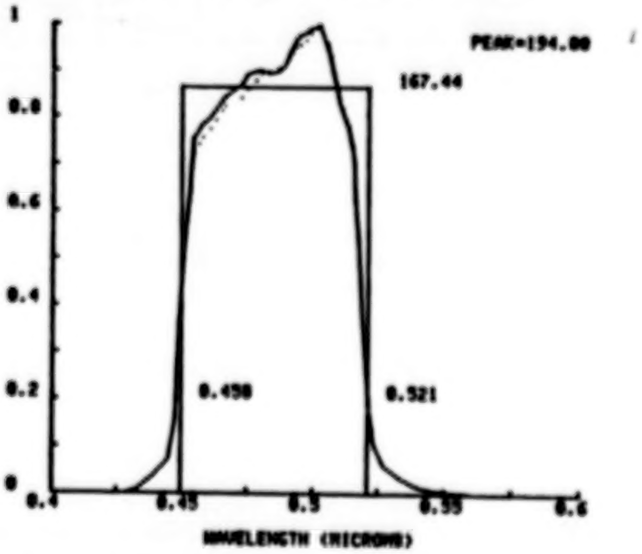

Figure 9. The equivalent passband (rectangular profile) to the TM band 1 spectral response. The dotted line is the profile after multiplying by the Labs and Neckel data.

Using the central wavelength and the peak response determined from this technique, the Herman code was used to calculate the radiance at the sensor for the first four TM bands as a function of solar zenith angle for lambertian ground reflectances of 0, 0.1, 0.25, 0.5 and 1.0. To give the reader an appreciation for the change in radiance with atmospheric condition, each graph shows the radiance for 100 km visibility (full line) and, in Figures 10, 12 and 13 the radiance for a Rayleigh atmosphere (dashed line). In Figure 11 the radiance is shown for an atmosphere with 100 km visibility, with and without the presence of ozone. Also marked on the graphs, as a horizontal dotted line, is the minimum saturation level for each band as stated by Barker(3).

We have marked on the graphs the measured reflectances of dry and damp gypsum in the various bands. However, we need to stress again that these reflectances are not corrected for the non-lambertian reflectance of our $BaSO_4$ reference panel. Any correction will lower these reflectances, and we might anticipate that values for solar zenith angles approaching 65° might have to be decreased by as much as 20% with respect to unity reflectance.

ACKNOWLEDGEMENTS

We wish to acknowledge the financial support provided by contract NAS5-27382, J. L. Barker, NASA/Goddard Space Flight Center, Project Scientist. We wish to thank B. M. Herman for the use of his radiative transfer code and J. A. Reagan for the use of a solar radiometer and both for useful discussions. In addition we wish to acknowledge the following organizations who are supporting or who plan to cooperate with our measurement program at White Sands: Atmospheric Sciences Laboratory, Canadian Center for Remote Sensing, NASA/Ames Research Center, NASA/Johnson Space Center, Purdue University, and U.S. Department of Agriculture.

REFERENCES

1) Kastner, C. J. and P. N. Slater (1982) "In-flight radiometric calibration of advanced remote sensing systems," SPIE Meeting San Diego. Conference 356.

2) Stair, R. (1953). Filter Radiometry and some of its Applications, J. Opt. Soc. Amer. 43, 971.

3) Barker, J. L. (1983). TM Sensor Radiometry, This Symposium.

4) Herman, B. M and S. R. Browning (1975). The effect of aerosols on the earth-atmosphere albedo, J. Atmos. Sci 32, 1430.

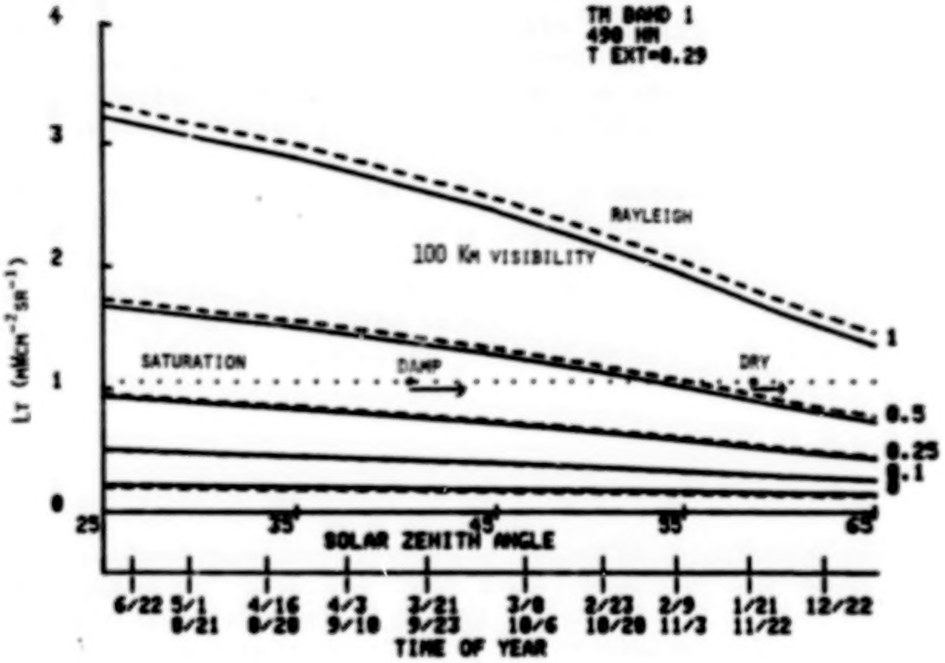

Figure 10. Atmospheric model data predicting that to the right of the dry and damp gypsum points on the dotted line TM band 1 will not be saturated at WSMR.

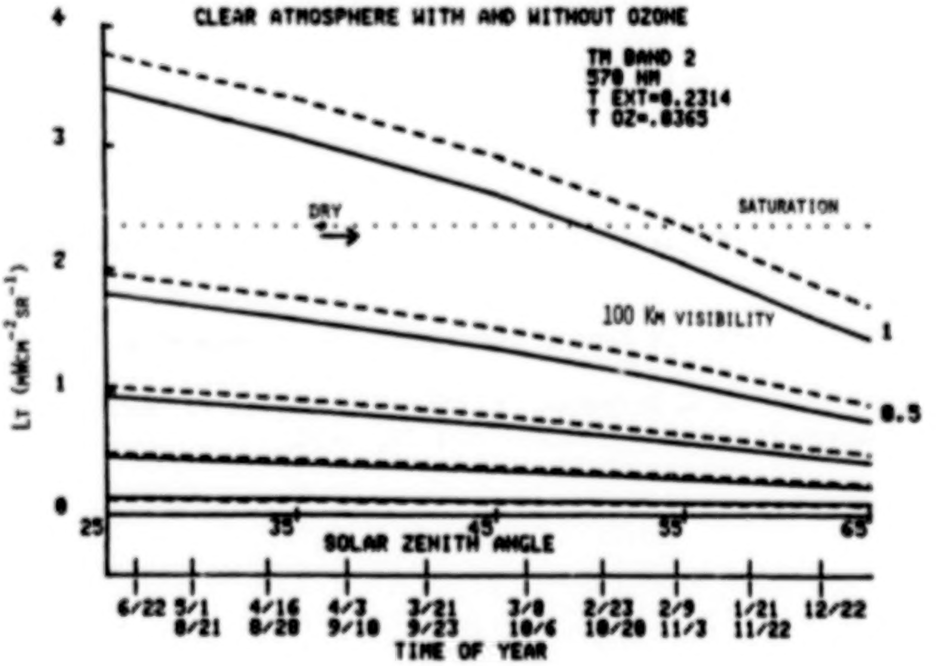

Figure 11. Atmospheric model data predicting that to the right of the dry gypsum point on the dotted line TM band 2 will not be saturated at WSMR. At no time of the year will damp gypsum cause saturation.

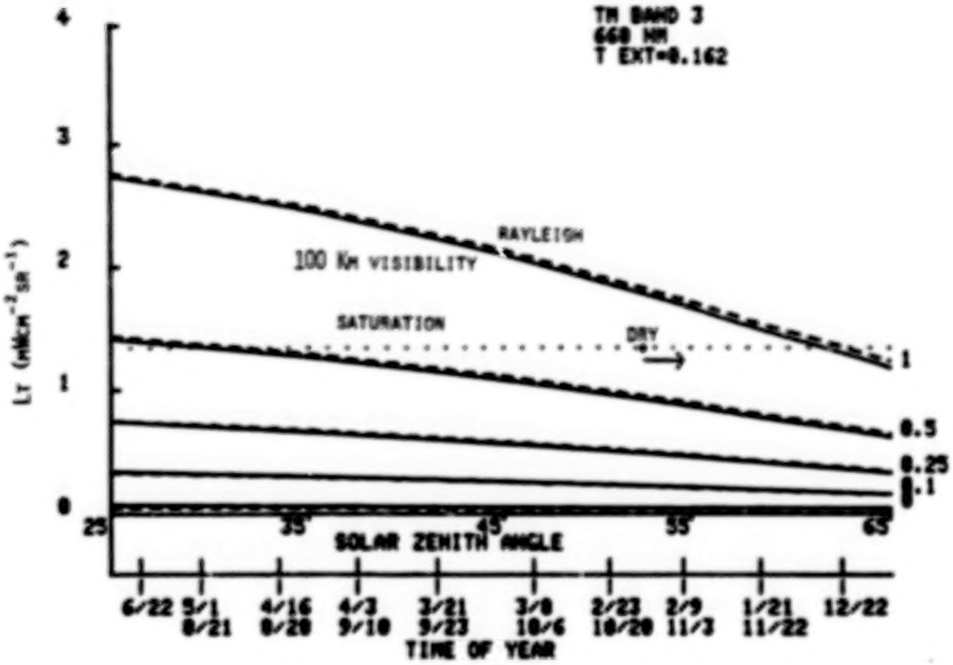

Figure 12. Atmospheric model data predicting that to the right of the dry gypsum point on the dotted line TM band 3 will not be saturated at WSMR. At no time of the year will damp gypsum cause saturation.

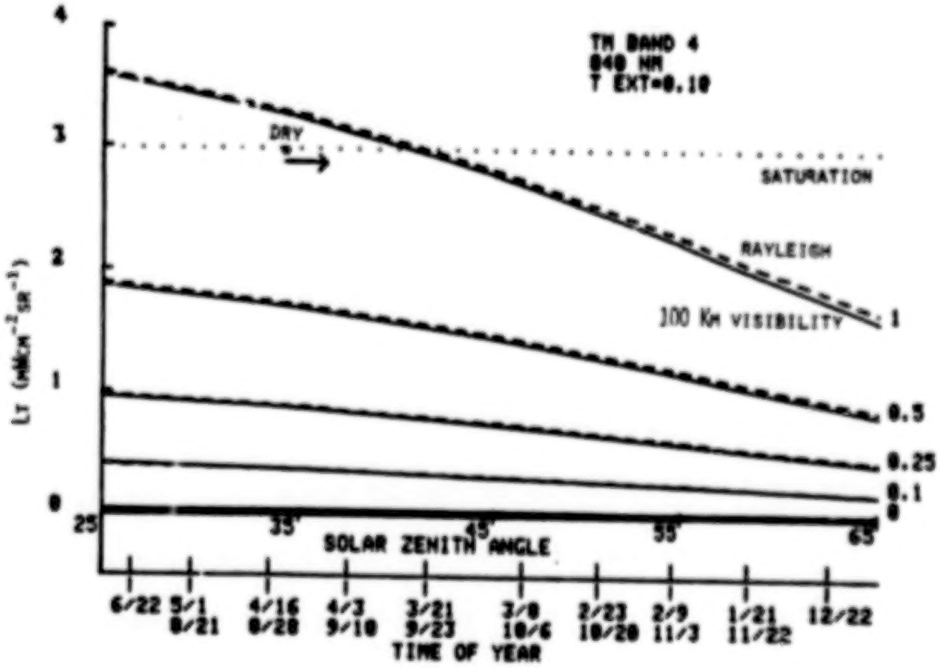

Figure 13. Atmospheric model data predicting that to the right of the dry gypsum point on the dotted line TM band 4 will not be saturated at WSMR. At no time of the year will damp gypsum cause saturation.

APPENDIX (AUGUST, 1983)

This appendix briefly presents the results obtained for the absolute calibration of TM bands 2, 3, and 4. The results are based on TM image data collected simultaneously with ground and atmospheric data at White Sands, New Mexico on January 3, 1983.

On that day, an 80 mm layer of snow covered our site. We determined the reflectance of the snow by using a Barnes radiometer with a $BaSO_4$ plate as a reference. Subsequent calibration of the plate allowed us to correct for its non-lambertian characteristics when solar-irradiated at a 60° zenith angle. These results are listed in Table 1.

Table 1. Snow reflectance values.

Band	Measured values	Reflectance of $BaSO_4$	Corrected values
1	0.961 ± 0.015	0.80 ± 0.017	0.769 ± 0.023
2	0.963 ± 0.014	0.79 ± 0.017	0.761 ± 0.023
3	0.957 ± 0.013	0.79 ± 0.017	0.756 ± 0.023
4	0.927 ± 0.011	0.79 ± 0.017	0.732 ± 0.022

Rayleigh spectral optical depths (τ_{Ray}) were determined for the effective center wavelengths of the TM bands (λ_c) from knowing that the barometric pressure was 889.5 mB. A solar radiometer using nine 10-nm bands in the visible and near ir was used to determine the total spectral optical depths, τ_T, at these 9 wavelengths. From these data the Mie and ozone optical depths (τ_{Mie} and τ_{oz}) were determined.

In bands 1, 2, and 3, the component of τ_T due to molecular absorption, τ_{abs}, is entirely due to ozone. Water vapor and CO_2 are present in addition to ozone in band 4. Their effects have been included in Table 2 which lists the values of the various atmospheric constituents in bands 1 through 4.

Table 2. Atmospheric values.

Band	λ_c(µm)	τ_T	τ_{Mie}	τ_{Ray}	τ_{abs}
1	0.485	0.2913	0.1475	0.1424	0.0014
2	0.57	0.2177	0.1382	0.0736	0.0059
3	0.66	0.1718	0.1282	0.0406	0.0030
4	0.84	0.1344	0.1099	0.0153	0.0092

Using the data in Table 2 as input to the radiative transfer code developed by B. M. Herman, the following quantities were calculated:

$E_{D,Dir}$: the direct solar irradiance at the ground = $\cos\theta_z \exp(-\tau_T \sec\theta_z)$

$E_{D,Dif}$: the diffuse solar irradiance at the ground

L_{Dir}: the direct radiance at the TM due to $E_{D,Dir} + E_{D,Dif}$

L_p: the path radiance at the TM = $L_T - (E_{D,Dir} + E_{D,Dif}) \frac{\rho}{\pi} \exp(-\tau_T \sec 5°)$

L_T: the total radiance at the TM

Table 3. Irradiances and radiances (normalized to unity solar exoatmospheric irradiance).

Band	Solar Zenith Angle	$E_{D,Dir}$	$E_{D,Dif}$	L_{Dir}	L_P	L_T
1	55°	0.345	0.185	0.097	0.033	0.1301
	65°	0.212	0.152	0.067	0.025	0.092
2	55°	0.392	0.145	0.105	0.024	0.129
	65°	0.253	0.122	0.043	0.019	0.092
3	55°	0.425	0.122	0.111	0.019	0.130
	65°	0.282	0.104	0.078	0.015	0.093
4	55°	0.454	0.095	0.112	0.014	0.126
	65°	0.308	0.082	0.079	0.011	0.090

Using the equivalent passband technique of Palmer and Tomasko[1] and the exoatmospheric solar spectral irradiance values of Labs and Neckel,[2] the values for the exoatmospheric irradiances within the TM passbands (ExΔλ), were calculated for the earth-sun distance on January 3. The required values of L_T for the solar zenith angle of 60° were found by interpolating between the 55° and 65° data from Table 3. These, when multiplied by their corresponding ExΔλ values, gave the radiances in mW/cm^2-sr in the TM passbands listed in Table 4.

Table 4. Exoatmospheric irradiances and the radiances at the TM in the TM passbands.

Band	Equivalent bandwidth in µm	$E_x\Delta\lambda$ mW/cm^2	L_T mW/cm^2-sr
1	0.0712	12.2	1.36
2	0.0884	13.8	1.52
3	0.0773	10.7	1.19
4	0.1345	13.7	1.47

By identifying our site on the CCT-B image, we determined which detectors scanned the area and how many samples each collected. Detectors 1, 2, 3, 15 and 16 collected 5, 3, 1, 2, and 4 samples respectively. We found the average digital count for each detector, then calculated the average detector spectral radiance using offset and gain values reported by Barker et al.[1] These spectral radiances were multiplied by the number of samples for each detector. The resultant products were added and then divided by the total number of samples, 15. Thus we derived a value for the average spectral radiance of our site as measured by the TM, proportionally weighted according to the number of samples per detector.

The final step in the calculation was to multiply the average spectral radiance at the TM by the equivalent passband to determine the radiance within each TM band (Table 4). These values are compared in Tables 5, 6 and 7.

Table 5. Calculation of radiance in TM band 2 from preflight calibration data[3] and comparison with inflight White Sands data.

Detector	Average Count	Average Spectral Radiance	Gain	Offset
3	139.0	17.04	8.014	2.41
2	143.7	17.42	8.117	2.33
1	146.2	17.52	8.174	2.99
16	141.5	17.43	7.979	2.43
15	147.5	17.71	8.195	2.83

Weighted average = 17.47 mW cm^{-2} sr^{-1} μm^{-1}
Equivalent band radiance from weighted average = 1.537 mW cm^{-2} sr^{-1}
Equivalent band radiance from Table 4 = 1.52 mW cm^{-2} sr^{-1}
Agreement = -1.0% AND +2.5% with reference to preflight calibration and December 8, 1982 inflight data[4] respectively.

Table 6. Calculation of radiance in TM band 3 from preflight calibration data[3] and comparison with inflight White Sands data.

Detector	Average Count	Average Spectral Radiance	Gain	Offset
3	165.0	15.40	10.590	1.89
2	169.7	15.86	10.602	1.57
1	171.6	15.73	10.777	2.13
16	167.8	15.85	10.484	1.63
15	172.5	15.88	10.769	1.53

Weighted average = 15.78 mW cm^{-2} sr^{-1} μm^{-1}
Equivalent band radiance from weighted average = 1.215 mW cm^{-2} sr^{-1}
Equivalent band radiance from Table 4 = 1.19 mW cm^{-2} sr^{-1}
Agreement = -1.8% and 3.0% with reference to preflight and December 8, 1982 inflight data[4] respectively.

Table 7. Calculation of radiance in TM band 4 from preflight calibration data[3] and comparison with inflight White Sands data.

Detector	Average Count	Average Spectral Radiance	Gain	Offset
3	133.0	11.89	11.019	1.96
2	132.0	12.02	10.817	1.94
1	134.2	12.00	10.972	2.53
16	132.0	12.01	10.828	2.00
15	131.5	12.05	10.771	1.69

Weighted average = 12.01 $mWcm^{-2}$ sr^{-1} μm^{-1}
Equivalent band radiance from weighted average = 1.609 $mWcm^{-2}$ sr^{-1}
Equivalent band radiance from Table 4 = 1.47 $mWcm^{-2}$ sr^{-1}
Agreement = -8.5% and -5.6% with reference to preflight and December 8, 1982 inflight data[4] respectively.

Comments

The experimental results presented in this appendix represent our only opportunity so far to conduct an inflight absolute calibration of the TM. The main purpose of the January 3, 1983 experiment, however, was to familiarize ourselves with the scientific and logistic problems involved and to gain some field experience to guide us in the design and development of improved measurement techniques and field equipment. It is encouraging that we were able, two months into the contract, using quickly assembled equipment and little prior experience, to obtain results for bands 2, 3, and 4 that fall between 1% and 8.5% of the NASA/SBRC values.

Other comments are briefly as follows:

1. The estimated uncertainty for our results of January 3, 1983 is ±5%. The estimated uncertainty for the preflight absolute calibration of the TM is ±6%.
2. Because of the limitations of the instruments used on January 3, τ_{abs} in band 4 due to water vapor and CO_2 could not be measured. Instead, the LOWTRAN code was used to compute the water vapor and CO_2 transmittances across band 4 at 5 cm^{-1} intervals. The water vapor transmittance was scaled, to account for the 44% relative humidity measured at White Sands on January 3, then averaged to find $\tau_{H_2O+CO_2}$. Finally, the measured value of $\tau_{oz} = 0.0003$ was added to provide τ_{abs}. The effect of an error in this estimate can be judged by noting

that the inclusion of water vapor and CO_2 lowered the predicted radiance level at the TM by only 2%.

3. Band 1 saturated over the snow field at White Sands. NASA'S data indicate that a saturation level of 255 counts corresponds to a radiance at the sensor of 1.14 $mWcm^{-2}sr^{-1}$ in TM band 1. Our estimate is that the snowfield provided a radiance level of 1.36 $mWcm^{-2}sr^{-1}$ at the sensor.
4. We made no attempt to collect atmospheric data for calibrating band 6.
5. The field equipment used on January 3, 1983 is incapable of measuring solar irradiance in bands 5 and 7. Even if the appropriate data had been available, the low snow reflectance of about 0.09 and 0.04 in bands 5 and 7 respectively would have adversely affected the calibration accuracy. Fortunately, White Sands, New Mexico is not often snow covered and the gypsum surface has a reflectance between 3 and 5 times the reflectance of snow in these bands, depending on whether the gypsum is damp or dry.
6. In reducing our data, we initially incorrectly assumed that published data for TM saturation levels were derived by integrating the spectral responses of the bands. This incorrect assumption can lead to errors as large as 20%. In Table 8 we list the weighted central wavelengths of the first four TM bands, their nominal halfwidths (as commonly reported in the literature), the accurate halfwidths (1/2 power points

from Santa Barbara Research Center transmittance data), equivalent halfwidth (used here), and normalized filter response, unweighted by solar irradiance data.

Table 8. Bandwidths for the first four TM bands.

TM Band	Weighted Central λ_c µm	Nominal Halfwidth	Accurate Halfwidth	Equivalent Halfwidth	Normalized Response
1	0.4855	0.07	0.066	0.0712	0.8473
2	0.5706	0.08	0.081	0.0884	0.8305
3	0.6587	0.06	0.069	0.0773	0.8669
4	0.8361	0.14	0.129	0.1345	0.9305

7. The January 3, 1983 experiment gave us several ideas on how to improve our measurement techniques. For example, we have since designed and built a cart for moving either the Barnes spectroradiometer or a new instrument under development, over the reference site. Together with the acquisition of low altitude imagery, this will allow us to make more accurate reflectance maps of the site. We have designed and built a new dual-radiometer system for accurately determining the non-lambertian characteristics of our reference reflectance panels. Finally, we have started the construction of two spectropolarimeters that will be accurately calibrated in an absolute sense using self-calibrated detectors. These spectropolarimeters will be used for more accurately measuring ground reflectances and atmospheric characteristics. They will

also be used to check the results of the radiative transfer program at ground and aircraft altitudes.

With these improvements, we hope to achieve our goal of an uncertainty of inflight absolute radiometric calibration of less than ±3%.

REFERENCES

1. Palmer, J. M. and M. G. Tomasko, "Broadband radiometry with spectrally selective detectors." Optics Letters, 5, pp. 208-210 (1980).
2. Neckel, H. and D. Labs, "Improved data of solar spectral irradiance from 0.33 to 1.25 μm." Solar Phys. 74, 231 (1981).
3. Barker, J. L., D. L. Ball, K. C. Leung, and J. A. Walker, "Prelaunch absolute radiometric calibration of the reflective bands on the Landsat-4 protoflight thematic mapper." These symposium proceedings.
4. Barker, J. L., R. B. Abrams, D. L. Ball, and K. C. Leung, "Characterization of Radiometric Calibration of Landsat-4 TM reflective bands." These symposium proceedings.

N85-21734

D7

D10

LANDSAT-4 THEMATIC MAPPER CALIBRATION AND ATMOSPHERIC CORRECTION

Warren A. Hovis
NOAA/National Environmental Satellite,
Data, and Information Service

The Landsat-4 Thematic Mapper, with its wide spectral coverage and digitization to 8 bits per word, is a large step forward in the direction of quantitative radiometry from the Multi Spectral Scanner (MSS). In order to utilize the quantitative accuracy built into the Thematic Mapper effectively, more attention must be paid to calibration before launch, changes of calibration with time in orbit, and atmospheric interference with the measurements, especially in the 450 to 520 nanometer band. All of these factors are important if we are to determine the upwelled radiance that would be measured at the surface. Recent experience with the Coastal Zone Color Scanner (CZCS) program has led to procedures wherein Rayleigh correction factors can be generated utilizing simultaneous surface truth data that empirically give correct upwelled surface radiances, despite errors in sensor calibration, solar spectral irradiance measurements, and reported values of Rayleigh optical depth. These techniques offer sensitive tests for change in calibration, especially at shorter wavelengths. Instruments, such as the CZCS, have shown that calibration changes first, and to the largest degree, at the shorter wavelengths, with lesser changes as wavelength increases. These techniques are utilized to calculate a Rayleigh correction factor that, together with geometric terms, will give an accurate correction for this portion of the atmospheric contribution to the signal. Long term observation of the Rayleigh corrected radiance over clear water will be a sensitive indicator of any change in calibration as the sensor ages in orbit.

INTRODUCTION

The increased radiometric quality of the Thematic Mapper over the Multi Spectral Scanner (MSS) offers a number of opportunities for more accurate research to be carried out. The extension of the spectral range into the blue and the near infrared, and the increase in digital accuracy by increasing the bits per word to eight from the six found in the MSS, make the Thematic Mapper more of a true radiometer than the MSS. To utilize the Thematic Mapper as a radiometer for quantitative measurements, a number of factors that were not nearly so important in the MSS data, must now be considered.

First is the calibration of the sensor prior to launch, and during flight. The prelaunch calibration, utilizing an internally illuminated integrating sphere, is not considered to be accurate to any better than ±5% because of errors inherent in transferring calibration from a National Bureau of Standard's (NBS) irradiance source to a large aperture internally illuminated sphere, providing the diffuse source for calibration. In addition to the errors in prelaunch calibration, because of the lack of an accurate source of diffuse radiation, another problem will be degradation of the sensor in orbit as observed on many past instruments: Although the Thematic Mapper contains an internal calibration source, that source does not illuminate the large optics of the scan mirror, primary mirror, and secondary mirror that are most exposed to the spacecraft atmosphere, and are most likely to degrade during flight. The CZCS on Nimbus-7, with a similar inflight calibration system, has shown a degradation of approximately 25% in the band at 443 nanometers, yet the internal calibration source shows no loss of sensitivity of the detector-amplifier system. The loss of sensitivity in the CZCS was noticed when the Rayleigh correction factors, utilized shortly after launch, began to produce much lower radiance values than would be expected after approximately nine months in orbit. The system was developed to monitor the calibration of the CZCS with time. It has proven to be quite effective and can be utilized to monitor the performance of the Thematic Mapper.

With the increased radiometric accuracy and the extension of the spectral range into the blue, atmospheric interference becomes a more important factor in carrying out absolute radiometry. In theory, the Rayleigh component of the atmosphere can be calculated if the solar spectral irradiance, Rayleigh optical depth, and ozone transmission are known, as well as the phase angle and solar zenith angle for the observation. Using what were thought to be the best values for the parameters of solar spectral irradiance, Rayleigh optical depth, and ozone transmission, and accurately determined geometric factors, the Rayleigh correction, when first applied to the CZCS instrument, resulted in negative radiances calculated over the ocean. Obviously, the errors in the reported values of the solar spectral irradiance, Rayleigh optical depth, ozone transmission, and the calibration of the instrument, had combined to produce an erroneous result. In order to produce correct radiances that would be observed at the surface, simultaneous measurements were carried out by ships with satellite overpass, and a product of factors was developed that, together with the geometric terms of phase angle and solar zenith angle, produce a Rayleigh correction that gives correct answers for upwelled radiance as measured at the surface. The same scheme that worked with the CZCS will be applied to the Thematic Mapper, and factors provided, so that accurate correction can be made for the Rayleigh contribution to the total signal.

RAYLEIGH BACKSCATTER CORRECTION

One of the problems inherent in the correction of the CZCS data for atmospheric attenuation was the lack of agreement among the various reported measurements of solar spectral irradiance throughout the visible and the near infrared. This problem is illustrated in Fig. 1 where the results of Johnson, Labs and Neckel, and the NASA standard are shown. Johnson's reported values are higher than those of Labs and Neckel and the NASA standard at virtually every wavelength. Those of Labs and Neckel are higher beyond approximately 490 nanometers than the NASA standard, and the NASA standard is higher at wavelengths less than 490 nanometers. For the CZCS program, the results of Labs and Neckel were chosen, but since all of the parameters were adjusted to give the correct value that would be measured at the surface, there is no guarantee that they are, indeed, the most correct result.

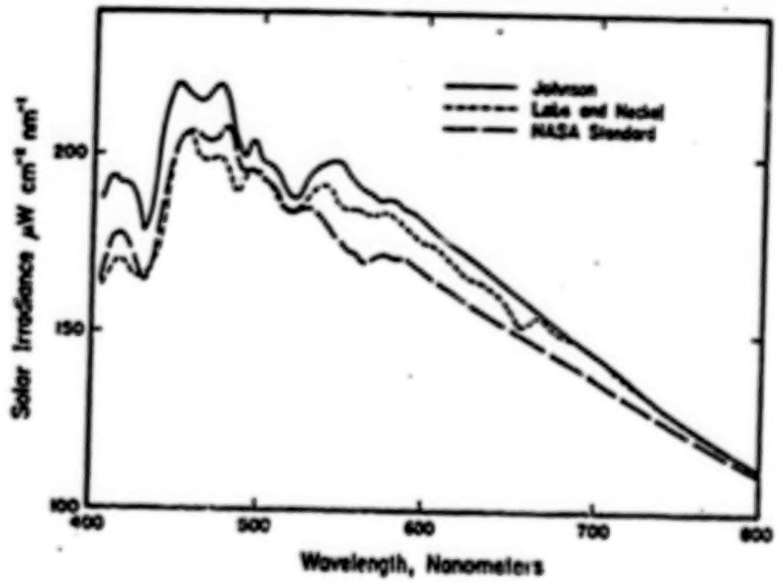

Fig. 1 Solar Spectral Irradiance

The Rayleigh optical depth for Air Mass one has been reported by a number of investigators, most recently from Frohlich and Shaw (Ref. 1), and is shown in Fig. 2. The steep change of the Rayleigh optical depth with the $(1/\lambda)^4$, presents some problem with the width of the spectral bands for the Thematic Mapper, and the fact that the bands are not rectangular or symmetric in shape. The system that will be reported here for determining the Rayleigh correction factors ignores this steep change of the Rayleigh optical depth and integrates the expected upwelled radiance of the ocean at the surface over the spectral response of the Thematic Mapper instrument bands 1 and 2. Although the Rayleigh optical depth itself is a smooth function, the solar spectral irradiance is not, and is illustrated in Fig. 3 where a calculated Rayleigh irradiance is shown utilizing the parameters that were developed for the CZCS. The letters "G.F." in Fig. 3, followed by (0.13), indicate that the geometric factors calculated for reasonable ranges of sun elevation angle and view angle from the scanner should come out to approximately 0.13. Typically, they range from 0.12 to 0.14. If the product of the geometric factors does not fall in this range, an error has been made in the calculation.

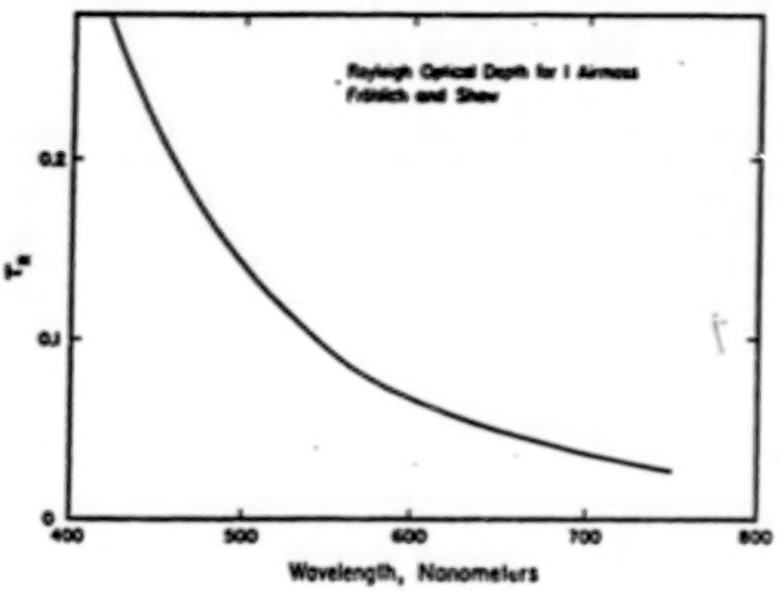

Fig. 2 Rayleigh Optical Depth

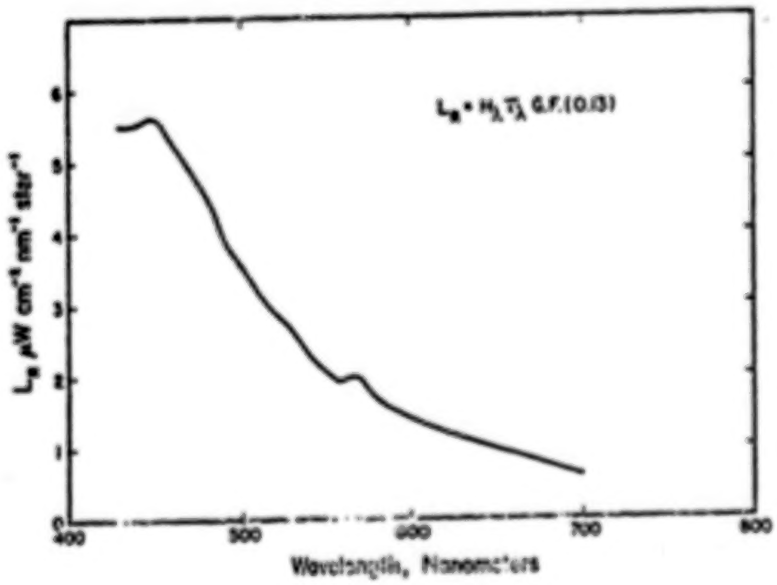

Fig. 3 Calculated Rayleigh Radiance

An illustration of the effect that Rayleigh backscatter alone will have on the measurements is shown in Fig. 4, wherein radiance scattered from the Pawnee Grasslands of the United States, as measured by a spectrometer on an aircraft, is summed with the calculated Rayleigh backscatter for its solar elevation angle of approximately 30 degrees. One can see that, especially in band 1 of the Thematic Mapper, even over this area consisting of soil with sparse grass coverage, the Rayleigh contribution is a considerable portion of the total signal measured with the contribution

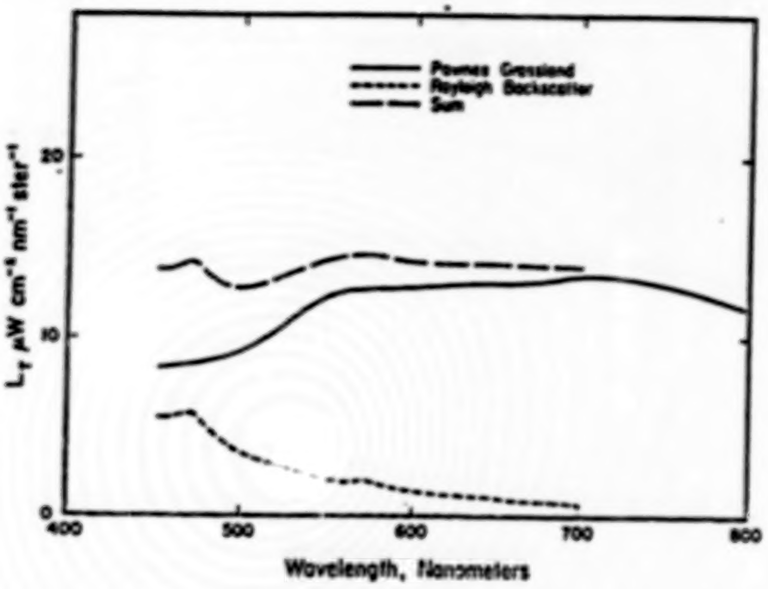

Fig. 4 Measured Radiance from Pawnee Grassland with Rayleigh Atmosphere Contribution

decreasing until approximately 700 nanometers where the Rayleigh contribution becomes negligible. It is obvious that if any attempt is made to analyze the surface content by either forming a spectrum, or taking ratios utilizing the two shorter wavelength bands of the Thematic Mapper, the atmospheric contribution must be considered in some way.

CALCULATION OF RAYLEIGH CORRECTION FACTORS

In order to calculate the Rayleigh correction factors for the Thematic Mapper, a scene was utilized where the Gulf Stream between the Keys in Florida was viewed on August 30, 1982, with a solar zenith angle at the center of the picture of 34 degrees, and a solar azimuth of 110 degrees. Utilizing data measured by ships in the CZCS program, the upwelled radiance was calculated for clear water in the first two bands of the Thematic Mapper. In band 1, the normalized radiance integrated under the Thematic Mapper response was 1.0 mW/(cm^2 µm ster), and this radiance was, in turn, adjusted for the solar elevation angle. Fig. 5 shows the response of the band 1 of the Thematic Mapper, together with the upwelled radiance that would be measured over clear water at the solar elevation angle of the scene. In the resultant calculation as follows, one finds that the phase angle for the area viewed with the clearest water was [illegible]1 degrees, and that after subtraction of the upwelled water radiance, the total atmospheric contribution was 4.2 mW/(cm^2 µm ster).

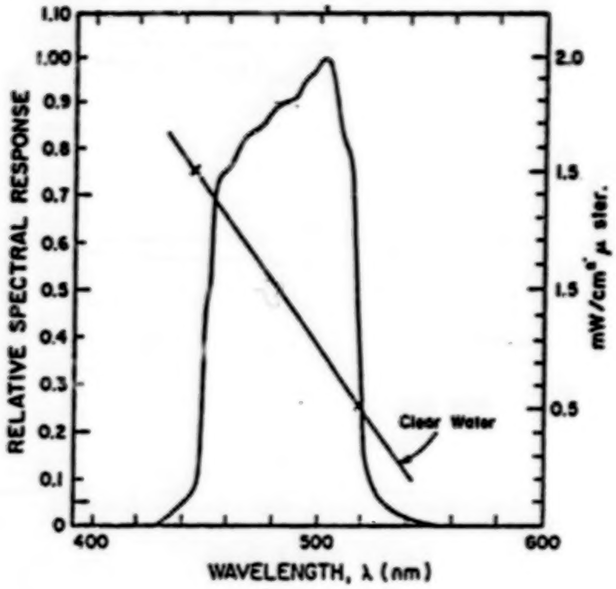

Fig. 5 Thematic Mapper Band 1 Response
with Clear Water Radiance

Rayleigh Correction--TM Band 1, Gulf Stream, August 30, 1982.

Solar Elevation = 56^o Solar Zenith (θ) = 34^o Solar Azimuth = 110^o
Phase Angle $\gamma = 31^o$ Normalized $L_{water} = 1.0$ mW/cm^2 µm ster
$L_w(SZ\ 34^o) = 0.83$ mW/cm^2 µm ster

$$L_{Total} = \frac{82 - 2.58}{15.784} = 5.03 \text{ mW/cm}^2 \text{ µm ster.} \quad (1)$$

$$L_{Rayleigh} = L_T - L_w = 5.03 - 0.83 = 4.20 \text{ mW/cm}^2 \text{ m ster.} \quad (2)$$

$$L_{Rayleigh} = \frac{1}{4\pi} (H_\lambda\ \tau_{R\lambda}\ T_{O_3}) \frac{3(1 + \cos^2\gamma}{4 \cos\theta}$$

$$= H_\lambda\ \tau_{R\lambda}\ T_{O_3} \times 5.97 \times 10^{-2} (1 + \cos^2\gamma)/\cos\theta$$

$$= H_\lambda\ \tau_{R\lambda}\ T_{O_3} \times 0.135 = 4.20 \text{ mW/cm}^2 \text{ µm ster.} \quad (3)$$

Therefore,

$$H_\lambda\ \tau_{R\lambda}\ T_{O_3} = 31.1 \text{ for subtropical summer.} \quad (4)$$

It should be emphasized here that the technique developed for the CZCS for removal of the aerosol contribution to the atmosphere is not applicable to the Thematic Mapper because of the lack of sensitivity in the near infrared. For this reason, a number of Rayleigh correction factors will have to be calculated before a final one can be determined over the clearest scene possible. Nevertheless, a preliminary factor of the product of the solar spectral irradiance, the Rayleigh optical depth and the ozone transmission is calculated as equal to 31.1 for the subtropical summer condition of the scene investigated. This factor, multiplied by the geometric terms, should give a good approximation of the Rayleigh contribution to the signal for the conditions of a subtropical summer. It should be mentioned that it has been assumed that the gain and offset given in the Goddard Prelaunch Calibration Document for the Thematic Mapper is absolutely correct, and that all corrections are made within the product of the solar spectral irradiance, Rayleigh optical depth, and ozone transmission. Although this may not be a valid assumption, something must be assumed to be stable in order to utilize this procedure.

The same procedure was utilized in band 2, as shown in Fig. 6, where the spectral response of the band is plotted against the steeply falling upwelled radiance from clear water. As can be seen in this Figure, the upwelled radiance is dropping to effectively 0 near the long wavelength end of band 2.

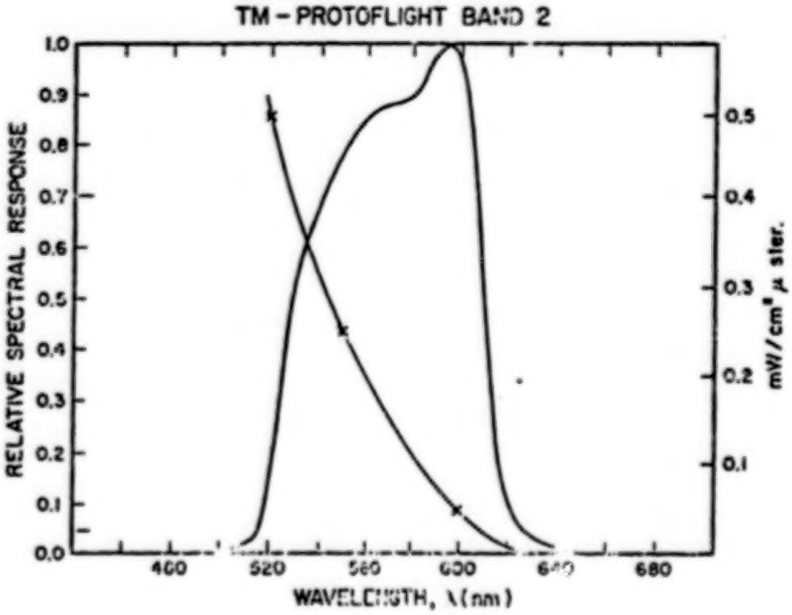

Fig. 6 Thematic Mapper Band 2 with Clear Water Radiance

Following the same procedure as used for band 1, a product of solar spectral irradiance, Rayleigh optical depth, and ozone transmission of 21.18 is arrived at for the subtropical summer condition.

Rayleigh Correction--TM Band 2, Gulf Stream, August 30, 1982

Solar Elevation = 56° Solar Zenith (θ) = 34° Solar Azimuth = 110°

Phase Angle = 31° Normalized L_{water} = 0.2 mW/cm^2 µm ster

$L_w(SZ\ 34^{\circ})$ = 0.17 mW/cm^2 µm ster

$$L_{Total} = \frac{27 - 2.44}{8.098} = 3.03\ mW/cm^2\ \mu m\ ster. \qquad (5)$$

$$L_{Rayleigh} = L_T - L_w = 2.86\ mW/cm^2\ \mu m\ ster = H_{\lambda}\ \tau_{R\lambda}\ T_{O_3} \times 0.135. \qquad (6)$$

Therefore,

$$H_{\lambda}\ \tau_{R\lambda}\ T_{O_3} = 21.18 \text{ for subtropical summer.}$$

It should be noted that one normally provides a Rayleigh optical depth for at least 16 separate conditions consisting of the four seasons, the tropics, the subtropics, the temperate zones, and the Arctic zones. It does not, at this time, appear possible to acquire sufficient data to provide enough statistics to get a valid measurement for each of those 16 conditions, so the effort in the future will be concentrated in the subtropics and temperate zones; namely, the areas covering the United States.

One factor that must be taken into account by those users intending to carry out radiometric measurements with the Thematic Mapper is that the Rayleigh contribution to the signal will change as the instrument scans from east to west. For some investigators, it may be perfectly adequate to calculate the Rayleigh contribution at the center of the picture and subtract it as a dc level from the entire picture, but it should be recognized that the data is not symmetrical with regard to the sun, and the Rayleigh contribution will be rising as the scan proceeds from east to west. Fig. 7 shows the calculated geometric term of $(1 + \cos^2\gamma)/\cos\theta$ for the August 30 scene in question. It also shows a calculated Rayleigh radiance at mW/(cm^2 µm ster) from the east to the west edge. The bars with the numbers ranging from 59 to 67 show the number of digital counts that would have to be subtracted from the scene through the appropriate range of angles in order to correct exactly as close as possible with the digital type data provided. This would, unfortunately, produce a discontinuity as each digital count is changed, but it is, nevertheless, necessary if the Rayleigh radiance is to be correctly removed from the signal. Thus, for accurate removal of the Rayleigh contribution, the solar elevation angle and the phase angle will have to be calculated for either every pixel within the scene that is examined, or an extrapolation utilized. In the CZCS program, it has been found that the calculation can be done for each two degrees of motion of the scan, and an extrapolation made between those calculations. Obviously, the degree of calculation and the range of extrapolation can be varied by each investigator to suit his particular need. It should also be noted that for the area chosen for the calculation of the Rayleigh factor for band 1, the total is far and away the largest portion of the signal.

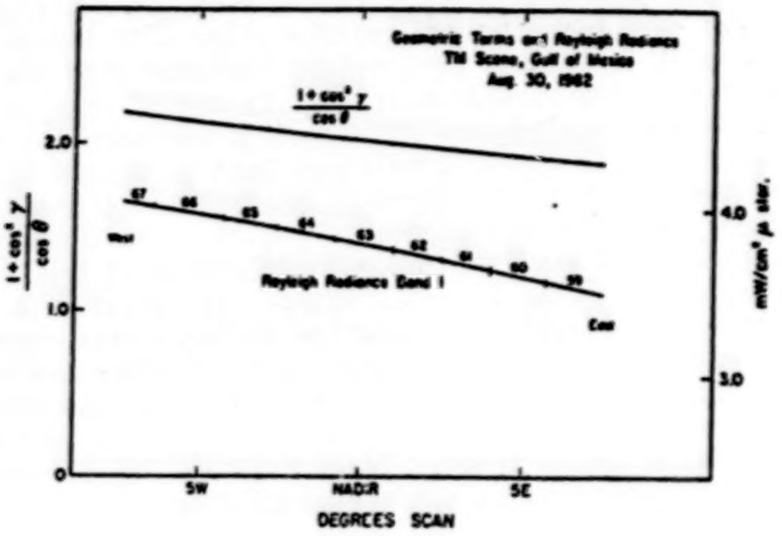

Fig. 7 Geometric Terms for Rayleigh Calculation and Rayleigh Radiance vs Scan Angle

Given this fact, each investigator will have to determine the total digital count seen by targets in the subtropical summer, and determine if a count of approximately 60 is a sufficient portion of the signal that removal is necessary.

As one encounters scenes at lower solar elevation angles than the 56 degrees found in the scene in question, it will be found that the Rayleigh contribution to the measured upwelled signal in all the bands, especially in bands 1 and 2, will increase, whereas the contribution from the surface will decrease because of the lower level of solar illumination at the surface. As more scenes become available that can be analyzed in this manner, the present Rayleigh factors will be corrected to attempt to arrive at an optimum factor for the various conditions that the Thematic Mapper will observe. Obviously, a sample of one is a start, and the factors given should be viewed in that context. Nonetheless, the factors are quite consistent with those that were measured with the CZCS program, and give evidence that the sensor calibration is reasonably accurate as of launch.

MONITORING CALIBRATION WITH TIME

It was important to determine Rayleigh correction factors as soon as possible after launch, because of the degradation that has been observed with the CZCS instrument after nine months in orbit, especially in the blue. Although no positive proof exists, it is assumed that the degradation is in the foreoptics since the internal calibration source shows no change in response. It is further assumed, based on other evidence, that the degradation is probably due to particulate distribution on the large optics of the scan mirror, the primary and secondary mirrors of the telescope. This degradation was detected when the Rayleigh correction factors, that have been derived shortly after CZCS launch, began to give exceptionally low values of upwelled radiance from the clear water after approximately nine months in orbit. By use of simultaneous ship measurements, and the knowledge of the upwelled radiance one would expect from clear water, a corrected formula has been developed for the CZCS that removes the effect of the degradation, and has allowed data reduction for over four years with satisfactory results. The Thematic Mapper data will be monitored in a similar manner to determine if the Rayleigh correction factor as derived shortly after launch, at sometime in the future begins to produce unacceptably low upwelled radiance measurements over clear water. As with the CZCS, the onboard calibration system of the Thematic Mapper does not include the large foreoptics of the system, and this then, together with potential aircraft flights in conjunction with Thematic Mapper overflights, offers the only way of detecting degradation in the sensor response as a function of time.

CONCLUSION

An early look at the Thematic Mapper data for atmospheric correction parameter shows that the parameters derived are consistent with those measured previously in the CZCS program, and indicate a reasonable level of accuracy for the calibration of the Thematic Mapper. More data is needed to gather statistics and to determine the best possible Rayleigh correction factors, and, of course, data will be needed over a period of time in order to assess what degradation, if any, occurs to the sensor performance during its life in space.

References

1. Frohlich, C., and G. E. Shaw, "New Determination of Rayleigh Scattering in the Terrestrial Atmosphere," Appl. Opt., pp. 1773-1775, June 1, 1980.

N85-21735

~~D70~~
D11

SCAN ANGLE AND DETECTOR EFFECTS IN THEMATIC MAPPER RADIOMETRY

Michael D. Metzler
William A. Malila
Environmental Research Institute of Michigan
Ann Arbor, Michigan 48107

Abstract

The effects on Thematic Mapper (TM) radiometry of scan angle and inter-detector differences were analyzed. Radiometric corrections currently performed were found to improve overall consistency of data, but some residual striping remains in the corrected data due to the quantization of signal values and other effects. A new type of banding was discovered which is related to the bidirectional scanning of TM. An initial empirical model was developed for correcting this effect in Band 1, but should receive additional development. The scan angle effects observed corresponded to those expected based on atmospheric considerations and scene characteristics. Low frequency scan-to-scan noise was detected in Band 1, Band 7 and to a lesser extent in Bands 2 and 3. The Band 1 detectors which exhibited this noise showed strong correlation in their variation.

INTRODUCTION

This investigation was directed at quantifying and understanding the scan-angle and detector effects observed in TM radiometry.

DATA AND METHODS OF ANALYSIS

The data set used for this study consisted of computer compatible tapes (CCT's) of raw data (CCT-BT), radiometrically corrected data (CCT-AT), and geometrically corrected data (CCT-PT) for two scenes, 40049-16262 (North Central Iowa) and 40037-16031 (Arkansas). Major emphasis was given to the unresampled (CCT-BT and CCT-AT) data to allow analysis of individual scan and detector effects. Although analysis was concentrated on the Iowa scene because of its cloud-free, relatively confirmation of results. The analyses were performed over the full frame of data for each band, for each detector within each band and for each scan direction.

Histograms of the frequency of occurrence of each quantized signal level were produced and analyzed for each step in the correction process (CCT-BT to CCT-AT to CCT-PT). Signal means and variances were computed, again before and after calibration. Across track profiles of the mean signal as a function of pixel number were generated for each scan direction by dividing the scene into forward and reverse scans and then computing the mean signal for each set of scans in a window 16 samples wide by 2992 lines (i.e., all forward or all reverse lines) long. Stepping the window across the scene produced relatively noise-free average scan lines exhibiting only gross scene content effects. Along track profiles were generated for each detector by computing the mean signal level for all the pixels in each scan line and then plotting the scan-line means for a given detector as a function of scan number (374 scans x 16 detectors = 5984 lines in full scene, CCT-BT or CCT-AT).

RESULTS

The overall quality of TM imagery was observed to be good. However, several effects were noted which could be significant in analysis of data from different scenes, from different areas within the same scene or for applications where small signal differences are important.

Scan Angle and Scan Direction Effects

Scan angle effects caused by atmospheric backscattering, changing optical path lengths, and ground bidirectional reflectance effects were expected. Figure 1 illustrates the mean signal level as a function of scan angle (pixel number) for each of the seven TM bands. The sharp peaks present are primarily due to urban areas (at pixels 800, 3300), larger bodies of water (pixels 4200-5200), or numerous smaller bodies of water. The feature of interest, however, is the overall decline in mean signal level in going from the western side of the scene to the eastern side. The effect is greatest in Bands 1 and 2 which decrease approximately 10%. Band 3 exhibits a somewhat less apparent angular effect, and the remaining reflective bands demonstrate an even lesser effect and more influence of scene composition. The thermal band, Band 6, also exhibits a similar pattern, with larger responses at the western edge, presumably due to viewing a greater percentage of sunlit scene components. However, this full-frame average scan line for the thermal band masks a distinctive scan-direction effect which is discussed in detail later.

Previous modeling work at ERIM for analyses of spaceborne scanner data has predicted atmospheric scan angle effects similar to those seen with this TM data [1,2]. Figure 2 is a plot of model results derived by us from the data set of Dave [3] for the MSS; their approximate TM equivalents are given. At the longer wavelengths, e.g., TM Bands 4, 5 and 7, atmospheric scan angle effects are reduced, and canopy shadowing and

FIGURE 1

SCAN–ANGLE EFFECT

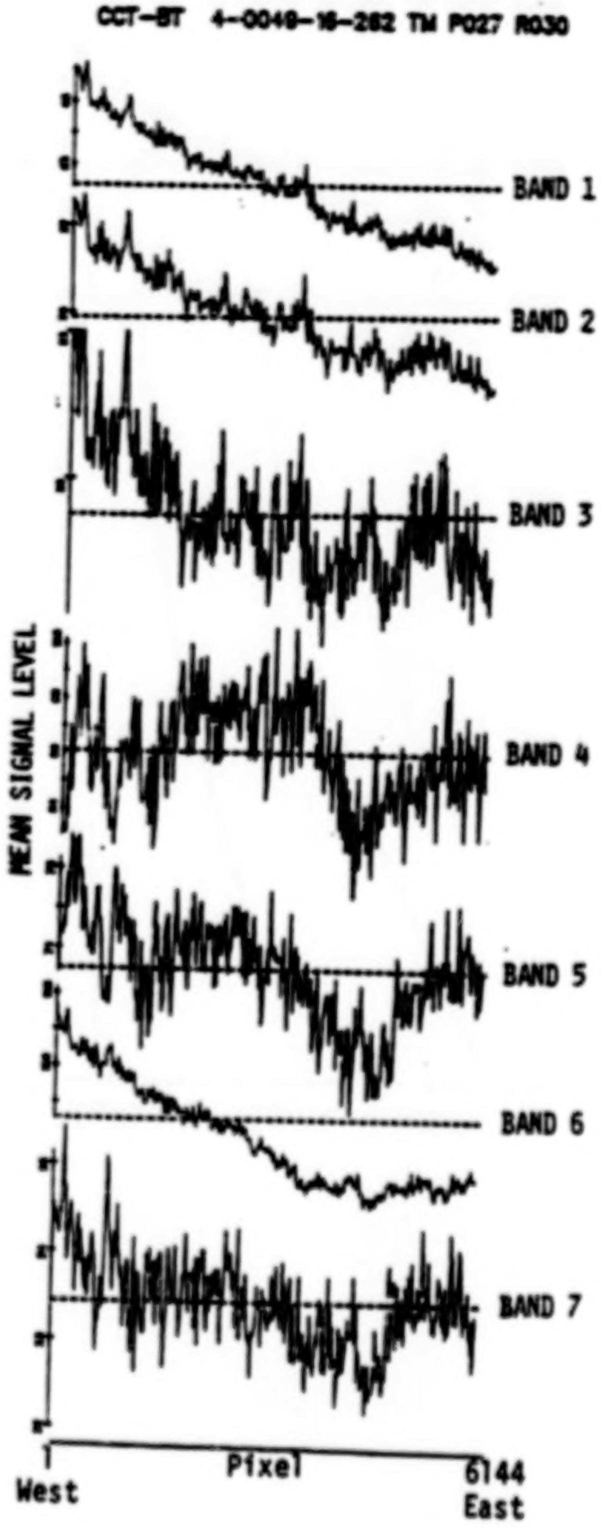

FIGURE 2

ATMOSPHERIC SCAN-ANGLE EFFECTS IN MSS BANDS (MODEL RESULTS)

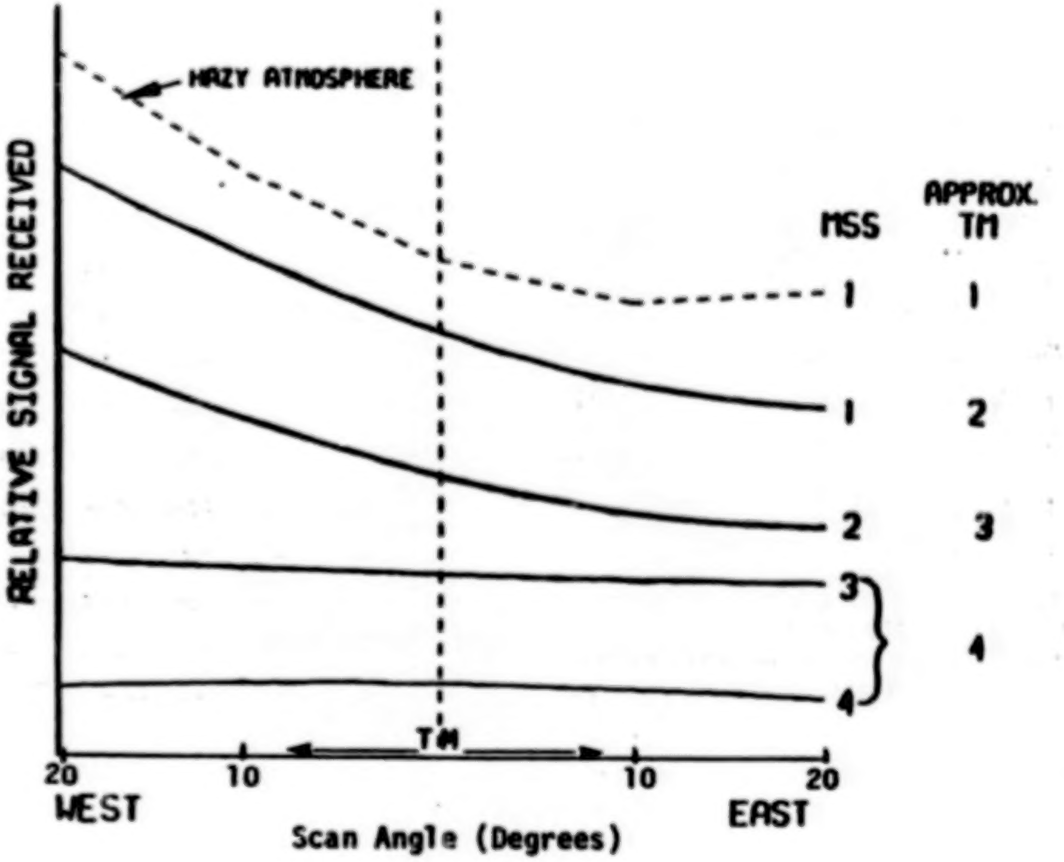

bidirectional reflectance effects become the predominant drivers of the observed scan-angle effect.

Quantification of the scan-angle effects in TM radiometry was complicated by a new effect which was discovered. Figure 3 illustrates the mean signal level as a function of scan angle for Bands 1 and 6 as in Figure 1, but in Figure 3 the forward and reverse scans are plotted separately. While the dominant effect is the expected scan angle effect, a systematic droop of signal values during the active scan tends to increase the observed scan angle effect for forward scans, and decrease it during reverse scans. This scan direction effect was detected to some extent for all of the reflective bands, and was most pronounced in Band 1. Band 6 also demonstrated a pronounced scan direction effect, but of a distinctly different nature (see Figure 3).

In order to characterize the scan direction effect, the ratio of forward scan signal level to reverse scan signal level was computed as a function of scan angle (pixel). These data (Figure 4) were then fit to an exponential decay model of the form

$$S(p) = \frac{S_o(p)}{1 + A[\exp(-KM) - 1]}$$

where

p = Pixel number, counting from West edge of scene

p_f, p_r = Pixel offsets to convert "p" to relative minor frame number

M = $p_f + p$ for forward scans
$p_r - p$ for reverse scans

$S_o(p)$ = Signal returned to sensor for pixel "p"

$S(p)$ = Corrected signal value for pixel "p"

K = Time constant (reciprocal of the number of pixels of active scan required for 63% of the decay to occur)

A = Factor determining magnitude of total decay

The model was fit with the constraint that A and K be identical for forward and reverse scans. The result of fitting this model to Band 1 of the Iowa scene is illustrated in Figure 4, and in Figure 5 the predicted signal decay during forward and reverse scans is shown. From this model, one can see that the decay begins prior to the first pixel, having decayed approximately 1% by that time. The total decay is approximately 2.25% by the end of the active scan. This results in the mean signal level of the forward scan being approximately 0.75 counts higher than the mean signal level of the reverse scan at the West end of the scene, and approximately 0.75 counts lower at the East end of the scene for Band 1.

FIGURE 3a

SCAN–DIRECTION EFFECT

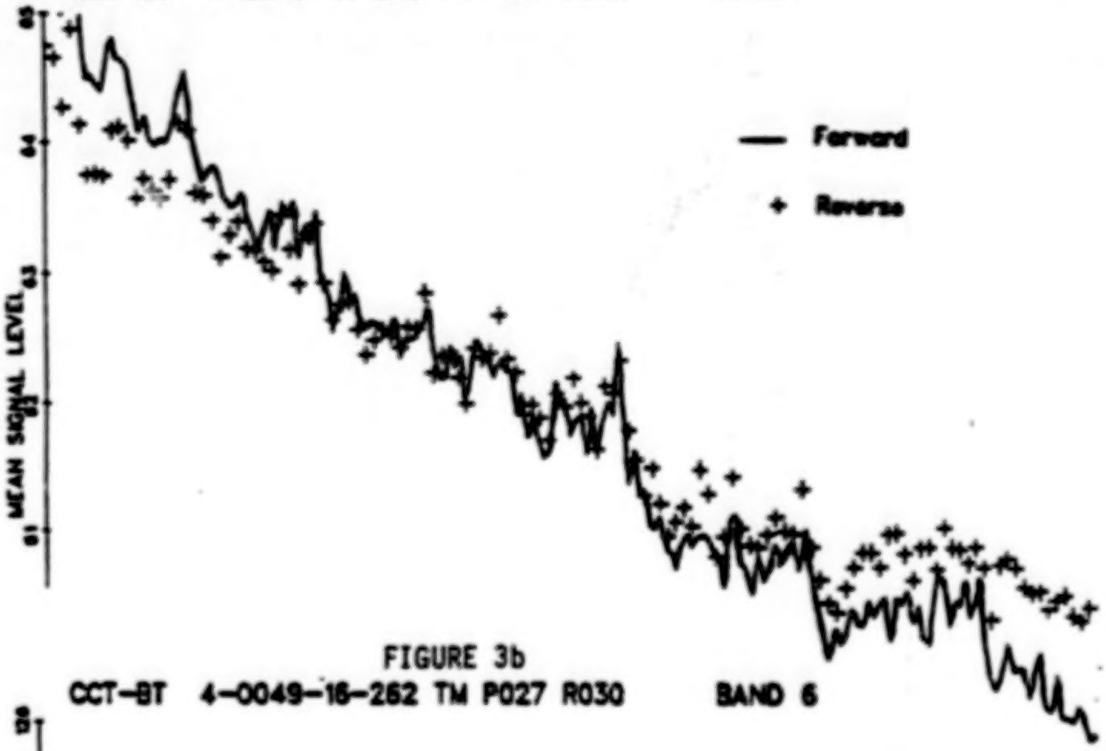
CCT-BT 4-0049-16-262 TM P027 R030 BAND 1

FIGURE 3b

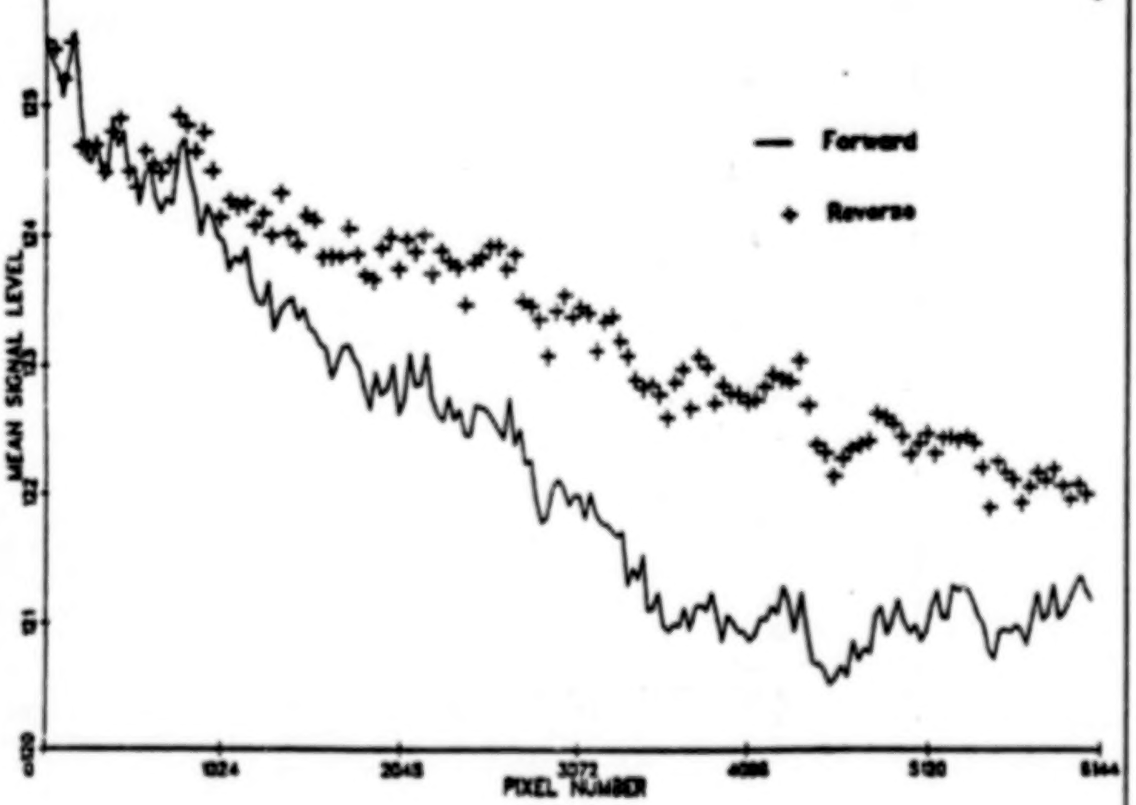
CCT-BT 4-0049-16-262 TM P027 R030 BAND 6

FIGURE 4

RATIO OF MEAN FORWARD TO MEAN REVERSE SCAN SIGNAL

Band 1

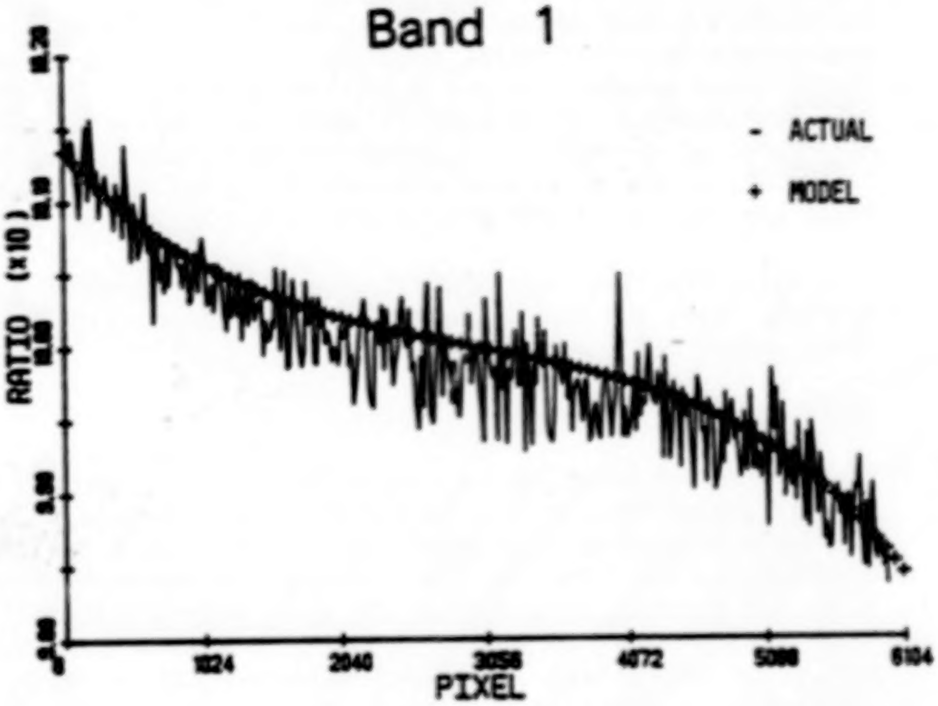

FIGURE 5

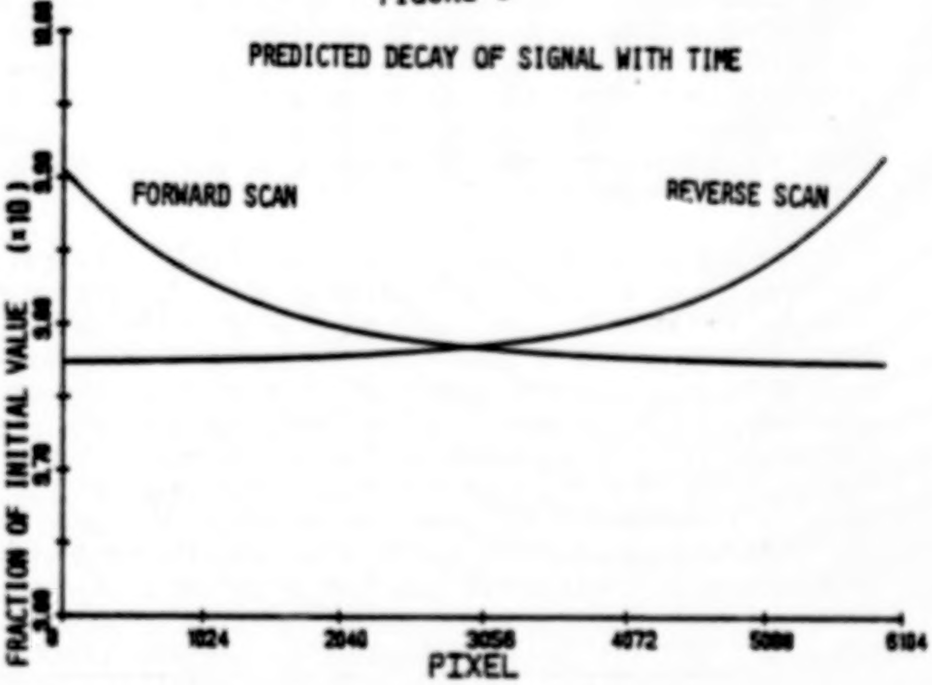

PREDICTED DECAY OF SIGNAL WITH TIME

For this case (Band 1, scene 40049-16262) the p_f and p_r required for the fit resulted in the exponential decay beginning at the time of DC restore (different times for the two scan directions). During DC restore, a dark (no radiance) level is presented to the detectors, and a DC level capacitor is charged to a value which results in approximately two signal counts. This charge is to be held for the entire scan, having a time constant on the order of minutes [4]. The empirically derived scan-direction effect model suggests that this charge may be decaying much faster (time constant of the order of 10 msec). Two problems exist with this explanation: 1) 10 msec is much, much less than minutes and 2) the magnitude of the effect appears to be proportional to the mean signal level, while the DC restore capacitor simply adds a set signal level. Final explanation of the effect awaits further investigation.

Any corrections for this scan-direction effect should be made an integral part of a single radiometric correction process to minimize quantization and roundoff errors.

Inter-Detector Calibration Effects

Horizontal striping is commonly found in imagery from sensors that scan arrays of detectors. To minimize the potential for striping among the 16 detectors in each band (four in Band 6), a histogram normalization technique is included in the radiometric correction processing. This technique attempts to equalize the means and variances of the quantization level histograms of each detector within a band by applying a gain and offset to the signals from each detector. Since this gain and offset is applied to a discrete function (histogram), and the result is still integer, the number of occupied quantization levels is not changed by the correction; only the total range they span is changed. This requires that some quantization levels within the expanded range be empty. The effect of this correction is illustrated in Figure 6. Although the histogram for an individual detector acquires some empty bins in the correction process (right-center), the histogram of the entire band is noticeably smoother (left-center). Of course, the cubic convolution resampling done in the geometric correction processing tends to equalize the histogram bin sizes even more (left-bottom).

The net effect of these corrections for a band with a fairly large variance, such as Band 4, illustrated here, is virtual elimination of any detector striping in the radiometrically corrected data. On the other hand, if a band has a lower variance, the histogram normalization is unable to equalize the means and variances of the detectors because of quantization limitations, and low level residual striping may exist after the correction. As an example, Figure 7 contains two plots for Band 2. The top plot is a trace of the mean signal level of each of the first 136 lines in a radiometrically and geometrically corrected image (CCT-PT). The lower plot was constructed by computing the mean signal level for each detector (on a CCT-AT) over the full frame and using these mean values to construct eight scans (128 lines) of data. Note the similarity of the two plots and the 17-line periodicity of the top trace compared with the

FIGURE 6

QUANTIZATION-LEVEL HISTOGRAMS
THEMATIC MAPPER BAND 4

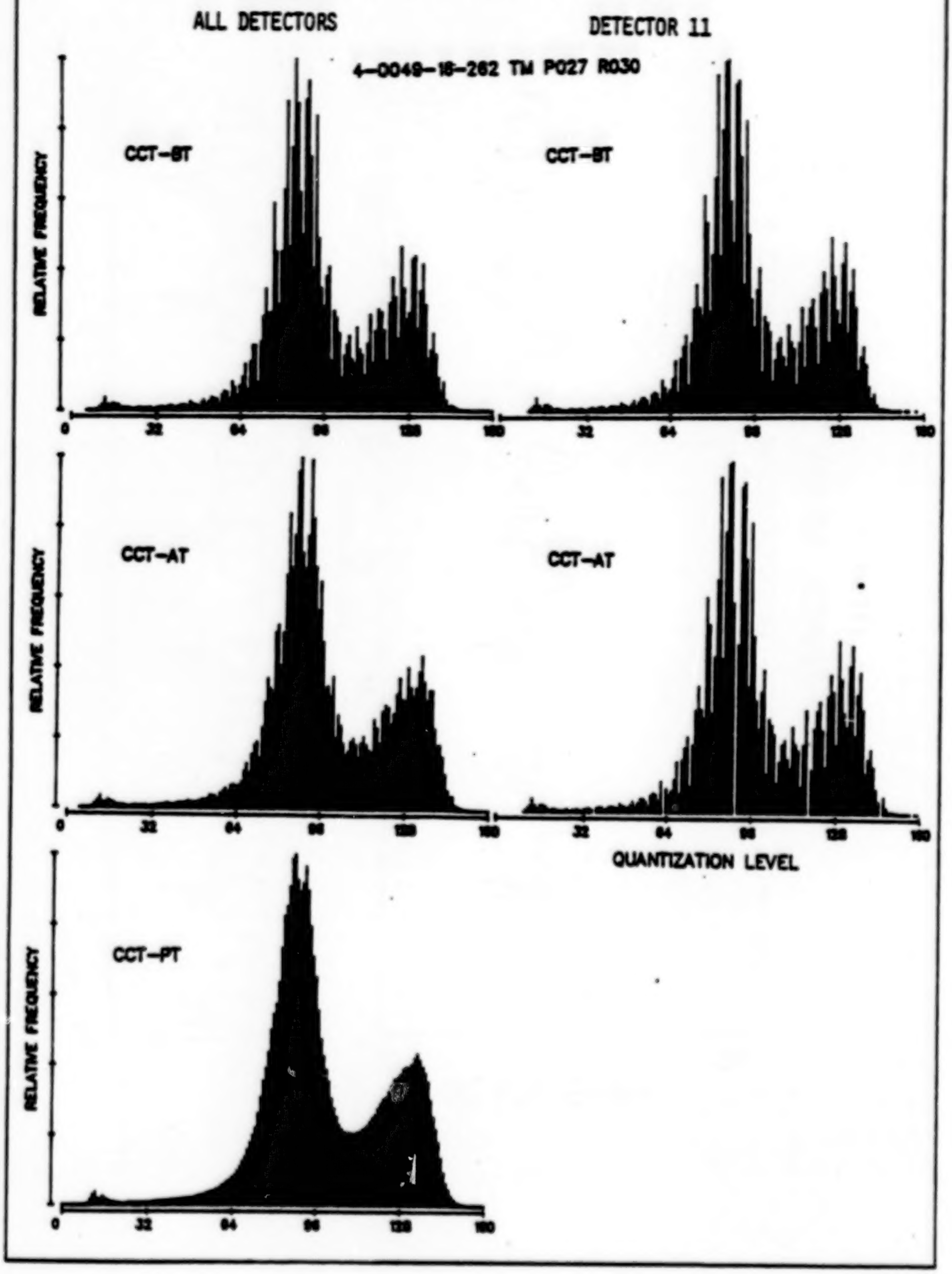

FIGURE 7

DOWN-TRACK MEAN SIGNAL

CCT-PT 4004916262 D02703082258 BAND 2

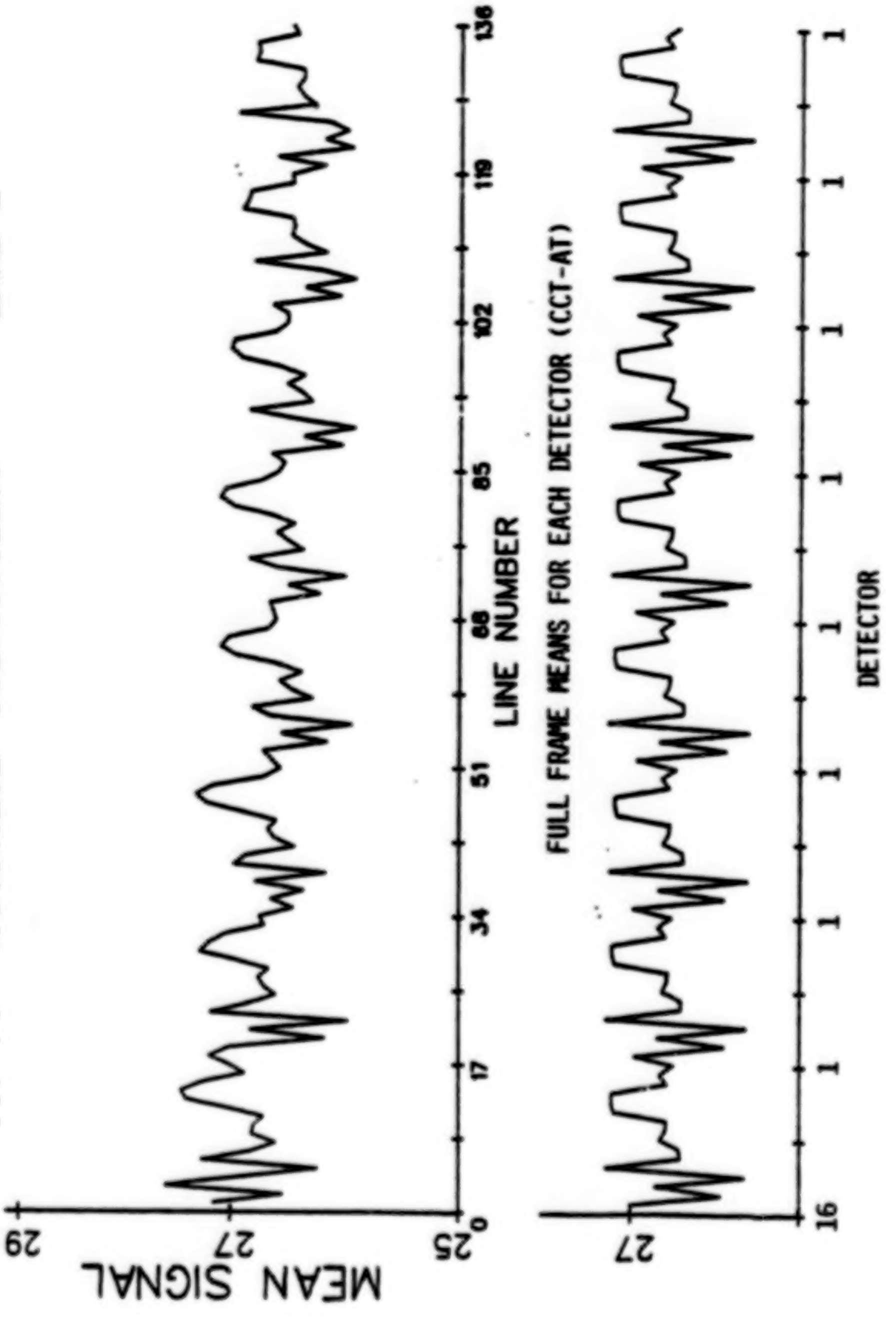

16-line period of the bottom. This 17- vs. 16-line period is due to the resampling to a slightly smaller pixel size in the geometrically corrected data. Note that this periodic fluctuation in mean signal level is not due to an error in the correction process; but stems from the round-off and/or truncation errors introduced when applying calibration transformations to discrete signals. The result is low level striping effects which will appear in the final image data even though the performance of the radiometric correction algorithm appears to be approaching its upper limits.

Low Frequency Noise

Analysis of low frequency noise (at or below scan mirror frequencies) produced the plots shown in Figures 8 and 9. In these figures, each trace is a plot of the mean signal level as a function of scan number for a given detector. The mean signal level for a detector for a scan is defined as the mean of all the pixels in that scan line. Figure 8 illustrates the consistent difference between forward and reverse scan signal levels for Band 6. As suggested by Figure 3b, the mean signal level for a forward scan is always lower than the mean signal for the following reverse scan, although the magnitude varies as one progresses down the frame.

Band 1, shown in Figure 9, contains several detectors which have significant low frequency variations. Detectors 4, 12, 10 and 8 have mean signal levels which vary between two states that are separated by approximately 2.0, 1.5, 1.0 and 0.75 signal counts, respectively. In other bands, this low frequency noise is much less evident, appearing in Band 2, Detector 1 (<0.5 count), Band 3, Detectors 1 and 16 (∿0.5 count each), Band 5, Detector 10 (<0.5 count) and Band 7, Detector 7 (∿0.5 count). Note that this low frequency variation may remain in the higher or lower state for several seconds, and is not to be confused with the high frequency, within-scan noise reported previously (as for Band 7, Detector 7) [5]. This low frequency effect could be serious in water-related applications where average signal levels are low.

Additional examination of the low frequency noise in Band 1 indicated that it was highly correlated between the noisy detectors (4, 12, 10 and 8). One would expect that within a given scan, the signal variations of each detector would be best correlated with the variations of the adjacent detectors, and least correlated with detectors spaced further in the array. Although this is strictly the case for Band 4, and generally true with the other bands, Band 1 is markedly different. The inter-detector correlation matrices for all seven bands are presented in Figures 10-16. As well as the above mentioned correlation of detectors 4, 12, 10 and 8 in Band 1, the tendency towards every-other detector correlation (odd/even detector effect) is quite noticeable in Bands 2, 3 and 7. The cause of this low frequency noise is under investigation; a preliminary hypothesis is that it is the result of the DC restore procedure locking onto the high (low) phase of the coherent noise reported elsewhere [6].

FIGURE 8

DOWN-TRACK TRACE OF SCAN-LINE MEAN SIGNAL FOR EACH DETECTOR IN BAND 6

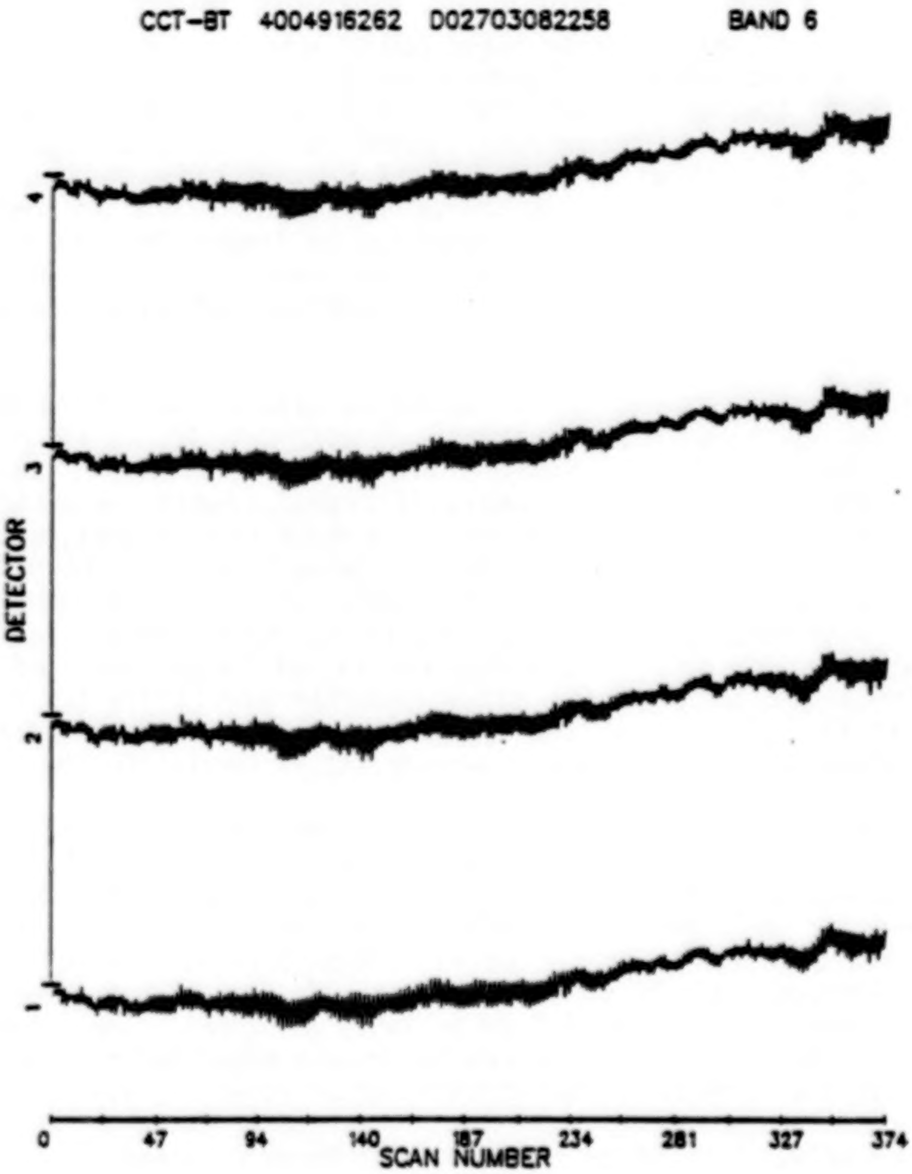

FIGURE 9

DOWN-TRACK TRACE OF SCAN-LINE MEAN SIGNAL FOR EACH DETECTOR IN BAND 1

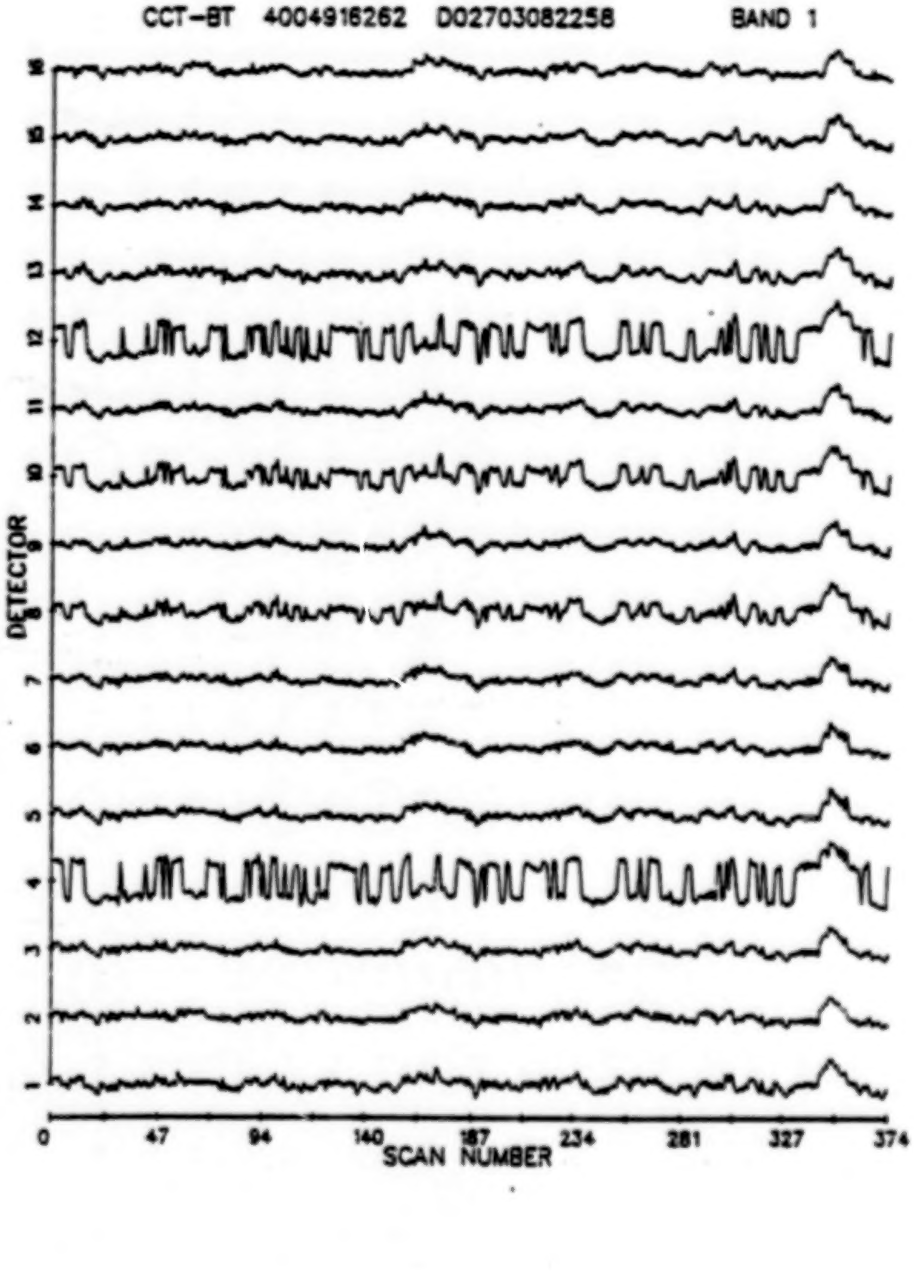

Correlation Matrix for Scan Line MEANS <1> BAND:1 CCT-BT 4004916262 (IOWA SCENE)

DET	1	2	3	4	5	6	7	8	9	10	11	12	13	14	15	16
1	1.00															
2	.82	1.00														
3	.90	.93	1.00													
4	.68	.19	.45	1.00												
5	.88	.87	.95	.48	1.00											
6	.80	.87	.92	.37	.95	1.00										
7	.84	.83	.91	.47	.94	.96	1.00									
8	.87	.55	.74	.87	.78	.71	.80	1.00								
9	.80	.74	.85	.50	.87	.90	.94	.80	1.00							
10	.81	.41	.63	.93	.68	.58	.68	.96	.72	1.00						
11	.85	.75	.86	.55	.88	.86	.91	.83	.94	.78	1.00					
12	.71	.23	.47	.98	.52	.40	.51	.90	.56	.96	.64	1.00				
13	.85	.64	.79	.70	.82	.77	.84	.89	.88	.87	.94	.78	1.00			
14	.82	.78	.84	.45	.86	.83	.86	.75	.85	.69	.92	.55	.92	1.00		
15	.82	.70	.82	.57	.83	.80	.85	.80	.88	.76	.93	.65	.95	.94	1.00	
16	.63	.81	.77	.09	.77	.78	.76	.47	.73	.36	.77	.19	.68	.87	.81	1.00

Note correlation of Detectors 4, 8, 10, 12 with each other and lack of correlation with others, especially Detectors 2 and 16.

FIGURE 10

CORRELATION BETWEEN DETECTORS OF LOW-FREQUENCY NOISE
TM BAND 1

Correlation Matrix for Scan Line MEANS <2> BAND:2 CCT-BT 4004916262 (IOWA SCENE)

DET	1	2	3	4	5	6	7	8	9	10	11	12	13	14	15	16
1	1.00															
2	.70	1.00														
3	.73	.67	1.00													
4	.72	.95	.63	1.00												
5	.83	.79	.91	.82	1.00											
6	.61	.90	.72	.91	.86	1.00										
7	.71	.74	.90	.74	.94	.88	1.00									
8	.62	.90	.67	.90	.82	.95	.86	1.00								
9	.78	.77	.84	.78	.92	.85	.94	.89	1.00							
10	.58	.87	.64	.87	.78	.92	.81	.96	.88	1.00						
11	.70	.70	.86	.69	.88	.80	.92	.82	.95	.85	1.00					
12	.55	.82	.67	.81	.77	.88	.81	.91	.86	.95	.89	1.00				
13	.84	.73	.77	.77	.88	.76	.84	.79	.92	.81	.91	.85	1.00			
14	.63	.85	.61	.86	.76	.86	.76	.89	.83	.92	.82	.94	.88	1.00		
15	.84	.71	.76	.74	.86	.73	.81	.76	.89	.78	.88	.81	.97	.86	1.00	
16	.40	.82	.44	.80	.59	.82	.62	.85	.67	.88	.66	.88	.68	.91	.69	1.00

Note every other detector correlation, i.e., evens with evens, odds with odds.

FIGURE 11

CORRELATION BETWEEN DETECTORS OF LOW-FREQUENCY NOISE
TM BAND 2

Correlation Matrix for Scan Line MEANS <3> BAND:3 CCT-BT 4004916262 (IOWA SCENE)

DET	1	2	3	4	5	6	7	8	9	10	11	12	13	14	15	16
1	1.00															
2	.58	1.00														
3	.91	.72	1.00													
4	.61	.84	.85	1.00												
5	.89	.72	.96	.85	1.00											
6	.69	.88	.83	.90	.90	1.00										
7	.82	.67	.92	.84	.95	.89	1.00									
8	.55	.67	.77	.88	.78	.83	.89	1.00								
9	.60	.63	.78	.84	.79	.80	.89	.97	1.00							
10	.70	.82	.79	.79	.84	.91	.86	.82	.85	1.00						
11	.78	.57	.85	.75	.86	.76	.90	.84	.90	.88	1.00					
12	.52	.82	.66	.78	.71	.85	.74	.78	.79	.93	.80	1.00				
13	.84	.62	.85	.68	.87	.78	.87	.71	.77	.88	.93	.81	1.00			
14	.59	.82	.70	.75	.74	.85	.74	.73	.74	.92	.78	.95	.86	1.00		
15	.88	.51	.84	.59	.85	.68	.83	.62	.70	.78	.88	.66	.95	.75	1.00	
16	.17	.79	.29	.50	.36	.65	.32	.39	.36	.66	.30	.77	.41	.78	.29	1.00

Note preference for "every other" detector correlation as in Band 2.

FIGURE 12

CORRELATION BETWEEN DETECTORS OF LOW-FREQUENCY NOISE
TM BAND 3

Correlation Matrix for Scan Line MEANS <4> BAND:4   CCT-BT 4004816262 (IOWA SCENE)

DET	1	2	3	4	5	6	7	8	9	10	11	12	13	14	15	16
1	1.00															
2	.99	1.00														
3	.97	.99	1.00													
4	.96	.97	.99	1.00												
5	.94	.96	.97	.99	1.00											
6	.92	.94	.96	.97	.99	1.00										
7	.90	.92	.94	.96	.97	.99	1.00									
8	.89	.91	.92	.94	.96	.98	.99	1.00								
9	.87	.89	.91	.92	.94	.96	.98	.99	1.00							
10	.86	.87	.89	.90	.91	.94	.95	.97	.99	1.00						
11	.85	.86	.88	.89	.90	.92	.94	.96	.97	.99	1.00					
12	.83	.85	.86	.86	.88	.90	.92	.93	.95	.97	.99	1.00				
13	.83	.84	.85	.86	.87	.89	.90	.92	.94	.96	.97	.99	1.00			
14	.82	.84	.84	.85	.86	.88	.89	.91	.93	.94	.96	.97	.99	1.00		
15	.82	.83	.84	.84	.85	.67	.88	.89	.91	.93	.94	.95	.97	.99	1.00	
16	.81	.63	.83	.83	.84	.86	.87	.88	.89	.91	.92	.94	.95	.97	.99	1.00

Note correlation structure as expected, i.e., decreasing correlation with increasing inter-detector distance.

FIGURE 13

CORRELATION BETWEEN DETECTORS OF LOW-FREQUENCY NOISE
TM BAND 4

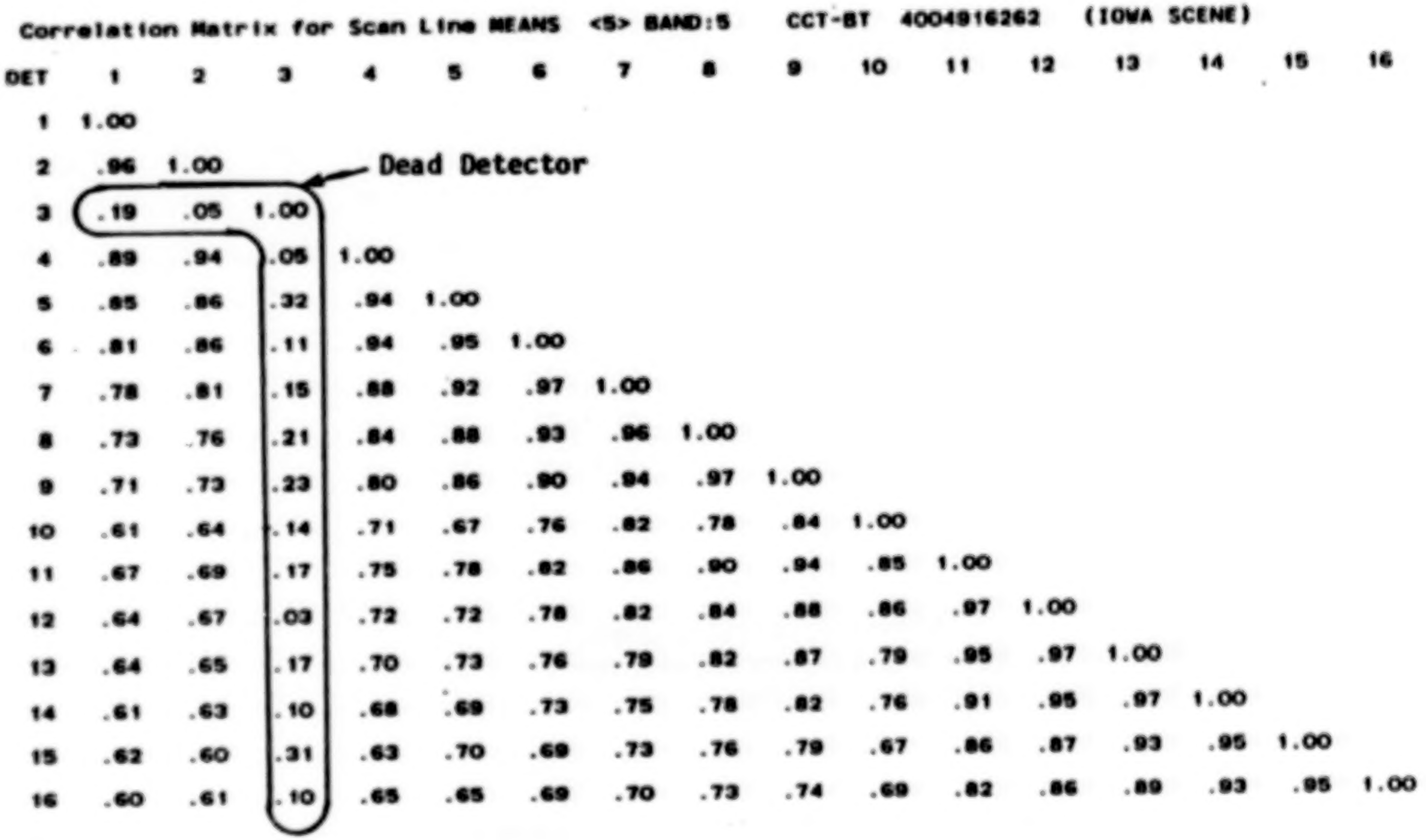

Correlation Matrix for Scan Line MEANS <5> BAND:5 CCT-BT 4004916262 (IOWA SCENE)

DET	1	2	3	4	5	6	7	8	9	10	11	12	13	14	15	16
1	1.00															
2	.96	1.00														
3	.19	.05	1.00													
4	.89	.94	.05	1.00												
5	.85	.86	.32	.94	1.00											
6	.81	.86	.11	.94	.95	1.00										
7	.78	.81	.15	.88	.92	.97	1.00									
8	.73	.76	.21	.84	.88	.93	.96	1.00								
9	.71	.73	.23	.80	.86	.90	.94	.97	1.00							
10	.61	.64	.14	.71	.67	.76	.82	.78	.84	1.00						
11	.67	.69	.17	.75	.78	.82	.86	.90	.94	.85	1.00					
12	.64	.67	.03	.72	.72	.78	.82	.84	.88	.86	.97	1.00				
13	.64	.65	.17	.70	.73	.76	.79	.82	.87	.79	.95	.97	1.00			
14	.61	.63	.10	.68	.69	.73	.75	.78	.82	.76	.91	.95	.97	1.00		
15	.62	.60	.31	.63	.70	.69	.73	.76	.79	.67	.86	.87	.93	.95	1.00	
16	.60	.61	.10	.65	.65	.69	.70	.73	.74	.69	.82	.86	.89	.93	.95	1.00

FIGURE 14

CORRELATION BETWEEN DETECTORS OF LOW-FREQUENCY NOISE
TM BAND 5

```
Correlation Matrix for Scan Line MEANS  <6> BAND:6    CCT-BT  4004816262   (IOWA SCENE)
DET     1      2      3      4
  1   1.00
  2    .99   1.00
  3    .99    .99   1.00
  4    .99    .99    .99   1.00
```

FIGURE 15

CORRELATION BETWEEN DETECTORS OF LOW-FREQUENCY NOISE
TM BAND 6

Correlation Matrix for Scan Line MEANS <7> BAND:7 CCT-BT 4004916262 (IOWA SCENE)

DET	1	2	3	4	5	6	7	8	9	10	11	12	13	14	15	16
1	1.00															
2	.78	1.00														
3	.94	.78	1.00													
4	.73	.95	.79	1.00												
5	.89	.70	.95	.77	1.00											
6	.68	.89	.73	.95	.77	1.00										
7	.72	.25	.74	.31	.81	.35	1.00									
8	.56	.83	.61	.88	.64	.94	.25	1.00								
9	.76	.67	.81	.72	.85	.78	.70	.81	1.00							
10	.48	.79	.51	.82	.53	.87	.13	.95	.75	1.00						
11	.74	.61	.77	.66	.82	.71	.70	.71	.93	.73	1.00					
12	.53	.73	.54	.77	.58	.81	.26	.86	.75	.92	.82	1.00				
13	.71	.58	.73	.62	.77	.65	.65	.66	.87	.68	.95	.82	1.00			
14	.61	.67	.61	.71	.65	.74	.41	.75	.75	.79	.85	.93	.90	1.00		
15	.71	.55	.72	.59	.75	.61	.65	.60	.82	.60	.89	.74	.95	.88	1.00	
16	.55	.70	.55	.72	.57	.74	.27	.76	.67	.79	.74	.88	.79	.93	.84	1.00

Note "every other" detector correlation as in Bands 2 and 3, poor correlation of Detector 7 with others.

FIGURE 16

CORRELATION BETWEEN DETECTORS OF LOW-FREQUENCY NOISE
TM BAND 7

SUMMARY AND CONCLUSIONS

The overall quality of Thematic Mapper image data is very good. The spatial resolution is excellent and the radiometric correction procedures currently in use are working well, although some residual effects may remain which can cause low-level striping. Small but significant scan-direction effects exist in the reflective bands; they appear to be correctable in the two scenes examined by use of an empirical model employing exponential decay terms. Refinement and extension of the initial correction model await further understanding of the sensor phenomena driving the effect. Band 6 has a unique scan-direction effect, markedly different from the effect observed in the reflective bands. Highly correlated low frequency noise in Band 1, Detectors 4, 8, 10 and 12, may be due to a coherent-noise/DC-restore interaction; however, this phenomenon requires further investigation. It is recommended that any new radiometric correction procedures be integrated into a single process to minimize quantization and round-off effects.

The shorter wavelength of Band 1 and a scan-angle range larger than previous Landsats both increase the magnitude of scan-angle effect due to atmospheric and scene bidirectional reflectance characteristics in Thematic Mapper data. For a number of applications, approaches to reduce these effects should be developed.

References

1. W.A. Malila and R.F. Nalepka, "Atmospheric Effects in ERTS-1 Data, and Advanced Information Extraction Techniques," Proceedings of the Symposium on Significant Results Obtained from the Earth Resources Technology Satellite-1, NASA Goddard Space Flight Center, 1973, pp.1097-1104.

2. W.A. Malila, J.M. Gleason and R.C. Cicone, "Atmospheric Modeling Related to Thematic Mapper Scan Geometry", Final Report NAS9-14819, NASA Johnson Space Center, 1976.

3. J.V. Dave, "Extensive Data Sets of the Diffuse Radiation in Realistic Atmospheric Models with Aerosols and Common Absorbing Gases," Solar Energy, 21:361-369.

4. J. Engle, Private Conversation, 29 January 1983.

5. J.L. Barker, Presented at Landsat-D Investigations Workshop, NASA Goddard Space Flight Center, May 1982.

6. H.H. Kieffer, E. Eliason, P. Chavez, R. Batson and W. Borgeson, Presentation at Second Landsat-4 Investigations Workshop, NASA Goddard Space Flight Center, January 1983.

N85-21736

THEMATIC MAPPER SPECTRAL DIMENSIONALITY AND DATA STRUCTURE*

E. P. Crist and R. C.Cicone
Environmental Research Institute of Michigan
Ann Arbor, Michigan 48107

INTRODUCTION

The Thematic Mapper (TM) embodies several improvements over the spectral characteristics of the Multispectral Scanner (MSS), including more total bands, narrower bandwidths, and greater total range of spectral coverage. These improvements suggest that TM data will carry more information than is available in MSS data with respect to scene characteristics. However, the degree of added information cannot be determined simply on the basis of the described spectral differences.

Experience with MSS data over agricultural regions has shown that, even though radiation is measured in four spectral bands, the vast majority of data variability is concentrated in a single plane within the four dimensional space. This phenomenon occurs because of correlations between adjacent bands, these correlations being the result of fundamental reflectance properties of scene classes. Since at least some of the TM bands resemble the MSS bands in terms of spectral sensitivity and/or proximity to one another, a like effect may be seen in TM data, i.e., the effective dimensionality of the data may be less than is suggested by the number of spectral bands.

In MSS data, any pair of untransformed bands provides a skewed view of the data plane. The Tasseled Cap Transformation developed by Kauth and Thomas [1] was designed to rotate MSS data such that the plane into which most agricultural data fall could be viewed "head-on". It thus serves to concentrate the greatest amount of total data variability into the fewest number of features. In addition, the data plane is oriented such that the features defining it can be readily interpreted with respect to physical characteristics of the scene being viewed.

---

*The work described herein was supported by the Earth Resources and Applications Division, NASA Johnson Space Center, under contract NAS9-16538.

PRECEDING PAGE BLANK NOT FILMED

PAGE III-442 INTENTIONALLY BLANK

The clear benefits of this transformation, and the success with which it has been used in MSS applications, prompted considerable interest in the possibility of a Tasseled Cap transformation for TM data. Holmes [2] and Badhwar and Henderson [3] carried out studies using TM data simulated from actual reflectance spectra (excluding the thermal band) to assess the potential for such a transformation. Holmes predicted the presence of at least three important dimensions in the data. Badhwar and Henderson predicted only two dimensions in agricultural data, defined by features similar to those of the MSS Tasseled Cap (i.e., Greenness and Brightness).

The work reported here was undertaken to more fully evaluate the dimensionality and structure of TM data, to compare the dimensionality and structure of TM and MSS data, and to assess the potential for a Tasseled Cap transformation of Thematic Mapper data, using field reflectance spectra to simulate TM and MSS signal counts. This work extends that of Holmes and Badhwar and Henderson by 1) using a data set which represents a wider range of agricultural crop conditions and soil types, 2) simulating actual signal counts based on pre-launch sensor characteristics 3) using a more sophisticated atmospheric model, 4) verifying the simulation with actual TM data, and 5) extending analysis beyond principal components to a more thorough, physically-based evaluation of TM data structure. A more complete description of this work is available in References 4 and 5.

MATERIALS AND METHODS

Data

Landsat-4 TM and MSS signal counts were simulated using reflectance spectra collected by and at Purdue/LARS for the NASA Johnson Space Center [6]. Included were data from three crops over three growing seasons, as well as data for a wide range of soil types. Data from the Dave atmospheric model [7] were used to derive top-of-atmosphere radiances for a clear day, and pre-launch composite detector response functions and absolute calibration data [8,9,10] were used to derive simulated signal counts for the two sensors. Only the reflective TM bands were simulated (i.e., the thermal band was excluded).

The final data set consisted of 1640 spectral samples from partially- or fully-vegetated plots and 636 spectra from soil samples (both field and laboratory measured). Because the original reflectance spectra and simulated atmospheric characteristics were identical in the simulation of TM and MSS data, a pure comparison of sensor spectral response and dynamic range was possible.

Analysis

Simulated TM signal counts were compared to actual data from a portion of an early TM scene, using band histograms. This comparison was carried out for the purpose of verifying the simulation. Principal components based on covariance matrices were then used to provide a starting point for the data transformations. For MSS data, whose variability is largely confined to a single plane, the first two principal components effectively defined that plane. In this case, all that was required to simulate a Tasseled Cap Transformation was to rotate the plane about the z-axis such that Greenness and Brightness equivalent features were defined. Such a process was followed both for the simulated MSS data and for a three-band TM analysis, using the three TM bands most similar to the MSS bands (TM bands 2, 3 and 4).

In more complex data structures, principal components may not effectively define the actual planes of data dispersion. Figure 1 shows the dispersion of six-band TM data as determined by the reported analyses. The principal components defined for data so dispersed will resemble those shown in Figure 2. Principal components define the directions of maximum data variability, but need not be at all related to the actual data structure, as driven by the physical properties of scene components.

In order to align the planes of TM Data dispersion with the coordinate axes, multi-dimensional rotations were applied, guided by visual inspection of the data plotted three dimensions at a time. Once defined, the transformation was applied to the entire data set, and both statistical (correlation) and subjective (visual) comparisons of sensors were made. In addition, the descriptive information accompanying the LARS reflectance spectra was used to begin to understand the physical drivers of spectral response in the TM Tasseled Cap space.

RESULTS AND DISCUSSION

Comparison to Real Data

Figure 3 shows the band histograms of the simulated Landsat-4 TM data and equivalent histograms for a portion of Landsat-4 TM scene 40037-16031 collected on 22 August 1982 over the Arkansas/Tennessee region. While the overall shapes are, for the most part, similar, in all cases the simulated data occupy a lower range of signal counts than the real data. However, given the known differences in sun elevation, haze level, and scene content between the simulated and actual data sets, the histograms indicate that the simulation provides an acceptable base for analysis of the spectral characteristics of TM data.

Three-Band TM Vs. MSS

Figure 4 shows the Tasseled Cap plane, as derived from the simulated data, for Landsat-4 MSS data, and for Landsat-4 TM bands 2, 3 and 4. The obvious similarity between the two is made even clearer in Figure 5, which directly compares the Greenness and Brightness features derived for the two data sets. In this agriculturally-oriented data set, the three TM bands provide a data space equivalent to the four MSS bands, but with greater dynamic range. The omission of the 0.9 to 1.1 μm region in the TM data (measured by MSS Band 4) causes no apparent loss of information in this agricultural data set. While this spectral region may be important for particular applications, the analyses reported here suggest that in general, the three TM bands can be assumed to provide an MSS-equivalent data space.

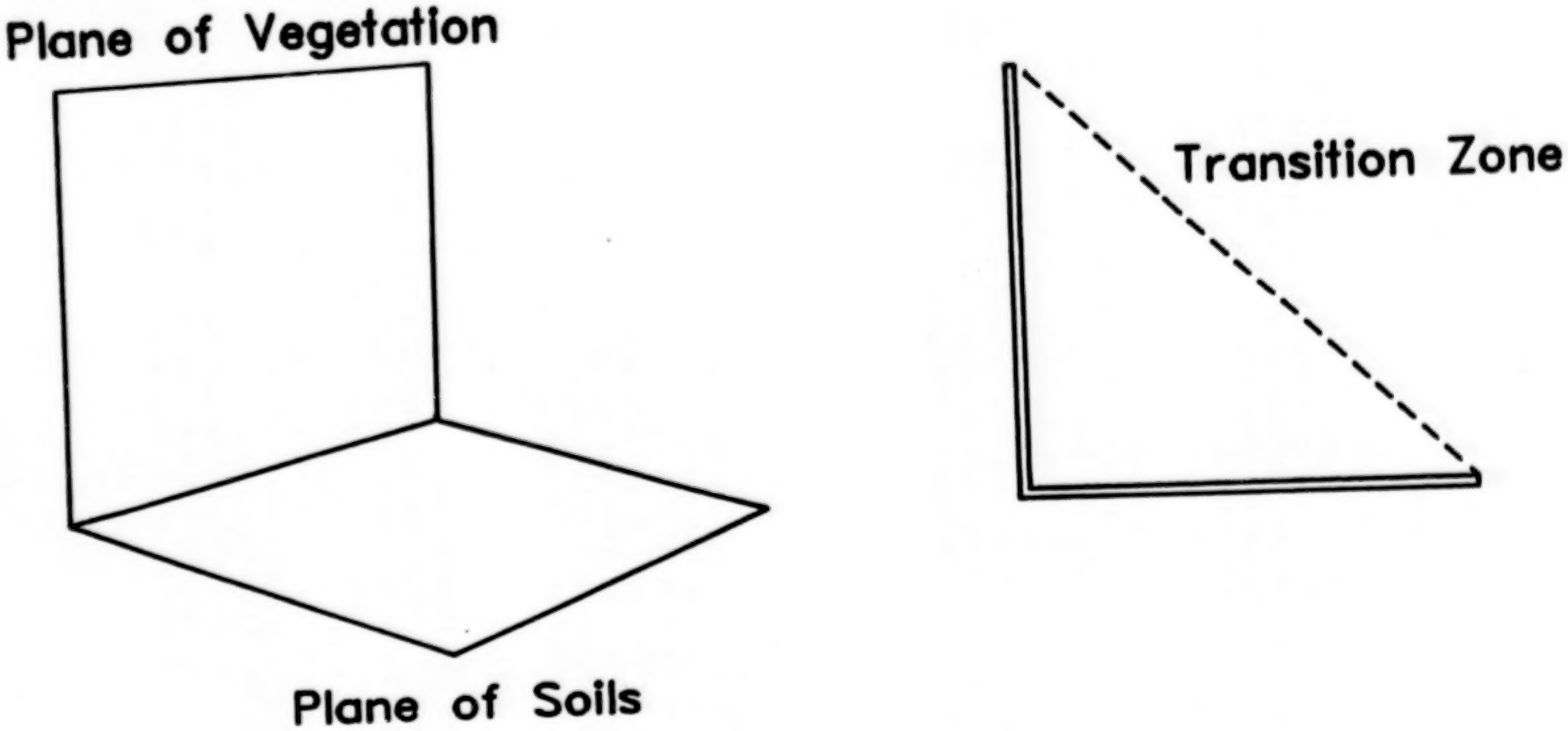
Plane of Vegetation
Transition Zone
Plane of Soils

Figure 1. Structure of Simulated Thematic Mapper Data

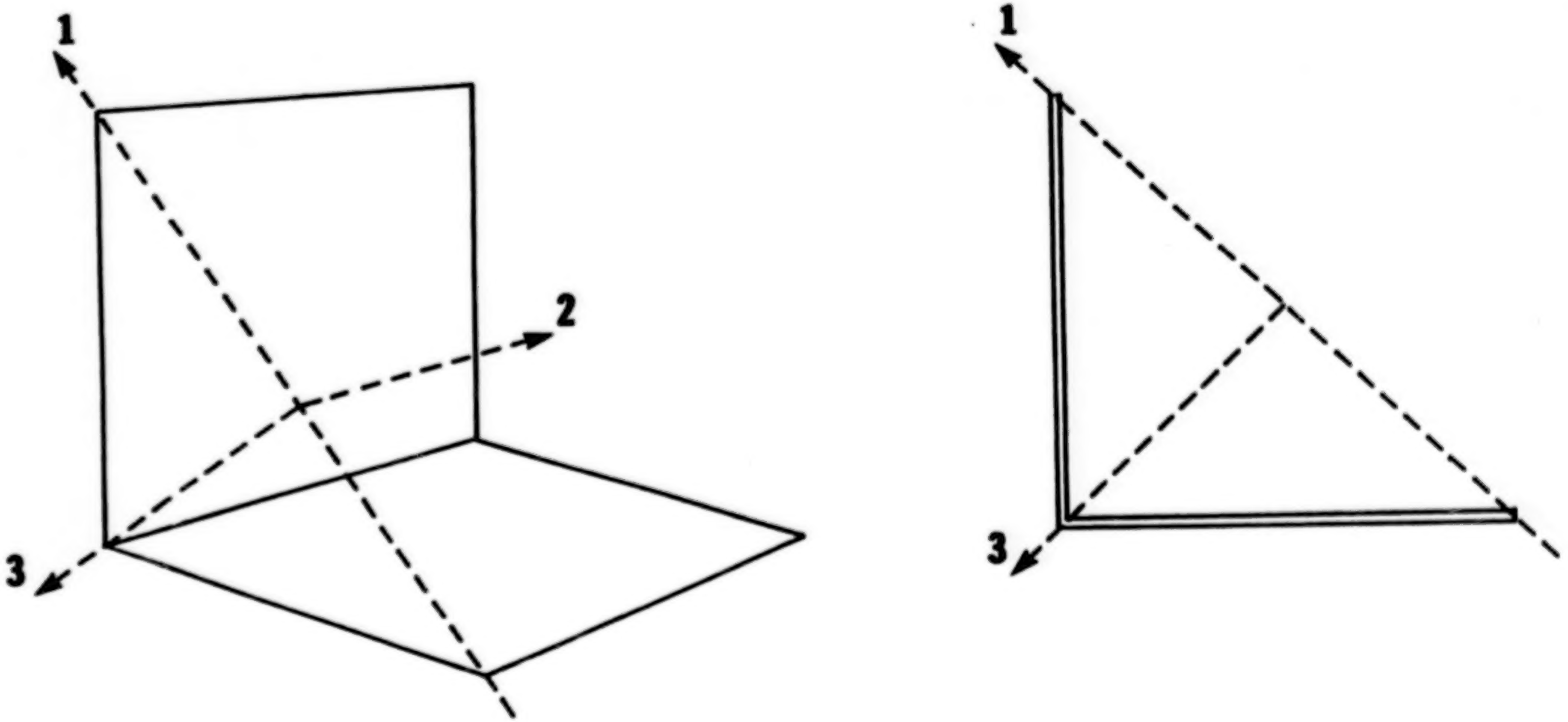

Figure 2. Principal Components of Complex Data Structure

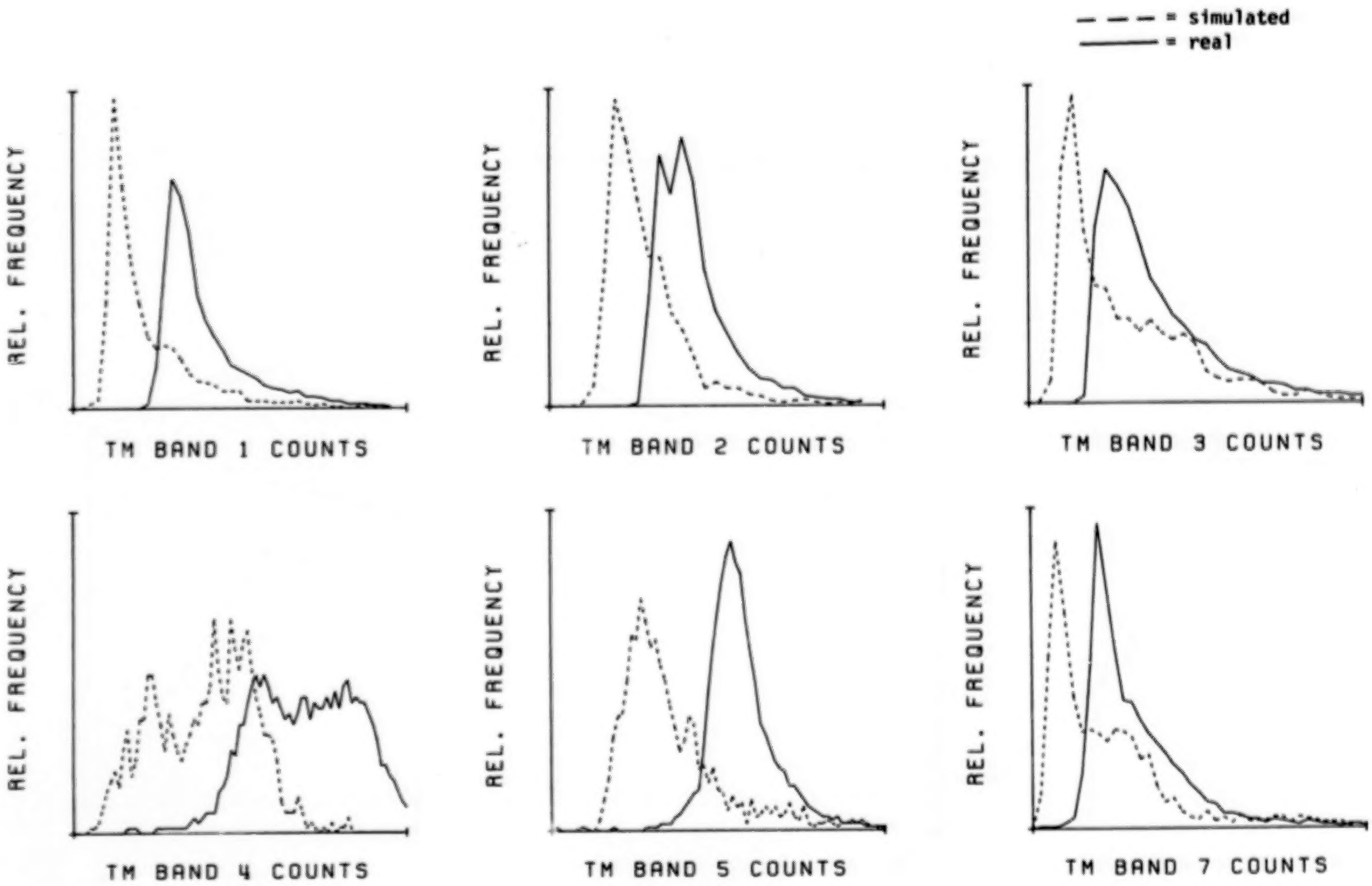

Figure 3. Comparison of Real and Simulated Data

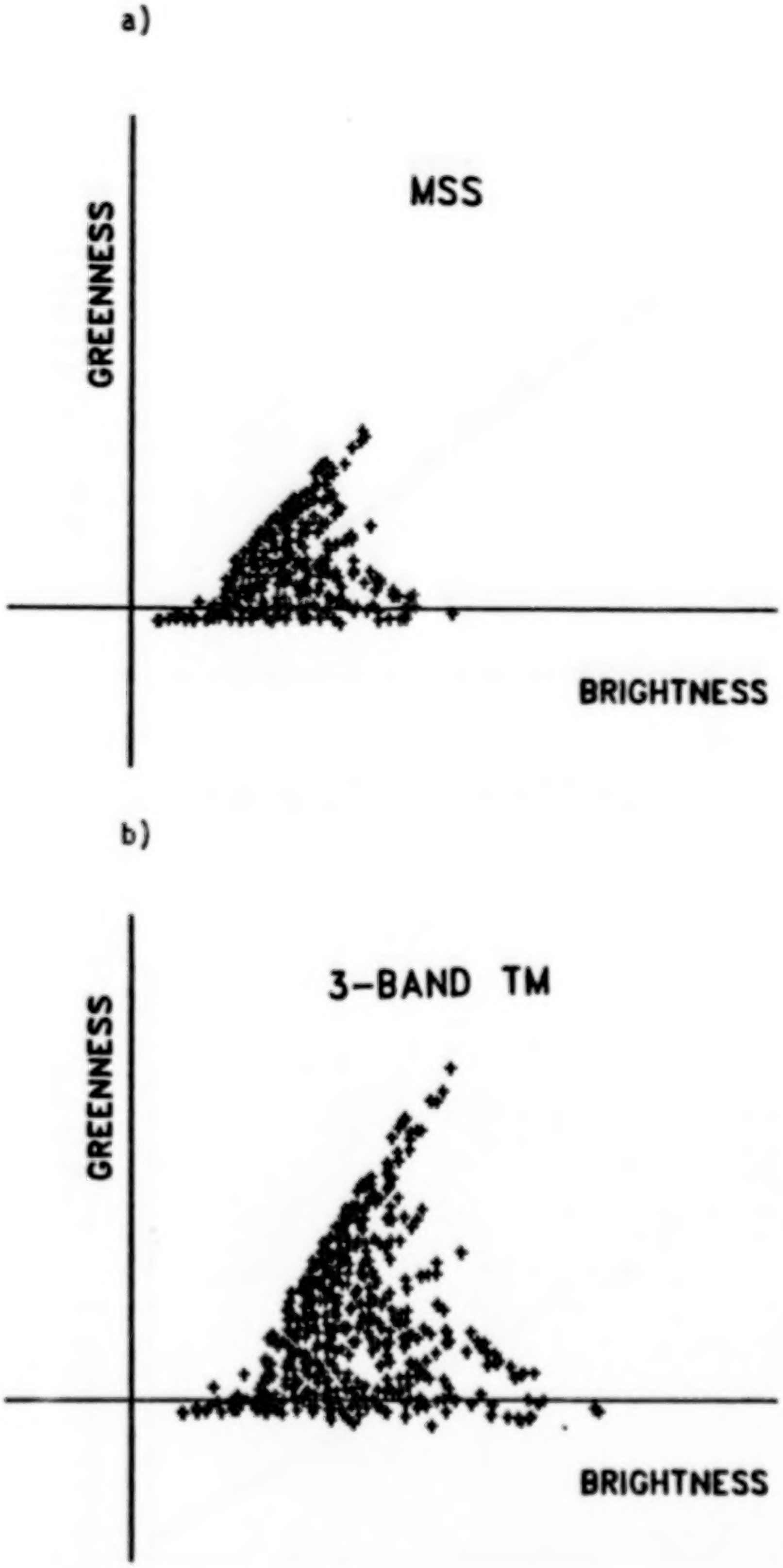

Figure 4. Simulated Landsat-4 MSS and 3 Band TM Tasseled Cap Plane

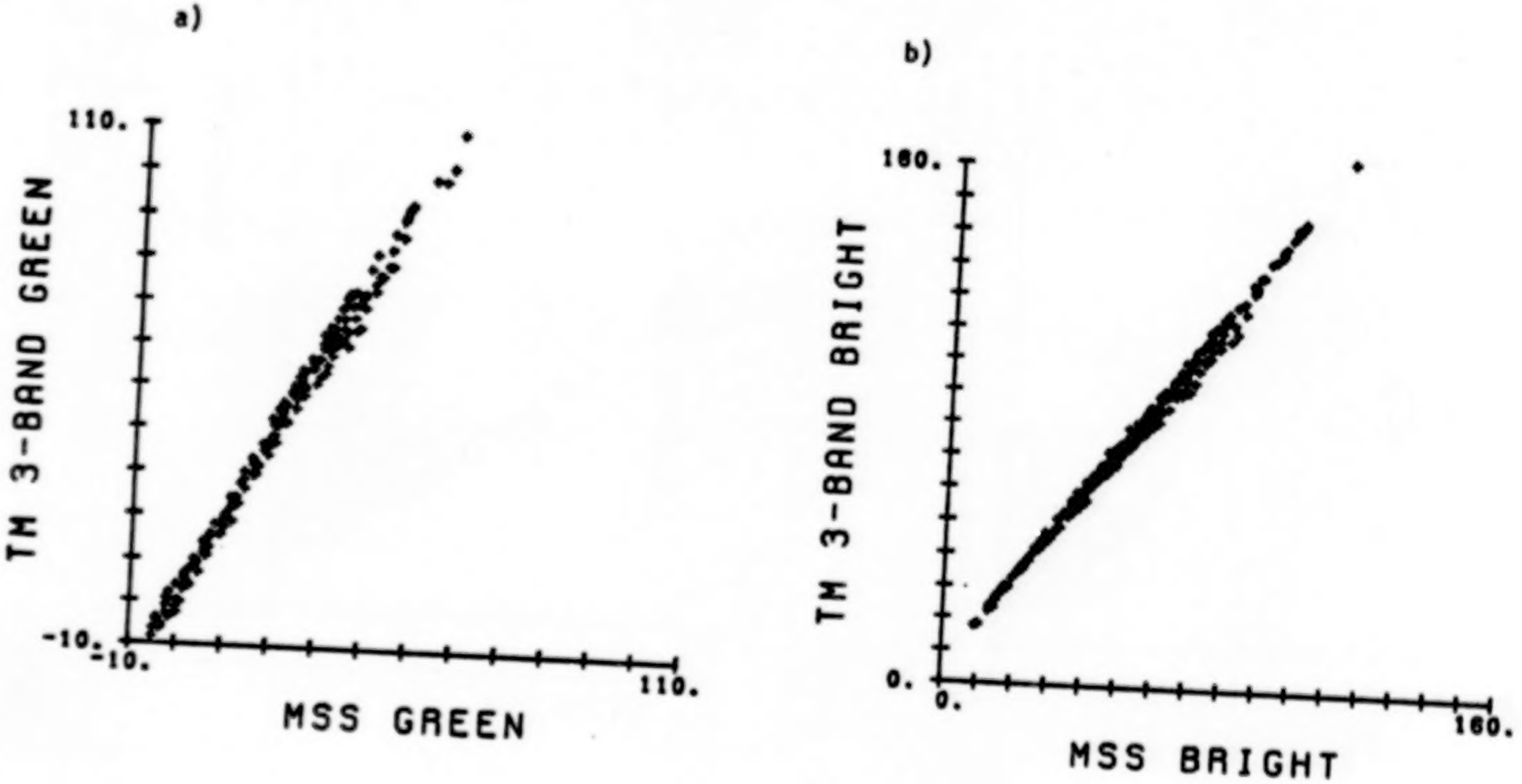

Figure 5. Comparison of Simulated Landsat-4 MSS and 3-Band TM Tasseled Cap Features

Six-Band Thematic Mapper Tasseled Cap

Data from the six reflective TM bands are primarily oriented into two perpendicular planes, as depicted in Figure 1. Thus, as suggested by Holmes, TM data provide at least one additional important dimension as compared to MSS data. The "Plane of Vegetation" shown in Figure 6 is essentially equivalent to the MSS or three-band TM Tasseled Cap planes. Figure 7 shows that the Greenness feature derived from the six-band TM data is very highly correlated to MSS Greenness (>0.99), while some small differences attributable to the influences of the longer infrared TM Bands can be seen in the Brightness features for the two sensors. In TM Greenness, the coefficients for the longer infrared bands are such that they cancel each other out, leaving a more MSS-like Greenness.

Rotating the data 90-degrees about the Greenness axis, we achieve a view of the edges of the two data planes, and the "Transition Zone" between them (Figure 8). Figure 9 provides the same perspective, but only particular samples of the data are plotted. Here one can see clearly that the "Plane of Vegetation" is occupied by data from fully-vegetated ground samples, while the "Plane of Soils" contains only soils data. Those data not displayed in Figure 9 are the samples of partial vegetated cover, where both vegetation and soil are visible to the sensors. These data are "in transition" between the Plane of Soils and the Plane of Vegetation. A third view, obtained by rotating the view in Figure 6 90-degrees about the Brightness axis, shows the Plane of Soils. It should be noted that all variation off the Plane of Vegetation, in either the Transition Zone or the Plane of Soils, is new information available in TM data but not detectable in MSS data.

The lesser features of the TM Tasseled Cap Transformation are illustrated in Figure 11. Even in the fourth feature, a degree of soils-related information is apparent. However, this information, along with any possible information in the fifth and sixth features, has not yet been analyzed in detail.

The transformation matrix for converting simulated Landsat-4 TM data to TM Tasseled Cap coordinates is provided in Table 1.

Physical Drivers in TM Tasseled Cap Space

The similarity of the TM Plane of Vegetation and the MSS Tasseled Cap plane suggests that the relationship between physical scene characteristics and spectral variation in the former should be much as described in Reference 1. While the greater dynamic range and improved signal-to-noise ratio of the Thematic Mapper may allow extraction of more detailed information from this plane, basic processes and influences should remain essentially unchanged, save for some influence of the longer-infrared bands on TM Brightness.

However, variation in the third dimension of the TM Tasseled Cap space cannot a priori be associated with MSS data variation, or explained in terms of physical processes in the MSS Tasseled Cap plane. The added dimension in the TM Tasseled Cap space may allow detection of entirely new

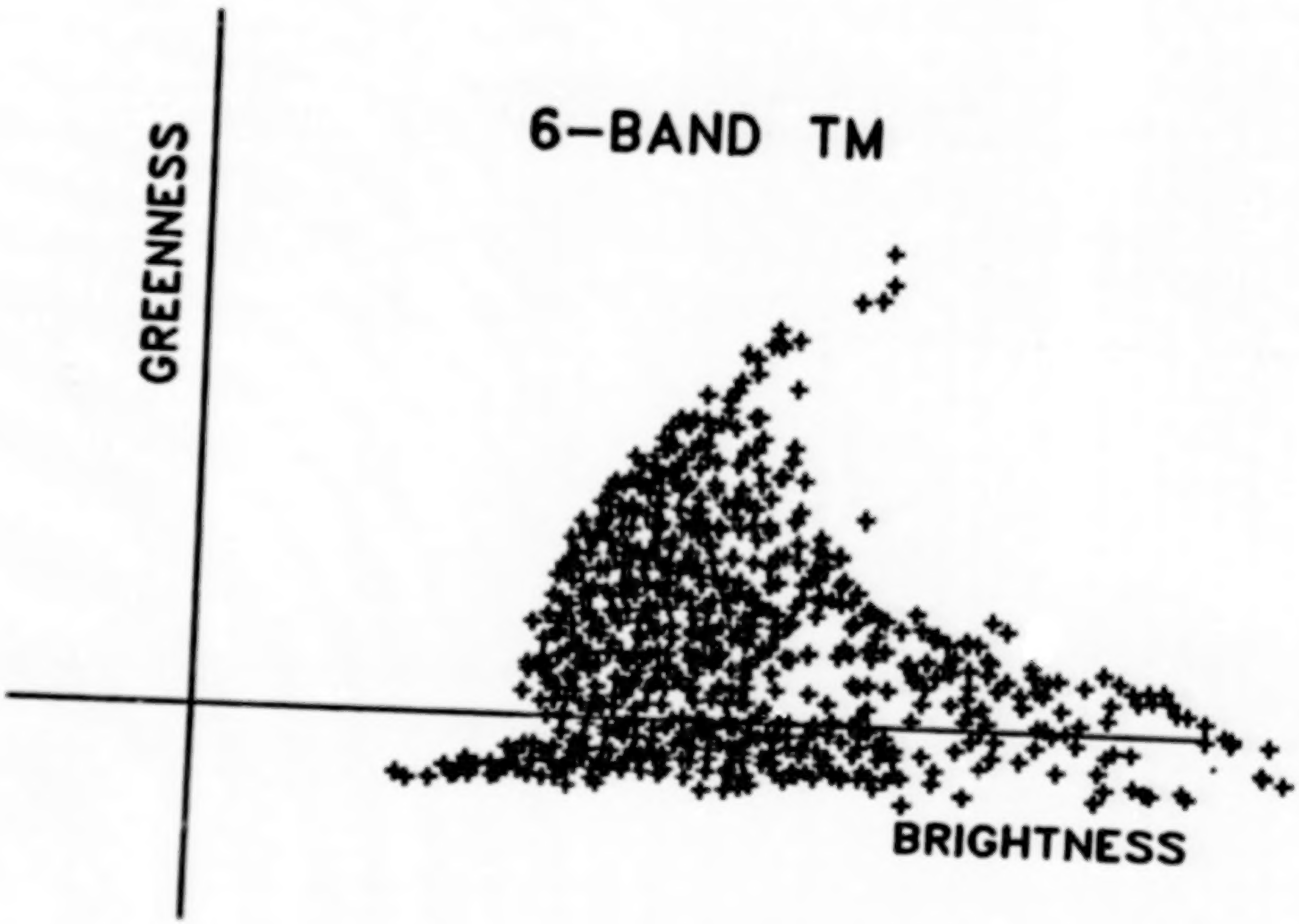

Figure 6. Plane of Vegetation in Simulated 6-Band TM Data

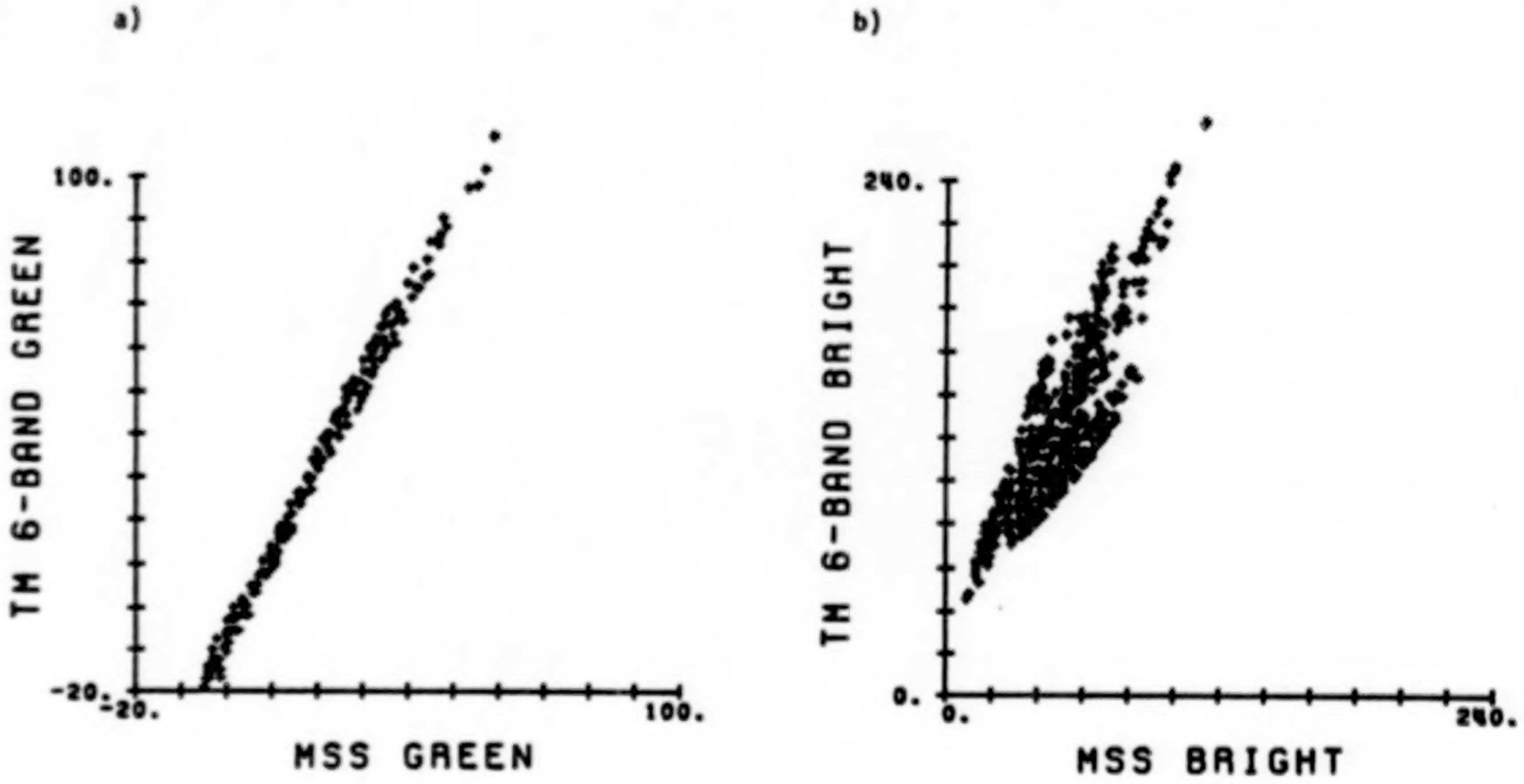

Figure 7. Comparison of Simulated Landsat-4 MSS and 6-Band TM Tasseled Cap Features

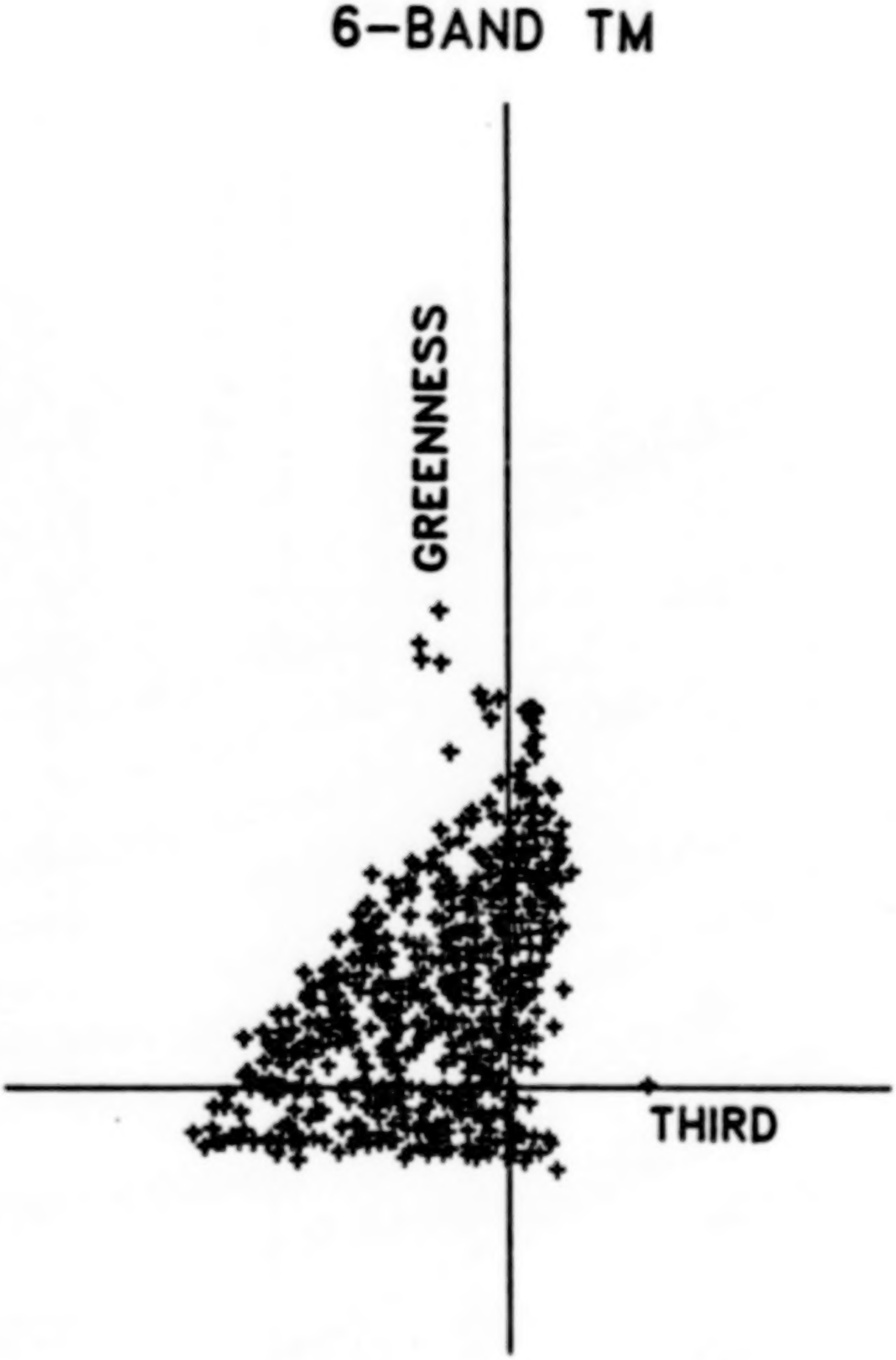

Figure 8. Transition Zone View of Simulated TM Tasseled Cap Space

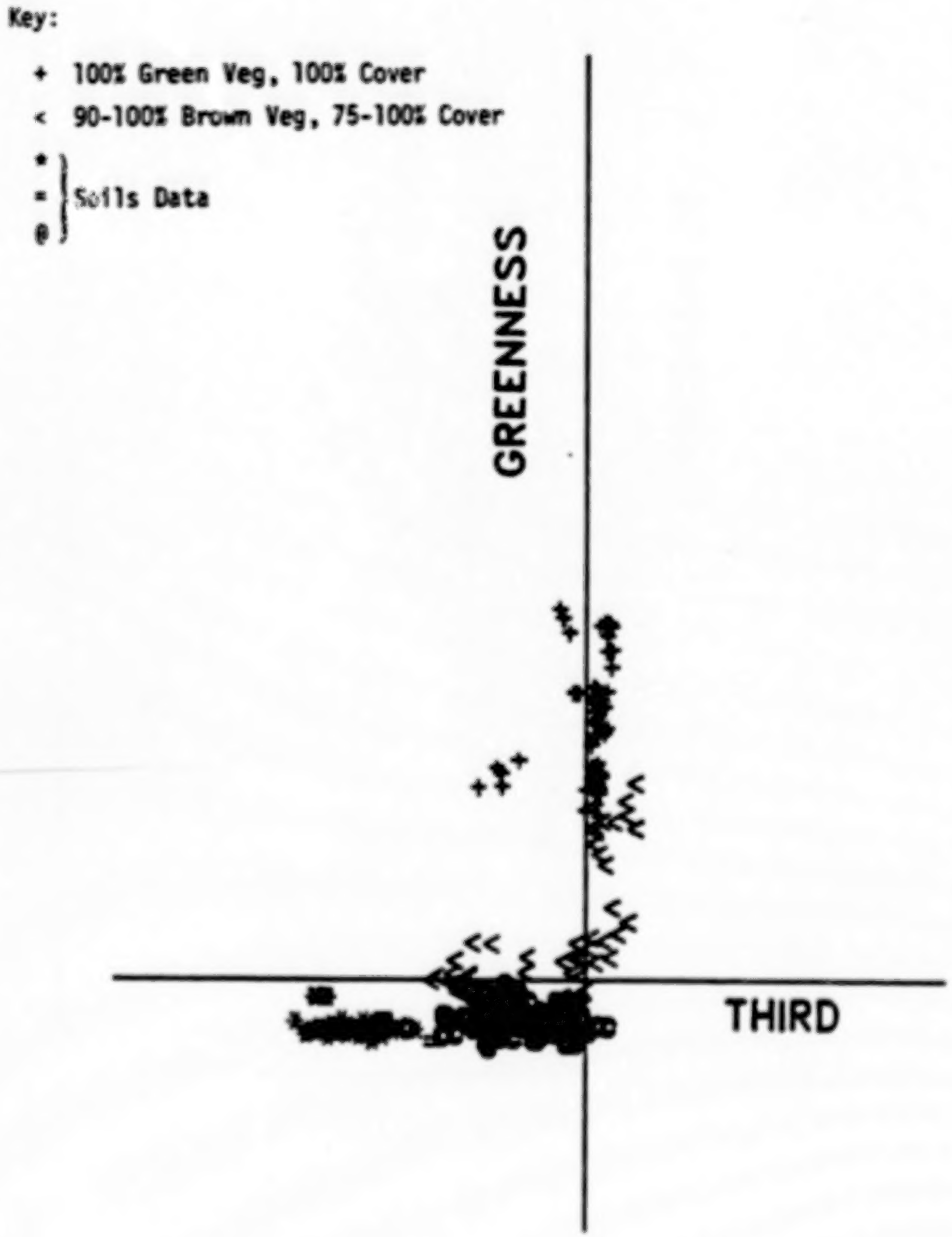

Figure 9. Transition Zone View - Data Samples

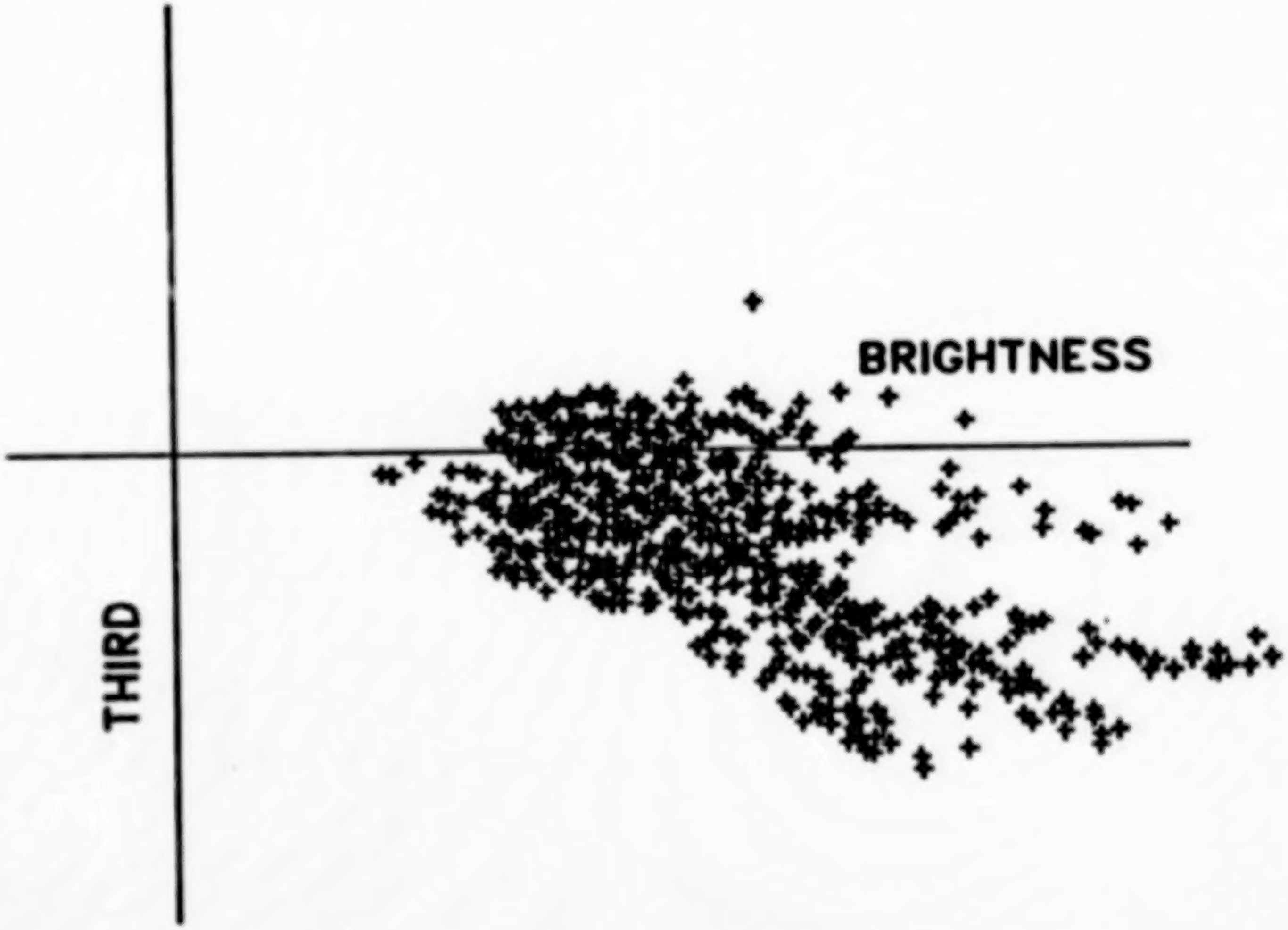

Figure 10. Plane of Soils in Simulated TM Tasseled Cap Space

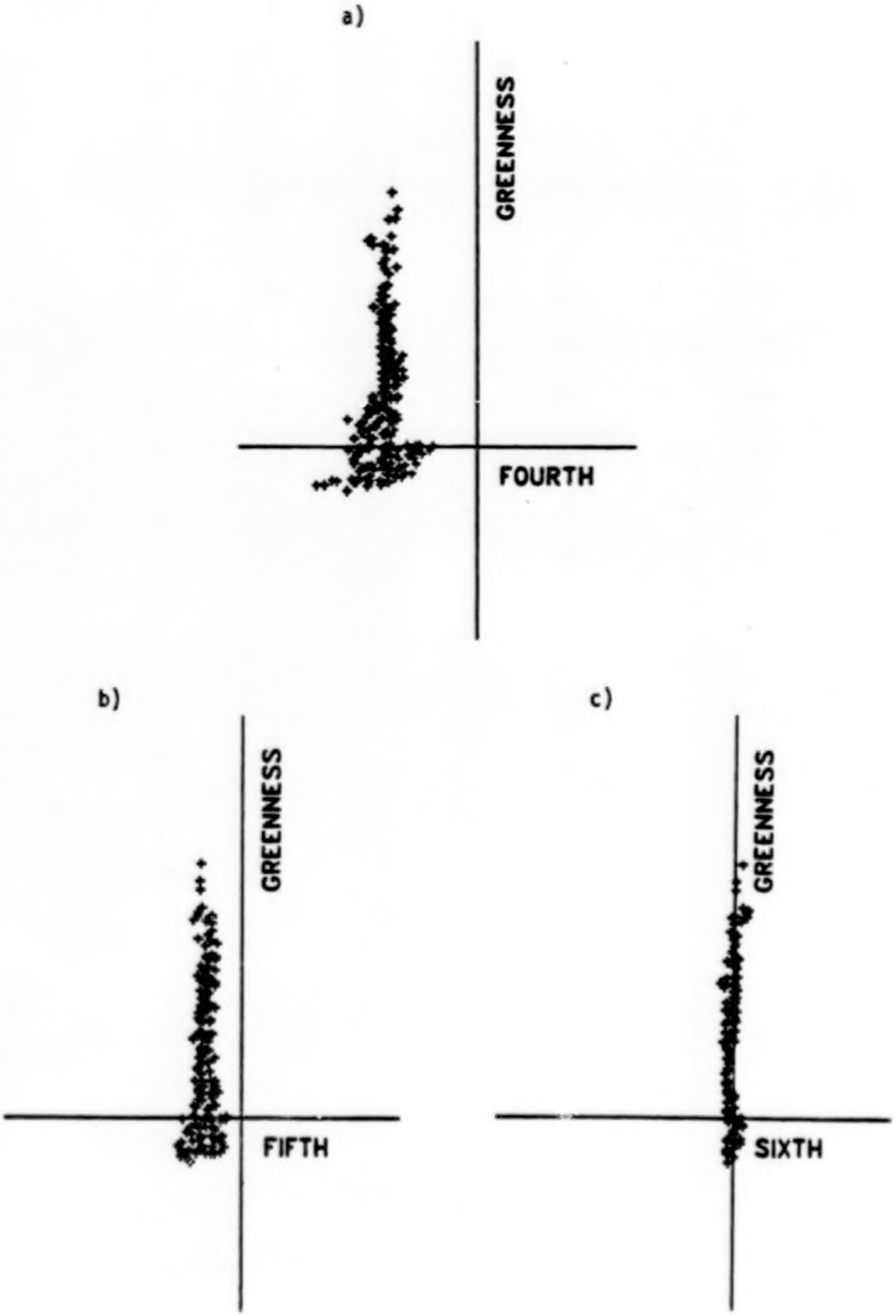

Figure 11. Lesser Features of Simulated TM Tasseled Cap Transformation

Table 1

TM TASSELED CAP TRANSFORMATION
SIMULATED DATA

.33	.33	.55	.43	.48	.25
-.25	-.16	-.41	.85	.05	-.12
.14	.22	.40	.26	-.70	-.46
-.83	.07	.42	-.08	.24	-.25
-.33	.05	.11	.11	-.47	.81
.11	-.90	.42	.07	-.02	.03

events, or may enhance the ability to detect various conditions or events which are also visible, if less readily identifiable, in the MSS Tasseled Cap plane. Two physical characteristics will be briefly discussed which fall into the latter category: the percentage of vegetation in the field of view and soil moisture status.

In the Plane of Vegetation, increases in the vegetation/soil ratio in the field of view are expressed as movement toward the "green arm". This effect is illustrated in Figure 12 using 100% green vegetation samples. A clear path can be traced from low vegetative cover to complete cover, with varying degrees of overlap. In the TM Tasseled Cap Transition Zone, a similar path can be traced (Figure 13). However, in this view canopy closure is associated with arrival at the Plane of Vegetation. Detection of percent cover is thus potentially easier in TM Tasseled Cap space for two reasons: 1) the spectral movement is now three-dimensional instead of two-dimensional, possibly allowing greater discrimination between less distinct classes and 2) full cover is represented by a plane perpendicular to the Third feature, rather than a less precise "green arm" which is at an angle to both the Greenness and Brightness axes, and as such is more difficult to define. Determination of the actual enhancement of percent-cover detection resulting from the third dimension in the TM Tasseled Cap space is a topic of current research.

Soil moisture status is expressed in the Brightness dimension of the Plane of Vegetation (or MSS Tasseled Cap plane), with drier soils appearing brighter. Figure 14 shows the soils data in the Plane of Soils, with three groups delineated: moist laboratory-meeasured soils, bare soil field plots and bare sand field plots. Because moisture content is the most obvious distinguishing feature between the lab soils and the "typical" field soils, the Third feature differences between these groups are likely associated with moisture variation. In addition, the field plot data (soil or sand) represent multi-temporal observations of a few homogeneous plots. Thus the variation within these two groups must be associated not with differences in intrinsic soil characteristics but with differences in soil conditions. In the course of a growing season, moisture status is perhaps the most likely of such conditions to vary.

Additional evidence of the effect of moisture on the Third feature is provided by the laboratory-measured soils data. Within the lab soils, variation in moisture percentage by weight occurs even though moisture tension is held constant [11]. Selecting pairs of samples from single soil series which show the maximum variation in moisture by weight and minimum variation in other potentially important properties thus provides another means of observing the effect of moisture status. Figure 15 illustrates the results, with arrows showing both the magnitude and direction of change in the Plane of Soils associated with an increase in moisture content. None of the other properties considered (including particle size distribution, organic matter content, and iron oxide content) showed as great a magnitude or directional preference of change as that associated with soil moisture.

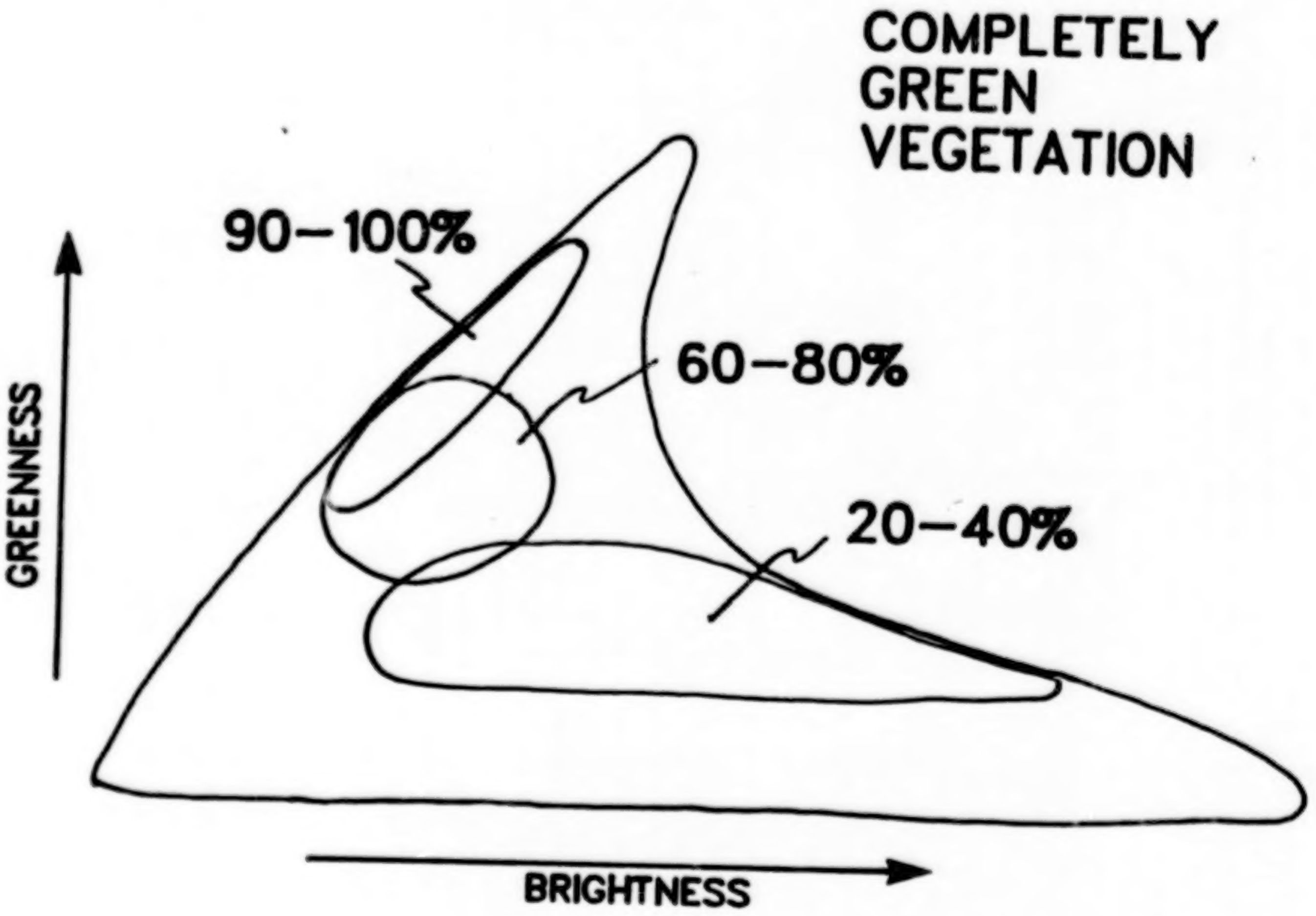
COMPLETELY
GREEN
VEGETATION
90–100%
60–80%
20–40%
GREENNESS
BRIGHTNESS

Figure 12. Effects of Increasing Vegetative Cover in the Plane of Vegetation

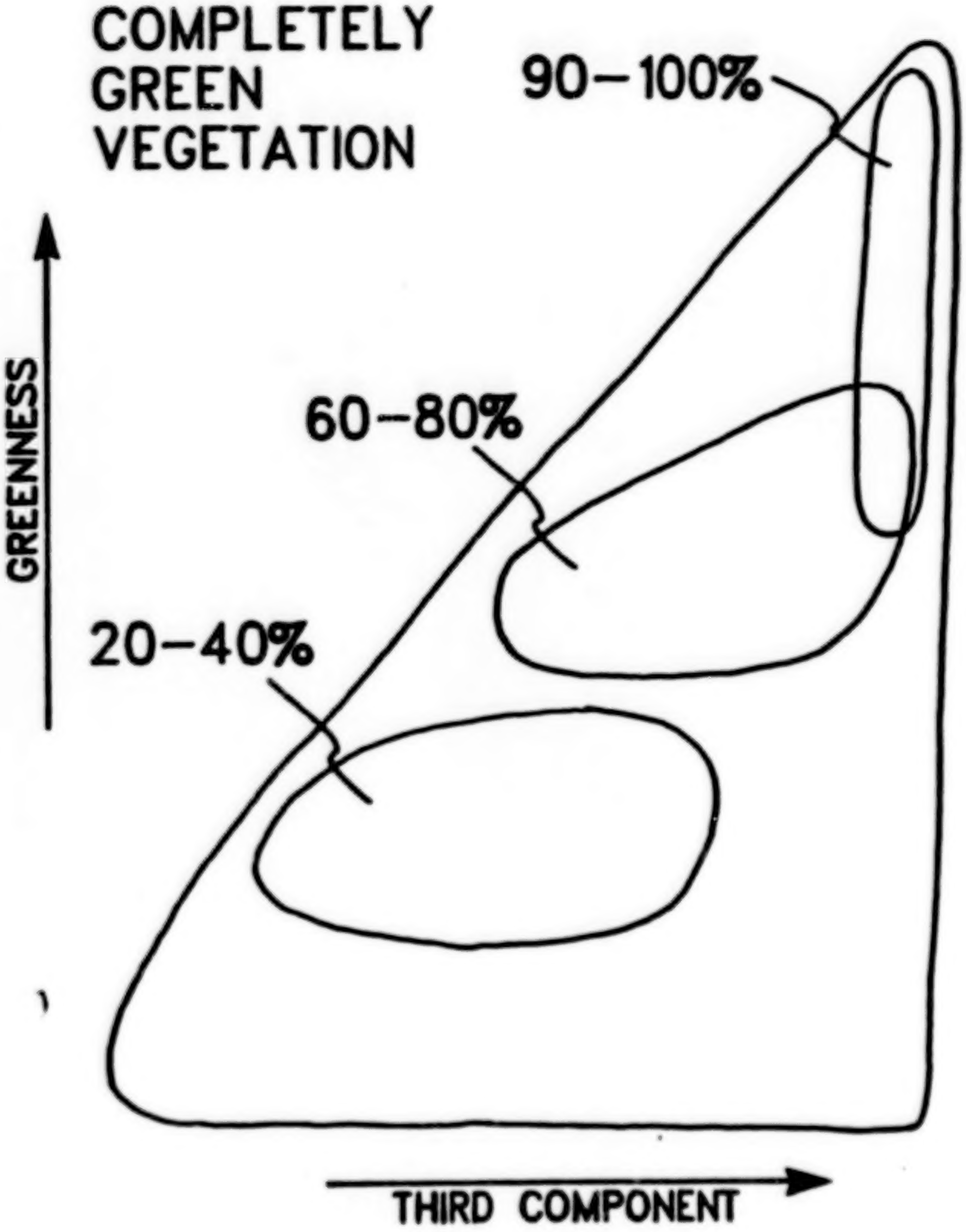
COMPLETELY GREEN VEGETATION
90–100%
60–80%
20–40%
GREENNESS
THIRD COMPONENT

Figure 13. Effects of Increasing Vegetative Cover in the Transition Zone

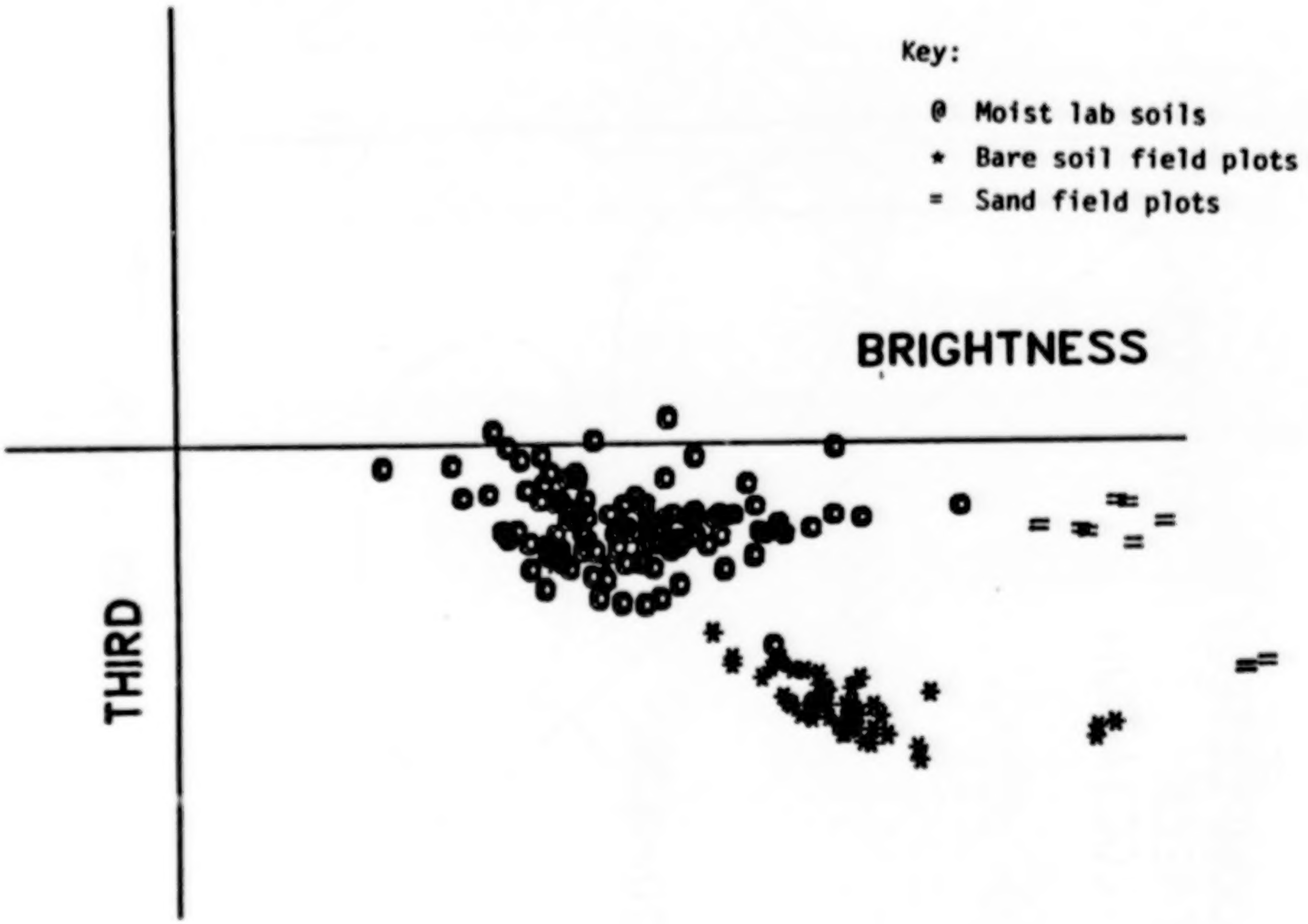

Figure 14. Dispersion of Soils Data in the Plane of Soils

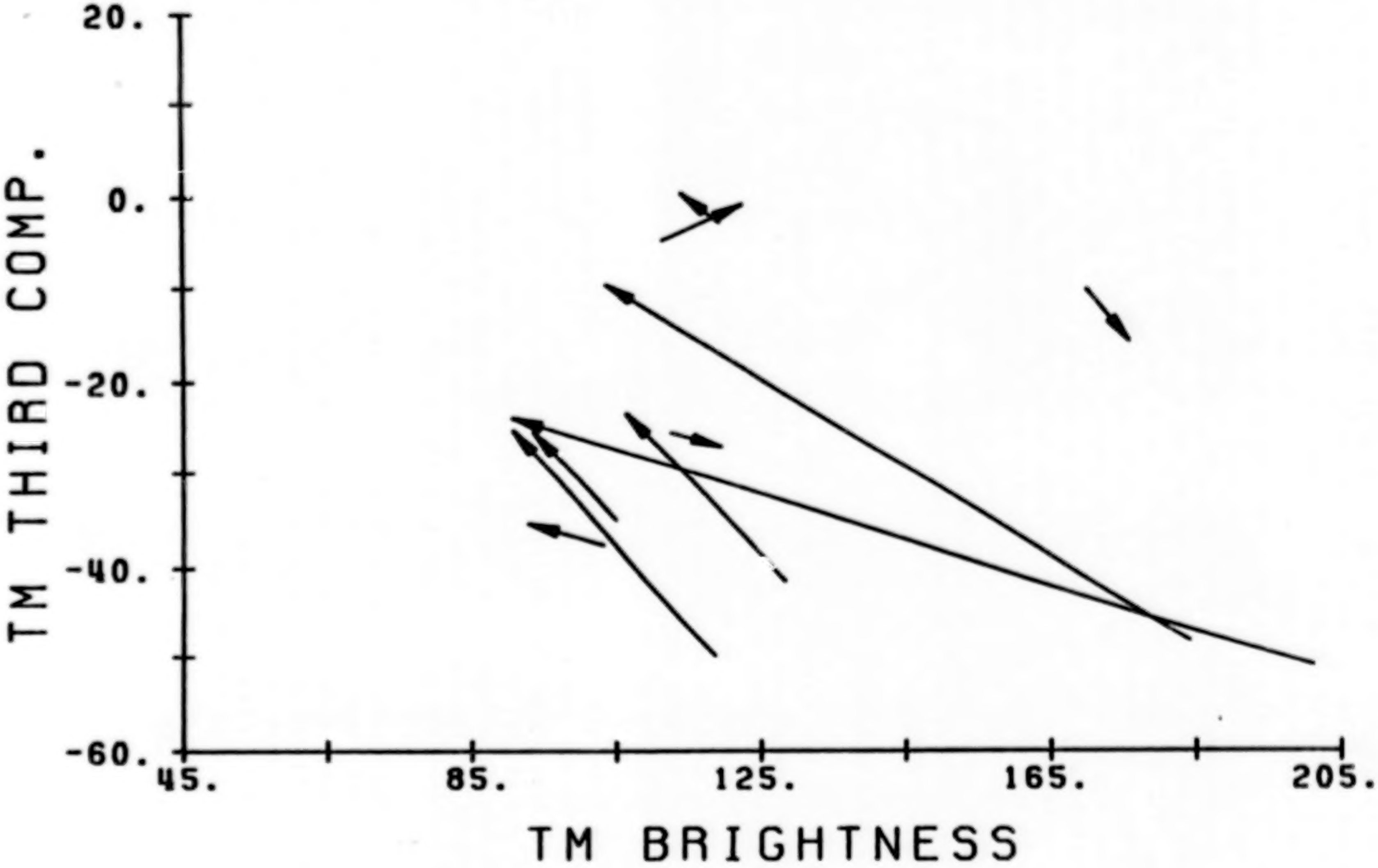

Figure 15. Magnitude and Direction of Change in Plane of Soils Associated With Increasing Percentage Moisture by Weight - Lab Soil Samples

The evidence is thus strong that soil moisture exerts an important influence on data in the Plane of Soils. Figure 14 can also be used to illustrate the enhanced ability to detect this effect as a result of the Third TM Tasseled Cap feature. While the drier bare soil and sand plots (lower Third feature values) are indeed brighter than the wetter (higher Third feature values) samples in their respective groups, all the sand plots are brighter than any of the bare soil plots, and many of the moist lab soils are as bright as some of the dry field soil plots. In the two dimensions of the TM Tasseled Cap Plane of Soils, however, the distinctions between moist lab soils and dry field soils, and between drier and wetter bare soil and sand plots, are much more apparent. One explanation may be that changes in Brightness appear to be correlated to relative changes in soil moisture, but a particular Brightness value cannot be associated with a particular soil moisture content. The Third TM Tasseled Cap feature, on the other hand, may be more directly associated with absolute moisture status. If this is the case, soil moisture content will be more easily measured using Thematic Mapper Tasseled Cap data.

SUMMARY AND CONCLUSIONS

A simulated Landsat-4 TM and MSS data set, representing three crops over three growing seasons and a wide variety of soil types, was used to evaluate the structure of TM data and to compare its characteristics to those of MSS data. TM Bands 2, 3 and 4, transformed to Tasseled Cap-like coordinates, provide an equivalent data space to MSS Tasseled Cap data, with greater dynamic range and no apparent loss of information resulting from the exclusion of the 0.9 to 1.1 μm region.

Data from the six reflective TM bands (excluding the thermal band) primarily occupy two planes and a "Transition Zone" between them. The "Plane of Vegetation" is comparable to the MSS Tasseled Cap plane, while the "Plane of Soils" and "Transition Zone" provide a new dimension of information unavailable from the MSS. This added dimension offers promise of improved ability to determine the relative mix of vegetation and soil in the sensor field of view and to estimate soil moisture status.

The added complexity of TM data over that collected by the MSS is such that full understanding of the potential uses for and physical effects in those data will only be achieved over time, as experience with both simulated and actual data is gained. Certainly the conclusions drawn in this paper must be tested and revised, as necessary, using actual TM data. What is clear, however, is that the improvement in spectral characteristics of the TM over the MSS, not to mention the greater spatial resolution, have resulted in a significant increase in the information content of the data.

References

1. Kauth, R.J. and G.S. Thomas, The Tasseled Cap -- A Graphic Description of the Spectral-Temporal Development of Agricultural Crops as Seen by Landsat, Proceedings of the Symposium on Machine Processing of Remotely Sensed Data, Purdue University, W. Lafayette, IN, 1976, pp.4B41-4B51.

2. Holmes, Q.A., Unpublished data, 1979.

3. Badhwar, G.D. and K.E. Henderson, A Comparative Study of the Thematic Mapper and Landsat Spectral Bands from Field Measurement Data, NASA Report SR-J0-04029, NASA Johnson Space Center, Houston, TX, 1981.

4. Crist, E.P. and R.C. Cicone, Application of the Tasseled Cap Concept to Simulated Thematic Mapper Data, Photogrammetric Engineering and Remote Sensing (submitted), 1983.

5. Crist, E.P. and R.C. Cicone, Comparison of the Dimensionality and Features of Simulated Landsat-4 MSS and TM Data, Remote Sensing of Environment (submitted), 1983.

6. Biehl, L.L., M.E. Bauer, B.F. Robinson, C.S.T. Daughtry, L.F. Silva and D.E. Pitts, A Crops and Soils Data Base for Scene Radiation Research, Proceedings of the Symposium on Machine Processing of Remotely Sensed Data, Purdue University, W. Lafayette, IN, 1982, pp.169-177.

7. Dave, J.V., Extensive Datasets of the Diffuse Radiation in Realistic Atmospheric Models with Aerosols and Common Absorbing Gases, Solar Energy, 21:361-369, 1978.

8. Barker, J.L., Spectral Characterization of Landsat-D Thematic Mapper Subsystems, NASA Technical Memorandum, NASA Goddard Space Flight Center, Greenbelt, MD, 1983.

9. Markham, B.L. and J.L. Barker, Spectral Characterization of Landsat-D Multispectral Scanner Subsystems, NASA Technical Memorandum 83955, NASA Goddard Space Flight Center, Greenbelt, MD, 1982.

10. Landsat-D Investigations Workshop, NASA Goddard Space Flight Center, Greenbelt, MD, 13-14 May 1982 (briefing materials).

11. Stoner, E.R. and M.F. Baumgardner, Physiochemical, Site, and Bidirectional Reflectance Factor Characteristics of Uniformly Moist Soils, LARS Technical Report 11679, Laboratory for Applications of Remote Sensing, Purdue University, W. Lafayette, IN, 1980.

N85-21737

Dee
13

MTF ANALYSIS OF LANDSAT-4 THEMATIC MAPPER

Robert Schowengerdt
Arizona Remote Sensing Center
University of Arizona
Tucson, Arizona 85721

INTRODUCTION

Measurement of a satellite sensor's MTF requires the use of a calibrated ground target, i.e. the spatial radiance distribution of the target must be known to a resolution at least four to five times greater than that of the system under test. Any radiance structure smaller than this will have a small effect on the calculated MTF. Calibration of the target requires either the use of man-made special purpose targets with known properties, e.g. a small reflective mirror or a dark-light linear pattern such as line or edge, or use of relatively high resolution underflight imagery to calibrate an arbitrary ground scene. Both approaches will be used in this program; in addition a technique that utilizes an analytical model for the scene spatial frequency power spectrum will be investigated as an alternative to calibration of the scene.

TM SYSTEM CHARACTERISTICS

The characteristics of digital scanning sensors such as the TM influence the selection of targets-of-opportunity or the design of special purpose targets for MTF measurement. The three most important sensor characteristics are:

Two-dimensional performance

The sampling and signal processing characteristics of the TM are different along-scan and across-scan (along-track). Thus, the MTF is at least bi-directional and therefore requires a two-dimensional target for measurement.

Sampled imagery

The TM produces sampled, digital imagery. The impact of this is that the relative sub-pixel location of the pixel (sample) grid and the scene affects the quality of the imagery. This effect, called sample-scene phase, has been analyzed in one-dimension by Park and Schowengerdt (1982).

Multispectral imagery

Target reflectance characteristics may vary from band-to-band causing a change in target contrast. Furthermore there may be small-scale spatial variations in reflectance that change from band-to-band.

PAGE III-466 INTENTIONALLY BLANK

PRECEDING PAGE BLANK NOT FILMED

The following conclusions about MTF target characteristics may be drawn from the above observations:

(1) The MTF should be measured in at least two directions, along- and across-scan.

(2) The sample-scene phase effect must be accounted for in MTF analysis. The most direct approach would be ensemble averaging over the range of possible phases.

(3) The spectral and spatial characteristics of any MTF target should be measured.

MTF MEASUREMENT TECHNIQUES

There are several ways to measure a satellite system's MTF. Absolute approaches require the use of known, special-purpose targets or independent calibration of arbitrary targets. Relative approaches permit only comparison of the quality of different data sets, for example between detectors. In all cases it is desirable to use targets with high spatial frequency content, i.e. edges, lines, points, etc. The techniques to be used in this project are:

Two-image analysis

This approach was originally applied to MTF measurement of the Landsat-1 MSS (Schowengerdt, 1976). It requires a near-simultaneous aircraft underflight with a sensor similar to that in the satellite. The aircraft imagery provides a high resolution calibration of an arbitrary scene in the same spectral bands as those of the satellite sensor.

Special targets

Candidate targets are high contrast edges, lines, combs (periodic bars), and point sources. Comb targets have signal-to-noise advantages at certain spatial frequencies. For all of these targets several parameters must be balanced to obtain a suitable target, for example the shape, contrast, size and material characteristics. The image of an edge, line, or point source is the Edge Spread Function (ESF), Line Spread Function (LSF) or Point Spread Function (PSF), respectively. Each is related in some manner to the MTF via Fourier transformation. For example, the magnitude of the 2-D Fourier transform of the PSF is the 2-D MTF and the magnitude of the 1-D Fourier transform of the LSF is a 1-D cross section of the 2-D MTF at a given azimuth angle. Furthermore the LSF is the derivative of the ESF.

Power spectrum analysis

The ensemble average of spatial frequency content for a statistical sample of image data is called the power spectrum. It may be used to compare relative data quality from detector-to-detector or between forward and reverse scans without calibrating the absolute spatial frequency content of the data.

RESEARCH PLANS

We plan to utilize all of the above techniques in this program to measure the TM MTF. Specifically the following is planned:

(1) Three TM/underflight acquisitions in the San Francisco area. The two-image analysis technique will be used on these data to measure TM MTF from three scene dates over a period of about one year. The NS001 scanner will likely be used in the aircraft underflights.

(2) Two or three TM acquisitions of the White Sands National Monument area will be used to image the black-on-white runway markers at the Shuttle land site (Northrup Strip). These markers are in the subpixel-to-pixel size range and are therefore possibly suitable for MTF measurement. In addition the feasibility of creating new, special-purpose targets in a similar manner is being pursued with the Army at the White Sands Missile Range. MTF measurements in the White Sands area have the advantage of collaboration with Dr. P. N. Slater and his radiometric measurement activities there. These data will be valuable for characterization of the atmospheric effect on MTF measurement.

(3) Targets-of-opportunity such as bridges, highways, etc. will be analyzed as available. Work has begun on analysis of the Washington DC scene acquired on November 2, 1982 (ID# 4020915140) in both the A and P formats to evaluate the relative image quality of each. There are several bridges and roads in the scene that are candidate targets. In addition, deployment of several small, reflective mirrors (Evans, 1974) is anticipated in conjunction with the San Francisco acquisitions. These mirrors will represent high intensity point sources and consequently are ideal for MTF measurements, if no sensor saturation occurs.

ACKNOWLEDGEMENTS

This research is being conducted jointly by the University of Arizona and NASA/Ames Research Center under the contract "An Investigation of Several Aspects of Landsat-D Data Quality," Robert C. Wrigley, principal investigator.

REFERENCES

1. Evans, W.E., "Marking ERTS Images with a Small Mirror Reflector," Photogrammetric Eng., Vol. 40, No. 6, 1974, pp. 665-671.

2. Park, S. K. and R. A. Schowengerdt, "Image Sampling, Reconstruction, and the effect of Sample-Scene Phasing," J. Appl. Opt. 21(17), 1982, pp. 3142-3151.

3. Schowengerdt, R. A., "A method for determining the operational imaging performance of orbital earth resources sensors," Proc. of the annual Am. Soc. of Photogrammetry Convention, February 1976, pp. 25-62.

N85-21738

D~~23~~
14

INTRABAND RADIOMETRIC PERFORMANCE OF THE LANDSAT 4 THEMATIC MAPPER

Hugh H. Kieffer, Eric M. Eliason, Pat S. Chavez, Jr.

U.S. Geological Survey, Flagstaff, Arizona 86001

Original photography may be purchased
from EROS Data Center
Sioux Falls, SD 57198

PRECEDING PAGE BLANK NOT FILMED

C-6

PAGE III-470 INTENTIONALLY BLANK

ABSTRACT

This preliminary report examines those radiometric characteristics of the Landsat 4 Thematic Mapper (TM) that can be established without absolute calibration of spectral data. Our analysis is based largely on radiometrically raw (B type) data of three daytime and two nighttime scenes; in most scenes, a set of 512 lines were examined on an individual-detector basis. Subscenes selected for uniform-radiance were used to characterize subtle radiometric differences and noise problems. We have discovered various anomalies with a magnitude of a few digital levels or less. Virtually all of this nonideal performance is incorporated into the fully processed (P type) images, but disguised by the geometric resampling technique.

The effective resolution in radiance is degraded by a factor of about 2 by the irregular width of the digital levels. Underpopulated levels are consistent over all bands and detectors, and are spaced an average of 4 digital numbers (DN) apart. In band 6, level 127 is avoided by a factor of 30. This behavior is masked by resampling in the P data. In the radiometrically corrected (A type) data, small differences--typically, 0.8 DN--exist between the average DN for the 16 detectors in each band; the standard deviations also differ, typically by 0.4 DN.

Several detectors exhibit a change of gain with a period of several scans; the largest effect is about 4%. These detectors appear to switch between two response levels during scan-direction reversal; all the affected detectors switch simultaneously. There is no apparent periodicity to these changes. This behavior can cause small apparent differences between forward and reverse scans for parts of an individual image.

The magnitude of interdetector variation is readily seen by making an image of the first derivative in the vertical (line) direction of a flat field and stretching progressively wider ranges to gray; most detectors differ from their neighbors by 1 or 2 DN.

At high-contrast boundaries, some of the detectors in band 5 commonly overshoot by several DN and require about 30 samples to recover; this behavior occurs erratically. A small asymptotic decrease in response occurs along scanlines.

The high-frequency noise level of each detector was characterized by the standard deviation of the first derivative in the sample direction across a flat field. By this measure, the noise level is: 1.6 to 2.5 DN in band 1, 0.3 to 1.6 DN in band 2, 0.5 to 1.4 DN in band 3, 0.4 to 0.8 DN in band 4, 1.3 to 1.8 DN in band 5, and 1.3 to 2.8 DN in band 7.

A coherent-sinusoidal-noise pattern is evident in detector 1 of band 3. One-dimensional Fourier transforms show that this "stitching" pattern has a period of 13.8 samples, with a peak-to-peak amplitude ranging from 1 to 5 DN. Oscillations of the same frequency but of less than half this amplitude also occur for two other detectors in this band. Noise with a period of 3.24 samples is pronounced for most of the detectors in band 1; to a lesser extent in bands 2, 3, and 4; and at or below background-noise levels in bands 5, 6,

and 7. We have adapted and applied a noise-removal algorithm that tracks the varying-amplitude periodic noise to reduce the coherent-noise of detector 1 in band 3; this algorithm appears to work quite well.

For two areas, we determined the correlation between the six reflective bands and used it to select three groups of bands whose aggregate first principal-components contain the greatest total informaiton. A composite of the first components of bands 1, 2, and 3, bands 5 and 7, and band 4, together containing 98% of the information in the reflectance bands, has reduced the effect of noise.

INTRODUCTION

This preliminary report discusses several intrinsic radiometric characteristics of the Landsat 4 Thematic Mapper (TM). Our report emphasizes the internal consistency of the radiometry and is based on characteristics of the TM data that would not be expected in a natural scene. In particular, we have studied the differences in behavior between detectors in each of the seven bands, the noise associated with each detector, and the apparent stability of each detector, albeit with a limited time base and number of samples. We have also examined an index of relative information content of the seven TM bands.

Our report concentrates on the small deviations from ideal behavior exhibited by the TM. We emphasize that its overall behavior is excellent; nonideal behavior is barely discernible in a typical image.

Much of our work is based on the Washington, D.C., scene obtained November 2, 1982, and parts of three flat-field scenes acquired at night or over the ocean. Although these scenes have several characteristics that make them desirable for such a study, we advise caution in extrapolating these results to permanent behavior of the instrument; the results for other scenes are incorporated herein where available.

TM data are available in three formats. B data are radiometrically and geometrically raw; that is, the only ground processing has been reformatting of the scene data to account for the bidirectional scan, so that each line proceeds in the same direction. The position in the image of each scan is determined from timing marks in the instrument, and alternate scans generally are significantly offset. A data are identical in format to B data, with no geometric differences; the only corrections are to the radiometry, using a separate radiometric lookup table for each detector for an entire scene, based on the detector response to internal-calibration light levels. P data result from geometrically resampling of the A data, using a cubic convolution algorithm, as much spacecraft-position and -attitude information as is available, and the positions of ground-control points where they are known and identified.

In using the A or B data for statistical analysis, the scan offset must be carefully corrected to ensure that the same scene areas are used for both forward and reverse scans. The geometric resampling techniques used in constructing the P data makes it impossible to recover the detector with which each pixel should be associated, and so these data cannot be used for studies of detector radiometry.

Thematic Mapper Operation

Some understanding of the operational mode of the TM is essential to understanding this study, and so we include a brief review of it here.

The TM contains seven spectral bands. Bands 1 through 4 are adjacent bands in the visible and immediate infrared, and the detectors are physically adjacent in the warm focal plane. The cold focal plane contains the detectors for bands 5 and 7, in the near-infrared, and for band 6, which responds to thermal emission. In each band except 6, 16 detectors are spaced by their own width in a direction normal to the scan direction. Within each band, the even-numbered and odd-numbered detectors are on separate modules, spatially separated by approximately three instantaneous fields of view (IFOV) in the scan direction. Band 6 contains four detectors, and the linear dimensions of each detector are 4 times as great as those of the corresponding detectors in the other bands; these four detectors are also staggered. The sets of detectors in the seven bands are spaced in the scan direction by separations of 25 to 45 fields of view.

The TM actively gathers data on both directions of scan-mirror motion; i.e., 16 lines of data are collected on the forward scan, and 16 on the reverse scan. An optical scanline corrector converts the saw-toothed scan pattern resulting from the motion of only the scan mirror and the spacecraft into a rectangular pattern, and both the forward and reverse scanlines in object space are essentially perpendicular to the spacecraft track. Some confusion can result from the fact that the formal numbering of the detectors is in reverse order from their relative position in an image; i.e., the line numbers in an image increase, whereas the detector designations of each scan decrease, from north to south. In this study, the first (top, or most northerly in daytime scenes) 16 lines of a scene are taken to be in the forward direction, the next 16 lines in the reverse direction, and so forth.

Data Used

Table 1 lists the data used in this report. Image areas smaller than a full scene are referred to by starting line, starting sample; number of lines, number of samples.

Table 1

THEMATIC-MAPPER SCENES USED IN THIS STUDY

Location	Path/row	Date	Scene Identification
Washington, D.C.-------	15/33	82 Nov 02	40109-15140
NE. Arkansas-----------	23/35	82 Aug 22	40037-16031
Cape Cod, Mass.--------	11/31	82 Dec 08	40145-14492 (first 512 lines)
Roanoke, Va------------	114/210	82 Nov 08	40115-02364 (first 512 lines)
Richmond, Va-----------	112/210	82 Aug 22	40037-02230 (first 512 lines)
Silver Bell, Ariz------	36/38	82 Nov 21	40128-17263 (512X512)

Our studies of both random and coherent noise have utilized flat fields (areas of a scene with nearly constant radiance), where possible. In the Washington, D.C., scene, this procedure included areas within the Chesapeake Bay immediately southeast of Annapolis, Md., that are 512 pixels square, and an area south of the confluence with the Potomac River where 1,024 successive samples were within the bay. We have also used the first 512 lines of scenes obtained at night over Richmond and Roanoke, Va., and a marine section of the Cape Cod, Mass., scene.

STATISTICAL BEHAVIOR OF THE DETECTORS

Data Populations

Histograms of scenes with a wide range of radiance show a clear tendency for an irregular width of the digital intervals. The apparent radiance interval associated with individual digital-number (DN) levels varies by a factor of more than 3. For example, in band 4 of the northeastern Arkansas scene, DN level 71 occurs less than a third as frequently as the average for adjacent levels. The most conspicuous characteristic is an undersampling of levels spaced about 4 DN apart. These levels are consistent over all the detectors in bands 1 through 4. In band 6 (but not band 1, 4, or 5), DN level 127 is underpopulated by a factor of 30. This irregularity in the width of digital intervals decreases the effective radiance resolution by a factor of about 2.

These effects are consistent in the B data, but they may be shifted in level by the radiometric lookup-table procedure used in generating the A data. This behavior is masked by geometric resampling in the P data.

Statistical Variations Between Detectors and Correlation With Scan Direction

The variations in response between detectors are nominally corrected through use of the radiometric lookup-tables, constructed for each detector for each scene through use of the eight levels of radiance provided by the inflight calibration wand. This correction, which forms the A data, is constant throughout a scene and has the characteristic of never mapping two levels into a single level. We have thus concentrated on characteristics that would not be completely corrected by use of the lookup-tables; these characteristics are variations of behavior within a scene, particularly with regard to scan direction.

Early analysis of A data revealed banding with a period of 16 lines, which suggests a difference in response between scan directions. On that basis, detector statistics for the forward and reverse directions were derived separately. Later, detailed statistics of individual lines revealed that the scan-to-scan variations were not strictly correlated with scan direction; instead, there were two response states between which the TM switched with a irregular period of 1 to 8 (or more) scans (see next subsection). Thus, the statistical differences between forward and reverse directions are not likely to be consistent from scene to scene, and represent a lower bound on scan-dependent variations.

The first 512 lines were extracted from several different scenes. The data for band 6 were decimated by a factor of 4 in both directions to undo the fourfold replication procedure involved in constructing the computer-compatible tapes; this decimation recovered the initial behavior of the detectors. Histograms were then constructed for each detector in both scan directions (spacing by 32 lines), for a total of 200 histograms of each scene. The minimum, maximum, and mode digital levels, and the levels that would exclude at least 1% of the data at both extremes, were determined. The mean and standard deviation were determined for 3 conditions: All data levels, all levels excluding the zero level, and for the DN-level range that excluded at least 1% at both extremes. The statistics including the zero level are necessary for determining the dark current in nighttime scenes. The statistics excluding the extremes of the distribution remove the effects of extreme data errors and small features of extreme radiance in the scene, such as small clouds or glint.

Summary statistics (all DN levels) for both daytime and nighttime scenes (Table 2) indicate a significant correlation with scan direction at high DN levels. For the northeastern Arkansas daytime scene, the response of every detector in bands 1 through 3 is higher in the forward than in the reverse direction. Table 2 lists the differences in the mean for the forward and reverse parts of this scene; the ranges of the reverse-minus-forward differences in the mean for the detectors in bands 1 through 7, respectively, are 0.28 to 0.79, 0.12 to 0.37, 0.03 to 0.49, -0.23 to 0.42, 0.00 to 0.35, -0.13 to -0.40, and 0.02 to 0.39. The largest difference occurs for detector 6 in bands 2, 3, 5, and 7, for detector 4 in bands 1 and 6, and for detector 1 in band 4. At low digital levels, scan-direction effects are generally insignificant--less than 0.1 DN for the water area of the Cape Cod scene and the two nighttime scenes studied (except the noisy detector 7 in band 7). The noise level, as determined by the standard deviation of all scans in the same direction, is nearly the same in both directions.

Level Shift

Examination of the data on an individual-line basis indicates that some detectors have a significant scan-direction effect that changes over time. The line averages for dark data spaced by 16 lines (corresponding to a single detector) commonly switch between two distinct levels, spaced a few tenths of a DN apart; the phase of this oscillation can reverse with a period of 1 to 8 scans. For example, in the Cape Cod scene, level shifts occurred after six, nine, five, six, and one scans (see Figure 1), in the Richmond scene after every two scans (after every reverse-forward pair), and in the Roanoke scene after nearly every scan (yielding a stronger forward-reverse difference). The absence of this behavior in some detectors demonstrates that these changes are not due to the scene content itself.

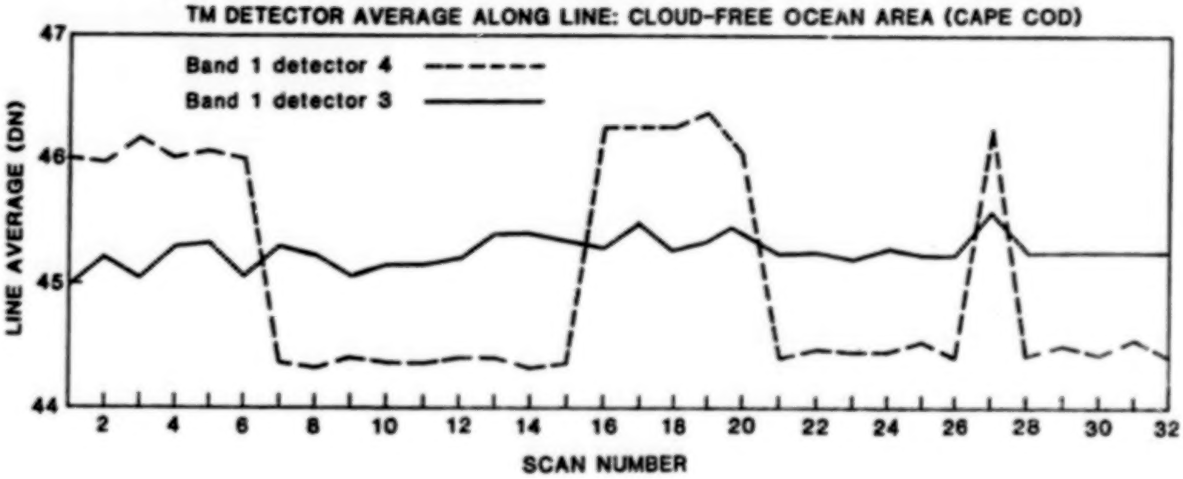

Figure 1. DN line average of two adjacent detectors (3 and 4, band 1) in the Cape Cod, Mass., scene as a function of scan number, showing Thematic Mapper detector-level shift. Detector 4 is an extreme case of level shift, where as detector 3 is more nearly typical.

Intrascene detector level shifts were observed in all nonthermal bands, ranging from a maximum of 2.07 DN in detector 4 of band 1 to a minimum of 0.18 DN in detector 14 of band 2, with an average level shift for all bands of 0.59 DN. A subscene array (starting line and sample, 1, 1025; number of lines and samples, 512, 1,024) of the Cape Cod B-type frame, consisting of a cloud-free area over the Atlantic Ocean, provided a uniform-radiance target for the analysis. The shift was determined as the difference between the maximum and minimum detector line averages, listed in Table 3.

Band 1 of a homogeneous Iowa farmland scene, with an average DN 1.4 times that of the ocean subscene, exhibits level shifts for the more strongly affected detectors (4, 10, and 12) also greater by a factor of 1.4. In nighttime scenes, where the DN level is approximately 2, this level shift is much reduced, typically being 0.3 DN. This correlation with scene brightness suggests that the cause of the level shift is a variation in gain.

The changes in line average are not evident in all detectors. For those detectors in which it occurs, shifts correlate between all detectors across all reflectance bands. The strongest correlation is between adjacent detectors on the same module (all even, or all odd, detectors in a band) (Figure 2).

Table 2

VARIATION OF RESPONSE WITH SCAN DIRECTION

Band	1	2	3	4	5	6	7
Band mean							
Arkansas---------	78.21	32.49	29.82	95.63	72.28	136.81	28.63
Cape Cod---------	44.85	14.15	11.70	6.87	4.56	---	3.32
Roanoke (night)--	2.29	2.27	2.29	2.14	2.61	---	2.35
Richmond (night)-	2.66	2.32	2.46	2.26	2.61	---	2.39
Reverse-forward mean							
Arkansas---------	0.55	0.24	0.30	-0.01	0.22	-0.29	0.20
Cape Cod---------	-0.05	0.00	0.01	0.02	0.01	---	0.01
Roanoke (night)--	-0.06	-0.04	-0.02	-0.02	0.00	---	0.01
Richmond (night)-	0.01	0.00	0.00	0.00	0.00	---	-0.01
Standard deviation							
Arkansas---------	14.23	7.20	10.64	25.19	18.51	9.72	13.14
Cape Cod---------	1.29	0.59	0.69	0.62	0.79	---	1.12
Roanoke (night)--	1.09	0.44	0.53	0.27	0.85	---	1.01
Richmond (night)-	1.13	0.46	0.57	0.38	0.85	---	1.02
Reverse-forward standard deviation							
Arkansas---------	0.03	0.08	0.15	0.02	0.14	1.10	0.26
Cape Cod---------	-0.01	-0.01	0.00	0.00	-0.01	---	0.00
Roanoke (night)--	-0.01	-0.02	0.01	-0.02	0.00	---	0.00
Richmond (night)-	0.00	0.00	0.02	0.00	0.00	---	0.00
Maximum reverse-forward mean (detector)							
Arkansas---------	0.79(4)	0.37(6)	0.49(6)	0.42(1)	0.35(6)	-0.40(4)	0.39(6)
Cape Cod---------	-0.09(16)	-0.03(15)	0.06(15)	0.04(12)	0.02(7)		0.10(7)
Roanoke (night)--	-0.12(2)	-0.19(1)	0.07(16)	-0.06(6)	0.08(7)		0.39(7)
Richmond (night)-	0.02	0.01	0.01	0.01	-0.02(2)		-0.21(7)

Table 3

THEMATIC MAPPER DETECTOR LEVEL SHIFT

Table entry for each detector is the maximum-minimum line average within a cloud-free ocean subscene near Cape Cod. Detectors marked by an asterisk were dead.

Band	1	2	3	4	5	7
Band mean	45	14	12	7	4	3
Detector						
1	0.72	1.15	1.12	0.38	0.34	0.54
2	0.53	0.38	0.85	0.58	0.48	0.55
3	0.64	0.49	0.85	0.41	0.27*	0.68
4	2.07	0.44*	0.35	0.42	0.27	0.45
5	0.56	0.56	0.89	0.49	0.47	0.58
6	0.39	0.28	0.55	0.49	0.36	0.56
7	0.38	0.39	0.74	0.59	0.48	1.33
8	0.89	0.22	0.41	0.43	0.49	0.59
9	0.49	0.34	0.50	0.59	0.33	0.52
10	1.07	0.25	0.56	0.62	0.93	0.79
11	0.54	0.34	0.60	0.59	0.34	0.60
12	1.71	0.34	0.67	0.68	0.35	0.66
13	0.67	0.43	0.85	0.63	0.33	0.67
14	0.51	0.18	0.69	0.57	0.35	0.42
15	0.57	0.51	1.19	0.69	0.49	0.55
16	0.52	0.34	1.46	0.85	0.35	0.62

ORIGINAL PAGE IS
OF POOR QUALITY

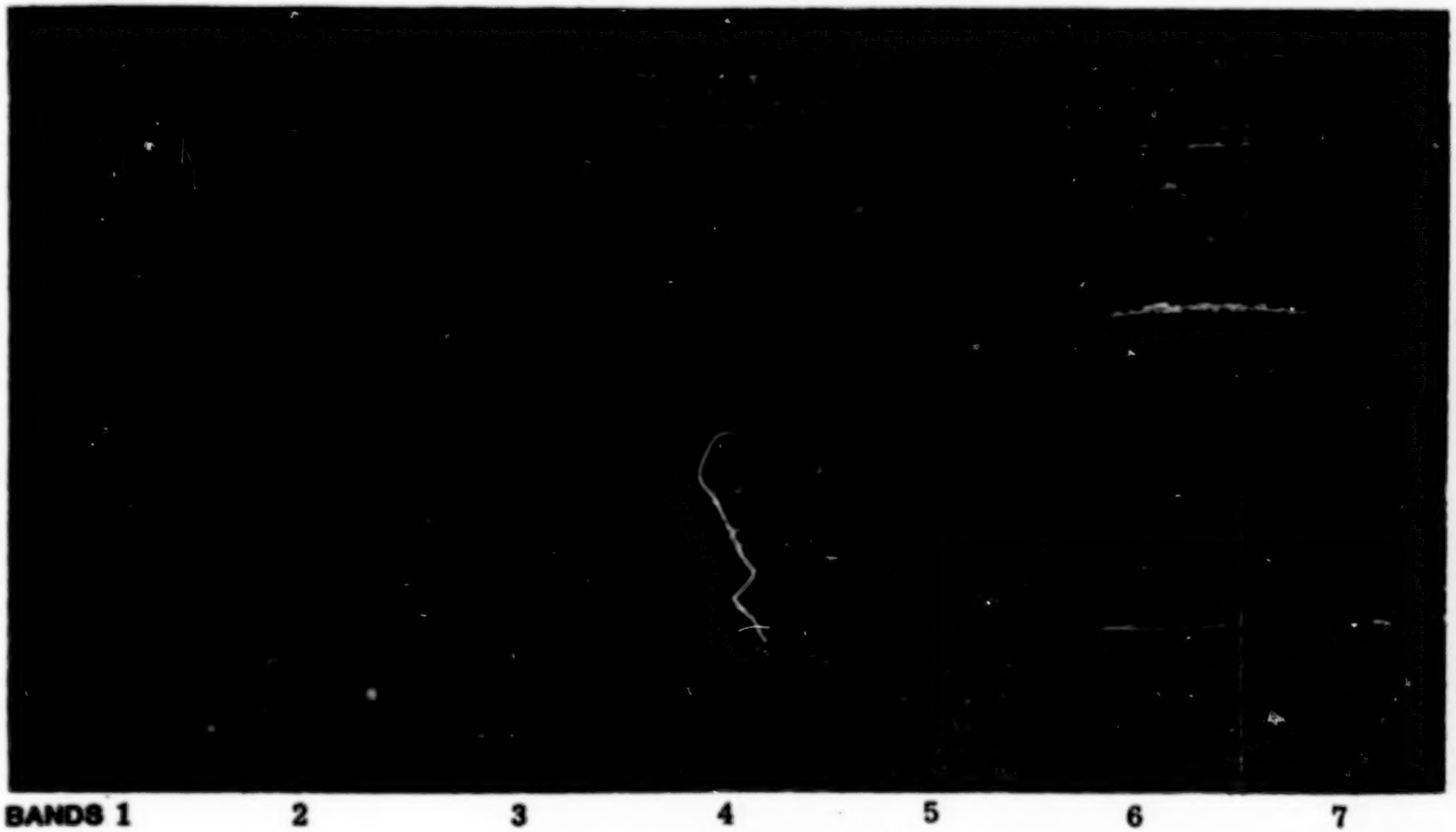

Figure 2. Mosaic of seven bands of Thematic Mapper B data over a cloud-free ocean area east of Cape Cod, Mass. This ocean subscene of 512 lines and 100 samples provides a uniform-radiance target used for graphic display of random and coherent-noise level. Each band was contrast enhanced to maximize visual inspection. Black-to-white DN levels are 41-50 for band 1, 12-17 for band 2, 10-14 for band 3, 5-9 for band 4, 2-7 for band 5, 87-92 for band 6, and 0-7 for band 7. High frequency graininess of bands 1, 3, and 4 is attributed to large amplitudes of 3.26-pixels per cycle coherent noise. "Stiching" pattern seen in band 3 results largely from 13.8 pixels per cycle coherent-noise in detector 1. Black lines in band 5 are due to dead detector 3. Detector 7 in band 7, which has the largest noise level, visually stands out as random alternation between black and white within a line. Between-band correlation of shift in line average within a given scene is visible as dark and light strips spanning across bands. an

The standard deviation does not appear to change when the level shift occurs. Also, the line averages rarely take intermediate values, but jump between two discrete levels. These observations suggest that a discrete level shift is occurring during the scan-mirror turnaround. The magnitude for the most strongly affected detector is about 4.5%.

The magnitude of this nonideal behavior remaining in the A data is visible in contrast-enhanced images of uniform fields, such as the Chesepeake Bay area (Figure 3). The variations in response can be graphically assessed quantitatively by taking the digital derivative in the direction normal to the scan direction (the vertical derivative) of this image and mapping progressively wider ranges to grey (Figure 4).

Stability of Dark Current Over Time

We compared the average values for each detector (except the thermal band 6) between the two nighttime scenes, obtained approximately 3 months apart. Changes were typically of about 0.1 DN, and all changes were less than 0.4 DN except for detector 1 of band 3 (0.47 DN) and detectors 4 and 12 of band 1 (1.77 and 1.56 DN, respectively).

DYNAMIC RESPONSE

The dynamic response of the TM appears generally to be excellent, with abrupt image edges for natural high-contrast borders; however, no quantitative measure of field-of-view definition has been made. We noted two low-frequency response problems.

Overshoot

Some of the detectors in band 5 exhibit an overshoot response when scanning across an abrupt boundary between two spatially large areas of significantly different average-brightness levels; the detector overestimates (overshoots) the change in brightness level for a finite time before recovering to the proper level.

This overshoot effect, evident in both the forward and reverse scan directions, is visible in the Washington, D.C., A data along the boundaries between the Chesapeake Bay (uniform in brightness) and the surrounding terrain (Figure 5). When the scanner crosses from the terrain (average DN, 55) to the bay (average DN, of 5), detectors 1, 2, 15, and 16 overshoot the change in brightness level, and so the density numbers are initially lower than the average value of the bay. The overshoot effect diminishes and completely disappears over a scan length of 30 pixels from the boundary. To quantify this effect, the first 15 pixels of the water at the terrain boundary were averaged and compared for each detector in the forward and reverse scan directions. Detector 1 was found to be lower in density number by an average of 0.47 DN, detector 2 by 0.73 DN, detector 15 by 0.78 DN, and detector 16 by 0.62 DN; the effect for the other 12 detectors was negligible.

Gain Sag

We looked for a variation in gain along each scanline by determining the differences in response between the forward and reverse scan directions as a function of sample position. The B data for a set of detectors in a band (generally all 16) were averaged for a set of 16 forward and 16 reverse scans

ORIGINAL PAGE IS
OF POOR QUALITY

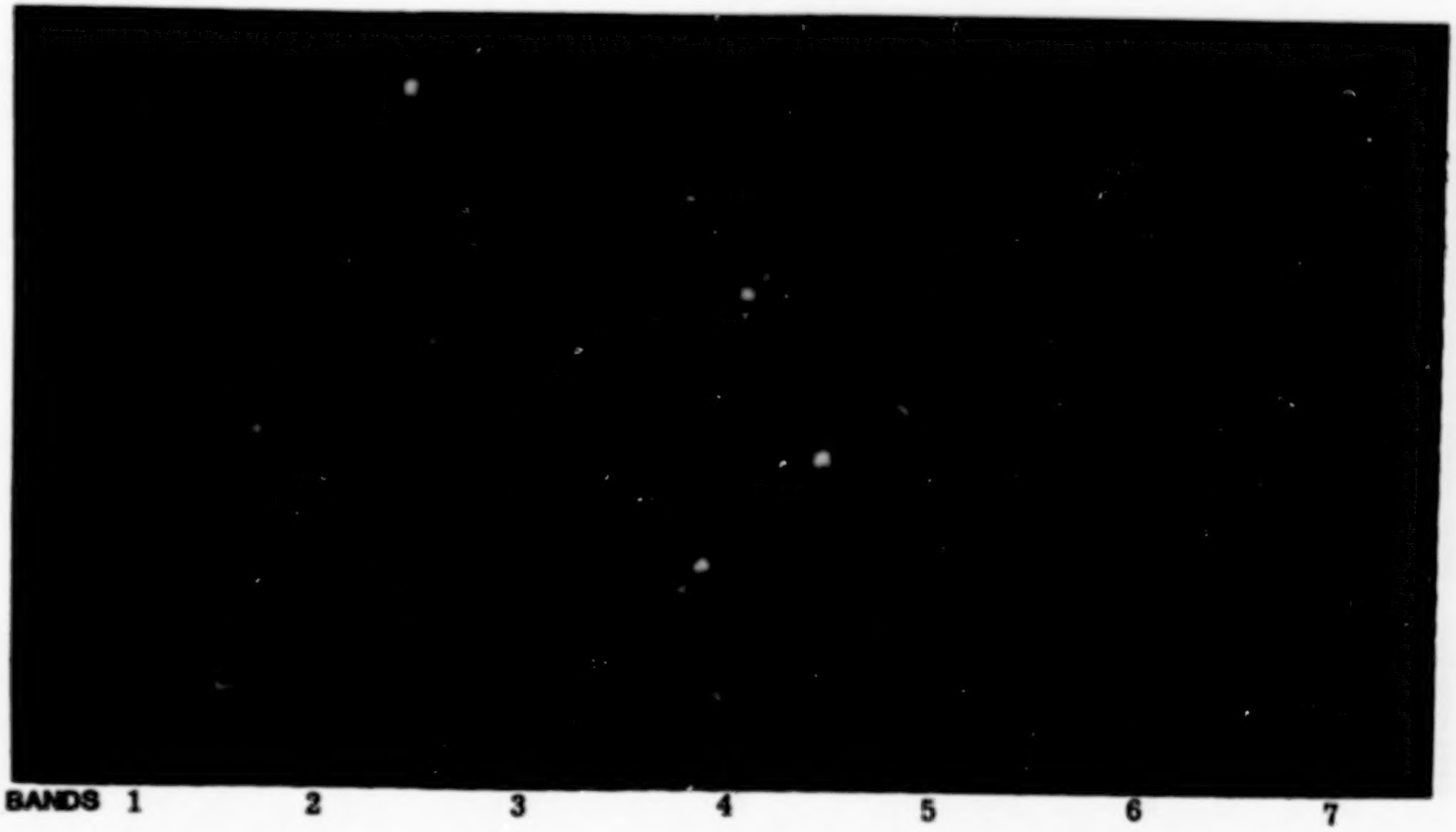

Figure 3. Seven-band mosaic of A-type Washington, D.C., subscene centered over Chesapeake Bay. After radiometric correction tables have been applied, residual detector striping is still visible.

ORIGINAL PAGE IS
OF POOR QUALITY

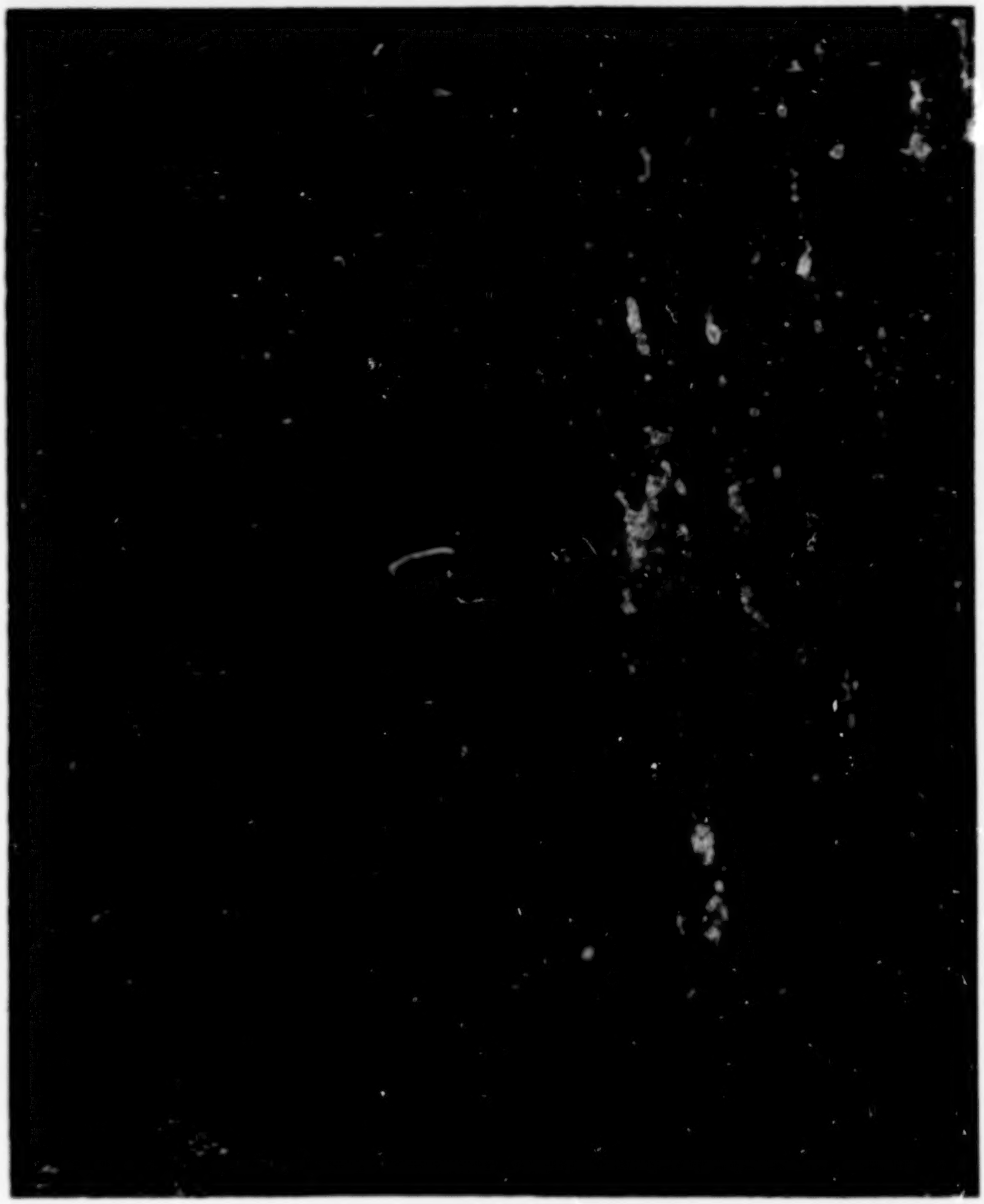

Figure 4. Vertical derivatives of bands 1 and 2 of Chesapeake Bay subscene A data. Interdetector variations after a radiometric correction are seen by making an image of the first derivative in the vertical direction of a flat field and stretching progressively wider ranges to gray. Top three images are of band 1, and from top to bottom, represent 0, ±1, and ±2 DN differences mapped to gray. Residual detector variations are visible even with a ±2 DN gray band. Bottom two images are of band 2 with 0 and ±1 DN mapped to gray. Little detector variation is visible after a ±1-DN stretch.

ORIGINAL PAGE IS
OF POOR QUALITY

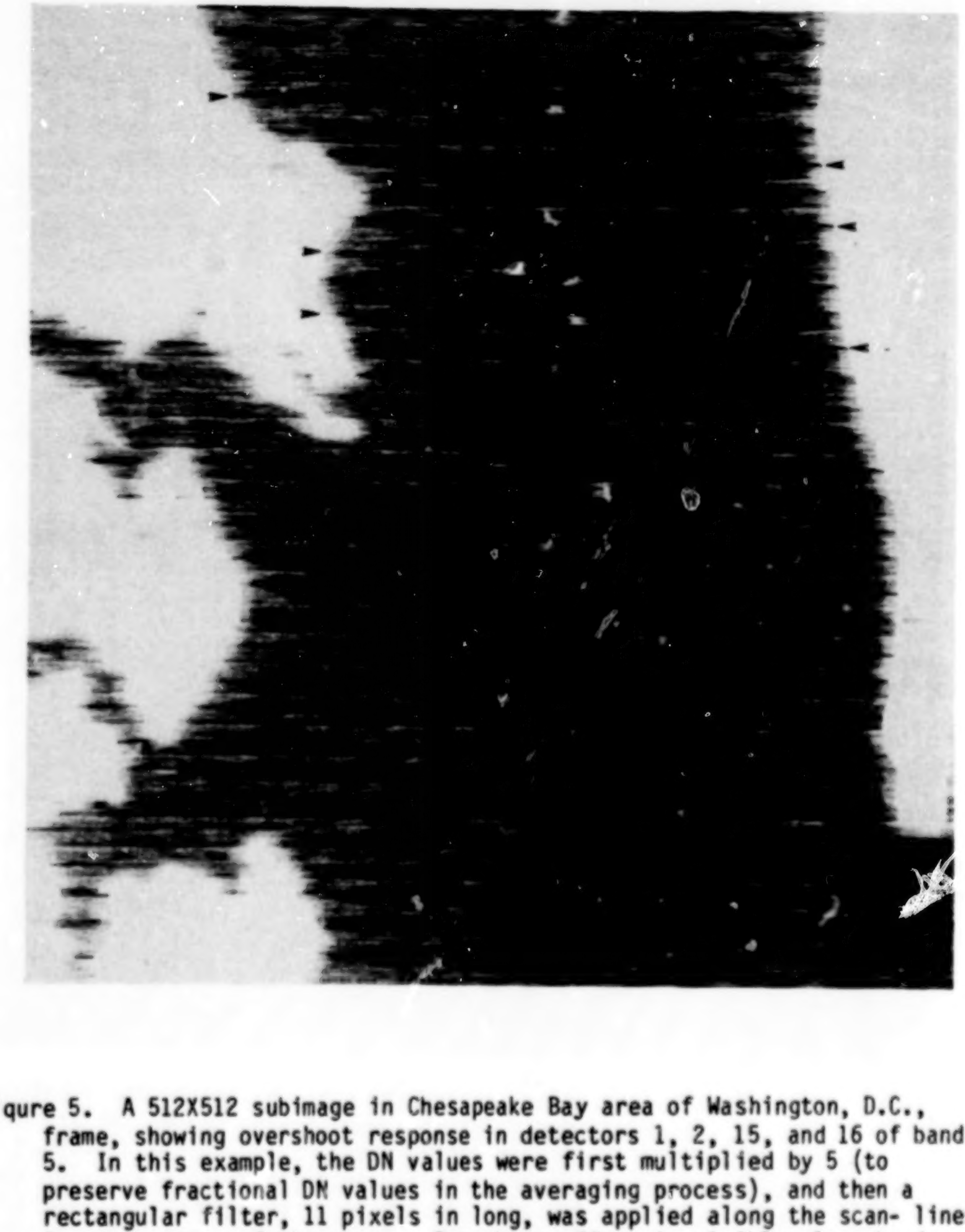

Figure 5. A 512X512 subimage in Chesapeake Bay area of Washington, D.C., frame, showing overshoot response in detectors 1, 2, 15, and 16 of band 5. In this example, the DN values were first multiplied by 5 (to preserve fractional DN values in the averaging process), and then a rectangular filter, 11 pixels in long, was applied along the scan- lines in water areas of the scene. Overshoot effect is visible along border between terrain (saturated in white) and water (darker areas). Visibility of this effect on both sides of the bay (arrows) indicates that the effect exists in both forward and reverse scan directions.

in 100 intervals of 60 samples each; each scan was across an image. These averages were subtracted to form 100 differences across the image, which we then examined for any consistent behavior.

The resulting curves are similar in shape to those for the difference between two exponentials of the same amplitude and period, decaying away from the starting end of the scan. In nighttime scenes (average DN, 2 or 3) or in the Cape Cod ocean scene (band 2 DN, 14; band 3 DN, 12), the drop in level is less than 0.1 DN, probably less than 0.05 DN. For higher radiance scenes (northwestern Iowa band 1 DN, 65; Cape Cod ocean band 1 DN, 46) the magnitude of the gain sag is approximately 0.5 DN, and the decay period about 1,200 samples.

HIGH-FREQUENCY NOISE

We determined the noise level of each detector by computing the first difference between samples (the "horizontal derivative") of the first 512 lines of four scenes and then determining the standard deviation for each detector in each scan direction. This technique measures the high-frequency noise and is immune to drift, sag, or scan-reversal gain changes. Table 4 lists the results for the Richmond nighttime scene.

There is a negligible dependence of noise on scan direction for any detector (detector 7 of band 7 shows a small effect in dark scenes due to clipping at zero, and small level changes with scan direction). Comparison of this measure of noise for the two nighttime scenes, spaced 3 months apart, showed little change, typically 0.1 DN, and less than 0.3 DN for all detectors.

Table 4

DETECTOR NOISE AS DETERMINED BY STANDARD DEVIATION OF HORIZONTAL DERIVATIVE

Band----- Detector	1	2	3	4	5	7
1	1.80	0.58	0.79	0.53	1.39	1.67
2	2.11	1.57	0.82	0.64	1.30	1.61
3	1.66	0.73	0.78	0.78	0.84*	1.38
4	1.64	1.10*	1.14	0.64	1.44	1.70
5	1.57	0.70	0.82	0.53	1.43	1.49
6	2.10	0.81	0.82	0.78	1.48	1.67
7	1.96	0.56	0.77	0.43	1.82	2.77
8	1.91	0.74	1.36	0.84	1.32	1.52
9	1.57	0.50	0.65	0.39	1.44	1.54
10	1.60	0.49	0.90	0.56	1.35	1.70
11	1.80	0.51	0.53	0.46	1.50	1.51
12	1.61	0.31	0.70	0.63	1.43	1.63
13	1.59	0.63	0.77	0.36	1.40	1.31
14	2.02	0.59	0.94	0.43	1.35	1.81
15	1.78	0.60	0.74	0.46	1.33	1.29
16	2.47	0.70	1.11	0.73	1.33	1.61
Mean	1.82	0.70	0.85	0.57	1.38	1.63

* Detector was dead.

Coherent Noise

Fourier analysis of two TM scenes revealed coherent-noise effects in the imaging system. Two B data subscenes, Cape Cod and Richmond (both with starting line 1, starting sample 1,025; with 512 lines and 1,024 samples), were selected for the analysis. The Richmond subscene, acquired at night and having no scene radiance, was used for determining coherent-noise at the dark-current level; and the Cape Cod subscene, consisting of a large area of cloud-free ocean and providing a uniform-radiance target, was used for monitoring coherent-noise at brightness levels above dark current. For all lines of the seven bands, a one-dimensional fast Fourier transform (FFT) was applied, and peak-to-peak amplitudes of the 512 FFT frequencies were determined. Averaging of the amplitudes of each Fourier component of the 32 scans in the 512-line subscene for each detector improved the statistics on the coherent-noise levels. Because of the uniform-radiance fields, the amplitudes of all Fourier components are attributed to either random or coherent-noise (except zero frequency). Typical background frequency amplitudes due to random detector noise for both subscenes fall within the range 0.01 - 0.06 DN for all bands.

The results of the FFT's exhibited several sharp peaks well above the background levels at certain frequencies. The Cape Cod subscene exhibited coherent-noise at 3.26, 13.65, 13.83, 14.22, and 17.35 pixels per cycle, and the Richmond scene at 2.51, 2.62, 3.23, 13.65, and 14.22 pixels per cycle.

In the Cape Cod subscene, the strongest, most consistent peak-to-peak amplitude-coherent-noise exists at 3.26 pixels per cycle and is evident with varying amplitude in almost all the detectors of bands 1 through 4. This noise is visible in areas of uniform-radiance and appears as a grainy high-frequency pattern, especially in bands 1, 3, and 4 (see Figures 2 and 3). Detector 16 of band 1 exhibits the greatest amplitude (1.12 DN). Coherent noise at 17.35 pixels per cycle is evident in almost all the detectors of bands 1 through 4, though much weaker in amplitude; detector 4 of band 1 exhibits the greatest amplitude (0.36 DN). Band 3 exhibits unusual coherent noise in detectors 1, 3, and 9. Detector 1 coherent-noise exists at 13.83 pixels per cycle with an amplitude of 0.55 DN, detector 3 at 13.62 pixels per cycle with an amplitude of 0.19 DN and detector 9 at 14.22 pixels per cycle with an amplitude of 0.28 DN. Because these noise levels are so close in period, they are probably related. The visual appearance of this noise is a "stitching" pattern occurring every 16th line as shown in Figures 2 and 6.

In the Richmond subscene, the strongest, most consistent peak-to-peak amplitude-coherent-noise exists at 3.23 pixels per cycle and is evident in almost all the detectors of bands 1 through 4. This coherent-noise is probably related to the noise at 3.26 pixels per cycle seen in the Cape Cod subscene but has been shifted in period by 0.03 pixels per cycle. The coherent noise at 17.35 pixels per cycle, also evident in the Cape Cod subscene, does not appear in the Richmond subscene. Detectors 1, 3, and 9 of band 3 in the Richmond subscene also exhibit coherent-noise near 13.6 pixels per cycle, with amplitudes of 0.53, 0.13, and 0.27 DN, respectively. In addition, detector 16 of band 3 exhibits coherent-noise at 2.51 pixels per cycle, with an amplitude of 0.12 DN. Detectors 4, 8, and 10 of band 4 exhibit coherent-noise at 2.62 pixels per cycle, with respective amplitudes of 0.13, 0.14, and 0.09 DN.

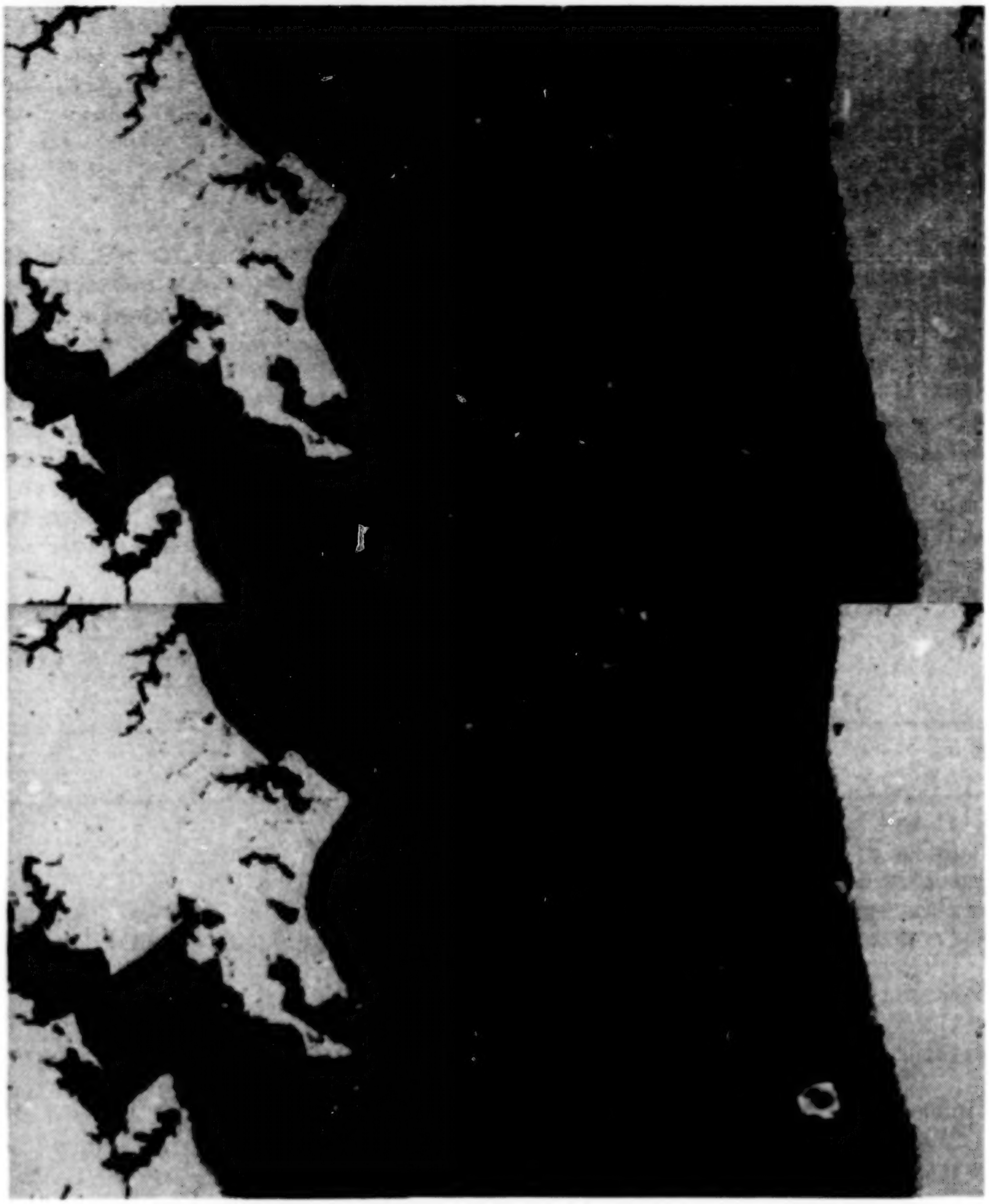

Figure 6. Band 3 of Washington, D.C., subscene, centered over Chesapeake Bay, showing before (top) and after (bottom) results of filter designed by Chavez and Soderblom (1974) for suppressing coherent-noise of stable period but varying amplitude. Filter was applied to "stitching" pattern of 13.8 pixels/per cycle only for detector 1, not detectors 3 or 9.

ORIGINAL PAGE IS
OF POOR QUALITY

No other coherent-noise with amplitudes greater than twice the background level were evident in the FFT's. Coherent-noise levels in bands 5 through 7 are only slightly above background (less than twice background) and are discernible only in large-scale statistics. Table 5 summarizes the coherent noise consistent in bands 1 through 4. We note that the amplitude of this coherent-noise is approximately the same in the Richmond and Cape Cod subscenes. Thus, the coherent-noise level is not a function of scene brightness and is an additive component to the signal.

The 13.8 pixels-per-cycle noise amplitude in detector 1 of band 3 varies considerably within a given scene. In the Washington, D.C., subscene, centered over the Chesapeake Bay, FFT's of individual lines showed the average amplitude to be 0.5 DN and the maximum amplitude 5.0 DN. We tried to remove the effects of the 13.8 pixels per cycle "stitching" pattern by using a spatial filter designed by Chavez and Soderblom (1974). This filter was designed to suppress an along-the-line oscillation that is stable in period but varies in amplitude. In determining the noise level, the filter compares the noisy line with the lines above and below (assumed to be noise free). Only differences at the 13.8 pixel-per-second sampling period between the noisy and noise-free lines are suppressed. Figure 6 shows the result before and after application of the filter to only detector 1.

Table 5

SUMMARY OF CONSISTENT COHERENT NOISE LEVELS

Band	1	2	3	4
Cape Cod subscene				
(3.26 pixels per cycle)				
Detector with maximum amplitude....	16	6	8	8
maximum amplitude..................	1.12	0.25	0.68	0.53
Average amplitude (all detectors)..	0.56	0.12	0.20	0.25
(17.35 pixels per cycle)				
Detector with maximum amplitude....	4	1	1	12
Maximum amplitude..................	0.36	0.16	0.20	0.17
Average amplitude (all detectors)..	0.21	0.08	0.07	0.06
Richmond Sub-scene				
(3.23 pixels per cycle)				
Detector with maximum amplitude....	16	6	8	8
Maximum amplitude..................	1.72	0.40	0.97	0.58
Average amplitude (all detectors)..	0.92	0.15	0.26	0.22

The high-frequency coherent-noise (period of 3.2 samples) is of constant amplitude. The "stitching"-pattern noise (period of 13.85 samples) differs in amplitude in the forward and reverse directions, and changes over time. Images specially processed to show coherent-noise indicate consistent phase relations between detectors and, in some images, between scans. These relations have not yet been quantified.

EFFECTS OF RESAMPLING

Generation of the P data involves use of a cubic convolution algorithm. Application of this 4-by-4 weighting scheme alters the magnitude of the radiometric irregularities of the TM detectors and generally reduces them because the behavior of adjacent detectors commonly differs. Nonetheless, such effects as level shift can easily be seen in uniform areas, e.g., bodies of water.

The cubic convolution algorithm can also yield, at high-contrast boundaries, digital levels significantly outside the imput range. For example, the P-data DN range for a north-south section through Dulles National Airport Terminal in band 1 is 58 to 237, whereas the A data DN range is 71 to 220. This radiance extension likely leads to erroneous results of automated statistical or classification routines; images based on such automated routines will exhibit apparent edge enhancement.

The resampling algorithm does not discriminate against null data bordering image data. Thus, its use results in fuzzy image edges with a 3-pixel-wide border of invalid data. To avoid adverse effects in applications involving scene statistics, these values should be reset to zero after resampling.

INTRABAND STATISTICAL ANALYSES OF THEMATIC MAPPER IMAGES

Because of the increased spatial resolution and the number of spectral bands in the TM imaging system relative to the Multispectral Scanner, it is difficult to process a large number of digital data quickly and efficiently. Methods which help sort, preselect, and (or) reduce the number of data that need to be processed and analyzed will need to be developed and implemented. One method that we found useful for this purpose is the optimum-index-factor (OIF) technique developed by Chavez et al. (1982). This technique, which compares the variance in each band with the cross-correlation between bands, can be used either to select a subset of bands that contain the most information with the least amount of duplication or to reduce the dimensionality of the data set and store as much of the total information as possible into a subset of bands or components. This method was used on TM data covering the Washington D.C. area and the Silver Bell copper mine test site near Tucson, Ariz. Table 6 details the band-correlation matrix for this latter area.

Table 6

THEMATIC MAPPER SIX BAND CORRELATION MATRIX (512X512),
SILVER BELL MINE AREA, TUCSON, ARIZONA.

Band	1	2	3	4	5	7
1	1.000					
2	0.956	1.000				
3	0.937	0.968	1.000			
4	0.828	0.877	0.917	1.000		
5	0.752	0.812	0.845	0.872	1.000	
7	0.763	0.811	0.848	0.870	0.955	1.000

The OIF technique was used to select that three-band combination out of the possible 20 which contains the most information with the least amount of duplication (the thermal band was not included). The combination selected for the Washington, D.C., area was TM bands 1, 4, and 5 (TM 1-4-5). The combination selected for the Silver Bell Mine area was TM 1-5-7; this combination was also selected for most of the other arid and semiarid areas we have studied. For the Silver Bell Mine area, combinations TM 1-4-5 and TM 1-3-5 were closely ranked to combination TM 1-5-7 by the OIF technique. Combinations TM 1-2-4 and TM 1-2-3 were ranked 19th and 20th (lowest), respectively. The three-band combinations were color composited; however, owing to color-printing restrictions, they are not included in this report.

Next, to minimize the amount of information excluded from a three-band combination but still to use only three components, "selective" principal-component analysis was used (Chavez et al., 1982). Most users of principal-component analysis would have used all six TM bands as input and thus would have generated six different components. In selective principal-component analysis, however, the correlation matrix is used instead to select sets of two or three bands for input to principal-component analysis. Bands with a high degree of correlation are identified as a set to be used as input, assuming that because of their high degree of correlation, most of the information will be mapped to the first principal-component. The other components are not used because they contain only a small amount of the total information, which commonly includes noise patterns in the data. For the Silver Bell Mine area, the two sets of TM bands identified for input to principal-component analysis were TM 1-2-3 and TM 5-7.

Figure 7 shows TM bands 1, 4, 5, and 7 for the Silver Bell Mine area, with linear-contrast stretches; Figure 8 shows principal-components 1, 2, and 3 of combination TM 1-2-3; and Figure 9 shows principal-components 1 and 2 of combination TM 5-7.

The proportions of the total variance in combination TM 1-2-3, mapped to components 1, 2, and 3, were 96.77, 2.57, and 0.66 percent, respectively. The proportions of the total variance mapped to components 1 and 2 of combination TM 5-7 were 98.36 and 1.62 percent, respectively. By combining the first

ORIGINAL PAGE IS
OF POOR QUALITY

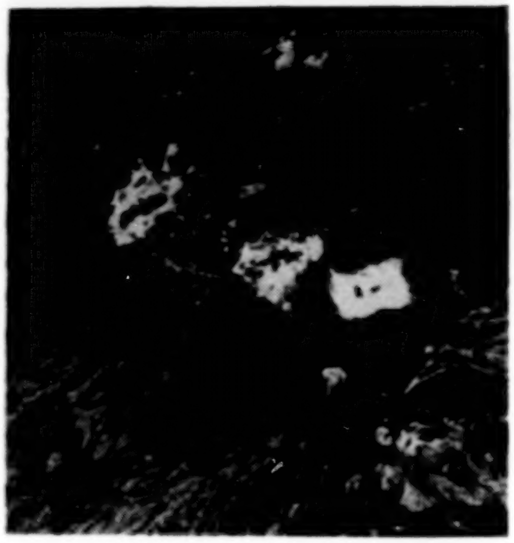

Figure 7a.
Landsat 4 TM image of band 1 (0.45-0.52 μm), with a linear-contrast stretch over 49-91 (42-DN range). Silver Bell copper mine is located in center.

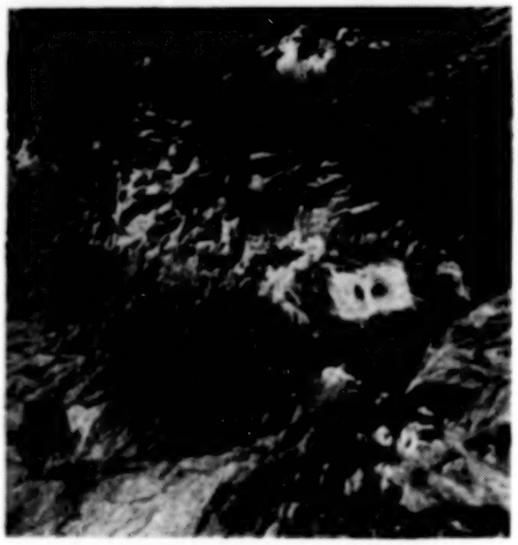

Figure 7b.
Landsat 4 TM image of band 4 (0.76-0.90 μm), with a linear-contrast stretch over 19-59 (40-DN range).

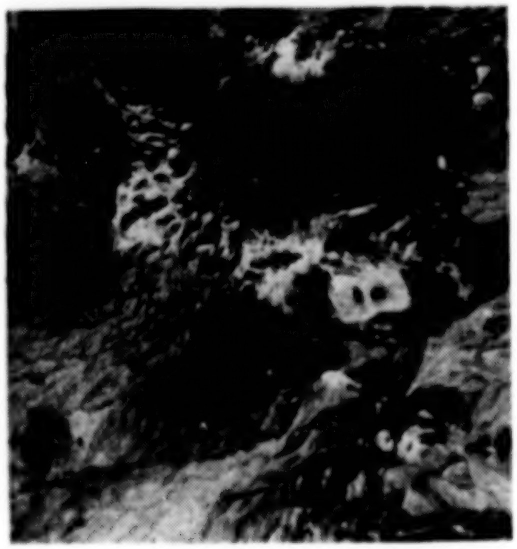

Figure 7c.
Landsat 4 TM image of band 5 (1.55-1.75 μm), with a linear-contrast stretch over 9-108 (99-DN range).

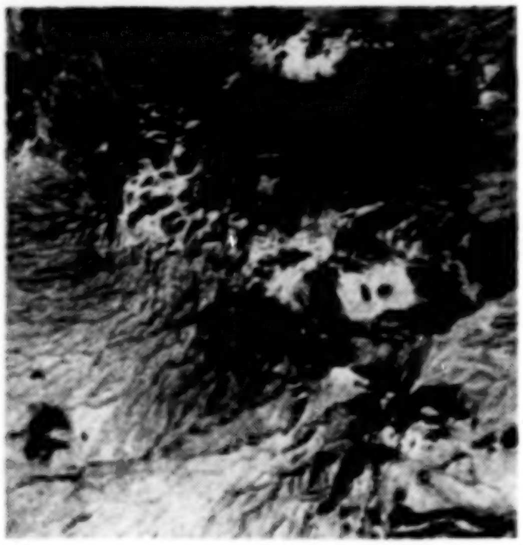

Figure 7d.
Landsat 4 TM image of band 7 (2.08-2.35 μm), with a linear-contrast stretch over 4-57 (53-DN range).

ORIGINAL PAGE IS
OF POOR QUALITY

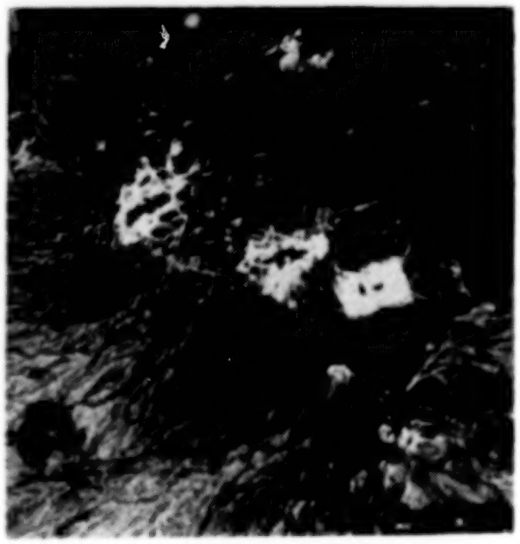

Figure 8a.
Principal component 1 of combination TM 1-2-3, with a linear-contrast stretch over 47-116 (69-DN range). The proportion of total variance in combination TM 1-2-3 mapped to principal component 1 is 96.77 percent.

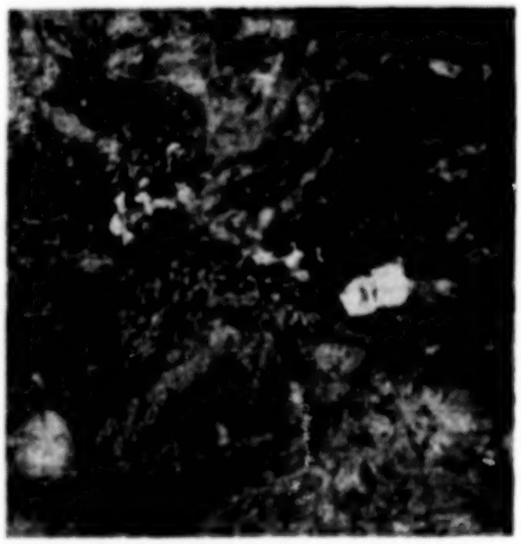

Figure 8b.
Principal component 2 of combination TM 1-2-3, with a linear-constrast stretch over 117-131 (14-DN range). The proportion of total variance in combination TM 1-2-3 mapped to principal component 2 is 2.57 percent. Note horizontal and vertical noise patterns in TM data.

ORIGINAL PAGE IS
OF POOR QUALITY

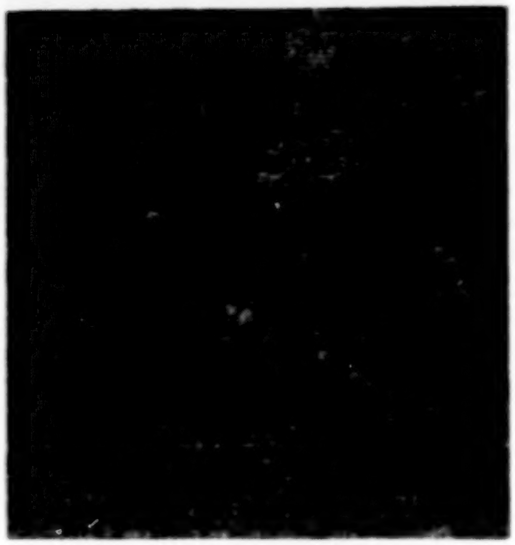

Figure 8c.
Principal component 3 of combination TM 1-2-3, with a linear-constrast stretch over 148-157 (9-DN range). Proportion of total variance in combination TM 1-2-3 mapped to principal component 3 is 0.66 percent. Note that most information shown in this component is a noise pattern not seen in component 2.

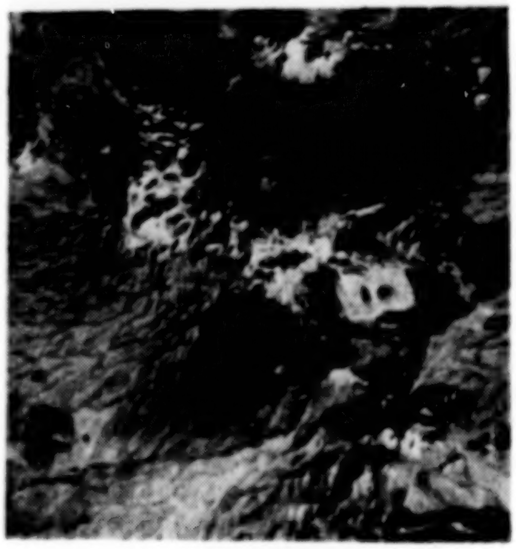

Figure 9a.
Principal component 1 of combination TM 5-7, with a linear-contrast stretch over 9-120 (111-DN range). Proportion of total variance of combination TM 5-7 mapped to principal component 1 is 98.36 percent.

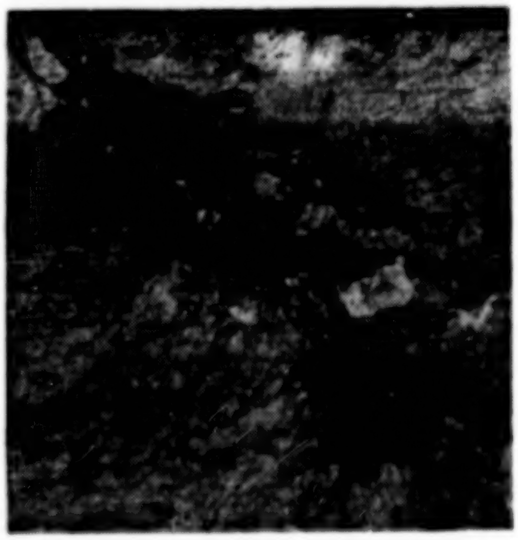

Figure 9b.
Principal component 2 of combination TM 5-7, with a linear-contrast stretch over 69-89 (20-DN range). Proportion of total variance combination of TM 5-7 mapped to principal component 2 is 1.64 percent. This image also shows a noise pattern contained in the TM data. Darker toned areas correspond closely to an alteration zone previously mapped by the Geosat committee and the Jet Propulsion Laboratory, using TM simulator data.

principal components of combinations TM 1-2-3 and TM 5-7 with TM band 4, a total of at least 98.3 percent of the variance of all six TM bands is obtained. These new subsets can now be used as input for color compositing, processing, and (or) analysis.

A note of caution is appropriate here. Although selective principal-component analysis can be used to generate a subset that contains most of the total information in the original data set, the discarded information should be visually evaluated to ascertain that the information of interest has not been isolated in one of the lower, unused components. In the Silver Bell Mine area, for example, principal-component 2 of combination TM 5-7 showed an alteration zone around the mining area that is of great interest to mining geologists. Here, the other 98 percent of the data can be discarded, and processing and analysis can be done on the reduced data set.

The images of components 2 and 3 of combination TM 1-2-3 (Figures 8b and 8c) and of component 2 of combination TM 5-7 (Figure 9b) show the various noise patterns that are present in the TM data. At least three different noise patterns are visible in these images in the horizontal and vertical directions.

CONCLUSIONS

This study has emphasized the radiometric deviations of the Thematic Mapper from ideal behavior. It should be remembered that its overall performance is a great improvement over that of previous Landsat scanners; many of the anomalies presented here are less than one digital level. All the larger effects could be reduced by ground processing; the only problem not addressable by ground processing is the irregular width of the digital levels.

In approximate order of decreasing seriousness, the major problems are: Level shifts, "stitching"-pattern noise, coherent noise at 3.2 pixels per cycle, gain sag, band 5 overshoot, and other coherent noise. Level shift, gain sag, and overshoot appear to be proportional to signal level; level shift and gain sag may represent well-defined and consistent changes of gain. Level shifts are irregular in time, but a small correlation exists between level and scan-mirror direction. Level shift could be easily corrected if it always occurred during scan-mirror reversal; the calibration-wand data might be sufficient to determine the times of level shift.

The 3.2 pixel per cycle coherent-noise has adequately short wavelength to be considerably reduced by cubic convolution resampling. Because corrections of less than 1 DN are relatively meaningless (and difficult to implement), the remaining problems are unlikely to have significant effect on the use of TM data.

By judicious selection of spectral groups and use of principal-components, most of the information in the six reflectance bands can be mapped into a three-color display; however, data of great geologic significance can be transformed into components formally containing little information. The improved spectral and spatial information provided by the TM have great potential benefit if the user is not overwhelmed by the sheer volume of data.

REFERENCES

Chavez, P. S., Jr., Berlin, G. L., and Sowers, L. B., 1982, "Statistical method for selecting Landsat MSS ratios": Special Issue of Journal of Allied Photographic Engineering, vol. 8, no. 1, p. 23-30.

Chavez, P. S., Jr. and Soderblom, L. A., 1974, "Simple High Speed Digital Image Processing to Remove Quasi-Coherent Noise Patterns": American Society of Photogrammetry Symposium, Washington, D.C., Proceedings: Falls Church, VA, p. 595-600.

N85-21739

D4/15

A PRELIMINARY EVALUATION OF LANDSAT-4 THEMATIC MAPPER DATA FOR THEIR GEOMETRIC AND RADIOMETRIC ACCURACIES

M. H. Podwysocki, N. Falcone,
L. U. Bender and O. D. Jones
U.S. Geological Survey

Original photography may be purchased
from EROS Data Center
Sioux Falls, SD 57198

INTRODUCTION

This report describes results of some preliminary analyses of Landsat-4 Thematic Mapper data for the NASA Landsat Image Quality Analysis program (LIDQUA). The work is being done under interagency agreement S-12407-C between the U.S. Geological Survey and NASA-Goddard Space Flight Center (GSFC).

Landsat-4 TM scenes for Washington, D.C. (40109-15140, November 2, 1982) Macon, Georgia (40050-15333, September 4, 1982) and Cape Canaveral, Florida (40036-14214, August 20, 1982) have been examined to determine their geometric and radiometric accuracy. In addition, parts of these scenes are also being analyzed to determine the ability to identify specific rock types with the added near-infrared TM bands at 1.6 and 2.2 um.

GEOMETRIC ANALYSIS

In order to assess whole scene geometric accuracy, each of the seven TM bands for the geometrically corrected (GSFC P-tape digital format) Washington, D.C. scene were contrast stretched and recorded on film using an Optronics P-1500 film writer. Thirty-eight well-defined control points (figs. 1a and b) were visually identified by comparing 1:24,000-scale topographic maps with TM band 3. Bender and Falcone[1] stated that the combined affect of map-position error (for maps meeting National Map Standards) and control-point identification error may yield a Root Mean Square Error (RMSE) of 12 m. A point marking device was used to drill 40 micrometer circular holes at the control points in the emulsion of the band 3 image. The control points then were were transferred and drilled onto images of bands 1, 5, and 7 using binocular vision and the drilled holes on band 3 as the "master". Therefore, any errors arising during the transfer of the control points from the map to

PRECEDING PAGE BLANK NOT FILMED

PAGE III-496 INTENTIONALLY BLANK

the band 3 image also are present in the other bands. Cartesian coordinates of each control point on each band then were measured by means of a photogrammetric comparator whose resolution is one micrometer.

Universal Transverse Mercator (UTM) projection coordinates for each of the control points were measured from the topographic maps and recorded to the nearest 5 m using a metric coordinate reader (a transparent plastic template). The UTM coordinates were transformed numerically to latitude-longitude and then to Space Oblique Mercator (SOM) coordinates.

The coefficients of two transformations, the similarity and the affine, were calculated by the least-squares method by using the measured comparator coordinates, and their respective UTM and SOM coordinates. The similarity transformation can be interpreted as a rotation, single change in scale and two translations:

$$x' = ax + by + x_o \qquad a = K \cos 0$$
$$y' = -bx + ay + y_o \qquad b = K \sin 0$$

when K is the scale change, 0 is the rotation, and x_o, y_o are the translations.

The affine transformation is a six-parameter transformation permitting two mutually perpendicular scale changes, two rotations (one defining the direction of the scale changes), and two translations:

$$x' = ax + by + x_o$$
$$y' = cx + dy + y_o$$

Table 1 shows the vector residuals resulting from each transformation for the four TM bands measured to date.

Table 1
ROOT MEAN SQUARE ERROR (RMSE) OF VECTOR RESIDUALS
FROM CONTROL MEASUREMENT

	UTM ground coordinates		SOM ground coordinates	
TM band	Similarity	Affine	Similarity	Affine
1	72 m	45 m	70 m	43 m
3	70 m	45 m	67 m	42 m
5	68 m	48 m	66 m	46 m
7	69 m	45 m	66 m	41 m

In all cases, the SOM projection fits the data slightly better, i.e. has a smaller RMSE, than the UTM projection, but little difference in shape exists between a scene recorded on film in either of the two map projections. The difference probably will be smallest for those areas in which the scene center coincides with a UTM central meridian; at these locations the higher order terms of the two projections are minimal.

Table 1 shows that the application of the affine transformation significantly reduces the root mean square error in all cases. One possible cause may be the film-writing device. A highly significant skewness had been observed in 1980 from tests of grids printed from the same device as used in this study (N. Falcone, U.S. Geological Survey, personal communication). At that time, it was hypothesized that it possibly was caused by lack of parallelism between the axis of the rotary drum and the axis of travel of the light source. In order to verify the 1980 findings, a new six by six grid, having 4 cm spacing, was written on film using a 50 micrometer aperture. The RMSE values are given in Table 2 along with those of the 1980 measurements:

Table 2
ROOT MEAN SQUARE ERROR OF VECTOR RESIDUALS
FROM GRID MEASUREMENTS

	Similarity	Affine
1980 Grid	136 micrometers	75 micrometers
1983 Grid	117 micrometers	21 micrometers

Although the values for the 1983 grid are smaller, a significant affine error is still indicated. Vector plots of residuals from the similarity transformation display an extremely high degree of correlation between the two sets of grids. Figures 2 and 3 are vector plots of residuals for the 1983 grids. Figure 2 indicates a general elongation inclined at 45° to the direction of the lead screw which moves the light source and a compression at 90° to the prior direction. Figure 3 is a plot of residuals remaining after the removal of first order errors. One can surmise, from examination of the residuals, that at least a third order polynomial is necessary to reduce the residuals to the same order of magnitude as the measuring errors (approximately 3 micrometers).

In order to assess the difference in shape between the UTM and SOM map projections, their respective sets of coordinates of the control points were fit together by the least-squares method. The similarity transformation results in a RMSE of 11.3 m for the 38 control points, whereas the affine transformation results in a value of 11.4 m. Because both projections are conformal, it is not surprising that the affine transformation does not reduce the residuals.

Band-to-band registration was checked for the Washington, D.C. scene viewing several small parts of the scene on an interactive video display device. Several strongly contrasting targets, such as airport runways and small ponds, were used to visually determine the offsets. By rapidly toggling between the TM bands on the interactive system it was found that bands 1 through 4 were coregistered nearly perfectly (fig. 4a). Using channels 1 through 4 as references, bands 5 and 7 were found to be displaced 1 to 2 pixels westward (fig. 4b). Band 6 was displaced 4 pixels eastward (fig. 4c), which effectively means it is displaced by one of its 120 m resolution units.

RADIOMETRIC ANALYSIS

A geometrically uncorrected version (GSFC A-tape digital format) of the Macon, Georgia scene was examined to determine some of the radiometric characteristics of the data. This included analysis of the 16 individual detectors in bands 1 through 5 and 7 and each of 4 detectors of channel 6. Systematic gaps were found within the limited range of digital numbers recorded for the scene. These can be attributed to the integer truncation of decimal numbers involved in the calibration procedure during production of the computer compatible tapes.

The potential of sensor striping caused by the separate gains and offsets required for each of the 16 sensors of the visible and near-infrared TM bands was investigated using the A-tape of the Macon scene. The four sensor thermal infrared band also was examined. Means and standard deviations were calculated on a modulo-16 basis. The results are summarized in table 3.

Table 3

COMPARISON OF DIGITAL NUMBER STATISTICS
FOR MODULO-16 STRIPING OF TM DATA

TM Channel	1	2	3	4	5	6	7
range of	85.5	34.2	30.6	74.5	66.8	126.0	22.7
sensor means	86.4	34.8	31.2	74.9	67.1	126.7	23.1
difference	0.9	0.6	0.5	0.4	0.3	0.7	0.4
range of							
standard	17.649	9.067	11.295	16.665	23.449	15.527	11.679
deviations	18.076	9.504	11.661	17.026	23.931	15.980	12.271
difference	0.427	0.437	0.366	0.361	0.482	0.453	0.592

The range of means is typically less than that of Landsat MSS values when the MSS data are scaled into 8-bit space. Enhanced-contrast images of parts of the Macon scene were recorded onto film and visually examined for evidence of striping. Striping is not evident in channels having sensors with a range of mean differences less than 0.4 between their high and low values. Striping becomes apparent when difference values reach 0.5 and becomes objectionable when values are greater than 0.6.

A banding also was noted for some of the TM bands over homogeneous targets such as water bodies. The banding appears clustered into two groups of 16 adjacent scanlines and appears to be related to the alternate back and forth sweeps of the pushbroom scanner.

P-tape data for the Florida scene were analyzed to assess the radiometric character of the banding. Because the data have been geometrically corrected and interpolated to a 28.5 m pixel size, the gathering of banding statistics was done on groups of 17 scanlines, which is an approximation to the required correction of a 30 m original pixel to the geometrically corrected pixel size of 28.5 m. The relationship should hold for at least a small contiguous group of scanlines. Two areas along the same groups of 17 scanlines were sampled over relatively homogeneous bodies of water. Statistics were contrasted for waters of Lake Weir, Florida, on the western side of the image, against the Atlantic Ocean waters located off Edgewater, Florida, near the east edge of the image (Tables 4 and 5).

TABLE 4

COMPARISON OF DIGITAL NUMBER STATISTICS, TWO HOMOGENEOUS WATER BODIES ALONG THE SAME, BUT OPPOSITE ENDS OF GROUPS OF 17 SCANLINES

Lake water

Scanlines	TM Band	1	2	3	4	5	6	7
2809-2825	Mean	78.97	29.07	23.01	17.22	9.41	131.51	4.24
	Std. Dev.	1.44	0.63	0.66	0.47	0.68	0.50	1.08
2826-2842	Mean	79.92	29.33	23.34	17.36	9.41	131.68	4.27
	Std. Dev.	1.46	0.61	0.73	0.49	0.78	0.47	0.96
2843-2859	Mean	78.74	29.00	23.00	17.15	9.36	131.68	4.31
	Std. Dev.	1.42	0.68	0.70	0.43	0.79	0.47	1.05
2860-2876	Mean	79.24	29.13	23.22	17.37	9.40	131.72	4.28
	Std. Dev.	1.54	0.68	0.74	0.52	0.79	1.45	1.04
2877-2893	Mean	78.57	28.82	22.95	17.07	9.38	131.71	4.31
	Std. Dev.	1.60	0.69	0.72	0.45	.74	0.46	1.04

Sample size for each group of scanlines = 272

TABLE 5

COMPARISON OF DIGITAL NUMBER STATISTICS, TWO HOMOGENEOUS WATER BODIES ALONG THE SAME, BUT OPPOSITE ENDS OF GROUPS OF 17 SCANLINES

Ocean water

Scanlines	TM Band	1	2	3	4	5	6	7
2809-2825	Mean	74.71	25.26	19.39	12.25	6.91	129.44	3.89
	Std. Dev.	1.42	0.69	0.68	0.66	0.92	0.61	1.01
2826-2842	Mean	73.44	24.78	18.83	11.03	6.84	128.89	3.82
	Std. Dev.	1.36	0.80	0.68	0.69	0.98	1.63	1.02
2843-2859	Mean	74.53	25.40	19.40	12.31	6.82	129.44	3.87
	Std. Dev.	1.31	0.69	0.72	0.75	0.92	0.67	1.04
2860-2876	Mean	73.49	24.95	18.94	11.16	6.69	129.17	3.85
	Std. Dev.	1.24	0.72	0.68	0.69	1.01	0.49	0.97
2877-2893	Mean	74.98	25.61	19.81	12.50	6.83	129.47	3.92
	Std. Dev.	1.48	0.63	0.71	0.68	0.95	0.70	1.05

Sample size for each group of scanlines = 272

Both these areas exhibited banding in the image data. The beginning of the groups of 17 scanlines was determined by using a harshly contrast-enhanced TM band 3 image and picking the beginning scanline on an interactive video analysis system. Examination of table 5 shows that the ocean waters have a consistent variation in mean values for groups of 17 adjacent scanlines, beginning with all channels having high mean values for the first group of 17 lines (2809-2825), and proceeding in an alternating low-high fashion for following groups of 17 lines. Digital values for the lake waters (table 4) show an opposite trend. The same initial group of scanlines shows consistently low values and proceeds in an alternating high-low fashion for following groups of 17 scanlines. Differences between adjacent groups of scanlines are greatest in TM channels 1 through 4, and appear negligible in TM band 5-7. The change in relative mean values across the image for adjacent groups of scanlines suggests an inherent and systematic change occurring, perhaps due to some decay factor imposed on the gain or offset values for opposite sweeps of the pushbroom scanner. Some crossover point must exist in the data, presumably near the center of the scanline, where digital numbers for opposite sweeps would be of equal value. It also suggests that this type of banding could not be corrected by a modulo-16 or -32 histogram equalization, even in the geometrically uncorrected A-tape data, unless correction factors which varied as a function of position along a scanline, were applied along groups of 32 scanlines.

PRELIMINARY SPECTRAL OBSERVATIONS

Specific band ratios were used to determine their effectiveness in defining vegetation and rock mineralogy for the Washington, D.C. scene. The TM 3/4 band ratio was selected to depict vegetation. Vegetation appears black to dark gray in this ratio because of its relatively low reflectance in band 3 due to the presence of chlorophyl absorption bands, and its high reflectance in band 4 due to a lack of chlorophyl absorption (Knipling, 1970). Geologic materials lack the strong contrast between TM bands 3 and 4 and thus would appear light gray to white in the ratio. The 5/2 band ratio was used to depict limonitic rocks. Limonitic rocks have low reflectances in bands 1 and 2 compared with band 3 due to a strong ferric-iron absorption band centered in the ultraviolet, but whose effects reach into the short wavelength visible part of the spectrum (Hunt and others, 1971; Hunt and Ashley, 1979). Nonlimonitic rocks and soils lack the absorption band in the ultraviolet, hence their spectral curves do not show the sharp drop between band 3 and bands 1 and 2. Most geologic materials have no absorption bands in TM band 5 and are quite bright in this region of the spectrum. Hence, a 5/2 band ratio image will appear relatively bright for limonitic rocks, whereas nonlimonitic rocks will appear dark.

Rocks which have minerals that contain hydroxyl or carbonate anions in their crystal lattices, have absorption bands (Hunt and Salisbury, 1971; Hunt and Ashley, 1979) in the bandpass of TM band 7. Hydroxyl-bearing minerals, those containing either Al-O-H or Mg-O-H bands, include: 1) clay minerals, 2) other sheet silicates such as the serpentine minerals, some of the micas, and talc, among others, and 3) sulfate minerals such as alunite and jarosite, which often are found as products of hydrothermal alteration processes. Carbonate minerals include calcite and dolomite, which are common constituents in the sedimentary rocks limestone and dolomite. Rocks containing these anions will have relatively low reflectance values in TM band 7, whereas rocks lacking these anions will have relatively higher reflectances. A 5/7 band ratio was evaluated to test the effectiveness of the 1.6- and 2.2-um bands in detecting rocks containing hydroxyl- or carbonate-bearing minerals. Areas containing rocks which have absorption bands in the 2.2-um region will appear light gray to white in the 5/7 ratio, whereas rocks lacking absorption bands in this region will appear dark gray to black. Similar bands were selected in prior studies to map clay-rich rocks using airborne Thematic Mapper Simulator (TMS) scanners (Podwysocki and Segal, in press; Rowan and Kahle, 1982; Ashley and Abrams, 1980). Preliminary results show that clay minerals containing absorption bands at 2.2 um, which are centered in TM band 7, can be readily detected when the band ratio images are suitably contrast-enhanced.

Figure 5a is a false-color infrared image which shows a 256 by 256 pixel area from the Washington, D.C. scene. A road construction project has laid bare clay-rich soils containing ferric iron oxide minerals. A color ratio composite image (fig. 5b) shows the clear barren area as white, which in the color assignments made to each ratio, indicates both ferric iron oxide and clay minerals. Ferric-iron-rich areas lacking clay minerals are portrayed as a cyan color. Vegetation appears red to magenta, depending upon its type and vigor. Spectrally flat areas (lacking both ferric iron and clay absorption bands) are green to yellow-green.

SUMMARY

Landsat-4 Thematic Mapper digital data were examined for several scenes in the eastern United States to characterize their geometric and radiometric accuracies. A small portion of one of the scenes also was processed using band ratioing in order to test the radiometric characteristics for mapping of spectrally dissimilar geologic materials.

Whole-scene accuracy was assessed by comparison of 38 image and topographic control points for four bands of a TM image of the Washington, D.C. area. The images were compared with both Universal Transverse Mercator and Space Oblique Mercator projections. Both similarity and affine transformations were applied using the least-squares method in order to fit the image control points to the map coordinates. Results show that the affine transformation provides a better fit of the image to the map projections, decreasing the root mean square error from an average of about 70 m for the similarity transformation to about 45 m for the affine transformation for both projections. Results show that little difference exists between the two projections for this TM scene. Analysis of the geometry of the film-writing device that was used to produce the TM images suggests a systematic error in the device, causing an elongation along one diagonal of the image and a foreshortening along the opposite diagonal. This distortion in the film-writer device accounts for most residual error found in the similarity transformation of the TM image data. Hence, geometric errors in the TM data itself, are of some value less than or equal to the RMSE values derived from the affine transformation.

Band-to-band registration for portions of the Washington, D.C. scene indicates subpixel misregistration in TM bands 1 through 4. TM bands 5 and 7 are displaced between 1 to 2 pixels from their corresponding points in the bands 1 through 4 and band 6 is displaced by 3 to 4 pixels from bands 1 through 4.

Analysis of the radiometric quality shows at least two types of scanline-related banding. Radiometric stripping occurs on a modulo-16 basis and is related to small shifts in gains and/or bias between each of the 16 detectors in each band. Stripping is most noticeable in band 1 and becomes less noticeable with increasing wavelength in the visible and near-infrared bands. The thermal band six also has relatively pronounced banding. Another type of banding appears as alternating groups of 16 lighter and darker scanlines. The effect is noticed over homogenous areas such as water bodies and is most pronounced along the edges of the scenes. The effect changes along the length of the groups of 16 scanlines. Along one edge of the scene, average values of the 16 scanlines alternate in a high-low fashion, whereas on the opposite side of the scene, values alternate in a low-high fashion for the same scanlines. The severity of the banding is worse in band 1 and becomes less and less noticeable towards the near infrared. TM band 6 is not affected by the phenomenon.

TM bands were ratioed in order to test the radiometric quality of the data for mapping geologic units with contrasting spectral characteristics. A 3/4 band ratio was processed to distinguish between vegetation and other materials. A 5/2 ratio was used to distinguish bwtween limonitic and nonlimonitic rocks and a 5/7 ratio was used to detect geologic materials which contained minerals having the hydroxyl or carbonate anion. Results showed that clay and limonite-rich rocks could be distinguished from limonitic rocks lacking clays. Rocks lacking both limonite and clays could also be distinguished.

REFERENCES

Ashley, R. P., and Abrams, M. J., 1980, Alteration mapping using multispectral images - Cuprite mining district, Esmeralda County, Nevada: U.S. Geological Survey Open-File Report 80-367, 17p.

Bender, L.U. and Falcone N. 1982, Landsat 3 RBV Imagery for Topographic Mapping: Proceedings, Fifth International Symposium on Computer-Assisted Cartography and ISP Commision IV; Cartographic and Data Band Application of Photogrammetry and Remote Sensing, p. 45-54.

Hunt, G. R., and Salisbury, J. W., 1971, Visible and near-infrared spectra of minerals and rocks: II-Carbonates: Modern Geology, v. 2, p. 22-30.

Hunt, G. R., and Ashley, R. P., 1979, Spectra of altered rocks in the visible and near infrared: Economic Geology, v. 74, p. 1612-1629.

Hunt, G. R., Salisbury, J. W., and Lenhoff, D. J., 1971, Visible and near-infrared spectra of minerals and rocks: III-Oxides and hydroxides: Modern Geology, v. 2, p. 195-205.

Knipling, E. B., 1970, Physical and physiological basis for the reflectance of visible and near-infrared radiation from vegetation: Remote Sensing of the Environment, v. 1, no. 3, p. 155-159.

Podwysocki, M.H., and Segal, D.B., 1983, Mapping of hydrothermally altered rocks using airborne multispectral scanner data, Marysvale, Utah mining district: Economic Geology, v. 78, p. 675-687.

Rowan, L.C., and Kahle, A.B. 1982, Evaluation of 0.46- to 2.36-um multispectral scanner images of the East Tintic mining district, Utah, for mapping hydrothermally altered rocks: Economic Geology, v 77, p. 441-452.

ORIGINAL PAGE IS
OF POOR QUALITY

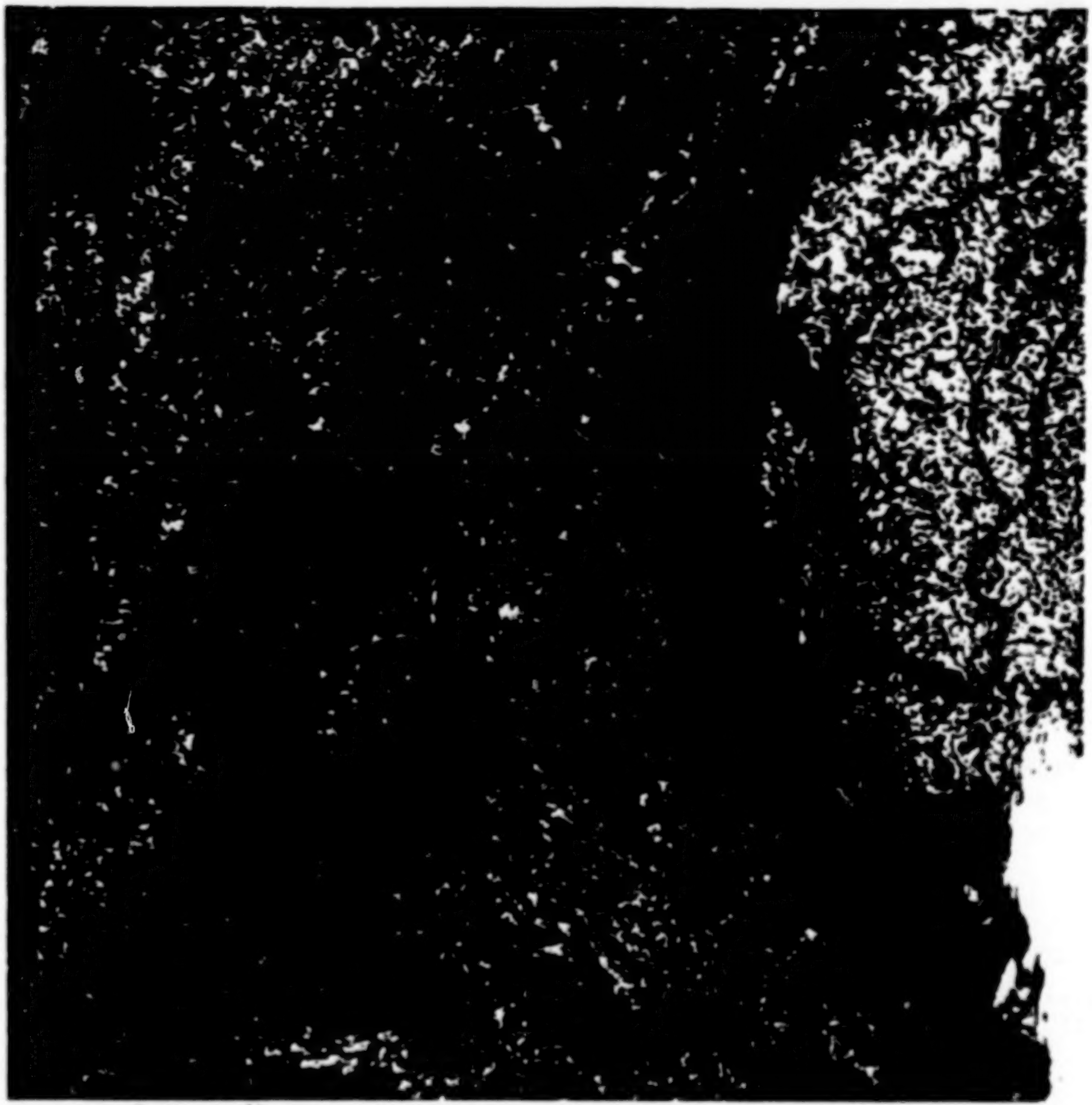

Figure 1a - Image of TM band 3 for the whole Washington, D.C. scene. Distance along the edge of the image is approximately 185 km.

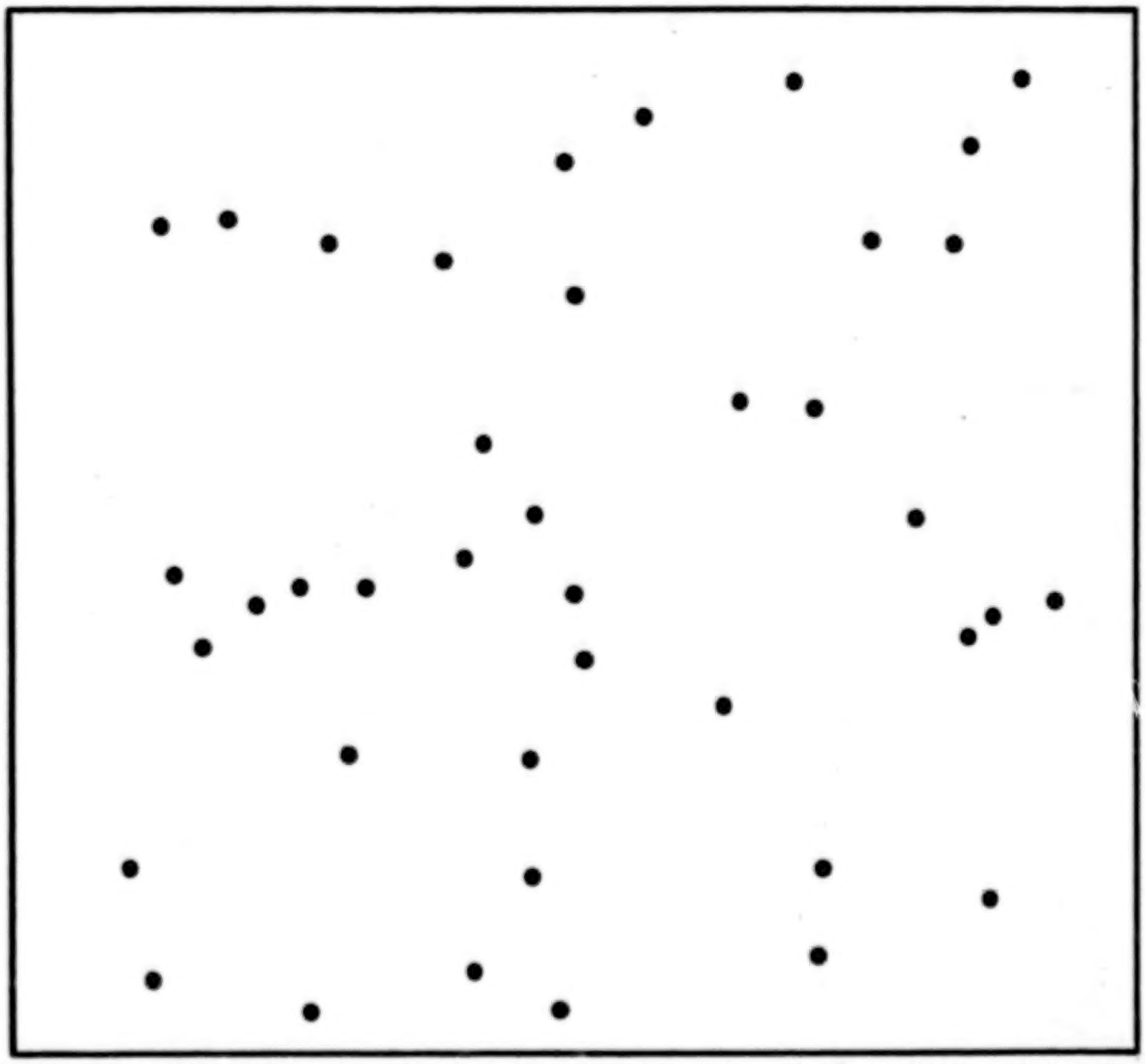

Figure 1b - Schematic map showing the distribution of 38 control points chosen for this study.

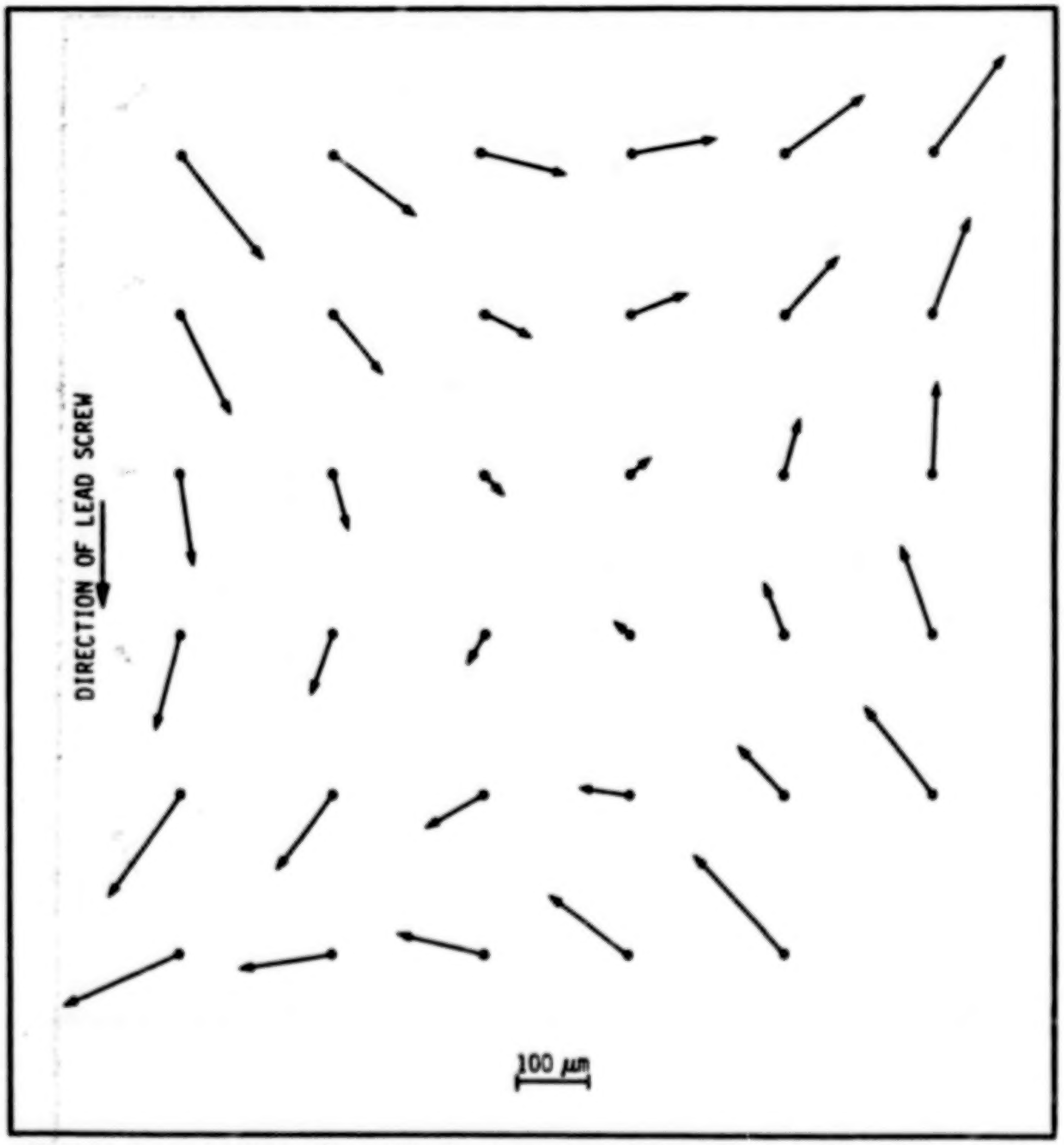

Figure 2 - A plot of residual errors resulting from application of the similarity transformation to the 4 cm-spaced grid data.

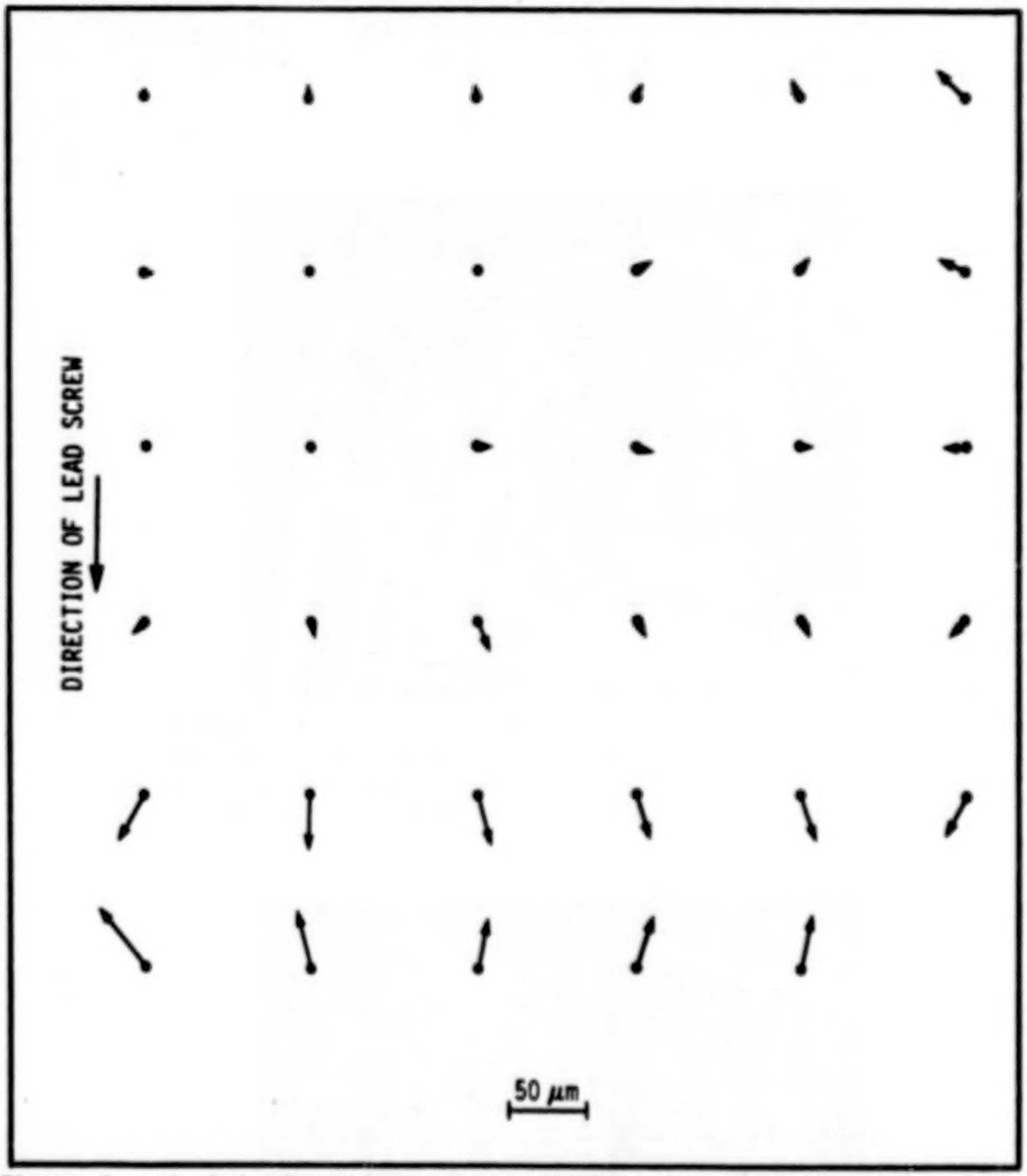

Figure 3 - A plot of residual errors resulting from the application of the affine transformation to the 4 cm-spaced grid data.

Figures 4 - Color-composite images (64 by 64 pixels) of TM bands projected on the CRT as red, green, and blue, respectively, for a portion of Dulles International Airport. The runways and small lake were used to study band-to-band registration. Distance along bottom edge of the image is approximately 1.8 km.

ORIGINAL PAGE IS
OF POOR QUALITY

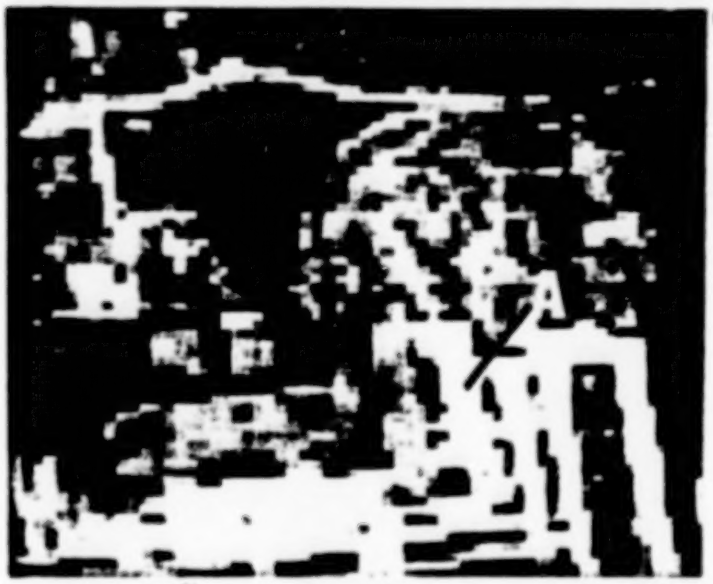

Figure 4a - A composite image of bands 4, 3, and 2. Misregister appears to be at the subpixel level. Note that the brightest portion of the airport parking ramp (A) is centered in the middle of the ramp (cf. fig. 4b).

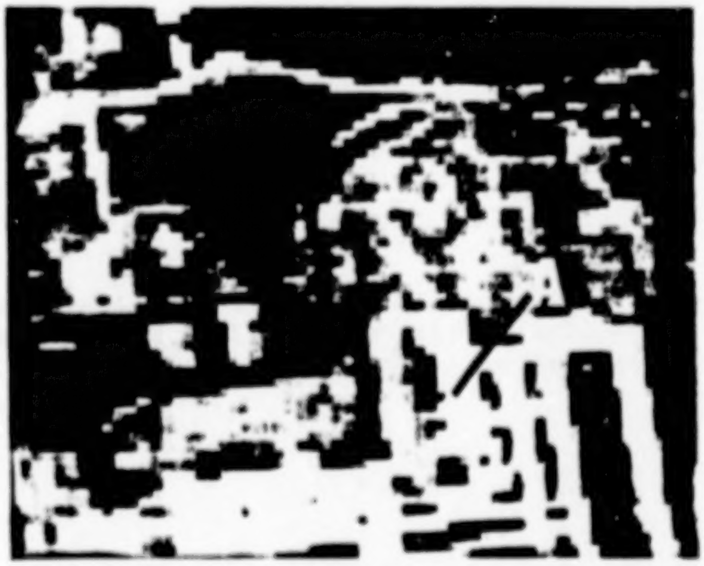

Figure 4b - A color-composite of bands 5, 3, and 2. Note that the brightest portion of the airport parking ramp (A) is shifted, indicating a westward shift of approximately one pixel for band 5.

ORIGINAL PAGE IS
OF POOR QUALITY

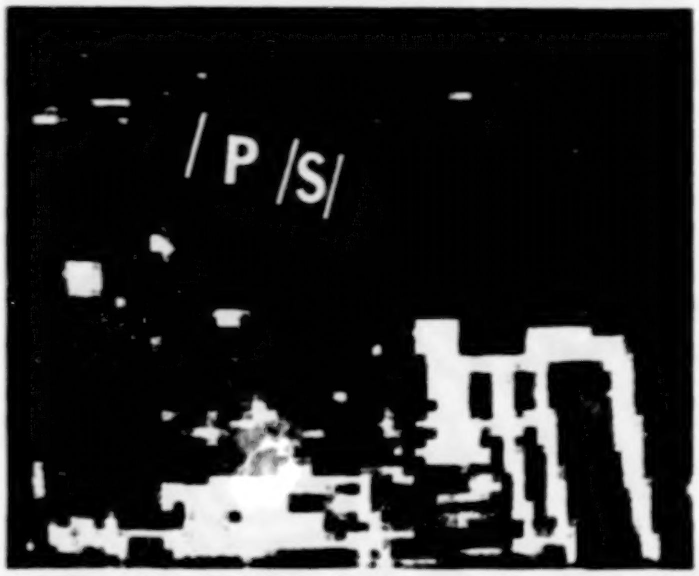

Figure 4c - A composite of bands 6, 3, and 2. The pond (P) appears shifted 4 pixels east in band 6, as noted by the dark "shadow" east of the pond.

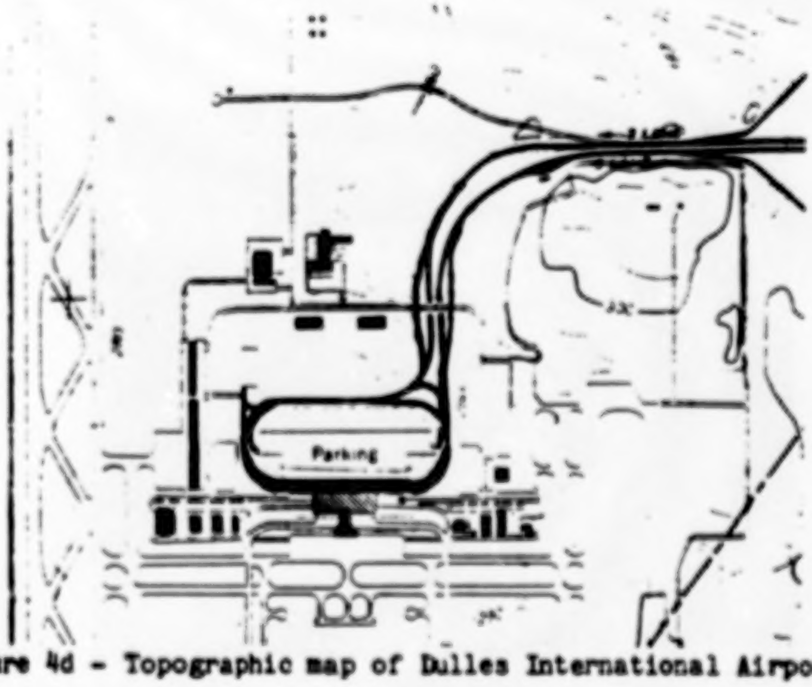

Figure 4d - Topographic map of Dulles International Airport.

SCALE 1:24 000

ORIGINAL PAGE IS
OF POOR QUALITY

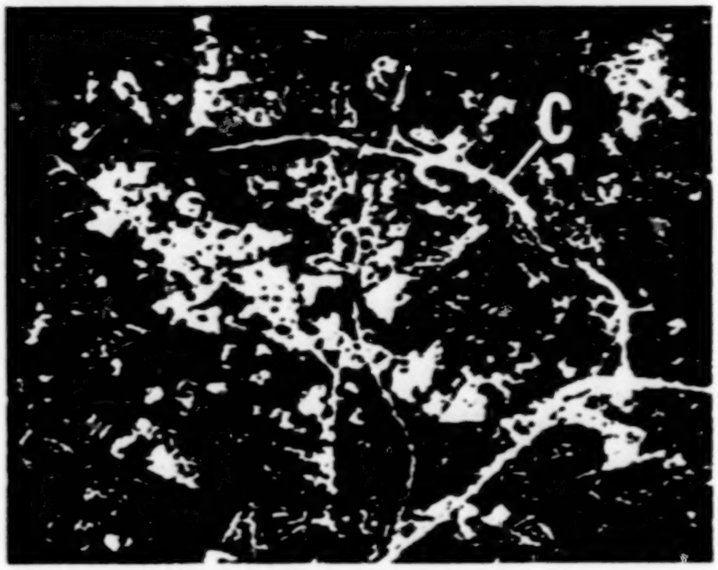

Figure 5a - A TM false-color infrared composite of bands 4, 3 and 2 projected as red, green, and blue, respectively. The bright white linear area in the northeast quadrant (C) is an area of disturbed ground along a highway right-of-way containing clay-rich limonitic soils. Distance across the bottom edge of the image is approximately 7.3 km.

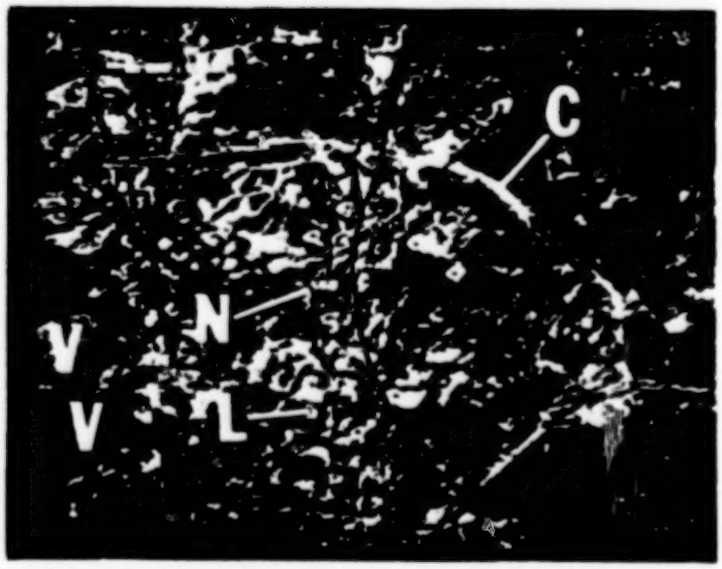

Figure 5b - A color-ratio-composite image of TM band ratios 3/4, 5/2 and 5/7 projected as green, blue and red, respectively. Areas of limonitic material (L) appear cyan, limonitic and clay-rich areas are white (C) bare areas containing neither limonite nor clay minerals are yellow-green to green (N). Vegetation appears in shades of red to magenta (V).

N85-21740

D
16

THE USE OF LINEAR FEATURE DETECTION TO INVESTIGATE THEMATIC MAPPER DATA PERFORMANCE AND PROCESSING

Charlotte M. Gurney
Systems and Applied Sciences Corporation
5809 Annapolis Road
Hyattsville, Maryland

INTRODUCTION

The objective of the work described is to investigate the geometric and radiometric characteristics of Thematic Mapper data through analysis of linear features in the data. The particular aspects considered are:

1. Thematic Mapper ground IFOV
2. Radiometric contrast between linear features and background
3. Precision of system geometric correction
4. Band-to-band registration
5. Potential utility of TM data for linear feature detection especially as compared to MSS data.

MODEL DESCRIPTION

In the context of this investigation linear features are defined as two close, parallel and opposite edges. Examples in remotely sensed data are features such as roads, rivers and bridges.

These features may be detected using a local operator which considers the arrangement of grey levels within a 5 by 5 pixel array. Details are given in Gurney (Ref. 1), and the model is described briefly below. Fourteen possible orientations of the linear feature in the local area are considered, these are illustrated in Fig. 1. For each orientation the sum of values in column B is compared to that in columns A and C. For dark linear features the sum in B must be less than both the sums in A and C by a given threshold. In addition B2 must be lower in value than both A2 and C2. For bright linear features the sums in A and C must be less than those in B. If these conditions are satisfied for any one of the 14 orientations then pixel B2 is considered as linear.

Original photography may be purchased
from EROS Data Center
Sioux Falls, SD 57198

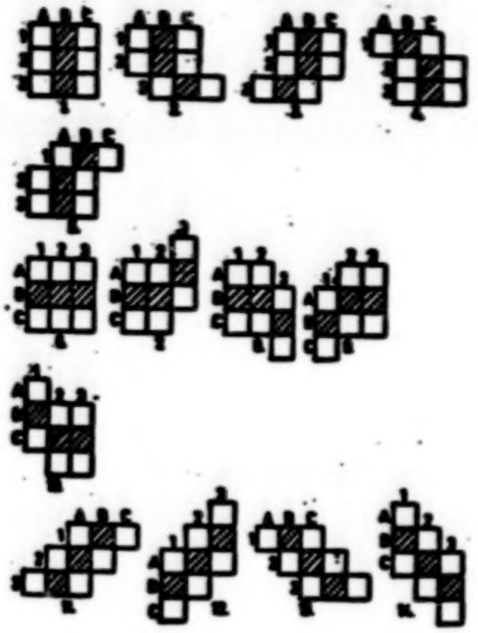

Fig. 1 Orientation of a Linear Feature Three Pixels Long Passing Through the Centre of an Array

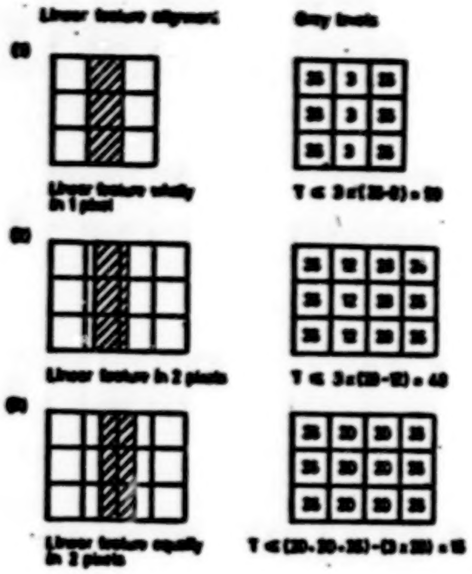

Linear feature alignment
Grey levels
Linear feature wholly in 1 pixel
Linear feature in 2 pixels
Linear feature equally in 2 pixels

Fig. 2 Variations in Threshold with Linear Feature Alignment with the Pixel Boundaries

Results depend on two factors: the contrast between line material and background material, and the width of the feature. Any given feature may be assumed to be of constant width and contrast over the area of study. Therefore by varying the detector threshold it is possible to vary the accuracy with which the feature is detected. At low thresholds all of a feature may be detected, as the threshold is increased less and less of the feature will be detected.

An additional factor which must be considered is the alignment of the linear feature with the pixel boundaries. A simplified schematic representation is illustrated in Fig. 2. If a feature occupies only a single pixel then a higher threshold may be used to detect it than if it is equally divided between two pixels. Thus there is a wide variability between thresholds required to detect the full range of conditions.

If it is assumed that the present material in a pixel is linearly proportional to its contribution to the reflectance, and if it is assumed that every alignment of the feature with the pixel boundaries is equally probable then it is possible to derive a set of expressions relating detector threshold to detection accuracy, and feature width and contrast. Complete derivations are given in Gurney (Ref. 2).

For lines up to 1 pixel wide:

$$T = 3bW - (3bW - bW/2)\,A \qquad (1)$$

where

T = detector threshold
A = % accuracy / 100
b = contrast = (|mean background - mean line|)/100
W = line width as % pixel width

Similarly for lines 1 - 2 pixels in width:

$$T = 300b - \left[\frac{3b\,(100 - W)}{2}\right] \left[1 + A\right] \qquad (2)$$

Similar expressions may be derived for features up to four pixels in width. Beyond this value detection using this model will not be possible.

Contrast measurements may be made by selecting training areas corresponding to known linear and background materials and using the mean grey level values in these areas. Since the contrast measurement is based upon mean values it is clear that a high variance in a training area will lead to results which conform less closely to the theoretical expectations of the model.

Using this model it is possible to select good thresholds for features of known width and contrast. Also, by applying the procedure at a given theshold and calculating observed detection accuracy then it is possible to estimate feature widths, assuming that the pixel size is known. If all parameters are known then it is possible to obtain an estimate of pixel size. All of these applications have been tested using digital MSS and RBV data with good results.

SCENE CONTRAST AND VARIABILITY

Using MSS data it is generally the case that only one, or maybe two, bands provide sufficient contrast to allow linear feature detection. With TM data there are more bands providing good contrast. This allows the possibility of independent verification from band to band of feature width estimations.

Figs. 3 - 10 illustrate the results of linear feature detection using part of a scene of Iowa for August 1982. Each of Figs. 3-8 corresponds to detection of bright linear features in bands 1, 2, 3, 4, 5 and 7 using the same threshold (9) in each case. Variations between results therefore correspond to variations in contrast and scene variability. Band 6 data, corresponding to the thermal infra-red channel, were not used since no features were detected.

Results indicate that bands 1 and 3 give the best performance, with band 2 providing similar results. Bands 5 and 7 also perform well, but there is evidence of increased 'noise' i.e., pixels detected as linear which do not correspond to any recognizable ground feature.

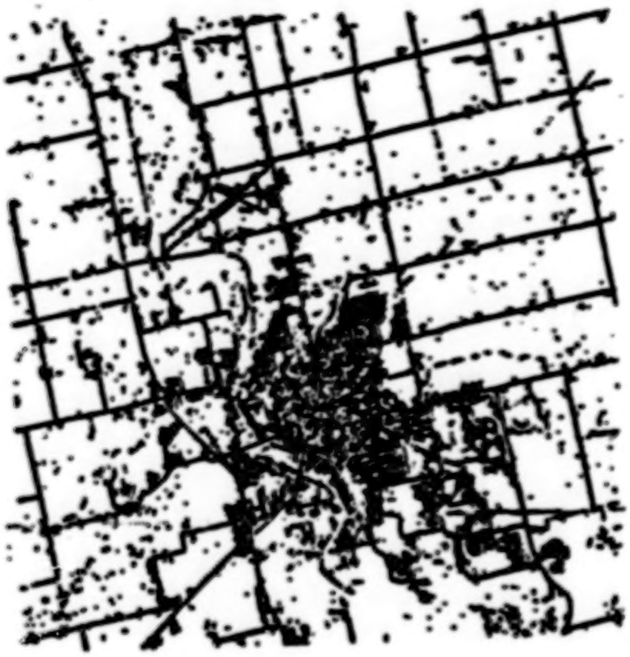

Fig. 3 Results of Linear Feature Detection for Iowa Test Area, Band 1

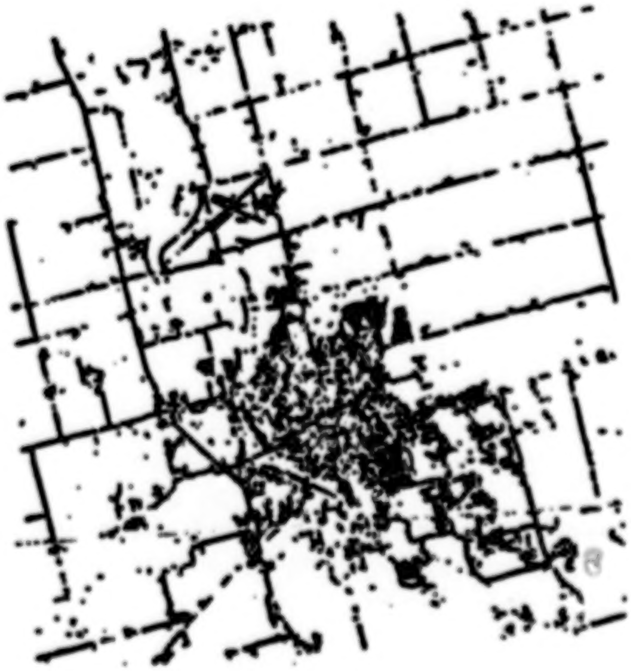

Fig. 4 Results of Linear Feature Detection for Iowa Test Area, Band 2

ORIGINAL PAGE IS
OF POOR QUALITY

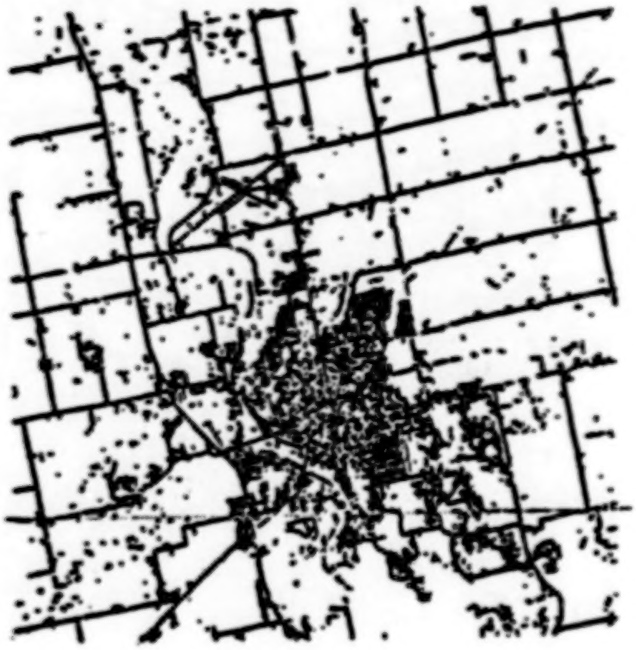

Fig. 5 Results of Linear Feature Detection for Iowa Test Area, Band 3

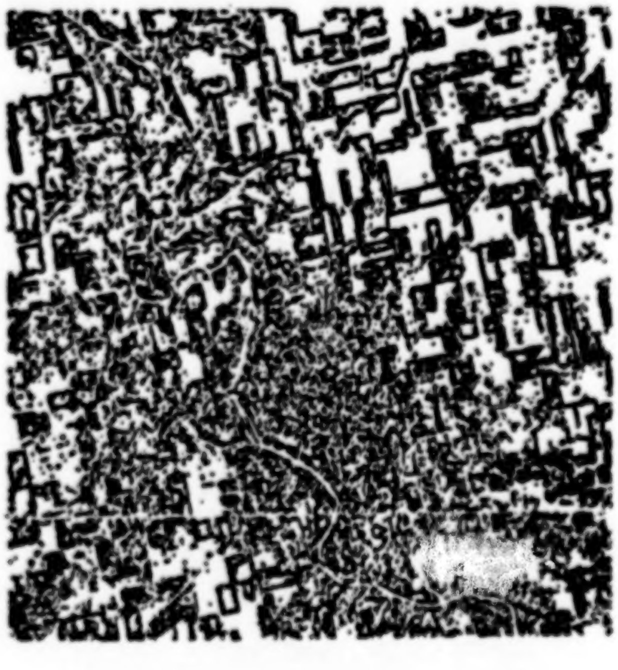

Fig. 6 Results of Linear Feature Detection for Iowa Test Area, Band 4

ORIGINAL PAGE IS
OF POOR QUALITY

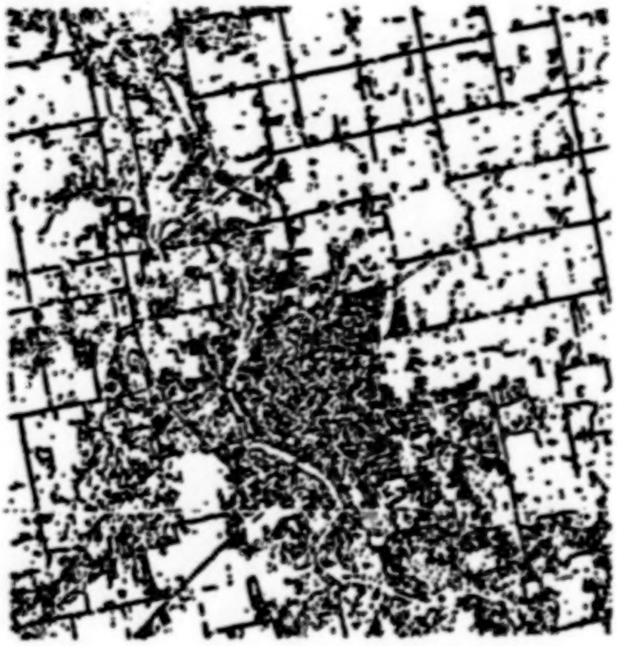

Fig. 7 Results of Linear Feature Detection for Iowa Test Area, Band 5

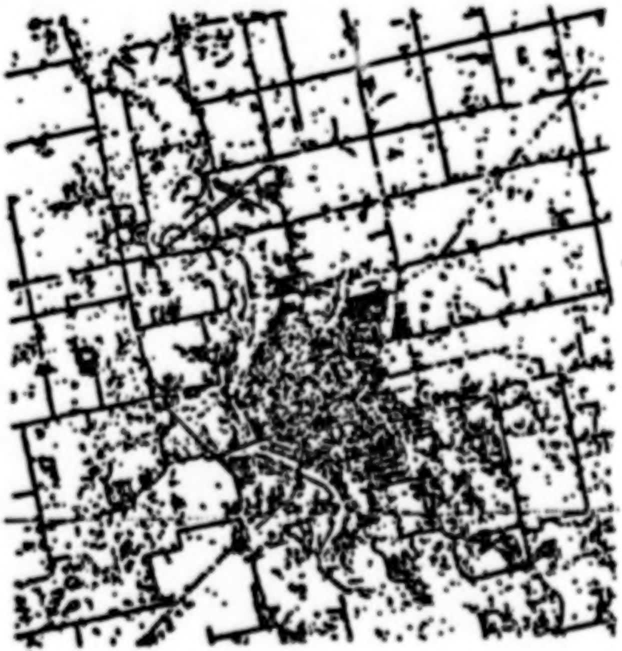

Fig. 8 Results of Linear Feature Detection for Iowa Test Area, Band 7

ORIGINAL PAGE IS
OF POOR QUALITY

Band 4 results are very different from those for the other bands. The road pattern is not apparent, and the response seems to be driven by a linear effect at field boundaries.

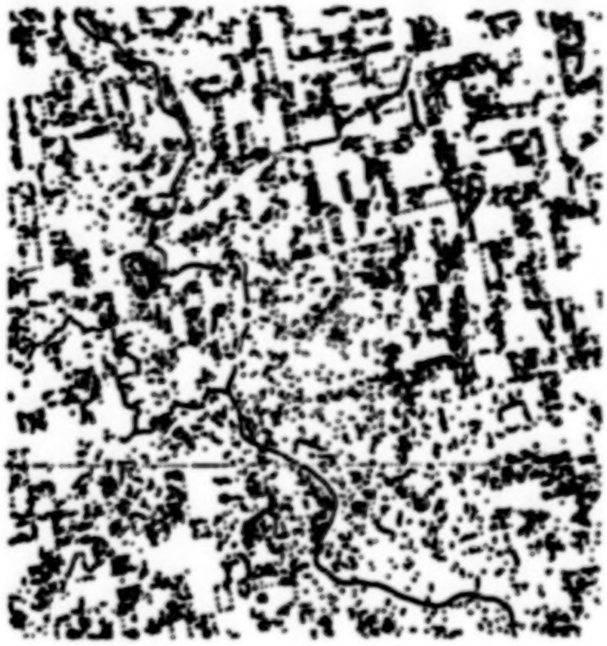

Fig. 9 Results of Linear Feature Detection for Iowa Test Area, Band 4, Dark Lines

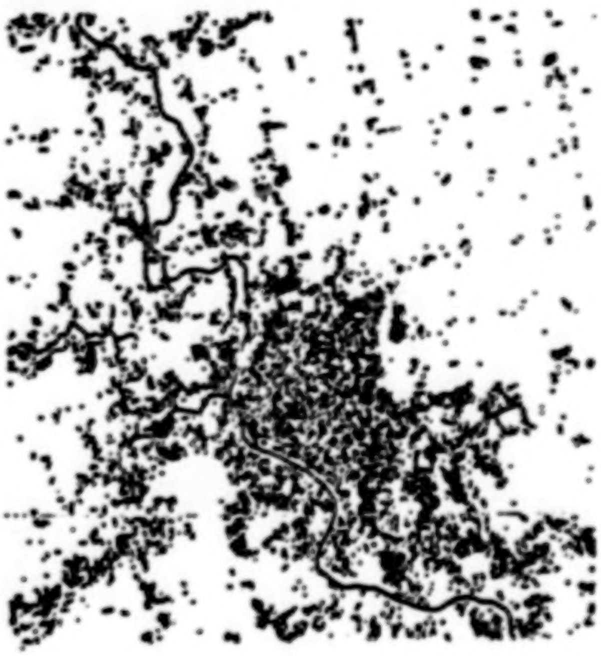

Fig. 10 Results of Linear Feature Detection for Iowa Test Area, Band 5, Dark Lines

Figs. 9 and 10 show the results of dark feature detection using bands 4 and 5. Other bands were unable to detect dark features successfully. Band 5 performs best in isolating the rivers without picking up excessive amounts of noise. Band 4 also show an interesting effect of evenly spaced 'dots' along field edges. The reasons for this effect are not known at present and will receive further study.

ESTIMATION OF LINEAR FEATURE WIDTHS

Estimation of feature widths using TM data was carried out in order to establish a lower limit on the width of detectable feature, and to confirm that the data are suitable for application of the model described previously.

Two test areas were selected which had different ground characteristics. The first corresponds to an area in North Carolina with a very homogeneous, flat background traversed by narrow gravel surfaced roads less than a pixel in width. The second corresponds to part of the Washington, D.C. beltway with a width between one and two pixels and traversing a much more variable background.

For each test area training areas were selected to establish line: background contrast. The line detection procedure was then applied at at least three different thresholds to each band of data for which contrast was sufficient to allow some degree of feature detection. For each of these the resulting detection accuracy was then calculated. Results were substituted in equations 1 and 2 in order to obtain an estimate of the feature width as a percent of the pixel width.

Tables 1 and 2 and Fig. 11 show results for the North Carolina area.

Table 1.

LINE: BACKGROUND CONTRASTS FOR NORTH CAROLINA TEST AREA

Band Number	Background		Line		Contrast	Deviation
	$\overline{X}$	σ	$\overline{X}$	σ		
1	64.5	1.5	107.4	14.9	.43	38.4
2	24.6	0.9	54.6	9.9	.30	36.3
3	21.7	2.6	69.3	15.6	.48	38.3
4	62.7	4.0	81.8	10.4	.19	75.4
5	41.8	6.8	139.6	26.4	.98	33.9
6	—	—	—	—	—	—
7	12.4	2.8	79.0	21.0	.67	35.8

Contrast = (|mean background - mean line|) /100.
Deviation = (σbackground + lineσ)/contrast.

Table 1 gives the contrast data and an additional parameter termed the deviation. The deviation is dependent on the amount of variation in the line and background data, and it essentially indicates the degree to which results are likely to accord with model predictions. High variances coupled with low contrast leads to considerable deviation from expected results. From previous experience using MSS data deviation values of 40 or less indicate very close correspondence between observed and predicted results.

Table 2.
RESULTS FOR NORTH CAROLINA TEST AREA.

	Detector Threshold	Observed Accuracy at 95% Confidence Level (%)	Estimated Road Width as % Pixel Size
BAND 1	9	81.7 - 87.5	21.8 - 25.8
	15	55.5 - 63.3	21.6 - 24.6
	18	35.4 - 43.2	19.8 - 21.8
	21	25.4 - 32.6	20.4 - 22.1
BAND 2	9	37.9 - 45.7	14.6 - 16.2
	12	32.5 - 40.1	18.3 - 20.0
	15	16.6 - 23.0	19.3 - 20.6
	18	7.1 - 11.7	21.2 - 22.2
BAND 3	12	75.0 - 81.6	22.2 - 26.0
	15	51.6 - 59.4	18.3 - 20.6
	18	36.8 - 44.6	18.0 - 19.9
	21	26.1 - 33.3	18.6 - 20.2
BAND 4	9	50.8 - 58.6	27.3 - 30.9
	12	34.4 - 42.0	29.5 - 32.4
	18	13.0 - 18.8	35.7 - 37.4
BAND 5	21	69.3 - 76.3	16.9 - 19.6
	24	63.0 - 70.4	17.2 - 19.7
	27	57.4 - 65.2	17.6 - 20.1
	36	45.1 - 53.1	19.6 - 22.0
BAND 7	18	61.1 - 68.7	18.2 - 20.9
	21	48.4 - 56.4	17.5 - 19.7
	24	42.2 - 50.2	18.4 - 20.5
	27	34.8 - 42.6	18.9 - 20.8

	Mean road width (%)	σ	Road width for 28.5 pixel
Excluding Band 4	20.0	2.0	5.7 metres
Including Band 4	21.5	4.7	6.1 metres

Table 2 lists the observed accuracies and calculated range of road widths for all bands and thresholds used. Results show a close correspondence between estimated widths at different bands and thresholds, with the exception of results for Band 4.

Band 4 gives a larger mean width and also shows more variability in the estimates for different thresholds. This is to be expected from the higher deviation value observed for this band. The estimated road width from all these data is about 6 metres assuming a 28.5 by 28.5 metre pixel.

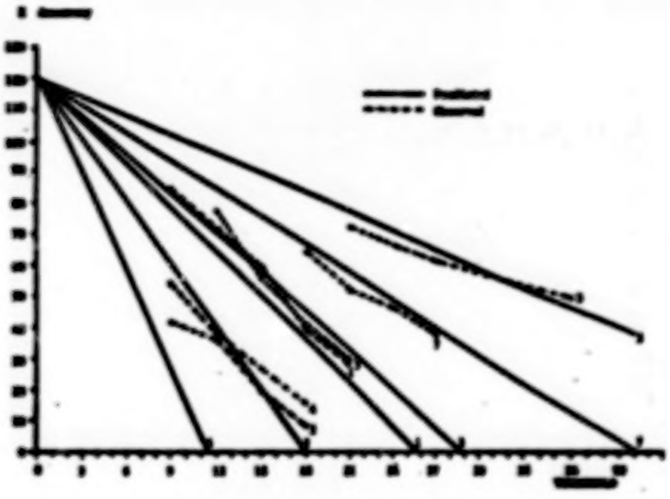

Fig. 11 Predicted vs. Observed Results for N. Carolina Test Area

Fig. 11 shows a plot of predicted results assuming a 6 metre road width, against actual observed results. There is a very close correspondence for all but the Band 4 data. The actual width of the roads in this area is not known at the time of writing, but is believed to be close to the estimate given here.

Table 3.
LINE: BACKGROUND CONTRASTS FOR WASHINGTON, D.C. TEST AREA

Band Number	Background		Line		Contrast	Deviation
	$\overline{X}$	σ	$\overline{X}$	σ		
1	56.6	1.6	73.2	8.5	.17	59.4
2	21.6	0.8	32.1	5.0	.11	52.7
3	22.8	1.96	36.6	7.3	.14	66.1
4	36.4	2.96	43.1	2.4	.07	76.6
5	38.6	5.7	60.7	10.1	.22	71.8
6	115.1	0.8	115.7	0.5	.01	130.0
7	13.1	2.3	28.2	8.4	.15	71.3

Contrast = (| Mean background - Mean line |)/100.
Deviation = (σbackground + σ line)/contrast.

Tables 3 and 4 and Figs. 12 and 13 show results for the Washington, D.C. area. Band 6 and Band 4 were included in the contrast measurement, but were not used subsequently because of the poor contrast levels observed. In general, contrasts are considerably lower than for the North Carolina area reflecting both the difference in materials and the lower sun angle of this November scene. Deviation values are also correspondingly higher.

Table 4.
RESULTS FOR WASHINGTON, D.C. TEST AREA

	Detector Threshold	Observed Accuracy % at 95% Confidence level	Estimated road width as % pixel size
BAND 1	15	83.6 - 94.6	172.5 - 176.9
	18	69.9 - 84.7	170.1 - 176.2
	21	47.9 - 65.3	171.2 - 179.5
	24	45.9 - 63.5	164.8 - 172.6
BAND 2	9	65.5 - 81.2	180.3 - 187.8
	15	31.9 - 49.3	173.1 - 182.1
	18	19.5 - 35.1	167.3 - 176.1
BAND 3	9	87.4 - 97.0	179.8 - 183.9
	15	68.3 - 83.3	170.1 - 176.4
	18	58.9 - 75.5	165.1 - 171.9
BAND 5	9	58.0 - 74.8	198.8 - 209.3
	18	32.7 - 50.1	196.9 - 209.6
	27	17.3 - 32.7	189.1 - 200.8
BAND 7	9	75.2 - 88.8	184.7 - 191.3
	15	31.9 - 49.3	189.3 - 201.1
	18	9.1 - 22.1	198.3 - 210.0

	Mean road width (%)	σ	Road width for 28.5 m pixel
Bands 1 - 3	174.96	5.14	49.9 metres
Bands 5, 7	198.30	6.63	56.5 metres

Estimated road widths are given in Table 4. These show a close correspondence between results in bands 1, 2, and 3 giving a width estimate of 175% of a pixel which is close to 50 metres for a 28.5 m pixel. The true width of the beltway is known to be 48-50 metres in this area so that this result corresponds very closely to the true width. However results for bands 5 and 7 give a width estimate close to 56 metres which is an over-estimate of the width.

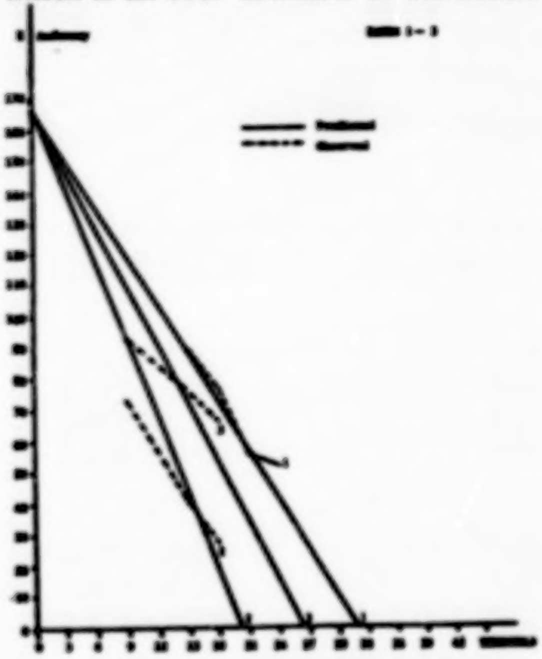

Fig. 12 Predicted vs. Observed Results for Washington, D.C. Test Area

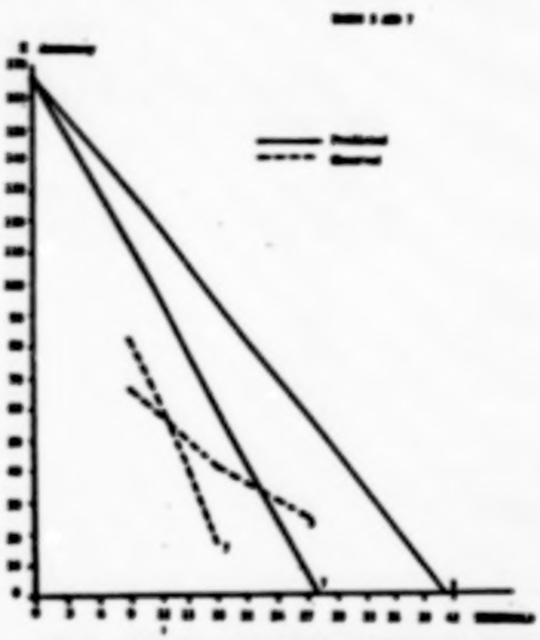

Fig. 13 Predicted vs. Observed Results for Washington, D.C. Test Area

Figs. 12 and 13 illustrate predicted against observed results assuming a road with of 50 metres. The correspondence is less close than for the North Carolina data, and is very poor indeed for bands 5 and 7. The deviation values for these bands are both very high. However, it is also possible that the Band 7 result is due to a mis-estimation of the contrast since the slope of the observed line could intercept the y axis at the same location as all other bands, as required by the model.

It is concluded that the model developed here may be used to estimate the width of unknown features in TM data. In optimum conditions with high contrast and homogeneous materials it appears possible to measure widths as little as one-quarter of a pixel. This has considerable potential for mapping purposes. Contrast levels observed compare favorably with those for MSS data, although variances and hence deviation levels tend to be greater. However, the increased dimensionality of the TM data allows independent verification of results from band to band so that the results may be considered to be more reliable. Pixel size is confirmed by these experiments to be 28.5 metres.

BAND: BAND REGISTRATION

Using linear feature detection results it is also possible to investigate band to band registration. Registration differences will be apparent as shifts in the locations of detected features from band to band.

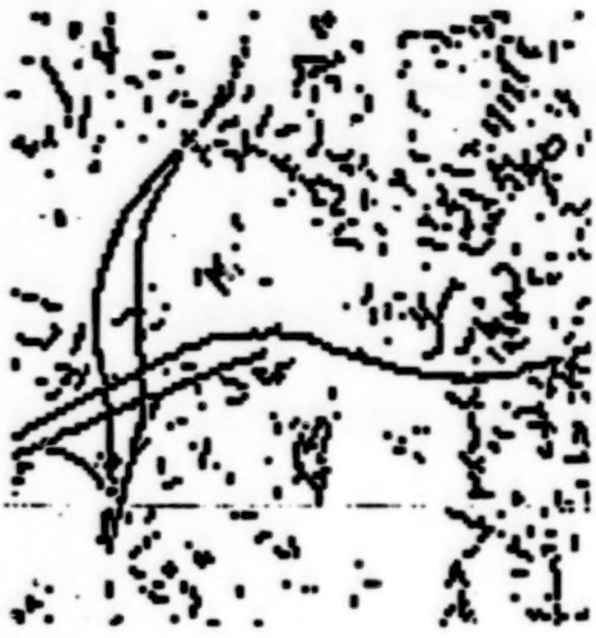

Fig. 14 I-95 Interchange, Bands 1 and 3 Superimposed

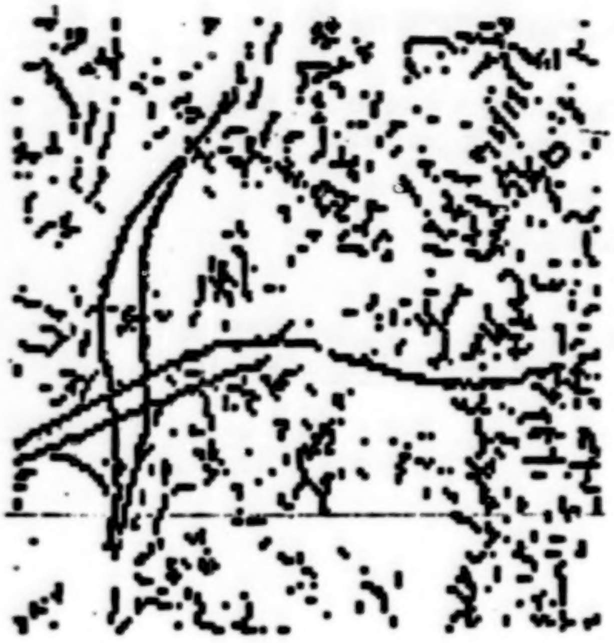

Fig. 15 I-95 Interchange, Bands 1 and 7 Superimposed

Figs. 14 and 15 illustrate the superposition of results of linear feature detection from part of the Washington, D.C. scene corresponding to the I-95: Beltway interchange. Fig. 14 shows bands 1 and 3 together; band 1 results are in black and band 3 in gray. There is clearly a close correspondence between the two. Fig. 15 shows bands 1 and 7 together. In this case there is a clear mis-registration with the band 7 data being shifted both to the right and down with respect to the band 1 data. This result was also observed for band 5 data against band 1. Bands 5 and 7 showed a slight difference that was difficult to assess because of the poor detection rate in band 5.

This method is less suitable for measurement of misregistration than it is for graphically illustrating that it exists. However, it does appear that there is a shift between primary and cold focal planes of less than 1 pixel in both directions that is apparently greater in the x direction than in the y direction.

CONCLUSIONS

It has been shown that TM data may be used to estimate TM pixel size and to illustrate band: band mis-registration. Further, the geometry and radiometry of the data are sufficiently precise to allow accurate estimation of the widths of linear features. In optimum conditions features one quarter of a pixel in width may be accurately measured. These results have considerable potential for applications for hydrological and topographic mapping.

ACKNOWLEDGEMENTS

The author would like to thank Mary Aloupis, Margaret Smith and Susan Sanzone for their help in preparing this paper.

REFERENCES

1. Gurney, C.M., Threshold selection for line detection algorithms, Trans Geosci and Remote Sensing Vol. GE-18, 2, 1980, pp 204-211

2. Gurney, C.M., The use of contextual information in remote sensing, Ph.D. thesis, University of Reading, 1980.

N85-21741

D17

SPATIAL RESOLUTION ESTIMATION OF LANDSAT-4 THEMATIC MAPPER DATA

Clare D. McGillem,
Paul E. Anuta and
Erick Malaret
Purdue University

I. INTRODUCTION

In order to verify that a satellite-borne remote sensing system is operating within specifications, it is necessary to estimate the system parameters by analysis of the measured data. One parameter of particular interest is the sensor point-spread function (PSF) which determines the resolution of the system.

It is possible to obtain useful estimates of the PSF by analyzing data resulting from scanning ground elements having identifiable geometric and radiometric structures. The data are processed in such a way as to estimate the coefficients in a basis function representation of the PSF or in some cases to directly provide the PSF itself.

The measured data can be expressed in the spatial domain as a convolution of the scene with an overall point-spread function:

$$g(x,y) = h(x,y) * f(x,y)$$

where $f(x,y)$ is the earth scene

$h(x,y)$ is the overall point-spread function of the sensor system

$g(x,y)$ is the resulting image

Given $g(x,y)$, we wish to determine $h(x,y)$. To do this, some deterministic element of the input $f(x,y)$ must be known or assumed. Although the theory can take into account the two-dimensional nature of the element, the initial experiments have been limited to the one-dimensional case. If the overall PSF is separable, i.e., if h(x,y) can be written as a product h(x)h(y), then this approach provides a direct estimate of the two components. Otherwise it generates cross sections through the two-dimensional PSF along the x and y axes.

Three scene elements that would be useful for this type of analysis are:

1. An impulse represented by a narrow-width discontinuity along a row or column of the data.

2. A step function represented by an abrupt change in gray level along a row or column of the data.

3. A rectangular pulse represented by a sequence of two steps in opposite directions along a row or column of the data.

Use of an impulse type scene element is the simplest since the sensor response is directly proportionate to the PSF. However, it is difficult to identify a discontinuity that is narrow enough that it may be considered to approximate an impulse. Some initial work was done using roads for this purpose. It was found, however, that because their width is not negligible, they consistently led to computed impulse response estimates that were too wide.

A general approach applicable to any type of (known) scene element has been developed. It is illustrated using scene elements of the second type listed above and gives results that appear to be in keeping with what would be expected based on the system specifications.

II. DATA SELECTION

There are a number of ways in which subsets of data from a scene can be selected for use in estimating parameters of the sensor. The one which is simplest to employ is to find a sequence of rows or columns in which a repetitive scene element of known geometrical configuration occurs. One example of this is a road that is bordered by constant reflectance materials on each side. It is not necessary that the reflectances be the same on each side, only that they be more or less constant. Another example is the border between fields containing different crops.

Because of the orbital inclination of Landsat and the propensity of man to arrange linear features, such as roads and field boundaries, in the cardinal compass directions, it is generally found that there is a spatial displacement in the scene coordinates of the linear elements from one row or column to the next. This has the desirable effect of providing a fine grid of samples of the system response when values from adjacent rows or columns are combined after correction for the spatial shift of the scene element. The procedure for combining the data is quite straightforward and can be illustrated as follows for a north-south road.

The coordinates of the peaks in the row data corresponding to the road are determined for a sequence of N rows. These data are then fitted with a least-squares straightline, providing an analytical expression for the road coordinates. The x-coordinates in each row are then modified by subtracting from them the least-squares estimate of the road location in that row. This converts the data to a coordinate system in which zero is the road center. Because of the small angular difference between the sensor coordinate system and the road direction, the change in road coordinates from row to row is only a fraction of the pixel spacing and so represents a sampled response to the scene element corresponding to a subpixel translation. By combining the data from a number of rows, a set of finely sampled data is found. These data can be graduated using splines or other smoothing functions to give an average response function from which to estimate the system point-spread function.

III. ESTIMATION PROCEDURE

A straightforward estimate of the system point-spread function can be obtained if it is represented in terms of a finite sum of basis functions. The simplest approach is to employ a sequence of rectangular pulses extending over the spatial extent of the PSF. This will give a staircase approximation to the PSF; but if narrow impulses are employed, the steps will be small and the fidelity will be good. A smooth curve can be passed through the approximation desired. In order for this procedure to be practical, it is necessary to know or estimate geometrical structure of the scene element producing the measured response. In the case of a road, it is desirable to know the width of the road, the intensity level on each side of the road, and the intensity level of the road itself. For a field boundary, all that is required is to know the intensities on each side of the boundary. Since the scene elements are selected on the basis of regions of uniform intensity on each side of a discontinuity, these levels can be found directly from the data. This is all that is required for a step type of discontinuity, such as a field boundary. In the case of a road, the peak value obtained when the sensor is centered on the road can be used. However, this value will be somewhat low and should be increased by a correction factor that can be computed from an initial analysis or from analysis of the step-response data.

Mathematically, the analysis procedure can be carried out as follows: Consider the case of a separable point-spread function, i.e., one in which the total PSF can be expressed as the product of a PSF in the x-direction (rows) and a PSF in the y-direction (columns). Only the x-direction analysis will be described; however, the y-direction analysis is exactly analagous. Let f(x) be the scene intensity as a function of the x-coordinate, let h(x) be the system PSF, and let g(x) be the system output. The output can be represented as the convolution of the scene and the PSF, i.e.,

$$g(x) = \int_{-\infty}^{\infty} f(\lambda)\ h(x-\lambda)\ d\lambda$$

Now let h(x) be represented using a finite set of nonoverlapping rectangular basis functions. h(x) is assumed to extend over an interval of $\pm$ P/2 and the rectangular basis functions are assumed to have unit heights and widths of T units. Thus

$$\hat{h}(x) = \sum_i c_i \,\mathrm{rect}\left(\frac{x-iT}{T}\right) \quad -P/2T \le i \le P/2T$$

$$\hat{g}(x) = \int_{-\infty}^{\infty} f(\lambda) \sum_i c_i \,\mathrm{rect}\left(\frac{x-\lambda-iT}{T}\right) d\lambda$$

$$= \sum_i c_i \,\phi_i\,(x)$$

where:

$$\phi(x) = \int_{-\infty}^{\infty} f(\lambda)\,\mathrm{rect}\left(\frac{x-\lambda}{T}\right) d\lambda$$

$$\phi_i(x) = \phi(x-iT)$$

The procedure is now to choose the unknown coefficients c_i so as to give the best approximation to $g(x)$. This can be done by minimizing the mean square error between the known (measured) $g(x)$ and the estimated value over the region (x_1,x_2). The integral squared error is:

$$E^2 = \int_{x_1}^{x_2} [g(x) - \hat{g}\,(x)]^2 \,dx$$

$$= \int_{x_1}^{x_2} [g(x) - \sum_i c_i \,\phi_i(x)]^2 \,dx$$

The coefficients c_i are found by solving the system of equations that results from setting the partial derivatives with respect to each coefficient equal to zero. The resulting expression for the c_is is:

$$\underline{c} = \underline{R}^{-1}\,\underline{b}$$

where $\underline{c}$ is a vector with elements c_i, $\underline{R}$ is a symmetric matrix with elements

$$r_{ij} = r_{ji} = \int_{x_1}^{x_2} \phi_i(x)\,\phi_j(x)\,dx$$

and $\underline{b}$ is a vector with elements

$$b_i = \int_{x_1}^{x_2} g(x)\,\phi_i(x)dx$$

For a typical problem, the PSF extent might be approximated by 20 or more coefficients extending over a spatial extent of 5-6 pixels. The solution would require computing the elements r_{ij} which are samples of the autocorrelation function of the input image convolved with the rectangular basis function, computing the b_i which are the projections of the output on the ith basis function, and then multiplying the inverse of the $\underline{R}$ matrix by the $\underline{b}$ vector. Because of the smoothing that was done in generating the original $\bar{g}(x)$ function, the solution will be well-behaved.

IV. EXPERIMENTAL RESULTS

The procedure that has been described is suitable for use with a variety of scene events that can be identified in Landsat imagery. The simplest case and the one that will be considered here is that of a boundary between two different intensity levels that extends in a north-south direction. This corresponds to an underlying functional form of a step discontinuity. Scene structures corresponding to field boundaries were selected from a rural area in Landsat-4 Thematic Mapper imagery of Webster County, Iowa* for use in the analysis. Data from consecutive rows on each side of the boundary were examined to be sure that no anomalous behavior was occurring. The least-squares straightline for the boundary representation was computed and the system response for consecutive rows adjusted to correspond to a boundary position on the x- direction of zero. Data for two different boundaries is shown in Figures 1 and 2. In Figure 1, fourteen scan lines are employed and in Figure 2, twelve scan lines.

The data of Figures 1 and 2 were smoothed using a cubic spline subroutine with five knots. The resulting response functions are shown in Figures 3 and 4 along with the assumed intensity level of the underlying scene. Data from the smoothed response functions were used to solve for the coefficients in the basis function representation of the PSF, as described previously. For this analysis, the PSF was assumed to be limited in extent to 9 sampling intervals and a total of 21 coefficients was calculated. The resulting PSFs are shown in Figures 5 and 6.

In interpreting the results of estimating the PSF of a sensor, it is convenient to use parameters that describe some of the general properties of the PSF. Two such parameters are the equivalent width, W_{eq}, and the half-amplitude width, $W_{\frac{1}{2}}$, of the main lobe. These are defined as:

1. Half amplitude width $W_{\frac{1}{2}}$ = width at which the magnitude of h(x) falls to one-half of its value at the origin.

2. Equivalent width $W_e = \dfrac{\int_{-\infty}^{\infty} h(x)\,dx}{h_{max}}$

This is the width of a rectangle having the amplitude of h(x) at its maximum and a width such that it has the same area as h(x). For the two scene elements analyzed, these parameters are as follows:

---

* The data used were from Band 4 (.76-.90 μm) of the Landsat-4 Thematic Mapper from Scene 40049-16264 obtained on Sept. 3, 1982 from the fully corrected P tape.

Table 1
RESULTS OF PSF WIDTH ESTIMATION

Parameter	Data Set 1	Data Set 2
W_{eq}	1.53	1.38
$W_{½}$	1.44	1.28

The units of W_{eq} and $W_{½}$ are sampling intervals. The sampling spacing for the Thematic Mapper imaging is 28.5 meters.

Because of the special nature of the underlying scene element that produced the data used in this analysis, there is an alternative way to estimate the point-spread function. The scene element can be modeled as a step superimposed on a constant background, i.e.,

$$f(x) = A + B\ u(x)$$

where A is the background and B is the amplitude change across the boundary. The output is then given by

$$g(x) = [A + B\ u(x)] * h(x)$$

Taking the derivative of both sides of this equation gives

$$\begin{aligned} g'(x) &= \frac{d}{dx}(A+B\ u(x)) * h(x) \\ &= B\ \delta(x) * h(x) \\ &= B\ \ h(x) \\ \therefore h(x) &= \frac{1}{B}\, g'(x) \end{aligned}$$

The PSF is therefore the derivative of the output (measured) function scaled by the amplitude of the step. This quantity can be computed directly from the smoothed representations given in Figures 3 and 4. The results of this computation are shown in Figures 7 and 8 along with the coefficients previously determined. It is seen that there is excellent agreement between these figures and the results of the more general solution given in Figures 5 and 6.

All of the estimates suggest the existence of sidelobes on the PSF. This is evidenced by the overshoot seen in Figures 3 and 4 and in the resulting PSF estimates in Figures 5-8. More extensive analysis using different scene structures will be required to accurately quantify the nature and extent of the sidelobe structure.

V. SUMMARY

The problem of estimating the overall point-spread function of multispectreal scanner systems was studied using real scene data and known geometric structures in the scene. A direct solution to an approximate form of the PSF was made along with a method using the derivative of an estimated edge response. Both results agreed closely. The TM scanner system specifications are given in line-spread function width and these values are listed with the experimental results in terms of meters in Table 2. The estimated values are very reasonable, considering the number of factors which could be influencing the result. The atmosphere will have a blurring effect on the overall PSF as well as on cubic convolution resampling effects and possible electronic effects not accounted for in the specification. Also, the specific definition of the LSF specification is not known nor is the actual altitude at the instant the data were acquired. Thus the nominal overall PSF half-amplitude width of 39 m is reasonable; however, a greater sample of scene objects should be evaluated to further verify this result.

Table 2

COMPARISON OF PSF WIDTH ESTIMATION RESULTS ON THEMATIC[2] MAPPER SPECIFICATIONS BASED ON ALTITUDE OF 705.3 km AND PIXEL SPACING OF 28.5 M.

Av. PSF Est. Width (Pixels)		Av. PSF EST. Width (Meters)		LSF Width μ Radians	LSF Width Meters
$W_{\frac{1}{2}}$	W_{eq}	$W_{\frac{1}{2}}$	W_{eq}		
1.36	1.45	38.8	41.3	43.2	30.5

REFERENCES

1. Kumar, R., and D. Fitzgerald. 1982. Geometric Correction Data Generation From Systematic Correction Data and Control-Point Location Errors for Thematic Mapper Data. Computer Sciences Corp. Report CSC/TR-82/.6002, Aug. 1982, for NASA/Goddard Space Flight Center, Greenbelt, MD 20771.

2. Landsat-D Investigations Workshop Notes. Thematic Mapper Characterizations, May 13-14, 1982, NASA/Goddard Space Flight Center, Greenbelt, MD 20771.

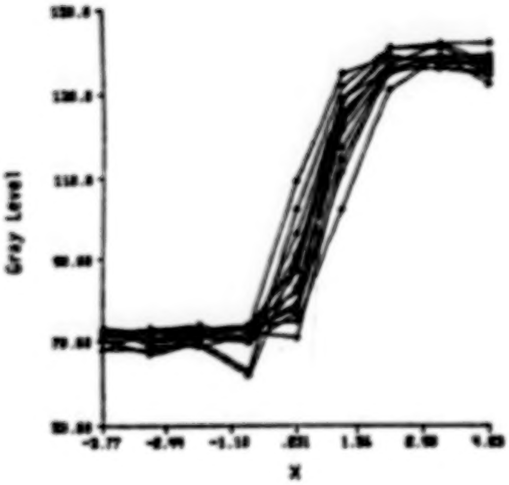

Fig. 1. Fourteen row responses from Reg. 1

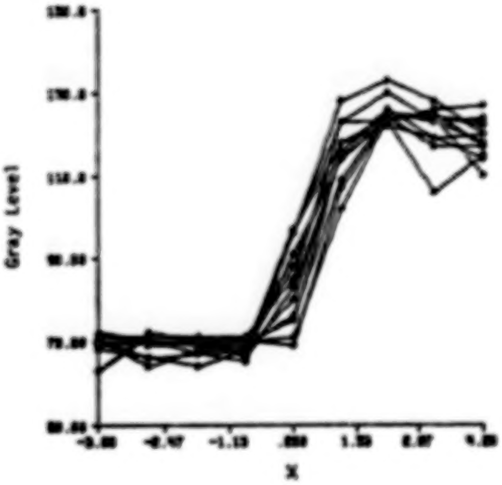

Fig. 2. Twelve row responses from Reg. 2.

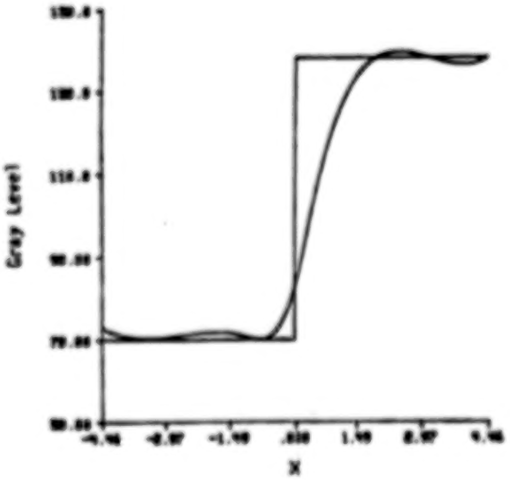

Fig. 3. Smoothed estimate of the row response from Region 1 and the underlying scene intensity.

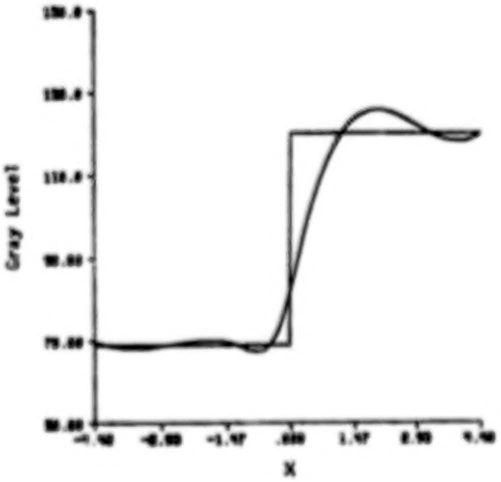

Fig. 4. Smoothed estimate of the row response from Region 2 and the underlying scene intensity.

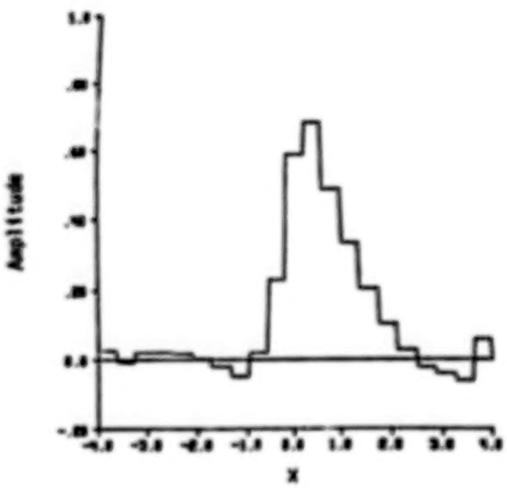

Fig. 5. PSF estimate from smoothed data from Region 1.

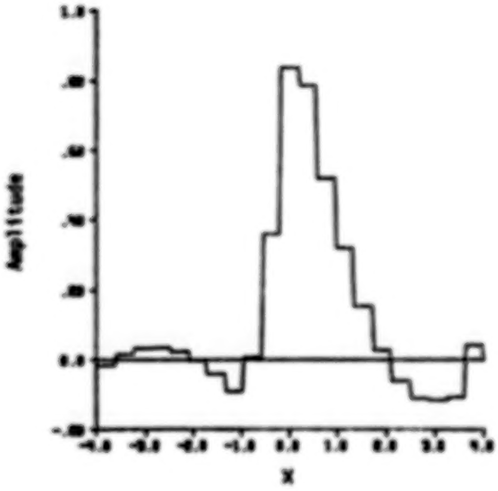

Fig. 6. PSF estimate from smoothed data from Region 2.

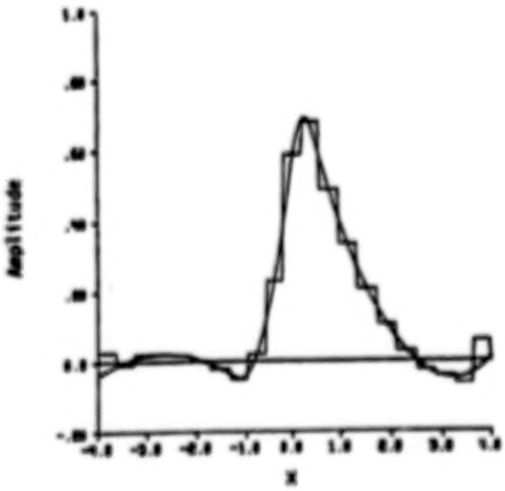

Fig. 7. PSF estimate as derivative of step response based on data from Reg. 1 superimposed on coefficient estimates given in Figure 5.

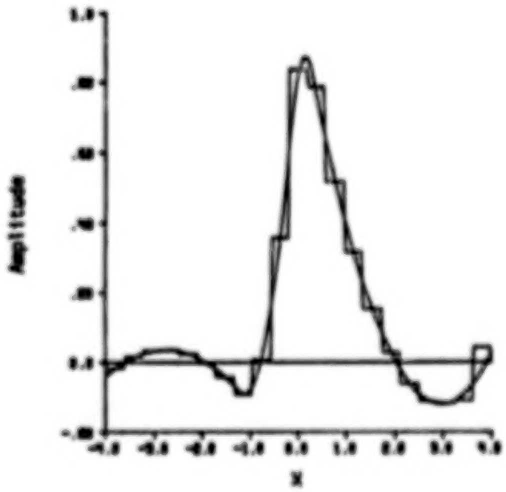

Fig. 8. PSF estimate as derivative of step response based on data from Reg. 2 superimposed on coefficient estimates given in Figure 6.

N85-21742 D18

AN ANALYSIS OF THE HIGH FREQUENCY VIBRATIONS IN EARLY THEMATIC MAPPER SCENES

John Kogut
Eliane Larduinat

Research and Data Systems, Inc.
10300 Greenbelt Road, Suite 206
Lanham, Maryland 20706

The motion of the mirrors in the Thematic Mapper (TM) and Multispectral Scanner (MSS) instruments, and the motion of other devices, such as the TDRSS antenna drive, and solar array drives onboard LANDSAT-4 cause vibrations to propagate through the spacecraft. These vibrations as well as nonlinearities in the scanning motion of the TM mirror can cause the TM detectors to point away from their nominal positions. The angular displacements of the nominal pointing direction of the TM detectors are measured by an onboard Angular Displacement Sensor (ADS), and by the spacecraft Dry Rotor Inertial Reference Unit (DRIRU). Data from these instruments are used to measure the high frequency along scan and cross scan vibrations acting on the TM during each scan.

Two computer programs, JITTER and SCDFT, were developed as part of the LANDSAT-D Assessment System (LAS), Products and Procedures Analysis (PAPA) program to evaluate the potential effect of high frequency vibrations on the final TM image. JITTER applies the operational TM Geometric Correction Operator (GCO)[1], to the Y component of the TM pixel XY locations, and finds the maximum deviation from perfect alignment (overlap and underlap) between the edges of successive TM scans. The SCDFT program analyzes the spectrum of the high frequency vibrations in each TM scene to determine in what frequency regions the high frequency vibrations are important.

PRECEDING PAGE BLANK NOT FILMED

PAGE III-536 INTENTIONALLY BLANK

The high frequency vibrations in 26 TM scenes between 4 and 50 days after LANDSAT-4 launch (July 20 to September 4, 1982) have been analyzed using the JITTER and SCDFT programs. These scenes represent the first scenes for which the CCT-ADDS tapes were processed. Fig. 1 shows how the 26 TM scenes are distributed over the time span considered.

FIGURE 1
DISTRIBUTION OF TM SCENES ANALYZED

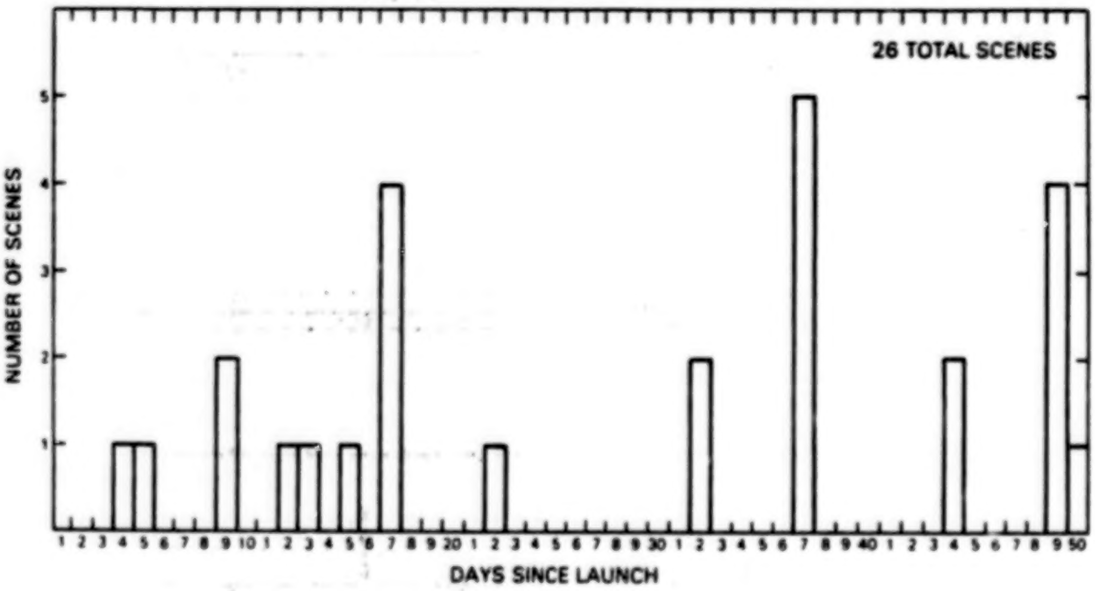

The date of launch for LANDSAT-4, July 16, 1982, is taken here as day 0 since launch. There were 6 days on which more than one scene was available, and the largest time over which no scene was available was the 9 days between day 23 and day 31 after launch.

The JITTER program computes the Y location of the pixels generated from detector 1 and detector 16 for each band (detector 4 for band 6), for each TM sweep. The Y value of the pixel center is computed using the TM GCO, which corrects the pixel location for along scan and cross scan high frequency vibrations using measurements available from the TM Systematic Correction Data (SCD).

The location of the pixel centers at the edges of the scan are then used to compute the amount by which successive scans underlap or overlap. The overlap or underlap for every 64th pixel in all 374 scans is computed, and a list of the scans with the 10 greatest overlaps and underlaps in the scene, and in which pixel they occur, is produced.

The maximum overlap and underlap for each of the 7 TM bands for the 26 scenes analyzed was compiled, and Figs. 2 through 8 show how these parameters change over the time span under consideration.

FIGURE 2
TM BAND 1
MAXIMUM PIXEL OVERLAP/UNDERLAP
BETWEEN SCANS

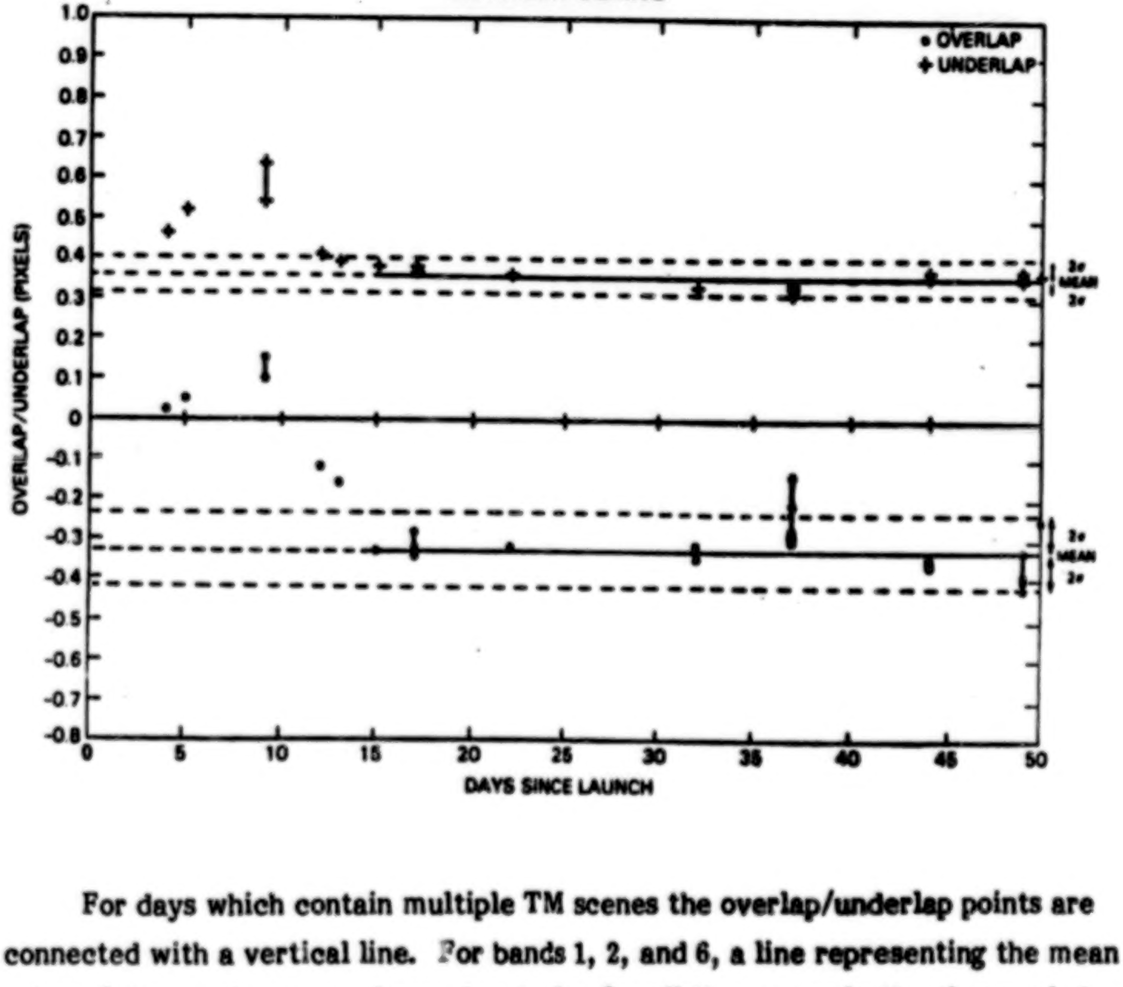

For days which contain multiple TM scenes the overlap/underlap points are connected with a vertical line. For bands 1, 2, and 6, a line representing the mean value of the maximum overlap and underlap for all the scenes in the time period between day 15 and day 50 since launch are given, as well as a line representing 2 standard deviations from the mean of these data sets.

FIGURE 3
TM BAND 2
MAXIMUM PIXEL OVERLAP/UNDERLAP BETWEEN SCANS

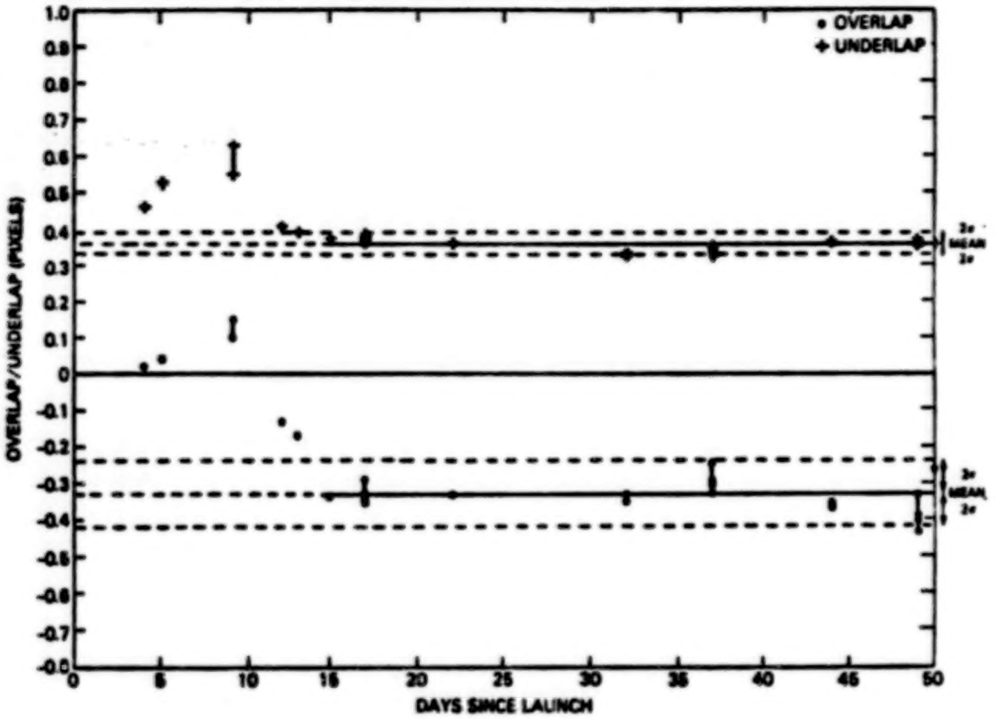

FIGURE 4
TM BAND 3
MAXIMUM PIXEL OVERLAP/UNDERLAP BETWEEN SCANS

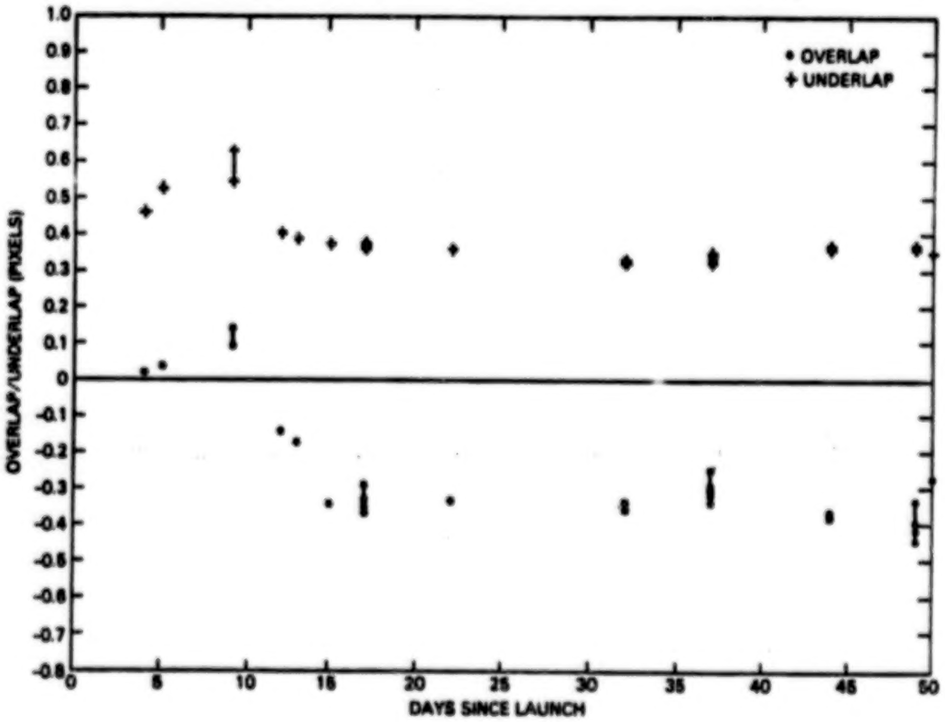

FIGURE 5
TM BAND 4
MAXIMUM PIXEL OVERLAP/UNDERLAP BETWEEN SCANS

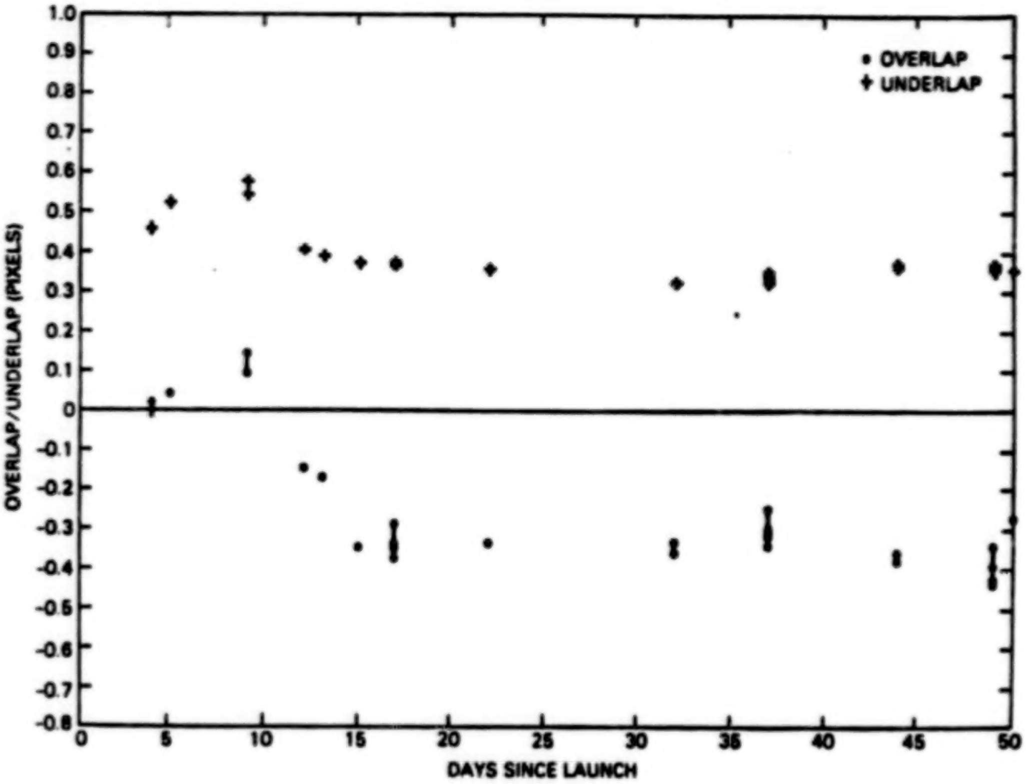

FIGURE 6
TM BAND 5
MAXIMUM PIXEL OVERLAP/UNDERLAP BETWEEN SCANS

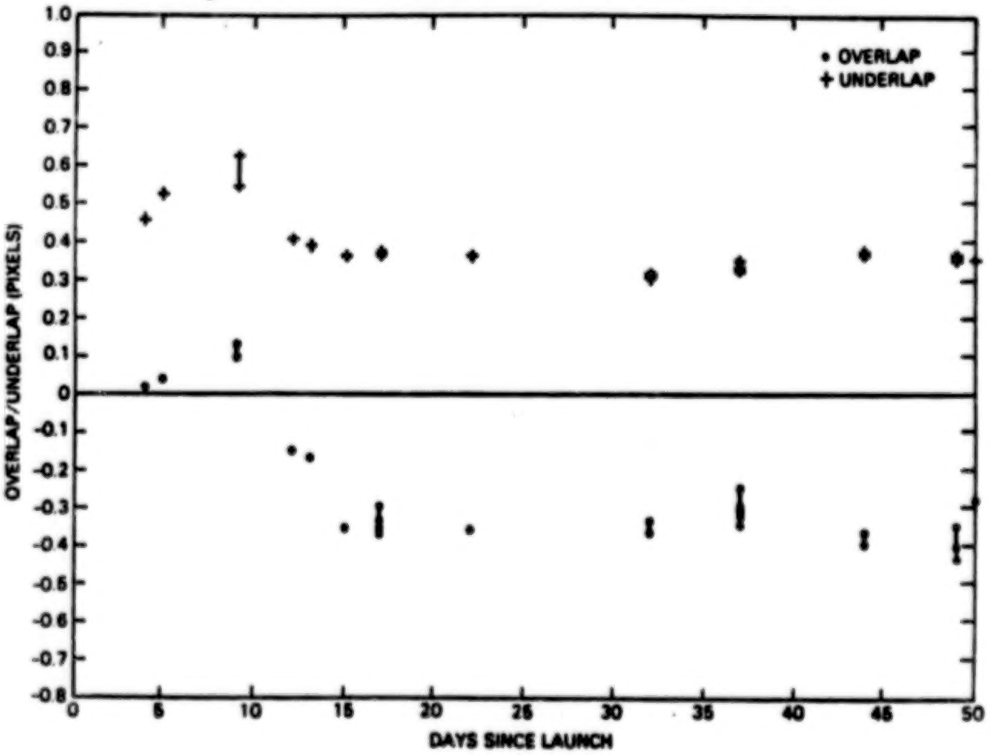

FIGURE 7
TM BAND 6
MAXIMUM PIXEL OVERLAP/UNDERLAP BETWEEN SCANS

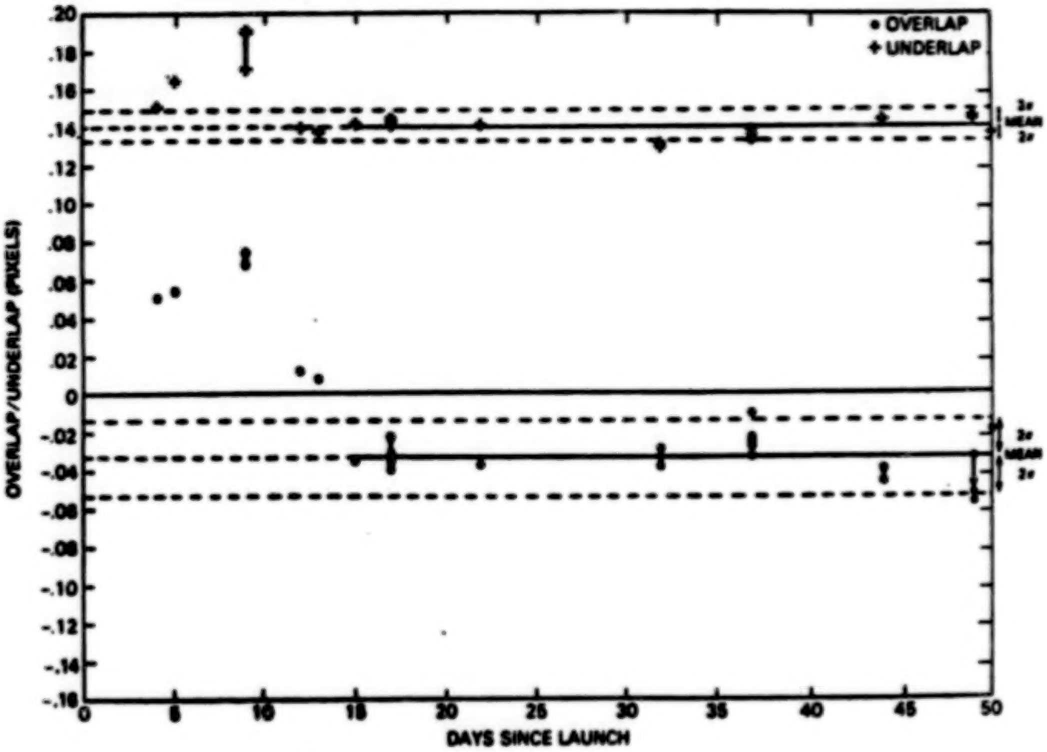

FIGURE 8
TM BAND 7
MAXIMUM PIXEL OVERLAP/UNDERLAP BETWEEN SCANS

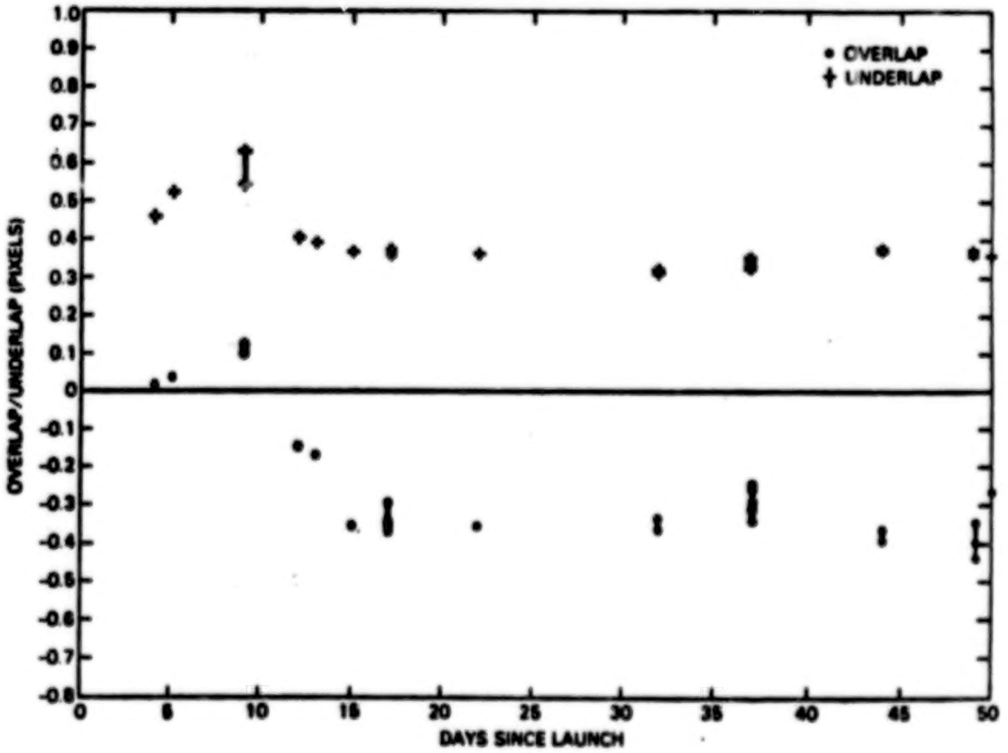

It can be seen that the values of the maximum overlap and underlap are practically identical for the reflective bands over the time period in question. This is to be expected since the computed overlap and underlap are primarily a measure of the impact of spacecraft altitude variations and high frequency vibrations, which should be the same for all bands. Since the maximum overlap and underlap is measured in pixels, the magnitudes of the measurements for band 6 will be correspondingly smaller because of the larger pixel size.

The strong underlap visible immediately after launch coincides with the time when the spacecraft high gain antenna boom was being deployed. The deployment began on day 5 since launch (July 21) and was completed on day 11 since launch (July 27). After day 15 since launch (July 31) the overlap and underlap appear to stabilize.

The mean and standard deviation of the maximum overlaps and underlaps for the 20 scenes between day 15 and day 50 since launch are given for all 7 bands in Table 1.

TABLE 1

TM MAXIMUM OVERLAP/UNDERLAP STATISTICS
FOR 20 SCENES FROM DAY 15 TO DAY 50 AFTER LAUNCH

	OVERLAP (PIXELS)		UNDERLAP (PIXELS)	
BAND	MEAN	STD. DEV.	MEAN	STD. DEV.
1	-0.326	0.046	0.356	0.019
2	-0.332	0.046	0.358	0.017
3	-0.337	0.047	0.360	0.017
4	-0.340	0.047	0.360	0.017
5	-0.345	0.049	0.358	0.018
6	-0.034	0.012	0.141	0.004
7	-0.344	0.049	0.349	0.017

The table shows that for the reflective bands the mean maximum overlap is about -0.34 pixels and the mean maximum underlap is about +0.36 pixels, with the variance of the overlap about 2.7 times that in the underlap. For band 6 the mean maximum overlap is -0.03 pixels; and the mean maximum underlap is 0.14 pixels.

The latitudes of the scenes which were examined ranged from 36.11°N to 46.02°N, so that the contributions to overlap and underlap arising from the different altitude of the spacecraft at different latitudes were about the same.

The other analysis of the high frequency vibrations involved determining the Fourier spectrum of the vibrations in each scene. The SCDFT program uses the technique of Compound Fourier Transforms[2] to find the spectrum of the high frequency vibrations in each of the 26 scenes analyzed. The along scan and cross scan high frequency matrices available every 2 milliseconds during each scan were used to generate vibration time series which spanned all the scans in a scene. The amplitude of the vibrations at each 3.5 Hz frequency interval between 3.5Hz and 84.0 Hz was computed for along scan vibrations and cross scan vibrations, and a separate spectrum was produced for the 4 time series formed from the along scan forward sweep, along scan reverse sweep, cross scan forward sweep, and cross scan reverse sweep data.

Figs. 9, 10 and 11 show typical examples of the spectrum for the 4 different time series.

FIGURE 9
TM ALONG SCAN H.F. VIBRATION SPECTRUM
(FORWARD SWEEP)
8-22-82 16^h 3^m 22^s SCENE

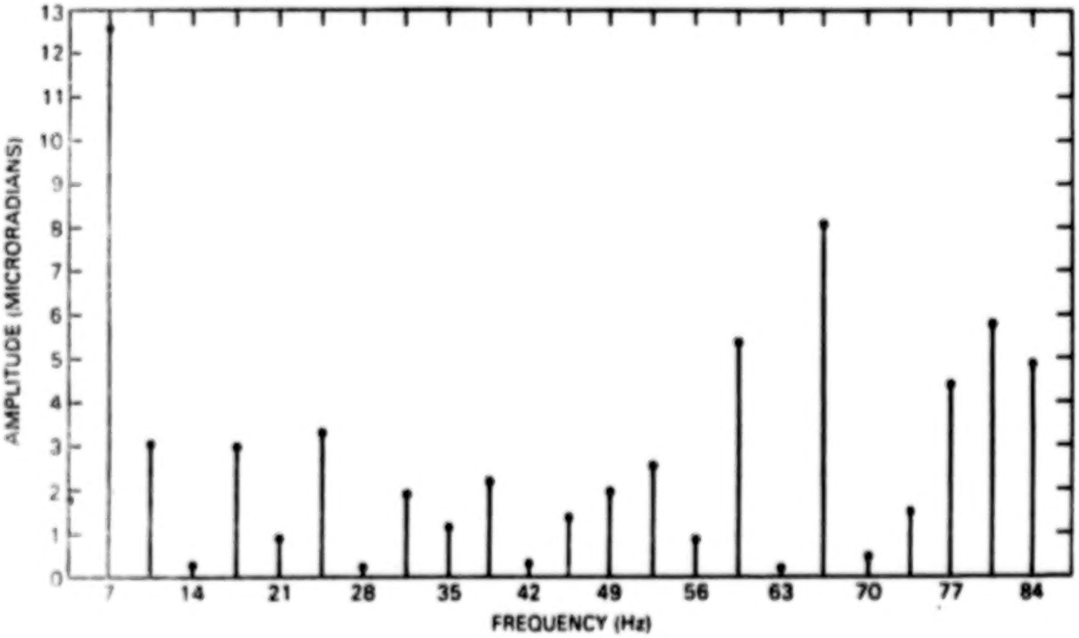

ORIGINAL PAGE IS
OF POOR QUALITY

FIGURE 10
TM ALONG SCAN H.F. VIBRATION SPECTRUM
(REVERSE SWEEP)
8-22-82 16^h 3^m 22^s SCENE

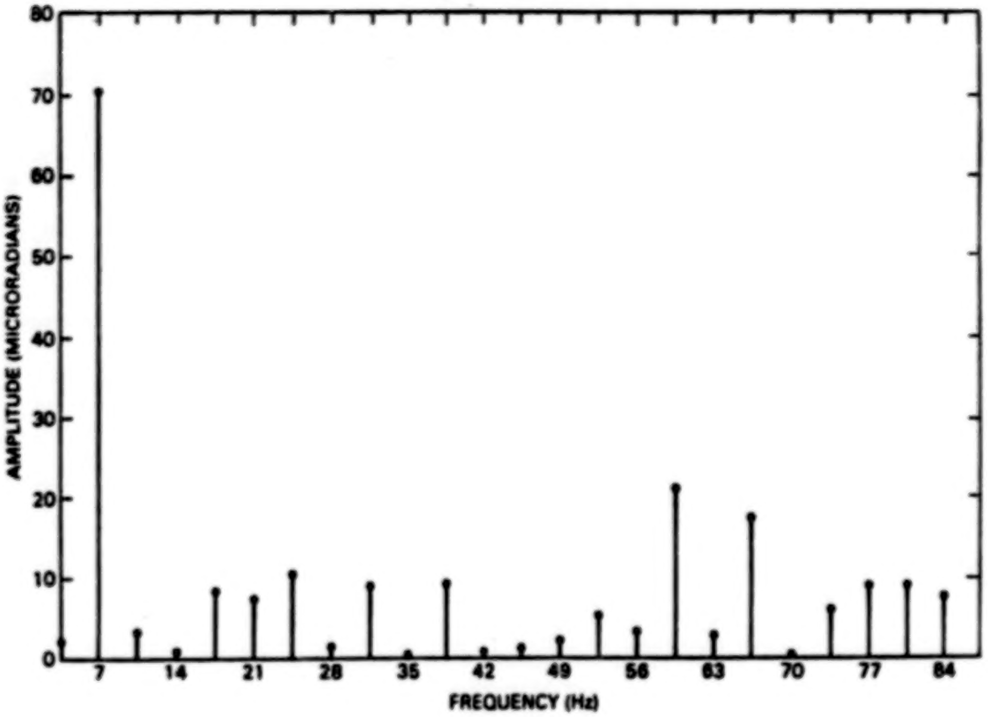

FIGURE 11
TM CROSS SCAN H.F. VIBRATION SPECTRUM
8-22-82 16^h 3^m 22^s SCENE

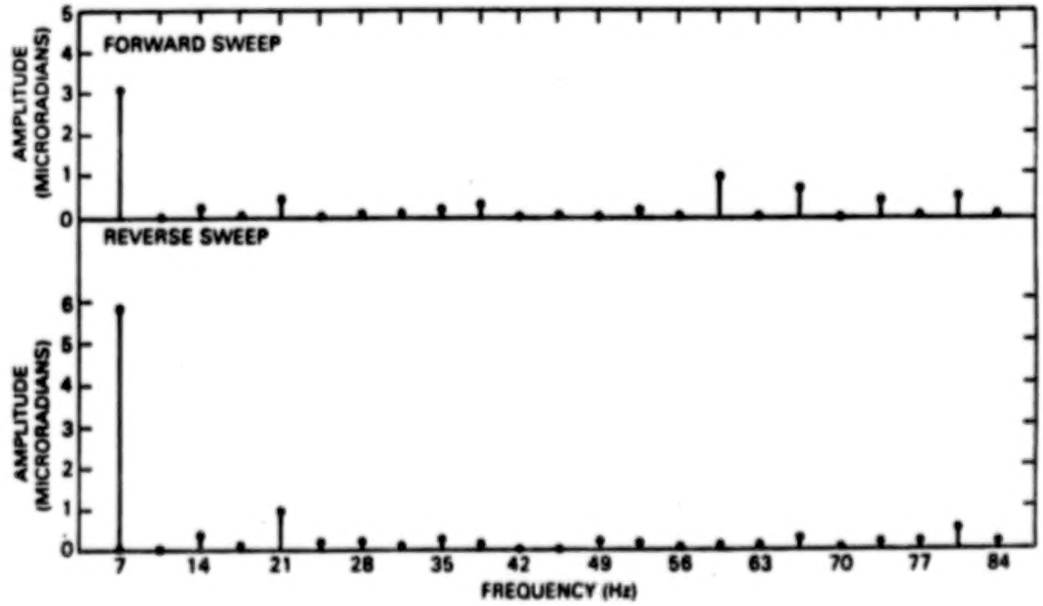

These spectra are from a TM scene on day 37 since launch (August 22, 1982). The peak amplitudes for the along scan vibrations are greater than for cross scan, with the spectral peaks for the reverse sweep along scan data having the highest amplitudes.

In the 26 scenes analyzed the highest spectral peaks appeared most often at specific frequencies for the different time series. Fig. 12 through Fig. 15 show how often the spectral peak with the largest amplitude (first peak) and the spectral peak with the next largest amplitude (second peak) occurred at various frequencies.

It can be seen that in all cases the strongest vibrations were measured at 7 Hz, which is the frequency of the TM mirror[3]. For the along scan data secondary peaks occured most often at 66.5 Hz and 59.5 Hz. For the cross scan data the secondary peaks occured most often at 21.0 Hz and again at 59.5 Hz. These frequencies are close to the odd harmonics of the TM mirror frequency (7 Hz), the MSS mirror frequency (13.62 Hz), and the solar array drive (19.66 Hz). For the along scan forward sweep data a strong spectral peak occurs at 77 Hz. The TM/F1 instrument also shows periodic vibrations at 77 Hz, and these preliminary results indicate that the TM/PF instrument may be exhibiting similar behavior.

Figs. 16 through 19 show how the amplitudes of the two largest spectral peaks observed in each scene change with time. Although there seem to be no major trends in the data over the time span considered here, the amplitudes may be increasing after day 50 from launch, and further data should be evaluated. Table 2 gives the mean and standard deviation of the spectral peaks with the two largest amplitudes measured in the 26 scenes.

TABLE 2

TM HIGH FREQUENCY VIBRATION STATISTICS FOR
26 SCENES FROM DAY 4 TO DAY 50 AFTER LAUNCH

	ALONG SCAN		CROSS SCAN	
	FWD	REV	FWD	REV
PEAK 1				
MEAN (MICRORADIANS)	15.9	79.7	6.7	3.7
STD. DEV. (MICRORADIANS)	2.3	9.8	1.5	1.5
PEAK 2				
MEAN (MICRORADIANS)	8.9	21.8	0.9	0.8
STD. DEV. (MICRORADIANS)	4.0	5.8	0.2	0.3

FIGURE 12
DISTRIBUTION OF FIRST TWO SPECTRAL PEAKS
FOR H.F. VIBRATION SPECTRUM

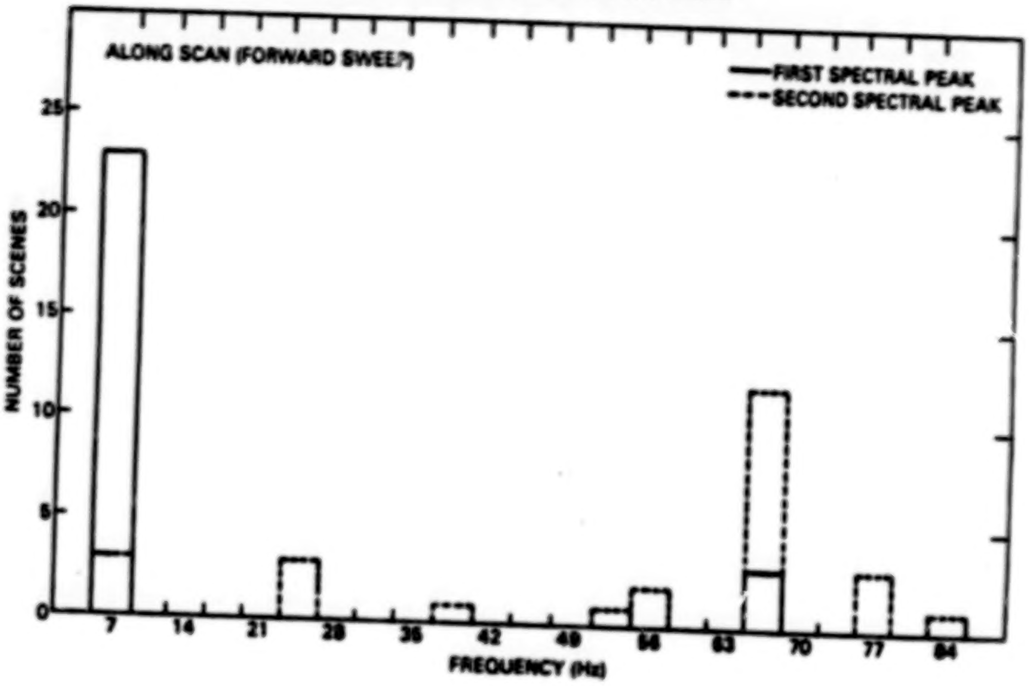

FIGURE 13
DISTRIBUTION OF FIRST TWO SPECTRAL PEAKS
FOR H.F. VIBRATION SPECTRUM

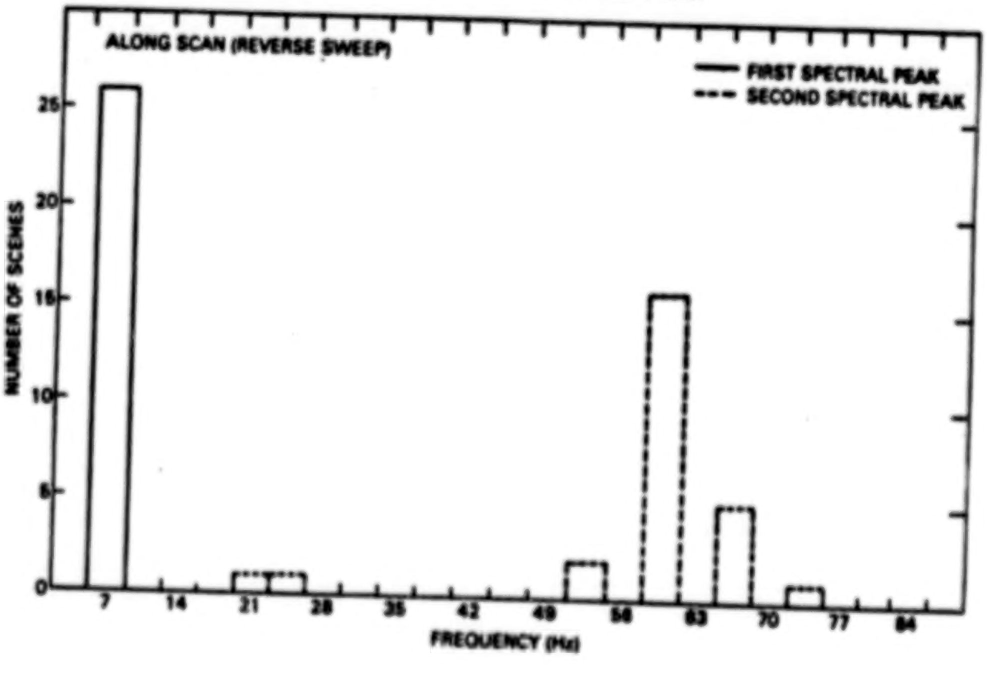

FIGURE 14
DISTRIBUTION OF FIRST TWO SPECTRAL PEAKS FOR H.F. VIBRATION SPECTRUM

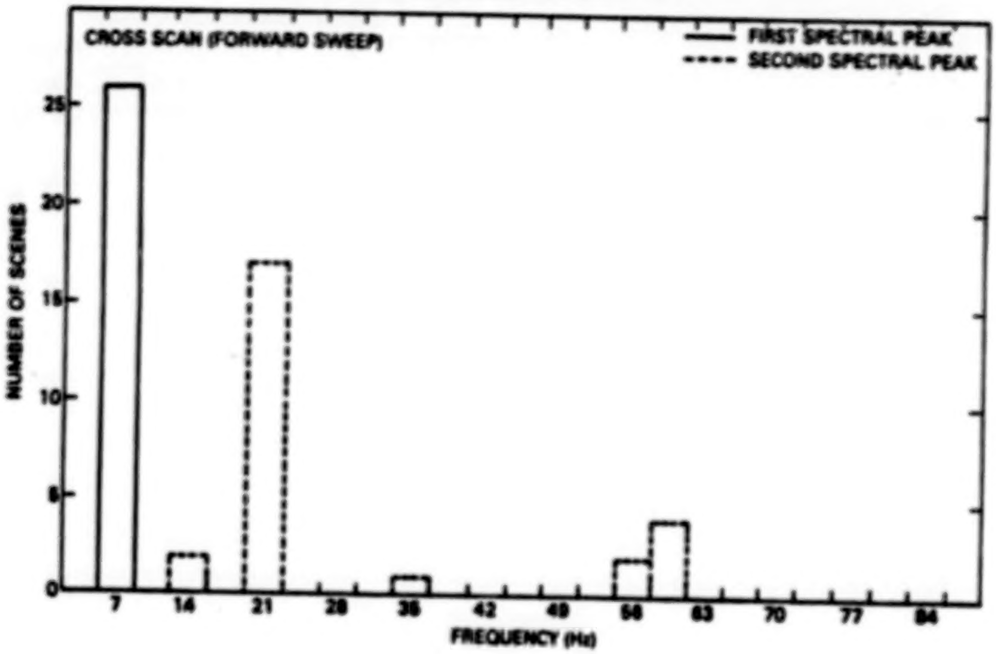

FIGURE 15
DISTRIBUTION OF FIRST TWO SPECTRAL PEAKS FOR H.F. VIBRATION SPECTRUM

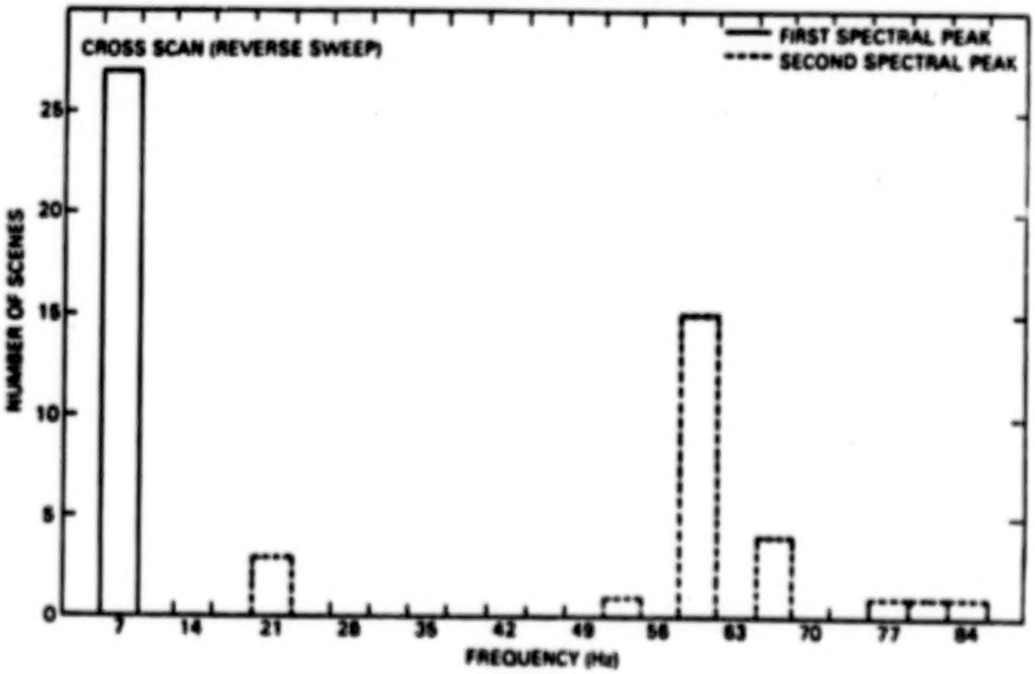

FIGURE 16
ALONG SCAN H.F. VIBRATION PEAK AMPLITUDES (FORWARD SWEEP)

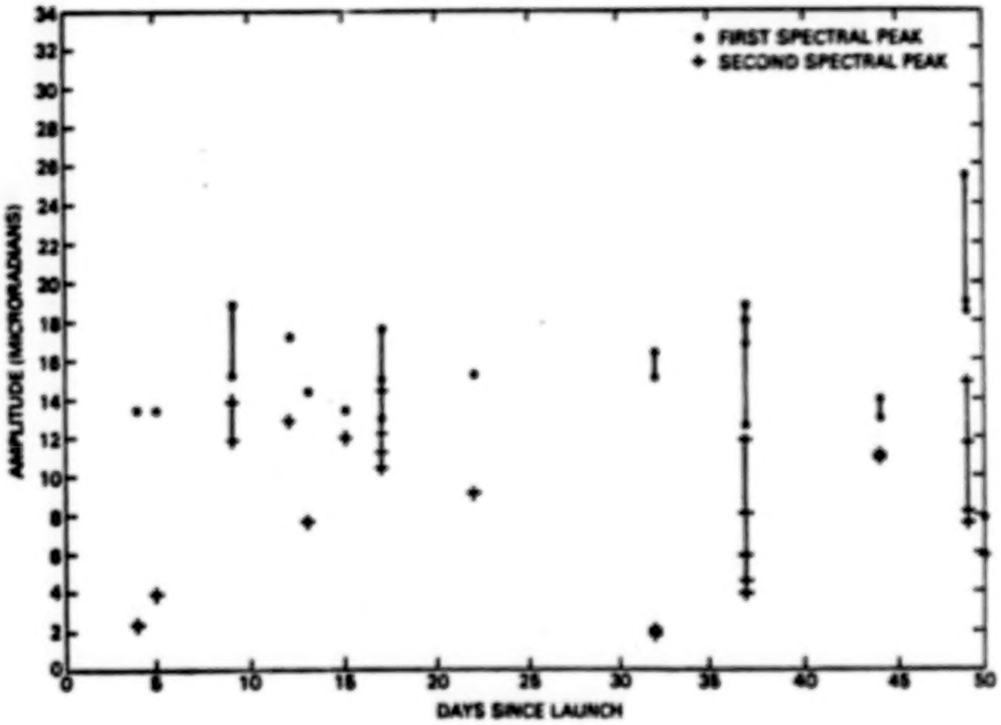

FIGURE 17
ALONG SCAN H.F. VIBRATION PEAK AMPLITUDES (REVERSE SWEEP)

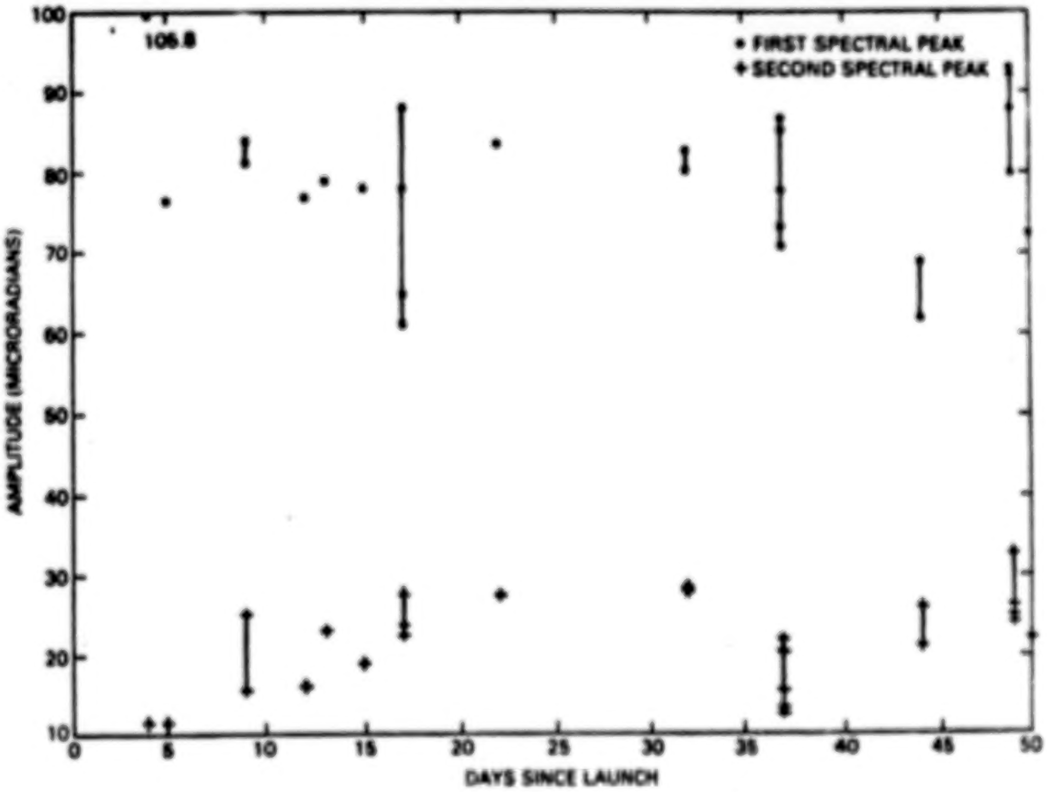

FIGURE 18
CROSS SCAN H.F. VIBRATION PEAK AMPLITUDES
(FORWARD SWEEP)

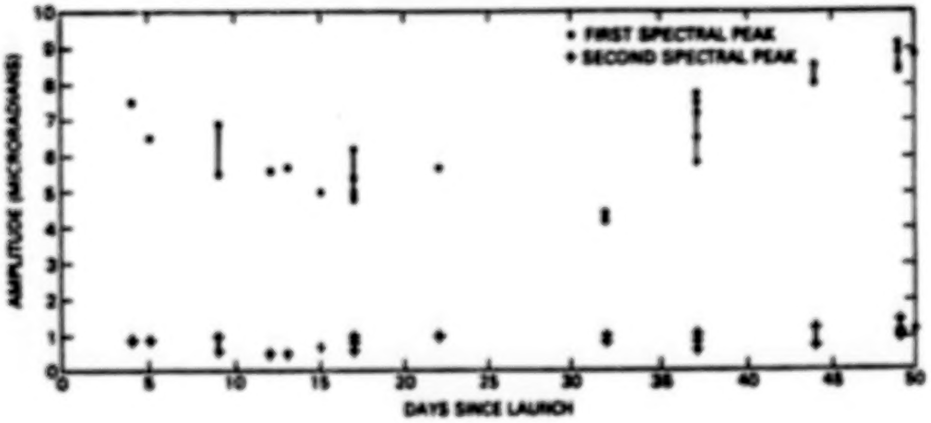

FIGURE 19
CROSS SCAN H.F. VIBRATION PEAK AMPLITUDES
(REVERSE SWEEP)

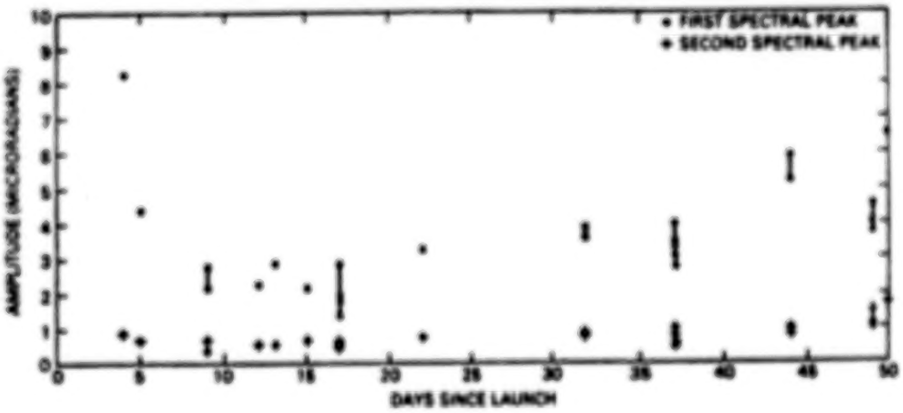

The largest amplitude for the along scan data is about 80 microradians which translates into about 1.88 pixels. The maximum cross scan amplitude is 6.7 microradians which translates into about 0.16 pixels.

The primary conclusions we have drawn from this study are that the maximum overlap and underlap which have been observed for early TM scenes are well within specifications for the ground processing system, and that the cross scan and along scan high frequency vibrations are also within the specifications cited for the flight system.

This work was supported by NASA contract NAS 5-27371. We would like to thank Dr. David Fischel, NASA/Goddard Space Flight Center for his assistance in this work.

REFERENCES

1. D. Fischel, "Thematic Mapper Geometric Correction Operator", LAS Memorandum, May 6, 1982

2. D. D. Meisel, "Fourier Transforms of Data Sampled in Unequally Spaced Segments", The Astronomical Journal, Vol. 84, No. 1, January 1979, pp. 116-126

3. E. Beyer, "An Overview of the Thematic Mapper Geometric Correction System (Draft)", General Electric Company, Valley Forge Space Center, 1982

N85-21743 D19

ASSESSMENT OF THEMATIC MAPPER BAND-TO-BAND REGISTRATION BY THE BLOCK CORRELATION METHOD

Don H. Card and Robert C. Wrigley
NASA Ames Research Center
Moffett Field, California 94035

Frederick C. Mertz and Jeff R. Hall
Technicolor Government Services, Inc.
Ames Research Center
Moffett Field, California 94035

INTRODUCTION

The configuration of the Thematic Mapper (TM) multispectral radiometer makes it especially susceptible to band-to-band misregistration. The non-cooled detectors of the visible and near-infrared spectral bands (TM bands 1-4) and the cooled detectors of the middle and thermal-infrared bands (TM bands 5-7) are located on physically separate focal planes in the sensor. In addition, there are several compensation devices in effect, such as the Scan Line Corrector (SLC), and the Attitude Displacement Sensor (Ref. 1). This creates the potential for inter-band misregistration, and could have serious consequences for the use of TM data in applications that rely on simultaneous observations. For example, Swain (Ref. 2) examined the effect of misregistration on classification accuracy of simulated TM data and showed that misregistration of 0.3 of a pixel (approx. 10 meters) could seriously degrade accuracy. The objective of the present study was to evaluate the magnitude of misregistration among the seven TM bands and to derive estimates of registration error that are sufficiently accurate for use in image correction.

There are several possible methods of quantifying band-to-band misregistration, some more subjective than others. A visual approach is to display black and white images on a video display screen at sufficient magnification (approx. 1x - 4x) and flicker between the two images of a band pair. For a quantitative assessment of the magnitude of misregistration, one can insert single pixel displacement in one band image of the pair, and for a given magnification, this results in a fractional pixel shift. For example, if the magnification is 4x, a single pixel displacement results in a 25%, or 0.25 pixel, shift. This can be repeated for increasing displacements until the misregistration appears negligible. The advantage of this method is its simplicity. Disadvantages are: 1) it is time consuming, and

PRECEDING PAGE BLANK NOT FILMED

PAGE III-552 INTENTIONALLY BLANK

therefore only a few local areas can be examined for a given image, 2) it is highly subjective, depending on visual acuity and analyst judgement, 3) it allows only a limited set of subpixel shifts, determined by the size of the video display screen, and 4) it cannot be used with uncorrelated bands (e.g., a visible band and the near infrared band) because of contrast reversals that cannot be entirely eliminated in a consistent manner.

Another approach, and one that is partially visual and partially quantitative, is to subtract the two band images being compared. This essentially performs an edge enhancement, in which misregistration results in erroneous edges in the difference image. Obviously, this method performs best when the misregistrations show up as odd patterns or anomalies in the difference image that can be related to the imaging system characteristics or to software problems. For example, an early TM image of the Detroit area showed an approximate single pixel misregistration of several apparently randomly located blocks of 16 or 17 lines by about 128 samples. Investigation revealed that the problem had been caused by a bug in the line insertion step in the pre-processing software, and was apparently corrected during routine de-bugging procedures. Although the problem was identified in the flickering technique, image subtraction graphically displayed the effect over large areas. More quantitative techniques could easily miss the pattern so well displayed by image subtraction. On the other hand, quantitative assessment of the misregistration would be difficult with this technique.

A third approach would be to lay out subpixel sized targets of high contrast in an area of a known imminent satellite overpass, such as mirrors or white patches on a dark background. This procedure would allow estimation of misregistration of a major fraction of a pixel and has the advantage that the target is known to have no spectral ambiguities; therefore, the possibility of a bias related to the difference in wavelength between the two bands would not be a problem. However, early work by Evans (Ref. 3) showed that the precision of this method is limited to 1/2 to 1 pixel due to a combination of several factors: the error in location of the IFOV over the targets, effects of electronic filtering on the data, and narrow angle forward scattering in the atmosphere (the adjacency effect). Such sub-pixel targets require great care in placement, so only a few targets could be set out over a given TM scene; hence, neither useful patterns nor a statistically meaningful number of target points could be observed.

The approach taken in this paper, and one selected after trying the differencing and flicker methods mentioned above, was the block correlation method. This technique statistically correlates rectangular blocks of pixels from one band image against blocks centered on identical pixels from a second band image. The block pairs are shifted in pixel increments both vertically and horizontally with respect to each other and the correlation coefficient for each shift position is computed. The displacement corresponding to the maximum correlation is taken as the best estimate of registration error for each block pair.

One of the earliest implementations of the method was the system developed at the Laboratory for Applications of Remote Sensing (LARS), Purdue University, West LaFayette, Indiana. The LARS procedure was developed for spatial registration of multi-spectral, multi-temporal digital imagery (Ref. 4). Historically, the registration software now resident on Ames Research Center's CDC 7600 computer was developed by the Center for Advanced Computation (CAC) of the University of Illinois at Urbana-Champaign for implementation on Ames' ILLIAC IV computer. The program was part of an interactive software system for remote sensing called EDITOR, developed in a joint project by NASA, USGS, CAC, and LARS (Ref. 5). Foreseeing the eventual demise of the ILLIAC IV, Ames personnel implemented the program on the CDC 7600, and eventually incorporated a Fast Fourier Transform (Ref. 4) to speed up the correlation computations.

METHOD

The image selected for the investigation was the Arkansas TM scene of August 22, 1982,in "P" (geometrically correct) format. EDITOR software was modified for a SEL 32/77 minicomputer at Ames to pre-process the data before input to the block correlation program. A systematic array of 17 blocks (square arrays of pixels) along-scan and 20 across-scan were selected and, with scene border deletions , this resulted in an array of 297 blocks that effectively covered the entire TM image. The primary blocks (64 pixels by 64 pixels) were selected from the TM band chosen to remain fixed in position, and the secondary blocks (32 pixels by 32 pixels) were selected from the TM band chosen to vary in position over the primary block. Each set of blocks, primary and secondary, was centered on the same TM pixel and the correlation coefficient was computed for every possible position of the secondary block within the primary block. The displacement (shift) of the center of the secondary block relative to that of the primary block corresponding to the maximum correlation was considered to be the best estimate of misregistration for the block pair. Subpixel accuracy was attempted by performing a bi-quadratic interpolation on the eight pixels surrounding the maximum correlation pixel, and fractional shift values for along-scan and across-scan directions were recorded. Mathematical formulas and algorithms for block correlation will not be discussed in this paper. The paper by Anuta (Ref. 4) is an excellent exposition of the Fast Fourier Transform approach to block correlation and includes the relevant formulas.

Edge enhancement was performed on the TM image in order to improve the estimation of shifts, especially in areas where correlation of unprocessed imagery was impossible, due to radiometric light-dark reversals between bands. Two operators were tried--one was the gradient operator implemented in the original version of the EDITOR correlation program:

$$\begin{aligned}|\mathrm{grad}\ F(i,j)| = {} & |F(i-1,j)-F(i,j)| + |F(i,j+1)-F(i,j)| \\ & + |F(j-1,i)-F(i,j)| + |F(i+1,j)-F(i,j)|\end{aligned}$$

for the pixel at line i and sample j, with radiometric value F(i,j). The other was the well-known Sobel operator (Ref. 6):

$$\begin{aligned}|\mathrm{grad}\ F(i,j)| = {} & |F(i-1,j+1)+2F(i,j+1)+F(i+1,j+1)-F(i-1,j-1) \\ & -2F(i,j-1)-F(i+1,j-1)| + |F(i+1,j-1)+2F(i+1,j) \\ & +F(i+1,j+1)-F(i-1,j-1)-2F(i-1,j)-F(i-1,j+1)|\end{aligned}$$

Results are presented in this paper for the EDITOR gradient operator, since it was the method that was operational in the block correlation program at the start of the project, and subsequent testing showed no improvement of shift estimates for selected band combinations using the Sobel operator.

Post-processing of the shift data was performed on an HP-3000 mini-computer using the MINITAB statistical package (Ref. 7) . Editing of the data consisted of deleting blocks (i.e., shift values corresponding to blocks) that had low correlation values. This procedure tended to eliminate blocks having obviously high positive or negative shifts. However, not all outliers were eliminated, therefore a further step was to discard exceptionally high shift values by keeping only those shifts within a specified threshold. This approach was somewhat subjective, and its consequences will be discussed in the following section.

RESULTS

Table 1 displays the fundamental results of the block correlation analysis for selected TM band combinations. The table shows the results of editing the shift data by discarding all shift values having corresponding correlations less than 0.6. In order to show that this editing procedure is not unreasonable, band pairs 3 versus 5 and 6 versus 7 were subjected to further editing. These pairs were selected because they showed the largest outliers in Table 1. Band pair 3 versus 5 was edited by discarding blocks that had shifts outside the range -3 to 3 pixels or had correlations < 0.6. Similarly, band pair 6 versus 7 was edited by discarding blocks that had shifts outside the range -10 to 10 or had correlations < 0.3. Table 2 displays the results, showing that the mean shift values are quite robust to the editing procedure (discarding shifts based on correlation thresholds and shift values). By restricting the shift values for band 3 versus band 5 , only two outliers were discarded and

Table 1

Descriptive statistics for band-to-band misregistration for selected Thematic Mapper band combinations (Arkansas scene - August 22, 1982). The first band listed in each set is the primary band for the correlations, and all correlation blocks having the correlation coefficient <.6 were discarded. (Unit of misregistration [shift] is in pixels.)

TM Bands	Shift Direction	Number of Blocks	Mean Shift	S.D.	Min Shift	Max Shift	95% Conf. Int. for Mean Shift
3 vs 1	Across-scan	256	-.04	.06	-.2	.2	(-.05,-.03)
	Along-scan	256	-.03	.06	-.4	.1	(-.04,-.02)
3 vs 4	Across-scan	44	-.03	.33	-1.0	1.1	(-.13,.07)
	Along-scan	44	.10	.38	-.4	1.9	(-.02,.22)
3 vs 5	Across-scan	217	.22	.73	-9.3	3.3	(.12,.32)
	Along-scan	217	.49	.41	-2.7	4.0	(.44,.54)
3 vs 7	Across-scan	264	.16	.20	-.4	2.2	(.14,.18)
	Along-scan	264	.49	.18	-.4	1.1	(.47,.51)
7 vs 5	Across-scan	280	.06	.09	-.5	.6	(.05,.07)
	Along-scan	280	-.01	.07	-.4	.3	(-.02,.0)
6 vs 7	Across-scan	4	-3.50	1.04	-4.7	-2.2	(-5.2,-1.8)
	Along-scan	4	-3.20	2.31	-4.9	.2	(-6.9,.48)

Table 2

Results of alternative editing for Band 3 vs Band 5 and Band 6 vs Band 7. (Unit of shift is in pixels.)

Restrictions: (3 versus 5) Correlations >.6, |shift|<3

(6 versus 7) Correlations >.3, |shift|<10

TM Bands	Shift Direction	Number of Blocks	Mean Shift	S.D.	Min Shift	Max Shift	95% Conf. Int. for Mean Shift
3 vs 5	Across-scan	215	.25	.25	-1.0	1.1	(.22,.28)
	Along-scan	215	.49	.25	-0.4	1.9	(.46,.52)
6 vs 7	Across-scan	96	-3.16	3.06	-9.9	8.2	(-3.8,-2.5)
	Along-scan	96	-2.96	2.65	-9.8	8.4	(-3.5,-2.4)

the mean shifts were affected only slightly; for band 6 versus band 7, the mean shifts shifts remained fairly stable, even though the sample size increased from 4 to 96 and the maximum absolute shift increased to 10. Table 3 displays mean shifts versus correlation threshold for band 3 versus 5, and indicates that the threshold for correlation of 0.6 in Table 1 is not unreasonable: for no restriction on either correlation or maximum shift, the mean shift estimates are reasonably close to those for correlation greater than 0.6. This illustrates again the robustness of the estimates of average shift.

In order to quantify somewhat the interpolation error involved in the use of a bi-quadratic fit to the correlations for obtaining subpixel shift estimates, band 3 was correlated against itself. All 297 blocks locked on with maximum correlation 1.0 at integral values of zero shift in each direction, as was to be expected. However, after interpolation, the average shifts were found to be 0.0006 and 0.0012 with standard deviations of 0.009 and 0.04 in the across-scan and along-scan directions, respectively. This indicates that interpolation error can safely be neglected.

The sign associated with the shift values in the tables indicates the relative direction of misregistration. A plus sign in the along-scan direction indicates a right shift, and a plus sign in the across-scan direction indicates a downward shift in the secondary band with respect to the primary band. Similarly, negative shifts would be to the left and upwards. In the tables, the primary band is always written first. For example, in Table 1, for bands 6 versus 7, with band 6 stationary, band 7 is to the left and upwards. The tables also show the number of blocks remaining after editing, the standard deviations, minima and maxima of the shifts, and a nominal 95% confidence interval around the mean shift based on the assumption of approximate normality of the shift distributions (after editing).

Table 1 shows that the target specification for TM band-to-band registration of 0.2 pixels is easily achieved for those band combinations within the same focal plane (bands 1 versus 3 and 3 versus 4 in the non-cooled focal plane, and bands 5 versus 7 in the cooled focal plane), with the exception of bands 6 versus 7. Band 6 presents special problems, which will be discussed below. Although the shift for band 3 versus band 4 was within the 0.2 pixel specification, the standard deviations of across-scan and along-scan shifts were higher than the 1-3 and 5-7 band pairs, and far fewer blocks were retained after editing (44 out of 297). The relatively poor performance for bands 3 and 4 is apparently the result of natural low correlation between a visible and a

Table 3

The effect of successive block deletion on estimates of band-to-band misregistration for Thematic Mapper bands 3 and 5 (Arkansas scene -- August 22, 1982). Band 3 was the primary band for the correlations. Blocks having correlation coefficients outside the range shown in the table were discarded. (Unit of shift is in pixels.)

Corr. Coef.	Shift Direction	Number of Blocks	Mean Shift	S.D.	Min Shift	Max Shift	95% Conf. Int. for Mean Shift
>.8	Across-scan	48	.17	.30	-1.0	.9	(.08,.26)
	Along-scan	48	.42	.26	-0.4	.9	(.34,.50)
>.6	Across-scan	217	.22	.73	-9.3	3.4	(.12,.32)
	Along-scan	217	.49	.41	-2.7	4.0	(.43,.55)
>.3	Across-scan	289	.33	1.23	-9.3	15.2	(.18,.47)
	Along-scan	289	.45	.90	-12.7	4.0	(.35,.55)
All	Across-scan	297	.26	1.67	-12.5	15.2	(.07,.45)
	Along-scan	297	.48	2.07	-16.0	16.0	(.24,.72)

near IR band. This is illustrated in Fig. 1, which compares histograms of the band 3 versus band 4 correlations with band 7 versus band 5 correlations. The mode of the distribution for anticorrelated bands 3 and 4 is approximately 0.3, whereas that of the distribution for correlated bands 7 and 5 is approximately 0.85, showing that the 3 versus 4 blocks correlated in general at lower values.

Table 1 also shows relatively larger and consistent shifts between bands in different focal planes(band 3 versus band 5 and band 3 versus band 7); the along-scan shift is larger than the permitted 0.3 pixel misregistration. This result confirmed the earlier experience with the flickering method, in which an approximate shift of a half pixel was noted in the along-scan direction when band 3 was flickered against band 5 on a video display screen. The shifts for band 3 versus band 5 and band 7 versus band 5 are remarkably consistent with each other--note that adding the 3-7 shifts to the 7-5 shifts equals the 3-5 shifts. This may be coincidental, but one might expect this kind of transitive relationship for real misregistration shifts. Given the fact that the data processing software for TM data can

```
Correlation  Number of
  Coeff.       Blocks
___________  _________
    -1.0         0
    -0.9         0
    -0.8         0
    -0.7         0
    -0.6         0
    -0.5         0
    -0.4         1     *
    -0.3        22     ***********
    -0.2        17     *********
    -0.1         0
     0.0         0
     0.1         1     *
     0.2        33     *****************
     0.3        70     ***********************************
     0.4        66     *********************************
     0.5        27     **************
     0.6        30     ***************
     0.7        19     **********
     0.8         5     ***
     0.9         4     **
     1.0         2     *
```

```
Correlation  Number of
  Coeff.       Blocks
___________  _________
    -1.0         0
    -0.9         0
    -0.8         0
    -0.7         0
    -0.6         0
    -0.5         0
    -0.4         0
    -0.3         0
    -0.2         0
    -0.1         0
     0.0         0
     0.1         0
     0.2         5     *
     0.3         0
     0.4         3     *
     0.5         7     **
     0.6         7     **
     0.7        44     *********
     0.8       112     ***********************
     0.9       112     ***********************
     1.0         7     **
```

(a) (b)

Fig. 1. Histograms of correlation coefficient (no deletions)
(a) Band 3 versus band 4 (each * represents 2 observations)
(b) Band 7 versus band 5 (each * represents 5 observations)

correct subpixel misregistrations, we suggest that the appropriate shifts to correct the misregistration between the uncooled and cooled focal planes would be 0.5 pixels along-scan and 0.2 pixels across-scan based on these results.

Band 6 presents a special problem, in that it had a very low correlation with band 7, and therefore editing was much more difficult as evidenced in Table 1 by the retention of only four blocks with correlations above 0.6. Flickering between bands 6 and 7 also showed poor visual correlation and verified an approximate four pixel shift. Fig. 2, a histogram of shifts for band 6 versus band 7 prior to editing, illustrates the difficulty of editing this band pair due to the large percentage of outliers and almost uniform nature of the distribution. Fig. 3 shows the histogram of shifts for band 3 versus band 5, for comparison with Fig. 2. (19 outliers were deleted from the data in Fig. 3 in order to show the shape of the distribution around the mean to better advantage.) As noted earlier, even with these difficulties, the shift estimates for band 6 versus band 7 seem to be quite robust to the editing procedure. Based on these results, we suggest correcting the band 6 misregistration by shifts of 3 pixels (28.5 meters) in both the along-scan and the across-scan directions.

```
Shift  Number of
         Blocks
       ---------
-16.0          8  ********
-15.0          7  *******
-14.0          4  ****
-13.0          2  **
-12.0          7  *******
-11.0          8  ********
-10.0          7  *******
 -9.0          5  *****
 -8.0          7  *******
 -7.0          6  ******
 -6.0         19  *******************
 -5.0         26  **************************
 -4.0         29  *****************************
 -3.0         25  *************************
 -2.0         20  ********************
 -1.0          9  *********
  0.0          9  *********
  1.0          5  *****
  2.0          5  *****
  3.0          6  ******
  4.0          7  *******
  5.0          2  **
  6.0         10  **********
  7.0          7  *******
  8.0          5  *****
  9.0           3  ***
 10.0          9  *********
 11.0          5  *****
 12.0          5  *****
 13.0          4  ****
 14.0         10  **********
 15.0          5  *****
 16.0         11  ***********
```

(a)

```
Shift  Number of
         Blocks
       ---------
-16.0         15  ***************
-15.0          7  *******
-14.0          4  ****
-13.0          8  ********
-12.0          8  ********
-11.0          3  ***
-10.0          2  **
 -9.0          8  ********
 -8.0          7  *******
 -7.0          4  ****
 -6.0         12  ************
 -5.0         17  *****************
 -4.0         29  *****************************
 -3.0         42  ******************************************
 -2.0         15  ***************
 -1.0         15  ***************
  0.0          7  *******
  1.0          8  ********
  2.0          6  ******
  3.0          4  ****
  4.0          6  ******
  5.0          4  ****
  6.0         10  **********
  7.0          2  **
  8.0         10  **********
  9.0          7  *******
 10.0          4  ****
 11.0          4  ****
 12.0          4  ****
 13.0          6  ******
 14.0          7  *******
 15.0          5  *****
 16.0          7  *******
```

(b)

Fig. 2. Histogram of shifts for band 6 versus band 7 (no deletions)
(a) Across-scan (b) Along-scan

```
Shift  Number of
         Blocks
       ---------
 -1.0          1  *
 -0.9          1  *
 -0.8          1  *
 -0.7          0
 -0.6          0
 -0.5          1  *
 -0.4          0
 -0.3          2  *
 -0.2          2  *
 -0.1          7  ****
  0.0         22  ***********
  0.1         52  **************************
  0.2         69  ***********************************
  0.3         53  ***************************
  0.4         25  *************
  0.5         13  *******
  0.6         12  ******
  0.7          6  ***
  0.8          2  *
  0.9          5  ***
  1.0          4  **
```

(a)

```
Shift  Number of
         Blocks
       ---------
 -0.8          1  *
 -0.7          1  *
 -0.6          0
 -0.5          0
 -0.4          1  *
 -0.3          0
 -0.2          1  *
 -0.1          5  *****
  0.0          4  ****
  0.1         11  ***********
  0.2         18  ******************
  0.3         44  ********************************************
  0.4         48  ************************************************
  0.5         43  *******************************************
  0.6         42  ******************************************
  0.7         26  **************************
  0.8         18  ******************
  0.9         12  ************
  1.0          3  ***
```

(b)

Fig. 3. Histograms of shifts for band 3 versus band 5 (blocks with |shift|>1 were deleted)
(a) Across-scan (each * represents 2 observations)
(b) Along-scan

CONCLUSIONS

For the band combinations studied:

(1) The misregistration of TM spectral bands within the non-cooled focal plane lie well within the 0.2 pixel target specification (TM bands 3 versus 1 and 3 versus 4).

(2) The misregistration between the middle IR bands (TM bands 5 and 7) is well within the 0.2 pixel specification.

(3) The thermal IR band (TM band 6) has an apparent misregistration with TM band 7 of approximately 3 pixels in each direction.

(4) TM band 3 has a misregistration of approximately 0.2 pixel in the across-scan direction and 0.5 pixel in the along-scan direction, with both TM bands 5 and 7.

Indications are that the block correlation method is a reasonable approach to the quantitative assessment of band-to-band misregistration. It is quite robust to the method of editing outliers and seems to result in estimates of registration error that are consistent with expectations.

REFERENCES

1. F. Gordon, Jr., "The Time-Space Relationships Among Data Points from Multispectral Spatial Scanners", International Journal of Remote Sensing, In press

2. P. H. Swain, A Quantitative Applications-oriented Evaluation of Thematic Mapper Design Specifications, Final Report LARS Grant Report 121680, Dec. 1980

3. W. E. Evans, "Marking ERTS Images with a Small Mirror Reflector," Photogrammetric Engineering, Vol. 40, 1974, pp. 665-671

4. P. E. Anuta, "Spatial Registration of Multispectral and Multitemporal Digital Imagery Using Fast Fourier Transform Techniques", IEEE Trans. on Geoscience Electronics, Vol. GE-8, No. 4, Oct. 1970 pp. 353-368

5. R. M. Ray, III, J.D. Thomas, W.E. Donovan, and P.H. Swain, Implementation of ILLIAC IV Algorithms for Multispectral Image Interpretation, Final Report, CAC Document No. 112, Center for Advanced Computation, University of Illinois at Urbana-Champaign, Urbana, Illinois, June 1974

6. R. O. Duda and P.E. Hart, Pattern Classification and Scene Analysis , John Wiley & Sons, 1973, pp. 271-272

7. T. A. Ryan, Jr., B.L. Joiner, and B.F. Ryan, MINITAB Student Handbook, Duxbury Press, North Scituate, Mass., 1976

N85-21744

Dg
20

TESTS OF LOW-FREQUENCY GEOMETRIC DISTORTIONS IN LANDSAT 4 IMAGES

R. M. Batson and W. T. Borgeson

U. S. Geological Survey
2255 No. Gemini Dr.
Flagstaff, Arizona 86001

INTRODUCTION

A series of tests was performed to investigate the geometric characteristics of Landsat 4 images. The first set of tests was designed to determine the extent of image distortion caused by the physical process of writing the Landsat 4 images on film. The second was designed to characterize the geometric accuracies inherent in the digital images themselves. Test materials consisted of film images of test targets generated by the Laser Beam Recorders (LBR) at Sioux Falls, the Optronics* Photowrite film writer at Goddard Space Flight Center, and digital image files of a strip 600 lines deep across the full width of band 5 of the Washington, D. C. Thematic Mapper scene. The tests were made by least-squares adjustment of an array of measured image points to a corresponding array of control points. The film test array consists of 25 test points, and the image test array consists of 60 test points, resulting in a model that can be used to characterize the low-frequency, random geometric distortions of the images. The tests were not suitable for examining jitter or similar high-frequency distortions because the spacing between control points is too large.

TEST PROCEDURES

All tests were made by least-square fitting of test arrays to control arrays. Control arrays are considered to be exact, and are determined either mathematically by generating arrays of test targets in the computer, or by precise measurement of control point locations on U.S.G.S. topographic maps. The test arrays are determined by physical measurement of film images, or by counting pixels in digital files.

PRECEDING PAGE BLANK NOT FILMED

Original photography may be purchased
from EROS Data Center
Sioux Falls, SD 57198

PAGE III-564 INTENTIONALLY BLANK

The least-square fit was done in three ways for each dataset. The first allowed magnification and rotation only. The second allowed differential magnification in X and Y along with rotation, and the third allowed not only rotation and differential X and Y magnification, but skew distortion of the image as well.

Coordinate measurements of points in the film image test array were made with a Mann* comparator with one micrometer least-count measurement capability. Coordinate measurements of control points on maps were made with an Altek* digitizer with 0.003 inch measurement capability. In each case, measurement error was reduced by measuring each array in four orientations differing by large random amounts. The four sets of measurements were then fitted together by least squares, allowing only rotation and translation of the measured arrays. Measurement blunders are easy to detect and eliminate by this method, and residual errors can then be reduced to some minimum average magnitude.

Test arrays of the locations of 25 targets on each of three film images (figure 1) were measured with the comparator by the method outlined above. The film images are printed on Estar-base film 0.007 inches thick; a standard film used to produce dimensionally stable images for photogrammetric use. Table 1 summarizes the results of the least-squares adjustment of the measured target locations to their nominal positions for each of the three images.

A total of 60 control points on the TM image were identified on USGS 1:24,000 topographic maps, and their UTM coordinates determined by direct measurement on the map sheets. These measurements were made with an Altek table digitizer, by measuring the rectangular coordinates of each point and of the four printed coordinate ticks nearest to each control point, to allow analytical adjustment for paper shrinkage. As in the film image tests above, measurements were made four times. After detection of measurement blunders, the mean location of each point was computed and placed in the control point array.

The image coordinates of each control point were measured in terms of lines and samples with a DeAnza* interactive digital image viewing system. Figure 2 shows the 51 line by 51 sample image segments for each control point. In each case, the central pixel is taken as the location of the point. Once again, the image array was fitted to the control array in three ways, with the results shown in table 2. Five of the original 60 points were eliminated from the process because of very large residual errors, which proved to be a result of misidentification of the image points.

C-7

Table 1
SUMMARY OF FILM RECORDER MEASUREMENT RESULTS
Units are micrometers

	Goddard Optronics	EROS LBR #1	EROS LBR #2
Nominal Pixel size:	25.0	57.0	57.0
Measurement error (i.e., standard error of four independent measurements of test images):	4.2	2.5	2.8
Standard error:			
Condition 1:	24.39	24.62	61.15
Condition 2:	23.89	20.17	57.17
Condition 3:	8.46	24.84	61.48
Condition 4:	5.64	8.95	28.48
Maximum value of ratio of X-magnification to Y-magnification:			
Condition 2:	.999068	1.000430	.999531
Condition 4:	.999801	1.000431	.999248
Maximum skew (degrees):			
Condition 3:	0.0415	0.0000	0.0083
Condition 4:	0.0414	-0.0141	-0.0197

Condition 1: Rigid array; skew held at 0 degrees, ratio of X-magnification to Y-magnification held at 1.0.

Condition 2: Skew held at 0 degrees, differential X and Y magnification permitted.

Condition 3: Skew allowed, ratio of X-magnification to Y-magnification held at 1.0.

Condition 4: Both skew and differential X and Y magnification allowed.

Table 2
SUMMARY OF IMAGE MEASUREMENT RESULTS

	X-magnification	Y-magnification	Skew (deg)	Standard error (m)
Condition 1	28.5054567	28.5054567	0.0000	36.41
Condition 2	28.5054270	28.5054011	0.0000	36.58
Condition 3	28.5054440	28.5054400	0.0018	36.58
Condition 4	28.5054123	28.5057287	-0.0023	36.76

CONCLUSIONS

The contribution of error caused by the film writers is somewhat variable, and should be measured at regular intervals. In the worst case measured in the current testing, slightly more than one pixel of error is typically contributed by the film writer. Overall standard errors can be reduced by more than a factor of two by allowing differential X- and Y-magnification and skew in the images. Unless further testing reveals that these errors are constant and unique to a given film writer, it will probably not be practical to attempt to improve image geometry by making such corrections.

The discrepancies in the TM image tested are essentially random, with negligible affine and skew components. The standard error in all cases is very nearly 37 meters, or approximately 1.3 pixels. It is reasonable to suggest that the source of this error is more likely a function ofthe accuracy with which the control point location is known and the accuracy with which the actual pixel containing the control point is selected than to a distortion in the TM image, and that planimetric mapping can be done to National Map Accuracy standards at any scale supported by the resolution of the image itself.

*Mention of specific products is for illustrative purposes only, and does not constitute endorsement by the U. S. Geological Survey.

ORIGINAL PAGE IS
OF POOR QUALITY

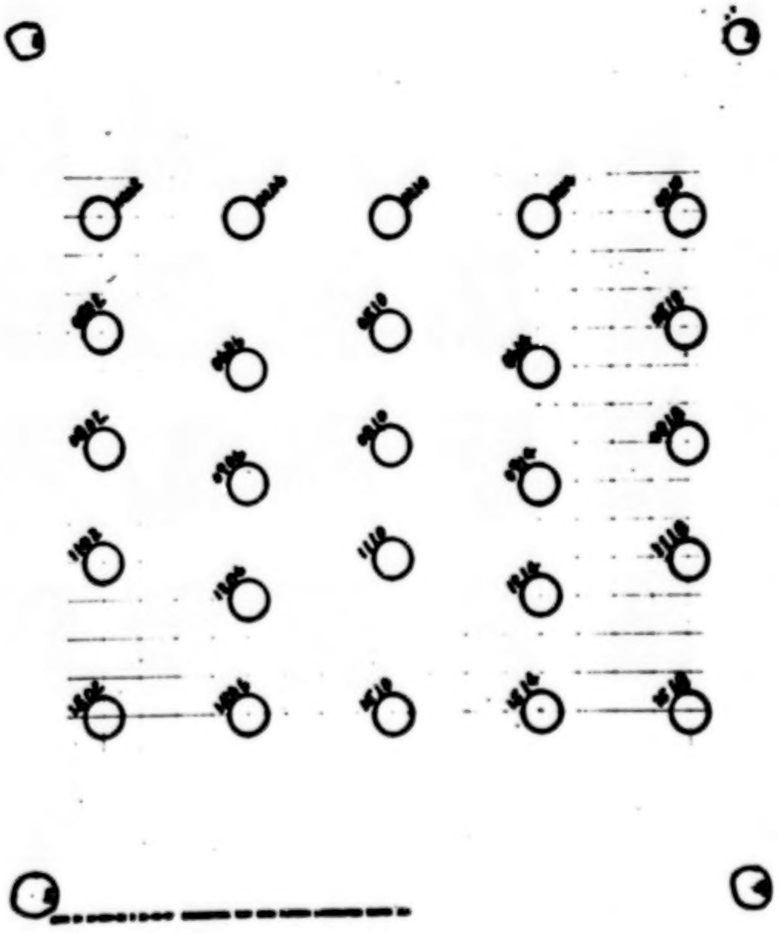

Figure 1. Example of film-writer test image.

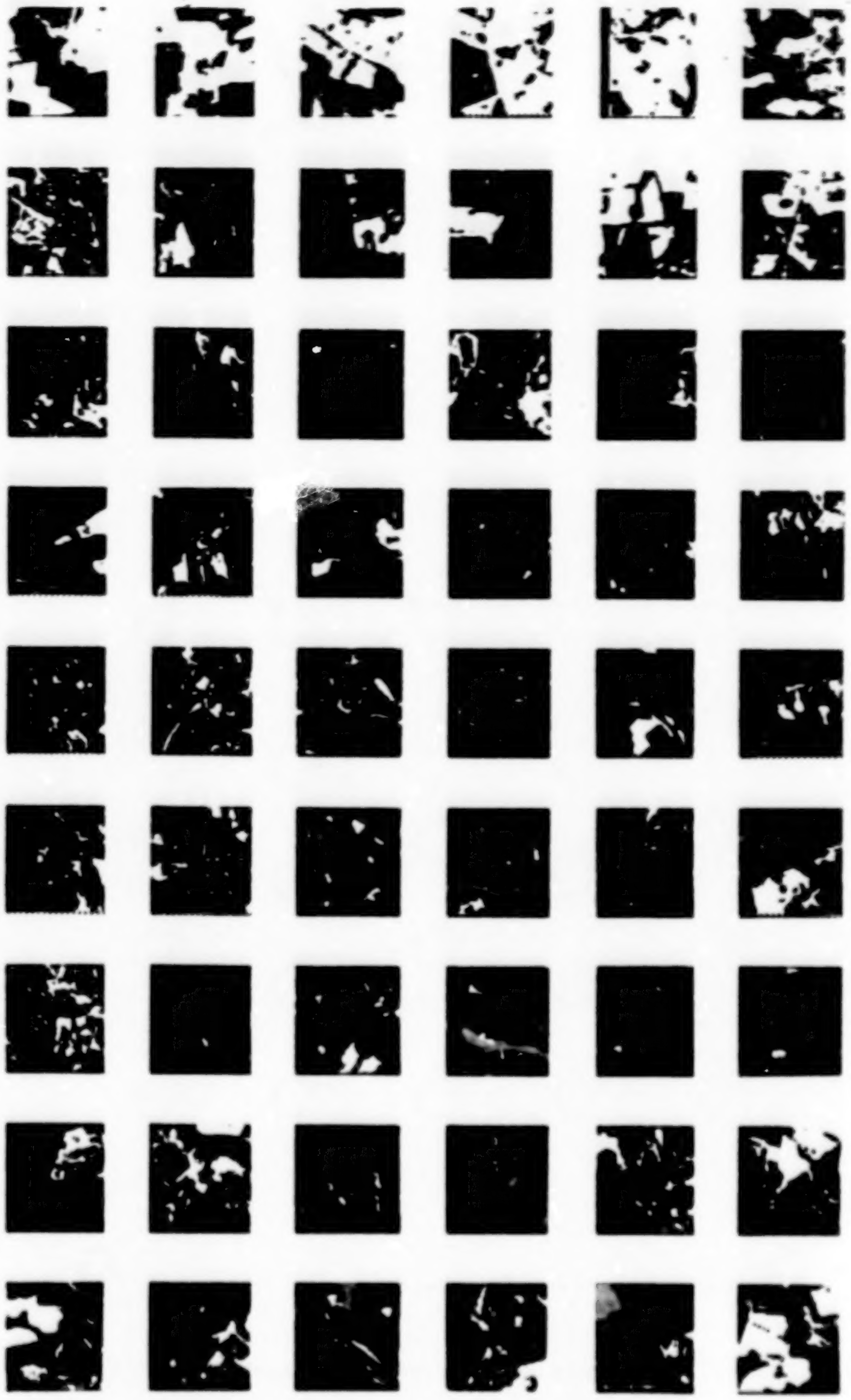

Figure 2. Images of control points used to test the geometry of band 5 of the TM image of the Washington, D.C. area.

ORIGINAL PAGE IS
OF POOR QUALITY

N85-21745

~~D20~~
21

INVESTIGATION OF TM BAND-TO-BAND REGISTRATION USING THE JSC REGISTRATION PROCESSOR

S. S. Yao and M. L. Amis

Lockheed Engineering and Management Service Company, Inc.
Houston, Texas

1. INTRODUCTION

When the Thematic Mapper (TM) imagery from Goddard Space Flight Center (GSFC) SCROUNGE system was first received and displayed at the Johnson Space Center (JSC) in the fall of 1982, its radiometric lucidity and geometric fidelity was judged far superior to the multispectral scanner (MSS) imagery. The MSS data from the Landsat series of satellites have served well as the mainstay of satellite imagery for the remote sensing community up to now. Therefore, there is great anticipation as to the utility of this new IM imagery to advance the field of remote sensing. As part of the scientific characterization effort, a task was initiated to make a quantitative evaluation of some of the geometric aspects of the TM imagery. The scenes selected for evaluation were the first few processed by GFSC through the SCROUNGE system; thus they did not represent the ultimate quality available geometry-wise for all TM images.

This paper discusses the TM band-to-band registration accuracy evaluation. In particular, the band-to-band registration accuracies of the TM data in the subpixel region were evaluated using the JSC registration processor which is ideally suited for this task. The JSC registration processor was also used to register one acquisition to another acquisition of multitemporal TM data acquired over the same ground track. The approach and the rationale behind the task, the description of the data set, the evaluation results, and the preliminary conclusions drawn from the study, are discussed in the following sections.

2. APPROACHES

Three TM scenes in P-tape format received at JSC from GSFC in the fall of 1982 provided the data set for this study. All three scenes have the same path number, 27, and row number, 31. Subscenes of the size 512 by 512 pixels were extracted to cover the Webster County, Iowa supersite in the Agriculture

Resources Inventory Survey Through Aerospace remote Sensing (AgRISTARS) study. The earliest acquisition was dated August 2, followed by a September 3, and then an October 21 acquisition. The total time span between the first and the third acquisition was 80 days, or five Landsat-4 cycles. The August 2 acquisition has only four bands, i.e., the three visible bands plus the first near infrared band. The other two acquisitions have all seven bands.

2.1 BAND-TO-BAND REGISTRATION ACCURACY EVALUATION

The detectors that imaged the seven-band TM data were placed in two groups onboard the Landsat-4 spacecraft (Beyer 1983). Detectors for band 1 to band 4 were located in the primary focal plane while those for band 5 to band 7 were in the cold focal plane. This arrangement, plus the fact that due to high spatial resolution, different detectors have slightly different instantaneous field of view (IFOV) during the scan mirror sweep, makes the band-to-band registration problem interesting. Ground processing software was designed to align within-focal-plane bands (e.g., bands 1 and 4) to 0.2 pixel accuracy, and between-focal-plane bands (e.g., bands 4 and 5) to 0.3 pixel accuracy.

Since finding image feature location to fractional pixel accuracy is required in band-to-band registration evaluation, the usual approach of image display, image zoom, and zoomed image flicker comparison is not satisfactory. A more precise and quantitative approach is needed. It was determined from previous experience that the JSC registration processor has the capability to make precise computations of the correlation peak locations. When data from two bands of the same scene are cross-correlated, the correlation peak location away from the center yields an offset that indicates both the magnitude and the direction of the misregistration.

2.1.1 JSC Registration Processor Capability

The JSC registration processor is designed to perform precise multitemporal registration of the Landsat imagery (Wolfe et al. 1982). The processor first performs a coarse correlation of two image acquisitions to remove gross translational offsets. It then computes correlation functions and iteratively estimates correlation peak locations to fractional pixel accuracies. By using this "fine correlation" capability, the band-to-band registration accuracies of the TM data can be precisely and quantitatively evaluated in the following manner: Assume that bands A and B images from the same TM scene are to be evaluated for registration accuracy. Band A image is first read in as the reference, where a reference edge image, E(A), is created. The edge image is made up of values 1 and zero, where the 1's represent 15 percent of the highest edge values computed by edge operator E. Band B image is then read in as the "overlay" image and its edge image, E(B), is created in a similar manner. The edge images are then separated into regularly spaced blocks of data, and each block of E(A) is correlated with the corresponding block of slightly larger size from E(B) via a user-specified correlation algorithm.

A reference block is often 50 pixels on each side. An overlay block will contain an additional 45-pixel border area. Up to 10 reference blocks can be spaced horizontally across an image in the column direction, and up to six blocks in the row direction. After the correlation functions are computed, each block will yield a peak offset location in column and row spacings, and up to 60 peak offset locations can be used to characterize the relation between E(A) and E(B), which in turn represents registration accuracy between bands A and B. If, for example, band A is identical to band B, autocorrelation is obtained instead of cross-correlation, and 60 zero-offset correlation peak location values should result. The precise fractional pixel location of the correlation peak computed from each block is iteratively estimated using a fourth order bivariate polynomial interpolation function derived from a 5 by 5 pixel area centered around the peak. From experiences gained running the system, together with some simulation studies already done, it has been shown that an accuracy of 1/15-pixel in peak location can be routinely achieved form the JSC registration processor.

2.1.2 Registration Accuracy Evaluation Procedure

The procedure used for evaluating the registration accuracy between TM band A and TM band B are summarized as follows:

a. Read in band A data and create edge image E(A), using edge image operator E.

b. Read in band B data from the same TM scene and create edge image E(B) using the same operator.

c. Select the cross-correlation function and the number of blocks per image to be correlated; perform cross-correlation.

d. Estimate the correlation peak offset location per block to fractional pixel accuracies and tabulate the results from all blocks.

e. Plot the line and column direction offset values on a scatterplot; then compute the mean and root-mean-square of the scatterplot to indicate overall registration performance between bands A and B.

f. Repeat all procedures for bands A and C, bands B and D, and so on.

2.2 Temporal Registration of TM Scences

The procedure used in evaluating the band-to-band registration accuracies of the single-acquisition TM data can be carried out one step further to register one acquisition to the other. Consider the registration of the September 3 subscene to the August 2 subscene. Band 4 of the August 2 subscene was chosen as the reference, and its edge image created. Over an agriculture area, the histogram of band 4 has the largest data range as compared to the histogram of the other bands. Thus band 4 often provides better contrast and, in turn, a better edge image. The September 3 acquisition was then read in, and its band 4 was used as the overlay image to be cross-correlated with the reference. Just like the band-to-band registration procedure mentioned, a set of peak offset locations are obtained. The coefficients of a distortion model (affine in this case) were then derived based on the block correlation peak offset locations, and the entire seven bands of the September 3 acquisition were resampled based on the distortion model established. Strictly speaking, only band 4 of the two acquisitions were precisely registered to each other. An attempt was made to use the combined edge images from bands 3 and 4 of the August 2 acquisition as a reference, then use it to cross-correlate with the combined edge images from bands 3 and 4 of the September 3 acquisition. Little difference was observed when the coefficients of the distortion models between the two attempts were compared.

The same procedure was used to register the October 21 acquisition to the August 2 acquisition. As a final product of the multitemporal registration, the four bands of the August 2 acquisition were combined with both the seven-band registered September 3 acquisition and the seven-band registered October 21 acquisition to form an 18-band TM data set over the Webster County, Iowa supersite. This multitemporally registered TM data set then became part of the data base for this supersite.

3. RESULTS

To evaluate the band-to-band registration accuracies of the TM SCROUNGE data and to register the three temporal acquisitions of the Webster County, Iowa scenes (Segment 893) together, the following options of the JSC registration processor were chosen.

a. Cloud detection and exclusion module was bypassed. Algorithms to detect cloud and cloud shadow automatically based on the seven band TM data have not yet been developed, and the three acquisition of Segment 893 were known to be cloud-free when the images were displayed on the Image Analysis Station screens.

b. A 3 x 3 edge operator based on a modified gradient formulation was employed. This edge operator was computational efficient. The formula for computing edge, G_{22}, at A_{22}, from the surrounding eight pixel values is

$$G_{22} = W_1 [\Delta D_1 + \Delta D_2] + W_2 [\Delta D_3 + \Delta D_4]$$

Where

$$\Delta D_1 = |A_{12} - A_{32}|$$
$$\Delta D_2 = |A_{21} - A_{23}|$$
$$\Delta D_3 = |A_{11} - A_{33}|$$
$$\Delta D_4 = |A_{13} - A_{31}|$$

and the weights (W's) were assigned

$$W_1 = 1.0$$
$$W_2 = 0.707$$

c. Only pixels that contained the highest 15 percent of edge values were included in the edge image. The 15 percent figure was empirically determined. It worked well for TM imagery.

d. To use the block correlation approach, eight horizontal blocks equally spaced across the image and five vertical blocks equally spaced along the image were specified. A total of 40 correlation peak offset locations were thus made available for accuracy evaluation.

e. The normalized cross-correlation function was used to determine the block correlation peaks. A threshold of 3.0 was used for peak-to-background ratio. The threshold was used to exclude some offset values which often came from false correlation peaks.

These options were selected to make the processor accept and process TM data more efficiently.

The band-to-band registration evaluation of the August 2 four-band subscene revealed no surprises. Since all bands were imaged from detectors on the same focal plane, very little band-to-band misregistration was found. The correlation peak offset locations were all found to be below the "noise level" of the JSC registration processor capabilities. Figure 1 shows three scatterplots of band-to-band registration of the seven band September 3 acquisition. Band 4 was used as the reference. Scatters for band 2 versus band 4 were small and well centered. Band 4 to band 5 scatters show definite bias in the upper right band quadrant, indicating misregistration in the subpixel range. Band 4 versus band 6 scatters show large bias in the column direction, indicating misregistration of around four pixels. Figure 2 shows the same three sets of scatterplots for the Octber 21 acquisition. Band 4 versus band 5 scatters were smaller and tighter as compared to the September 3 results. Nevertheless a bias was still evident. The band 4 to band 6 scatterplots on the other band, show much larger scatter from only few data points. Most of the 40 peak offset values were rejected by the software. Only 11 data points survived the test, and again, a bias in the column direction was quite prominent.

Table 1 is a summary of the band-to-band registration evaluation results with column and row offsets given both in terms of the average values as well as the root-mean-square (rms) values. All values were in terms of pixel spacing.

TABLE 1- SUMMARY OF BAND-TO-BAND REGISTRATION RESULTS

		RMS offsets (pixels)		Average offsets	
Acquisition date	Bands	Column	Row	Column	Row
September 3, 1982	2 vs 4	0.45	0.28	-0.02	-0.17
	4 vs 5	2.65	1.35	0.79	0.89
	4 vs 6	3.73	0.80	3.68	0.53
October 21, 1982	2 vs 4	0.17	0.12	-0.06	-0.01
	4 vs 5	0.53	0.38	0.28	0.33
	4 vs 6*	2.16	1.45	1.39	1.18

*Only 11 data points are available

The block correlation offset results for registering band 4 of the September 3 acquisition to that of August 2 acquisition is shown in Figure 3. The arrows give both the magnitude and the direction of the offsets at each block locations. The circles indicates failed or rejected correlation offset values. Figure 4 presents the same results in scatterplot format. The rms errors in both the column and the row directions are also shown. Figures 5 and 6 show the same type of graphs for the October 21 to August 2 registration. Because of the 80-day time lapse in acquisitions, ground cover type variations caused the correlation to be not as "tight" and the rms errors in both the column and the row directions increased.

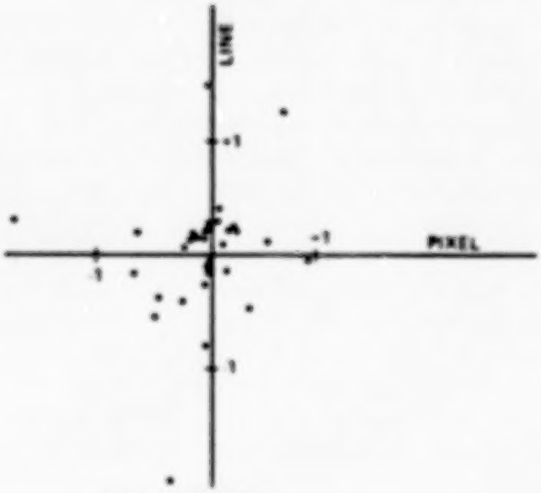

BAND 2 VS BAND 4
LINE AVERAGE OFFSET 0.013 PIXEL
COLUMN AVERAGE OFFSET -0.17 PIXEL

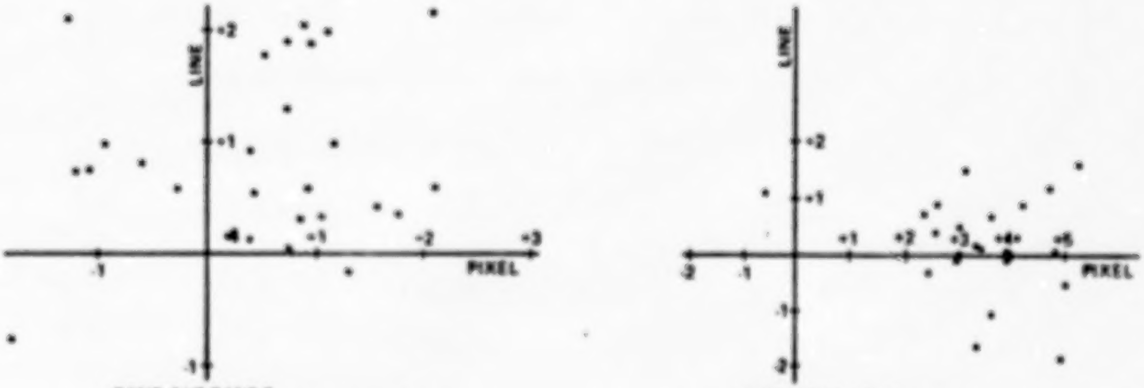

BAND 4 VS BAND 5
LINE AVERAGE OFFSET 0.79 PIXEL
COLUMN AVERAGE OFFSET 0.89 PIXEL

BAND 4 VS BAND 6
LINE AVERAGE OFFSET +0.53 PIXEL
COLUMN AVERAGE OFFSET +3.88 PIXEL

Fig. 1 Evaluation of TM Band-to-Band Registration
(September 3, 1982 Acquisition)

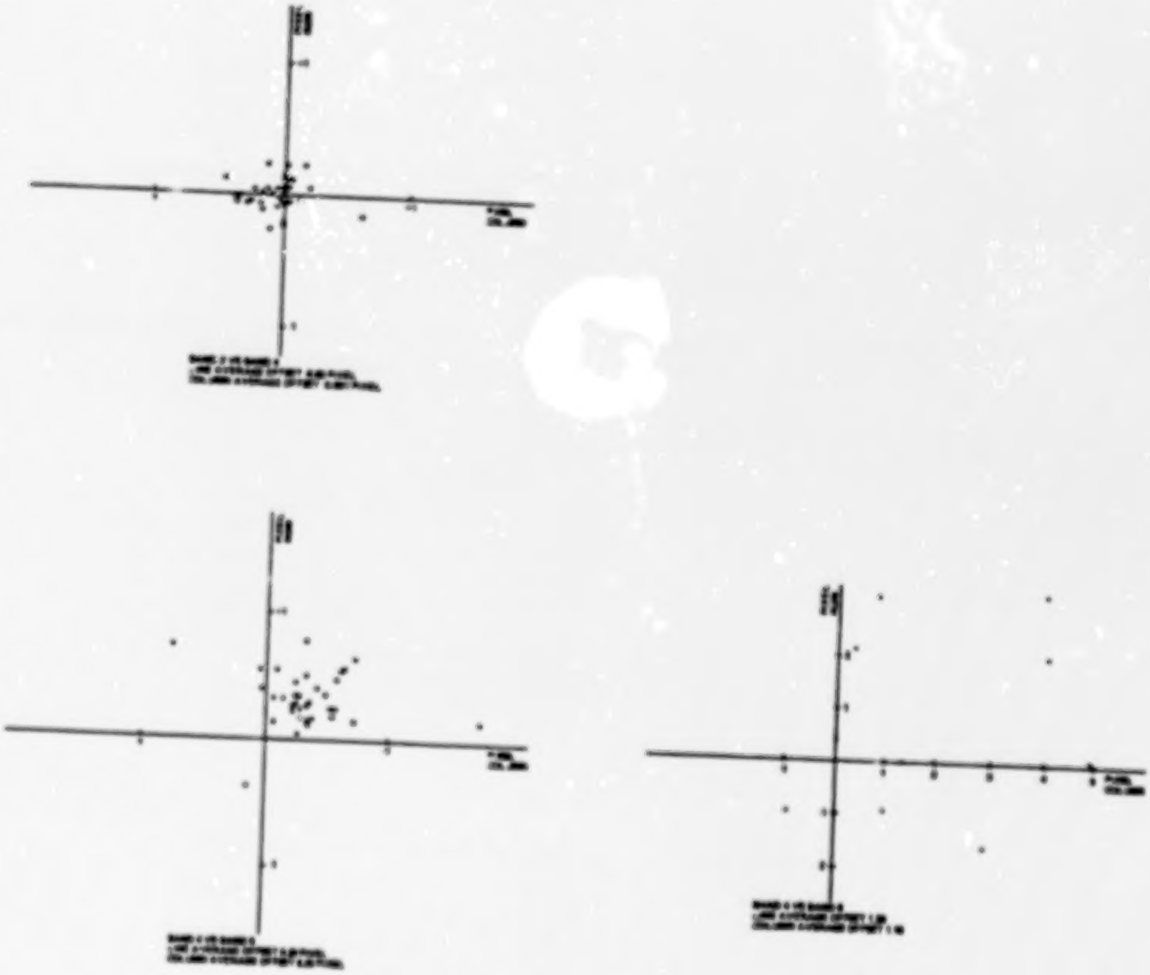

Fig. 2 Evaluation of TM Band-to-Band Registration
(October 21, 1982 Acquisition)

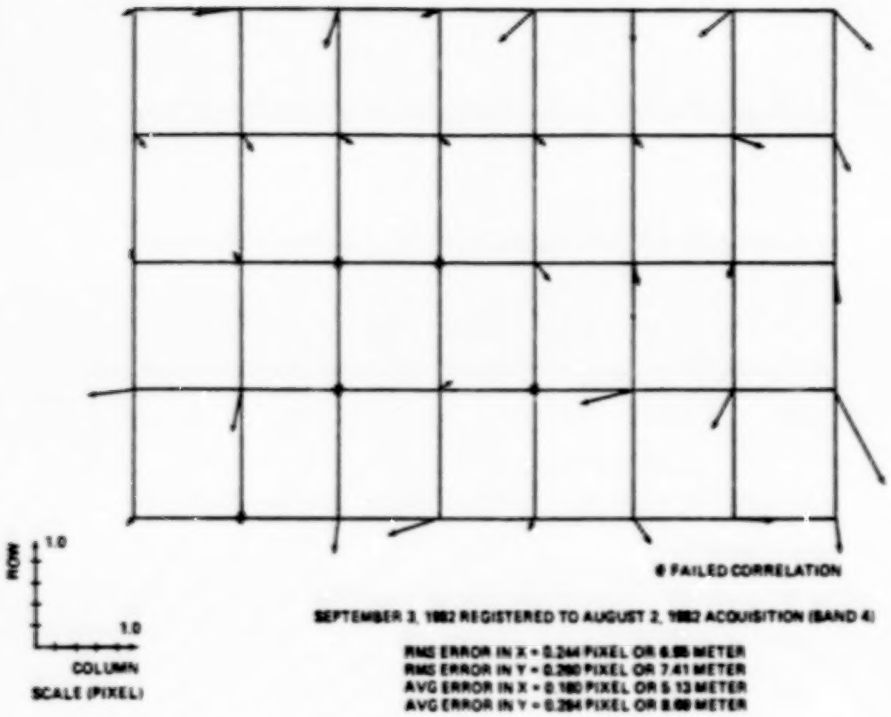

Fig. 3 Block Correlation Offset for Segment 893 (September 3 Registered to August 2, 1982 Acquisition - Band 4)

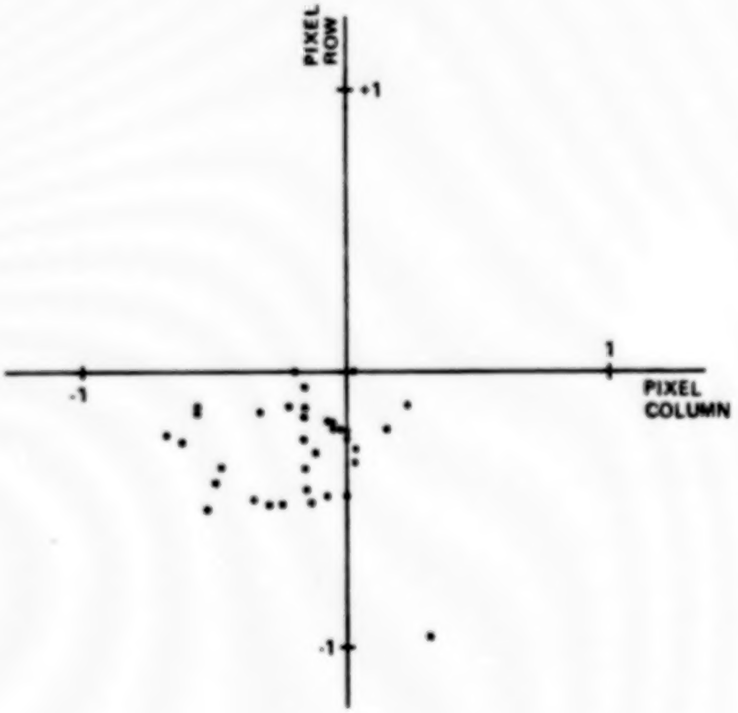

Fig. 4 Error Scatterplot for Segment 893 (September 3 Registered to August 2, 1982 Acquisition - Reference)

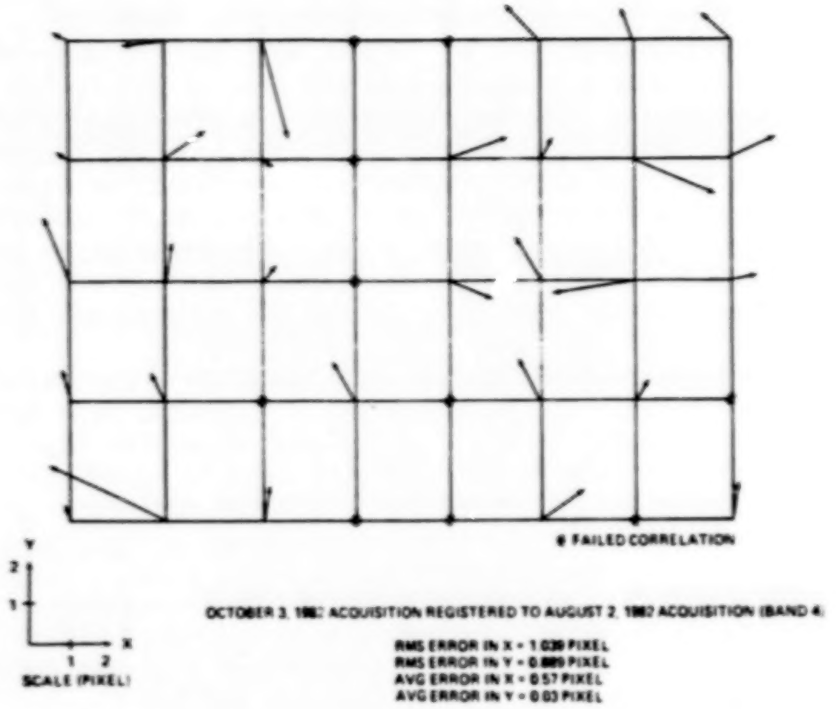

Fig. 5 Block Correlation Offset for Segment 893 (October 21 Registered to August 2, 1982 Acquisition - Band 4)

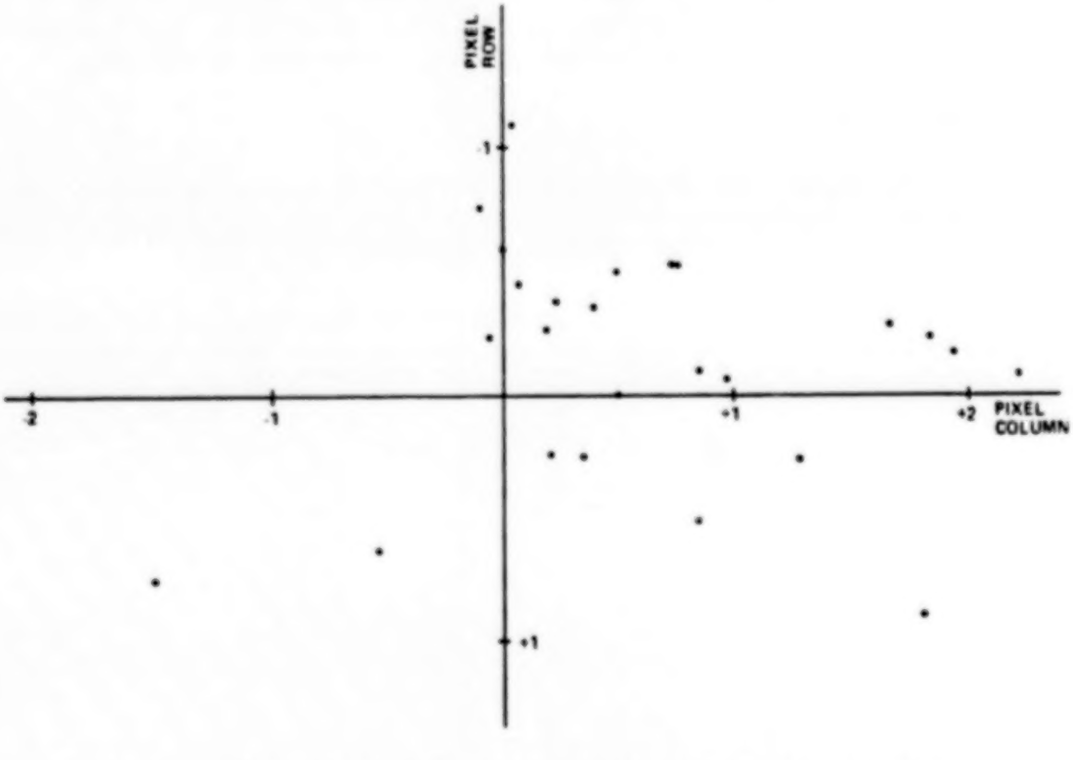

Fig. 6 Error Scatterplot for Segment 893 (October 21 Registered to August 2, 1982 Acquisition - Reference)

4. CONCLUSION

The JSC registration processor was effectively used to evaluate TM band-to-band registration over a subscene area the size of 512 by 512 pixels to fractional pixel accuracy. The same processor was also successfully used to temporally register three acquisitions of TM data over the Webster County, Iowa supersite to fractional pixel accuracies. The characteristics of the processor that enabled these results to be obtained quantitatively was the block correlation approach based on edge images. The correlation peak offset locations were also iteratively estimated to fractional pixel accuracies. In addition, quality assurance checks were also carried out to weed out false peak offsets.

The within-focal-plane bands of the TM SCROUNGE data was found to be well registered to each other. The between-focal-plane bands have definite offsets, the offsets being larger in the scan (column) direction than in the along scan (row) direction. Fractional pixel offsets were found between bands 1 to 4 in the primary focal plane and bands 5 and 7 in the cold focal plane. The thermal band (band 6) was found to have a much larger offset (up to four pixels) in the scan direction when compared to the other bands. These results have been confirmed by other investigators attending the Landsat-4 Scientific Characterization Early Results Symposium held at GSFC in February 1983. When the JSC registration processor was used to precisely register temporally three acquisitions of the TM data together over the Webster County, Iowa supersite, a data base consisting of 18 bands all registered to each other was made available to the user. In this case, the thermal band images were manually moved in the column direction to nullify the offsets.

To further explore the capabilities of the JSC registration processor, plans are being developed to (a) output the registered imagery in the Universal Transverse Mercator Projection; (b) register TM data to the Synthetic Aperture Radar (SAR) data, and (c) register ground truth data to TM data.

5. REFERENCES

1. Eric P. Beyer, "An Overview of the Thematic Mapper Geometric Correction System," *Proceedings of Symposium on Landsat-4 Early Results Scientific Characterization*, GSFC, Maryland, February 1983.

2. R. H. Wolfe, Jr., et al., "Landsat Image Registration for Agriculture Applications," *Eighth International Symposium on Machine Processing of Remotely Sensed Data*, Purdue University, West Lafayette, Indiana, July 1982.

N85-21746

D41
22

GEODETIC ACCURACY OF LANDSAT 4 MULTISPECTRAL SCANNER AND THEMATIC MAPPER DATA

J. M. Thormodsgard and D. J. DeVries

EROS Data Center, U.S. Geological Survey

INTRODUCTION

EROS Data Center is evaluating the geodetic accuracy of Landsat-4 data from both the Multispectral Scanner (MSS) and Thematic Mapper (TM) processing systems. Geodetic accuracy is a measure of the precision of Landsat data registration to the Earth's figure.

The assessment of the geometric accuracy of Landsat data generally requires locating ground control points (distinct features in an image) and calculating a surface fit, with the residuals (differences between the surface and the ground control points) indicating the accuracy. While this method provides the internal geometric consistency within a Landsat scene, it does not give the Landsat 4 user an appreciation of the geodetic accuracy or registration to the Earth's figure. This paper describes a geodetic accuracy assessment of several MSS and TM scenes, based on the geodetic referencing information supplied on a standard Landsat 4 computer compatible tape (CCT).

Landsat 4 data are geometrically corrected using all known sensor (detector array geometry, mirror scan), spacecraft (attitude and altitude variations), and terrestrial (Earth's rotation) geometric distortions to produce a system-corrected geometric product. Based on past performance of Landsat processing systems, this product can be expected to have good internal scene accuracy. However, geodetic (latitude and longitude) registration to the Earth's surface is significantly less accurate. A system-corrected scene has geodetic errors which are primarily translational; shifting the scene to a known geodetic location would result in a significantly improved geometric product.

To overcome the geodetic registration problem, a ground control point (GCP) library was developed for Landsats 2 and 3; the library is being edited and expanded for use with Landsat 4 data. This GCP library consists of 32- by 32-pixel areas extracted from individual Landsat scenes and referenced to a latitude and longitude location. These GCP's are then correlated with Landsat scenes to identify control points which further refine the geodetic accuracy of the Landsat data. This GCP-corrected product has small internal geometric errors and small geodetic errors depending on the distribution and number of GCP's which properly correlate with the Landsat scene.

In previous Landsat processing systems, no easy means of geodetically referencing the data was supplied on the standard CCT, and therefore the latitude and longitude of a pixel could not be calculated. The standard Landsat 4 CCT's have the information necessary to geodetically reference every pixel in the scene. The accuracy of the translation from geodetic location to pixel location depends on the precision of the geometric processing applied to the data; GCP-corrected data will be more accurate than system-corrected data. Therefore, measuring the accuracy of this translation results in an assessment of the geodetic accuracy of the data. The procedure is based on comparing the calculated image location, computed with the geodetic referencing algorithms given below, with the true image location visually located on a display device.

Geodetic Referencing Algorithms

Data provided on the standard Landsat 4 MSS and TM CCT's describe the rectangular map projection coordinate grid overlaying the image coordinate grid. To perform a translation from the map projection grid to the image grid, the angle of rotation between the two grid systems, and the coordinates of one location in both grid systems, are necessary. These values are contained in the header record of an MSS CCT and in the first ancillary record of a TM CCT, and consist of:

Map projection indicator,

Orientation angle of map projection,

WRS (World Reference System) scene center latitude and longitude,

WRS pixel offset from scene center.

The standard map projection applied to Landsat 4 MSS and TM data is the Space Oblique Mercator (SOM), although Universal Transverse Mercator (UTM) and Polar Stereographic (PS) map projections are available upon request, with PS being available for areas above 65°N. latitude and below 65°S. latitude.

A map projection grid at the orientation angle θ from the image grid at the WRS scene center ($\phi c,\lambda c$) is illustrated in Fig. 1. The WRS scene center is given in latitude and longitude, which can be converted to map projection coordinates. The vertical location or line coordinate of the WRS scene center is fixed while the sample coordinate can be computed given the WRS offset or horizontal shift in number of pixels giving the image coordinates ($Sc,\ell c$) at the WRS center. Thus, a simple translation of axes gives the image coordinates (s,ℓ) of a geodetic location (ϕ,λ):

$$\Delta s = \Delta x \cos\theta - \Delta y \sin\theta,$$

$$\Delta \ell = \Delta x \sin\theta + \Delta y \cos\theta,$$

$$s = s_c + \Delta s/\text{pixel size},$$

$$\ell = \ell_c - \Delta \ell/\text{pixel size}.$$

Where:

$\Delta x,\Delta y$ = displacement in projection coordinates (meters) between (ϕ,λ) and ($\phi c,\lambda c$), and

$\Delta s,\Delta \ell$ = displacement in image coordinates between (ϕ,λ) and ($\phi c, \lambda c$).

PROCEDURE

The latitude and longitude of a distinct feature on a 1:24,000-scale map are converted to line and sample coordinates using the geodetic referencing algorithms. An image subscene surrounding this calculated image location is displayed, the cursor is placed on the actual or true image location of the feature, and the pixel offsets from the calculated image location are computed. Maps are selected which result in an even distribution of 15 to 20 GCP locations throughout the image. Accuracy of the visual selection of the image locations is estimated to be 1.5 MSS pixels or 1.0 TM pixel.

RESULTS

Results of the testing and the geodetic accuracy of three MSS scenes and two TM scenes are presented on Figs. 2 through 6. The arrows represent the offset direction from the calculated image location of the GCP's to the actual image location. The table contains the latitude and longitude and the calculated and actual image location of the GCP's. The offset or difference between the calculated and actual image location, as well as the offset vector magnitude or pixel error, are presented. Note the pixel size for MSS is 57 m and 28.5 m for TM.

The two MSS scenes illustrated in Figs. 2 and 3 were system-corrected products with a root-mean-square (RMS) geodetic registration error of approximately 57 pixels or 3,200 m. The error is primarily a translational shift which is demonstrated by the high means and low standard deviations of the pixel offsets. An anomaly in the Washington, D.C., scene (Fig. 3) was the direction of the translational shift in the sample directon; all the other MSS and TM system-corrected scenes had the largest shift in the line (along-track) direction. Since Landsat's major positional error is in the along-track direction, the Washington, D.C., scene appears inconsistent.

The MSS GCP-corrected product (Fig. 4) had an RMS error of approximately 6 pixels or 325 m. There were only two GCP's out of 13 which correlated on this image; both points are located in the lower left corner of the image.

The TM system-corrected scenes (Figs. 5 and 6) had RMS errors of approximately 44 and 35 pixels or 1,250 and 1,000 m, respectively. As with the MSS data, the error is largely translational. A GCP-corrected TM product was not available to evaluate because a TM GCP library does not yet exist.

CONCLUSIONS

Conclusive statements concerning the geodetic accuracy of Landsat 4 data, based on such a small sampling of scenes, is impossible. However, the results provide a few interesting observations. For example, Landsat 4 MSS system-corrected errors were larger than were expected based on the authors' knowledge of the geometric accuracy of the data from Landsats 2 and 3. Also, the TM system-corrected scenes were more accurate than the MSS scenes by a factor of three. As the spacecraft platform for these two sensors is the same, this result cannot be explained, but a comparison of concurrently acquired MSS and TM data might clarify this situation. Finally, the single MSS GCP-corrected product evaluated had good geodetic accuracy considering the poor distribution of the two GCP's applied in the registration.

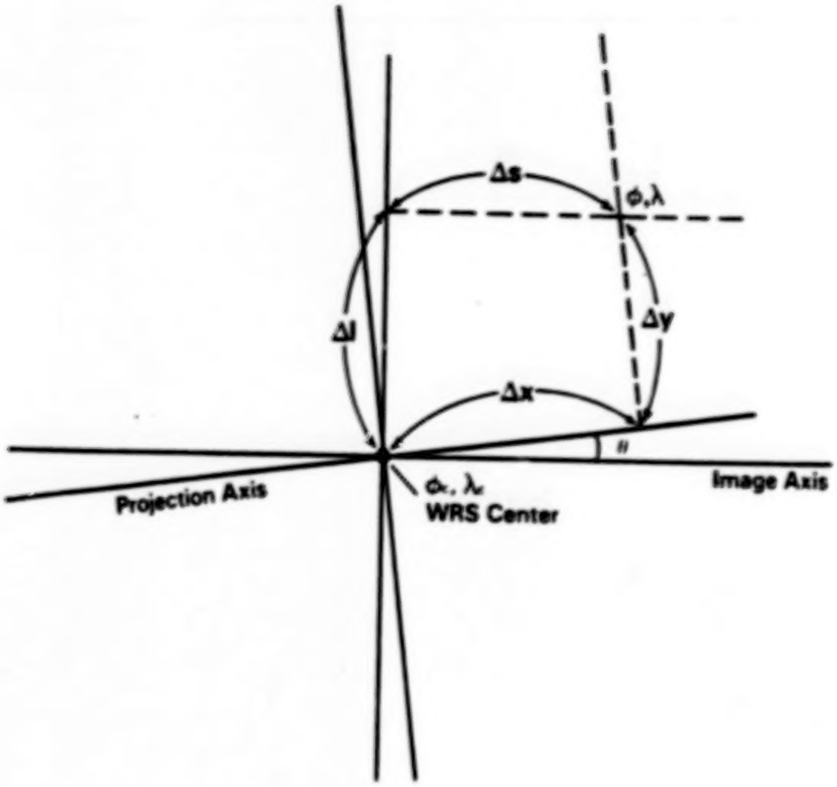
Δs
φ,λ
Δl
Δy
Δx
θ
Projection Axis
Image Axis
ϕ_c, λ_c
WRS Center

Fig. 1. Referencing a Landsat scene to the Earth's figure. The map projection grid at the orientation angle θ from the image grid at the WRS center.

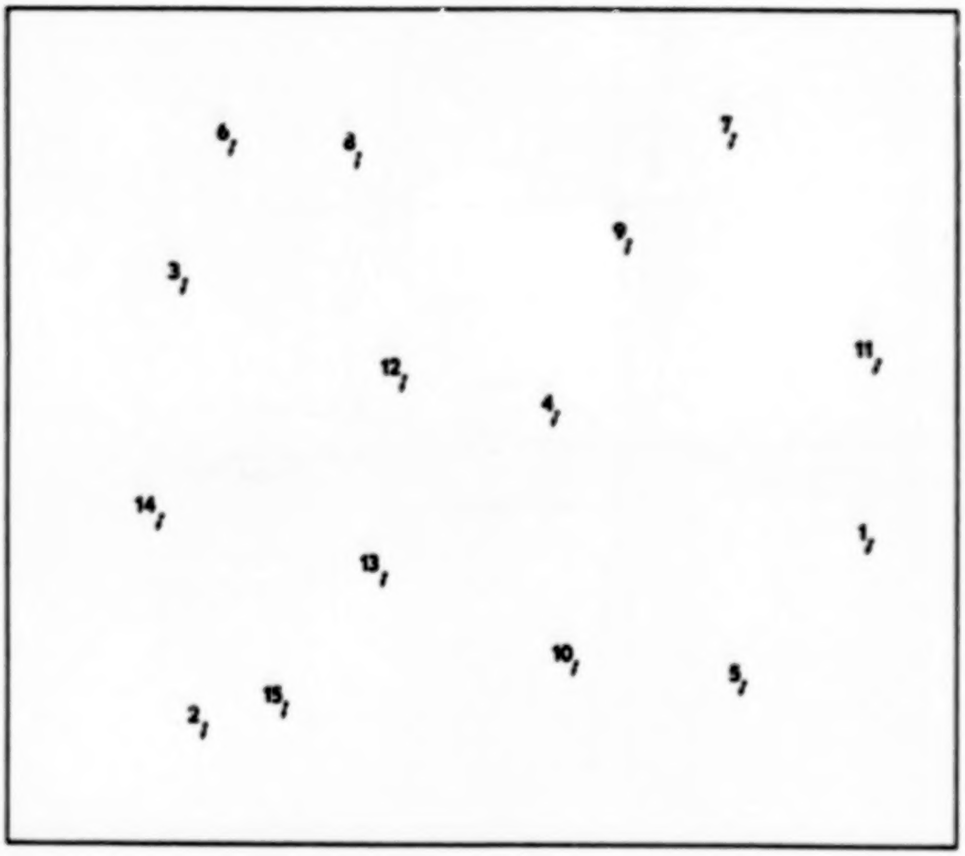

Point	Lat. DD	Lat. MM	Lat. SS	Long. DD	Long. MM	Long. SS	Calculated Line	Calculated Sample	Actual Line	Actual Sample	Offset Line	Offset Sample	Pixel Error
1	34	16	43	-117	27	2	1886	3251	1941	3234	-55	17	57.57
2	34	9	51	-119	3	35	2558	729	2608	711	-50	18	53.14
3	34	58	19	-118	56	23	976	658	1028	637	-52	21	56.08
4	34	36	50	-118	7	6	1437	2076	1491	2056	-54	20	57.58
5	34	3	56	-117	48	21	2397	2761	2451	2744	-54	17	56.61
6	35	12	34	-118	46	33	476	639	530	819	-54	20	57.58
7	35	3	35	-117	37	24	442	2704	499	2683	-57	21	60.75
8	35	8	31	-118	28	31	524	1334	581	1313	-57	21	60.75
9	34	54	20	-117	52	59	812	2348	869	2329	-57	19	60.08
10	34	9	41	-118	10	0	2317	2153	2369	2133	-52	20	55.71
11	34	36	10	-117	21	48	1241	3275	1299	3256	-58	19	61.03
12	34	43	41	-118	26	51	1310	1516	1364	1494	-54	22	58.31
13	34	22	44	-118	33	52	2011	1447	2063	1426	-52	21	56.08
14	34	33	23	-119	4	45	1810	571	1860	549	-50	22	54.63
15	34	10	39	-118	51	35	2478	1044	2530	1024	-52	20	55.71

	Offset Line	Offset Sample
MEAN =	53.9	19.9
*STD. =	2.6	1.6

RMS Error = 57.49 pixels

* Standard deviation from the mean

Fig. 2. MSS ground control points. Los Angeles, December 10, 1982, Path 41, Row 36, Scene ID 84014717565. System-corrected UTM projection.

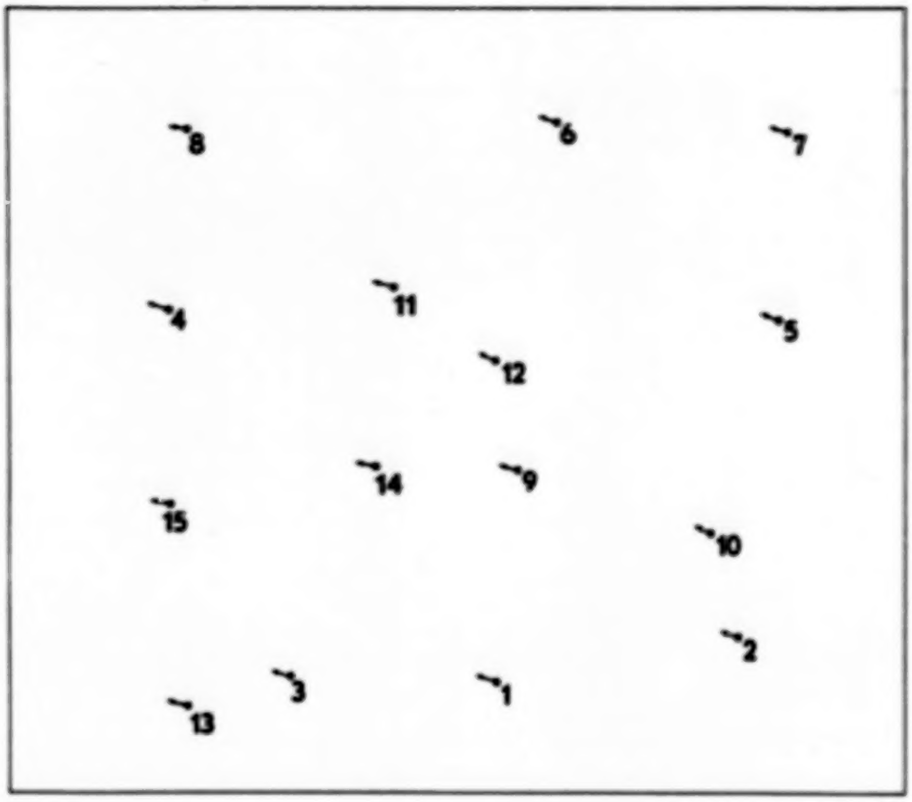

	LAT			LON			CALCULATED		ACTUAL		OFFSET		PIXEL
POINT	DD	MM	SS	DD	MM	SS	LINE	SAMPLE	LINE	SAMPLE	LINE	SAMPLE	ERROR
1	38	20	12	-76	50	31	2554	1923	2537	1865	17	58	60.44
2	38	19	32	-76	11	58	2391	2895	2370	2836	21	59	62.63
3	38	25	26	-77	21	15	2529	1120	2512	1068	17	52	54.71
4	39	10	10	-77	30	54	1143	621	1131	567	12	54	55.32
5	38	54	51	-75	56	39	1191	3057	1179	3007	12	50	51.42
6	39	22	57	-76	24	55	432	2183	419	2122	13	61	62.37
7	39	15	57	-75	49	37	485	3099	476	3046	9	53	53.76
8	39	30	12	-77	22	58	467	703	457	651	10	52	52.95
9	38	44	13	-76	41	5	1743	2015	1729	1963	14	52	53.85
10	38	32	22	-76	13	24	1989	2780	1976	2724	13	56	57.49
11	39	7	53	-76	55	9	1054	1524	1042	1468	12	56	57.27
12	38	[illegible]7	20	-76	41	39	1328	1922	1314	1866	14	56	57.72
13	38	24	36	-77	38	7	2632	701	2613	649	19	52	55.36
14	38	47	35	-77	2	23	1735	1463	1721	1411	14	52	53.85
15	38	48	00	-77	35	36	1872	631	1858	573	14	58	59.67
										MEAN =	14.1	54.7	
										*STD. =	2.2	2.2	

RMS ERROR = 56.69 pixels

*Standard deviation from the mean

Fig. 3. MSS ground control points. Washington, D.C., November 2, 1982, Path 15, Row 33, Scene ID 84010915140. System-corrected UTM projection.

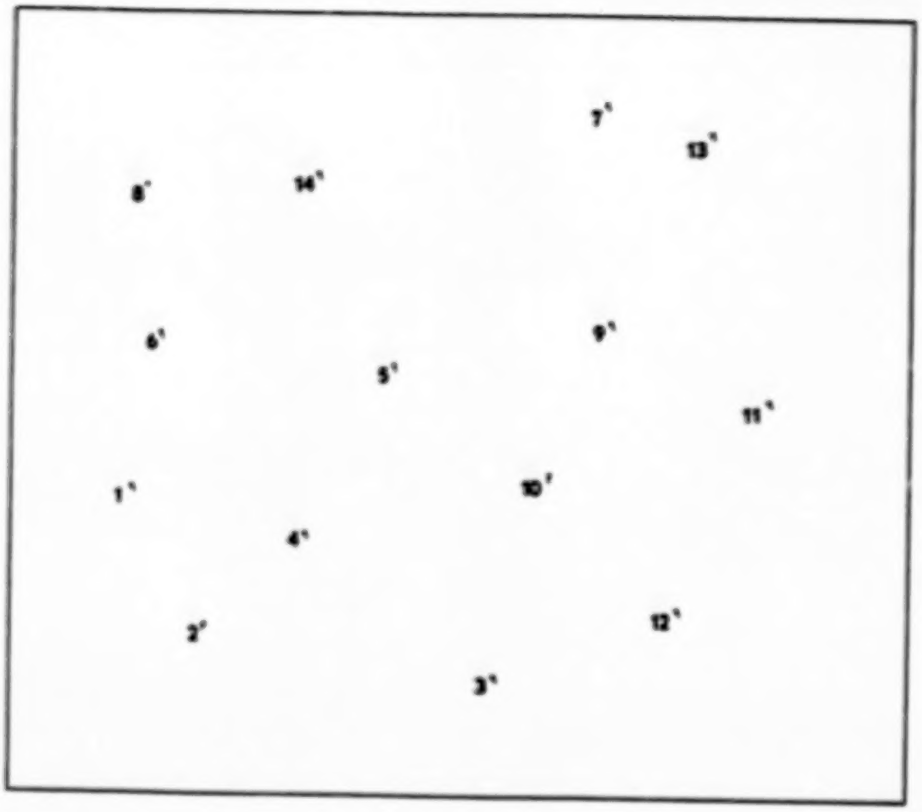

Point	Lat. DD	Lat. MM	Lat. SS	Long. DD	Long. MM	Long. SS	Calculated Line	Calculated Sample	Actual Line	Actual Sample	Offset Line	Offset Sample	Pixel Error
1	33	7	28	-87	2	9	1805	586	1807	592	-2	-6	6.32
2	32	50	35	-86	57	50	2326	792	2327	790	-1	2	2.24
3	32	39	19	-86	18	38	2507	1912	2510	1913	-3	-1	3.16
4	32	58	47	-86	41	18	1989	1194	1992	1197	-3	-3	4.24
5	33	16	58	-86	25	37	1336	1517	1342	1518	-6	-1	6.08
6	33	25	20	-86	58	7	1215	600	1219	600	-4	0	4.00
7	33	43	18	-85	48	59	324	2351	331	2354	-7	-3	7.62
8	33	42	36	-86	57	11	659	533	659	533	0	0	0.00
9	33	16	53	-85	53	26	1188	2381	1194	2387	-6	-6	8.49
10	33	1	12	-86	6	13	1750	2126	1754	2125	-4	1	4.12
11	33	5	9	-85	32	49	1464	3001	1468	3003	-4	-2	4.47
12	32	42	53	-85	50	34	2261	2650	2263	2653	-2	-3	3.61
13	33	37	20	-85	34	39	446	2768	455	2770	-9	-2	9.22
14	33	40	50	-86	32	19	603	1207	611	1209	-8	-2	8.25
										MEAN =	4.2	2.3	
										*STD. =	2.7	1.9	

RMS Error = 5.73 pixels

*Standard deviation from the mean

Fig. 4. MSS ground control points. Central Alabama, December 7, 1982, Path 20, Row 37, Scene ID 84014415472. GCP-corrected SOM projection.

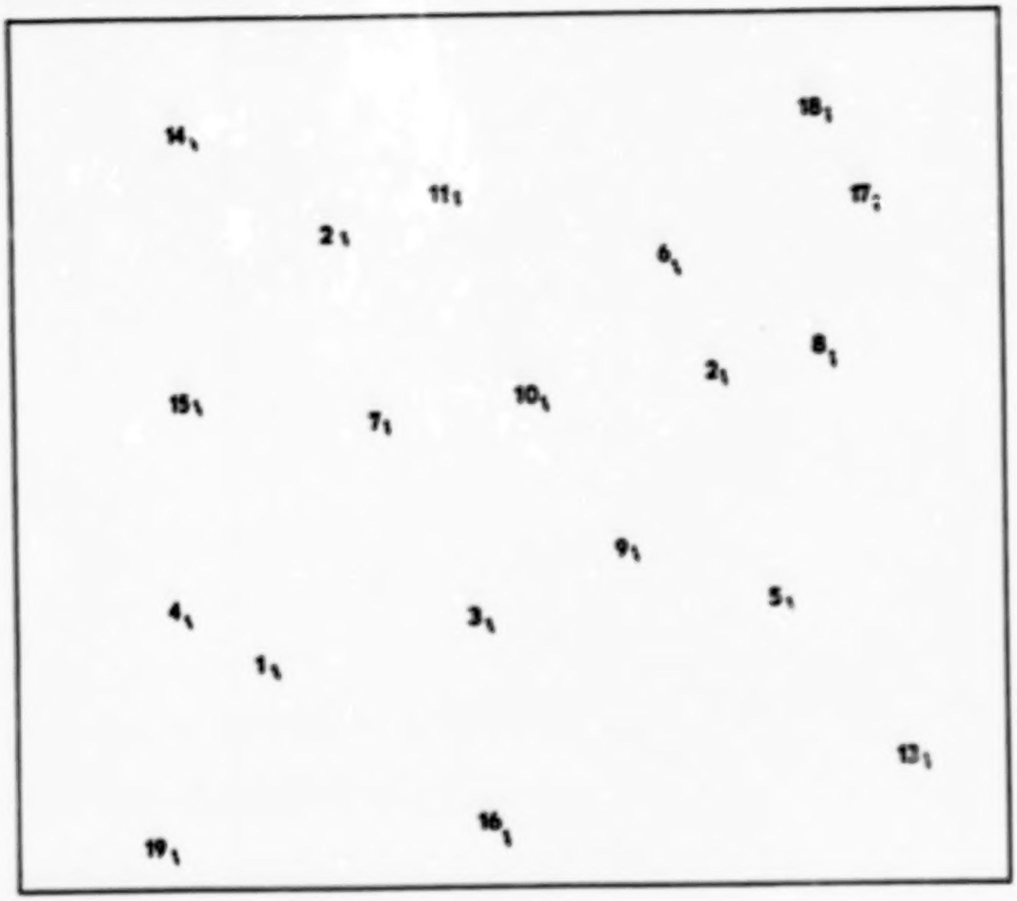

Point	Lat. DD	Lat. MM	Lat. SS	Long. DD	Long. MM	Long. SS	Calculated Line	Calculated Sample	Actual Line	Actual Sample	Offset Line	Offset Sample	Pixel Error
1	45	44	3	-98	18	37	4469	1864	4505	1872	-36	- 8	36.88
2	46	26	31	-97	54	30	1546	2381	1582	2390	-36	- 9	37.11
3	45	44	0	-97	45	3	4166	3361	4200	3371	-34	-10	35.44
4	45	51	3	-98	29	48	4122	1276	4158	1284	-36	- 8	36.88
5	45	39	36	-96	58	40	4004	5487	4036	5496	-32	- 9	33.24
6	46	15	41	-97	5	38	1779	4679	1813	4689	-34	-10	35.44
7	46	6	36	-97	54	13	2812	2655	2846	2664	-34	- 9	35.17
8	46	3	6	-96	44	29	2374	5788	2406	5798	-32	-10	33.53
9	45	48	20	-97	21	5	3664	4370	3698	4379	-34	- 9	35.17
10	46	5	41	-97	30	30	2650	3718	2684	3725	-34	- 7	34.71
11	46	28	17	-97	35	39	1261	3188	1296	3195	-35	- 7	35.69
12	46	4	0	-97	1	55	2485	5005	2519	5014	-34	- 9	35.17
13	45	20	27	-96	44	21	5079	6394	5110	6402	-31	- 8	32.02
14	46	39	37	-98	13	41	883	1363	918	1375	-35	- 7	35.69
15	46	12	42	-98	21	26	2668	1372	2705	1379	-37	- 7	37.66
16	45	22	13	-97	50	13	5599	3418	5633	3426	-34	- 8	34.93
17	46	17	50	-96	32	56	1325	6089	1358	6098	-33	- 9	34.21
18	46	28	17	-96	36	48	701	5770	734	5779	-33	- 9	34.21
19	45	27	39	-98	39	35	5701	1133	5738	1141	-37	- 8	37.85
										MEAN =	34.3	8.5	
										*STD. =	1.7	1.0	

RMS Error = 35.35 pixels

*Standard deviation from the mean

Fig. 5. TM ground control points. Aberdeen, SD, September 24, 1982, Path 30, Row 28, Scene ID 40070-16442. System-corrected SOM projection.

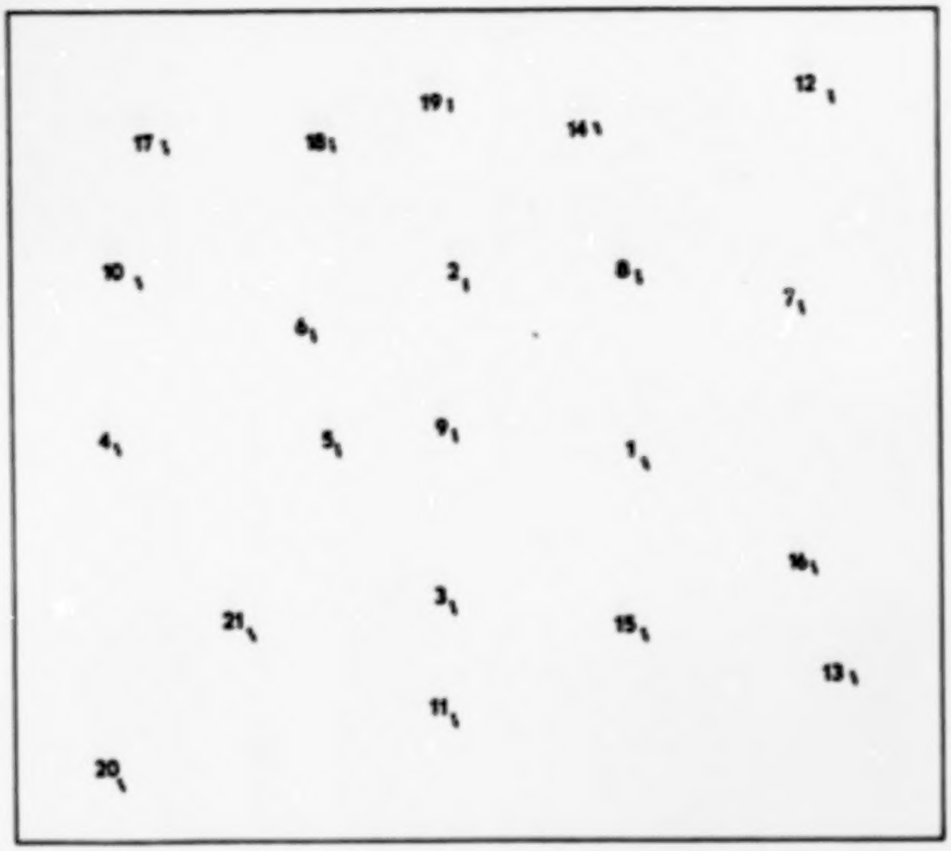

Point	Lat. DD	Lat. MM	Lat. SS	Long. DD	Long. MM	Long. SS	Calculated Line	Calculated Sample	Actual Line	Actual Sample	Offset Line	Offset Sample	Pixel Error
1	40	12	18	-89	54	40	3216	4771	3257	4781	-41	-10	42.20
2	40	35	49	-90	16	15	1920	3429	1963	3439	-43	-10	44.15
3	40	1	15	-90	27	3	4225	3320	4268	3331	-43	-11	44.38
4	40	26	1	-91	11	51	3112	847	3158	858	-46	-11	47.30
5	40	20	42	-90	39	11	3096	2493	3140	2503	-44	-10	45.12
6	40	33	24	-90	39	24	2287	2332	2331	2343	-44	-11	45.35
7	40	25	39	-89	27	26	2103	5931	2143	5941	-40	-10	41.23
8	40	32	32	-89	50	9	1884	4739	1926	4749	-42	-10	43.17
9	40	19	38	-90	21	31	3001	3369	3043	3380	-42	-11	43.42
10	40	42	51	-91	4	11	1905	1015	1951	1025	-46	-10	47.07
11	39	49	0	-90	30	26	5039	3302	5082	3312	-43	-10	44.15
12	40	47	34	-89	16	24	600	6185	641	6195	-41	-10	42.20
13	39	44	17	-89	31	2	4772	6282	4812	6294	-40	-12	41.76
14	40	49	40	-89	52	12	812	4425	854	4435	-42	-10	43.17
15	39	53	53	-89	59	40	4438	4754	4478	4765	-40	-11	41.48
16	39	57	33	-89	33	20	3950	6000	3990	6011	-40	-11	41.48
17	40	57	14	-90	56	26	918	1223	962	1235	-44	-12	45.61
18	40	53	22	-90	31	23	939	2482	985	2494	-46	-12	47.54
19	40	55	28	-90	12	21	630	3379	673	3388	-43	- 9	43.93
20	39	48	59	-91	18	44	5476	923	5522	932	-46	- 9	46.87
21	40	2	24	-90	55	25	4411	1914	4455	1925	-44	-11	45.35

MEAN =	42.9	10.5
*STD. =	2.1	0.9

RMS Error = 44.19 pixels

*Standard deviation from the mean

Fig. 6. TM ground control points. Galesburg, IL, October 16, 1982, Path 24, Row 32, Scene ID 40092-16092. System-corrected SOM projection.

Index of Authors

	Summary*		Proceedings**	
Authors	Volume	Page	Volume	Page
Abrams, R.	I	90	II	47
	I	116	II	147
			II	373
Abrams, M.			IV	127
Ackleson, S.	II	137	IV	325
Aepli, T.	I	15		
Alford, W.	II	69	I	1
	II	85	I	9
			I	143
Amis, M.	II	60	III	571
Anderson, J.	II	82	I	119
Anderson, W.	II	129	IV	281
Anuta, P.	II	1	III	321
	II	53	III	527
Baker, J.	II	149	IV	369
Ball, D.	I	90	I	25
	I	116		
	I	130	II	47
			II	147
			II	277
			II	373
Balick, L.	II	129	IV	281
Barker, J.	I	90	I	23
	I	116		
	I	127	II	1
	I	130	II	47
	I	140	II	147
	I	186	II	235
	II	73	II	277
			II	373
			III	1
			III	233
Bartolucci, L.	II	1	III	321
Batson, R.	II	59	III	565
Bender, L.	II	35	III	497
Bennett, D.	II	81	I	77
Bernstein, R.	I	108	IV	25
Beyer, E.	I	92	II	87
Bizzell, R.	II	113	IV	153
	II	133	IV	299
Blodget, H.	II	160	IV	403
Boatwright	II	141	IV	337
Borgeson, W.	II	59	III	565
Brooks, J.	I	101	I	177
	II	91		
Brumfield			IV	403
Bryant, N.	II	46		
Butlin, T.	I	190		
Card, D.	II	55	III	553
Carnes, J.	II	113	IV	153
Castle, K.	II	15	III	389
Chavez, P.	II	33	III	471
Cicone, R.	II	28	III	443
Collins, A.			II	221
Colwell, R.	II	98	IV	91
Conel, J.	II	109	IV	127
Crist, E.	II	28	III	443
Dean, E.	II	1	III	321
DeGloria, S.	II	98	IV	91
Deschamps, P.	II	21		
DeVries, D.	II	62	I	133
			III	581
Dickinson, K.	I	189	III	257
Dinguirard, M.	II	15	III	389
Dozier, J.	II	142	IV	349
Duff, P.	I	190		
Duggin, M.	II	64		
Dykstra, J.	II	103	IV	119
Eliason, E.	II	33	III	471
Engel, J.	I	41		
	I	65		
Everett, J.	II	103	IV	119
Ezra, C.	II	15	III	389
Falcone, N.			III	497
Feuquay, J.	II	129	IV	281
Fischel, D.	I	106		
Fitzerald, A.	I	190	II	275
Fleming, E.	I	189	III	257
Friedman, S.	II	46		
Fusco, L.	I	199	III	309
	II	7	III	359
	II	40		
Gayler, J.	II	149	IV	369
Gervin, J.	II	167	IV	415
			IV	421
Gillespie, A.			IV	127
Gokhman, B.	II	46		
Goodenough, D	I	189	II	221
			III	257
Guertin, F.	II	81	I	77
			II	221
Gunther, F.	I	116	II	147
Gurney, C.	II	50	III	513
Haas, R.	II	129		
Hall, J.	II	55	III	553
	II	113	IV	153
Hardisky, M.	II	121	IV	251
Hardy, J.	II	149	IV	369
Haydn, R.	II	116	IV	217
Henderson, K.	II	148	IV	359
Holm, R.	II	15	III	389
Houston, A.	II	148	IV	359

Index of Authors

Authors	Summary* Volume	Summary* Page	Proceedings** Volume	Proceedings** Page
Hovis, W.	II	20	III	411
Imhoff, M.	II	69	I	1
			I	9
			I	143
Irons, J.	I	62	II	15
	II	93	IV	7
	II	116	IV	237
Jackson, M.	II	149	IV	369
Jackson, R.	II	15	III	389
Jones, O.	II	35	III	497
Justice, C.	I	199	III	309
Kahle, A.			IV	127
Kastner, C.	II	15	III	389
Kieffer, H.	II	33	III	471
Kimmer, E.	II	91	I	177
Klemas, V.			IV	251
	II	137	IV	325
Kogut, J.	II	54	III	537
Lang, H.	II	109	IV	127
Lansing, J.	I	186	III	233
Larduinat, E.	II	54	III	537
Latty, R.	II	93	IV	7
	II	116	IV	237
Lauer, D.	II	129	IV	281
Leung, K.	I	90	II	47
	I	130	II	277
			II	373
Likens, W.	II	87	I	159
Logan,	II	46		
Lotspiech, J.	I	108	IV	25
Lozano, F.	II	1		
Lu, Y.	II	167	IV	415
			IV	421
			IV	431
Lyon, J.	I	106		
Malaret, E.	II	1	III	527
	II	53		
Malila, W.	II	23	I	57
	II	76	III	421
Marcell, R.	II	160	IV	403
	II	167	IV	421
Markham, B.	I	127		
	II	73	I	23
	II	93	II	1
	II	116	II	235
	II	135	IV	7
			IV	237
			IV	313
MacDonald, R.	II	113	IV	153
McGillem, C.	II	1	III	527
	II	53		
Mehl, W.	I	199	III	309
			III	359

Authors	Summary* Volume	Summary* Page	Proceedings** Volume	Proceedings** Page
Mertz, F.	II	55	III	553
Metzler, M.	II	23	III	421
Middleton, E.	II	171	IV	431
Mimms, D.	II	35		
	II	85	I	9
			I	143
Mulligan, P.			IV	415
Murphy, J.	I	190	I	77
	II	81	III	275
Nelson, R.	II	93	IV	7
	II	116	IV	237
Palmer, J.	II	15	III	389
Park, W.			III	275
Paylor, E.	II	109		
Pitts, D.	II	113	IV	153
	II	148	IV	359
Price, J.	II	128	IV	271
Prior, H.	II	133	IV	299
Podwysocki, M.	II	35	III	497
Quattrochi, D.	II	111	IV	131
Rasool, S.	II	21		
Reyna, E.	II	113	IV	153
Rice, D.	II	76	I	57
Ritchie, J.	II	141	IV	337
Sadowski, F.	II	129	IV	281
Salisbury, J.	II	35		
Savage, R.	II	15	III	389
Schiebe, F.	II	141	IV	337
Schoch, L.	II	64		
Schott, J.	I	181	III	221
Schowengerdt, R.	II	32	III	467
Seevers, P.	II	129	IV	281
Sekhon, R.	II	171	IV	431
Sheffield, C.	II	103	IV	119
Short, N.	II	114	IV	163
Slater, P.	II	15	III	389
Sorensen, C.	II	113	IV	153
Stauffer, M.	II	93	IV	7
	II	116	IV	237
Strome, W.	I	120	II	221
Sturdevant, J.	II	129	IV	281
Su, J.	II	91	I	177
Thompson, D.			IV	359
Thormodsgard, J	II	62	I	133
			III	581
Toll, D.	I	93	IV	7
	I	116	IV	237
	I	153	IV	387
Townshend, J.	II	149	IV	369
Trevese, D.	II	7		
Usery, E.	II	83	I	123
Valdes, J.	II	1		

Index of Authors

Authors	Summary*		Proceedings**	
	Volume	Page	Volume	Page
Valenzuela, C.	II	1		
Walker, J.	I	130	II	277
Walker, R.	II	46		
Waltz, F.	II	129	IV	281
Webb, W.	I	1		
Welch, R.	II	83	I	123
Williams, D.	II	93	IV	1
	II	119	IV	7
			IV	237
Witt, R.	II	160	IV	403
	II	171	IV	431
Wrigley, R.	II	55	I	159
	II	87	III	553
Yao, S.	II	60	III	571
	II	113	IV	153
Yu, K.	II	53		
Zobrist, A.	II	46		

* Landsat-4 Science Investigations Summary, John L. Barker, ed., 2 volumes (NASA Conference Publication CP-2326) available through Government Printing Office, National Technical Information Service (NTIS). Accession Numbers N84-30359 and N84-30380 5285 Port Royal, Springfield, VA 22161, Phone 800-336-4700 or (703) 487-4650.

** Landsat-4 Science Characterization Early Results, John L. Barker, ed., 4 volumes NASA Conference Publication.

END

DATE

FILMED

MAY 23 1985